Studies towards Reductive Aromatizations of Polyaromatic Hydrocarbons and Synthesis of Precursors for *on-Surface* Synthesis of Nanographenes

Kumulative Dissertation

zur Erlangung des Grades Doktor der Naturwissenschaften
(Dr. rer. nat.)

dem Fachbereich Chemie
der Philipps-Universität Marburg

vorgelegt von

M. Sc. Simon Werner
aus Biedenkopf

Marburg an der Lahn
2021

Licensing

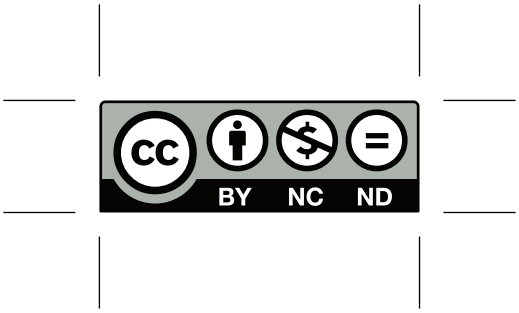

Die vorliegende Arbeit wurde unter Anleitung von Herrn Prof. Dr. Jörg Sundermeyer in der Zeit von November 2017 bis September 2021 am Fachbereich Chemie der Philipps-Universität Marburg angefertigt.

Vom Fachbereich Chemie der Philipps-Universität Marburg mit der Hochschulkennziffer 1180 als Dissertation am 28.09.2021 angenommen.

Tag der Einreichung: 28.09.2021

Tag der Disputation: 08.11.2021

Erstgutachter: Prof. Dr. Jörg Sundermeyer

Zweitgutachter: Prof. Dr. J. Michael Gottfried

Selbstständigkeitserklärung

Gemäß § 10 Abs. 1 der Promotionsordnung der Mathematisch-Naturwissenschaftlichen Fachbereiche und des Medizinischen Fachbereichs für seine mathematisch-naturwissenschaftlichen Fächer der Philipps-Universität Marburg vom 15.07.2009.

Ich erkläre, dass eine Promotion noch an keiner anderen Hochschule als der Philipps-Universität Marburg, Fachbereich Chemie, von mir versucht wurde und versichere, dass ich meine vorgelegte Dissertation

Studies towards Reductive Aromatizations of Polyaromatic Hydrocarbons and Synthesis of Precursors for on-Surface Synthesis of Nanographenes

selbstständig, ohne unerlaubte Hilfe Dritter angefertigt und andere als die in der Dissertation angegebenen Hilfsmittel nicht benutzt habe. Alle Stellen, die wörtlich oder sinngemäß aus veröffentlichten oder unveröffentlichten Schriften entnommen sind, habe ich als solche kenntlich gemacht. Dritte waren an der inhaltlich-materiellen Erstellung der Dissertation nicht beteiligt; insbesondere habe ich hierfür nicht die Hilfe eines Promotionsberaters in Anspruch genommen. Kein Teil dieser Arbeit ist in einem anderen Promotions- oder Habilitationsverfahren verwendet worden. Mit dem Einsatz von Software zur Erkennung von Plagiaten bin ich einverstanden.

Marburg, den 28.09.2021

Simon Werner

Erklärung zur kumulativen Dissertation

Ich versichere dass, die im kumulativen Teil der Dissertation mit dem Titel

Studies towards Reductive Aromatizations of Polyaromatic Hydrocarbons and Synthesis of Precursors for on-Surface Synthesis of Nanographenes

Aufgeführten Anteile der Autoren an den verfassten Publikationen und Manuskripten korrekt und vollständig dargelegt sind.

Der kumulative Teil umfasst die Kapitel 3.1 bis 3.9.

Marburg, den 28.09.2021

Simon Werner

Prof. Dr. Jörg Sundermeyer

Abstract

Polyaromatic hydrocarbons (PAHs) are of great research interest as they are candidates for many technical applications. PAHs find already application in organic solar cells (OSCs), organic field-effect transistors (OFETs) and organic light-emitting diodes (OLEDs). Especially in case of the miniaturization of electronic components, they are becoming increasingly important in large-scale applications. For an optimal application, tailor-made properties such as a precisely defined (optical) HOMO-LUMO gap or the highest possible fluorescence quantum yields with the narrowest possible emission are crucial. The most effective tool to precisely tune these properties is chemical functionalization.

The first part of this cumulative doctoral thesis deals with the reductive functionalization of polyaromatic hydrocarbons. This novel approach, previously described in only few examples in literature, utilizes a one-step functionalization of oxidatively generated precursor molecules using the cheapest and easiest-to-handle reducing agents possible, such as zinc. This strategy results in fourfold functionalized electron-rich ethers, silyl ethers, pivaloates or even triflates. As electron-rich counterparts to the rylenediimide dyes described many times in literature and in addition to the pyrene dyes, which have also been studied photochemically in great detail, the syntheses and properties of fourfold functionalized diazapyrenes, peropyrenes and their higher homologous terropyrenes and quarterropyrenes as well as violanthrenes are described in a total of five accepted publications. Furthermore, a materials chemistry application perspective for the synthesis of (N-doped) Carbon Nanoparticles is presented. Via UV-Vis and photoluminescence spectrometry as well as cyclic voltammetry, the (opto-)electronic properties are discussed in the context of the influence of the different functionalizations. Quantum chemical DFT calculations are discussed and are used for a deeper understanding of the electronic influences of the different substitutions.

In the second part of this work, collaborative projects with surface chemists from the Gottfried group and others are presented in four publications. In recent years, the surface-assisted synthesis of nanographenes and graphene nanoribbons has become increasingly important for the synthesis and characterize of these unfunctionalized graphene derivatives, which are often difficult to investigate due to poor solubility. For this purpose, porous nanographenes such as Kekulen or a C108 nanographene as well as porous graphene nanoribbons are prepared on single-crystalline noble metal surfaces via surface-supported Ullmann reaction and subsequent cyclodehydrogenations. For this, suitable halogenated precursors were designed and synthesized within the scope of this work. The influence of the nature of the surface on the resulting products as well as the individual electronic properties of the porous nanographene structures is investigated by means surface analytic methods such as *Scanning tuneling spectroscopy* (STS) or *angle resolved photoelectron spectroscopy* (ARPES).

Kurzzusammenfassung

Polyaromatische Kohlenwasserstoffe (PAKs) sind von großem Forschungsinteresse, da sie vielseitige technische Anwendungen finden. So finden PAKs schon heute ihren Einsatz in organischen Solarzellen (OSCs), organischen Feldeffekttransistoren (OFETs) und organischen Leutdioden (OLEDs). Gerade im Hinblick auf die Miniaturisierung elektronischer Bauteile kommt ihnen zunehmend auch eine großtechnische Bedeutung zu. Für einen optimalen Einsatz entscheidend sind vor allem maßgeschneiderte Eigenschaften wie eine genau definierter (optischer) HOMO-LUMO Abstand oder möglichst hohe Fluoreszenzquantenausbeuten bei möglichst schmalbandiger Emission. Das wirkungsvollste Werkzeug um diese Eigenschaften präzise einstellen zu können, ist die chemische Funktionalisierung.

Der erste Teil dieser kumulativen Dissertation befasst sich mit der reduktiven Funktionalisierung von polyaromatischen Kohlenwasserstoffen. Diese bisher in der Literatur nur in wenigen Beispielen beschriebene Herangehensweise geht von einer einstufigen Funktionalisierung oxidativ generierter Vorläufermoleküle unter Verwendung möglichst günstiger und einfach zu handhabender Reduktionsmittel wie beispielsweise Zink aus. Das Ergebnis dieser Strategie sind sind vierfach funktionalisierte, elektronenreiche Ether, Silylether, Pivaloate oder auch Triflate. Als elektronenreiche Gegenstücke zu den in der Literatur vielfach beschriebenen Rylendiimid-Farbstoffen und in Ergänzung zu den ebenfalls photochemisch genauestens untersuchten Pyrenfarbstoffen werden in insgesamt fünf akzeptierten Publikationen die Synthesen und Eigenschaften von funktionalisierten Diazapyrenen, Peropyrenen und ihren höheren homologen Terropyrenen und Quarterropyrenen sowie Violanthrene diskutiert. Zusätzlich wird eine materialchemische Anwendungsperspektive für die Synthese von (N-dotierten) kohlenstoff Nanopartikeln vorgestellt. Über UV-Vis und Photolumineszenz-Spektrometrie sowie Cyclovoltammetrie werden die (opto-)elektronischen Eigenschaften im Zusammenhang mit dem Einfluss der verschiedenen Funktionalisierungen diskutiert. Quantenchemische DFT-Rechnungen werden vergleichend diskutiert und dienen dem tiefergehenden Verständnis der elektronischen Einflüsse der Substitutionen.

Im zweiten Teil dieser Arbeit werden Kooperationsprojekte mit Oberflächenchemikern der Arbeitsgruppe Gottfried *et al.* vier Publikationen vorgestellt. In den letzten Jahren ist der oberflächengestützte Synthese von Nanographenen und Graphen-Nanobändern eine zunehmende Bedeutung zugekommen. Diese in Lösung oft aufgrund von Schwerlöslichkeit nur unzureichend charakterisierbaren unfunktionalisierten Graphenderivate werden auf Oberflächen synthetisiert und charakterisiert. Dazu werden mit Hilfe geeigneter halogenierter Prekursoren, die im Rahmen dieser Arbeit dargestellt werden sollten, auf einkristallinen Edelmetalloberflächen poröse Nanographene wie Kekulen oder ein C108 Nanographen sowie poröse Graphen-Nanobänder über oberflächengestützte Ullmann Reaktionen und nachfolgenden Cyclodehydrogenierungen hergestellt. Hierbei wird insbesondere der Einfluss der Art der Oberfläche auf die entstehenden Produkte sowie die individuellen elektronischen Eigenschaften der porösen Nanographenstrukturen mittels Analytik auf der Oberfläche (*Scaning tuneling spectroscopy* (STS), *angle resolved photoelectron spectroscopy* (ARPES)) diskutiert.

I Contents

List of Figures

List of Schemes

I.1 List of abbreviations

AFM Atomic Force Microscopy

$CHCl_3$ Chloroform

CNT Carbon Nanotube

CV Cyclovoltammetry

DAP Diazaperopyrene

DCM Dichloromethane

DDP Diphenyldibenzoperylene

DFT Density Functional Theory

DMF Dimethylformamide

DMSO Dimethylsulfoxide

DPV Differential Pulse Voltammetry

EtOAc ethyl acetate

GNR Graphene Nanoribbon

NDI Naphthalene Diimide

NTCDI Napthalenetetracarboxylic diimide

ncAFM non-contact Atomic Force Microscopy

NP Nanoparticle

PDI Perylene Diimide

PL Photoluminescence

PTCDI Perylenetetracarboxylic diimide

SEM Scanning Electron Microscopy

STM Scanning Tunneling Microscopy

TEM Transition Electron Microscopy

TD-DFT Time-dependent Density Functional Theory

TLC Thinlayer Chromatography

UV-Vis Ultraviolet-visible

I.2 Scientific Curriculum Vitae

I.2.1 Publications Reductive Aromatizations and Dye Chemistry

1. S. Werner, T. Vollgraff, J. Sundermeyer: *„Zugang zu funktionalisierten Pyrenen, Peropyrenen, Terropyrenen and Quarterropyrenen über Reductive Aromatisierung“*, *Angew. Chem.* **2021**, *133*, 13743–13748; *„Access to functionalized Pyrenes, Peropyrenes, Terropyrenes and Quarterropyrenes via Reductive Aromatization“*, *Angew. Chem. Int. Ed.* **2021**, *60*, 13631–13635.

2. S. Werner, T. Vollgraff, J. Sundermeyer: *„Tetrasubstituted Peropyrenes Formed by Reductive Aromatization: Synthesis, Functionalization and Characterization“*, *Chem. Eur. J.* **2021**, *27*, 11065–11075.

3. S. Werner, T. Vollgraff, Q. Fan, K. Bania, J. M. Gottfried, J. Sundermeyer: *„Reductive O-Triflylation of Naphthalene Diimide: Access to Alkyne- and Amine-functionalized 2,7-Diazapyrenes“*, *Org. Chem. Front.* **2021**, *8*, 5013–5023.

4. S. Werner, T. Vollgraff, J. Sundermeyer: *„Rylene- and Diaza-rylene-derived Cobalt Clusters for the Solid-State Pyrolysis towards Undoped and N-doped Carbon Nanoparticles“*, *Dalton Trans.* **2021**, *50*, 14374–14383.

5. S. Werner, J. Sundermeyer: *„Synthesis of Unsymmetrically Functionalized Violanthrenes by Reductive Aromatization of Violanthrone 79“*, **2021**, *32*, 1855–1860.

I.2.2 Publications Surface Synthesis of Porous Nanographene Derivatives

6. Q. Fan, D. Martin-Jimenez, S. Werner, D. Ebeling, T. Koehler, T. Vollgraff, J. Sundermeyer, W. Hieringer, A. Schirmeisen, J. M. Gottfried: *„On-Surface Synthesis and Characterization of a Cycloarene: C108 Graphene Ring“*, *J. Am. Chem. Soc.* **2020**, *142*, 894-899.

7. A. Haags, A. Reichmann, Q. Fan, L. Egger, H. Kirschner, T. Naumann, S. Werner, T. Vollgraff, J. Sundermeyer, L. Eschmann, X. Yang, D. Brandstetter, F. C. Bocquet, G. Koller, A. Gottwald, M. Richter, M. G. Ramsey, M. Rohlfing, P. Puschnig, J. M. Gottfried, S. Soubatch, and F. S. Tautz: *„Kekulene: On-Surface Synthesis, Orbital Structure, and Aromatic Stabilization“*, *ACS Nano* **2020**, *14*, 15766-15775.

8. J. Martinez-Castro, R. Bolat, Q. Fan, S. Werner, H. H. Arefi, T. Esat, J. Sundermeyer, C.

Wagner, J. M. Gottfried, R. Temirov, M. Ternes, F. S. Tautz: *„Disentangling the Complex Electronic Structure of the Large Organic Adsorbate Cycloarene C108“*, *ACS Nano*, under Revision (submitted: 14.09.2021).

9. Q. Fan, S. Werner, T. Koehler, T. Vollgraff, J. Sundermeyer, W. Hieringer, J. M. Gottfried: *„Porous Graphene Nanoribbon and Porous Nanographene by Precursor- and Substrate-Controlled On-Surface Synthesis“*, *manuscript in preparation*, **2021**.

I.3 Patent

J. Sundermeyer, E. Baal, S. Werner, *„Multi-functionalized [cd,ml]-anelated Perylenes and their Homologs“*, *WO 2019/229134 A1*, **2019**.

I.4 Conference Contributions

Poster: S. Werner, Q. Fan, D. Martin-Gimenez, T. Vollgraff, A. Schirmeisen, J. M. Gottfried, J. Sundermeyer, *„Formation of graphene nanodots and graphene nanoribbons via organometallic intermediates“*, 23^{rd} European Conference on Organometallic Chemistry, Helsinki, 16.06.2019 - 20.06.2019.

I.5 CV

[11.2017 – 09.2021] **PhD student**, group of Prof. Dr. Sundermeyer (organic materials chemistry) *„Studies towards Reductive Aromatizations of Polyaromatic Hydrocarbons and Synthesis of Precursors for On-Surface Synthesis of Nanographenes“*

[10.2015 – 09.2017] **M.Sc. Studies**, Philipps-University Marburg (very good, 1.0)

01.2017 – 09.2017 **M.Sc. Thesis**, interdisciplinary project between physical and organic chemistry, groups of Prof. Dr. Hilt and Prof. Dr. Gottfried, *„Synthesis of brominated terphenyls and investigation of their reactivity on different metal surfaces“*

[10.2012 – 09.2015] **B.Sc. Studies**, Philipps-University Marburg (excellent, 0.9)

09.2014 **Industrial internship**, Adolf Wagner GmbH (Biedenkopf), construction chemistry

04.2015 – 08.2015 **B.Sc. Thesis**, organic chemistry, group of Prof. Dr. Hilt *„Synthese neuartiger Precursoren zur oberflächengestützten* Ullmann*-Kupplung im Hochvakuum“*

[09.2005 – 06.2012] **Abitur**, Gymnasium Lahntalschule Biedenkopf (excellent, 1.0)

[01.12.1992] Date of birth, Biedenkopf

1 Introduction

1.1 Graphene, Graphene Nanoribbons and Nanographenes

Graphene is a permanently conducting two-dimensional material, consisting of a fully conjugated C_{sp2}-carbon system densest packed in a honeycomb lattice. In graphite, single graphene layers are interacting via VAN-DER-WAALS forces.[1, 2] It is a material with outstanding capabilities since the delocalization of the π-electrons perpendicular to the molecular plane leads to non-bandgap conductive behavior, interesting for the use in electronical devices.[1, 2]
Graphene monolayers can be easily prepared by mechanical exfoliation of HOPG as described by NOVOSELOV and GEIM[2] or by epitaxially growth *via on-surface* thermal decomposition of hydrocarbons like ethylene,[3] since graphene is the thermodynamically most favorable structure of all conjugated (hydro)carbons on surface.[4] Another preparation method is the seggregation of carbon containing alloys.[5] As shown in Figure 1.1,[A] 2D graphene is the stem form of all other derivatives consisting of graphitic carbon, such as graphene nanoribbons and nanotubes (1D) or molecular nanographenes and fullerene buckyballs (0D).[1]

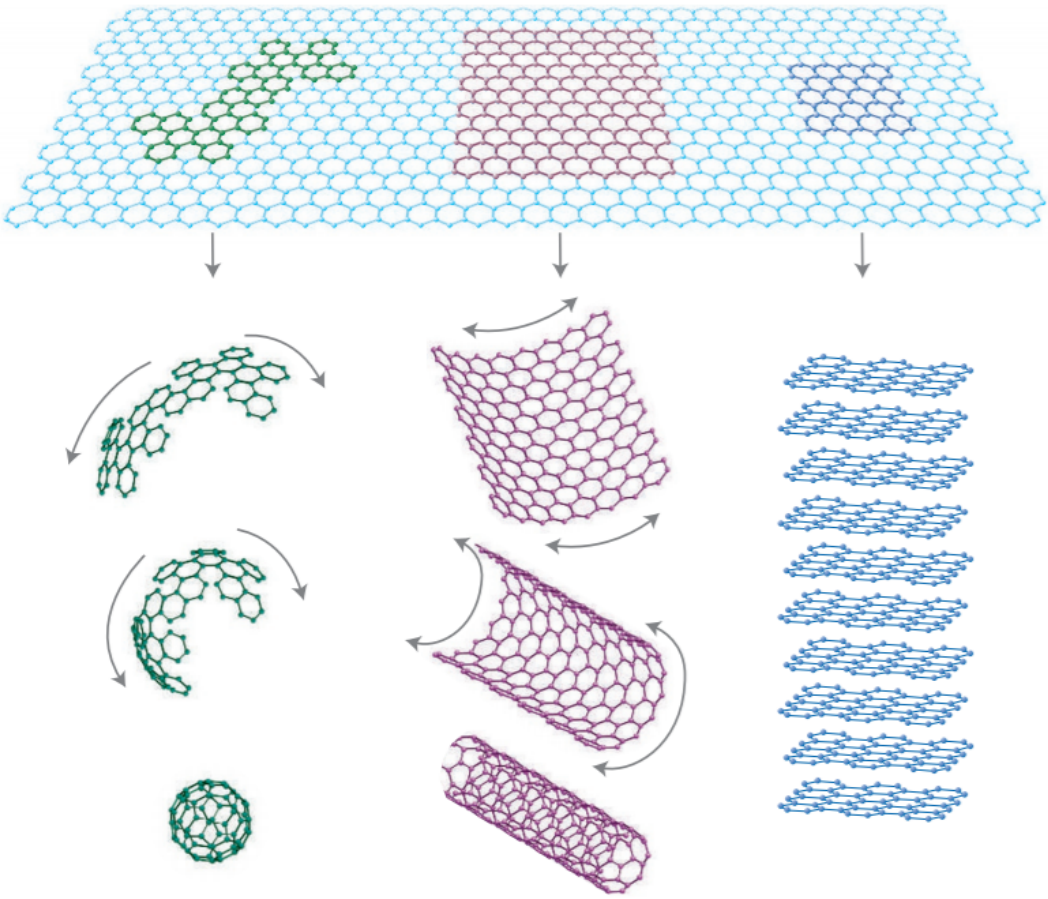

Fig. 1.1 The 2D, planar graphene is incorporated in 0D fullerenes, 1D carbon nanotubes, 1D graphene nanoribbons or 0D nanographenes.[1]

[A] Reprinted with permission of ref.[1], Copyright ©2007, Rights Managed by Springer Nature

1 Introduction

The drawback of graphene - in comparison to semiconductors like silicon - is the absence of a band gap between the valence band and the conductive band.[6] Although electronical characteristics like conductivity can be controlled with an electric field,[2, 6] the existence of a defined band gap is crucial for many electronic devices such as field effect transistors.[7] Field effect transistors (FETs) use an electric field to amplify, switch and control electronic power and were described firstly by Lilienfeld in the year 1930.[8] The electric field is controlled by the conductivity of the transistor material. In semiconducting materials this is realized by either electrons (*n*-channel FET) or holes (*p*-channel FET).[9]
In graphene, the bandgap-size can be controlled by limitation of the dimensions of the network.[6] For this purpose, *top down* strategies have been explored that cut the 2D-material graphene into pieces with defined sizes.[6, 10] In the last years, *top down* approaches such as cutting graphene sheets via laser lithography and masks into narrow graphene bands led to structures of a width of minimal 20 nm limited by the lithography process acuracy.[11, 12] Larger structures could also be obtained by unzipping carbon nanotubes as described by Tour and co-workers.[13] But since the electronic properties of a graphene stripe (graphene nanoribbon, GNR) change with the stripe's width from semiconducting to semimetal behaviour[14, 15] only small width GNRs can be used as potential semiconducting FET materials.[6]

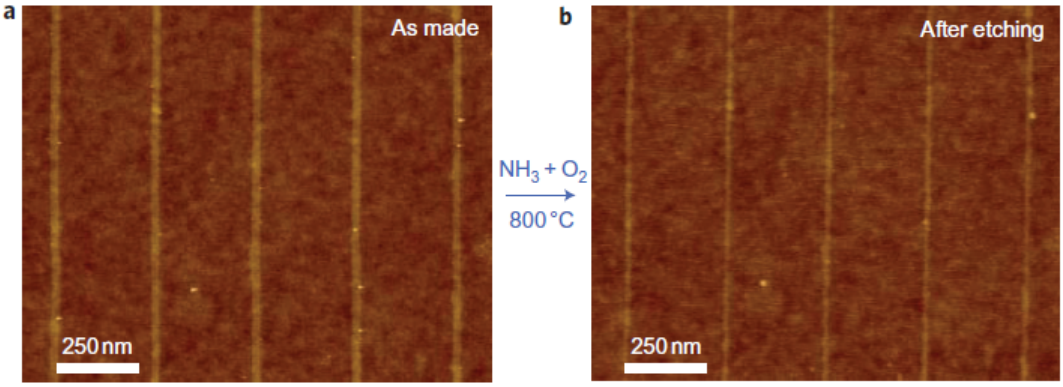

Fig. 1.2 AFM images of GNRs produced by Wang and Dai (a) before and (b) after the etching process.[10]

A successful *top down* approach to obtain GNRs with widths smaller than 5 nm was described by Wang and Dai using a subsequent gas phase etching process.[10] After laser lithography and application of more reducing etching conditions (O_2 and NH_3) under Ar atmosphere at 800 °C, GNR structures which could be used in FETs at room temperature were obtained.[10] They possessed a sufficiently large band gap to provide transistor on/off switching rates of 10^4.[10] Figure 1.2[B] shows AFM images of GNRs before and after etching.[10]
But besides that, it remains a yet unsolved challenge to fabricate narrower GNRs with the *top down* approach.[16] Therefore, the so-called *bottom up* fabrication of GNRs using chemical reactions to covalently link molecular precursors to defined graphene polymers appears to be more promising.[16] Applying this approach, the molecular precursor design is crucial for the shape

[B] Reprinted with permission of ref.[10], Copyright ©2010, Rights Managed by Springer Nature

and the width of the GNR.

In 2010 MÜLLEN, FASEL and co-workers reported firstly the atomically precise and controlled *bottom up* synthesis of a GNR by using two different molecular precursors as shown in Figure 1.3 (a) and (b).[17]C The shown *on-surface* synthesis sequence consists of an ULLMANN coupling reaction at 200-250 °C to covalently link the brominated precursors and subsequent planarization *via* cyclodehydrogenation at 700 K.

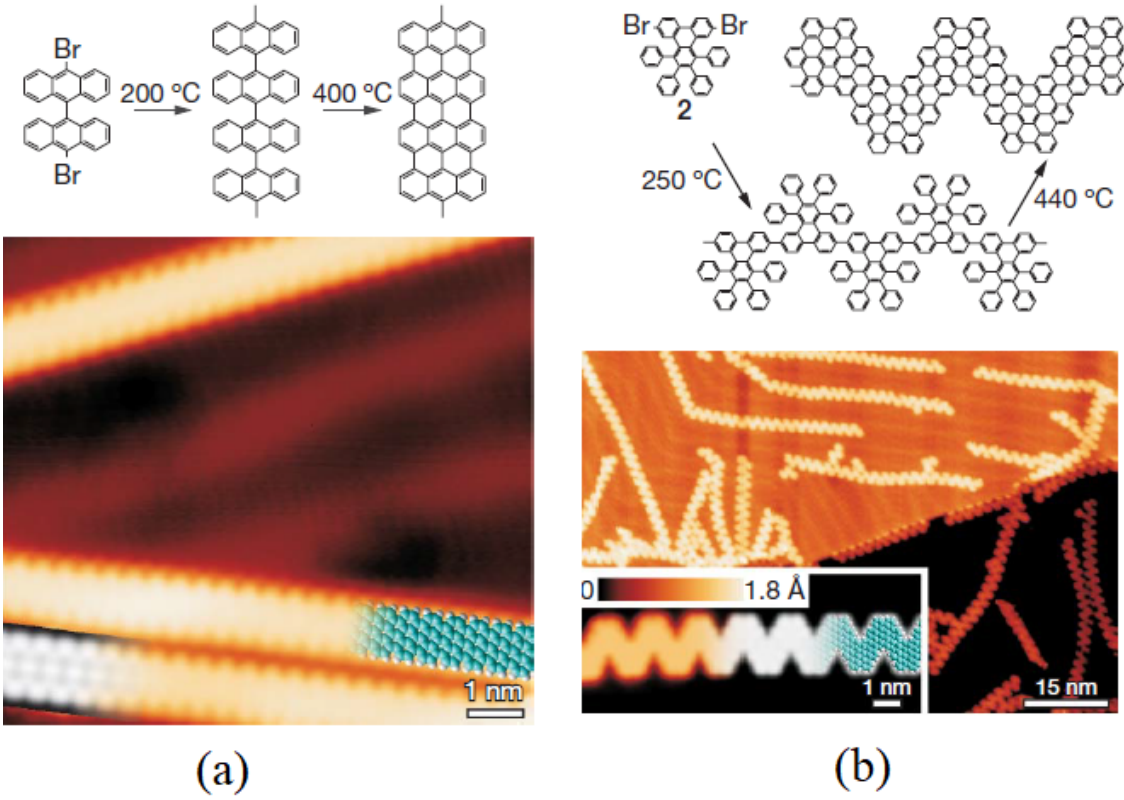

Fig. 1.3 Two different GNRs produced by FASEL, MÜLLEN and co-workers: (a) straight 7-AGNR; (b) chevron-type GNR.[17]

The GNR shown in Figure 1.3 (a) is an armchair GNR with a width of N=7 carbon atoms (7-AGNR) and a band gap of 1.6 eV. 1.3 (b) shows a chevron-type GNR with alternating N=6 and N=9 segments, possessing the same band gap.[17] For comparison, the band gap of bulk crystalline silicon is 1.09 eV.[18]

Today, the synthesis of many different linear armchair GNRs such as 3-AGNR[19] (band gap 1.15 eV), 5-AGNR[19, 20] (2.8 eV), 9-AGNR[21, 22] (1.4 eV), 13-AGNR[23] (1.4 eV), 14-AGNR[24] and 21-AGNR[24] have been realized. Furthermore, the electronic structures of N-doped GNRs with a larger band gap have been explored[25, 26] as well as B-doped GNRs.[27] Recently, O-doped

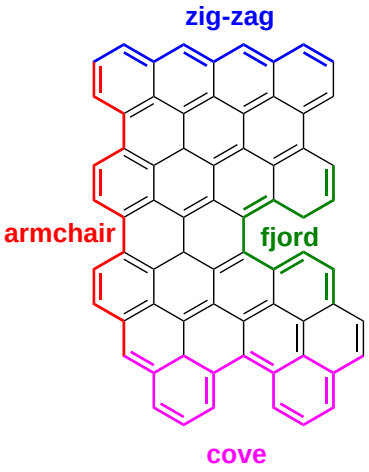

Fig. 1.4 Graphene edges.

[C] Adopted with permission of ref.[17],

PTCDA based 7-AGNRs containing alternating four- and eight-membered rings (band gap 1.38 eV) has been synthesized by Zhong *et al.*[28] They report that the utilization of four and eight membered rings narrows the band gap.[28] The shape of the edges also influences the electronical structure. Figure 1.4 shows four possible modes: armchair edges, cove edges, fjord edges and zig-zag edges.[29] Besides this, also chevron-type edges exist (see figure 1.2 (b)). Nakae *et al.* synthesized only 1.45 nm wide cove edged (N=7) GNRs under ambient pressure on Au(111), which could be transferred onto an insulating oxidized Si-wafer and contacted with Pd on both sides leading to a nanoelectronic transistor with a length of 500 nm and a width of 250 nm.[30] The measured on/off ratios were comparable to those of *top down* synthesized GNRs due to the length inhomogenity of the *bottom up* synthesized GNR (see Figure 1.5 (a).[30]D) The chemical structure of chevron-type GNRs makes it possible to fuse individual ribbons to broader GNRs containing pores. This can also be a versatile tool to adjust the ribbon's bandgap.[31, 32] Müllen reported the synthesis of soluble *tert*-butyl substituted cove edged GNR-oligomers with band gaps around 1.90 eV determined by UV-Vis spectroscopy.[29]

The synthesis and the electronical properties of a zig-zag edged N=6 GNR have also been reported.[33] A non contact AFM image is shown in Figure 1.5 (c).[33]E This GNR possesses a comparable large bandgap (1.6 eV) like AGNRs with similar width, but possesses spin-polarized edge states along the zig-zag edges.[34]

Shorter fragments of the zig-zag edged GNRs or nanographenes also possess a partial open-shell biradical character, indicating a high intrinsic electron mobility.[35]

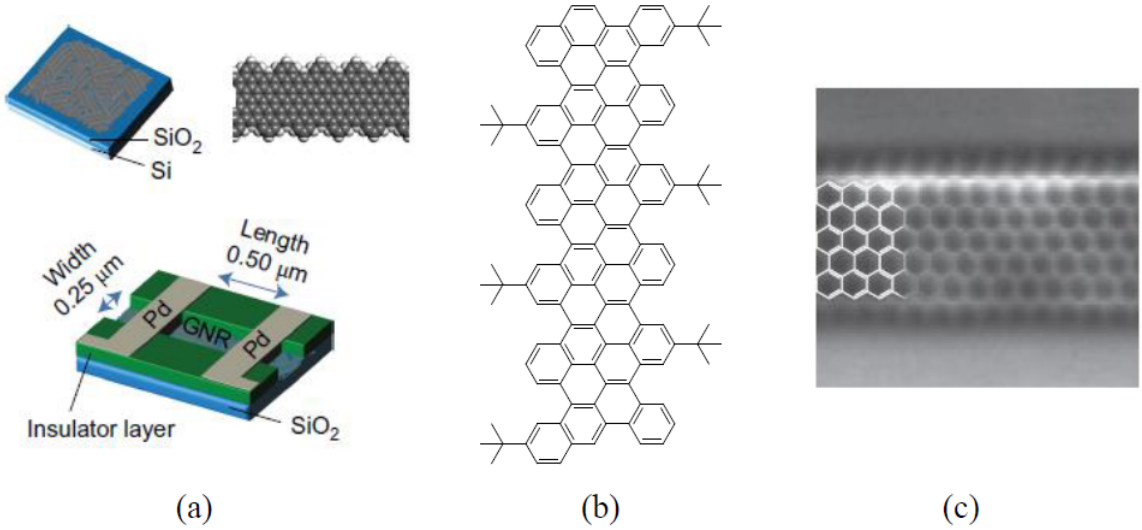

Fig. 1.5 (a) Cove edged GNRs used in a FET by Nakae *et al.*;[30] (b) soluble oligomeric cove edged graphene fragment synthesized by Müllen and co-workers[29]; (c) zig-zag edged GNR synthesized by Müllen, Fasel and co-workers.[33]

[D]Reprinted with permission of ref.[30], Copyright ©2017, Rights Managed by Springer Nature.
[E]Reprinted with permission of ref.[33], Copyright ©2016, Rights Managed by Springer Nature.

1.1.1 Porous (Nano)graphenes

As discussed previously, limitation of the outer dimensions from graphene sheet to graphene nanoribbons is an established successful strategy to open a bandgap in graphene and to obtain semiconducting properties. Another possibility is to prepare nanoribbons or nanographene with defined inner pores.

Nanoporous graphenes with pores in regular distances and arrangement (graphene nanomesh) surrounded by nanoribbons with widths <10 nm leads to room temperature bandgaps due to atomic scale disorder.[36, 37] Therefore, their use in room temperature field effect transistors is possible.[36, 37] Another important application possibility of nanoporous graphene is its function as nano-scaled sieve. Nanoporous graphene proved to be a separator for nucleic acid polymers (DNA, RNA)[38] or electrolyte separator for different charged species in electric cells.[39] Other separating applications were demonstrated for hydrated halogenide ions,[40] alkalimetal cations,[41] gases such as hydrogen, methane, CO or He.[42–44] Especially the separation ability of salt ions have been demonstrated to be useful for water purification devices.[45, 46] The presented applications have in common that selectivity for a selected ion or gas species can be achieved by the pore's size. Therefore, selective *bottom up* synthesis strategies for nanoporous graphene species are highly demanded. One successful example by Mugarza and Pena relies on the selective intermolecular fusion of GNRs substituted with phenyl groups leading to areas of fused GNRs with regular pores and a bandgap of 1 eV (Scheme 1.1 (a)).[32]F Utilizing intramolecular cyclodehydrogenations for the synthesis of a porous nanographene equipped with three pores by reacting a non-planar precursor on Au(111) was demonstrated by Fasel and Feng (Scheme 1.1 (b)).[47]G The synthesized C78 nanographene exhibits a comparably large HOMO-LUMO gap of 3.0 eV. Recently, macrocycles with very large pores consisting of 26 subunits were synthesized.[48] Since *bottom up* synthesis is the most accurate way of preparing GNRs with taylored shape and

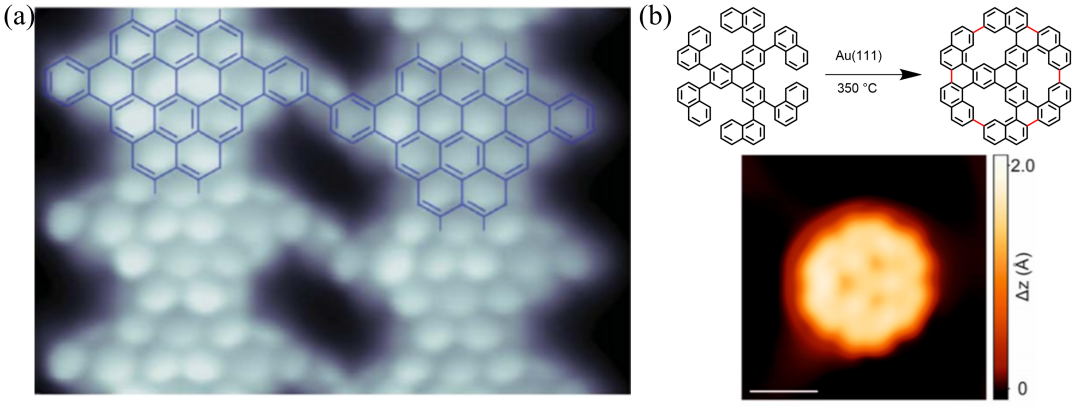

Scheme 1.1 (a) nc-AFM image of a porous graphene nanosheet on Au(111);[32] (b) synthesis and STM image of a porous nanographene on Au(111) (scale bar = 1 nm).[47]

corresponding reproducable electronical properties important for device fabrication, the next chapter deals with reaction types of organic molecules on surface for building up GNRs or various nanographenes.

[F] Reprinted with permission of ref.[32], Copyright ©2018, Rights Managed by the American Association for the Advancement of Science.

[G] Reprinted with permission of ref.[47], Copyright ©2019, Rights Managed by the American Chemical Society.

1.2 *On-surface* reactions

On-surface reactions of organic precursors provide the most versatile tool for *bottom up* synthesis of organic nanostructures. Thus, different recent reviews deal with this topic.[49–53] Many reactions have been reported on metal surfaces, but dehalogenation and dehydrogenation reactions have found most applications for nanographene synthesis and are shortly presented below.

1.2.1 Dehalogenative reactions

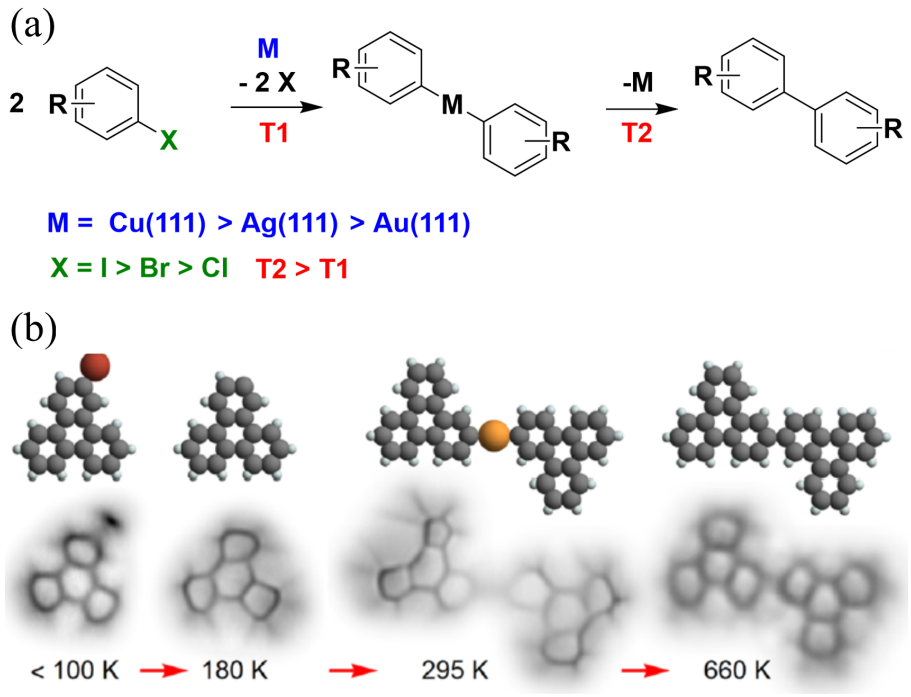

Scheme 1.2 (a) General reaction scheme for *on-surface* Ullmann couplings; (b) monitored reaction steps of an Ullmann homocoupling reaction on a Cu(111) surface by nc-AFM.[54]

The most prominent dehalogenation reaction is the Ullmann reaction, first described in solution by Ullmann 1902.[55] This reaction uses the metal catalyzed cleavage of aryl-halogen-bonds. First, a metalorganic dimer is formed by an oxidative insertion into two C-halogen-bonds, which were previously homolytically cleaved. The decomposition under further heating *via* reductive elimination of the metal center results in a homocoupling product (see Scheme 1.2 (a) and (b) for nc-AFM images of the intermediates[H]).[54, 56] The *on-surface* Ullmann reaction is understood to proceed *via* a radical mechanism.[54] This reaction was performed firstly by tip induced C-I cleavage[57] until Grill *et al.* found in 2007 that C-halogen-bonds can be cleaved by heat treatment on surface.[58] Since Lafferentz *et al.* found that C-I-bonds react at lower temperatures than C-Br-bonds, hierarchic 2D-structures were synthesized by selective couplings at different temperatures.[59] In a comparative study between *bis*-iodinated and *bis*-brominated terphenyl precursors, the lower reaction temperature of the iodinated precursor led to longer GNRs with fewer defects than in the case of the *bis*-brominated precursors. This can be explained by the

[H]Reprinted with permission of ref.[54], Copyright ©2017, Rights Managed by the American Chemical Society.

larger temperature window between dehalogenative coupling and cyclodehydrogenation preventing unwanted cross-talk between the different reaction channels.[52] Chlorinated precursors have been also used by Liu *et al.*, possessing a lower reactivity than the brominated ones.[60] This leads especially on the lowly reactive Au(111) surface to side reactions, since cyclodehydrogenation takes place at the activation temperature of C-Cl bonds.[61]
Until today, Ullmann reactions have been established for many different substrate types (*e.g.* stepped Au(10 7 7)[62]) with the insight that reactivities and also reaction mechanisms depend on the substrate.[63] Fan, Gottfried *et al.* found that control of the structure's geometry is possible on the stage of the reversibly formed organometallic network *via* slow precursor deposition onto a surface held at reaction temperature.[64, 65]
Also semiconducting titanium dioxide surfaces are suitable substrates for Ullmann reactions.[66] This is of special interest, since the strong electronic coupling of GNRs to noble metal surfaces makes it difficult to transfer them to insulating or semiconducting surfaces for device fabrication. Additionally, a more precise determination of their electronical bandgaps is possible without the electron-pushing effect of a noble metal surface. Other C-halogen-bonds apart from aryl-bonds can also undergo dehalogenative couplings. Sonogashira reactions of aryl chlorides, bromides and iodides with terminal alkynes on Au(111)[67] and Ag(100)[68] have been reported as well as alkenyl bromide homocouplings (Cu(110))[69] or homocouplings of alkyl halogenides (Wurtz reactions, on Cu(110) and Au(111)).[70] All of them proceed *via* radical mechanisms. The common feature of the presented dehalogenative couplings is the reaction selectivity which arises from the weakness of C-halogen-bonds in comparison to C-H-bonds. For this reason, strong C-F-bonds do not react this way.[71, 72] Very recently, Gottfried *et al.* described an *on-surface* interpolymer dehydrofluorination approach (HF zipping) of fluorinated poly-phenylenes to synthesize a planar nonbenzoid carbon allotrop biphenylene network consisting of 4- and 8-membered rings.[73]

1.2.2 Dehydrogenative reactions

Apart from Ullmann couplings, *on-surface* dehydrogenation reactions proved to be very important for the formation of nanographene or graphene nanoribbons. More than 100 years ago, dehydrogenative intramolecular reactions between aromatic C-H bonds were discovered by Scholl.[74, 75] In solution, the C-H bonds are activated for the reaction by several *Lewis*-acidic oxidants such as $AlCl_3$,[74, 75] $FeCl_3$,[76] $CuCl_2$[77] or combinations of *Lewis*-acid and oxidants such as $BF_3{\cdot}OEt_3$ with PIFA or combinations of Broensted-acids and oxidants such as trifluoromethyl sulphonic acid and DDQ.[76, 78] The mechanism of Scholl-reactions in solution has not been completely clarified until today. Two possible reaction pathways have been examined which describe the reaction either processing *via* arenium cation[78, 79] or radical cation[80] intermediate. For both possible mechanisms, the driving force of the reaction is the formation of a larger aromatic system.[78]
One drawback of the synthesis of large planar aromatic systems without bulky substituents in solution is their lack of solubility in common organic solvents. Therefore, an alternative method to access and characterize such large polyaromatic systems is the synthesis *via* surface-assisted cyclodehydrogenations. This was first observed by Müllen and Wöll in the case of the planarization of hexaphenylbenzene derivatives on Cu(111) to hexabenzocoronene.[78] In 2011, a

systematic study by Fasel on the cyclodehydrogenation of cyclohexa-*o*-*p*-*o*-*p*-*o*-*p*-phenylene to tribenzocoronene on Cu(111) showed that this *on-Surface* reaction involves a cascade of intramolecular aryl-aryl couplings with the electron-rich noble metal surface as a catalyst for the evolution of hydrogen and also as a stabilizer of the radical intermediates (Scheme 1.3 (b) for corresponding STM images[I]) through *van-der-Waals* interactions.[81]

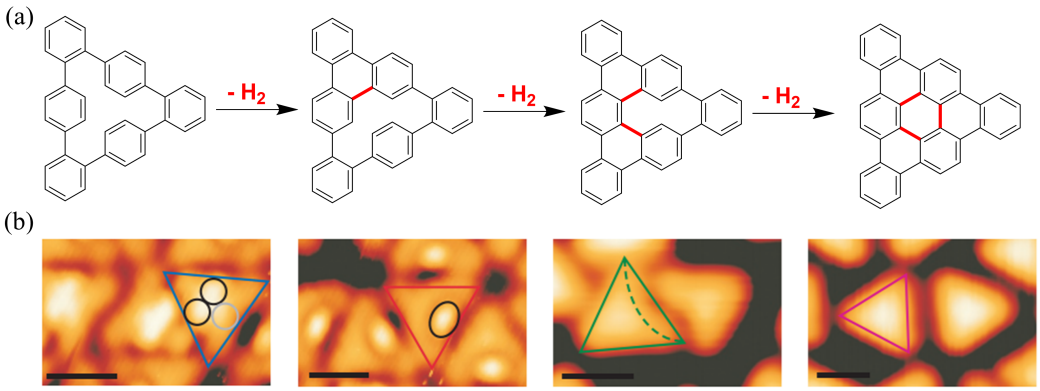

Scheme 1.3 (a) Cyclodehydrogenation reaction of cyclohexa-*o*-*p*-*o*-*p*-*o*-*p*-phenylene to tribenzocoronene on Cu(111); (b) Corresponding STM images of the reaction steps (scale bar = 1 nm).[81]

Due to the catalytical activity of noble metal surfaces for hydrogen formation, the thermally initiated cyclodehydrogenation proceeds at relatively low temperatures (400 °C).[81] As shown in Scheme 1.3, cyclodehydrogenations can be utilized for the synthesis of planar long-chained GNRs, demonstrating that multistep intramolecular cyclodehydrogenations deliver defect-free GNRs in high yields.[17, 52] Not only aromatic C-H bonds can be employed in the cyclodehydrogenation process for GNR synthesis, but also C-H bonds of methyl groups can be activated.[33, 82] This is opposed to the reaction scope of the Scholl reaction in solution that is limited to aromatic C-H activations. *On-surface* cyclodehydrogenations can also deliver reaction products that would not be formed in solution due to high molecular torsion. That can be reduced on surface by interaction with the noble metal surface.[83] Furthermore, complex ring rearrangements can be observed, leading to non-benzoid nanographenes.[84, 85] Cyclodehydrogenations are also useful for the intermolecular fuse of poly-phenylene chains or even poly-azulene chains towards GNRs.[86, 87]

The homo-coupling of terminal alkynes, known as Glaser-coupling,[88] can also be performed on noble metal surfaces and therefore can also be understood as an *on-surface* dehydrogenative coupling. First reported by Barth *et al.* 2012[89], this coupling already occours at 370 K on Ag(111) and also on Au(110) and Au(111) at similar temperatures.[90] A potential application for this reaction is the synthesis of graphyne, a two-dimensional network of benzene linked by alkyne groups or graphdyne nanowires.[91, 92] This has been demonstrated by Gross and co-workers in the synthesis of a cyclic all-sp-hybridisized [C18]-carbon via STM tip manipulation.[93]

[I] Reprinted with permission of ref.[81], Copyright ©2011, Rights Managed by Springer Nature.

1.3 Carbon Nanotubes

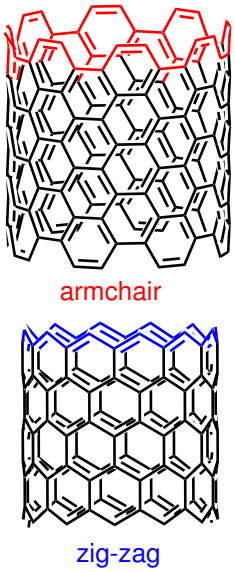

Fig. 1.6 CNT symmetry.

Another important allotrope of graphitic carbon are carbon nanotubes (CNTs). They consist of graphene tubes with typical diameters in the nanometer range but lengths up to 50 cm.[94] Their discovery by Iijima and Bethune was accidentaly, since they intended to study carbon anodes in carbon arc chambers.[95, 96] CNTs can be devided into single walled tubes (SWCNTs) and multi-walled tubes (MWCNTs). Whereas SWCNTs possess diameters of only around 1 nm, MWCNT can posess diameters of more than 100 nm and consist of many layers of nested SWCNTs.[97] Although their intrinsical insolubility limits the characterization of CNTs in solution on molecular level, the atomic structure of the SWCNTs determines their capabilities. Roling up the hexagonal graphene lattice from different directions can produce SWCNTs with two main symmetries: zig-zag *vs.* armchair (Fig. 1.6).[98] Roling angles between this two main structures can produce chiral CNTs.[99]
The symmetry has a huge impact on the electronical properties: compared to the 2D-semimetalic graphene-sheet, SWCNTs with armchair symmetry possess metallic conducting properties[100] and may carry electric current densities 1000 times higher than Cu wires.[101] Their special electric conductivity mode in one dimension along the tube axis is referred to as ballistic conductance.[102] Zig-zag SWCNTs or SWCNTs deviating from the idealistic two symmetry types can exhibit distinct bandgaps up to 2 eV, making them semiconducting.[103] MWCNTs, which are easily accessible for industrial production even in ton scale,[104] exhibit usually metallic conducting properties due to overlapping bands of many SWCNTs. They are of high technological interest mainly due to their mechanical properties: measured tensile strengths and elastic modulus identify them as strongest and also stiffest materials that are yet known with specific strengths up to 300 times higher than high-carbon steel.[105, 106] These properties are accompanied by the advantage of their low specific weight in comparison to metals or alloys, which is especially interesting for possible applications. However, the controlled selective synthesis of distinct zigzag and armchair SWCNTs is not possible today and their separation remains challenging.[107]
Their discussed unique properties make them to promising candidates for many applications. A few are briefly mentioned:

- as chemosensors for gases.[108]
- as thin-film flexible nanomaterial transistors.[109]
- as electrochemical energy storage materials.[110]
- as multi-level data storage materials.[111]
- as photovoltaic materials.[112]
- as human healthcare and biomedical devices.[113]

Therefore, efficient and precise strategies for the synthesis of CNTS are required.

1.3.1 Synthesis of Carbon Nanotubes

As mentioned above, the first generation of CNTs described by Iijima and Bethune in 1991 was obtained by electric arc discharge at carbon anodes.[95, 96] This procedure was already used a few years ago to synthesize C60 buckminster fullerene.[114] The high temperature used during the arc discharge (>1700 °C) leads to partial sublimation of the anodic carbon and nanotube growth.[115] Although it is possible to synthesize CNTs in gram-scale with this method and with only few defects,[116] the high reaction temperature is a drawback for industrial applications.
Alternatively, CNTs can be produced via laser plasma ablation of graphite on metal targets or C/metal composites.[117, 118] Depending on the metal target, MWCNTs or SWCNTs (especially in the case of a Co/Ni mixture) were obtained.[117, 118] This strategy was more effective for SWCNT synthesis and less expensive with the plasma being induced thermally with ethylene and ferrocene as carbon sources.[119] This is understandable, since CNTs could be detected in flames of ethylene.[120]

The most common method for CNT growth also in large quantities and industrial production is the chemical vapour deposition (CVD).[122, 123] This method relies on CNT growth on catalytically active nanoparticles in a reaction chamber with a gaseous carbon source at elevated temperatures (700 °C).[122, 123] The metal particles mostly consist of combinations of Fe, Ni or Co and are produced either by reduction of the corresponding metal oxides or described recently by Hampp by laser patterned stainless steel.[124, 125] The size of the grown CNTs depends on the morphology of the catalyst nanoparticles. For CNT growth initiation, a process gas (typically ammonia or nitrogen) is deposited together with the carbon source (typically ethylene, acetylene or methane).[126] Although the growth mechanism is still not elucidated completely, it is known that firstly the formed carbon on the nanoparticle's surface dissolves in the nanoparticles under alloy formation until saturation, initiating the CNT growth starting from carbidic nanoparticles with the nanoparticle situated at the growing end of the nanotube (see SEM image in Figure 1.7[121]J) or at its base, depending on the nature of the substrate.[127, 128] A scale-up for larger production volumes is possible, if oxides like aluminium oxide are used as catalyst support.[126] Subsequent acid or heat treatment is required in order to remove the metal nanoparticles from the grown carbon nanotubes,[129] but nevertheless the scalability of the methodology, the relatively low production costs as well as the possibility to directly grow and align the CNTs on the desired substrates makes this process highly relevant for industry.[130] Still a drawbac is the limited control over the different diameters in MWCNTs or the exclusive synthesis of SWCNTs with semiconducting or metallic properties.[107, 121, 131]

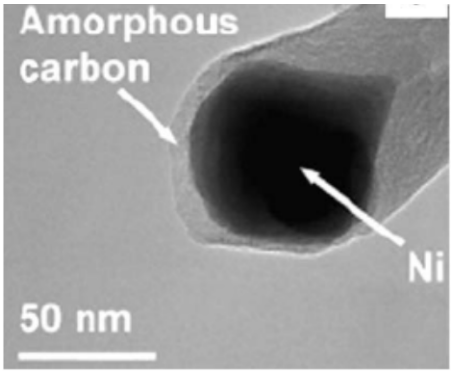

Fig. 1.7 Ni nanoparticle on a CNT tip (TEM image).[121]

[J]Reprinted with permission of ref.[121], Copyright ©2008, Rights Managed by Elsevier.

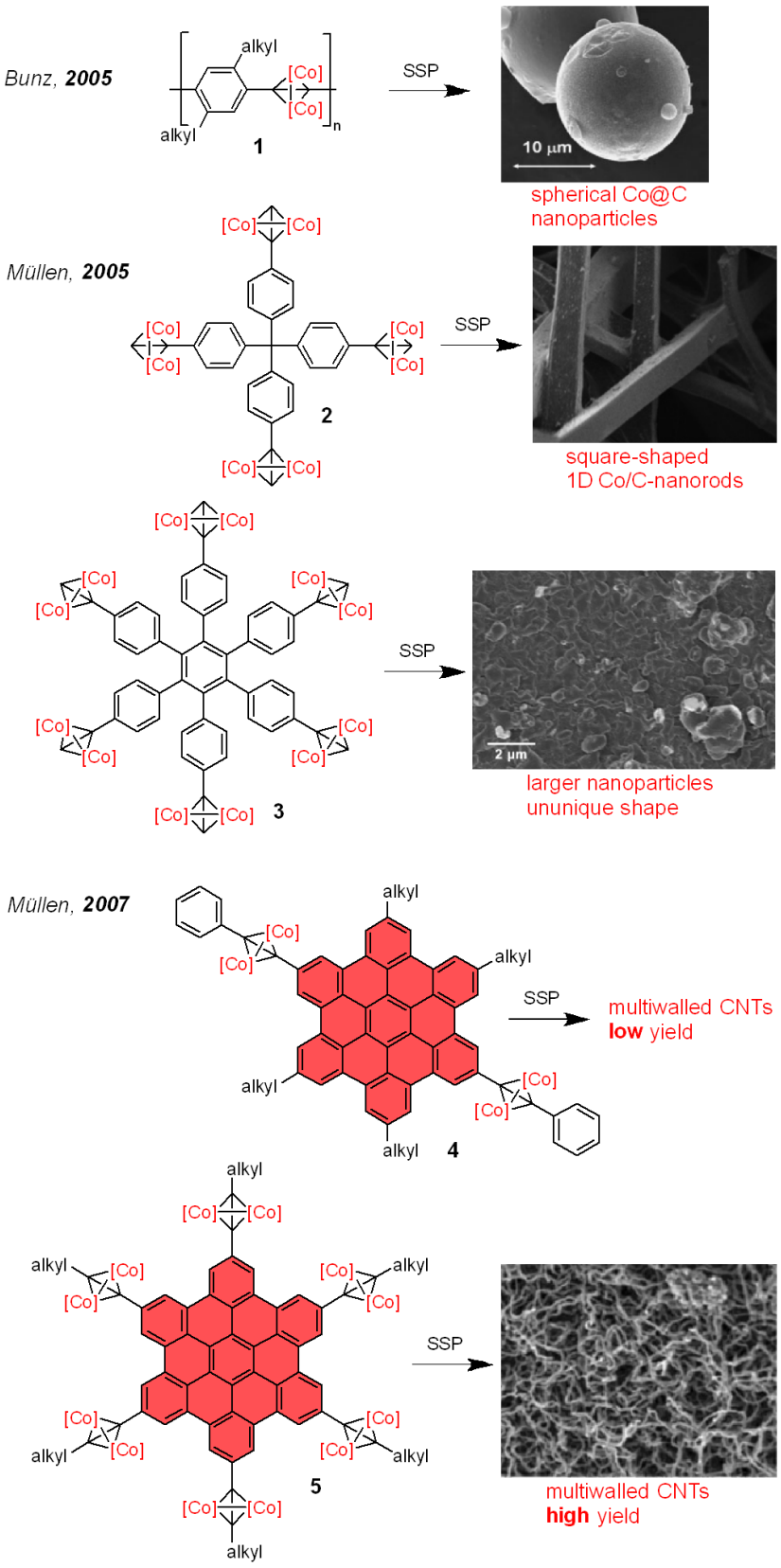

Fig. 1.8 Selected Co-complexes for SSP and SEM images of the pyrolysis products.[132–135]

The most promising approach for a control of the CNT shape is the solid-state pyrolysis (SSP) with organometallic compounds acting both as carbon source and catalyst. They are pyrolyzed in quartz glass ampoules under vacuum to form CNTs in a high temperature (800-1000 °C) carbonization process.[136] The advantage over the above discussed heterogeneous approaches are the homogeneously embedded catalyst atoms in the carbon matrix.[136] Early studies revealed that ferrocene[137, 138] and $Fe(CO)_5$[139] as effective organometallic precursors for the SSP. Work by Bunz and Vollhardt identified cobalt carbonyl complexes derived from arylated alkynes as promising organometallic SSP precursors for the synthesis of carbon nanoparticles (CNPs) and CNTs.[140–142] Studying various cobalt carbonyls, Müllen *et al.*[132–134] and Bunz *et al.*[135] found that in the case of SSP, the organometallic precursor's shape is crucial for the pyrolysis outcome (see Figure 1.8 for selected examples). Accordingly, SSP of dicobalthexacarbonyl functionalized poly(*p*-phenylenethynylene) (**1**) led to cobalt-

carbon spheres with distributed cobalt NPs in a carbon matrix.[135]K In contrast to that, the usage of a tetrakis(4-ethynylphenyl)-methane (**2**) derived Co-complex led to one-dimensional square-shaped cobalt-carbon rod fiber structures.[132]L Interestingly, ill-defined larger particles were obtained, when non-planar hexaphenyl-benzene cobalt cluster **3** was pyrolyzed.[133]M High yields of CNTs with bamboo-shape (laminar built multi-walled CNTs with wall segments of irregular lengths)[134] were obtained in the case of cobalt clusters containing planar graphitic aromatic backbones (*e.g.* hexa-peri-hexabenzocoronenes **4** and **5**)N, illustrating the importance of the precursor's shape and planarity for the bottom-up synthesis of nanostructures.[136] A second critical issue is a suitable Co to C ratio, because enough catalytically active Co-nanoparticles need to be formed since **4** leads to lower CNT yield like **5**.[133]

1.4 Polyaromatic hydrocarbons in solution

Graphene does not only play a role in surface science. In solution chemistry, the structural class of polyaromatic hydrocarbons (PAHs) plays an important role for more than 100 years. The development of selective reactions in order to obtain precise chemical structures enabled many applications for PAHs also considered as molecular nanographenes.[143] Especially an in-depth understanding of the structure and (opto-)electronic properties relations of PAHs led to many applications, for example in organic light emitting diodes (OLEDs),[144, 145] organic field effect transistors (OFETs),[146] organic solar cells (OSCs) or fluorescence-based applications (*e.g.* for organic laser devices[147] or medicinical applications[148]) with PAHs consisting of for their special purposes optimized chemical structures.

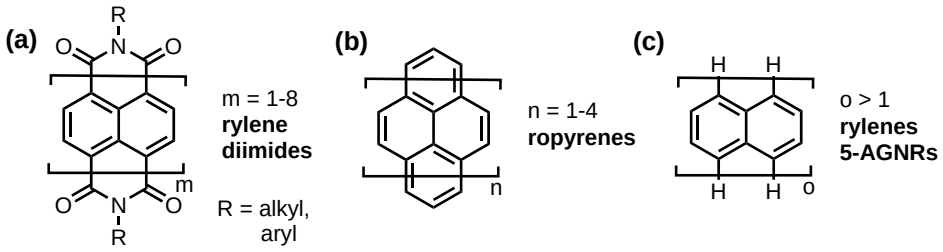

Fig. 1.9 Different structural motifs of oligo and poly-naphthalenes (a) rylene diimides; (b) ropyrenes; (c) rylenes (5-armchair GNRs).

The following sections will focus on PAHs consisting of *peri*-fused oligo-naphthalenes as shown in Figure 1.8. The most investigated structural type of this family are rylene diimides as electron acceptor-type materials (Fig. 1.9 (a)) with perylene bisimides (m=2) as most prominent and widely explored examples.[149] Pyrene (n=1) is the archetypical and most in-depth studied and applicated family member of the ropyrenes (Fig. 1.9 (b)).[150] They are the electron-rich counterparts of rylene diimides and structurally related to rylenes, which are oligomeric or polymeric fused *peri*-naphthalenes.[151] Poly-naphthalene is also known as 5-armchair GNR.[152]

[K]Reprinted with permission of ref.[135], Copyright ©2005, Rights Managed by Wiley VCH.
[L]Reprinted with permission of ref.[132], Copyright ©2005, Rights Managed by Wiley VCH.
[M]Reprinted with permission of ref.[133], Copyright ©2007, Rights Managed by Wiley VCH.
[N]Reprinted with permission of ref.[134], Copyright ©2005, Rights Managed by Wiley VCH.

1.4.1 Rylene Diimides

For nearly 100 years, naphthalene bisimide and bisanhydride (NTCDI, NTCDA) as well as their higher perylene homologues PTCDI and PTCDA have been synthesized in industrial scale (Scheme 1.4).[151]

The synthesis of naphthalic bisimides (Scheme 1.4 (a)) starts from pyrene (**6**), which is first chlorinated using gaseous chlorine, followed by hydrolysis of **7** to **8** and oxidation employing sodium hypochlorite in order to obtain the n-type semiconductor NTCDA.[153, 154] NTCDA can be converted to NTCDI by the use of concentrated ammonia or into various alkyl or aryl amines via condensation under acidic conditions.[153, 155] The synthesis of perylene bisimides (scheme 1.9 (b)) starts from acenaphthene (**9**), which is oxidized to the corresponding naphthalene monoanhydride **10** via vanadium pentoxide mediated air-oxidation,[151] followed by ammonolysis to the monoimide **11**. This is the starting point for a KOH mediated air-oxidation at high temperatures (300 °C), in order to dimerize naphthalene monoimide in peri-position to the n-type semiconductor PTCDI. PTCDI itself can be converted to the well-known insoluble red pigment PTCDA under acidic conditions at high temperature. During this step, other aryl- or alkyl-amines can be introduced via condensation reaction at acidic conditions.[151]

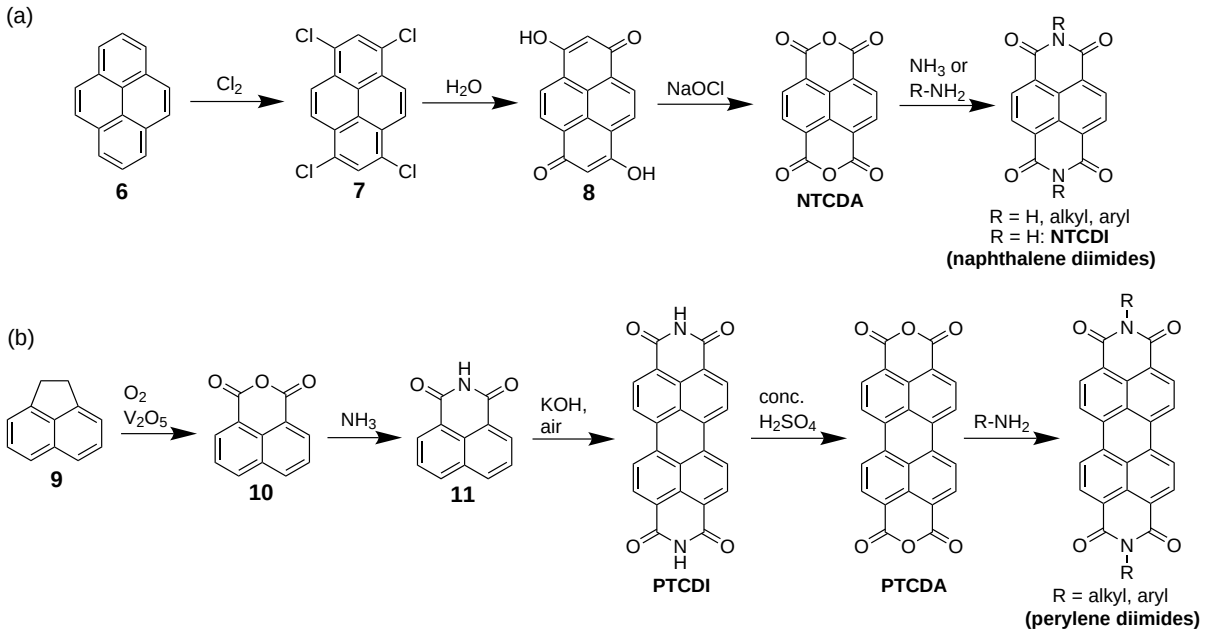

Scheme 1.4 (a) Industrial synthesis of naphthalic bisanhydride (NTCDA) and the corresponding bisimides; (b) Industrial synthesis of perylene bisanhydride (PTCDA) and the corresponding bisimides.

Although PTCDA itself finds application in OFETs,[156] its insolublity is a drawback for many solution-based applications *e.g.* for photophysical processes in OSCs.[157] Therefore, many synthetic approaches to introduce solubility enhancing groups and tune the electronical properties have been established.[149, 158] This includes either introduction of solubility enhancing sterically demanding imide groups while maintaining the electronical properties of NTCDI/PTCDI or altering both the electronic properties and improving the solubility by introducing substituents at

the rylene scaffold.[149, 158] Apart from the extensively studied naphthalene (NDIs) and perylene diimides (PDIs), also higher homologue rylene diimides have been accessed and their capabilities have been studied.[159] Their synthesis is more complex than the synthesis of PDIs and NDIs and requires a multi-step modular construction of the oligo-rylene scaffold.[160]

Müllen and co-workers built up higher rylene diimides like terrylene diimide (TDI **16**, Scheme 1.5 (a)) and other longitudinally extended rylene diimides with up to eight naphthalene subunits via Suzuki-Miyaura cross-coupling of 1,4-bisbromonaphthalene (**12**) and corresponding borylated naphthalene (**11**) - or higher rylene-monoimides. Afterwards, the resulting oligoperinapthalenediimides (**13**) were planarized by use of air oxidation using potassium hydroxide/ethanol as base for the formation of radical cation intermediates, which were dimerized intramolecularly and oxidized by either air or DDQ.[161–163]

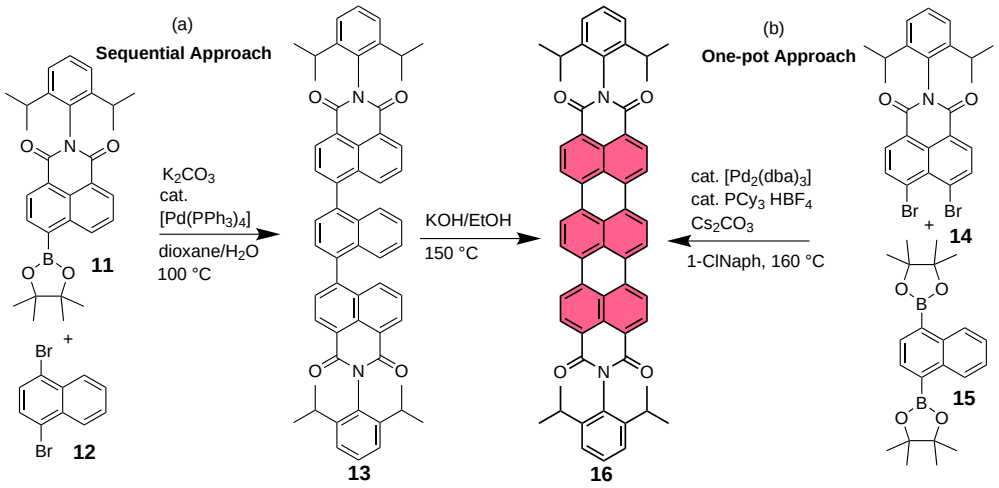

Scheme 1.5 (a) Approach for the stepwise construction of higher rylene disimides such as terrylene diimide **16** by Müllen and (b) one-pot approach by Würthner.

More recently, Würthner *et al.* found that a reaction of peri-bisbrominated naphthalene imide **14** and bis-borylated naphthalene **15** with catalytic amounts of $[Pd_2(dba)_3]$ and tricyclohexylphosphine as ligand furnished the corresponding bisimides in a one-pot tandem Suzuki-Miyaura cross-coupling/Heck-reaction (Scheme 1.5 (b)).[164–166] This reaction requires moderately high temperatures (160 °C) and 1-chloro-naphthalene as effective solvent for large aromatic reaction intermediates.[166]

The optoelectronical capabilities of the higher rylene bisimides could be altered in a comprehensive way, since the absorption and emission spectra of the higher rylene diimides are shifted bathochromically by approx. 90 nm per additional naphthalene unit.[159, 160] Furthermore, the molar attenuation coefficients also increase nearly linearly (see Figure 1.10[167]O) and are shifted in the NIR region for the higher homologues.[159, 160] For example, water-soluble quarterrylene diimides with attached polyethylene glycol groups were used as versatile dyes for biological imaging and photothermal cancer therapy due to their biosafe low energy absorption and emission (> 700 nm) and high fluorescence quantum yields.[168] Due to their high thermal and chemical stability as well as excellent photostability, rylene diimides have many applications today.[159]

[O]Reprinted with permission of ref.[167], Copyright ©2014, Rights Managed by the American Chemical Society.

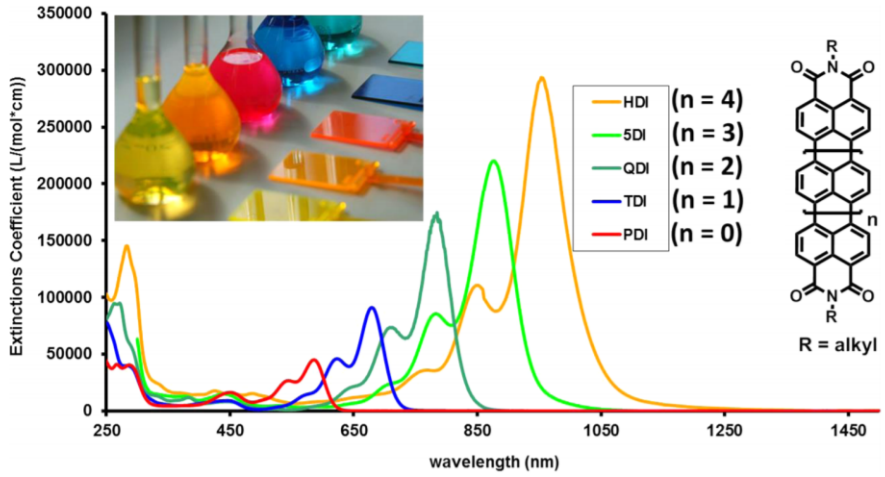

Fig. 1.10 UV-Vis-NIR spectra of a homologous rylene diimide series.[167]

1.4.2 Rylenes and Anthenes

Rylenes are closely related to rylene diimides. But in contrast to them, rylenes possess terminal zig-zag units and are more electron-rich than rylene diimides.[169] They also build up a homologous family by peri-extension of the naphthalene units. Perylene (**36**) itself is a prominent member of this class with many applications due to its inertness, photostability, high absorption coefficient and excellent fluorescence capabilities.[170] Higher homologues such as quarterropyrene have been made accessible via oxidative dimerization of perylene (**36**) using the oxidation system DDQ/$Sc(OTf)_3$ which was first reported by Johnson.[151]
Allthough its synthesis is quite simple, application of unsubstituted quarterropyrene remained limited due to its low solubility.[151] A concept for the synthesis of more soluble rylenes reported by Müllen relies on a modular construction as described before for rylene diimides. A Suzuki-Miyaura cross-coupling is followed by a Scholl reaction utilizing $FeCl_3$ or $CuCl_2$ in combination with $AlCl_3$ as oxidant (Scheme 1.6).[171, 172] Solubility is enhanced by substitution of the terminal naphthalene rings with *tert*-butyl groups (**18**). However, the limit of this approach is reached with penterrylene (**20**), which is already to insoluble for ^{1}H NMR analysis.[171, 172] The trend of the shift in absorption spectra is similar to rylene diimides, but with slightly blueshifted maxima due to weaker intramolecular donor-acceptor interactions in the case of rylenes.[169]

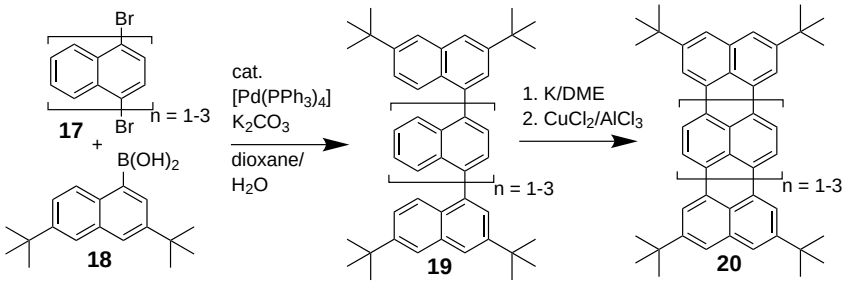

Scheme 1.6 Modular approach towards rylenes reported by Müllen.[171, 172]

The laterally extended higher homologues of rylenes are anthenes, formally regarded as longitudinally fused oligo-anthracenes and also classified as 9-armchair graphene nanoribbons (7-aGNRs).[17] As described above for the homologous family of rylenes, a series of homologous anthenes exists in literature.[169] They are accessible by reductive functionalization of the corresponding anthenequinones.[173] Interestingly, in the case of anthenes does not only the HOMO-LUMO energy gap, but also the solubility and chemical stability decrease with homologization. The higher anthenes even show an increasing open-shell biradical character.[169] This can be explained with the aromatic electron sextett theory of Clar, since the open-shell resonance structure allows the formal formation of more stable aromatic sextetts.[169] Unsubstituted bisanthene (**24**) was first synthesized by Clar via reduction of bisanthenequinone (**23**) with zinc dust in quinoline followed by oxidative dehydrogenation on air (Scheme 1.7).[174]

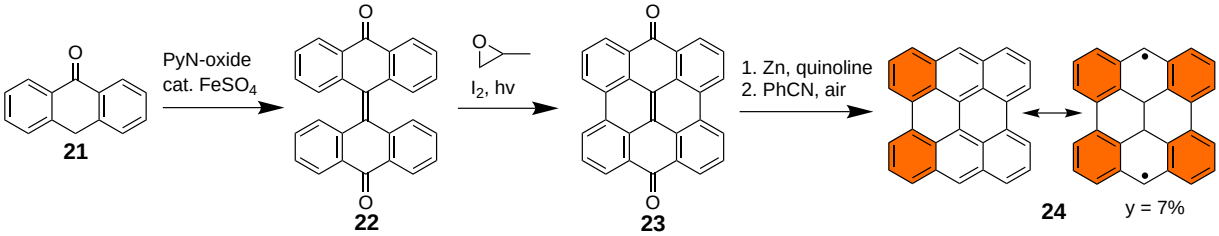

Scheme 1.7 First synthesis of bisanthene (**24**) reported by Clar, its corresponding open-shell resonance structure and determined biradical character (y).[174]

The blue-colored PAH **24** (absorption maximum: 662 nm) shows limited stability on air (singlett-oxygen)[175] due to its high lying HOMO and a singlett biradical character of y = 7%.[176, 177] The stability of bisanthenes can be enhanced by introduction of bulky or electron-withdrawing substituents in central peri-position (meso-position), where the spin density is maximal.[173, 176, 177] A strategy for the synthesis of teranthene (**34**) and quarteranthene (**35**) has been developed by the group of Kubo.[176, 177] They studied the crossover from closed-shell to open-shell structures by homologization and found an increasing biradical character (y) from **34** (y = 54%) to **35** (y = 91%), which could not be studied by NMR spectroscopy anymore.[177] The increasing biradical character from bisanthene **24** to quarteranthene **35** could also be demonstrated in a shortening of the central $C(sp_2)$-$C(sp_2)$ single bonds towards quinoide $C(sp_2)$=$C(sp_2)$ double bonds (from 1.467 Åto 1.414 Å).[177]

The synthesis strategy for **34** and **35** relies on a multi-step procedure and is shown in Scheme 1.8: It starts with a nucleophilic addition of lithiated **25** to anthraquinones **26** and **27** and is subsequently followed by a reductive aromatization employing the system NaI/NaH_2PO_2 to acieve anthryl derivatives **28** and **29**. Partial cyclization accompanied by demethylation of **28** and **29** was carried out with KOH/quinoline to yield the incompletely ring-closed quinones **30** and **31** which were treated with mesitylmagnesium bromide in the presence of $CeCl_3$ and further underwent reductive aromatization to generate the partially cyclized compounds **32** and **33**. The complete cyclization was promoted by $DDQ/Sc(OTf)_3$ to yield the anthenes **34** and **35**, which exhibited moderate stability in solution with a half-life times of around 3 days upon exposure to air and light at room temperature.[176, 177]

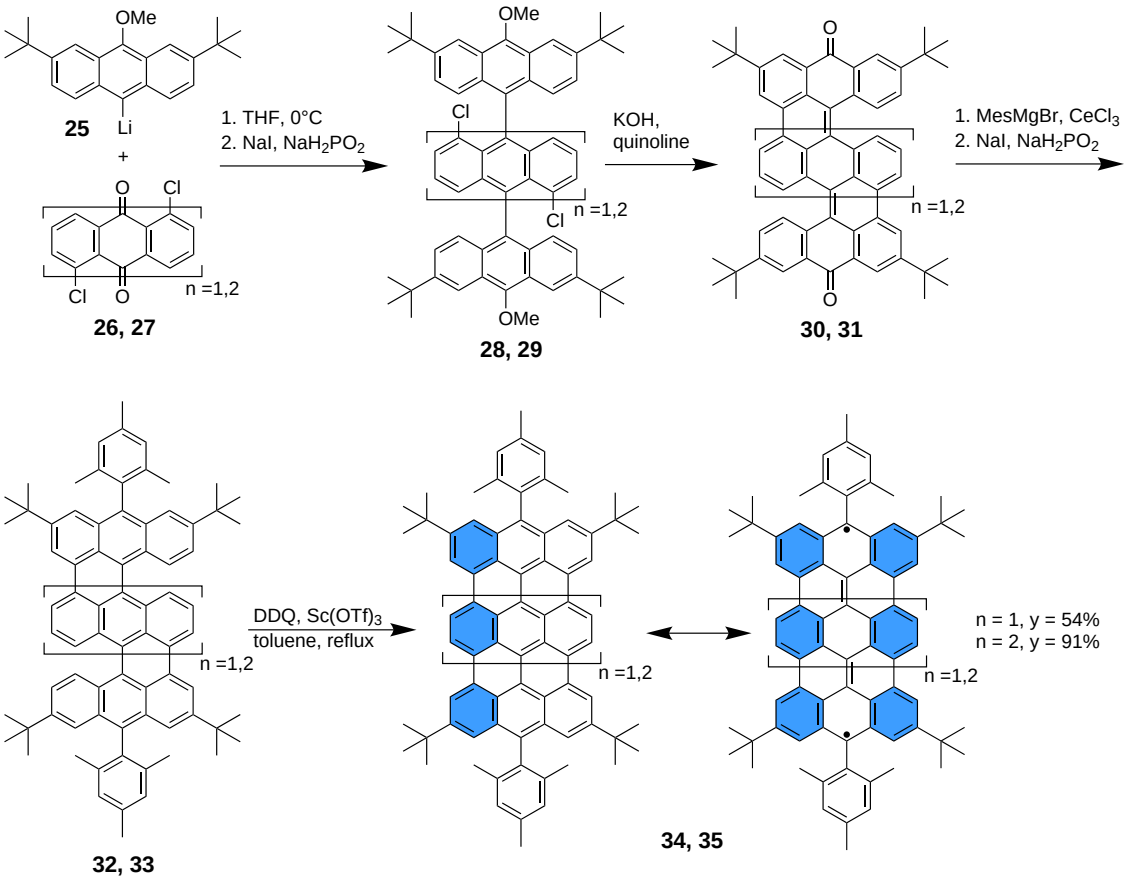

Scheme 1.8 Synthesis route towards teranthene **34** and quarteranthene **35** reported by Kubo.[176, 177]

1.4.3 Ropyrenes

In the 1940s, Clar discovered several synthetic approaches towards different PAHs. The most in-depth studied PAH among them was dibenzoperylene (**38**). Because of its close structural relationship to both known systems at that time - perylene (**36**) and pyrene (**6**) - he named the new PAH peropyrene.[178] His synthesis route based on a reductive dimerization of phenalenone (**37**) in a salt melt consisting of Zn, $ZnCl_2$ and NaCl under harsh conditions (300 °C) similar to above showed synthesis of bisanthene (**24**). With this method, he also accessed the PAHs violanthrene (**41**) and isoviolanthrene (**40**) from ketone **39**. Clar used **38** as a model to study the aromaticity of different benzene rings in PAHs. This led him to the formulation of the aromatic π-sextet rule towards the stability of aromatic systems (see Scheme 1.9 with highlighted Clar-sextetts).[179]

The Clar-synthesis of peropyrene (**38**) has been improved by Pogodin and Agranat to proceed at lower temperatures with higher yields by either application of McMurry reaction conditions (Zn/low valent titanium species as reducing agents) or by radical dimerization with the intermediate formation of an instable thioketone with P_2S_5.[180, 181] Alternatively, an oxidative dimerization approach using a corresponding metacyclophane and DDQ as oxidant was also described.[182] After beeing neglected for some decades, the research on peropyrene found a

renaissance when optical properties of PAHs were systematically studied.[183] In course of that, the ability of singlet fission in PAHs was studied, which can occur if the singlet and triplet state in photo-exited PAHs are energetically sufficiently separated.[184–186]
Especially for application in dye-sensitized solar cells (DSCs) this process was found to be important.[185, 186] For geometrically rigid PAHs such as perylene,[187] pentacene[188] or suitably functionalized perylene diimides,[189] the singlett fission process has been found. In the case of peropyrene (**38**), earlier studies revealed its photoconducting properties[190] and also fluorescence quenching capabilities in solution.[191] In 2013, a study of Bardeen investigated the ability of unsubstituted peropyrene as singlett fission material in solution and in crystalline state.[192] They found that only in the crystalline state, the energetical separation of singlet and triplet state is significant, but still too small for singlett fission.[192] Thus, crystal engineering via substitution of the peropyrene scaffold was required.

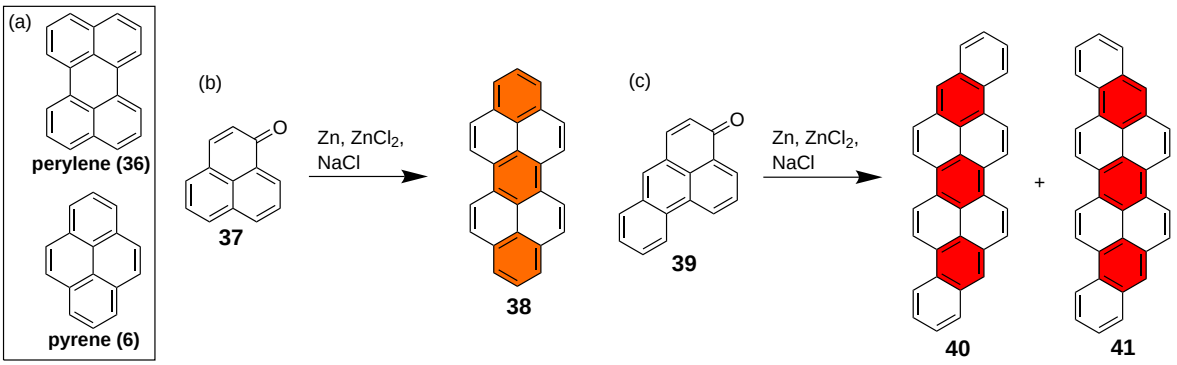

Scheme 1.9 (a) Chemical structures of perylene (**36**) and pyrene (**6**); (b) Clar-synthesis of peropyrene (**38**); (c) Clar-synthesis of violanthrene (**41**) and isoviolanthrene (**40**).[178, 179]

Until now, several approaches in order to obtain substituted peropyrenes are known. Many of them require multi-step synthetic procedures and only allow the synthesis of peropyrenes in small scale. Terminal 2,9-substituted peropyrenes were synthesized by Kamada *et al.*[193] The authors could demonstrate that the variation of groups in 2,9-position (*n*-Bu, *t*-Bu or Ph) could significantly affect the crystallization behaviour and the formation of triplet excitons could be verified for the phenyl-substituted congener (Scheme 1.10 (a)).[193] Nevertheless, their synthesis strategy based on eight steps!
Another approach towards peropyrenes with substitutions in the bay area was presented by Chalifoux.[194–196] The key of this synthesis strategy are benzanulations of internal alkynes that lead to π-extensions of a central phenyl or pyrene unit which result in twisted peropyrenes and also higher homologue terropyrenes that possess high solubility due to the non-planar backbone.[194, 195] Out-of-plane twist angles up to 32° were realized (see XRD structure in Scheme 1.10 (b)[P]). This leads to a redshift of the UV-Vis and fluorescence spectra and also to high fluorescence quantum yields (Scheme 1.10 (b)).[194] For the critical cyclization step, the group presented trifluoro sulphonic acid-mediated[194, 195] and $InCl_3$-catalyzed[196] approaches

[P] Reprinted with permission of ref.[196], Copyright ©2018, Rights Managed by the Royal Chemical Society.

with up to 50% yield for the cyclization step. The major drawback of this versatile strategy, that could also be applicated for 5-aGNR synthesis,[152] is the occurence of incomplete cyclized side products which can hardly be separated from the desired products.

Approaches by Miao[197] and later also Feng[198] to highly twisted peropyrenes were realized by oxidative Scholl reactions using DDQ in trifluorosulphonic acid as oxidant (Scheme 1.10 (c)). Using suitable tetranaphthyl-diphenylbenzene or even tetrapyrenyl-substituted precursors built up by sequential Suzuki-Miyaura couplings[198] or Diels-Alder reactions,[197] peropyrenes with four annulated naphthyl or pyrene units with torsion angles larger than 50° were achieved. Due to the energetically highly disfavored twisted aromatic system that is formed, the yields in the last step are comparably low (<10%).[197, 198] Due to the low π-stacking ability, the twisted peropyrenes show lower charge carrier mobilities,[197] but large Stokes shifts leading to NIR-fluorescence and also small optical HOMO-LUMO energy gaps.[198]

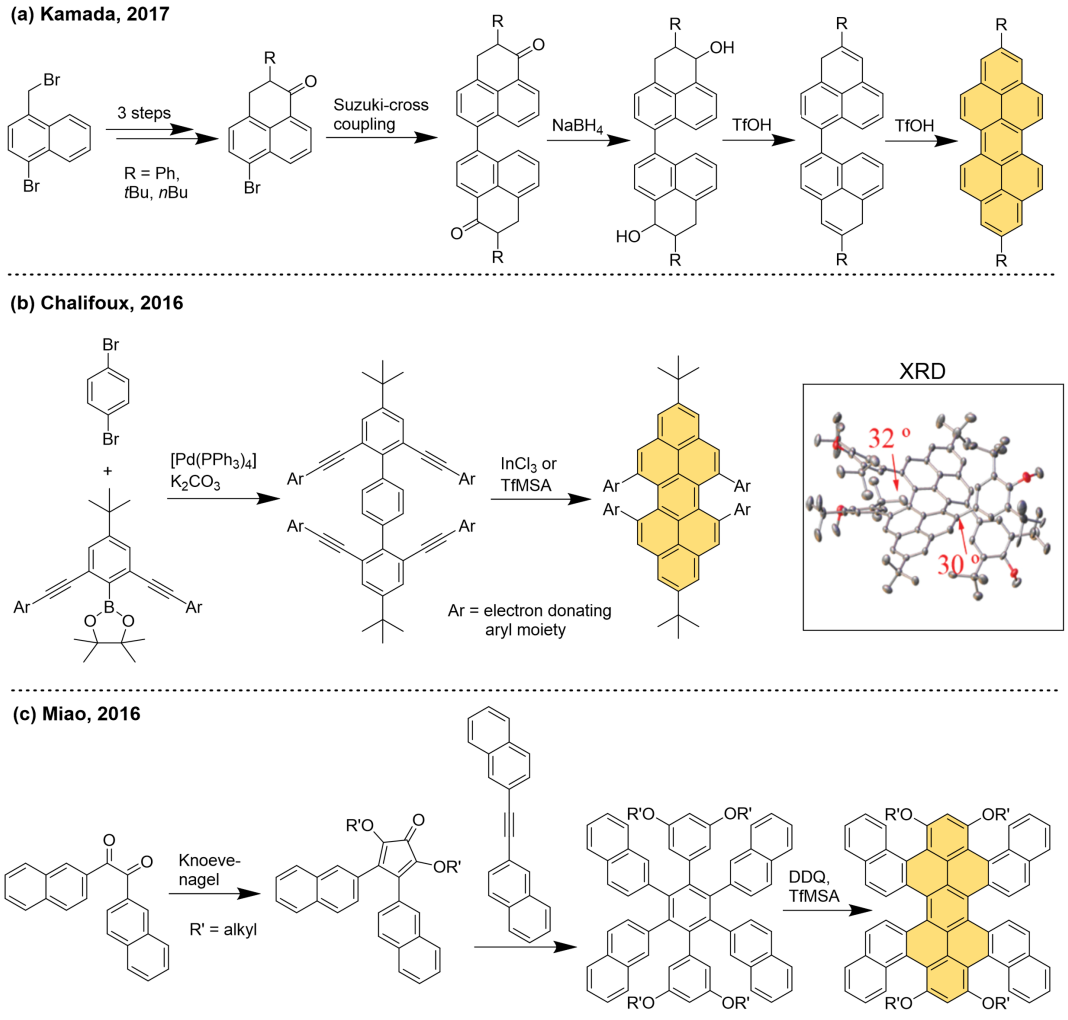

Scheme 1.10 Approaches to substituted peropyrenes by (a) Kamada *et al.*;[193] (b) by Chalifoux *et al.* and exemplary XRD structure of a highly distorted peropyrene;[194–196] (c) by Miao *et al.*[197]

1.4.4 Aza-based ropyrenes

The group of GADE developed the structural family of 1,3,8,10-tetraaza peropyrenes(TPAPs)[199] and also the structural closely related smaller 1,3,6,8-tetraaza pyrenes.[200] In terminal positions, they introduced electron-withdrawing perfluoroalkyl groups via condensation of the corresponding perfluoroalkyl carboxylic acid chlorides with their previously reported diamino-perylene (**43**) or naphthalene (**42**) diimines.[201] The perfluoroalkyl groups lowered the energy level of the frontier molecular orbitals, making the tetraaza pyrenes and peropyrenes stable electron-accepting dyes with typically two distinct reduction potentials. They also enlarged fluorescence quantum yields significantly (>30%).[201]
But the key of their diverse scientific work are selective core halogenations of the tetraaza pyrenes and peropyrenes with bromine (**47**, **49**) or dichloroisocyanuric acid (**46**, **48**) (Scheme 1.11 (a)).[200, 202] The halogenated congener **49** served as a precursor for a variety of chemical transformations (Scheme 1.1a (b)) and proved to be a good n-type semiconductor for OFETs according to its lowly low lying LUMO.[200, 202–205] Many different chemical transformations, such as SONOGASHIRA cross couplings to yield alkinylated derivatives or SUZUKI-MIYAURA cross couplings in order to obtain arylated tetraaza peropyrenes were possible.[206] Furthermore, aryl amines, phenolates and thiophenolates could be introduced by either BUCHWALD-HARTWIG cross-coupling or nucleophilic substitution.[206, 207] The thioaryl ether derivatives could be transferred into sulfoxides by selective oxidation of the sulphur atoms.[207] Additional functionalization of the C-Br groups was possible by use of Umpolung reactions with *n*-butyl lithium. Trapping of the tetralithiated TPAPs with several electrophiles resulted in silylated, stannylated or phospine derivatives of TPAPs, which can subsequently be transferred into fluorinated or trifluoromethylated TPAPS.[204, 208]
The functionalizations had a large impact on the opto-electronical properties of the TPAPS: Core halogenation led to an enlarged HOMO-LUMO bandgap and lower lying frontier molecular orbitals. This makes the halogenated compounds candidates for n-type semiconductors. Furthermore, the fluorescence properties are also strongly improved (quantum yields > 80%).[203, 204] Especially the variety of electron-withdrawing and electron-donating functional groups introduced by post-functionalizations could be used for fine-tuning of absorption and emission spectra. A variation of absorption maxima wavelengths over 200 nm, from 470 nm for electron-poor halogenated compounds to 670 nm for electron-rich thiol or amine substituents was achieved.[201, 207]
The introduction of dendrimeric electron-donating (oligo-)thienyl groups via SUZUKI-MIYAURA cross-coupling led to the formation of TPAPs that exhibit not only small HOMO-LUMO energy gaps, but also spacially separated HOMO and LUMO KOHN-SHAM orbitals.[209] This characteristic leads to improved charge mobilities.
The electron-deficient perhalogenated TPAPs or derivatives substituted with CF_3-groups are characterized by very low lying LUMO energies below -3.0 eV, a fact that characterizes them as very capable electron acceptors, which can form stable radical anions or even dianions by chemical reduction with potassium graphite.[210, 211]
The functionalization of TPAPs with amine or pyridine groups also opened the door for the design of water-soluble fourfold-charged methylated or protonated derivatives, that could be

applicated as biological fluorescence probes with the special opportunity to interact as DNA quadruplex binders with low cytotoxity.[212, 213]

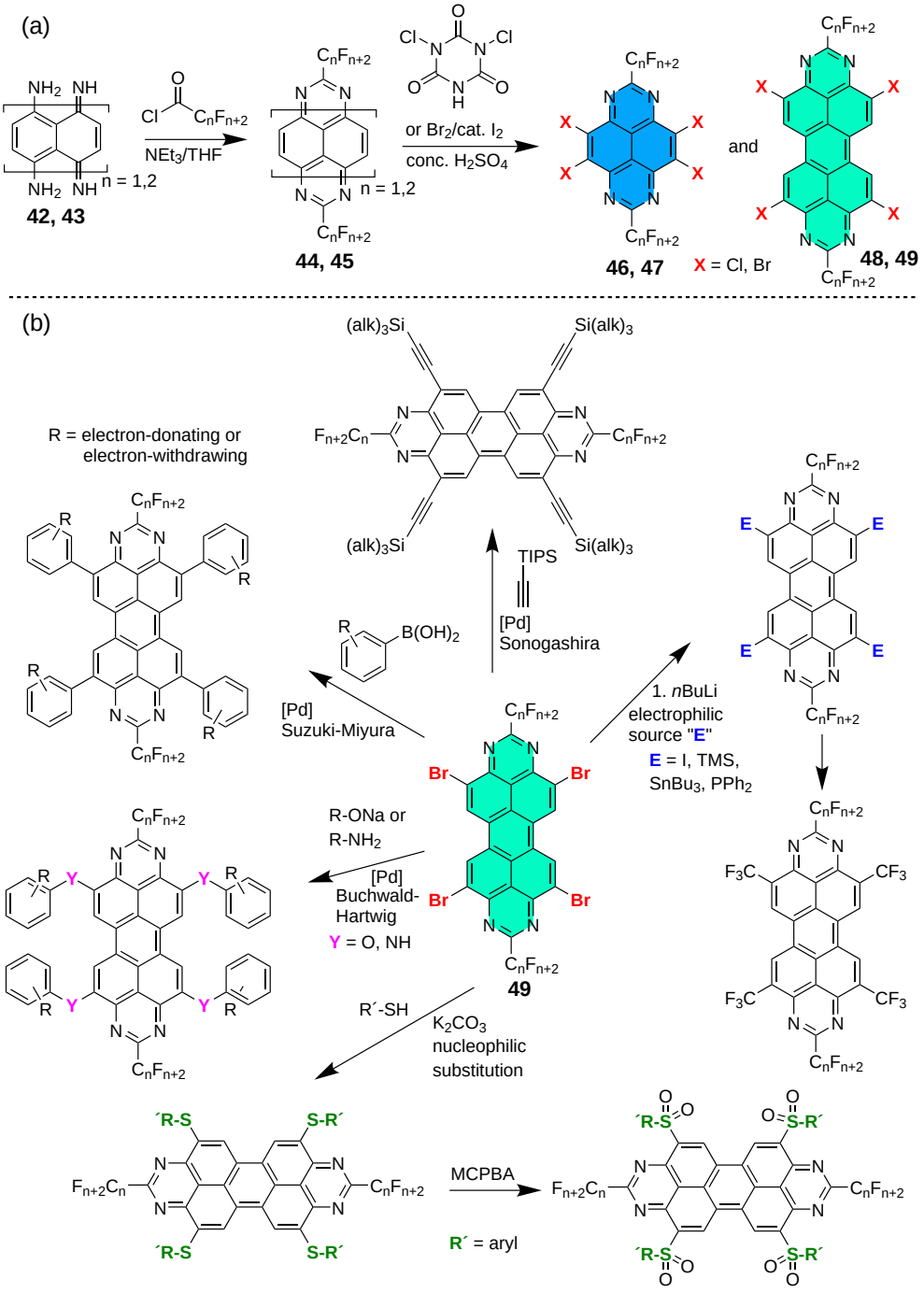

Scheme 1.11 Overview of GADE's research towards tetraaza(pero)pyrenes: (a) selective halogenizations; (b) post-fuctionalizations.

Recently, CHEN reported on a regioisomeric, in bay positions *N*-doped 5,6,12,13-tetraazaperopyrene, which possessed different crystal packing structures and slightly bathochromic shifted absorption and emission spectra compared to GADES 1,3,8,10-tetraaza peropyrenes.[214] This illustrates the importance of the position of the nitrogen atoms at the peropyrene's backbone.
Another possible nitrogen doping position in pyrenes and peropyrenes are the terminal 2,7- or

2,9-positions, respectively. Replacement of phenyl rings with pyridinyl rings is known to alter the electronic properties of PAHs dramatically, since especially the LUMO energy is lowered due to the higher electronegativity of the nitrogen atoms.[215, 216] Despite the fact that the terminally nitrogen substituted oxidated stem systems of 2,7-diazapyrene (**52**) and 2,9-diazaperopyrene (**53**), NTCDI and PTCDI, are known for more than 100 years, there was a lack of effective syntheses for **52** and **53**.[217, 218] They could be synthesized by a two step protocol via reduction of NTCDI's carbonyl groups to CH_2 groups with borane followed by oxidative aromatization with MnO_2 (Scheme 1.12).[219, 220] But **52** and **53** were too insoluble for further functionalizations.[221] They found application as bidentate ligands for coordination of metal ions or recognition of porphyrines in supramolecular coordination chemistry.[220, 222–224] Water solubility was achieved by synthesis of *N*-methylated or *N*-arylated biscationic systems, which served as graphene-exfoliation reagents[225] or DNA-sensing reagents[220] by making use of their DNA intercalation ability acompanied by high fluorescence quantum yields in aqueous systems.[226]

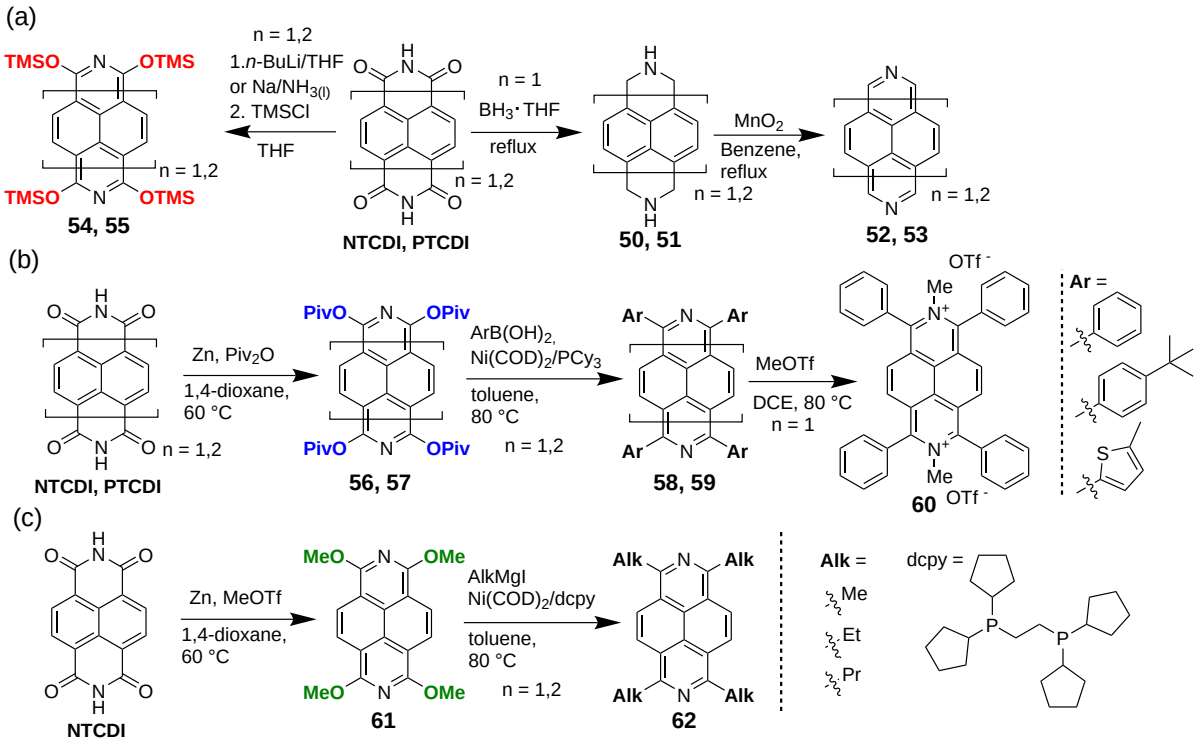

Scheme 1.12 Reductive functionalizations of NTCDI and PTCDI: (a) reductive silylation approach by Sachdev towards **54** and **55**[227] and two-step synthesis protocol towards **52** and **53**;[219] (b) and (c) reductive functionalization and post-functionalizations reported by Miyake.[228–230]

In 2011, Sachdev patented an approach way to reductively silylate NTCDI or PTCDI to soluble 1,3,6,8-tetrakis(trimethylsiloxy)-2,7-diazapyrene (**54**) or -diazaperopyrene (**55**) either by using *n*-butyl lithium in THF or sodium in liquid ammonia as reducing agent (Scheme 1.12).[227]
By employing zinc as non-toxic, easy to handle reducing agent, the group of Miyake published in 2018 a method for reductive pivaloation of NTCDI and PTCDI to **56** and **57**.[228] Since pivaloyl groups are known to react as leaving groups in Ni-catalyzed Suzuki-Miyaura cross-coupling reactions,[231, 232] they also reported several examples of tetraarylated diaza(pero)pyrenes (**58**,

59), allthough the scope of possible introducable aryl substituents was limited.[228] But they showed that the arylated tetraazapyrenes **58** have improved electron-transport capabilities compared to tetraarylated pyrenes due to the *N*-doping (Scheme 1.12).[228, 233] Furthermore, the dicationic species **60** was obtained by *N*-methylation with MeOTf.[229] One year later, they could apply this strategy to PTCDI in order to synthesize 1,3,8,10-tetraarylated diazaperopyrenes[234] and to anthracene diimides.[235] When methyl triflate was used instead of pivaloyl anhydride as trapping reagent in the reductive aromatization step, 1,3,6,8-tetramethoxy-2,7-diazapyrene (**61**) was obtained, which served as precursor for Ni-catalyzed KUMADA cross-couplings with alkyl grignards accessing tetraalkylated diazapyrenes (**62**), which could be used for fine tuning of the solid-state packing of diazapyrenes in crystalline state.[230]

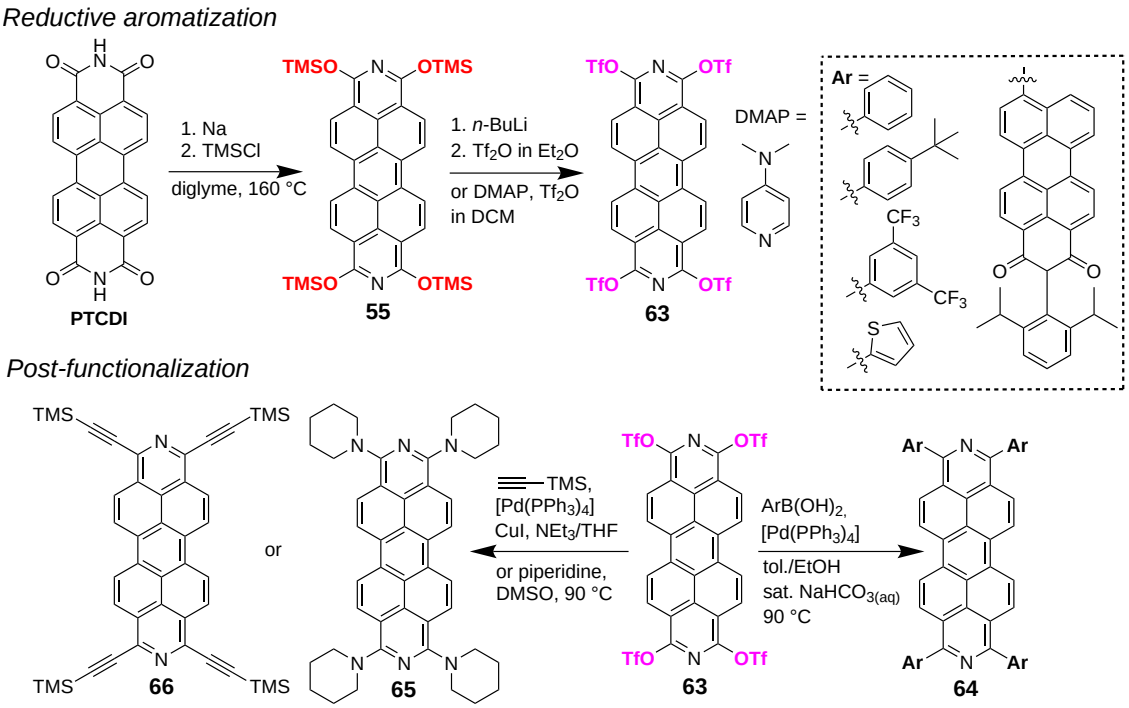

Scheme 1.13 Reductive silylation and *O*-triflination of PTCDI followed by Pd-catalyzed cross-coupling reactions and nucleophilic substitutions described by BAAL.[236, 237]

Meanwhile, a facile a reductive silylation approach of PTCDI developed by BAAL was also published.[236, 237] Herein, Na was used as reducing agent in high-boiling diglyme as solvent in order to furnish silylether **55** in up to 55% yield in a 70 g scale.[236, 237] Treatment of the silylether with *n*-butyl lithium in diethyl ether at low temperatures (-78 °C) gave the tetralithoxy derivative, which could be trapped *in situ* with triflate anhydride in order to furnish 1,3,8,10-tetratriflyl-diazaperopyrene (**63**) (Scheme 1.13). This could also be obtained in a one-pot procedure in dichloromethane using DMAP as activating reagent for both the siloxygroups and Tf_2O.[236, 237] As a big advantage in comparison to diazaperopyrene tetrapivaloate (**57**), the corresponding tetratriflate **63** showed to be not only more effective in SUZUKI-MIYAURA reactions. Different functionalized tetraarylated congeners **64** were obtained in higher yields and also post-functionalizations like SONOGASHIRA cross couplings to obtain tetraalkinylated **66** or nucleophilic substitution by piperidine toward **65** were possible (Scheme 1.13).[236, 237]

1.4.5 Kekulene and Cycloarenes

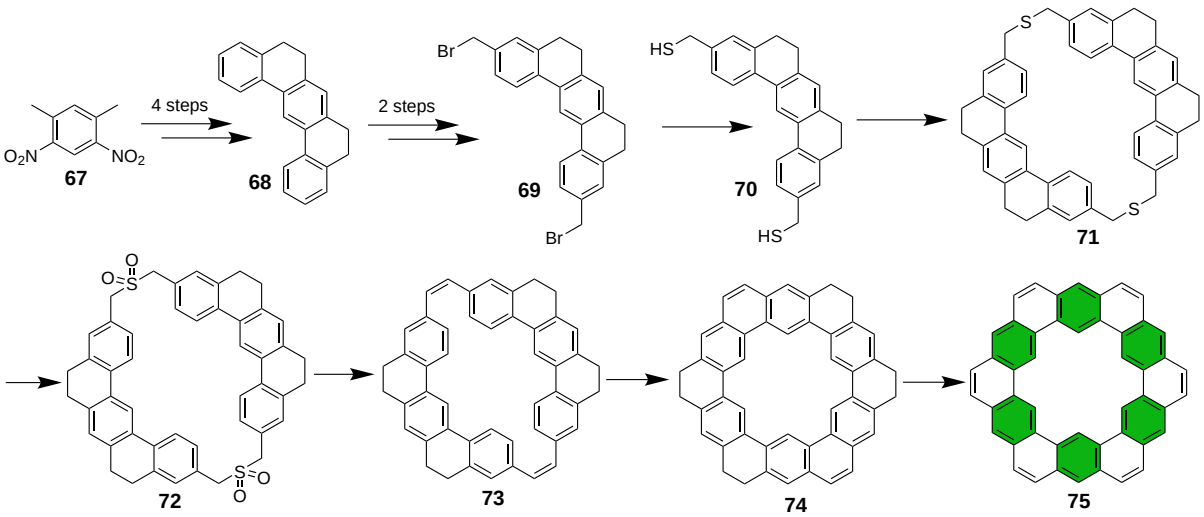

Scheme 1.14 Synthesis of Kekulene described by Diederich and Staab.[238] Clar electron sextetts are marked in green.

Cycloarenes have attracted broad scientific interest due to their unique geometrical properties (consisting of fully annulated benzene rings with inner cavity) and electronic properties (their π-electrons are delocalized within individual benzoid sextett rings rather than being globaly delocalized).[239, 240] The most prominent family member is Kekulene (**75**), which was first synthesized by Diederich and Staab in 1978 (Scheme 1.14).[238] Their multistep-procedure (12 steps in total) starts with dinitro xylene (**67**), which was converted over four steps to tetrahydrobenzo[*m*]tetraphene (**68**). This could be transferred via bromomethylation and thiolation into **70**, which could be nucleophilically coupled with **69** to cyclic **71**. After sulphur oxidation and desulphurization, cyclophane **73** was formed, which could be converted into **75** by photocyclization to **74** and subsequent oxidation. **75** could be obtained as orange crystals from hot trichlorobenzene.

Today, substituted derivatives of Kekulene[241] have been synthesized and additionally the larger homologues Septulene[242] and curved Octulene[243] have been synthesized during the last years as well as recently extended Kekulenes.[244] An access to a highly strained curved pentulene was possible in form of its π-extended polyaromatic congener.[245] Furthermore, nitrogen-doped Kekulene derivatives are known as substituted congeners with two[246] or six[247] nitrogen atoms in the inner cavity as well as three nitrogen atoms in the inner and outer positions.[248] In 2016, Müllen reported the synthesis of a large insoluble C216 nanographene as extended coronoid and extended version of Kekulene.[249]

Interestingly, all these selected examples for cycloarenes follow the Clar model of a maximum number of π-electron sextetts and thus tend not to follow a global model of aromaticity (referred to as superaromaticity[250, 251]). This is indicated furthermore by the fact that the inner protons of the cycloarenes are deshilded in proton NMR, whereas the concept of a global aromaticity model predicts a diamagnetic anisotropy, leading to magnetically unaffected shielded inner protons like in the case of annulenes.[252]

To the knowledge at the start of this doctoral thesis in 2017, there was a lack of reported syntheses and characterizations of larger π-extended cycloarenes.

2 Purpose of this work

In this doctoral thesis, two main research areas are investigated:
1) the synthesis of novel fourfold substituted (diaza-)ropyrene structures by reductive aromatization and their characterization and 2) the design, synthesis and characterization of precursors for novel *on-Surface* synthesized porous nanographenes or graphene nanoribbons.

2.1 (Diaza-)ropyrenes by reductive aromatizations

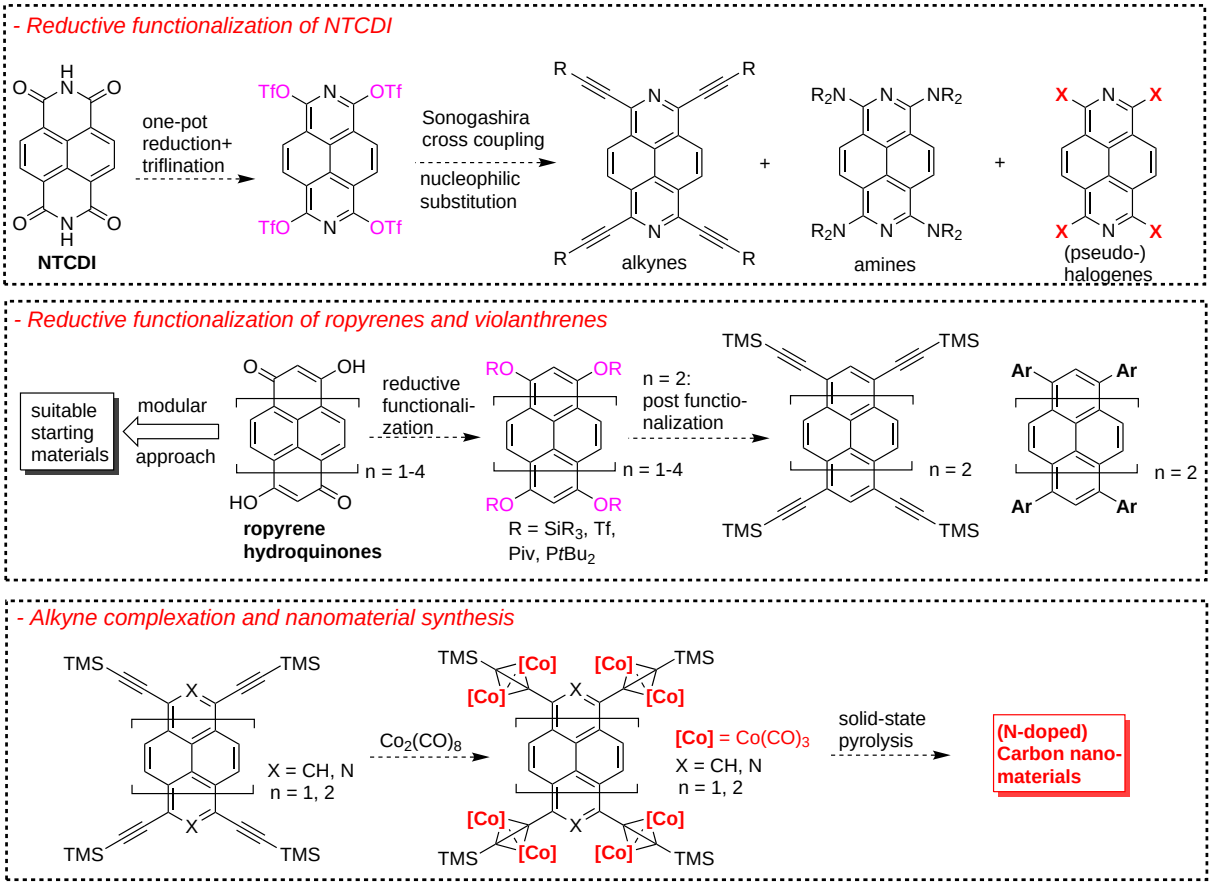

Scheme 2.1 Main goals for the reductive access to functionalized ropyrenes.

Following up previous work by Baal in our research group regarding reductive silylation of PTCDI using Na as reductant and subsequent triflination/post-functionalization and with respect to contemporaneous reductive pivaloations of NTCDI/PTCDI by Miyake, novel rylene-type PAH structures are accessed by reductive functionalization approaches. Four main goals are focused (*c.f.* Scheme 2.1):

- Employment of zinc as easy to handle and air stable reducing agent for reductive functionalization of NTCDI and dihydroxy ropyrenequinones.
- Development of one-pot reductive triflination synthesis strategies for NTCDI and further

functionalization of the obtained diazapyrene tetratriflate *via* SONOGASHIRA cross-coupling and nucleophilic substitution.

- Reductive generation and functionalization of purely carbon based peropyrenes and their higher homologues terropyrenes and quarterropyrenes and also related violanthrenes. Especially for the chemical class of peropyrenes, post-functionalization approaches (*e.g.* cross couplings or complexation reactions) were established.
- Metalorganic complex synthesis and characterization of Co-carbonyl complexes from novel (diaza)-ropyrene tetraalkynes and their solid state pyrolysis towards novel (nitrogen doped) carbon nanomaterials as well as their material-chemical characterization (SEM, TEM, powder-XRD).

The synthesized PAHs are characterized by means of X-ray crystallography in solid state and in solution. Therefore, the frontier molecular energies are experimentally determined by cyclovoltammetry and their optical HOMO-LUMO energy gaps by UV-Vis and phololuminescence spectroscopy. Furthermore, the dyes are characterized by determination of their extinction coefficients and fluorescence quantum yields. (TD-)DFT calculations are performed in order to theoretically understand fundamental trends in spectroscopy and to theoretically model the frontier molecular orbitals and their energies. Based upon experimental work and theoretical calculations, a structure-properties relation should be deduced in order to understand the substituent's impact on the (opto-)electronic properties of the resulting tetrasubstituted ropyrenes.

2.2 Precursors for novel nanographene structures

In corporation with the surface science group of Prof. GOTTFRIED, novel nanographene structures are developed. The main task is the development of suitable (halogenated) precursors that can form nanographenes and graphene nanoribbons by ULLMANN reactions and cyclodehydrogenations after UHV deposition on single crystalline noble metal surfaces. The focus lies on the generation of porous 2D-, 1D- and 0D-graphene structures with defined ratio, structure and arrangement of the pores. Of special interest are stable molecular precursors that are capable to form porous cycloarenes derived from the archetype Kekulene with armchair or zig-zag edges as well as fractal 2D structures (Scheme 2.2). Since the most atomically precise way to build up nanographene on metal surfaces is the *bottom-up* approach, the synthesis of precursor libraries should also be beneficial in order to understand the role of the precursor geometry for the *on-surface* reaction outcome in order to improve *bottom-up* synthesis strategies.
Additionally, parallel to the *on-surface* generation of molecular porous nanographenes, attempts for the synthesis and characterization of molecular nanographenes in solution are performed by modifying the precursors with solubilizing groups, since only few reported examples of porous nanographenes in solution are known to date.

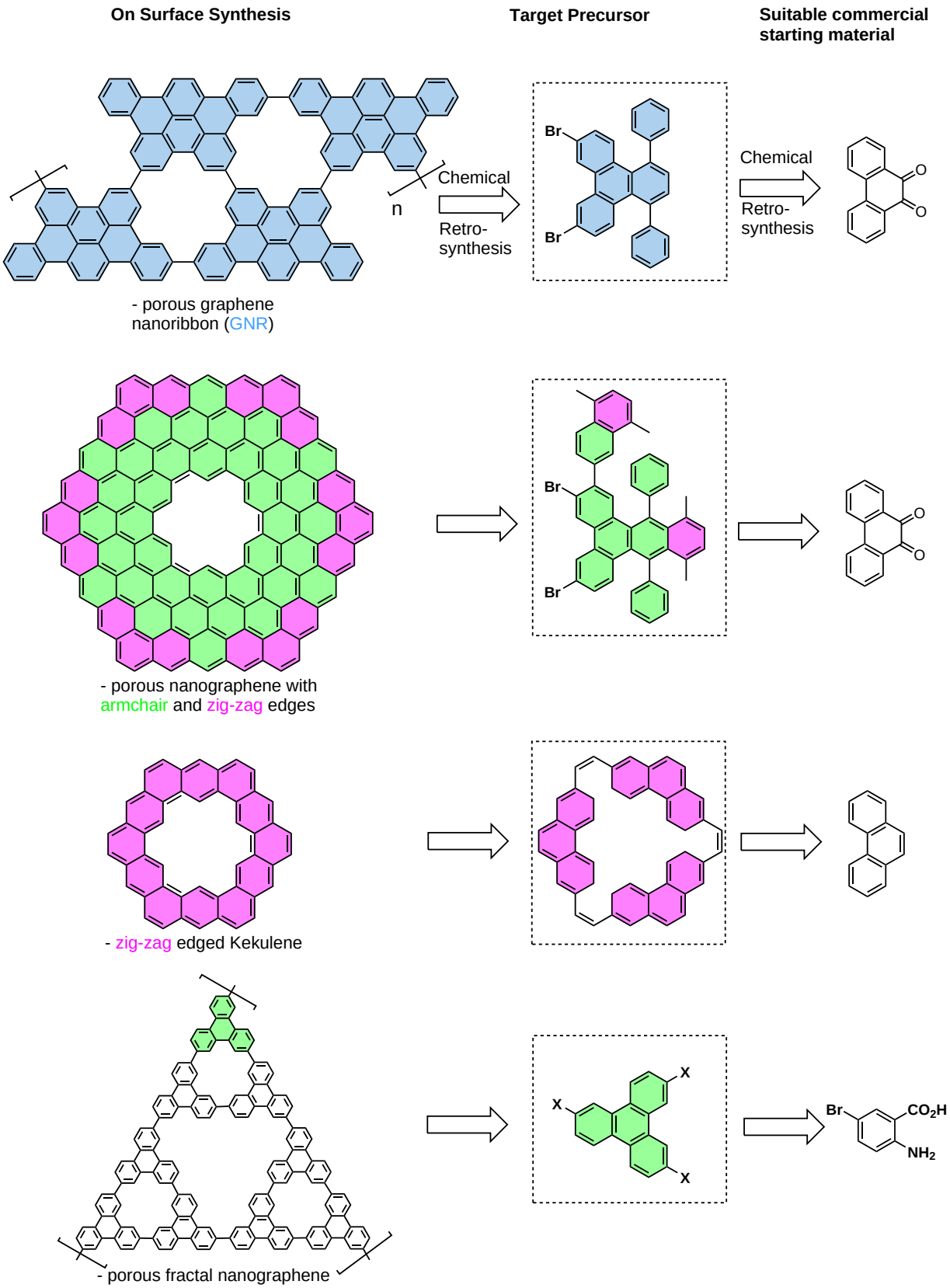

Scheme 2.2 Main retrosynthetical steps for target nanographenes and suitable precursors. The aimed structures are porous GNR, porous cyclic nanographenes with different edge structures and Sierpiński fractal structures.

3 Cumulative Part

When printing this PhD thesis, five publication with me as first author (Publication 1-5) were accepted. In Publication 6, I am equally contributing first author and in Publication 7 as well as in manuscripts 8 and 9 I was co-author.

This cumululative chapter devides into two thematic groups of publications. Publications 1-5 describe an approach for reductive aromatizations of (diaza-)ropyrenes and post-functionalizations. Publication 1 introduces the reductive silylation of dihydroxy-ropyrenequinones using zinc as reducing agend in order to obtain tetrafold silylated ropyrenes from pyrene up to quarterropyrene. In Publication 2, the functional class of tetrafold peropyrenes is in-dept studied with different examples of reductive aromatizations as well as post-functionalizations as Suzuki- or Sonogashira-cross couplings. In Publication 3 and 5, these concepts are applied on reductive functionalization of naphthalene diimide (Publication 3) and violanthrone 79 (Publication 5). Publication 4 describes the cobalt carbonyl complex synthesis from different (diaza-)ropyrene alkynes and their application in the solid-state pyrolysis towards carbon nanomaterials. This work follows up previous work of Dr. Baal in the group of Prof. Dr. Sundermeyer, who investigated the reductive functionalization of perylene diimide (PTCDI). All synthetic work as well as characterization (optical spectroscopy and cyclovoltammetry) are done by myself if not noted otherwise. Furthermore, DFT calculations were performed by myself with the purpose to theoretically support and understand the observed trends of the electronical impact of the applied substituents.

Publications 6-8 are cooperation works together with surface scientists (especially Dr. Fan in the group of Prof. Dr. Gottfried in Marburg). The *on-Surface* reactions of different organic precursors synthesized by myself towards porous nanographene C108 (Publication 6 and 8), Kekulene (Publication 7) or surface controlled generation of either porous GNRs or nanographene (Publication 9) is described. The described used precursors required multi-step organic syntheses and retrosynthetical planning performed by myself as well as purification and full characterization of the precursors.

Each publication is summarized briefly and the respective article is appended and also relevant supporting experimental procedures (synthesis) are shown in this chapter. Permissions and supporting material with NMR spectra and theoretical calculations of the publications are shown in the appendix. In chapter 3.10, yet unpublished additional work is briefly discussed. The shown crystal structures were solved and refined by T. Vollgraff and the solution is part of his PhD Thesis.

3.1 Publication 1: Access to functionalized Pyrenes, Peropyrenes, Terropyrenes and Quarterropyrenes via Reductive Aromatization

Citation: S. Werner, T. Vollgraff, J. Sundermeyer, *Angew. Chem.* **2021**, *133*, 13743-13748; *Angew. Chem. Int. Ed.* **2021**, *60*, 13631-13635.[A]

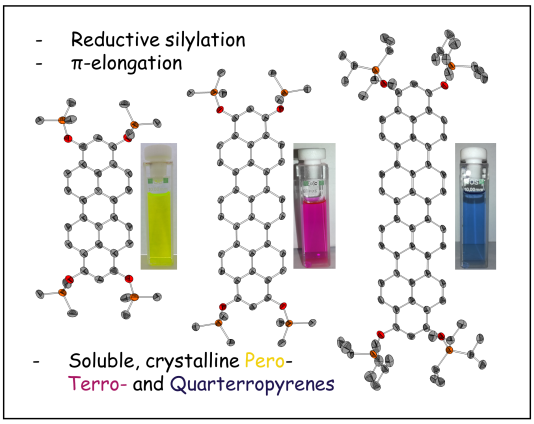

Summary: This communication deals with the reductive access to novel derivatives of the ropyrene family: tetrasubstituted pyrene-, peropyrene-, terropyrene- and quarterropyrene-silyl ethers are described. Within this context, the first published example of a quarterropyrene was synthesized and characterized. The corresponding ropyrene scaffold was built up by a modular approach: brominated hydroxy-perinaphthenone was reacted with (bi-)naphthyl-bisboronic acid pinacolesters in a Suzuki-Miyaura reaction followed by a caesium-hydroxide mediated air oxidation of the resulting oligo-naphthyls. The key step was a reductive silylation of the insoluble hydroxy-ropyrenequinones with Zn/R_3SiCl to the corresponding fourfold silylated ropyrenes. Bulky TIPS-groups enable a high solubility so that even a quarterropyrene silylether is characterizable in solution. The resulting ropyrenes were characterized via X-ray crystallography showing that π-stacking determines their arrangement in solid state. Furthermore, UV-Vis and photoluminescence measurements are discussed in the paper, showing a bathocromical shift of absorption and emission maxima of approx 80 nm per additional naphthalene unit as well as nearly linearly increasing extinction coefficients. Cyclovoltammetry supported by DFT calculations shows lower oxidation potentials and thus lower lying HOMO levels for the higher homologues, indicating a higher oxidation tendency. This was in-depth studied by an oxidation titration of quarterropyrene in order to spectroscopically characterize its radical cation.

Own Contribution: All experimental work was done by myself as well as characterization by spectroscopical (UV-Vis/PL) and electrochemical (CV/DPV) measurements and (TD-)DFT calculations. T. Vollgraff solved and refined the crystal structures. NMR and mass spectra were recorded by service departments of the faculty. Prof. Dr. J. Sundermeyer initiated and supervised this study and was available as valuable discussion partner. The manuscript was written by myself with valuable feedback of Prof. Dr. J. Sundermeyer.

[A]Reproduced with permission of S. Werner, T. Vollgraff, J. Sundermeyer, *Angew. Chem. Int. Ed.*, **2021**, *133*, 13743-13748, Copyright ©2021, Rights Managed by Wiley VCH.

GDCh Communications Angewandte International Edition Chemie

Check for updates

How to cite: Angew. Chem. Int. Ed. 2021, 60, 13631–13635
International Edition: doi.org/10.1002/anie.202100686
German Edition: doi.org/10.1002/ange.202100686

Organic Dyes

Access to Functionalized Pyrenes, Peropyrenes, Terropyrenes, and Quarterropyrenes via Reductive Aromatization

*Simon Werner, Tobias Vollgraff, and Jörg Sundermeyer**

In memory of Professor Siegfried Hünig

Abstract: *Herein we report a versatile concept for the synthesis of fourfold functionalized, soluble pyrenes, peropyrenes, terropyrenes, and quarterropyrenes. They were obtained by a modular stepwise approach towards the rylene scaffold via Suzuki–Miyaura cross coupling, oxidative cyclodehydrogenation in the presence of caesium hydroxide under air, and finally zinc-mediated reductive silylation. The silylated reaction products were characterized by X-ray crystallography. The first example of a synthesized and crystallized quarterropyrene is presented and its oxidation reaction investigated. The functionalized ropyrenes were systematically characterized by means of UV/Vis–NIR and photoluminescence spectroscopy showing a bathochromic shift of 80 nm per naphthalene unit and a nearly linear increase of the extinction coefficients. Cyclic voltammograms and DFT calculations identify them as electron-rich dyes and show a narrowing of the electrochemically determined HOMO–LUMO gap and lower oxidation potentials for the higher homologues.*

Polyaromatic hydrocarbons (PAHs) offer a huge variety of applications related to their unique (opto-)electronic properties, for example in materials for organic electronics and photovoltaics.[1] Studies elucidating structure–property relations gave rise to the synthesis of nanographenes with defined structures and tailored properties.[2] Especially the edge structure and width determine their electronical properties (band structure).[3] The family of poly-perinaphthalenes (rylenes, see Figure 1 b), also known as 5-armchair graphene nanoribbons (5-AGNRs), is a broadly studied class of PAHs.[4] Compared to other GNRs their simple structure, broad spectral light absorbance[5] and singlet fission properties,[6] as well as length-dependent band gap sizes[7] were motivation for intensive research efforts.[8] With regard to molecular and soluble rylene compounds beyond the archetypical family of perylene diimides (PDIs, see Figure 1 a),[9] higher homologue rylene diimides were synthesized by the group of Müllen using a modular approach of cross couplings starting from halogenated perylene or naphthalene monoimides and their corresponding boronic acid esters followed by oxidative cyclizations to form the rylenes.[10–15] Thereby, rylene diimides with up to eight naphthalene units were formed, and also terrylene and quarterrylene were accessed.[10–17]

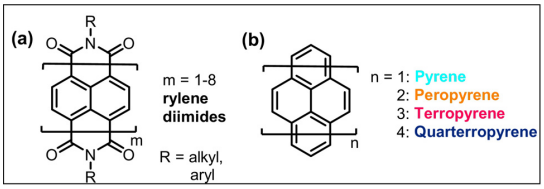

Figure 1. Chemical structures of a) the substance class of rylene diimides and b) pyrene and its higher homologues.

Another model system for molecular rylenes is peropyrene (Figure 1 b, $n = 2$).[18] Peropyrene is a potential candidate for singlet fission materials[19] and effective synthesis strategies for substituted peropyrenes were developed during the past years.[17,20–22] Terropyrenes, for example, the unsubstituted stem system[23] or bent varieties for cyclophane syntheses,[24] are rare in literature. All published strategies required multi-step organic syntheses, especially for accessing the higher homologues, terropyrenes.[21,22,25,26] Key of the synthesis route reported by Chalifoux and co-workers are π-extentions of aromatic systems using two- or tetrafold alkynylated precursors in acid-mediated[21,22,27] or $InCl_3$-catalyzed benzannulations.[25]

Inspired by the modular construction principle of higher rylene diimide dyes[11,13,15] and the novel reductive functionalization approaches for naphthalene diimide (NTCDI)[28] and perylene diimide (PTCDI)[29,30] in our group and in the group of Miyake, we intended to reductively access higher homologue ropyrenes. The precursors **2**, **3**, **11**, and **12** of the final peropyrenes, terropyrenes, and quarterropyrenes are synthesized in analogy to the modular synthesis of soluble, liquid crystalline dihydroxy-ropyrene-quinones reported by Buffet and Bock (Scheme 1).[31] Peropyrenequinone **2** was directly reduced and silylated, reacting with Zn as reducing agent in the presence of trimethylsilyl chloride to the orange air sensitive peropyrene silylether **4**. Zinc turned out to be the best reducing agent. It is readily available, non-toxic, and processable even under non-inert conditions. For reductive silylation of the smaller dihydroxy pyrenequinone **2** we could introduce four triisopropylsilyl groups, leading to highly soluble pyrene-tetrasilyl ether **5** in rather poor yield. Next,

[*] S. Werner, T. Vollgraff, Prof. Dr. J. Sundermeyer
Fachbereich Chemie and Material Science Center (WZMW)
Philipps-Universität Marburg
Hans Meerwein Strasse 4, 35032 Marburg (Germany)
E-mail: JSU@staff.uni-marburg.de
Supporting information and the ORCID identification number(s) for the author(s) of this article can be found under: https://doi.org/10.1002/anie.202100686.

GDCh Communications Angewandte International Edition Chemie

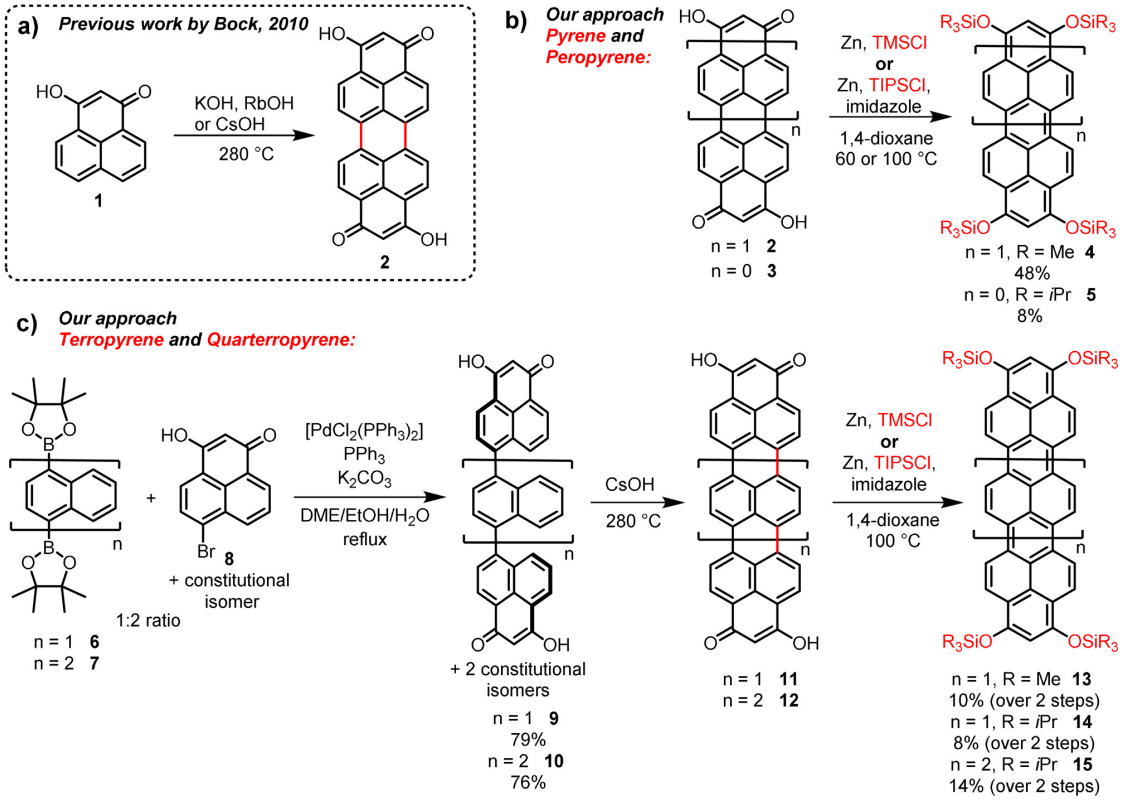

Scheme 1. a) Previously reported synthesis of dihydroxy-peropyrenequinone (**2**); b) our approaches for the synthesis of peropyrene-silylether **4** and pyrene-silylether **5** by reductive functionalization; c) the higher homologue terropyrene-silylethers **13** and **14** and quarterropyrene-silylether **15** by modular approaches.

we turned our attention to the application of a similar reduction protocol to obtain the higher homologues of **2**, terropyrenequinone **11** and quarterropyrenequinone **12**.

11 and **12** were synthesized in a facile two-step protocol starting with bis-boronic acid pinacol esters **6**[32] and **7**[33] together with peri-brominated hydroxyphenalenone **8** under standard Suzuki–Miyaura coupling conditions in a 1:2 ratio. The resulting ter- and quarternaphthyls **9** and **10** could be isolated as inseparable isomer mixture (see SI) by a simple precipitation due to protonation with diluted acetic acid and subsequent washing with methanol. Non-planar **9** and **10** were heated in a CsOH melt for three hours to 280 °C in a Ni-crucible on air until the gas evolution ceased. We chose CsOH as base because of the improved intercalation and interaction capabilities of caesium cations with intermediately formed aromatic anions. **11** and **12** were isolated as insoluble dark blue solids that were directly used for further transformations. Surprisingly, **11** and **12** reacted under similar conditions as **2** with zinc and trialkylsilyl chlorides in dioxane despite their insolubility at 100 °C. The resulting silylated products were soluble since their capability of π–π stacking is reduced due to the sterically demanding silyl groups. Hence, a similar terropyrene-trimethylsilylether **13**, as a higher homologue to **4**, could be isolated as purple-red solid. After activating triisopropylsilyl chloride with imidazole, a reductive silylation of **11** and even **12** yielded the air stable terropyrene-triisopropyl silylether **14** and royal blue colored quarterropyrene-triisopropylether **15** with superior solubility, high purity, however low yields. Both **14** and **15** could be isolated by column chromatography with dichloromethane. We further synthesized a congener of **15** with *n*-butyl groups in both terminal positions and TMS groups (**S4**) in order to improve the solubility, but the solubilizing effect of non-bulky butyl groups was not significantly more effective. Unfortunately, all attempts to synthesize a higher homologue penterropyrene were not successful so far, since the corresponding penterropyrene-quinone was too insoluble for further transformations. The good solubility of our silylated rylenes **4**, **13**, and **15** in chlorinated solvents made it possible to obtain X-ray diffractive single crystals via slow gas phase diffusion of *n*-pentane (Figure 2). Trimethylsilyl ethers **4** and **13** crystallize in the monoclinic space group $P2_1/c$ with π–π stacking pairs ($d_{\pi\text{-}\pi}$ = 3.30 Å (**4**) and 3.64 Å (**13**)) of molecules oriented in a herringbone arrangement for **13**. Quarterropyrene **15** crystallizes in the monoclinic spacegroup $P2_1/n$ being the first investigated quarteropyrene in the crystalline state to the best of our knowledge. Its bulkier TIPS groups do not prevent the face-to-face π–π stacking interactions in the solid state

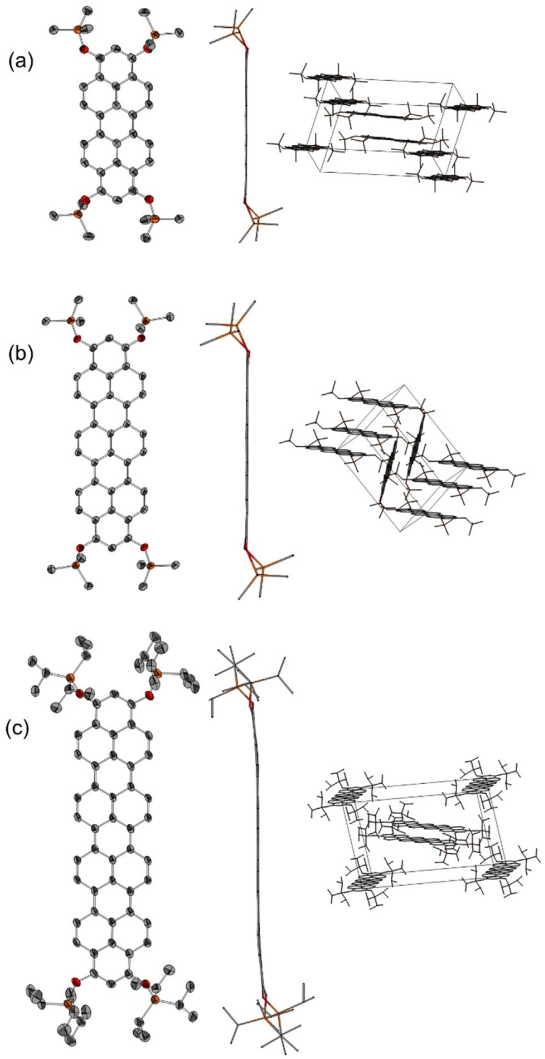

Figure 2. Solid state structures (left: front view, center: side view, and right: packing structure) of a) **4**; b) **13**, and c) **15**. Hydrogen atoms are omitted for clarity and thermal ellipsoids are shown at the 50% probability level.[38]

($d_{\pi-\pi}$ = 3.36 Å) but induce a slight bending of the rylene backbone in comparison to the trimethylsilyl-substituted homologues **4** and **13** and lead to a transversal intermolecular displacement in order to minimize steric repulsions.

The (opto-)electronical properties of the rylenes **4**, **5**, **13**, **14**, and **15** were investigated by UV/Vis–NIR and photoluminescence spectroscopy as well as cyclovoltammetry. The optical spectra and cyclovoltammogramms of both quaterropyrene silylethers **13** and **14** were almost identical (see Figure S7). Typical for rylene dyes,[11,13] the absorption spectra are dominated by the lowest-energy $S_1 \leftarrow S_0$-transition. The absorption maxima (λ_{max}) and extinction coefficients (ε) increase nearly linearly with each additional naphthalene unit [a bathochromic shift of about 80 nm and an increase of the extinction coefficient from λ_{max} = 390 nm (ε = 24 500 L mol^{-1} s^{-1}) for **5** to λ_{max} = 634 nm (ε = 128 200 L mol^{-1} s^{-1}) for **15** (Figure 3a)] with extinction coefficients in slightly smaller magnitudes compared to the related rylene diimides.[11,13] All four compounds showed nearly no concentration-dependent absorption maxima (see Figure S2–S6). TD-DFT (see Figure S13) supports the trend also regarding the oscillator strengths of the λ_{max} transitions. The mirrored emission spectra reveal a similar trend with Stokes shifts of around 15 nm. **4**, **13**, and **15** show strong vibronic progressions indicating, together with the narrow Stokes shift, small reorganization energies.[34] A broadening of the bands can be observed for the higher homologues. Measured fluorescence quantum yields (Φ_{PL}, see SI) were only moderately high in case of **4** (0.30), lower for **13** (0.08) and **14** (0.06), and undetectably low in **4** and **15** with bulky rotating TIPS groups most likely deactivating the fluorescence through reorganization energy loss. The predictable evolution of optical properties can also be rationalized with the Kohn–Sham molecular orbitals of the HOMO and LUMO for **4**, **5**, **13**, and **15**, being of similar modular symmetry (Figure 3d). The frontier molecular orbital energies were experimentally assigned using cyclic voltammetry (Figure 3c). The electron-rich dyes **4**, **5**, **14**, and **15** show two pronounced and quasi-reversible oxidation potential waves, whereas only **14** shows one and **15** shows two not fully reversible reduction potential waves within the electrochemical window of dichloromethane. In comparison to reported arylated pero- and terropyrenes, **5** and **14** show lower oxidation potentials and are therefore more electron-rich.[25] Additionally, a narrowing of the electrochemically determined HOMO–LUMO gap with the growing π-system could be observed. The experimental HOMO energies were referenced to the vacuum energy level of the ferrocene/ferrocenium redox couple (−4.8 eV,[35] see Figure S8–S12) and the LUMO energy was accessed with the help of the optical HOMO–LUMO gap (determined from the intersection wavelength of normalized UV/Vis and PL spectra[36]). Both experiment and theory show an energy gap (E_g) narrowing from E_g = 3.02 eV (theory 3.48 eV) for pyrene **5** to 1.93 eV (theory 1.96 eV) to **15**, respectively (see Table 1). This is indicated by higher HOMO and lower LUMO energies (from experimentally −5.01 eV (HOMO) and −2.04 eV (LUMO) of **5** to −4.62 eV (HOMO) and −2.73 eV (LUMO) for **15**), with theoretical values supporting the observed trends. In comparison with arylated ropyrenes, silylether substitution leads to higher HOMO levels.[25]

The high HOMO value of **15** and also the existence of a non-zero baseline in the NIR region of the UV/Vis spectrum gave rise to the assumption that minor amounts of the oxidation product **[15]**$^+$ are present after column chromatography with dichloromethane, also observed for other electron-rich PAHs and resulting from traces of acid in the presence of air.[37] In order to study the oxidation product of **15**, we added the oxidant nitrosyl tetrafluoroborate ($NOBF_4$) in a UV/Vis–NIR titration experiment. Upon addition of excess (10 equiv) of $NOBF_4$ a gradual color change from blue to turquoise green and broad NIR absorption bands appearing at 820 and 1050 nm (Figure 4) were observed. Addition of

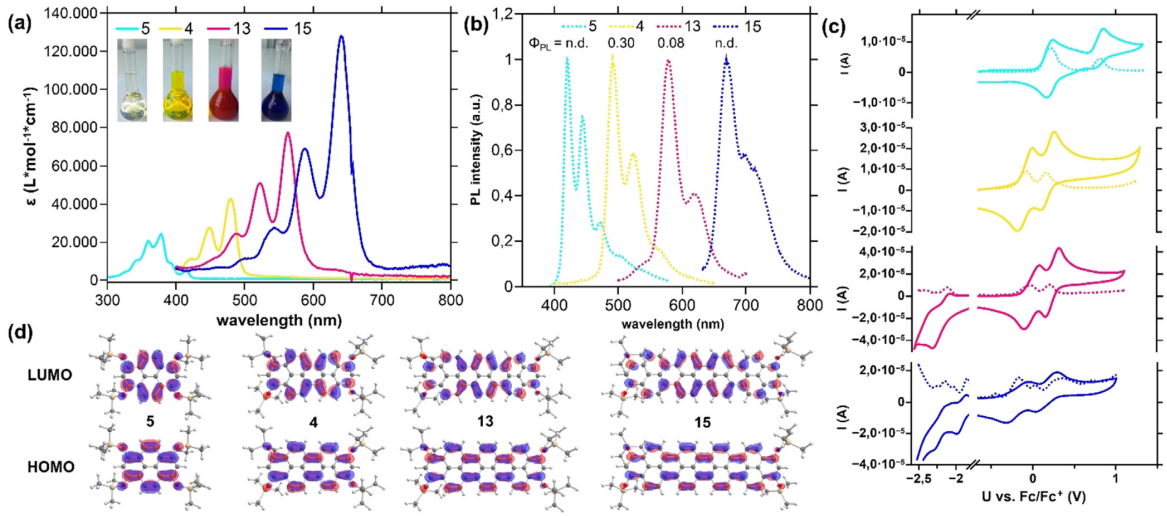

Figure 3. a) UV/Vis–NIR spectra of **4**, **5**, **13**, and **15** ($c \approx 1 \times 10^{-5}$ M) in CH_2Cl_2 and photographs of the corresponding solutions (inset). b) Normalized emission spectra of **4**, **5**, **13**, and **15** in CH_2Cl_2 ($c \approx 1 \times 10^{-7}$ M, $\lambda_{ex.} = 350$ nm). c) Cyclic voltammograms of **4**, **5**, **14**, and **15** (measured in CH_2Cl_2, 0.1 M *n*-Bu_4NPF_6, 100 mV s^{-1} scan rate, glassy carbon working electrode, platinum reference electrode) and corresponding differential pulse voltammograms (DPV, dashed lines, 10 mV s^{-1} scan rate). d) HOMO and LUMO of **5**, **4**, **13**, and **15** calculated by DFT (TIPS groups simplified by TMS, B3LYP, def-2/TZVPP, isoval. 0.03 a.u.).

Table 1: Summary of experimentally and theoretically determined HOMO and LUMO energies of **4**, **5**, **14**, and **15**.

	$E_{HOMO,exp.}$ [eV][a]	$E_{LUMO,exp.}$ [E_g] [eV][b]	$E_{HOMO,theo.}$ [eV][c]	$E_{LUMO,theo.}$ [E_g] [eV][c]
5	−5.01	−2.04 [3.02]	−4.59	−1.11 [3.48]
4	−4.71	−2.16 [2.55]	−4.54	−1.85 [2.69]
14	−4.80	−2.66 [2.14]	−4.32	−2.02 [2.20]
15	−4.62	−2.73 [1.89]	−4.27	−2.33 [1.94]

[a] Electrochemically determined oxidation and reduction potentials referring to Fc/Fc^+ as internal standard ($E_{HOMO}(fc) = -4.8$ eV): $E_{HOMO,exp} = -4.8$ eV $- E_{1/2,ox1}$. [b] Determined HOMO and LUMO energies based on the optical HOMO–LUMO energy gap [E_g]: $E_{LUMO,exp} = E_{HOMO,exp} + E_{g,opt}$. [c] Calculated HOMO and LUMO energies, level of theory: def2-TZVPP/B3LYP, for carthesian coordinates (XYZ) of optimized geometries see Table S1–S4.

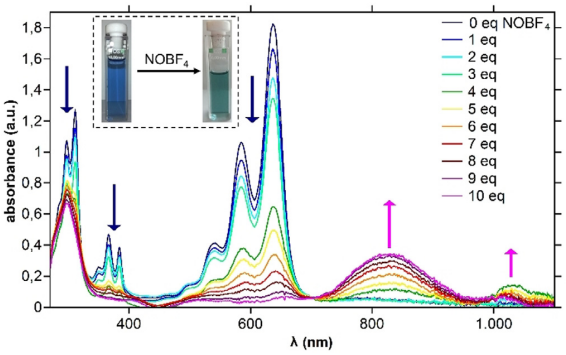

Figure 4. Changes in the UV/Vis–NIR absorption spectrum of **15** during titration with $NOBF_4$ in CH_2Cl_2/acetonitrile. Inset: Color change after addition of 10 equiv of $NOBF_4$.

more than 10 equiv $NOBF_4$ had no further effect. Using ^{1}H NMR, the formation of a paramagnetic compound could be observed by the absence of distinct signals. TD-DFT calculations (see SI, Figure S15) of **[15]**$^+$ describe the novel band at 1050 nm as SOMO–LUMO transition.

In summary, we report a facile and efficient access to the higher homologues of peropyrene by a modular and scalable synthetic bottom-up approach with a reductive aromatization by Zn/R_3SiCl as a key step towards functionalized, soluble, and easily isolable electron-rich rylene silylethers. Supported by comprehensive experimental spectroscopy and spectrometry, the influence of the enlargement by naphthalene units on the HOMO–LUMO gap was rationalized by spectroscopy, CV, and DFT calculations. As $OSiR_3$ groups can be converted to OTf functionalities for further transformations,[30] we are convinced that our new synthesis strategy allows an efficient general synthetic entry into novel functionalized PAHs for high-performance organic electronic materials.

Supporting Information available: Additional experimental details, NMR spectra, CV/DPV measurements, UV/Vis and TD-DFT spectroscopy, cartesian coordinates of calculated structures (XYZ), and XRD data. The CIF files of the presented structures are provided.

Acknowledgements

Financial support by the LOEWE Program of Excellence of the Federal State of Hesse (LOEWE Focus Group PriOSS "Principles of On-Surface Synthesis") is gratefully acknowledged. Open access funding enabled and organized by Projekt DEAL.

Conflict of interest

The authors declare no conflict of interest.

Keywords: crystallography · cyclovoltammetry · fluorescence · organic dyes · reductive aromatization

[1] a) S. Yang, R. E. Bachman, X. Feng, K. Müllen, *Acc. Chem. Res.* **2013**, *46*, 116 – 128; b) M. J. Allen, V. C. Tung, R. B. Kaner, *Chem. Rev.* **2010**, *110*, 132 – 145; c) T. M. Figueira-Duarte, K. Müllen, *Chem. Rev.* **2011**, *111*, 7260 – 7314; d) J. Mei, Y. Diao, A. L. Appleton, L. Fang, Z. Bao, *J. Am. Chem. Soc.* **2013**, *135*, 6724 – 6746; e) J. Wu, W. Pisula, K. Müllen, *Chem. Rev.* **2007**, *107*, 718 – 747.

[2] a) S. Seifert, K. Shoyama, D. Schmidt, F. Würthner, S. Seifert, K. Shoyama, D. Schmidt, F. Würthner, *Angew. Chem. Int. Ed.* **2016**, *55*, 6390 – 6395; *Angew. Chem.* **2016**, *128*, 6500 – 6505; b) A. Narita, X.-Y. Wang, X. Feng, K. Müllen, *Chem. Soc. Rev.* **2015**, *44*, 6616 – 6643; c) Q. Chen, S. Thoms, S. Stöttinger, D. Schollmeyer, K. Müllen, A. Narita, T. Basché, *J. Am. Chem. Soc.* **2019**, *141*, 16439 – 16449; d) J. Liu, B.-W. Li, Y.-Z. Tan, A. Giannakopoulos, C. Sanchez-Sanchez, D. Beljonne, P. Ruffieux, R. Fasel, X. Feng, K. Müllen, *J. Am. Chem. Soc.* **2015**, *137*, 6097 – 6103.

[3] a) V. Barone, O. Hod, G. E. Scuseria, *Nano Lett.* **2006**, *6*, 2748 – 2754; b) L. Yang, C.-H. Park, Y.-W. Son, M. L. Cohen, S. G. Louie, *Phys. Rev. Lett.* **2007**, *99*, 186801.

[4] Y.-W. Son, M. L. Cohen, S. G. Louie, *Phys. Rev. Lett.* **2006**, *97*, 216803.

[5] T. M. Halasinski, J. L. Weisman, R. Ruiterkamp, T. J. Lee, F. Salama, M. Head-Gordon, *J. Phys. Chem. A* **2003**, *107*, 3660 – 3669.

[6] T. Minami, S. Ito, M. Nakano, *J. Phys. Chem. Lett.* **2012**, *3*, 2719 – 2723.

[7] a) J. L. Brédas, *J. Chem. Phys.* **1985**, *82*, 3808 – 3811; b) A. Kimouche, M. M. Ervasti, R. Drost, S. Halonen, A. Harju, P. M. Joensuu, J. Sainio, P. Liljeroth, *Nat. Commun.* **2015**, *6*, 10177.

[8] a) T. Kitao, M. W. A. MacLean, K. Nakata, M. Takayanagi, M. Nagaoka, T. Uemura, *J. Am. Chem. Soc.* **2020**, *142*, 5509 – 5514; b) H. Zhang, H. Lin, K. Sun, L. Chen, Y. Zagranyarski, N. Aghdassi, S. Duhm, Q. Li, D. Zhong, Y. Li, K. Müllen, H. Fuchs, L. Chi, *J. Am. Chem. Soc.* **2015**, *137*, 4022 – 4025.

[9] F. Würthner, C. R. Saha-Möller, B. Fimmel, S. Ogi, P. Leowanawat, D. Schmidt, *Chem. Rev.* **2016**, *116*, 962 – 1052.

[10] Y. Avlasevich, S. Müller, P. Erk, K. Müllen, *Chem. Eur. J.* **2007**, *13*, 6555 – 6561.

[11] L. Chen, C. Li, K. Müllen, *J. Mater. Chem. C* **2014**, *2*, 1938 – 1956.

[12] N. G. Pschirer, C. Kohl, F. Nolde, J. Qu, K. Müllen, *Angew. Chem. Int. Ed.* **2006**, *45*, 1401 – 1404; *Angew. Chem.* **2006**, *118*, 1429 – 1432.

[13] T. Weil, T. Vosch, J. Hofkens, K. Peneva, K. Müllen, *Angew. Chem. Int. Ed.* **2010**, *49*, 9068 – 9093; *Angew. Chem.* **2010**, *122*, 9252 – 9278.

[14] D. Uersfeld, S. Stappert, C. Li, K. Müllen, *Adv. Synth. Catal.* **2017**, *359*, 4184 – 4189.

[15] Z. Yuan, S.-L. Lee, L. Chen, C. Li, K. S. Mali, S. de Feyter, K. Müllen, *Chem. Eur. J.* **2013**, *19*, 11842 – 11846.

[16] a) A. Bohnen, K.-H. Koch, W. Lüttke, K. Müllen, *Angew. Chem. Int. Ed. Engl.* **1990**, *29*, 525 – 527; *Angew. Chem.* **1990**, *102*, 548 – 550; b) E. Clar, *Chem. Ber.* **1948**, *81*, 52 – 63.

[17] R. Thamatam, S. L. Skraba, R. P. Johnson, *Chem. Commun.* **2013**, *49*, 9122 – 9124.

[18] E. Clar, *Ber. Dtsch. Chem. Ges. A/B* **1943**, *76*, 328 – 333.

[19] V. M. Nichols, M. T. Rodriguez, G. B. Piland, F. Tham, V. N. Nesterov, W. J. Youngblood, C. J. Bardeen, *J. Phys. Chem. C* **2013**, *117*, 16802 – 16810.

[20] a) K. Uchida, T. Kubo, D. Yamanaka, A. Furube, H. Matsuzaki, R. Nishii, Y. Sakagami, A. Abulikemu, K. Kamada, *Can. J. Chem.* **2017**, *95*, 432 – 444; b) W. Yang, G. Longhi, S. Abbate, A. Lucotti, M. Tommasini, C. Villani, V. J. Catalano, A. O. Lykhin, S. A. Varganov, W. A. Chalifoux, *J. Am. Chem. Soc.* **2017**, *139*, 13102 – 13109; c) Y. Yang, L. Yuan, B. Shan, Z. Liu, Q. Miao, *Chem. Eur. J.* **2016**, *22*, 18620 – 18627.

[21] W. Yang, W. Chalifoux, *Synlett* **2017**, *28*, 625 – 632.

[22] W. Yang, J. H. S. K. Monteiro, A. de Bettencourt-Dias, V. J. Catalano, W. A. Chalifoux, *Angew. Chem. Int. Ed.* **2016**, *55*, 10427 – 10430; *Angew. Chem.* **2016**, *128*, 10583 – 10586.

[23] T. Umemoto, T. Kawashima, Y. Sakata, S. Misumi, *Tetrahedron Lett.* **1975**, *16*, 1005 – 1006.

[24] a) B. L. Merner, L. N. Dawe, G. J. Bodwell, *Angew. Chem. Int. Ed.* **2009**, *48*, 5487 – 5491; *Angew. Chem.* **2009**, *121*, 5595 – 5599; b) B. L. Merner, K. S. Unikela, L. N. Dawe, D. W. Thompson, G. J. Bodwell, *Chem. Commun.* **2013**, *49*, 5930 – 5932.

[25] W. Yang, R. R. Kazemi, N. Karunathilake, V. J. Catalano, M. A. Alpuche-Aviles, W. A. Chalifoux, *Org. Chem. Front.* **2018**, *5*, 2288 – 2295.

[26] Y. Gu, R. Muñoz-Mármol, S. Wu, Y. Han, Y. Ni, M. A. Díaz-García, J. Casado, J. Wu, *Angew. Chem. Int. Ed.* **2020**, *59*, 8113 – 8117; *Angew. Chem.* **2020**, *132*, 8190 – 8194.

[27] W. Yang, J. H. Monteiro, A. de Bettencourt-Dias, W. A. Chalifoux, *Can. J. Chem.* **2017**, *95*, 341 – 345.

[28] T. Nakazato, T. Kamatsuka, J. Inoue, T. Sakurai, S. Seki, H. Shinokubo, Y. Miyake, *Chem. Commun.* **2018**, *54*, 5177 – 5180.

[29] Y. Nakamura, T. Nakazato, T. Kamatsuka, H. Shinokubo, Y. Miyake, *Chem. Eur. J.* **2019**, *25*, 10571 – 10574.

[30] J. Sundermeyer, E. Baal, S. Werner, WO 2019/229134 A1, **2019**.

[31] a) N. Buffet, E. Grelet, H. Bock, *Chem. Eur. J.* **2010**, *16*, 5549 – 5553; b) N. Buffet, H. Bock, FR 2930944 A1, **2009**; c) N. Buffet, H. Bock, WO 2009141562 A2, **2009**; N. Buffet, *PhD Thesis*, Université de Bordeaux 1, **2008**.

[32] D. Alezi, Y. Belmabkhout, M. Suyetin, P. M. Bhatt, Ł. J. Weseliński, V. Solovyeva, K. Adil, I. Spanopoulos, P. N. Trikalitis, A.-H. Emwas, M. Eddaoudi, *J. Am. Chem. Soc.* **2015**, *137*, 13308 – 13318.

[33] H. Jia, Y. Gao, Q. Huang, S. Cui, P. Du, *Chem. Commun.* **2018**, *54*, 988 – 991.

[34] J. R. Lakowicz, *Principles of fluorescence spectroscopy*, Springer, New York, **2010**.

[35] B. Dandrade, S. Datta, S. Forrest, P. Djurovich, E. Polikarpov, M. Thompson, *Org. Electron.* **2005**, *6*, 11 – 20.

[36] P. Klán, J. Wirz, *Photochemistry of organic compounds. From concepts to practice*, Wiley, Chichester, **2009**.

[37] Q. Chen, D. Wang, M. Baumgarten, D. Schollmeyer, K. Müllen, A. Narita, *Chem. Asian J.* **2019**, *14*, 1703 – 1707.

[38] Deposition Numbers 2055267 (**4**),2055268 (**13**), and 2055269 (**15**) contain the supplementary crystallographic data for this paper. These data are provided free of charge by the joint Cambridge Crystallographic Data Centre and Fachinformationszentrum Karlsruhe Access Structures service www.ccdc.cam.ac.uk/structures.

Manuscript received: January 15, 2021
Revised manuscript received: March 11, 2021
Accepted manuscript online: March 16, 2021
Version of record online: May 7, 2021

Angewandte Chemie
Eine Zeitschrift der Gesellschaft Deutscher Chemiker

Supporting Information

Access to Functionalized Pyrenes, Peropyrenes, Terropyrenes, and Quarterropyrenes via Reductive Aromatization

*Simon Werner, Tobias Vollgraff, and Jörg Sundermeyer**

anie_202100686_sm_miscellaneous_information.pdf

Additional experimental data for synthesis

Synthesis of a butyl-substituted quarteropyrene-trimethylsilyl ether (S4)

As first attempt for the synthesis of a soluble quarteropyrene tetra-silylether, we synthesized a quarteropyrene trimethylsilylether (S4), terminal functionalized with *n*-butyl groups (see scheme S1). The synthesis route is analogous as discussed in the main text. As a first step, we reacted binaphthyl-bisboronic acid pinacolester with 6-bromo-2-butyl-3-hydroxy-1*H*-phenalen-1-one (S1) to form quarternaphthyl S2 in moderate yields (37%). S2 shows a slightly improved solubility in comparison with its non-butylated congener 10, so a purification by column chromatography was possible. Nevertheless, the cyclodehydrogenated reaction product S3 from the CsOH-melt air oxidation reaction of S2, was as insoluble as the non-butylated counterpart 12. In a final step, S3 was reacted with Zn and TMSCl to form silylether S4, proceeding with a yield (14% over 2 steps) comparable to the in the main text discussed reductive silylations of terropyrenequinone 11 and quarterropyrenequinone 12. The solubility of S4 in organic solvents as chloroform is moderate, so the acquisition of a proton NMR spectra was possible at elevated temperature (50 °C), but no 13C NMR or single crystals for XRD measurements could be obtained. It can be concluded that S4 is less soluble than quarteropyrene triisopropylsilylether 15, meaning that the TIPS groups prevent the quarteropyrene core much better from **π-π-stacking** interactions than butyl groups in combination with a TMS-substitution.

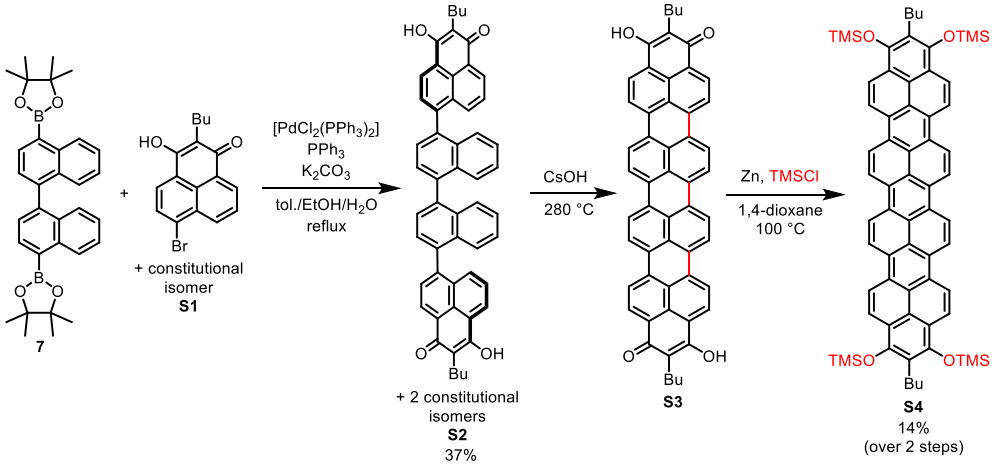

Scheme S1. Synthetic route towards butyl-substituted quarterropyrene trimethylsilyl ether **S4**.

S4 shows an absorption maximum at 634 nm in DCM with a nearly equal UV-Vis-NIR spectrum in comparison to 15. The broadened bands in comparison to lighter homologue trimethylsilyl ethers indicate the weak solubility of S4. The cyclic voltammogram in DCM shows two reduction waves (-2.00 V and -1.82 V vs. Fc/Fc^+) and two oxidation waves (0.24 V and 1.24 V vs. Fc/Fc^+), none of them being fully reversible (figure S1).

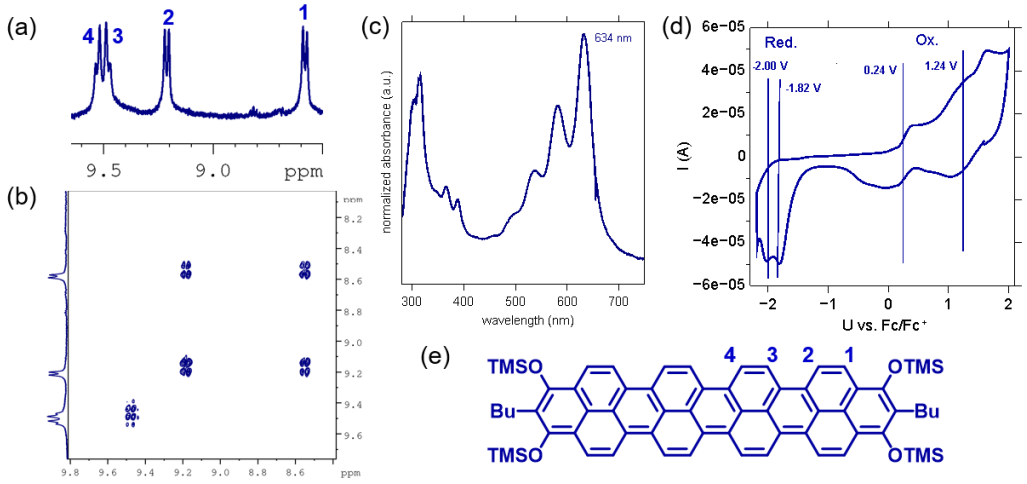

Figure S1. (a) Aromatic region of ^{1}H NMR spectrum of **S4** in $CDCl_3$ (323 K, 500 MHz); (b) COSY-NMR (500 MHz, $CDCl_3$) of the aromatic region of **S4**; (c) UV-Vis spectrum of **S4** measured in DCM; (d) cyclic voltammogram of **S4** in DCM (Scan rate 50 mV/s, electrolyte: nBu$_4$NPF$_6$, vs. Fc/Fc^+); (e) chemical structure of **S4** with assigned aromatic protons from NMR.

Attempts for the reductive aromatization towards penteropyrenes

The strategy of terminal butyl functionalization was also applied in the case of the synthesis of a penteropyrene, the higher homologue of quarteropyrene (Scheme S2). Therefore, ternaphthyl-bis boronic acid pinacolester S6 as central building block was synthesized by a Suzuki Miyaura cross coupling of 1,4-dibromonaphthalene (S4) in excess (3 eq) with naphthalene bis boronic acid pinacolester 6, leading to dibromo-ternaphthyl S5 in moderate yield (40%). S5 was subsequently converted to S6 by Miyaura borylation. S6 could be analogously to the binaphthyl congener 7 reacted with hydroxy-phenalenone S1 to the non-planar pentanaphthyl S7, which could be isolated in good yields (70%). The following cyclodehydrogenative oxidation led to the black powder S8. Suffering even more from insolubility than quarterropyrenequinone S3, the penterropyrenequinone-analogue S8 did not react in silylation reactions, even treatment with Zn, TIPSCl in the presence of imidazole under reflux in dioxane did not lead to a detectable product formation by mass spectrometry. The only evidence for traces of conversion of S8 was a slightly dark green colored DCM solution after extraction the residue and filtration, eventually indicating a red shifted absorption maximum with respect to the dark blue colored lighter homologue quarteropyrene.

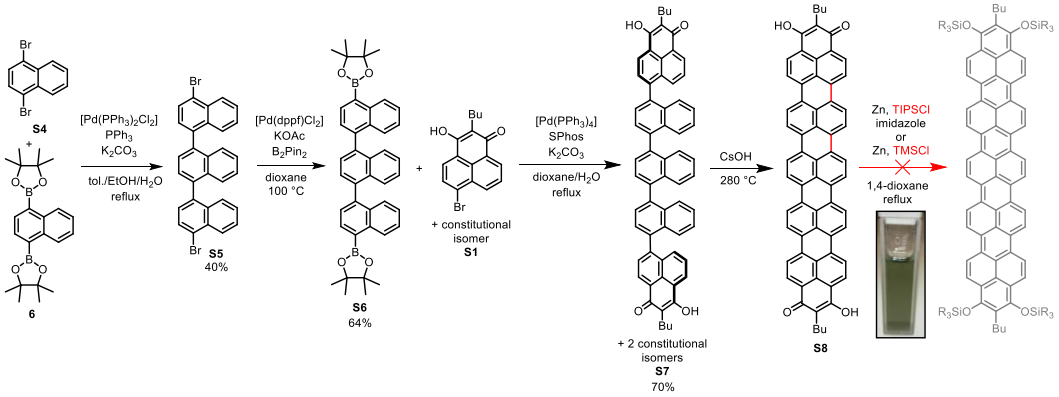

Scheme S2. Attempted synthetical route towards penterropyrenes**.**

Experimental

*1,4-bis(4,4,5,5-tetramethyl-1,3,2-dioxaborolan-2-yl)naphthalene (**6**)*

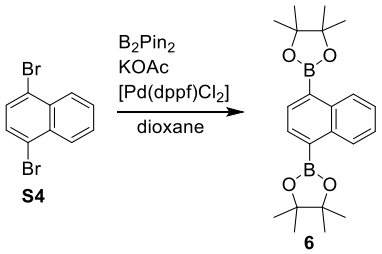

According to a literature known procedure[18], 1.00 g (3.51 mmol, 1.0 eq) 1,4-dibromonaphthalene (**S4**), 1.80 g (18.30 mmol, 5.2 eq) dry KOAc, 2.05 g (8.11 mmol, 2.3 eq) bis(pinacolato)diboron and 75 mg (0.10 mmol, 3 mol%) [Pd(dppf)Cl_2] were evacuated and back-flushed with argon in a flame-dried Schlenk flask. Thereto, 25 mL anhydrous dioxane were added and the mixture stirred for 2 d at 100 °C under argon atmosphere. After cooling to room temperature, 20 mL water and 20 mL ethyl acetate were added and the organic phase was separated. The aqueous phase was extracted with ethyl acetate (2x 30 mL). The combined organic phases were dried over MgSO4 and the crude product was purified by column chromatography on silica (*n*-hexane/ethyl acetate 20:1). 1.05 g (2.76 mmol, 79 %) of **6** were obtained as colorless solid. ^{1}H NMR (300.1 MHz, $CDCl_3$): δ_H = 1.42 (s, 24H, 4 x C(CH_3)$_2$), 7.48-7.54 (m, 2H), 8.02 (s, 2H), 8.72-8.78 (m, 2H) ppm. ^{13}C NMR (75.5 MHz, $CDCl_3$): δ_C = 25.1, 83.9, 126.0, 128.8, 134.4, 136.7 ppm. The analytical data are in accordance with the literature.[18]

*4,4'-dibromo-1,1'-binaphthyl (**S10**)*

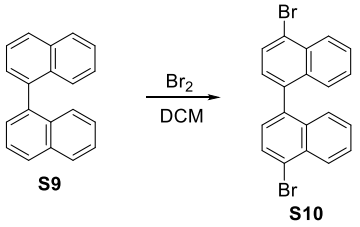

According to a literature known procedure[19], 1.00 g (3.94 mmol, 1.0 eq) 1,1'-binaphthyl (**S9**) were dissolved in 30 mL DCM and cooled to 0°C. Under exclusion of light, 0.8 mL (15.7 mmol, 4.0 eq) bromine were added dropwise over the course of 15 min at 0 °C and stirred for further 2 h at room temperature. To this, 30 mL *n*-pentane were added and a colorless solid was formed. The suspension was filtered and the solid was washed with n-pentane (20 mL) and dried in vacuo. 1.39 g (3.39 mmol, 86 %) of **S10** were obtained as off-white solid. ^{1}H NMR (300.1 MHz, $CDCl_3$): δ_H = 7.28-7.35 (m, 6H), 7.55-7.65 (m, 2H), 7.90 (d, $^3J_{H,H}$ = 7.6 Hz, 2H), 8.36 (d, $^3J_{H,H}$ = 7.6 Hz, 2H) ppm. ^{13}C NMR (75.5 MHz, $CDCl_3$): δ_C = 123.2, 127.1, 127.1, 127.5, 127.6, 128.3, 129.6, 132.1, 134.1, 137.8 ppm. The analytical data are in accordance with the literature.[19]

*4,4'-bis(4,4,5,5-tetramethyl-1,3,2-dioxaborolan-2-yl)-1,1'-binaphthalene (**7**)*

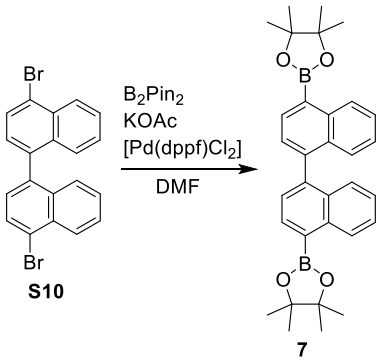

According to a literature known procedure[19], 1.35 g (3.30 mmol, 1.0 eq) 4,4'-dibromo-1,1'-binaphthyl (**S10**)**,** 1.95 g (20.00 mmol, 6.9 eq) dry KOAc, 2.09 g (8.20 mmol, 2.5 eq) bis(pinacolato)diboron and 75 mg (0.10 mmol, 3 mol%) [Pd(dppf)Cl_2] were evacuated and back-flushed with argon in a flame-dried Schlenk flask. Thereto, 15 mL anhydrous DMF were added and the mixture stirred for 18 at 100 °C under argon atmosphere. After cooling to room temperature, 20 mL methanol were added and the precipitate filtered. The resulting solid was washed with water and methanol (20 mL) and recrystallized in THF/n-hexane. 1.32 g (2.61 mmol, 79 %) of **7** were obtained as off-white solid. ^{1}H NMR (300.1 MHz, $CDCl_3$): δ_H = 1.46 (s, 24H, 4 x C(CH_3)$_2$), 7.24 (t, $^3J_{H,H}$ = 7.5 Hz, 2H), 7.36 (d, $^3J_{H,H}$ = 8.2 Hz, 2H), 7.45-7.55 (m, 4H), 8.19 (d, $^3J_{H,H}$ = 7.0 Hz, 2H), 8.87 (d, $^3J_{H,H}$ = 8.4 Hz, 2H) ppm. ^{13}C NMR (75.5 MHz, $CDCl_3$): δ_C = 27.1, 84.0, 125.7, 126.4, 126.9, 127.0, 128.7, 132.6, 135.2, 137.1, 142.3 ppm. The analytical data are in accordance with the literature.[19]

*4,4''-dibromo-1,1':4',1''-ternaphthalene (**S5**)*

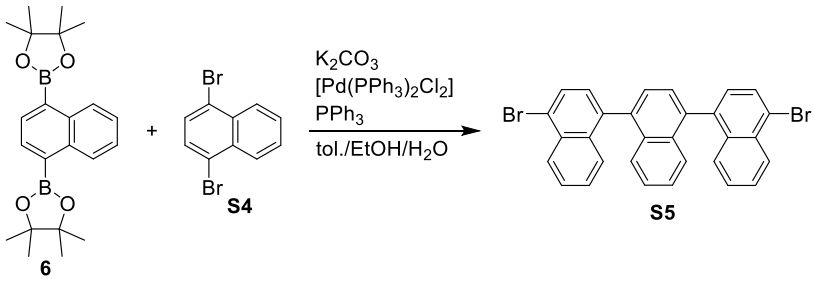

In a Schlenk flask, 1.25 g (4.30 mmol, 3.0 eq) 1,4-dibromonaphthalene (**S4**)**,** 545 mg (1.43 mmol, 1.0 eq) **6** and 1.19 g (8.60 mmol, 6.0 eq) K_2CO_3 were dissolved in 40 mL toluene, 10 mL ethanol and 5 mL water and subsequently degassed. Under argon atmosphere, 50 mg (0.07 mmol, 5 mol%) [Pd(PPh3)2Cl2] and 36 mg (0.14 mmol, 10 mol%) triphenyl phosphine were added and it was refluxed for 18 h. After cooling to room temperature, 20 mL water were added and the organic phase was separated. The aqueous phase was extracted with ethyl acetate (2x 30 mL). The combined organic phases were dried over $MgSO_4$ and the crude product was purified by column chromatography on silica (*n*-hexane/chloroform 20:1). 305 mg (0.57 mmol, 40 %) of **S5** were obtained as colorless solid. ^{1}H NMR (300.1 MHz, $CDCl_3$): δ_H = 7.25-7.32 (m, 2H), 7.38-7.70 (m, 12H), 7.78 (dd, $^3J_{H,H}$ = 7.6, Hz, $^4J_{H,H}$ = 3.6 Hz, 2H), 8.39 (d, $^3J_{H,H}$ = 8.6 Hz, 2H) ppm. ^{13}C NMR (75.5 MHz, $CDCl_3$): δ_C = 123.0, 126.5, 126.6, 127.0, 127.3, 127.4, 127.6, 127.6, 127.8, 127.8, 128.8, 130.0, 132.4, 132.2, 134.6, 138.2, 139.0 ppm. The analytical data are in accordance with the literature.[19]

*4,4''-bis(4,4,5,5-tetramethyl-1,3,2-dioxaborolan-2-yl)-1,1':4',1''-ternaphthalene (**S6**)*

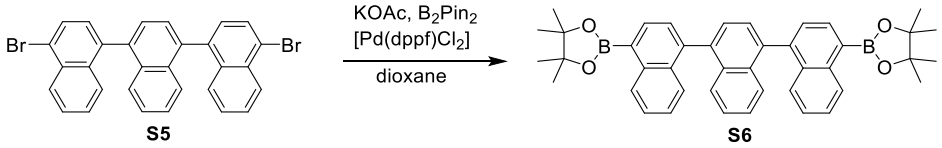

According to a literature known procedure[19], 300 mg (0.56 mmol, 1.0 eq) 4,4''-dibromo-1,1':4',1''-ternaphthalene (**S5**), 330 mg (3.36 mmol, 6.0 eq) dry KOAc, 427 mg (1.68 mmol, 3.0 eq) bis(pinacolato)diboron and 20 mg (0.03 mmol, 3 mol%) [Pd(dppf)Cl_2] were evacuated and back-flushed with argon in a flame-dried Schlenk flask. Thereto, 20 mL anhydrous dioxane were added and the mixture stirred for 18 h at 100 °C under argon atmosphere. After cooling to room temperature, 20 mL water and 20 mL ethyl acetate were added and the organic phase was separated. The aqueous phase was extracted with ethyl acetate (2x 30 mL). The combined organic phases were dried over MgSO4 and the crude product was purified by column chromatography on silica (*n*-hexane/ethyl acetate 4:1). 225 mg (0.36 mmol, 64 %) of **S6** were obtained as colorless solid, from which excess of bis(pinacolato)diboron was removed by washing with diethyl ether (10 mL). ^{1}H NMR (300.1 MHz, CD_2Cl_2): δ_H = 1.47 (s, 24H, 4 x C(C*H*$_3$)$_2$), 7.22-7.28 (m, 2H), 7.30-7.45 (m, 4H), 7.49-7.66 (m, 8H), 8.21 (dd, $^3J_{H,H}$ = 7.0, Hz, $^4J_{H,H}$ = 3.5 Hz, 2H) 8.89 (dd, $^3J_{H,H}$ = 8.8 Hz, $^4J_{H,H}$ = 2.2 Hz, 2H) ppm. ^{13}C NMR (75.5 MHz, CD_2Cl_2): δ_C = 25.2, 84.4, 126.1, 126.3, 126.6, 127.1, 127.3, 127.5, 127.6, 129.2, 133.1, 133.2, 135.5, 137.5, 138.9, 142.4 ppm. The analytical data are in accordance with the literature.[19]

*6-bromo-3-hydroxy-1H-phenalen-1-one (**8**)*

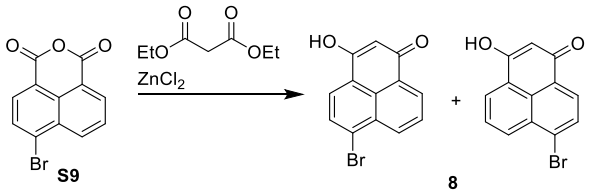

In a flame dried Schlenk flask, 6 mL diethylmalonate were added to 2.00 g (7.20 mmol, 1.0 eq) 6-bromo naphthalene anhydride (**S9**) and 2.00 g (14.40 mmol, 2.0 eq) dry $ZnCl_2$ under argon atmosphere. The suspension was stirred at 185 °C for 6 h, until the gas evolution ceased and the red mixture solidified. 200 mL 2M aqueous KOH were added and the red solution filtered. The filtrate was cooled with an ice bath and 200 mL 2M acetic acid were added carefully. The resulting yellow to brown precipitate was collected by filtration, washed with water and dried at 120 °C overnight. 1.60 g **8** (5.85 mmol, 81 %) were obtained as brown solid. ^{1}H NMR (300.1 MHz, DMSO-d_6): δ_H = 5.38 (s, 1H), 7.72 (t, $^3J_{H,H}$ = 7.8 Hz, 1H), 7.92 (d, $^3J_{H,H}$ = 7.8 Hz, 1H), 7.99 (d, $^3J_{H,H}$ = 7.7 Hz, 1H), 8.20 (dd, $^3J_{H,H}$ = 8.3 Hz, $^4J_{H,H}$ = 4.2 Hz, 2H) ppm. ^{13}C NMR (75.5 MHz, DMSO-d_6): δ_C = 105.3, 127.9, 128.2, 129.1, 130.1, 130.8, 131.5, 131.6, 132.5, 133.2, 133.6 ppm (C-O not detected). HR-MS (APCI-) m/z clcd. for [$C_{13}H_6BrO_2$]$^-$: 279.9537 (found: 279.9545). IR (ATR), $\tilde{\nu}$ = 3019 (w), 2216 (w), 2170 (w), 1958 (w), 1622 (s), 1554 (vs), 1338 (m), 1254 (m), 1212 (m), 1024 (w), 942 (w), 805 (m), 768 (m), 649 (w), 521 (w) cm^{-1}.
Note: **8** consists of two possible inseparable constitutional isomers leading to broadened ^{1}H NMR signals.

*6-bromo-2-butyl-3-hydroxy-1H-phenalen-1-one (**S1**)*

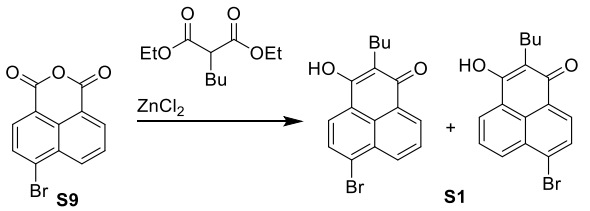

In a flame dried Schlenk flask, 5 mL diethyl butylmalonate were added to 1.00 g (3.60 mmol, 1.0 eq) 6-bromo naphthalene anhydride (**S9**) and 1.00 g (7.20 mmol, 2.0 eq) dry $ZnCl_2$ under argon atmosphere. The suspension was stirred at 185 °C for 4 h, until the gas evolution ceased and the red mixture solidified. The solid was taken up with a mixture of chloroform and ethyl acetate (250 mL) and washed with 250 mL water and 250 mL brine. The organic layer was separated and dried over Na_2SO_4 and filtered through a plug of neutral aluminum oxide, which was rinsed with 100 mL acetone. The solvent was concentrated to 20 mL and 100 mL *n*-pentane were added. Pure product crystalized at -20 °C from this mixture. 510 mg **S1** (1.55 mmol, 43 %) were obtained as orange solid. ^{1}H NMR (300.1 MHz, DMSO-d_6): δ_H = 0.90 (t, $^3J_{H,H}$ = 7.0 Hz, 3H, Bu*H*), 1.40-1.48 (m, 4H, Bu*H*), 2.62 (t, $^3J_{H,H}$ = 7.3 Hz, 2H, Bu*H*), 7.87 (t, $^3J_{H,H}$ = 7.9 Hz, 1H), 8.09 (d, $^3J_{H,H}$ = 7.9 Hz, 1H), 8.17 (d, $^3J_{H,H}$ = 7.9 Hz, 1H), 8.39 (dd, $^3J_{H,H}$ = 7.1 Hz, $^4J_{H,H}$ = 2.5 Hz, 2H), 10.55 (s, 1H, O*H*) ppm. ^{13}C NMR (75.5 MHz, DMSO-d_6): δ_C = 14.3, 22.6, 30.9, 118.5, 127.0, 127.1, 127.7, 128.0, 128.5, 128.6, 130.1, 131.1 ppm (C-O not detected). HR-MS (APCI-) m/z clcd. for [$C_{17}H_{14}BrO_2$]$^-$: 331.0164 (found: 331.0180). IR (ATR), $\tilde{\nu}$ = 3079 (w), 2950 (m), 2921 (m), 2861 (w), 1688 (w), 1616 (m), 1550 (vs), 1457 (w), 1367 (w), 1172 (s), 1104 (m), 1019 (m), 845 (w), 773 (w), 693 (w), 560 (w) cm^{-1}.
Note: **S1** consists of two possible inseparable constitutional isomers leading to broadened ^{1}H NMR signals.

*3-hydroxy-7-(4-(3-hydroxy-1-oxo-1H-phenalen-6-yl)naphthalen-1-yl)-1H-phenalen-1-one (**9**)*

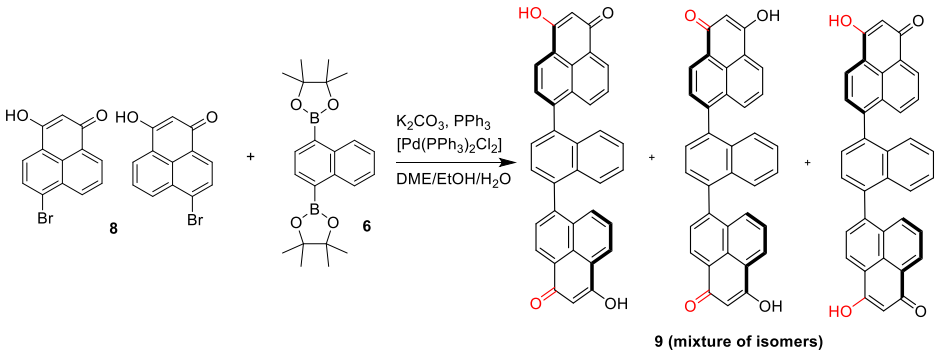

In a Schlenk flask, 417 mg (1.09 mmol, 1.0 eq) boronic acid pinacol ester **6**, 725 mg (2.65 mmol, 2.4 eq) 6-bromo-3-hydroxy-1*H*-phenalen-1-one (**8**, isomer mixture) and 1.83 g (13.2 mmol, 12.0 eq) K_2CO_3 were dissolved in 20 mL dimethoxyethan, 10 mL ethanol and 5 mL water and degassed thoroughly. Under argon atmosphere, 77 mg (0.11 mmol, 10 mol%) $[Pd(PPh_3)_2Cl_2]$ and 53 mg (0.20 mmol, 20 mol%) triphenylphosphine were added and the reaction mixture was heated to reflux for 18 h. After cooling down to room temperature, 2 M acetic acid (50 mL) was added and a yellow precipitate was formed. The yellow solid was collected by filtration and washed with water (50 mL), methanol (50 mL) and diethyl ether (50 mL) and dried in vacuo. 448 mg (0.87 mmol, 80 %) of the yellow solid **9** were obtained and directly used for the next step. Note: due to the insoluble nature of the product, some aromatic impurities could not be removed completely from the product. ^{1}H NMR (300.1 MHz, DMSO-d_6): δ_H = 6.10 (s, 2H), 7.30-8.10 (br m, 12H), 8.15-8.40 (br m, 4H), 11.87 (br s, 2H, O*H*) ppm. ^{13}C NMR not recorded due to low solubility. HR-MS (APCI-) m/z clcd. for $[C_{36}H_{19}O_4]^-$: 515.1289 (found: 515.1292). IR (ATR), $\tilde{\nu}$ = 3056 (w), 3006 (w), 1775 (m), 1736 (m), 1626 (m), 1573 (s), 1510 (m), 1362 (w), 1302 (m), 1186 (m), 1119 (m), 1021 (w), 846 (w), 750 (vs), 720 (s), 694 (vs), 541 (s), 514 (m) cm^{-1}.
Note: **9** consists of inseparable constitutional isomers leading to broadened ^{1}H NMR signals.

*3-hydroxy-7-(4'-(3-hydroxy-1-oxo-1H-phenalen-6-yl)-[1,1'-binaphthalen]-4-yl)-1H-phenalen-1-one (**10**)*

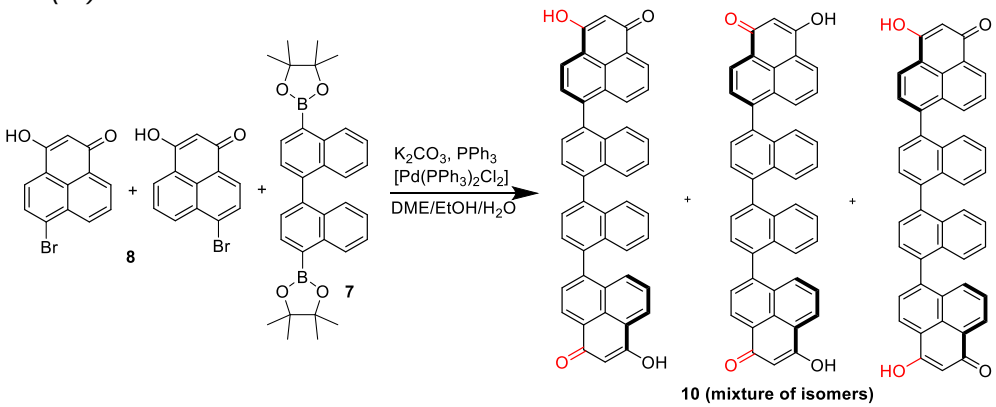

In a Schlenk flask, 600 mg (1.19 mmol, 1.0 eq) boronic acid pinacol ester **7**, 840 mg (3.09 mmol, 2.6 eq) 6-bromo-3-hydroxy-1*H*-phenalen-1-one (**8**, isomer mixture) and 1.97 g (14.3mmol, 12.0 eq) K_2CO_3 were dissolved in 30 mL dimethoxyethan, 5 mL ethanol and 5 mL water and degassed thoroughly. Under argon atmosphere, 85 mg (0.12 mmol, 10 mol%) $[Pd(PPh_3)_2Cl_2]$ and 139 mg (0.53 mmol, 40 mol%) triphenylphosphine were added and the reaction mixture was heated to reflux for 18 h. After cooling down to room temperature, 2 M acetic acid (50 mL) was added and a yellow precipitate was formed. The yellow solid was collected by filtration and washed with water (50 mL), methanol (50 mL) and diethyl ether (50 mL) and dried in vacuo. 581 mg (0.90 mmol, 76 %) of the yellow solid **10** were obtained and directly used for the next step. Note: due to the insoluble nature of the product, some aromatic impurities could not be removed completely from the product. ^{1}H NMR (300.1 MHz, DMSO-d_6): δ_H = 6.11 (s, 2H), 7.05-8.05 (br m, 18H), 8.30-8.60 (br m, 4H), 11.92 (br s, 2H, O*H*) ppm. ^{13}C NMR not recorded due to low solubility. HR-MS (APCI-) m/z clcd. for $[C_{46}H_{25}O_4]^-$: 641.1758 (found: 641.1758). IR (ATR), $\tilde{\nu}$ = 3057 (w), 2997 (w), 2357 (w), 2149 (w), 1919 (w), 1626 (s), 1567 (vs), 1514 (s), 1481 (m), 1366 (m), 1300 (m), 1237 (m), 1204 (w), 839 (m), 764 (vs), 721 (m), 693 (m), 540 (m) cm^{-1}.
Note: **10** consists of inseparable constitutional isomers leading to broadened ^{1}H NMR signals.

*2-butyl-7-(4'-(2-butyl-3-hydroxy-1-oxo-1H-phenalen-6-yl)-[1,1'-binaphthalen]-4-yl)-3-hydroxy-1H-phenalen-1-one (**S2**)*

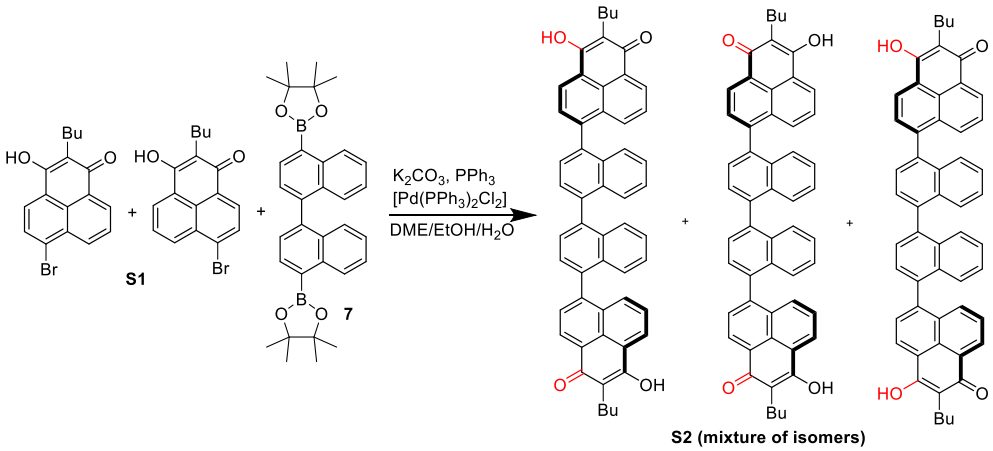

In a Schlenk flask, 860 mg (1.70 mmol, 1.0 eq) boronic acid pinacol ester **7**, 1.35 g (4.03 mmol, 2.5 eq) 6-bromo-2-butyl-3-hydroxy-1*H*-phenalen-1-one (**S1**, isomer mixture) and 1.50 g (10.9 mmol, 6.4 eq) K_2CO_3 were dissolved in 20 mL toluene, 10 mL ethanol and 5 mL water and degassed thoroughly. Under argon atmosphere, 119 mg (0.17 mmol, 10 mol%) $[Pd(PPh_3)_2Cl_2]$ and 89 mg (0.34 mmol, 40 mol%) triphenylphosphine were added and the reaction mixture was heated to reflux for 18 h. After cooling down to room temperature, 2 M HCl (50 mL) was added and the organic phase was separated. The aqueous phase was extracted with chloroform (2 x 50 mL). The combined organic phase was dried over $MgSO_4$ and purified via column chromatography on silica (first, side products were eluated using chloroform, product **S2** was eluated using ethyl acetate/acetone 10:1). 480 mg (0.64 mmol, 37 %) of the yellow solid **S2** were obtained. ^{1}H NMR (300.1 MHz, DMSO-d_6): δ_H = 0.88-1.02 (m, 6H, Bu*H*), 1.20-1.65 (m, 12H, Bu*H*), 7.20-8.05 (br m, 18H), 8.30-8.60 (br m, 4H), 10.53 (br s, 2H, O*H*) ppm. ^{13}C NMR not recorded due to low solubility. HR-MS (APCI-) m/z clcd. for $[C_{54}H_{41}O_4]^-$: 753.3010 (found: 753.3038). IR (ATR), $\tilde{\nu}$ = 3268 (w), 2953 (w), 2925 (m), 2868 (w), 2020 (w), 1938 (w), 1705 (w), 1621 (m), 1557 (s), 1431 (m), 1213 (m), 1187 (w), 848 (w), 719 (vs), 661 (w), 544 (w) cm^{-1}.
Note: **S2** consists of inseparable constitutional isomers leading to broadened ^{1}H NMR signals.

*2-butyl-7-(4''-(2-butyl-3-hydroxy-1-oxo-1H-phenalen-6-yl)-[1,1':4',1''-ternaphthalen]-4-yl)-3-hydroxy-1H-phenalen-1-one (**S7**)*

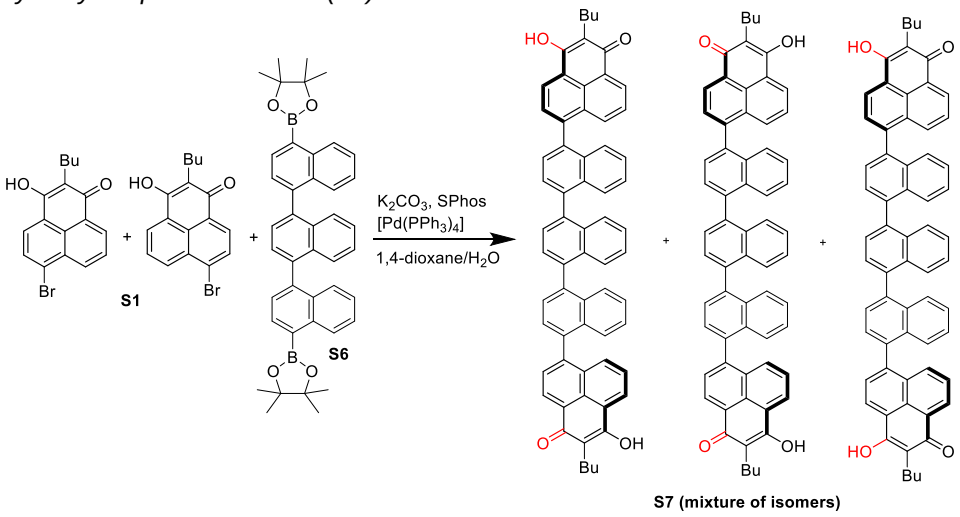

In a Schlenk flask, 200 mg (0.32 mmol, 1.0 eq) boronic acid pinacol ester **S6**, 256 mg (0.80 mmol, 2.5 eq) 6-bromo-2-butyl-3-hydroxy-1*H*-phenalen-1-one (**S1**, isomer mixture) and 531 mg (3.84 mmol, 12.0 eq) K_2CO_3 were dissolved in 10 mL dioxane and 3 mL water and degassed thoroughly. Under argon atmosphere, 37 mg (0.03 mmol, 10 mol%) $[Pd(PPh_3)_4]$ and 25 mg (0.06 mmol, 20 mol%) SPhos were added and the reaction mixture was heated to 100 °C and stirred for 3 d. After cooling down to room temperature, 2 M HCl (20 mL) was added and the organic phase was separated. The aqueous

phase was extracted with chloroform (3 x 20 mL). The combined organic phase was dried over $MgSO_4$ and filtered. The solvent was evaporated and the residue suspended in 50 mL methanol. The precipitate was collected by filtration and was washed with diethyl ether (20 mL). 196 mg (0.22 mmol, 70 %) of the yellow solid **S7** were obtained. ^{1}H NMR (300.1 MHz, DMSO-d_6): δ_H = 0.80-1.05 (m, 6H, Bu*H*), 1.10-1.60 (m, 12H, Bu*H*), 7.30-8.00 (br m, 24H), 8.35-8.65 (br m, 4H), 10.52 (br s, 2H, O*H*) ppm. ^{13}C NMR not recorded due to low solubility. HR-MS (APCI-) m/z clcd. for $[C_{64}H_{47}O_4]^-$: 880.3514 (found: 880.3494). IR (ATR), $\tilde{\nu}$ = 2958 (w), 2930 (w), 2108 (w), 2020 (w), 1943 (w), 1705 (w), 1616 (m), 1565 (vs), 1440 (w), 1216 (m), 1204 (w), 1189 (w), 848 (w), 719 (vs), 709 (w), 653 (w), 546 (w) cm^{-1}.
Note: **S7** consists of inseparable constitutional isomers leading to broadened ^{1}H NMR signals.

*3,8-dihydroxypyrene-1,6-dione (**3**)*

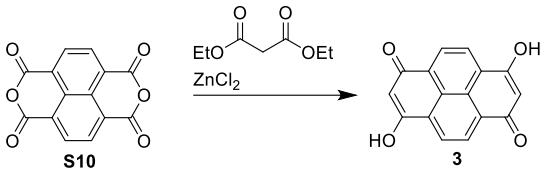

In a flame dried Schlenk flask, 10 mL diethylmalonate were added to 1.00 g (3.73 mmol, 1.0 eq) naphthalene dianhydride (**S10**) and 2.00 g (14.40 mmol, 3.9 eq) dry $ZnCl_2$ under argon atmosphere. The suspension was stirred at 185 °C for 3 h, until the gas evolution ceased and the black mixture solidified. 100 mL 2M aqueous KOH were added and the brown solution filtered. The filtrate was cooled with an ice bath and 100 mL 2M acetic acid were added carefully. The resulting yellow to brown precipitate was collected by filtration, washed with water and methanol and dried at 120 °C overnight. 692 mg of **3** were obtained as brown solid. Due to the insolubility of **3**, no NMR measurements could be acquired and **3** was directly used for the next step without further purification HR-MS (APCI-) m/z clcd. for $[C_{16}H_7O_4]^-$: 263.0350 (found: 263.0357). IR (ATR), $\tilde{\nu}$ = 3064 (w), 2654 (w), 2369 (w), 2189 (w), 1676 (m), 1556 (vs), 1451 (vs), 1363 (s), 1289 (vs), 1234 (vs), 1193 (s), 1040 (m), 903 (w), 833 (m), 801 (m), 740 (w), 650 (w), 595 (w) cm^{-1}. The analytical data are in accordance to the literature.[20]

3,10-dihydroxydibenzo[cd,lm]perylene-1,8-dione (2)

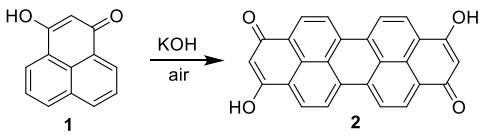

According to a literature known procedure[20], 1.96 g (10.00 mmol, 1.0 eq) 3-hydroxy-1H-phenalen-1-one (**1**) and 10 g mortared KOH pellets were homogenized. It was heated to 285 °C for 2 h in a Ni crucible open to air. In that time, a purple melt was formed and gas evolution ceased. After cooling to room temperature, the melt was taken up in water (100 mL), filtered and the purple filtrate was acidified with 2M acetic acid to pH = 5 and a brown precipitate was formed. The precipitate was ultrasonicated for 5 min and collected by filtration. The dark brown, insoluble solid was washed with water, methanol, THF and diethyl ether until the filtrate remains colorless. After drying at 120 °C overnight, 1.28 g of **2** were obtained as blackish-brown solid. Due to the insolubility of **2**, no NMR measurements could be acquired and it was directly used for the next step without further purification. IR (ATR), $\tilde{\nu}$ = 3174 (w), 3107 (w), 3012 (w), 2778 (w), 2256 (w), 2140 (w), 2103 (w), 2050 (w), 1921 (m), 1902 (w), 1870 (w), 1762 (w), 1585 (m), 1544 (m), 1509 (w), 1073 (vs), 955 (m), 923 (w), 803 (m), 660 (w), 591 (m), 460 (vs) cm^{-1}. The analytical data are in accordance to the literature.[20]

*3,12-dihydroxybenzo[rst]dinaphtho[8,1,2-cde:2',1',8'-klm]pentaphene-1,10-dione (**11**)*

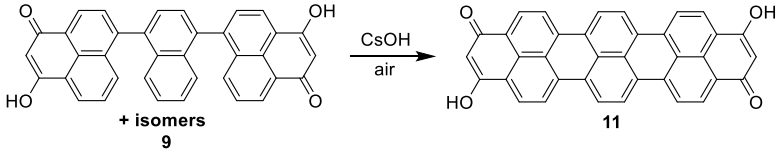

In a Ni crucible open to air, 390 mg (0.76 mmol, 1.0 eq) of **9** (isomer mixture) and 4.0 g monohydrated CsOH were homogenized. It was heated to 285 °C for 2 h on air. In that time, a purple-blue melt was formed and gas evolution ceased. After cooling to room temperature, the melt was taken up in water (100 mL), and the blue suspension was

acidified with 2M acetic acid to pH = 5 and a purple-blue precipitate was formed. The precipitate was ultrasonicated for 5 min and collected by filtration. The purple, insoluble solid was washed with water, methanol, THF and diethyl ether until the filtrate remains colorless. After drying at 120 °C overnight, 212 mg of **11** were obtained as purple solid. Due to the insolubility of **11**, no NMR measurements could be acquired and it was directly used for the next step without further purification. IR (ATR), ṽ =3669 (w), 2359 (w), 2279 (w), 2207 (m), 2169 (w), 2092 (m), 2049 (w), 1989 (m), 1961 (w), 1901 (w), 1689 (s), 1611 (vs), 1545 (s), 1497 (s), 1357 (m), 1238 (vs), 1184 (s), 999 (m), 800 (m), 711 (m), 648 (m) cm^{-1}.

*3,14-dihydroxybenzo[rst]benzo[12,1]tetrapheno[7,8,9-cde]naphtho[2,1,8-klm]pentaphene-1,12-dione (**12**)*

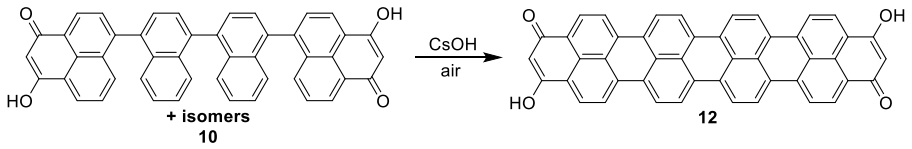

In a Ni crucible open to air, 582 mg (0.91 mmol, 1.0 eq) of **10** (isomer mixture) and 6.0 g monohydrated CsOH were homogenized. It was heated to 285 °C for 2 h on air. In that time, a blackish-blue melt was formed and gas evolution ceased. After cooling to room temperature, the melt was taken up in water (200 mL), and the blue suspension was acidified with 2M acetic acid to pH = 5 and a dark blue precipitate was formed. The precipitate was ultrasonicated for 5 min and collected by filtration. The purple, insoluble solid was washed with water, methanol, THF and diethyl ether until the filtrate remains colorless. After drying at 120 °C overnight, 429 mg of **12** were obtained as blackish-blue solid. Due to the insolubility of **12**, no NMR measurements could be acquired and it was directly used for the next step without further purification. IR (ATR), ṽ = 3860 (w), 3759 (w), 2195 (w), 2152 (w), 2078 (w), 1998 (w), 1680 (m), 1655 (w), 1605 (w), 1539 (s), 1356 (w), 1311 (w), 1299 (m), 1172 (s), 1051 (m), 1042 (w), 800 (s), 755 (w), 706 (m), 560 (w) cm^{-1}.

*2,13-dibutyl-3,14-dihydroxybenzo[rst]benzo[12,1]tetrapheno[7,8,9-cde]naphtho[2,1,8-klm]pentaphene-1,12-dione (**S3**)*

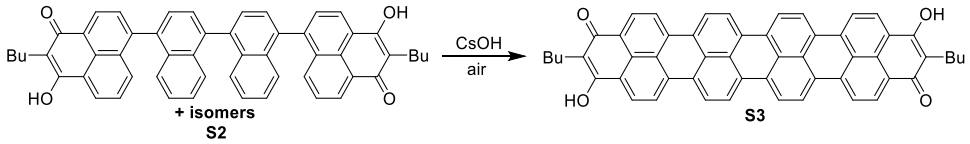

In a Ni crucible open to air, 385 mg (0.51 mmol, 1.0 eq) of **S2** (isomer mixture) and 4.0 g monohydrated CsOH were homogenized. It was heated to 285 °C for 2 h on air. In that time, a blackish-blue melt was formed and gas evolution ceased. After cooling to room temperature, the melt was taken up in water (200 mL), and the blue suspension was acidified with 2M acetic acid to pH = 5 and a dark blue precipitate was formed. The precipitate was ultrasonicated for 5 min and collected by filtration. The purple, insoluble solid was washed with water, methanol, THF and diethyl ether until the filtrate remains colorless. After drying at 120 °C overnight, 260 mg of **S3** (0.35 mmol, 68 %) were obtained as blackish-blue solid. Due to the insolubility of **S3**, no NMR measurements could be acquired and it was directly used for the next step without further purification. IR (ATR), ṽ = 3911 (w), 3860 (w), 3757 (w), 3711 (w), 2370 (w), 2198 (w), 2151 (w), 2073 (w), 1995 (w), 1681 (m), 1608 (w), 1544 (vs), 1356 (m),, 1297 (m), 1174 (s), 1050 (m), 801 (s), 702 (m), 658 (m), 553 (m) cm^{-1}.

*2,13-dibutyl-3,14-dihydroxybenzo[rst]benzo[12,1]tetrapheno[7,8,9-cde]naphtho[2,1,8-klm]pentaphene-1,12-dione (**S8**)*

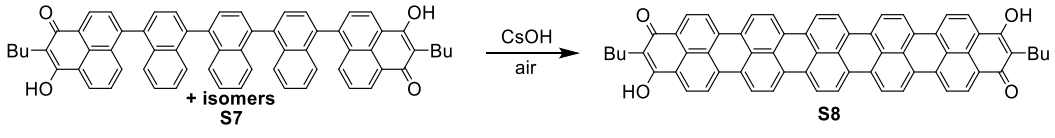

In a Ni crucible open to air, 175 mg (0.20 mmol, 1.0 eq) of **S7** (isomer mixture) and 3.5 g monohydrated CsOH were homogenized. It was heated to 285 °C for 2 h on air. In that time, a black melt was formed and gas evolution ceased. After cooling to room temperature, the melt was taken up in water (200 mL), and the black suspension was acidified with 2M acetic acid to pH = 5 and a black precipitate was formed. The precipitate was ultrasonicated for 5 min and collected

by filtration. The purple, insoluble solid was washed with water, methanol, acetone, THF and diethyl ether until the filtrate remains colorless. After drying at 120 °C overnight, 93 mg of **S8** were obtained as black solid. Due to the insolubility of **S8**, no NMR measurements could be acquired and it was directly used for the next step without further purification. IR (ATR), $\tilde{\nu}$ = 3831 (w), 3727 (w), 2356 (w), 2312 (w), 2196 (m), 2121 (w), 2042 (w), 1991 (w), 1952 (w), 1550 (m), 1186 (s), 802 (s), 749 (m), 707 (m), 644 (w) cm^{-1}.

*1,3,6,8-tetrakis((triisopropylsilyl)oxy)pyrene (**5**)*

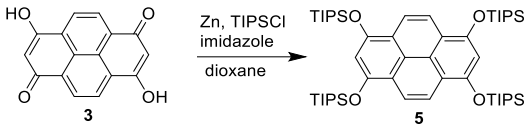

Pyrenequinone (**3**, 264 mg, 1.0 mmol, 1.0 eq), Zn dust (523 mg, 8.0 mmol, 8.0 eq), imidazole (545 mg, 8.0 mmol, 8.0 eq) and triisopropyl chloride (1.7 mL, 8.0 mmol, 8.0 eq) were heated to 90 °C for 18 h under argon atmosphere in 20 mL 1,4-dioxane. The brownish solution was cooled to room temperature, filtered and the solvent was evaporated in vacuo. The brown residue was purified by column chromatography over neutral aluminum oxide (eluent: DCM), the solvent was removed in vacuo and the residual yellow oil was dissolved in 30 mL *n*-pentane and precipitated at -80 °C. 78 mg (0.08 mmol, 8%) of the off-white solid **5** were obtained after removing the supernatant and drying in vacuo. ^{1}H NMR (500.1 MHz, $CDCl_3$): δ_H = 1.19 (d, $^{3}J_{H,H}$ = 7.5 Hz, 72H, $(CH_3)_2CH$), 1.44 (hept, $^{3}J_{H,H}$ = 7.5 Hz, 12H, $(CH_3)_2CH$), 7.02 (s, 2H, *H*a), 8.06 (s, 4H, *H*b) ppm. ^{13}C NMR (125.8 MHz, $CDCl_3$): δ_C = 13.5, 18.3, 107.5, 118.4, 118.6, 127.9, 149.5 ppm. HR-MS (LIFDI+) m/z clcd. for $[C_{52}H_{90}O_4Si_4]^+$: 890.59161 (found: 890.59229). IR (ATR), $\tilde{\nu}$ = 2945 (m), 2866 (m), 2043 (w), 1950 (w), 1590 (m9, 1500 (m), 1464 (m), 1388 (w), 1309 (vs), 1193 (m), 1153 (m), 928 (w), 889 (s), 689 (m), 621 (w9, 497 (w) cm^{-1}. λ_{max} (abs.) = 380 nm (DCM, ε = 24405 $L{\cdot}mol^{-1}{\cdot}cm^{-1}$). λ_{max} (em.) = 419 nm (DCM). CV: $E_{1/2}(Ox_1)$ = 0.26 V (vs. Fc/Fc^+), $E_{1/2}(Ox_2)$ = 0.77 V (vs. Fc/Fc^+).

*1,3,8,10-tetrakis((trimethylsilyl)oxydibenzo[cd,lm]-perylene (**4**)*

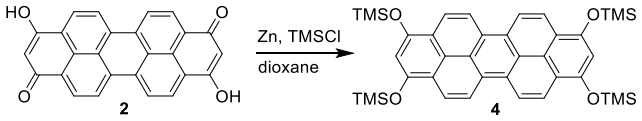

Peropyrenequinone (**2**, 778 mg, 2.0 mmol, 1.0 eq), Zn dust (1.05 g, 16.0 mmol, 8.0 eq) and trimethylsilyl chloride (2.0 mL, 16.0 mmol, 8.0 eq) were stirred for 3 h under argon atmosphere at 100 °C in 40 mL 1,4-dioxane. The greenish solution was cooled to room temperature and all volatile components were removed in vacuo. The residue was taken up in 40 mL of dichloromethane and filtered. After removing the solvent under vacuum, the crude product was washed with *n*-pentane. 647 mg (0.95 mmol, 48%) of **4** were obtained as an orange solid. X-ray suited single crystals of **4** were grown by slow gas phase diffusion of *n*-pentane into a saturated DCM solution of **4** at -18 °C. ^{1}H NMR (500.1 MHz, $CDCl_3$): δ_H = 0.46 (s, 36H, $Si(CH_3)_3$), 7.17 (s, 2H, *H*a), 8.46 (d, $^{3}J_{H,H}$ = 9.4 Hz, 4H, *H*b), 8.98 (d, $^{3}J_{H,H}$ = 9.6 Hz, 4H, *H*c) ppm. ^{13}C NMR (125.8 MHz, $CDCl_3$): δ_C = 0.7, 109.0, 118.7, 120.2, 121.5, 124.0, 125.5, 128.0, 150.1 ppm. HR-MS (EI+) m/z clcd. for $[C_{36}H_{46}O_4Si_4]^+$: 678.24409 (found: 678.24731). IR (ATR), $\tilde{\nu}$ = 3072 (m), 2954 (w), 2864 (w), 1624 (w), 1596 (w), 1554 (m), 1504 (m), 1482 (w), 1423 (w),1393 (w), 1352 (w), 1292 (w), 1251 (m), 1190 (m), 1167 (s), 1147 (w), 1089 (w), 915 (w), 873 (m), 838 (m), 785 (w), 749 (w), 681 (w), 645 (w), 559 (w) cm^{-1}. λ_{max} (abs.) = 479 nm (DCM, ε = 42896 $L{\cdot}mol^{-1}{\cdot}cm^{-1}$). λ_{max} (em.) = 495 nm (DCM). CV: $E_{1/2}(Ox_1)$ = -0.09 V (vs. Fc/Fc^+), $E_{1/2}(Ox_2)$ = 0.17 V (vs. Fc/Fc^+).

*1,3,10,12-tetrakis((trimethylsilyl)oxy)benzo[rst]dinaphtho[8,1,2-cde:2',1',8'-klm]pentaphene (**13**)*

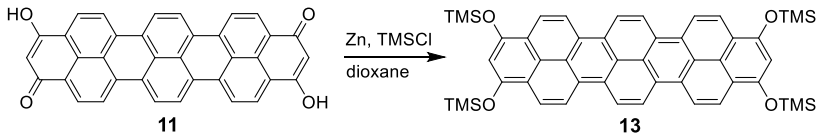

Teropyrenequinone **11** (153 mg, 0.3 mmol, 1.0 eq), Zn dust (315 mg, 4.8 mmol, 16.0 eq) and trimethylsilyl chloride (0.6 mL, 4.8 mmol, 16.0 eq) were stirred for 2 h under argon atmosphere at 100 °C in 40 mL 1,4-dioxane. The red solution was cooled to

room temperature and all volatile components were removed in vacuo. The residue was taken up in 20 mL of dichloromethane and filtered. After removing the solvent under vacuum, the crude product was washed with *n*-pentane. 45 mg (0.06 mmol, 10% over 2 steps) of **13** were obtained as an orange solid. X-ray suited single crystals of **13** were grown by slow gas phase diffusion of *n*-pentane into a saturated DCM solution of **13** at room temperature. ^{1}H NMR (500.1 MHz, $CDCl_3$): δ_H = 0.52 (s, 36H, Si(CH_3)$_3$), 7.24 (s, 2H, *H*a), 8.59 (d, $^{3}J_{H,H}$ = 9.3 Hz, 4H, *H*b), 9.17 (d, $^{3}J_{H,H}$ = 9.5 Hz, 4H, *H*c), 9.42 (s, 4H, *H*d) ppm. ^{13}C NMR (125.8 MHz, $CDCl_3$): δ_C = 0.8, 109.0, 118.7, 120.2, 122.2, 122.6, 123.7, 124.4, 124.9, 126.5, 127.8, 150.6 ppm. HR-MS (LIFDI+) m/z clcd. for $[C_{48}H_{50}O_4Si_4]^+$: 802.27861 (found: 802.27765). IR (ATR), $\tilde{\nu}$ = 2958 (w), 1592 (m), 1499 (m), 1391 (m), 1350 (w), 1301 (s), 1257 (w), 1188 (w), 1149 (w), 1021 (w), 878 (s), 848 (vs), 784 (m), 756 (w), 409 (w) cm^{-1}. λ_{max} (abs.) = 563 nm (DCM, ε = 77431 L·mol^{-1}·cm^{-1}). λ_{max} (em.) = 577 nm (DCM). CV: $E_{1/2}(Ox_1)$ = -0.04 V (vs. Fc/Fc$^+$), $E_{1/2}(Ox_2)$ = 0.25 V (vs. Fc/Fc$^+$).

*1,3,10,12-tetrakis((triisopropylsilyl)oxy)benzo[rst]dinaphtho[8,1,2-cde:2',1',8'-klm]pentaphene (**14**)*

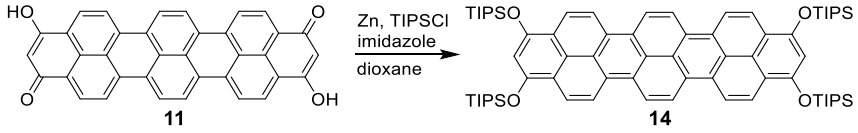

Teropyrenequinone **11** (180 mg, 0.35 mmol, 1.0 eq), Zn dust (190 mg, 2.91 mmol, 8.3 eq), imidazole (198 mg, 2.91 mmol, 8.3 eq) and triisopropyl chloride (0.6 mL, 2.9 mmol, 8.3 eq) were heated to 95 °C for 18 h under argon atmosphere in 20 mL 1,4-dioxane. The red solution was cooled to room temperature, diluted with 20 mL DCM and filtered over a pad of neutral aluminum oxide and rinsed with additional 50 mL DCM. The solvent was removed in vacuo and the purple residue was washed with diethyl ether (20 mL) and *n*-pentane (20 mL). 62 mg (0.05 mmol, 8% over 2 steps) of the purple-red solid **14** were obtained after drying in vacuo. ^{1}H NMR (500.1 MHz, $CDCl_3$): δ_H = 1.27 (d, $^{3}J_{H,H}$ = 7.5 Hz, 72H, $(CH_3)_2CH$), 1.57 (hept, $^{3}J_{H,H}$ = 7.5 Hz, 12H, $(CH_3)_2CH$), 7.27 (s, 2H, *H*a), 8.70 (d, $^{3}J_{H,H}$ = 9.4 Hz, 4H, *H*b), 9.14 (d, $^{3}J_{H,H}$ = 9.6 Hz, 4H, *H*c), 9.35 (s, 4H, *H*d) ppm. ^{13}C NMR (125.8 MHz, $CDCl_3$): δ_C = 13.5, 18.3, 107.5, 118.0, 119.9, 122.2, 122.5, 123.8, 124.4, 124.7, 126.5, 127.9, 151.5 ppm. HR-MS (LIFDI+) m/z clcd. for $[C_{72}H_{98}O_4Si_4]^+$: 1138.65421 (found: 1138.65888). IR (ATR), $\tilde{\nu}$ = 2944 (w), 2894 (w), 2866 (w), 1589 (w), 1497 (m), 1463 (s), 1389 (m), 1348 (s), 1299 (s), 1259 (m), 1187 (m), 1147 (w), 1019 (m), 860 (m), 781 (s), 681 (w) cm^{-1}. λ_{max} (abs.) = 572 nm (DCM, ε = 129393 L·mol^{-1}·cm^{-1}). λ_{max} (em.) = 587 nm (DCM). CV: $E_{1/2}(Red_1)$ = -2.21 V (vs. Fc/Fc$^+$), $E_{1/2}(Ox_1)$ = 0.00 V (vs. Fc/Fc$^+$), $E_{1/2}(Ox_2)$ = 0.24 V (vs. Fc/Fc$^+$).

*((2,13-dibutylbenzo[rst]benzo[12,1]tetrapheno[7,8,9-cde]naphtho[2,1,8-klm]pentaphene-1,3,12,14-tetrayl)tetrakis(oxy))-tetrakis(trimethylsilane) (**S4**)*

Quarteropyrenequinone **S3** (75 mg, 0.10 mmol, 1.0 eq), Zn dust (52 mg, 0.80 mmol, 8.0 eq) and trimethylsilyl chloride (0.2 mL, 1.6 mmol, 16.0 eq) were stirred for 3 h under argon atmosphere at 100 °C in 10 mL 1,4-dioxane. The dark blue solution was cooled to room temperature and all volatile components were removed in vacuo. The residue was taken up in 20 mL of dichloromethane and filtered. After removing the solvent under vacuum, the crude product was washed with *n*-pentane (10 mL). 22 mg (0.02 mmol, 14% over 2 steps) of **S4** were obtained as a dark blue solid. ^{1}H NMR (500.1 MHz, $CDCl_3$): δ_H = 0.48 (s, 36H, Si(CH_3)$_3$), 1.05 (t, $^{3}J_{H,H}$ = 7.5 Hz, *H*a), 1.26-1.35 (m, 8H, *H*b), 1.52-1.56 (m, 4H, *H*c), 8.58 (d, $^{3}J_{H,H}$ = 9.0 Hz, 4H, *H*d), 9.21 (d, $^{3}J_{H,H}$ = 9.5 Hz, 4H, *H*e), 9.48 (d, $^{3}J_{H,H}$ = 9.7 Hz, 4H, *H*f), 9.52 (d, $^{3}J_{H,H}$ = 9.7 Hz, 4H, *H*g) ppm. ^{13}C NMR not acquired due to low solubility. HR-MS (LIFDI+) m/z clcd. for $[C_{66}H_{70}O_4Si_4]^+$: 1038.43511 (found: 1038.43595). IR (ATR), $\tilde{\nu}$ = 2957 (m), 2940 (w), 1614 (s), 1500 (m), 1471 (w), 1326 (w), 1252 (m), 1221 (m), 1148 (m), 846 (vs), 784 (m), 755 (m), 658 (w) cm^{-1}. λ_{max} (abs.) = 634 nm (DCM). CV: $E_{1/2}(Red_2)$ = -2.00 V (vs. Fc/Fc$^+$), $E_{1/2}(Red_1)$ = -1.82 V (vs. Fc/Fc$^+$), $E_{1/2}(Ox_1)$ = 0.29 V (vs. Fc/Fc$^+$), $E_{1/2}(Ox_2)$ = 1.24 V (vs. Fc/Fc$^+$).

*1,3,10,12-tetrakis((triisopropylsilyl)oxy)benzo[rst]dinaphtho[8,1,2-cde:2',1',8'-klm]pentaphene (**15**)*

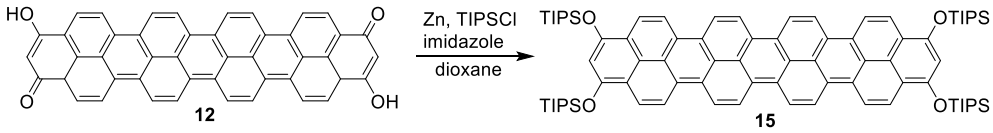

Quarteropyrenequinone **12** (189 mg, 0.30 mmol, 1.0 eq), Zn dust (320 mg, 4.80 mmol, 16.0 eq), imidazole (327 mg, 4.80 mmol, 16.0 eq) and triisopropyl chloride (1.0 mL, 4.8 mmol, 16.0 eq) were heated to 110 °C for 3 h under argon atmosphere in 20 mL 1,4-dioxane. The dark blue solution was cooled to room temperature, diluted with 20 mL chloroform and filtered over a pad of neutral aluminum oxide and rinsed with additional 50 mL DCM. The solvent was removed in vacuo and the dark blue residue was washed with methanol (20 mL), diethyl ether (20 mL) and *n*-pentane (20 mL). 68 mg (0.05 mmol, 14% over 2 steps) of the dark blue solid **15** were obtained after drying in vacuo. X-ray suited single crystals of **15** were grown by slow gas phase diffusion of *n*-pentane into a saturated DCM solution of **15** at room temperature. ^{1}H NMR (300.1 MHz, CD_2Cl_2): δ_H = 1.28 (d, $^{3}J_{H,H}$ = 7.4 Hz, 72H, $(CH_3)_2CH$), 1.56 (hept, $^{3}J_{H,H}$ = 7.5 Hz, 12H, $(CH_3)_2CH$), 7.26 (s, 2H, *H*a), 8.69 (d, $^{3}J_{H,H}$ = 9.5 Hz, 4H, *H*b), 9.10 (d, $^{3}J_{H,H}$ = 9.0 Hz, 4H, *H*c), 9.33 (br s, 8H, *H*d, *H*e) ppm. ^{13}C NMR (125.8 MHz, $CDCl_3$): δ_C = 12.4, 13.5, 17.8, 18.3, 107.5, 118.0, 119.9, 122.2, 122.3, 122.8, 123.7, 123.9, 124.4, 125.4, 126.8, 127.8, 151.6 ppm. HR-MS (LIFDI+) m/z clcd. for $[C_{82}H_{102}O_4Si_4]^+$: 1262.68551 (found: 1262.68521). IR (ATR), $\tilde{\nu}$ = 2948 (w), 2895 (w), 2866 (w), 1590 (w), 1498 (m), 1464 (s), 1389 (m), 1349 (m), 1300 (s), 1260 (m), 1186 (s), 1146 (w9, 1019 (m), 995 (w), 861 (m), 780 (vs), 681 (m) cm^{-1}. λ_{max} (abs.) = 642 nm (DCM, ε = 128215 L·mol^{-1}·cm^{-1}). λ_{max} (em.) = 670 nm (DCM). CV: $E_{1/2}(Red_2)$ = -2.19 V (vs. Fc/Fc$^+$), $E_{1/2}(Red_1)$ = -1.92 V (vs. Fc/Fc$^+$), $E_{1/2}(Ox_1)$ = -0.18 V (vs. Fc/Fc$^+$), $E_{1/2}(Ox_2)$ = 0.17 V (vs. Fc/Fc$^+$).

3.2 Publication 2: Tetrasubstituted Peropyrenes Formed by Reductive Aromatization: Synthesis, Functionalization and Characterization

Citation: S. Werner, T. Vollgraff, J. Sundermeyer, *Chem. Eur. J.* **2021**, *27*, 11065-11075.[B]

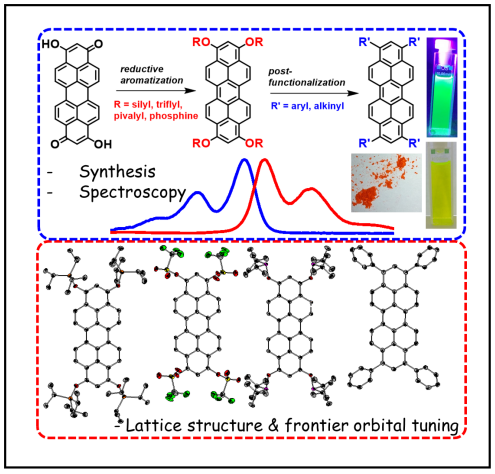

Summary: This full paper is a follow-up study of the reductive functionalization strategy introduced in Publication 1 with focus on novel peropyrene 1,3,8,10-tetra functionalization motifs. In a first reduction step of dihydroxy-peropyrenequinone, a symmetrical functionalization of the peropyrene backbone introducing silylethers, pivaloyl-, triflyl- and also phosphinite-groups was demonstrated by utilization of *n*-butyl lithium or zinc as inexpensive reducing agents. Furthermore, the potential to use the corresponding tetrapivaloate and tetratriflate in transition metal catalyzed cross couplings was explored leading to three different 1,3,8,10-tetraaryl- and one tetraalkynyl-peropyrene. The influence of nine different substituents on the optoelectronic properties of the functionalized peropyrenes was investigated in solid state by means of X-ray crystallography, in solution by means of UV-Vis and PL spectroscopy. Their redox properties were studied via cyclovoltammetry. Fluorescence quantum yields up to 84% and absorption maxima ranging between 440 and 525 nm could be observed. By comparison with DFT and TD-DFT calculations, it could be elucidated that introduction of a broad variety of substituents leads to peropyrenes with easily finetunable HOMO and LUMO energies ranging in a HOMO-LUMO gap window of 0.8 eV. Furthermore, it could be verified that terminal 2,9-substituents do not affect the HOMO/LUMO energies, since these positions do not contribute to the frontier Kohn-Sham molecular orbitals. The frontier molecular orbital energies and chemical stability identify the target molecules as promising candidates for hole transporting semiconductors.

Own Contribution: All experimental work was done by myself as well as characterization by spectroscopical (UV-Vis/PL) and electrochemical (CV/DPV) measurements and (TD-)DFT calculations. T. Vollgraff solved and refined the crystal structures. NMR and mass spectra were recorded by service departments of the faculty. Prof. Dr. J. Sundermeyer initiated and supervised this study and was available as valuable discussion partner. The manuscript was written by myself with feedback of Prof. Dr. J. Sundermeyer.

[B]Reproduced with permission of S. Werner, T. Vollgraff, J. Sundermeyer, *Chem. Eur. J.*, **2021**, *27*, 11065-11075,

Chemistry–A European Journal | Full Paper
doi.org/10.1002/chem.202101101
Chemistry Europe
European Chemical Societies Publishing

Tetrasubstituted Peropyrenes Formed by Reductive Aromatization: Synthesis, Functionalization and Characterization

Simon Werner,[a] Tobias Vollgraff,[a] and Jörg Sundermeyer*[a]

Abstract: The chromophore class of 1,3,8,10-tetrasubstituted peropyrenes was effectively synthesized from peropyrenequinone via a Zn-mediated reductive aromatization approach. In one step, a symmetric functionalization of the peropyrene backbone introducing silylethers (**2**,**3**), pivaloyl (**4**), triflyl (**5**) and also phosphinite (**6**) groups was established. Furthermore, the potential of using **4** and **5** in transition metal catalysed cross couplings was explored leading to 1,3,8,10-tetraaryl (**8**-**11**) and tetraalkynyl (**7**) peropyrenes. The influence of various substituents on the optoelectronic properties of these π-system extended peropyrenes was investigated in solid state by means of X-ray crystallography, in solution by means of UV-Vis and fluorescence spectroscopy and by their redox properties studied via cyclic voltammetry. By comparison with DFT and TD-DFT calculations, it could be elucidated that introduction of a broad variety of substituents in such versatile one or two step procedures leads to peropyrenes with easily tunable HOMO and LUMO energies ranging in a gap window of 0.8 eV. The frontier molecular orbital energies identify the target molecules as promising candidates for hole transporting semiconductors.

Introduction

Polyaromatic Hydrocarbons (PAHs) with atomically precise defined structures have received broad research interest in the past decade because of their manifold applications, for example their use in organic light-emitting diodes (OLED) or organic field effect transistors (OFET) and organic solar cells (OSC).[1–4] One of the first versatile synthetic approaches to PAHs were described at the beginning of the past century by Scholl et al.[5,6] In 1943, Clar reported the synthesis of dibenzoperylene, named peropyrene because of its structural consistence of both PAH systems perylene and pyrene.[7] Peropyrene served as model for studying the aromaticity of different benzene rings in PAH and let him define the aromatic π-sextet rule with respect to the stability of aromatic systems (see Scheme 1).[8–10] Since then, research on peropyrene has been neglected for some decades. This changed in the context of systematic investigations of the relationship between structure and (optical) properties of PAHs.[11] For example in polyacenes such as pentacene,[12,13] large energetical separations between the triplet (T_1) and the singlet (S_1) state made it possible to consider these compounds as singlet fission materials potentially utilizable for solar cell applications.[14–16] This photophysical process was also observed in perylene[17,18] and perylene diimides.[19] Earlier work reported on photoconductivity[20] and fluorescence quenching properties[21] of peropyrene in solution suggesting that peropyrene could also be a singlet fission material in solution. In 2013, Bardeen and co-workers reported on the photophysical properties of peropyrene in solution and solid state, showing that the S_1 energy is significantly lowered in crystalline state.[22]

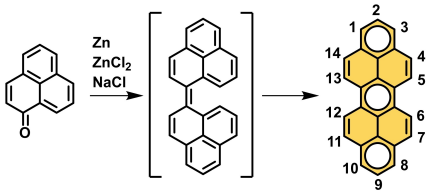

Scheme 1. Clar-synthesis of peropyrene and the in situ formed biphenalenylidene intermediate. The C–H positions of peropyrene are numbered and the π-sextets according to Clar are highlighted.[7,8]

However, the use of peropyrenes as a crystalline singlet fission material requires the development of synthesis strategies for substituted peropyrenes with tunable properties both in solution and film as well as in the crystalline state. The original synthesis by Clar yielded peropyrene via reductive coupling of 1-phenalenone using a salt melt consisting of Zn, $ZnCl_2$ and NaCl under harsh conditions at 300 °C (Scheme 1).[7]

Pogodin, Agranat and co-workers modified the reductive dimerization strategy using milder conditions such as low valent titanium reagents related to McMurry reaction conditions with $TiCl_4$/$LiAlH_4$ in tetrahydrofuran.[23] Alternatively, P_2S_5 in benzene[24] was used in order to dimerize two phenalenone

[a] S. Werner, T. Vollgraff, Prof. Dr. J. Sundermeyer
Fachbereich Chemie and Material Science Center
Philipps-Universität Marburg,
Hans-Meerwein-Straße 4, 35032 Marburg (Germany)
E-mail: JSU@staff.uni-marburg.de

Supporting information for this article is available on the WWW under https://doi.org/10.1002/chem.202101101

Chemistry–A European Journal | Full Paper doi.org/10.1002/chem.202101101 | Chemistry Europe European Chemical Societies Publishing

radicals to biphenalenylidene, which in situ forms peropyrene via electrocyclization. Experimental evidence for this mechanism was reported by Uchida et al. who isolated dihydroperopyrene, the electrocyclization product of biphenalenylidene, which forms peropyrene after oxidation.[25] Beer et al. used the dimerization of phenalenyl radical cations in the synthesis of functionalized peropyrenes.[26] Peropyrene was also synthesized via intramolecular dehydrogenative C–C-bond coupling of metacyclophane and subsequent oxidation using DDQ.[27]

So far, approaches for the synthesis of functionalized peropyrenes in 2- and 9-position require multistep synthesis protocols.[28] A more convenient protocol was developed by Chalifoux and co-workers who built up the peropyrene scaffold by acid mediated intramolecular benzannulation of internal alkynes (Scheme 2a).[29–31] This approach enables the functionalization of the bay positions of peropyrene and leads therefore to twisted peropyrens with up to 18° out of plane twist angle and axial chirality.[30] The most twisted representative is a tetranaphthyl annulated peropyrene built up via oxidative Scholl dehydrogenation of a tetranaphthyl-diphenylbenzene precursor reported by the group of Miao (Scheme 2b)[32] and later extended with pyrene functionalities by Feng.[33] Recently, these authors also accessed a dicyclopenta-fused peropyrene via alkyne annulation approach.[34]

Since many peropyrene syntheses require low-yield aromatization steps or multistep synthesis approaches, we aimed to establish a higher yield synthetic approach with only a short number of steps. Thereby we were able to obtain peropyrenes with a yet undescribed 1,3,8,10-substitution pattern. Recently, the group of Mateo-Alonso described a reductive mono- and dialkylation of a non-hydroxylated peropyrenequinone.[35,36] But they could not separate the two formed 1,8- and 1,9-isomers.[36] We used bis-hydroxylated peropyrenequinones[37] as precursors, allowing an new approach to symmetric fourfold peropyrene substitution. Recently, we demonstrated the potential of a reductive O-silylation strategy in the synthesis of peropyrene's higher homologues, terropyrene and quarterropyrene.[38] As a key step, we modified and applied the reductive aromatization step recently reported for the reductive functionalization of perylene diimide (PTCDI)[39,40] by using Zn instead of Na as bench stable and less powerful reducing agent. In the following we add proof, that this protocol is perfectly suitable for the introduction of different functional groups via post-functionalization of reactive triflyl and pivaloyl peropyrene key intermediates (Scheme 2c).

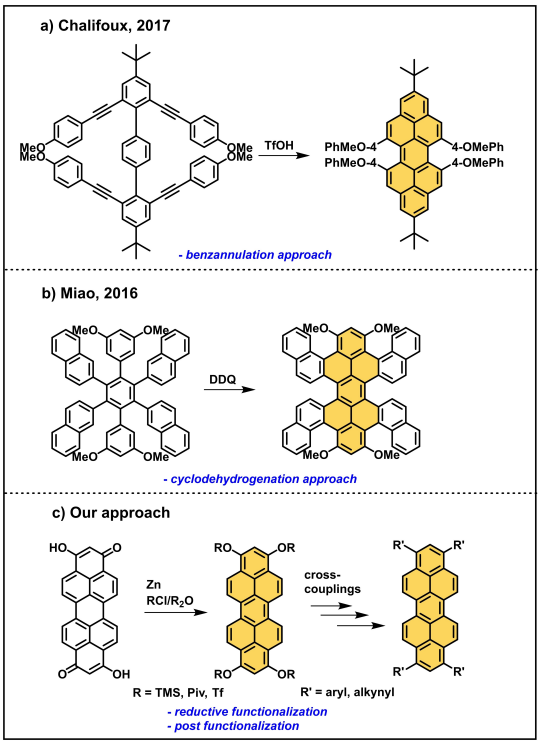

Scheme 2. a) TfOH-mediated benzannulation approach for the synthesis of bay-substituted peropyrens by Chalifoux,[30] b) Miao's synthesis of highly twisted peropyrenes via Scholl reaction,[32] and c) our approach for the synthesis of 1,3,8,10-tetrasubstituted peropyrenes via reductive aromatization and post-functionalization.

Results and Discussion

Synthesis

Starting point for our reductive aromatization strategy was peropyrenequinone (**1**), synthesized according to a protocol of Bock.[37] **1** is a purple pigment, which is almost insoluble in common organic solvents. However, when suspended together with an excess (8 eq) of zinc dust and trimethylsilyl chloride in 1,4-dioxane at 60–80 °C, a green, fluorescent solution appears which yields the corresponding reduced 1,3,8,10-tetrasiloxy peropyrene **2** in a yield of 48% (Scheme 3). Reductive trimethylsilylations are already known for anthracene-9,10-dione. They are privileged due to the activation of zinc by trimethylsilyl chloride.[41]

The analogous reaction conditions using Mg turnings instead of Zn dust yielded only traces of product **2**, whereas the reaction failed completely when Na or C_8K were used as reducing agent instead. This can be explained with the higher reduction potential of Na and C_8K compared to Zn, which might lead to undesirable overreduction to product radical anions or activation of the relatively acidic protons of peropyrenequinone in 2- and 9-position. The moderately air sensitive orange solid **2** could be easily purified from zinc dichloride and excess zinc by dissolving the crude product in dichloromethane, filtration and removing the solvent, since the polymeric zinc chloride dioxane adduct is insoluble in chlorinated solvents.[38] An air stable product can be obtained, when **1** is reacted with triisopropylsilyl chloride (TIPSCl) instead of TMSCl. Notable, a moderate yield of 20% of peropyrene **3** could only be achieved by using imidazole as equimolar activation reagent for triisopropylsilyl chloride. Chemically more robust **3** could be purified by column

Chemistry–A European Journal | Full Paper doi.org/10.1002/chem.202101101 | Chemistry Europe European Chemical Societies Publishing

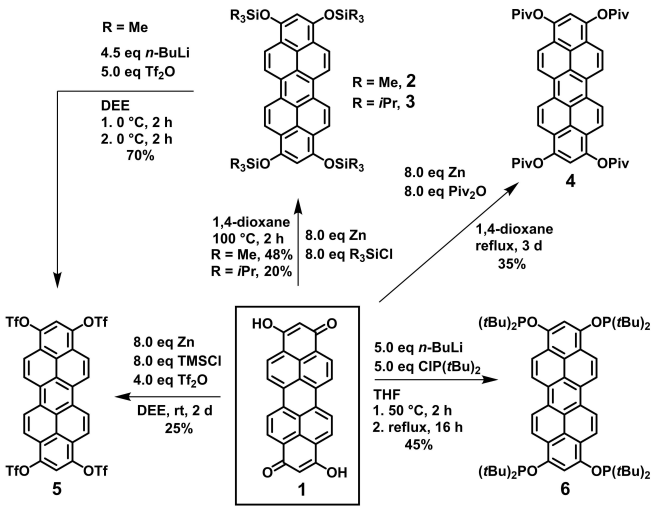

Scheme 3. Reductive aromatization strategies to convert peropyrenequinone **1** to the corresponding peropyrene silylethers **2** and **3**, pivaloate **4**, triflate **5** and phosphinite **6** under mild conditions using Zn or *n*-butyl lithium as reducing agent.

chromatography on silica. Its lower reactivity compared to **2** is due to the higher steric demand of TIPSCl versus TMSCl. In order to synthesize peropyrenes with carboxyl ester groups in 1,3,8,10-position which provide a possibility for further functionalization, i.e. in cross coupling reactions, a direct reduction of **1** to corresponding tetrapivaloyl-substituted peropyrene **4** was accomplished in moderate yield (35%) by refluxing **1** with 8 eq of zinc dust and pivalic anhydride for 3 days. Recently, this reductive pivalation strategy was also used Miyake et al. for their functionalization of naphthalene diimide (NTCDI) to tetrapivaloxy-2,7-diazapyrene[42] and of perylene diimide (PTCDI) to tetrapivaloxy-2,7-diazaperopyrene.[43] The corresponding pivaloates were subjected to Ni-catalysed cross couplings. In contrast to trimethylsilyl ether **2**, pivalate **4** is air stable and moisture insensitive, thus a purification by column chromatography on silica was possible.

We discovered, that silylether **2** can easily be deprotected and activated via stoichiometric reaction with 4 eq. of *n*-butyl lithium at 0 °C in diethyl ether: Desilylation is observed, formation of silane *n*-$BuSiMe_3$ and a purple suspension of 1,3,8,10-tetralithoxy peropyrene. Slow addition of trifluoromethanesulfonic acid anhydride (Tf_2O) to this in situ prepared suspension of an activated form of **2** allowed to isolate tetratriflate **5** in good yield of 70%, whereas lithium triflate remains in solution. Due to the high reactivity of the triflate groups, **5** is air sensitive. Direct treatment of **1** with zinc, TMSCl and Tf_2O also yields **5** in a one-pot approach, however in lower yields (25%) and with a larger amount of undesired side products difficult to separate. **1** could be directly reduced and converted to 1,3,8,10-tetralithoxy peropyrene by applying 6 eq. of *n*-butyl lithium as base and reducing agent in tetrahydrofurane (THF). By treating this tetra-lithoxy intermediate with di-*tert*-butylchlorophosphine in THF, air sensitive peropyrene 1,3,8,10-tetraphosphinite **6** was obtained in good yield (45%). After an *ortho*-directed CH-activation, **6** might serve as a PCP pincer ligand[44–49] for binuclear transition metal complexes. This fourfold O-phosphination can also be accomplished starting from trimethylsilyl ether **2**, its desilylation with *n*-BuLi and quenching in situ formed ArO–Li intermediates by *t*-Bu_2PCl. Contrastingly, the in situ Zn reduction method failed, since chlorophosphines are prone to form P–P bonds[50] under reductive conditions needed to reduce peropyrenequinone **1**. After discovering the reductive functionalization of **1** with activatable groups, we explored the scope of possible post functionalization reactions. Therefore, pivaloate **4** and triflate **5** were subjected to transition metal catalysed cross coupling reactions (Scheme 4).

Aryl triflates are known to display similar reactivity in Pd catalysed cross coupling reactions as aryl bromides.[51] Therefore, triflate **5** was first reacted with trimethylsilyl acetylene under Sonogashira cross coupling conditions at 2.5 mol% ratio per triflate functional group (10 mol% per **5**).[52] Under optimized conditions, using CuI and $[Pd(dppf)Cl_2]$ as catalyst in a mixture of triethylamine and tetrahydrofuran, 10% of the corresponding peropyrene-tetraalkyne **7** was isolated as a dark red solid after preparative TLC. We suppose that the rather low yield results from a partial product decomposition during the necessary chromatographic purification. So far, other alkyne substituents (e.g. phenylacetylene) only led to complex inseparable product mixtures under these reaction conditions.

Next, we reacted **5** under typical Suzuki-Miyaura cross coupling conditions using $[Pd(PPh_3)_4]$ as catalyst and potassium carbonate as mild base in dioxane/water and 2.5 mol% catalyst ratio per triflate functional group (10 mol% per **5**). Two representative reactions using 2-thienylboronic acid and 3,5-bis (trifluoromethyl)phenyl boronic acid were chosen in order to

Chemistry–A European Journal
Full Paper
doi.org/10.1002/chem.202101101
Chemistry Europe
European Chemical Societies Publishing

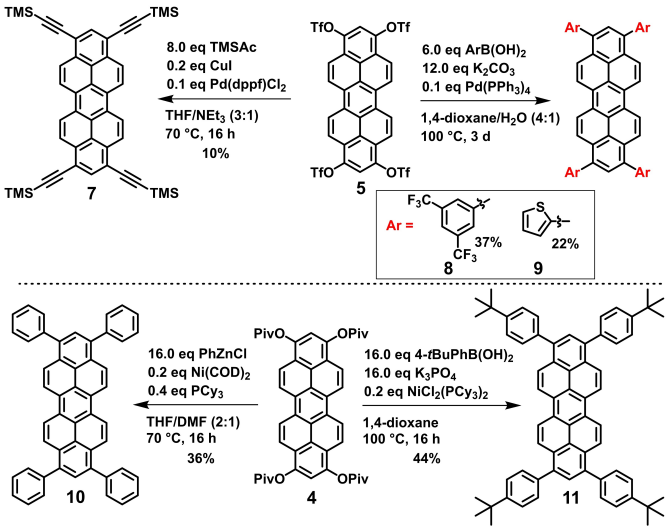

Scheme 4. Post-functionalization of triflate **5** and pivalate **4** in Ni and Pd catalysed cross-coupling reactions for the formation of alkenyl (**7**)- and aryl (**8**-**11**)-functionalized peropyrenes.

synthesize tetraaryl-peropyrenes with four electron-donating 1-thienyl groups or four moderately electron-withdrawing 1,3-trifluromethylphenyl groups. Both tetraaryl-peropyrenes **8** and **9** were isolated in 37% (**8**) and 22% (**9**) yield as air stable orange-reddish solids after column chromatography. Interestingly, no impurities from side-products bearing less than four aryl groups were detected under this protocol. Nevertheless, the moderate yields show that triflate **5** tends to decompose to a certain extent, probably due to its limited stability towards water/K_2CO_3.

Aryl pivaloates had been developed to be reactive substrates in Ni catalysed cross-coupling reactions. They might serve as economically and ecologically friendlier alternative to Pd-catalysed Ar–Ar′ couplings of aryl halides and triflates.[53–58] Therefore, we explored the reactivity of tetrapivaloate **4** in two representative Ni-catalysed cross-couplings. The first uses [Ni(COD)$_2$] as Ni(0) precatalyst and tricyclohexylphosphine in 5 mol% ratio per pivaloate functional group (20 mol% per **4**) and aryl zinc reagents in a Negishi-type cross-coupling protocol.[54] Thus, an excess of PhZnCl prepared in situ from PhLi and $ZnCl_2$ in THF converted **4** into tetraphenyl peropyrene **10** in 34% yield after column chromatography. Improved Ni-catalysed cross coupling protocols use the cheaper and bench stable precatalyst [$NiCl_2(PCy_3)_2$] and an excess of an aryl boronic acid as coupling reagent and reducing agent for the Ni(II) precatalyst.[56] Under such water-free Suzuki-Miyaura cross-coupling conditions in dioxane with K_3PO_4 as base,[56] it was possible to synthesize 4-*tert*-butylphenyl substituted peropyrene **11**. The yield 44% seems to be moderate, nevertheless it is 81% (av.) per coupling step, slightly higher than in the Pd-catalysed cross-couplings of triflate **5**. Comparable yields were obtained in Ar–Ar′ couplings with tetrapivaloxy-2,7-diazapyrenes.[42] However, the scope of achievable peropyrene substituents compatible with the Ni catalysed cross coupling protocol is limited. Other examples of aryl derivatives such as **8** or **9** could not be synthesized under nickel mediated conditions. In conclusion, pivaloate **4** turned out to be a more stable but less reactive alternative to triflate **5** for the synthesis of tetraaryl peropyrenes. All synthesized tetraaryl-peropyrenes **8**–**11** show an excellent stability towards water and air which makes them to promising candidates for further investigations applying them in organic semiconductor or OLED devices.

Crystallography

In order to study the molecular and lattice structure of 1,3,8,10-tetrasubstituted peropyrenes with respect to their functional groups, single crystals were grown from a saturated *n*-pentane solution at −20 °C (**6**) and via slow diffusion of *n*-pentane vapor into saturated dichloromethane or chloroform solutions at room temperature (**3**, **5**, **10** and **11**). Figure 1 displays their molecular and crystal lattice structures in form of their unit cells.[59] Silyl ether **3** crystallizes in monoclinic space group $P2_1/c$ with pairs of molecules arranged in a herringbone arrangement with 90° angles between different slipped stacks. All other compounds **5**, **6**, **10** and **11** crystallize in triclinic space group $P\bar{1}$ with a molecular and crystallographic inversion centre at the central peropyrene backbone defining symmetry related substituents in 1,3,8,10-positions. Steric demand of triisopropyl silyl groups in **3** and bis-*tert*-butylphosphanyl substituents in **6** prevent their peropyrene backbones from any π-stacking. Molecules rather pack in a staggered manner. In contrast, triflate-substituted peropyrene **5** forms π-stacked dimers with

Chemistry–A European Journal
Full Paper
doi.org/10.1002/chem.202101101
Chemistry Europe
European Chemical Societies Publishing

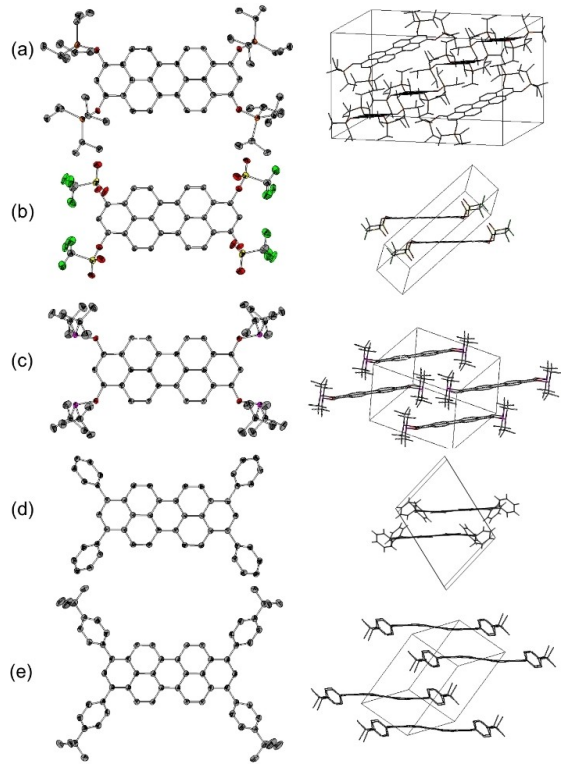

Figure 1. Molecular and lattice structures of (a) **3**, (b) **5**, (c) **6**, (d) **10** and (e) **11**. Ellipsoids are shown at 50% level; all hydrogen atoms and solvent molecules are omitted for clarity.[59]

an intermolecular distance of 3.37 Å. Such dimers are also observed in phenyl substituted peropyrene **10** and *tert*-butylphenyl substituted congener **11**, both with slightly larger intermolecular distances of 3.67 Å and 3.68 Å, respectively. The latter are induced by an out of plane twist of the phenyl groups with respect to the peropyrene plane: the dihedral angels are 53.4° and 50.6° for **10** and 55.5° and 49.5° for **11**.

The different substituents on the peropyrene backbone do not only influence the capability of π-stacking but also the planarity of the peropyrene backbone measured as torsion angle of neighbouring naphthalene units. The twist is not at similar level as observed for substituents in bay positions.[30]

Little distortion is observed for triflate **5** (0.3°) and phosphinite **6** (0.7°). In triisopropyl silyloxy-substituted **5** (2.5°) or phenyl-substituted **10** (2.3°) the twist angle gets higher and reaches a maximum at *p-tert*-butylphenyl-substituted **11** (4.9°). Only silyl ether **3** crystallizes in the same monoclinic space group $P2_1/c$ as unsubstituted peropyrene.[22] The herringbone structural motif associated with parent peropyrene was identified to be responsible for a low energy gap between T_1 and S_1 states in crystalline state, thus for poor ability for singlet fission.[15,22] In contrast, **5**, **6**, **10** and **11** crystallize in space group $P\bar{1}$. Therefore, this particular substituent pattern provides a handle for peropyrene crystal engineering, a topic previously demonstrated for other substitution patterns of peropyrene.[26,28]

Optical Spectroscopy

The influence of different substituents in 1,3,8,10-position on optical properties of 2–11 was investigated by UV/Vis and photoluminescence (PL) spectroscopy (Figure 2 and Table 1). All spectra were recorded in dichloromethane. A dependency of the energy of absorption and emission maxima from concentration in solution was not observed. Aggregation in solution tends to be small.

Compounds **2**–**11** also show pronounced vibronic progression fine structures with spacings of ~30 nm, typical for the π*←π transition of other perylene derivatives[60,61] and parent peropyrene.[22] Only alkynyl substituted 7 and 2-thienyl substituted 9 display a less distinct vibronic progression, probably due to aggregation effects. The emission bands are mirror images of the corresponding absorption bands, indicating similar molecular conformation of the electronic ground state and excited state.[62] Triflate 5 is the only derivative displaying only weak fluorescence due to an overlay of the first vibronic

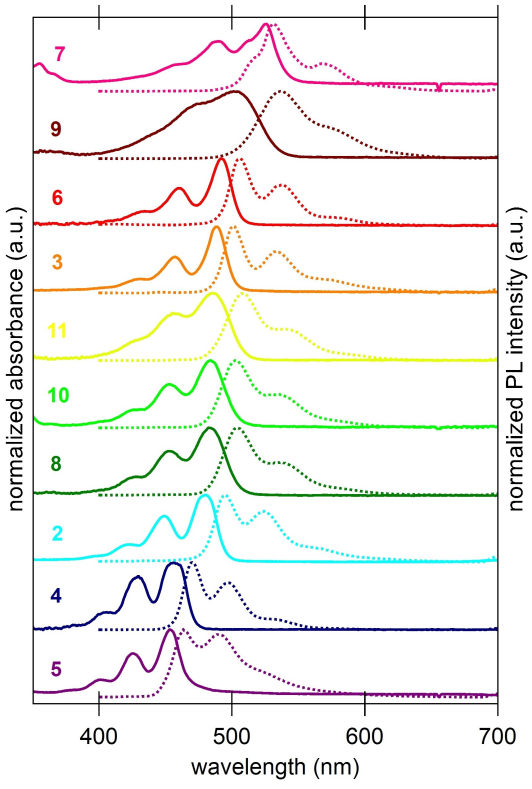

Figure 2. Normalized absorption and corresponding photoluminescence (PL) spectra (dashed) of 2–11 in dichloromethane.

Chemistry–A European Journal | Full Paper doi.org/10.1002/chem.202101101 | Chemistry Europe European Chemical Societies Publishing

Table 1. Absorption and emission data of **2**–**11** ordered in decreasing HOMO-LUMO gap.

Compound substituent R)	$\lambda_{max,abs.}$ (nm) [ε (10^{-4} L mol^{-1} cm^{-1})]	$\lambda_{max,em.}$ (nm) [Φ_{PL}]	Stokes shift (eV)	$E_{g,opt}$ (eV)[a]
5 (OTf)	453 [3.42]	464 [0.02]	0.07	2.70
4 (OPiv)	456 [5.55]	470 [0.02]	0.08	2.67
2 (OTMS)	479 [4.29]	495 [0.30]	0.08	2.54
8 ($(CF_3)_2C_6H_3$)	482 [1.11]	502 [0.52]	0.10	2.51
10 (Ph)	483 [6.17]	500 [0.51]	0.09	2.52
11 (tBuC$_6$H$_4$)	485 [9.19]	506 [0.66]	0.11	2.49
3 (OTIPS)	488 [8.27]	500 [0.84]	0.06	2.51
6 (OP(tBu$_3$)$_2$)	492 [7.49]	506 [0.72]	0.07	2.48
9 (2-thienyl)	505 [7.12]	537 [0.25]	0.14	2.38
7 (TMSA)	526 [4.85]	531 [0.37]	0.02	2.35

[a] Determined from the intersection wavelength of normalized absorption and emission spectra.

progression mode with the fluorescence maximum. All other compounds show a qualitatively strong fluorescence. It seems that triflate groups trigger fluorescence quenching effects as it was discussed by Gade et al. for tetrabrominated tetraaza-peropyrenes.[63] Congeners **2**–**11** do show neither shifts of the UV-Vis maxima in their concentration-dependent UV-Vis spectra (see Figures S1–S10) nor solvatochromic effects. Aryl substituted compounds **8**, **9** and **11**, in particular, display high molar attenuation coefficients (ε), whereas acceptor-substituted **4** and **5** show lower values of ε. In general, the absorption and emission maxima are ranging over 72 nm and reflect the electron donating or withdrawing effects of the substituents: The electron-poor triflate **5** (454 nm) displays most hypsochromically shifted, the electron-rich trimethylsilyl alkynyl substituted 7 (526 nm) most bathochromically shifted maxima. The determined fluorescence quantum yields (Φ_{PL}, determined by dilution method[62] in DCM (see Supporting Information and Table 1) are high (up to 84%) for electron-rich compounds **3** and **6** and slightly lower for aryl-substituted congeners (up to 66%) owed supposedly due to higher reorganization energy losses.[62] The quantum yields are as high as those of comparable diazaperopyrenes[43] or twisted peropyrenes.[31] Remarkably, fluorescence is nearly deactivated (Φ_{PL} = 2%) for electron-deficient substituents (**4** and **5**).

Our findings show that a precise fine tuning of absorption and emission maxima of peropyrenes is possible by substituent variation within the 1,3,8,10substitution pattern introduced here. Next to triflate **5**, pivaloate **4** is more hypsochromically shifted, whereas next to alkynyl derivative **7**, silylethers **2** and **3** and especially phosphinite **6** are more (~25-30 nm) bathochromically shifted.

It is evident, that all three aryl substituted derivatives **8**, **10** and **11** display very similar absorption maxima around 483 nm, which leads to the conclusion that the nature of +I or -I substituents attached to the benzene ring, *p*-tBu (**11**) vs. 3,5-CF_3 (**8**) vs. H / none (**10**) does not influence the HOMO-LUMO gap significantly (Figure 4). They are orange-coloured solids and form yellow solutions with green fluorescence (Figure 3).

In contrast aryl substituents with +M effect such as 2-thienyl groups in **9** lead to a significant bathochromic shift to 505 nm in the absorption. Not unexpectedly, conjugation to an electron-rich π-system such as thiophene in **7** (or alkyne in **9**) is

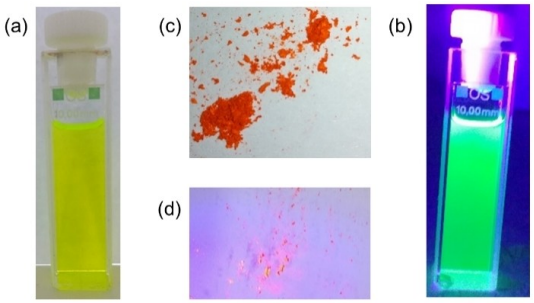

Figure 3. Photographs of peropyrene **8** in solution (~10^{-5} M) under (a) ambient light; (b) under UV-light (366 nm) and as powder under (c) ambient light and (d) under UV-light (366 nm).

triggering the HOMO-LUMO gap more efficiently. In order to rationalize the individual influence of substituents in this respect, we calculated the ground state geometries of **2**–**11** at def2-TZVPP/B3LYP level of theory (see Supporting Information, Tables S2–S11 for cartesian coordinates of the optimized geometries). The frontier Kohn-Sham orbitals support our experimental observation that substituents in 1,3,8,10-position influence the electronic properties. The HOMO and LUMO are delocalized all over the peropyrene core. However, the participation of substituent orbitals on both HOMO and LUMO coefficients particular at 1,3,8,10-positions is increasing in the order Ph (**10**) < 2-thienyl (**7**) < alkynyl (**9**) (Figure 4) whereas no significant changes are observed for differently substituted phenyl substituents (**8**, **10** and **11**).

The trend in the absorption spectra is also reflected by TD-DFT calculations at def2-TZVPP/PBE level of theory assigning the absorption maxima mostly to HOMO-LUMO (S_0 to S_1) transitions (see Figure S21 and Table S1 for details). The mirrored photoluminescence spectra are following the same trend with only small Stokes shifts (10-20 nm) typically observed for rigid chromophores such as well-studied perylene diimides.[60,61] Thienyl substituted **8** displays a larger Stokes shift and broader absorption and emission bands indicating geometry changes between ground state and excited state, in other words a large reorganization energy. Contrastingly, alkyne derivative **7** displays a very small Stokes shift of 5 nm indicating similar

Chemistry–A European Journal
Full Paper
doi.org/10.1002/chem.202101101
Chemistry Europe
European Chemical Societies Publishing

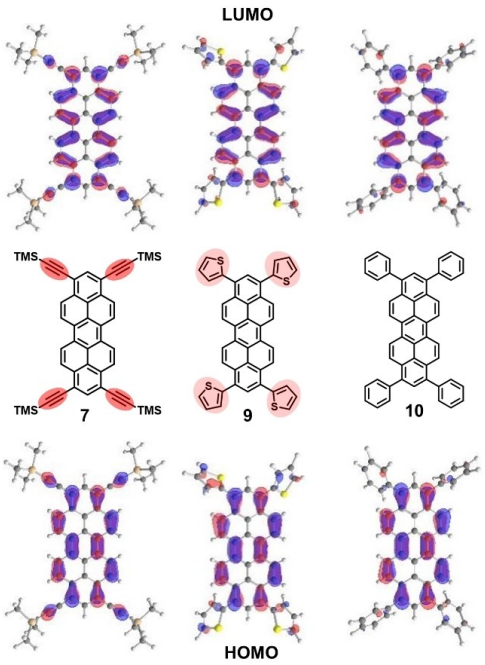

Figure 4. Molecular orbitals of **7** (left), **9** (centre) and **10** (right) (def2-TZVPP/B3LYP level of theory, isoval. 0.03 a.u.) in comparison.

molecular geometries in ground state and excited state with almost no energy loss by molecular reorganization between absorption and fluorescence. Similar observations were made for other alkynyl substituted aromatic systems.[40,63] Finally, we approximated the magnitude of the optical energy gaps as the energy of the intersection wavelength of the normalized absorption and emission spectra (Table 1).[64] Not surprisingly, the trend of the optical gap narrowing in the range 2.70 eV for **5** to 2.38 eV for **7** follows previously discussed trend in bathochromically shifted absorption and emission spectra. This trend is in accord with peropyrenes functionalized only in 1- and 8-position.[35,36]

Electrochemistry and theoretical modelling of the frontier orbital energies

Electrochemical properties of these 1,3,8,10-substituted peropyrenes were investigated by cyclic voltammetry (CV) and differential pulse voltammetry (DPV) vs. ferrocene as internal standard (Figure 5 and Table 2, Figures S13–S22). Only triflate **5** and pivaloate **4** showed irreversible redox behaviour and decomposition during CV data acquisition under the defined parameters. All aryl substituted derivatives **8**–**11** display two almost reversible oxidation waves and one reversible reduction wave underlining their electron rich PAH character. In addition, **8** and **9** display a second quasi reversible reduction wave. As expected, 3,5-CF_3-substituted aryl derivative **8** is the easiest to be reduced and the most difficult to be oxidized, whereas phenylogue *tert*-butyl derivative **11** is easiest to be oxidized and most difficult to be reduced. We were surprized to find, that thienyl substituted heteroaryl congener **9** tends to be in the middle range, less easily oxidized and less easily reduced than just mentioned phenyl derivatives tuned to only one extreme (Figure 2). The accessibility of first oxidation and reduction potentials in this arene substituent series observable as metastable radical anion and radical cation species allows to

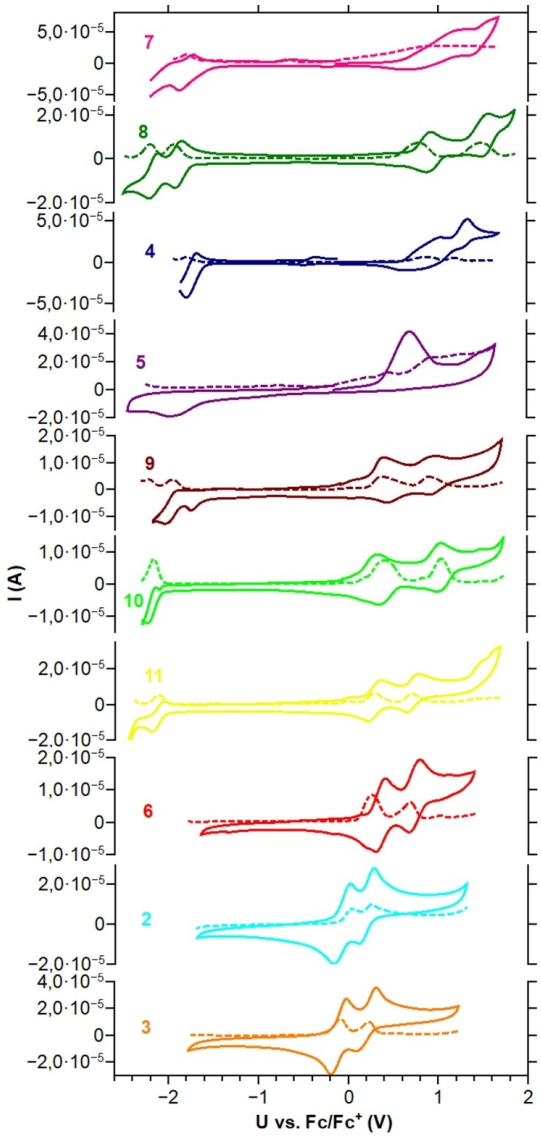

Figure 5. Cyclic voltammograms of **2**–**11** (measured in CH_2Cl_2, 0.1 M *n*-Bu_4NPF_6, 50 mV s^{-1} scan rate, glassy carbon electrode) and their corresponding differential pulse voltammograms (DPV, dashed lines, 10 mV s^{-1} scan rate).

Chemistry–A European Journal | Full Paper doi.org/10.1002/chem.202101101 | Chemistry Europe European Chemical Societies Publishing

Table 2. Electrochemical Data of **2**–**11**.

Compound	$E_{1/2,Red1}$ (V)	$E_{1/2,Ox1}$ (V)	$E_{1/2,Ox2}$ (V)	$E_{HOMO,exp}$ (eV)[a]	$E_{LUMO,exp}$ (eV)[b]
3 (OTIPS)	–	−0.11	0.21	−4.69	−2.18
2 (OTMS)	–	−0.07	0.19	−4.73	−2.19
6 (OP(tBu$_3$)$_2$)	–	0.23	0.61	−5.03	−2.55
11 (tBuC$_6$H$_4$)	−2.12	0.29	0.73	−5.09	−2.60
10 (Ph)	−2.18	0.34	1.00	−5.14	−2.62
9 (2-thienyl)	−1.94[c]	0.43	0.94	−5.23	−2.85
5 (OTf)	≈−1.9	≈−0.7	–	−5.50	−2.80
4 (OPiv)	−1.73	0.83	1.30	−5.63	−2.93
8 ((CF$_3$)$_2$C$_6$H$_3$)	−1.88[d]	0.90	1.53	−5.70	−3.19
7 (TMSA)	−1.81	0.99	–	−5.79	−3.44

[a] Determined using literature methods by referencing on Fc/Fc^+ as internal standard (E_{HOMO} (fc) = -4.8 eV) added after data acquisition: $E_{HOMO,exp} = -4.8\ eV - E_{1/2,ox1}$. [b] Determined with help of the optical gap ($E_{g,opt}$, see Table 1): $E_{LUMO,exp} = E_{HOMO,exp} + E_{g,opt}$. [c] $E_{1/2,Red2} = -2.20$ V. [d] $E_{1/2,Red2} = -2.17$ V.

discuss a narrowing of the electrochemical window within the aryl substituted species **8** (2.77 eV) up to **9** (2.37 eV) as it is also the case for the optically determined energy gaps.

Beyond the limits of these aryl derivatives first oxidation potentials are ranging from −0.11 V for TIPS-substituted derivative **3**, the easiest to be oxidized in this series and 0.99 V for alkynyl derivative **7**, the most difficult to be oxidized. All representatives with –$OSiR_3$ (**2**, **3**) and –OPR_2 (**6**) functional groups do not display a reversible reduction wave within the electrochemical window of dichloromethane, but two pronounced oxidation waves. This reflects their low electron affinities and also their oxidation (air) sensitivity. In contrast to that, electron-poor tetrapivaloate **4** and tetratriflate **5** show one reduction potential due to the electron affinity of their electron-withdrawing pivaloate or triflate groups. Alkynyl congener **7** represents not only a species most difficult to be oxidized ($E_{1/2,Ox1} = 0.99$ V) but also nearly the easiest to be reduced ($E_{1/2,Red1} = -1.81$ V). **7** shows also the narrowest optical energy gap according to UV-Vis and PL measurements.

In order to relate experiment and theory, experimental HOMO energies were registered from the first oxidation potential determined by differential pulse voltammetry (DPV) vs. Fc/Fc^+ assuming an ionization potential of 4.8 eV for ferrocene[65] (Table 2).

The experimental LUMO energy was determined with help of the optical gap energies determined from the UV-Vis spectra (Table 1) and the HOMO energies. Both were compared to the calculated orbital energies. Def2-TZVPP/B3LYP reproduced the experimentally determined frontier molecular energies best. The experimental HOMO levels range from −5.70 eV for alkyne **7** to −4.69 eV for electron-rich silyl ether **3**. But also other peropyrenes with electron-deficient substituents such as **4**, **5** or **8** show HOMO energies below −5.5 eV corresponding to high first oxidation potentials. The LUMO energies vary from −3.44 eV for **7** to −2.18 eV for **3**, respectively. The high lying HOMOs of **2** and **6** go also in hand with their air sensitivity. We conclude that relatively large orbital coefficients at peropyrene 1,3,8,10-positions allow to tune absolute LUMO and HOMO energies as well as their energy gap by the electronic character of introduced substituents (Figure 6). Namely, electron-withdrawing substituents such as pivaloate (**4**) or 3,5-bis (trifluoromethyl)phenyl (**8**) lead to low-lying frontier orbitals, whereas electron-donating substituents such as TIPS–O (**3**), TMS–O (**2**) and 2-thienyl (**9**) lead to energetically high-lying frontier orbitals. However, as observed for highly reactive triflate **5**, low lying frontier molecular orbitals do not automatically guarantee any stability of electrochemically generated radical anions (or cations) under ambient conditions.

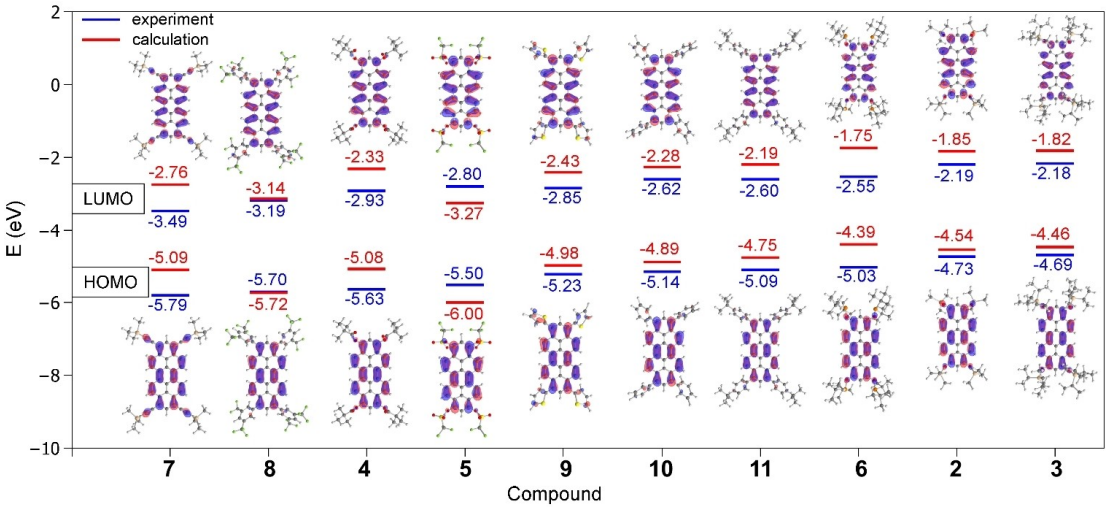

Figure 6. Energy diagram of experimental HOMO and LUMO energies of **2**–**11** determined via HOMO from first oxidation potential vs. Fc/Fc^+ from CV/DPV and HOMO-LUMO gap from UV-Vis measurements in comparison to calculated HOMO and LUMO energies of **2**–**11** (def2-TZVPP/B3LYP). The corresponding Kohn-Sham orbitals of HOMO and LUMO of **2**–**11** are shown as insets (isoval. 0.03 a.u.).

Chemistry–A European Journal | Full Paper doi.org/10.1002/chem.202101101 | Chemistry Europe European Chemical Societies Publishing

The experimental HOMO and LUMO values are in accord with values of alkoxy-substituted peropyrenes which were proven to be hole-transporting semiconductors.[35,36] The calculated HOMO and LUMO energies and calculated HOMO-LUMO energy gap also follow this trend and are compared with experimental ones in Figure 5. Especially the calculated energy gap is in good agreement with the experimental values. Calculated absolute HOMO and LUMO energy values lie generally higher than experimental ones. Best agreement between experimental and calculated frontier MO energies is obtained for aryl peropyrenes **8**, **9** and **10** as well as for silyl ethers **2** and **3**.

Effect of additional 2- and 9-substituents

In order to study the influence of substituents in terminal 2,9-positions, we introduced phenyl groups by simply following the reductive functionalization and aromatization strategy at 2,9-bisphenyl peropyrene hydroxyquinone **12** synthesized analogously to terminal unsubstituted peropyrene hydroxyquinone **2**. Two model compounds, tetrasilyl ether **13** and tetrapivaloate **14**, were synthesized applying our protocol with zinc as reducing agent (Scheme 5). The syntheses proceeded with slightly lower yields than in case of their congeners **2** and **4** without phenyl substituents. Again, pivaloate **14** turned out to be air stable whereas silyl ether **13** hydrolyses slowly on air. The solubility of the sterically more crowded and rigid compounds **13** and **14** is significantly lower than in the case of **2** and **4**.

A comparison of absorption and emission spectra of silyl ethers **2** and **13** or pivaloates **4** and **14** reveals, that absorption and emission maxima, thus the HOMO-LUMO gap are essentially the same. Additional phenyl substituents at 2- and 9-positions do not drastically change optical properties (Figure 7 (a)). Only the Stokes shift is slightly smaller in **13** and **14** than in unsubstituted pendants **2** and **4**. This is indicating a higher rigidity of the peropyrenes **13** and **14** substituted in 2,9-position. The nearly identical absorption and emission spectra can be rationalized by DFT calculations at def2-TZVPP/B3LYP level of theory (Tables S12 and S13). The optimized geometries of **13** and **14** show that the phenyl groups in 2,9-position are oriented nearly perpendicular with respect to the molecular plane of the peropyrene backbone, conjugative effects are not expected. Furthermore, the orbital coefficients at ring positions 2 and 9 are small, so that substituents at these positions do not affect and contribute significantly to the HOMO and LUMO (Figure 7 (b)), thus to the HOMO→LUMO transition. The calculated HOMO and LUMO energies of **13** and **14** also differ only slightly from those of **2** and **4**. These experimental and computational findings let us conclude that variation of the

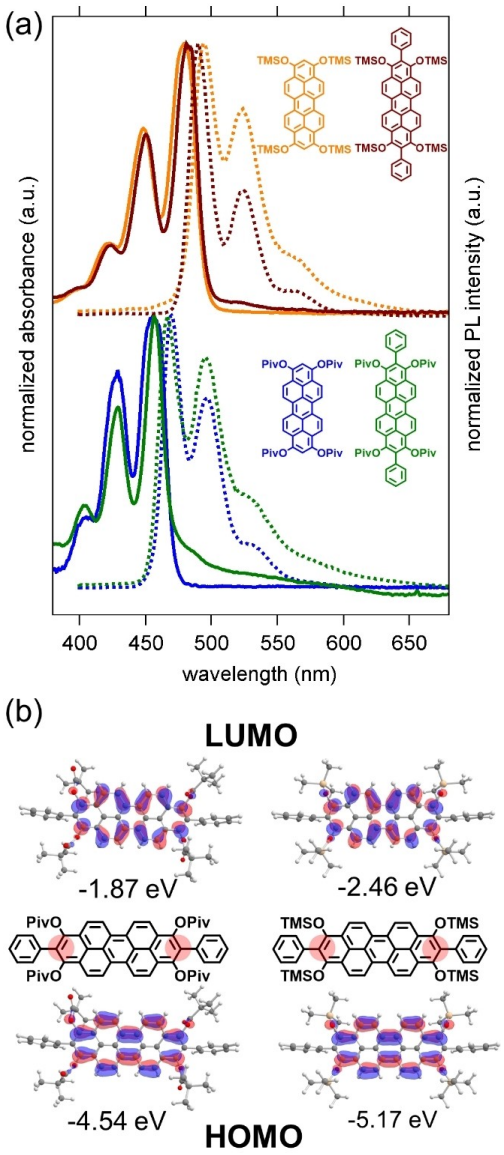

Figure 7. (a) Comparison of absorption and photoluminescence spectra (dashed lines) of **2** and **13** and **4** and **14** recorded in DCM; (b) Kohn-Sham orbitals of HOMO and LUMO of **13** and **14** and their energies calculated by DFT (def2-TZVPP/B3LYP level of theory).

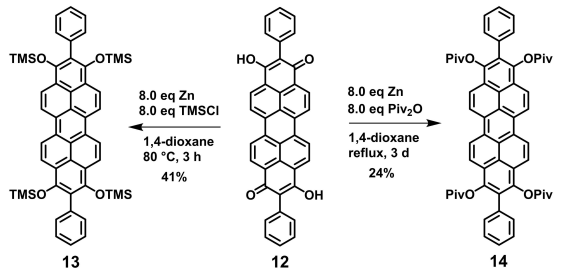

Scheme 5. Synthesis of peropyrenes **13** and **14** substituted and reductively functionalized in 1,2,3,8,9,10-positions.

Chemistry–A European Journal | Full Paper doi.org/10.1002/chem.202101101 | Chemistry Europe European Chemical Societies Publishing

terminal 2- and 9- position is much less effective for fine tuning optical properties than variations at 1,3,8,10-positions.

Conclusions

We presented a versatile access to 1,3,8,10- and 1,2,3,8,9,10-functionalized peropyrenes. Four siloxy groups (**2**, **3**), pivaloyl (**4**) and triflyl groups (**5**) were introduced via Zn mediated reductive aromatization and functionalization of readily available quinoid precursors. Another strategy uses *n*-butyl lithium as base and reducing agent in order to successfully introduce four phosphinite groups (**6**). Triflyl and pivaloyl substituted peropyrenes **4** and **5** were applied in post-functionalization via Pd- and Ni-catalysed cross-coupling reactions leading to uncommon tetraaryl and tetraalkynyl peropyrenes (**8**-**11** and **7**). The electron-donating or withdrawing functional groups did not only influence the π-stacking in the lattice of XRD structurally characterized representatives **3**, **5**, **6**, and **10** but also the absolute energy of frontier orbitals and HOMO-LUMO gap extracted from experimental UV-Vis, photoluminescence and cyclic voltammetry measurements: Absorption maxima were ranging from 426 nm to 526 nm, while HOMO and LUMO energies were varying from −5.66 eV to −4.66 eV and −2.92 eV to −2.12 eV, respectively. DFT calculations support these experimental trends. Our synthetic strategy allows to tailor the optoelectronic properties of peropyrenes for applications such as in hole-conducting semiconductors or fluorescence emitters.

Acknowledgements

Financial support by the LOEWE Program of Excellence of the Federal State of Hesse (LOEWE Focus Group PriOSS "Principles of On-Surface Synthesis") is gratefully acknowledged. Open access funding enabled and organized by Projekt DEAL.

Conflict of Interest

The authors declare no conflict of interest.

Keywords: cyclic voltammetry · crystallography · fluorescence · peropyrenes · reductive aromatization

[1] M. Ball, Y. Zhong, Y. Wu, C. Schenck, F. Ng, M. Steigerwald, S. Xiao, C. Nuckolls, *Acc. Chem. Res.* **2015**, *48*, 267–276.
[2] T. M. Figueira-Duarte, K. Müllen, *Chem. Rev.* **2011**, *111*, 7260–7314.
[3] J. Mei, Y. Diao, A. L. Appleton, L. Fang, Z. Bao, *J. Am. Chem. Soc.* **2013**, *135*, 6724–6746.
[4] J. Wu, W. Pisula, K. Müllen, *Chem. Rev.* **2007**, *107*, 718–747.
[5] R. Scholl, C. Seer, R. Weitzenböck, *Ber. Dtsch. Chem. Ges.* **1910**, *43*, 2202–2209.
[6] R. Scholl, J. Mansfeld, *Ber. Dtsch. Chem. Ges.* **1910**, *43*, 1734–1746.
[7] E. Clar, *Ber. dtsch. Chem. Ges. A/B* **1943**, *76*, 458–466.
[8] E. Clar, *The Aromatic Sextet*, Wiley, London, **1972**.
[9] I. Gutman, I. Agranat, *Polycyclic Aromat. Compd.* **2006**, *2*, 63–73.
[10] M. Solà, *Front. Chem.* **2013**, *1*, 22.
[11] R. Rieger, K. Müllen, *J. Phys. Org. Chem.* **2010**, *6*, 315–325.
[12] J. Lee, P. Jadhav, M. A. Baldo, *Appl. Phys. Lett.* **2009**, *95*, 33301.
[13] A. Rao, M. W. B. Wilson, J. M. Hodgkiss, S. Albert-Seifried, H. Bässler, R. H. Friend, *J. Am. Chem. Soc.* **2010**, *132*, 12698–12703.
[14] S. Singh, W. J. Jones, W. Siebrand, B. P. Stoicheff, W. G. Schneider, *J. Chem. Phys.* **1965**, *42*, 330–342.
[15] M. B. Smith, J. Michl, *Chem. Rev.* **2010**, *110*, 6891–6936.
[16] I. Paci, J. C. Johnson, X. Chen, G. Rana, D. Popović, D. E. David, A. J. Nozik, M. A. Ratner, J. Michl, *J. Am. Chem. Soc.* **2006**, *128*, 16546–16553.
[17] W. G. Albrecht, H. Coufal, R. Haberkorn, M. E. Michel-Beyerle, *Phys. Status Solidi* **1978**, *89*, 261–265.
[18] W. G. Albrecht, M. E. Michel-Beyerle, V. Yakhot, *Chem. Phys.* **1978**, *35*, 193–200.
[19] W. E. Ford, P. V. Kamat, *J. Phys. Chem.* **1987**, *91*, 6373–6380.
[20] Y. Kamura, H. Inokuchi, J. Aoki, S. Fujisawa, *Chem. Phys. Lett.* **1977**, *46*, 356–359.
[21] U. Wenzel, H.-G. Löhmannsröben, *J. Photochem. Photobiol. A* **1996**, *96*, 13–18.
[22] V. M. Nichols, M. T. Rodriguez, G. B. Piland, F. Tham, V. N. Nesterov, W. J. Youngblood, C. J. Bardeen, *J. Phys. Chem. C* **2013**, *117*, 16802–16810.
[23] S. Pogodin, I. Agranat, *Org. Lett.* **1999**, *1*, 1387–1390.
[24] S. Pogodin, I. Agranat, *J. Am. Chem. Soc.* **2003**, *125*, 12829–12835.
[25] K. Uchida, S. Ito, M. Nakano, M. Abe, T. Kubo, *J. Am. Chem. Soc.* **2016**, *138*, 2399–2410.
[26] L. Beer, S. K. Mandal, R. W. Reed, R. T. Oakley, F. S. Tham, B. Donnadieu, R. C. Haddon, *Cryst. Growth Des.* **2007**, *7*, 802–809.
[27] T. Umemoto, T. Kawashima, Y. Sakata, S. Misumi, *Tetrahedron Lett.* **1975**, *16*, 1005–1006.
[28] K. Uchida, T. Kubo, D. Yamanaka, A. Furube, H. Matsuzaki, R. Nishii, Y. Sakagami, A. Abulikemu, K. Kamada, *Can. J. Chem.* **2017**, *95*, 432–444.
[29] W. Yang, W. Chalifoux, *Synlett* **2017**, *28*, 625–632.
[30] W. Yang, G. Longhi, S. Abbate, A. Lucotti, M. Tommasini, C. Villani, V. J. Catalano, A. O. Lykhin, S. A. Varganov, W. A. Chalifoux, *J. Am. Chem. Soc.* **2017**, *139*, 13102–13109.
[31] W. Wang, J. H. S. Monteiro, A. de Bettencourt-Dias, V. J. Catalano, A. Chalifoux, *Angew. Chem.* **2016**, *128*, 10583-10586; W. Wang, J. H. S. Monteiro, A. de Bettencourt-Dias, V. J. Catalano, A. Chalifoux, *Angew. Chem. Int. Ed.* **2016**, *55*, 10427–10430..
[32] Y. Yang, L. Yuan, B. Shan, Z. Liu, Q. Miao, *Chem. Eur. J.* **2016**, *22*, 18620–18627.
[33] Y. Hu, G. M. Paternò, X.-Y. Wang, X.-C. Wang, M. Guizzardi, Q. Chen, D. Schollmeyer, X.-Y. Cao, G. Cerullo, F. Scotognella, K. Müllen, A. Narita, *J. Am. Chem. Soc.* **2019**, *141*, 12797–12803.
[34] J. Ma, Y. Fu, J. Liu, X. Feng, *Beilstein J. Org. Chem.* **2020**, *16*, 791–797.
[35] M. Martínez-Abadía, G. Antonicelli, A. Saeki, M. Melle-Franco, A. Mateo-Alonso, *J. Org. Chem.* **2019**, *84*, 3270–3274.
[36] M. Martínez-Abadía, G. Antonicelli, A. Saeki, A. Mateo-Alonso, *Angew. Chem. Int. Ed.* **2018**, *57*, 8209–8213; *Angew. Chem.* **2018**, *130*, 8341–8345.
[37] N. Buffet, E. Grelet, H. Bock, *Chem. Eur. J.* **2010**, *16*, 5549–5553.
[38] S. Werner, T. Vollgraff, J. Sundermeyer, *Angew. Chem. Int. Ed.* **2021**, DOI: https://doi.org/10.1002/anie.202100686; *Angew. Chem.* **2021**, DOI: https://doi.org/10.1002/ange.202100686; .
[39] J. Sundermeyer, E. Baal, S. Werner, *WO 2019/229134 A1* **2019**.
[40] E. Baal, M. Klein, K. Harms, J. Sundermeyer, E. Baal, M. Klein, K. Harms, J. Sundermeyer, *Chem. Eur. J.* under revision, **2021**..
[41] A. Castellan, M. Daney, J.-P. Desvergne, M.-H. Riffaud, H. Bouas-Laurent, *Tetrahedron Lett.* **1983**, *24*, 5215–5218.
[42] T. Nakazato, T. Kamatsuka, J. Inoue, T. Sakurai, S. Seki, H. Shinokubo, Y. Miyake, *Chem. Commun.* **2018**, *54*, 5177–5180.
[43] Y. Nakamura, T. Nakazato, T. Kamatsuka, H. Shinokubo, Y. Miyake, *Chem. Eur. J.* **2019**, *25*, 10571–10574.
[44] P. Bhattacharya, J. A. Krause, H. Guan, *Organometallics* **2011**, *30*, 4720–4729.
[45] P. Bhattacharya, J. A. Krause, H. Guan, *J. Am. Chem. Soc.* **2014**, *136*, 11153–11161.
[46] I. Göttker-Schnetmann, P. White, M. Brookhart, *J. Am. Chem. Soc.* **2004**, *126*, 1804–1811.
[47] L. P. Press, A. J. Kosanovich, B. J. McCulloch, O. V. Ozerov, *J. Am. Chem. Soc.* **2016**, *138*, 9487–9497.
[48] Y. Li, J. A. Krause, H. Guan, *Organometallics* **2018**, *37*, 2147–2158.
[49] S. D. Timpa, C. M. Fafard, D. E. Herbert, O. V. Ozerov, *Dalton Trans.* **2011**, *40*, 5426–5429.
[50] S. Zhang, H. Neumann, M. Beller, *Chem. Eur. J.* **2018**, *24*, 67–70.
[51] A. F. Littke, C. Dai, G. C. Fu, *J. Am. Chem. Soc.* **2000**, *122*, 4020–4028.
[52] Q.-Y. Chen, Z.-Y. Yang, *Tetrahedron Lett.* **1986**, *27*, 1171–1174.

Chemistry–A European Journal | Full Paper doi.org/10.1002/chem.202101101 | Chemistry Europe European Chemical Societies Publishing

[53] A. R. Ehle, Q. Zhou, M. P. Watson, *Org. Lett.* **2012**, *14*, 1202–1205.
[54] B.-J. Li, Y.-Z. Li, X.-Y. Lu, J. Liu, B.-T. Guan, Z.-J. Shi, *Angew. Chem. Int. Ed.* **2008**, *47*, 10124–10127; *Angew. Chem.* **2008**, *120*, 10278–10281.
[55] T. Mesganaw, N. K. Garg, *Org. Process Res. Dev.* **2012**, *17*, 29–39.
[56] K. W. Quasdorf, X. Tian, N. K. Garg, *J. Am. Chem. Soc.* **2008**, *130*, 14422–14423.
[57] B. M. Rosen, K. W. Quasdorf, D. A. Wilson, N. Zhang, A.-M. Resmerita, N. K. Garg, V. Percec, *Chem. Rev.* **2011**, *111*, 1346–1416.
[58] T. Shimasaki, M. Tobisu, N. Chatani, *Angew. Chem. Int. Ed.* **2010**, *49*, 2929–2932; *Angew. Chem.* **2010**, *122*, 2991–2994.
[59] Deposition numbers Deposition Numbers 2072185 (for **3**), 2072186 (for **5**), 2072187 (for **6**), 2072188 (for **10**), 2072189 (for **11**) contain the supplementary crystallographic data for this paper. These data areprovided free of charge by the joint Cambridge Crystallographic Data Centre and Fachinformationszentrum Karlsruhe Access Structures service.
[60] C. Huang, S. Barlow, S. R. Marder, *J. Org. Chem.* **2011**, *76*, 2386–2407.
[61] F. Würthner, C. R. Saha-Möller, B. Fimmel, S. Ogi, P. Leowanawat, D. Schmidt, *Chem. Rev.* **2016**, *116*, 962–1052.
[62] J. R. Lakowicz, *Principles of Fluorescence Spectroscopy*, Springer, New York, **2010**.
[63] S. Geib, S. C. Martens, M. Märken, A. Rybina, H. Wadepohl, L. H. Gade, *Chem. Eur. J.* **2013**, *19*, 13811–13822.
[64] P. Klán, J. Wirz, *Photochemistry of organic compounds. From Concepts to Practice*, Wiley, Chichester, **2009**.
[65] B. Dandrade, S. Datta, S. Forrest, P. Djurovich, E. Polikarpov, M. Thompson, *Organic Electron.* **2005**, *6*, 11–20.

Manuscript received: March 26, 2021
Accepted manuscript online: May 25, 2021
Version of record online: June 15, 2021

Supporting Information

Tetrasubstituted Peropyrenes formed by reductive aromatization: Synthesis, Functionalization and Characterization

Simon Werner [a],Tobias Vollgraff [a], and Jörg Sundermeyer*[a]

[a] S. Werner, T. Vollgraff, Prof. Dr. J. Sundermeyer
Fachbereich Chemie and Materials Science Center
Philipps-Universität Marburg, Hans-Meerwein-Straße 4
35043 Marburg (Germany)
E-Mail: JSU@staff.uni-marburg.de

Experimental Section

Methods and devices

All preparative operations were conducted by using standard Schlenk techniques and solvents were dried according to common procedures[1] and passed through columns of aluminium oxide, 3 Å molecular sieves and R3-11G-catalyst (BASF) or stored over molecular sieves (3 Å or 4 Å). Peropyrenequinone (**1**)[2,3] and 3-hydroxy-2-phenyl-1*H*-phenalen-1-one[4] were synthesized according to literature method.

The XRD data collection was performed on a Stoe Stadivari diffractometer or a Bruker D8 Quest diffractometer by the XRD analytic department of Fachbereich Chemie, Universität Marburg. Information concerning the used hardware, and software used for data collection, cell refinement and data reduction as well as structure refinement can be reviewed in the electronic supplement tables and CCDC 2072185–2072189. After solution (SHELXT)[5] and refinement process (SHELXL 2017/1)[6] the data were validated by using Platon.[7] All graphic representations were created with Diamond 4.[8]

^{1}H and proton decoupled ^{13}C NMR spectra were recorded in automation or by the NMR service of Fachbereich Chemie with a Bruker Avance II 300 spectrometer, a Bruker Avance II HD 300, DRX 400 or Avance III 500 spectrometer. All spectra were recorded at ambient temperature. ^{1}H and ^{13}C NMR spectra were calibrated using residual proton signals of the solvent (CD_2Cl_2: δ_H = 5.32 ppm, δ_C = 53.84 ppm, $CDCl_3$: δ_H = 7.26 ppm, δ_C = 77.16 ppm). Multiplicity is abbreviated as follows: s (singlet), d (doublet), t (triplet), q (quartet), qt (quintet), m (multiplet), br (broad). HR-APCI mass spectra were acquired with a LTQ-FT Ultra mass spectrometer (Thermo Fischer Scientific). The resolution was set to 100.000. HR-EI mass spectra were acquired with an AccuTOF GCv 4G (JEOL) Time of Flight (TOF) mass spectrometer. An internal or external standard was used for drift time correction. The LIFDI ion source and FD-emitters were purchased from Linden ChroMasSpec GmbH (Bremen, Germany). IR spectra were recorded in a glovebox on a Bruker Alpha ATR-FT-IR spectrometer.

Absorption spectra were recorded with a Varian Cary-5000 UV/Vis/NIR spectrophotometer in 10 mm cuvettes in dichloromethane with concentrations of 10 μM with a scan rate of 600 nm/min. Emission spectra were recorded with a Varian Cary Eclipse Spectrophotometer in 10 nm cuvettes in dichloromethane with a scan rate of 600 nm/min. Cyclic voltammetry (CV) and differential pulse voltammetry (DPV) measurements were carried out on a rhd instruments TSC 1600 closed electrochemical workstation under nitrogen atmosphere in a glovebox (Labmaster 130, MBraun); working electrode: glassy carbon; counter electrode: platinum crucible; reference electrode: platinum wire pseudo reference electrode. The samples were measured in dichloromethane and calibrated using ferrocene as internal standard added in the final sweep after CV data collection. Dichloromethane was filtered through an aluminum oxide pad prior to use. Tetrabutylammonium hexafluorophosphate ($TBAPF_6$; >99.0 %) was used as electrolyte for electrochemical analysis. The measurements were carried out at a concentration of 100 mmol/L of electrolyte.

Density functional theory (DFT) calculations using the B3LYP[9–11] functional were performed. The def2-TZVPP[12–14] basis set was used with RIJDX auxiliary base set[15,16], employing the resolution-of-identity approximation.[17,18] Further D3-dispersion correction[19] was considered by applying Becke−Johnson damping.[20–23] Structural optimizations and TD-DFT calculations were performed using Orca 3.0.3.[24] The atomic coordinates for geometry optimization were taken from XRD structures, if possible. The structurally optimized molecules were used for TD-DFT calculations using the PBE[25,26] functional (PBE0-D3/def2-TZVPP), employing the resolution-of-identity approximation for both Coulomb integrals and HF exchange integrals.[18]

Synthesis

Synthesis of 1,3,8,10-tetrakis((trimethylsilyl)oxydibenzo[*cd*,*lm*]-perylene (2). Peropyrenequinone (**1**, 778 mg, 2.0 mmol, 1.0 eq), Zn dust (1.05 g, 16.0 mmol, 8.0 eq) and trimethylsilyl chloride (2.0 mL, 16.0 mmol, 8.0 eq) were stirred for 3 h under argon atmosphere at 100 °C in 40 mL 1,4-dioxane. The greenish solution was cooled to room temperature and all volatile components were removed in vacuo. The residue was taken up in 40 mL of dichloromethane and filtered. After removing the solvent under vacuum, the crude product was washed with *n*-pentane. 647 mg (0.95 mmol, 48%) of **2** were obtained as an orange solid. ^{1}H NMR (300.1 MHz, $CDCl_3$): δ_H = 0.47 (s, 36H, $Si(CH_3)_3$), 7.42 (s, 2H, *H*2, *H*9), 8.47 (d, $^{3}J_{H,H}$ = 9.4 Hz, 4H, *H*4, *H*7, *H*11, *H*14), 8.99 (d, $^{3}J_{H,H}$ = 9.6 Hz, 4H, *H*5, *H*6, *H*12, *H*13) ppm. ^{13}C NMR (75.5 MHz, $CDCl_3$): δ_C = 0.7, 108.2, 118.1, 119.5, 120.8, 123.4, 124.9, 127.3, 149.4 ppm. HR-MS (EI+) m/z clcd. for $[C_{36}H_{46}O_4Si_4]^+$: 678.24409 (found: 678.24731). IR (ATR), $\tilde{\nu}$ = 3072 (m), 2954 (w), 2864 (w), 1624 (w), 1596 (w), 1554 (m), 1504 (m), 1482 (w), 1423 (w),1393 (w), 1352 (w), 1292 (w), 1251 (m), 1190 (m), 1167 (s), 1147 (w), 1089 (w), 915 (w), 873 (m), 838 (m), 785 (w), 749 (w), 681 (w), 645 (w), 559 (w) cm^{-1}. λ_{max} (abs.) = 479 nm (DCM, $\varepsilon = 4.29 \cdot 10^{-4}$ L·mol^{-1}·cm^{-1}). λ_{max} (em.) = 495 nm (DCM). CV: $E_{1/2}(Ox_2)$ = 0.19 V (vs. Fc/Fc^+), $E_{1/2}(Ox_1)$ = - 0.07 V (vs. Fc/Fc^+).

Synthesis of 1,3,8,10-tetrakis((triisopropylsilyl)oxy)dibenzo[*cd*,*lm*]-perylene (3). Peropyrenequinone (**1**, 389 mg, 1.0 mmol, 1.0 eq), Zn dust (503 mg, 8.0 mmol, 8.0 eq), imidazole (545 mg, 8.0 mmol, 8.0 eq) and triisopropyl chloride (1.7 mL, 8.0 mmol, 8.0 eq) were refluxed for 18 h under argon atmosphere in 20 mL 1,4-dioxane. The brownish green solution was cooled to room temperature, filtered over a pad of neutral aluminium oxide and washed with 50 mL dichloromethane, subsequently. After removing the solvent under vacuum, the crude product was washed with 20 mL methanol and 20 mL *n*-pentane and dried in vacuo. 203 mg (0.20 mmol, 20%) of an orange solid were obtained after drying in vacuo. X-ray suited single crystals could be obtained by layering a saturated solution of **3** in dichloromethane with *n*-pentane at –18 °C. ^{1}H NMR (300.1 MHz, CD_2Cl_2): δ_H = 1.25 (d, $^{3}J_{H,H}$ = 7.4 Hz, 72H, $(CH_3)_2CH$), 1.54 (hept, $^{3}J_{H,H}$ = 7.6 Hz, 12H, $(CH_3)_2CH$), 7.24 (s, 2H, *H*2, *H*9), 8.60 (d, $^{3}J_{H,H}$ = 8.1 Hz, 4H, *H*4, *H*7, *H*11, *H*14), 8.97 (d, $^{3}J_{H,H}$ = 9.5 Hz, 4H, *H*5, *H*6, *H*12, *H*13) ppm. ^{13}C NMR (75.5 MHz, CD_2Cl_2): δ_C = 13.8, 18.4, 107.9, 118.3, 120.1, 121.9, 125.8, 128.3, 151.5 ppm. HR-MS (LIFDI+) m/z clcd. for $[C_{52}H_{94}O_4Si_4]^+$: 1014.62291 (found: 1014.62294). IR (ATR), $\tilde{\nu}$ = 2940 (m), 2862 (m), 1592 (w), 1499 (w), 1461 (m), 1351 (w), 1287 (vs), 1189 (m), 1086 (m), 1002 (w), 971 (vs), 824 (s), 781 (vs), 718 (w), 633 (vs), 582 (w) cm^{-1}. λ_{max} (abs.) = 488 nm (DCM, $\varepsilon = 8.27 \cdot 10^{-4}$ L·mol^{-1}·cm^{-1}). λ_{max} (em.) = 500 nm (DCM). CV: $E_{1/2}(Ox_2)$ = 0.21 V (vs. Fc/Fc^+), $E_{1/2}(Ox_1)$ = - 0.11 V (vs. Fc/Fc^+).

Synthesis of dibenzo[*cd*,*lm*]perylene-1,3,8,10-tetrayltetrakis(2,2-dimethyl-propanoate) (4). Peropyrenequinone (**1**, 3.80 g, 9.8 mmol, 1.0 eq), Zn dust (5.18 g, 78.0 mmol, 8.0 eq) and pivalic anhydride (15.9 mL, 78.0 mmol, 8.0 eq) were refluxed for 3 d under argon atmosphere in 200 mL 1,4-dioxane. The brownish green solution was cooled to room temperature, filtered over a pad of neutral aluminium oxide and washed with 200 mL dichloromethane, subsequently. After removing the solvent in fine vacuum, the crude product was suspended in 200 mL *n*-pentane and filtered. 2.43 g (3.35 mmol, 34%) of the brown solid **4** were obtained after drying in vacuo. ^{1}H NMR (300.1 MHz, CD_2Cl_2): δ_H = 1.63 (s, 36H, C(CH_3)$_3$), 7.69 (s, 2H, *H*2, *H*9), 8.13 (d, $^{3}J_{H,H}$ = 9.4 Hz, 4H, *H*4, *H*7, *H*11, *H*14), 8.87 (d, $^{3}J_{H,H}$ = 9.6 Hz, 4H, *H*5, *H*6, *H*12, *H*13) ppm. ^{13}C NMR (75.5 MHz, $CDCl_3$): δ_C = 27.7, 39.9, 114.7, 120.5, 121.9, 123.0, 125.7, 126.5, 144.6, 177.2 ppm. HR-MS (APCI+) m/z clcd. for $[C_{46}H_{47}O_4]^+$: 727.3265 (found: 727.3272). IR (ATR), $\tilde{\nu}$ = 2964 (m), 2873 (w), 1751 (s), 1603 (w), 1480 (w), 1422 (w), 1395 (w), 1296 (m), 1173 (w), 1112 (vs), 1029 (w), 941 (w), 897 (w), 787 (w), 759 (w) cm^{-1}. λ_{max} (abs.) = 456 nm (DCM, $\varepsilon = 5.55 \cdot 10^{4}$ L·mol^{-1}·cm^{-1}). λ_{max} (em.) = 470 nm (DCM). CV: $E_{1/2}(Ox_2)$ = 1.30 V, $E_{1/2}(Ox_1)$ = 0.82 V, $E_{1/2}(Red_1)$ = -1.73 V.

Synthesis of dibenzo[*cd*,*lm*]perylene-1,3,8,10-tetrayltetrakis-(trifluoromethanesulfonate) (5). Route A: Peropyrenequinone (**1**, 184 mg, 0.5 mmol, 1.0 eq) and Zn dust (262 mg, 4.0 mmol, 8.0 eq) were suspended in 20 mL diethyl ether and trimethylsilyl chloride (0.5 mL, 4.0 mmol, 8.0 eq) were added dropwise. After cooling to 0 °C, trifluoromethanesulfonic anhydride (1.2 mL, 2.0 mmol, 4.0 eq) was added dropwise over 30 min. The reaction solution was stirred at room temperature for 2 d. After removing the solvent under vacuum, the crude product was dissolved in 20 mL dichloromethane, filtered and the solvent removed under reduced pressure. The residue was washed with *n*-pentane and dried. 110 mg (0.12 mmol, 23%) of **5** were obtained as brown solid.
Route B: 475 mg (0.7 mmol, 1.0 eq) of **2** were suspended in 100 mL diethyl ether and cooled to 0 °C. Over a period of 30 min, 1.3 mL (3.1 mmol, 4.4 eq) *n*-butyl lithium (2.43 M, *n*-hexane) were added dropwise. The purple suspension was stirred for 2 h at room temperature, cooled down to 0 °C and trifluoromethanesulfonic anhydride (1.9 mL, 3.1 mmol, 4.4 eq) was added dropwise over 30 min. After stirring at room temperature for 3 h, **5** was precipitated from the brownish reaction mixture at –18 °C, filtered and dried in vacuo after washing with *n*-pentane and diethyl ether. 440 mg (0.49 mmol, 70%) of **5** were obtained. X-ray suited single crystals were obtained by slow diffusion of *n*-pentane into a saturated solution of **5** in dichloromethane. Note: due to the instability of **5**, decomposition products could not be removed completely and therefore it was used for the next steps directly without further purification. ^{1}H NMR (300.1 MHz, $CDCl_3$): δ_H = 8.21 (s, 2H, *H*2, *H*9), 8.71 (d, $^{3}J_{H,H}$ = 9.5 Hz, 4H, *H*4, *H*7, *H*11, *H*14), 9.50 (d, $^{3}J_{H,H}$ = 9.6 Hz, 4H, *H*5, *H*6, *H*12, *H*13) ppm. ^{13}C NMR (125.8 MHz, $CDCl_3$): δ_C = 113.8, 117.7, 120.3, 120.7, 124.2, 125.8, 126.2, 126.5, 141.9 ppm. ^{19}F NMR (235.3 MHz, $CDCl_3$): δ_H = -72.6 (s) ppm. HR-MS (LIFDI+) m/z clcd. for $[C_{30}H_{10}F_{12}O_{12}S_4]^+$: 917.88635 (found: 917.88694). IR (ATR), $\tilde{\nu}$ = 2932 (w), 2232 (w), 2027 (w), 1600 (w), 1423 (m), 1302 (m), 1284 (m), 1236 (vs), 1180 (m), 1136 (m), 1092 (m), 1025 (m), 942 (w), 900 (w), 791 (w), 723 (w), 699 (m), 619 (w), 523 (w) cm^{-1}. λ_{max} (abs.) = 454 nm (DCM, $\varepsilon = 3.42 \cdot 10^{4}$ L·mol^{-1}·cm^{-1}). λ_{max} (em.) = 494 nm (DCM), CV: $E_{1/2}(Ox_1) \approx$ -0.7 V (vs. Fc/Fc^+), $E_{1/2}(Red_1) \approx$ -1.9 V.

Synthesis of 1,3,8,10-tetrakis((di-*tert*-butylphosphaneyl)oxy)dibenzo-[*cd*,*lm*]perylene (6). Peropyrenequinone (**1**, 776 mg, 2.0 mmol, 1.0 eq) was suspended in THF (40 mL). At room temperature, 4.1 mL (10.0 mmol, 5.0 eq) *n*-butyl lithium (2.43 M, *n*-hexane) were added dropwise. The purple reaction mixture was stirred for 2 h at 50 °C, until the gas evolution ceased. After cooling to room temperature, 2.45 mL (12.8 mmol, 6.5 eq) di-*tert*-butylchlorophosphine were added and the mixture was refluxed for 18 h. After cooling to room temperature, the solvent was removed in fine vacuum. The crude product was dissolved in 60 mL dichloromethane and filtered. After evaporating the solvent under reduced pressure, the brown residue was washed with *n*-pentane. 463 mg (0.48 mmol, 24%) of the brown solid **6** were obtained after drying in vacuo. Single crystals suitable for XRD measurements were obtained from a saturated solution of **6** in *n*-pentane at -18 °C. ^{1}H NMR (300.1 MHz, $CDCl_3$): δ_H = 1.33 (d, 72H, $^{3}J_{P,H}$ = 11.8 Hz, P(C(CH_3)$_3$)$_2$), 8.52 (t, 2H, $^{4}J_{P,H}$ = 5.2 Hz, *H*2, *H*9), 8.67 (d, $^{3}J_{H,H}$ = 9.4 Hz, 4H, *H*4, *H*7, *H*11, *H*14), 8.98 (d, $^{3}J_{H,H}$ = 9.6 Hz, 4H, *H*5, *H*6, *H*12, *H*13) ppm. ^{31}P NMR (101 MHz, $CDCl_3$): δ_P = -151.7 (s) ppm. ^{13}C NMR (75.5 MHz, $CDCl_3$): δ_C = 27.7 (d, $^{2}J_{P,C}$ = 15.6 Hz), 36.3 (d, $^{1}J_{P,C}$ = 26.7 Hz), 103.6, 116.5, 120.0, 121.0, 125.6, 128.0, 154.3 (d, $^{3}J_{P,C}$ = 10.8 Hz) ppm. HR-MS (LIFDI+) m/z clcd. for $[C_{58}H_{82}O_4P_4]^+$: 966.51635 (found: 966.51486). IR (ATR), $\tilde{\nu}$ = 2941 (m), 2896 (w), 2863 (w), 1624 (w), 1595 (m), 1559 (w), 1497 (m), 1473 (w), 1389 (w), 1275 (vs), 1179 (m), 1130 (m), 1075 (m), 1011 (w), 958 (m), 853 (w), 772 (s), 707 (w), 679 (w), 635 (w), 612 (w), 557 (w) cm^{-1}. λ_{max} (abs.) = 492 nm (DCM, $\varepsilon = 7.49 \cdot 10^{4}$ L·mol^{-1}·cm^{-1}). λ_{max} (em.) = 506 nm (DCM). CV: $E_{1/2}(Ox_2)$ = 0.60 V, $E_{1/2}(Ox_1)$ = 0.23 V (vs. Fc/Fc^+).

Synthesis of 1,3,8,10-tetrakis((trimethylsilyl)ethynyl)dibenzo[*cd*,*lm*]-perylene (7). Triflate **5** (194 mg, 0.2 mmol, 1.0 eq) and trimethylsilyl acetylene (0.25 mL, 1.6 mmol, 8.0 eq) were dissolved in THF (6 mL) and triethylamine (2 mL), copper iodide (8 mg, 0.04 mmol, 20 mol%) and $[Pd(dppf)Cl_2]$ (15 mg, 0.02 mmol, 10 mol%) were added and the reaction mixture was stirred for 16 h at 70 °C, until complete conversion of **5** could be detected via TLC. After removing all volatiles in fine vacuum, the residue was taken up in dichloromethane (20 mL) and filtered over neutral aluminium oxide. Further purification could be achieved via preparative TLC (*n*-pentane/DCM 3:1). The red fraction at the solvent front was collected and the product precipitated using n-pentane at -18 °C. 15 mg (0.02 mmol, 10%) of the dark red solid **7** could be isolated after filtration and drying in vacuo. ^{1}H NMR (300.1 MHz, $CDCl_3$): δ_H = 0.45 (s, 36H, Si(CH_3)$_3$), 8.43 (s, 2H, *H*2, *H*9), 8.76 (d, $^{3}J_{H,H}$ = 9.3 Hz, 4H, *H*4, *H*7, *H*11, *H*14), 9.22 (d, $^{3}J_{H,H}$ = 9.5 Hz, 4H, *H*5, *H*6, *H*12, *H*13) ppm. ^{13}C NMR (75.5 MHz, $CDCl_3$): δ_C = 0.2, 101.3, 103.3, 117.9, 118.3, 122.1, 124.0, 124.3, 125.4, 125.8, 126.0, 131.9, 132.0, 132.2, 133.1, 134.4 ppm. HR-MS (EI+) m/z clcd. for $[C_{46}H_{46}Si_4]^+$: 710.26766 (found: 710.26695). IR (ATR), $\tilde{\nu}$ = 3357 (w), 3177 (w), 2922 (w), 2851 (m), 2776 (w), 2206 (w), 2119 (w), 1954 (w), 1895 (w), 1820 (w), 1633 (m), 1605 (m), 1465 (m), 1414 (w), 1061 (w), 1036 (w), 940 (w), 855 (s), 754 (s), 658 (w), 563 (w) cm^{-1}. λ_{max} (abs.) = 526 nm (DCM, $\varepsilon = 4.85 \cdot 10^{4}$ L·mol^{-1}·cm^{-1}). λ_{max} (em.) = 531 nm (DCM), CV: $E_{1/2}(Ox_1)$ = 0.99 V, $E_{1/2}(Red_1)$ = -1.81 V (vs. Fc/Fc^+).

Synthesis of 1,3,8,10-tetrakis(3,5-bis(trifluoromethyl)phenyl)dibenzo-[*cd*,*lm*]perylene (8). 184 mg (184 mg, 0.2 mmol, 1.0 eq) of triflate **5**, 310 mg (3.2 mmol, 12.0 eq) potassium carbonate, 310 mg (1.2 mmol, 6.0 eq) (3,5-bis(trifluoromethyl)phenyl)boronic acid and 23 mg (0.02 mmol, 10 mol%) $[Pd(PPh_3)_4]$ were stirred in 3 mL 1,4-dioxane and 1 mL water under argon atmosphere for 3 d at 110 °C. After complete conversion of **5** was detected via TLC, the reaction mixture was cooled down to room temperature and 10 mL water and 10 mL dichloromethane were added. The aqueous phase was separated and extracted with 10 mL dichloromethane. The combined organic layers were dried over $MgSO_4$. The crude product was purified by column chromatography (*n*-pentane/dichloromethane (1:1). 86 mg (0.07 mmol, 37%) of **8** were obtained as an orange solid. ^{1}H NMR (300.1 MHz, CD_2Cl_2): δ_H = 8.10 (s, 4 H, *p*-Ph*H*), 8.11 (s, 2H, *H*2, *H*9), 8.24 (s, 8 H, o-Ph*H*), 8.41 (d, $^3J_{H,H}$ = 9.5 Hz, 4H, *H*4, *H*7, *H*11, *H*14), 9.40 (d, $^3J_{H,H}$ = 9.7 Hz, 4H, *H*5, *H*6, *H*12, *H*13) ppm. ^{13}C NMR (125.8 MHz, $CDCl_3$): δ_C = 120.2, 121.9 (m), 122.4, 123.6, 124.5, 124.9, 125.0, 126.0, 126.2, 126.7, 129.2, 129.3, 130.9, 130.9, 132.3 (q, $^1J_{C,F}$ = 33.5 Hz), 134.7, 142.7 ppm. ^{19}F NMR (235.3 MHz, $CDCl_3$): δ_H = -62.6 (s) ppm. HR-MS (EI+) m/z clcd. for $[C_{58}H_{22}F_{24}]^+$: 1174.13383 (found: 1174.13295). IR (ATR), $\tilde{\nu}$ = 2961 (w), 1617 (w), 1464 (m), 1408 (m), 1335 (s), 1278 (m), 1182 (vs), 1078 (m), 1020 (w), 897 (w), 868 (w), 848 (m), 794 (w), 707 (w) cm^{-1}. λ_{max} (abs.) = 482 nm (DCM, $\varepsilon = 1.11 \cdot 10^{-5}$ L·mol^{-1}·cm^{-1}). λ_{max} (em.) = 502 nm (DCM). CV: $E_{1/2}(Ox_2)$ = 1.53 V, $E_{1/2}(Ox_1)$ = 0.90 V, $E_{1/2}(Red_1)$ = -1.88 V (vs. Fc/Fc$^+$), $E_{1/2}(Red_2)$ = -2.17 V (vs. Fc/Fc$^+$).

Synthesis of 1,3,8,10-tetra(thiophen-2-yl)dibenzo[*cd*,*lm*]perylene (9). 184 mg (184 mg, 0.2 mmol, 1.0 eq) of triflate **5**, 310 mg (3.2 mmol, 12.0 eq) potassium carbonate, 154 mg (0.12 mmol, 6.0 eq) 2-thienylboronic acid and 23 mg (0.02 mmol, 10 mol%) $[Pd(PPh_3)_4]$ were stirred in 3 mL 1,4-dioxane and 1 mL water under argon atmosphere for 3 d at 110 °C. After complete conversion of **5** was detected via TLC, the reaction mixture was cooled down to room temperature and 10 mL water and 10 mL dichloromethane were added. The aqueous phase was separated and extracted with 10 mL dichloromethane. The combined organic layers were dried over $MgSO_4$. The crude product was purified by column chromatography (*n*-pentane/dichloromethane (3:1). 28 mg (0.04 mmol, 22%) of **9** were obtained as a red solid. ^{1}H NMR (300.1 MHz, CD_2Cl_2): δ_H = 7.35 (dd, $^3J_{H,H}$ = 5.1 Hz, $^4J_{H,H}$ = 3.6 Hz, 4H), 7.53 (dd, $^3J_{H,H}$ = 3.5 Hz, $^4J_{H,H}$ = 1.1 Hz, 4H), 7.62 (d, $^3J_{H,H}$ = 4.1 Hz, 4H) 8.36 (s, 2H, *H*2, *H*9), 8.85 (d, $^3J_{H,H}$ = 9.5 Hz, 4H, *H*4, *H*7, *H*11, *H*14), 9.32 (d, $^3J_{H,H}$ = 9.7 Hz, 4H, *H*5, *H*6, *H*12, *H*13) ppm. ^{13}C NMR (75.5 MHz, $CDCl_3$): δ_C = 123.7, 125.6, 125.8, 126.2, 126.8, 127.8, 128.6, 128.7, 129.3, 129.8,131.2, 132.4, 132.4, 142.2 ppm. HR-MS (EI+) m/z clcd. for $[C_{42}H_{22}S_{24}]^+$: 654.06043 (found: 654.06152). IR (ATR), $\tilde{\nu}$ = 2958 (m), 2923 (m), 2853 (w), 2188 (w), 2160 (m), 2031 (m), 2012 (w), 1908 (w), 1259 (w), 1090 (m), 1018 (m), 793 (s), 751 (m), 687 (m) cm^{-1}. λ_{max} (abs.) = 505 nm (DCM, $\varepsilon = 7.12 \cdot 10^{-4}$ L·mol^{-1}·cm^{-1}). λ_{max} (em.) = 537 nm (DCM). CV: $E_{1/2}(Ox_2)$ = 0.94 V, $E_{1/2}(Ox_1)$ = 0.41 V, $E_{1/2}(Red_1)$ = -1.94 V (vs. Fc/Fc$^+$), $E_{1/2}(Red_2)$ = -2.20 V (vs. Fc/Fc$^+$).

Synthesis of 1,3,8,10-tetraphenyldibenzo[cd,lm]perylene (10). To a solution of 450 mg (3.3 mmol, 16.5 eq) dried zinc chloride dissolved in 4 mL THF were added dropwise 2.2 mL (3.2 mmol, 16 eq) phenyl lithium (1.43 M in dibutyl ether) at 0 °C. After stirring for 1 h at room temperature, the solution of the zinc organyl was added to a solution of 146 mg (0.2 mmol, 1.0 eq) pivalate **4**, 12 mg (0.04 mmol, 20 mol%) $[Ni(COD)_2]$ and 22 mg (0.08 mmol, 40 mol%) PCy_3 in 2 mL DMF. The reaction mixture was then stirred for 16 h under exclusion of light at 70 °C. After complete conversion of **4** was detected via TLC, the reaction mixture was cooled down to room temperature and 10 mL water and 10 mL dichloromethane were added. The aqueous phase was separated and extracted with 10 mL dichloromethane. The combined organic layers were dried over $MgSO_4$. The crude product was purified by column chromatography (*n*-pentane/dichloromethane (3:1). The solvent was evaporated and the product washed with *n*-pentane. 45 mg (0.07 mmol, 36%) of **10** were obtained as an orange solid. X-ray suited single crystals could be obtained by layering a saturated solution of **10** in dichloromethane with *n*-pentane at -18 °C. ^{1}H NMR (300.1 MHz, CD_2Cl_2): δ_H = 7.53-7.57 (m, 4H, *p*-Ph*H*), 7.59-7.66 (m, 8H, *m*-Ph*H*), 7.74-7.79 (m, 8H, *o*-Ph*H*), 8.14 (s, 2H, *H*2, *H*9), 8.54 (d, $^3J_{H,H}$ = 9.5 Hz, 4H, *H*4, *H*7, *H*11, *H*14), 9.23 (d, $^3J_{H,H}$ = 9.7 Hz, 4H, *H*5, *H*6, *H*12, *H*13) ppm. ^{13}C NMR (75.5 MHz, $CDCl_3$): δ_C = 123.1, 123.1, 125.5, 125.8, 126.1, 127.8, 128.3, 128.6, 129.7, 130.9, 137.7, 141.2 ppm. HR-MS (EI+) m/z clcd. for $[C_{50}H_{30}]^+$: 630.23475 (found: 630.23280). IR (ATR), $\tilde{\nu}$ = 3057 (m), 3027 (m), 2926 (w), 2247 (w), 1956 (w), 1897 (w), 1598 (m), 1484 (m), 1439 (w), 1351 (w), 1255 (w), 1185 (w), 954 (w), 904 (s), 835 (w), 790 (vs), 698 (vs), 648 (w), 540 (w) cm^{-1}. λ_{max} (abs.) = 483 nm (DCM, $\varepsilon = 6.17 \cdot 10^{-4}$ L·mol^{-1}·cm^{-1}). λ_{max} (em.) = 500 nm (DCM). CV: $E_{1/2}(Ox_2)$ = 1.00 V, $E_{1/2}(Ox_1)$ = 0.34 V, $E_{1/2}(Red_1)$ = -2.18 V (vs. Fc/Fc$^+$).

Synthesis of 1,3,8,10-tetrakis(4-(tert-butyl)phenyl)dibenzo[cd,lm]-perylene (11). 146 mg (0.2 mmol, 1.0 eq) of pivalate **4**, 570 mg (3.2 mmol, 16.0 eq) (4-(tert-butyl)phenyl)boronic acid, 679 mg (3.2 mmol, 16.0 eq) dried potassium phosphate and 28 mg (0.04 mmol, 20 mol%) $[NiCl_2(PCy_3)_2]$ were dissolved in 3 mL 1,4-dioxane and stirred for 18 h at 110 °C under argon atmosphere. After removal of all volatile components in vacuo, the residue was taken up in 20 mL dichloromethane and filtered over neutral aluminium oxide. The crude product was crystalized from dichloromethane/n-pentane (1:1) at -18 °C. 75 mg (0.08 mmol, 44%) of **11** could be isolated as brownish orange needles. ^{1}H NMR (300.1 MHz, CD_2Cl_2): δ_H = 1.33 (s, 36H, C(C*H*$_3$)$_3$), 7.63 (d, 8H, $^3J_{H,H}$ = 8.3 Hz, *o*-Ph*H*), 7.69 (d, 8H, $^3J_{H,H}$ = 8.3 Hz, *m*-Ph*H*), 8.12 (s, 2H, *H*2, *H*9), 8.57 (d, $^3J_{H,H}$ = 9.4 Hz, 4H, *H*4, *H*7, *H*11, *H*14), 9.22 (d, $^3J_{H,H}$ = 9.7 Hz, 4H, *H*5, *H*6, *H*12, *H*13) ppm. ^{13}C NMR (125.8 MHz, $CDCl_3$): δ_C = 31.6, 34.9, 122.8, 123.9, 125.5, 125.9, 126.2, 128.2, 129.9, 130.6, 137.6, 138.3, 150.4 ppm. HR-MS (EI+) m/z clcd. for $[C_{66}H_{62}]^+$: 854.48515 (found: 854.48231). IR (ATR), $\tilde{\nu}$ = 2958 (s), 2904 (w), 2865 (w), 1928 (w), 1881 (w), 1602 (w), 1497 (m), 1462 (m), 1394 (w), 1270 (w), 1113 (m), 1050 (w), 1014 (w), 903 (s), 837 (m), 791 (w), 725 (w), 597 (w) cm^{-1}. λ_{max} (abs.) = 485 nm (DCM, $\varepsilon = 9.19 \cdot 10^{-4}$ L·mol^{-1}·cm^{-1}). λ_{max} (em.) = 506 nm (DCM). CV: $E_{1/2}(Ox_2)$ = 0.73 V, $E_{1/2}(Ox_1)$ = 0.29 V, $E_{1/2}(Red_1)$ = -2.12 V (vs. Fc/Fc$^+$).

Synthesis of 3,10-dihydroxy-2,9-diphenyldibenzo[*cd*,*lm*]perylene-1,8-dione (12). 4.0 g (14.7 mmol, 1.0 eq) 3-hydroxy-2-phenyl-1*H*-phenalen-1-one and 20 g potassium hydroxide were heated in a Ni crucible for 3 h at 285 °C on air. During the reaction, the melt turned black. After cooling to room temperature, the solid was taken up in 1 l water, filtered and precipitated with 200 mL of 2 M acetic acid. The purple precipitate was filtered and washed with water and hot methanol. The solid was dried

at 120 °C overnight. 880 mg (3.3 mmol, 22%) of the purple solid **12** were obtained and directly used for further stages, since a characterization was not possible due to the insolubility in organic solvents. HR-MS (APCI+) m/z clcd. for $[C_{38}H_{19}O_4]^+$: 539.1289 (found: 539.1309). IR (ATR), $\tilde{\nu}$ = 3466 (w), 3050 (w), 1608 (m), 1549 (vs), 1404 (m), 1374 (m), 1232 (vs), 1178 (s), 1093 (s), 951 (w), 856 (m), 810 (w), 776 (m), 738 (m), 636 (w), 499 (w) cm^{-1}.

Synthesis of ((2,9-diphenyldibenzo[cd,lm]perylene-1,3,8,10-tetrayl)-tetrakis(oxy))tetrakis(trimethylsilane) (13). Peropyrenequinone **12** (590 mg, 1.06 mmol, 1.0 eq), Zn dust (556 g, 8.5 mmol, 8.0 eq) and trimethylsilyl chloride (1.1 mL, 8.5 mmol, 8.0 eq) were stirred for 3 h under argon atmosphere at 100 °C in 40 mL 1,4-dioxane. The greenish solution was cooled to room temperature and all volatile components were removed in vacuo. The residue was taken up in 40 mL dichloromethane and filtered. After removing the solvent under vacuum, the crude product was washed with *n*-pentane. 360 mg (0.43 mmol, 41%) of **13** were obtained as an orange solid. ^{1}H NMR (300.1 MHz, $CDCl_3$): δ_H = -0.04 (s, 36H, Si(C*H*$_3$)$_3$), 7.42 (t, $^3J_{H,H}$ = 6.8 Hz, 2H, *p*-Ph*H*), 7.52 (t, $^3J_{H,H}$ = 7.4 Hz, 4H, *m*-Ph*H*), 7.67 (d, $^3J_{H,H}$ = 7.1 Hz, 4H, *o*-Ph*H*), 8.49 (d, $^3J_{H,H}$ = 9.4 Hz, 4H, *H*4, *H*7, *H*11, *H*14), 9.07 (d, $^3J_{H,H}$ = 9.6 Hz, 4H, *H*5, *H*6, *H*12, *H*13) ppm. ^{13}C NMR (75.5 MHz, $CDCl_3$): δ_C =0.5, 119.7, 120.6, 122.3, 125.5, 126.7, 127.5, 128.2, 132.9, 136.4, 148.8 ppm. HR-MS (FD+) m/z clcd. for $[C_{50}H_{54}O_4Si_4]^+$: 830.30991 (found: 830.31051). IR (ATR), $\tilde{\nu}$ = 2952 (w), 2922 (w), 1583 (w), 1471 (w), 1398 (m), 1355 (w), 1308 (m), 1250 (s), 1144 (m), 1092 (m), 1029 (m), 845 (vs), 789 (m), 723 (m), 617 (w), 582 (w) cm^{-1}.

Synthesis of 2,9-diphenyldibenzo[cd,lm]perylene-1,3,8,10-tetrayl tetrakis(2,2-dimethylpropanoate) (14). Peropyrenequinone **12** (900 mg, 1.67 mmol, 1.0 eq), Zn dust (872 mg, 13.3 mmol, 8.0 eq) and pivalic anhydride (2.7 mL, 13.3 mmol, 8.0 eq) were refluxed for 3 d under argon atmosphere in 200 mL 1,4-dioxane. The brownish green solution was cooled to room temperature, filtered over a pad of neutral aluminium oxide and washed with 100 mL dichloromethane subsequently. After removing the solvent in fine vacuum, the crude product was suspended in 50 mL *n*-pentane and filtered. 250 mg (0.34 mmol, 22%) of the brown solid **14** were obtained after drying in vacuo. ^{1}H NMR (300.1 MHz, CD_2Cl_2): δ_H = 1.19 (s, 36H, C(C*H*$_3$)$_3$), 7.32-7.48 (m, 10H, Ph*H*), 8.27 (d, $^3J_{H,H}$ = 9.4 Hz, 4H, *H*4, *H*7, *H*11, *H*14), 9.23 (d, $^3J_{H,H}$ = 9.5 Hz, 4H, *H*5, *H*6, *H*12, *H*13) ppm. ^{13}C NMR: not recorded due to insolubility. HR-MS (APCI+) m/z clcd. for $[C_{58}H_{55}O_4]^+$: 879.3891 (found: 879.3903). IR (ATR), $\tilde{\nu}$ = 2959 (w), 2925 (w), 2854 (w), 1751 (vs), 1633 (m),1598 (m), 1477 (w), 1395 (w), 1367 (w), 1263 (m), 1217 (m), 1100 (s), 1027 (m), 789 (m), 756 (m), 731 (m), 699 (w) cm^{-1}.

3.3 Publication 3: Reductive *O*-Triflylation of Naphthalene Diimide: Access to Alkyne- and Amine-functionalized 2,7-Diazapyrenes

Citation: S. Werner, T. Vollgraff, Q. Fan, K. Bania, J. M. Gottfried, J. Sundermeyer, *Org. Chem. Front.* **2021**, *8*, 5013–5023.[C]

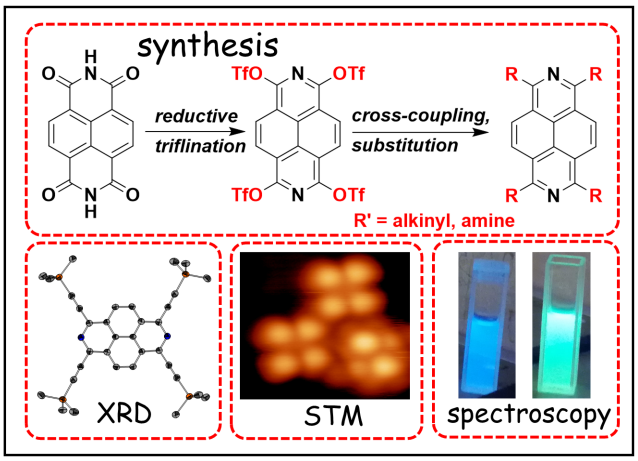

Summary: This article describes an application of the reductive functionalization strategy (Publication 1, 2) on naphthalene diimide (NTCDI). It is in line with previous work on reductive functionalizations of perylene diimide (PTCDI) in our group which was performed by E. Baal. With respect to previous published work on corresponding 2,7-diazapyrene pivaloates and tetraaryl-2,7-diazapyrenes by Miyake *et al.*, the work deals with silylation and triflination. In a one-pot procedure, up to 3 gram of the corresponding 2,7-diazapyrene tetratriflate could be isolated. It is exemplarily demonstrated, that the tetratriflate can serve as a starting material for Sonogashira cross-couplings and nucleophilic aromatic substitutions towards novel diazapyrene-tetraalkynes and -tetraamines. The compounds are studied by X-ray crystallography as well as optical (UV-Vis, PL) spectroscopy and cyclic voltammetry. By introduction of different substituents, a variation of absorption and emission maxima in a range of 100 nm is possible as well as tuning of the redox properties which are supported by DFT calculations. It could be demonstrated that tetra-trimethylsilylacetyl substituted 2,7-diazapyrene could be successfully sublimed in ultra-high vacuum and investigated on a Cu(111) surface by scanning tunneling spectrometry (STM).

Own Contribution: All experimental work was done by myself as well as characterization by spectroscopical (UV-Vis/PL) and electrochemical (CV/DPV) measurements and (TD-)DFT calculations. K. Bania assisted in chemical synthesis within his Bachelor thesis and T. Vollgraff solved and refined the crystal structures. NMR and mass spectra were recorded by service departments of the faculty. Dr. Q. Fan performed UHV depositions and STM analysis under supervision of Prof. Dr. M. Gottfried. Prof. Dr. J. Sundermeyer initiated and supervised this study and was available as valuable discussion partner. The manuscript was written by myself with valuable feedback of all authors.

[C] Reproduced with permission of S. Werner, T. Vollgraff, Q. Fan, K. Bania, J. M. Gottfried, J. Sundermeyer, *Org. Chem. Front.* **2021**, *8*, 5013–5023, Copyright ©2021, Rights Managed by the Royal Society of Chemistry.

ORGANIC CHEMISTRY FRONTIERS

CHINESE CHEMICAL SOCIETY

ROYAL SOCIETY OF CHEMISTRY

RESEARCH ARTICLE

View Article Online
View Journal | View Issue

Cite this: *Org. Chem. Front.*, 2021, **8**, 5013

Reductive *O*-triflylation of naphthalene diimide: access to alkyne- and amine-functionalized 2,7-diazapyrenes†

Simon Werner, Tobias Vollgraff, Qitang Fan, Kevin Bania, J. Michael Gottfried and Jörg Sundermeyer *

Herein we report the facile reductive *O*-triflylation and *O*-silylation of naphthalene diimide as a scalable one-step approach. The resulting highly reactive 1,3,6,8-tetratriflato-2,7-diazapyrene was prepared at the 3 gram scale and serves as a versatile platform for further functionalizations *via* Sonogashira cross coupling or nucleophilic aromatic substitution by piperidine or iodide leading to tetrasubstituted diazapyrenes with tunable optoelectronic properties. Fine tuning is demonstrated by means of absorption and emission maxima varying within a range of more than 100 nm. The different diazapyrenes are characterized by means of XRD diffraction, UV-Vis and photoluminescence spectroscopy as well as cyclic voltammetry and TD-DFT calculations. The applicability of so far unaccessible tetra-1-alkynyl diazapyrenes for organic molecular beam epitaxy (OMBE) is demonstrated by characterization of a sub-monolayer on Cu(111) using scanning tunneling microscopy (STM).

Received 7th June 2021,
Accepted 30th June 2021

DOI: 10.1039/d1qo00862e

rsc.li/frontiers-organic

Introduction

Functionalized polyaromatic hydrocarbons (PAHs) are a promising and evolving group of functional materials with manifold applications in the field of organic electronics.[1–4] The desired properties can be achieved *via* precise regioselective chemical functionalisation of PAH systems as a versatile tool to alter their photophysical, electrochemical and chemical properties.[5–8] Functionalized pyrene derivatives attracted tremendous research interest, not least due to their pronounced volatility in OMBE.[3] Photophysical properties like long-lived excimer formation and high fluorescence quantum yields as well as excellent charge mobilities made functionalized pyrenes into archetypical fluorophores and organic semiconductors.[9–12] As a consequence, selective chemical functionalisation of pyrene at different positions was widely studied.[3] A common approach for the 1,3,6,8-tetrafunctionalisation is electrophilic bromination with an excess of bromine.[13,14] The reactivity of 1,3,6,8-tetrabromopyrene was investigated in Suzuki,[15,16] Sonogashira[17] and Buchwald–Hartwig cross-couplings[18,19] as well as in nucleophilic aromatic substitutions with thiols.[20] The substituents prevent strong aggregation behaviour and therefore fluorescence quenching and make applications such as *e.g.* blue dopants for organic light emitting diodes (OLEDs) possible.[21,22] The complementary terminal 2,7-positions of perylenes could be functionalized by Marder *et al.* by Ir-catalyzed C–H borylations.[23,24] The obtained bis-borylated pyrenes served as versatile platforms for C–C coupling reactions, even unsymmetrical functionalization.[25]

Heteroaromatic PAHs incorporating [=N–] instead of [=CH–] units typically display energetically lower HOMO and LUMO frontier orbitals with consequences in their photophysical, electronic and electrochemical properties.[26–28] With respect to pyrene derivatives, Gade *et al.* presented the synthesis and functionalization of n-type semiconducting 1,3,6,8-tetraazapyrenes.[29] Recently, Langer *et al.* reported the synthesis of functionalized 2-azapyrenes.[30] In this report, we focus on functionalized 2,7-diazapyrenes, which are less investigated than the corresponding pyrenes. Unsubstituted parent 2,7-diazapyrene is synthesized in a two-step procedure involving the reduction of the carbonyl groups of naphthalene diimide (NTCDI, **1**)[31,32] with borane[33,34] followed by oxidative aromatisation with MnO_2.[33] However, due to its insolubility, parent 2,7-diazapyrene could not be functionalized in a way comparable to pyrene.[35–37]

1,3,6,8-Tetrasubstituted diazapyrenes were reported by Sachdev (Scheme 1).[38] **2a** was obtained from NTCDI *n*-butyl

Fachbereich Chemie and Material Science Center (WZMW), Philipps-Universität Marburg, Hans Meerwein Straße 4, 35032 Marburg, Germany.
E-mail: JSU@staff.uni-marburg.de

†Electronic supplementary information (ESI) available: NMR spectra, CV/DPV measurements, UV/Vis and TD-DFT spectroscopy, cartesian coordinates of the calculated structures (*XYZ*), XRD data, and the CIF files of the presented structures. CCDC 2087065, 2087066 and 2087067. For ESI and crystallographic data in CIF or other electronic format see DOI: 10.1039/d1qo00862e

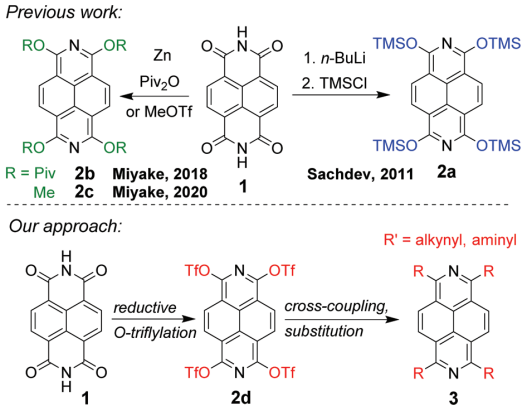

Scheme 1 Previously reported 1,3,6,8-functionalized diazapyrenes and our reductive triflylation approach.

lithium or sodium in liquid ammonia as a reducing agent and TMS chloride.[38] In 2018 and 2019 Miyake *et al.* reported a reductive *O*-pivaloylation of NTCDI and perylene dianhydride (PTCDI), using Zn and pivalic anhydride in dioxane leading to tetra pivaloates **2b** (Scheme 1).[39,40] Conversion of NTCDI with zinc and methyl triflate as electrophiles led to tetramethoxy derivative **2c**.[41] The corresponding 1,3,6,8-tetrapivaloyl-2,7-diazapyrene (**2b**) and 1,3,6,8-tetramethoxy-2,7-diazapyrene (**2c**) were further transformed in Ni-catalyzed Suzuki–Miyaura cross couplings leading to tetraaryl-2,7-diazapyrenes and tetraalkyl-2,7-diazapyrenes with intrinsically higher electron mobility than pyrenes.[39,41] Structural and electronic tuning *via* complexation of α-hydroxylated tetraaryl-2,7-diazapyrenes with boron Lewis acids was communicated only recently.[42] We demonstrated the reductive *O*-silylation of quinoid PAH precursors by zinc/R_3SiCl as a strategy to synthesize functionalized peropyrenes and their higher homologues terropyrene and quarterropyrene.[43] Such *O*-silyl derivatives of peropyrenes were shown to be versatile intermediates towards tetrapivaloates and triflates, which served as versatile synthons and key compounds for C–C cross-coupling reactions.[44] The aim of this paper is to synthesise 1,3,6,8-tetratriflato-2,7-diazapyrene (**2d**) and with this key compound in hand, tetra-amino (**3a**) and tetra-alkynyl derivatives (**3b** and **3c**) of this class of topical compounds that were not accessible so far were synthesized.

Results and discussion

Synthesis

Based on the current studies of tetratriflato-2,9-diazaperopyrenes[45] we intended to apply our synthetic strategy of reductive triflylation of NTCDI in order to get access to a synthetically valuable platform 1,3,6,8-tetratriflato-2,7-diazapyrene (**2d**). Aryl triflates promise to be more reactive than the corresponding pivaloates both in transition-metal catalysed cross coupling reactions and in uncatalyzed nucleophilic aromatic substitutions.[44]

Reductive *O*-silylation and aromatization of **1** was accomplished with 8 eq. of zinc and 8 eq. of trimethylsilyl chloride (TMSCl) in 1,4-dioxane (Scheme 2). A similar reducing system was used in the more common reduction of anthracene-9,10-dione.[46] Silylether **2a** is forming in ethers as solvent at room temperature. Compared to THF or diethyl ether, 1,4-dioxane gave the best yield of 68% after only 6 h at room temperature. The preparation of sterically more demanding triisopropyl silylether (TIPS) **2e** required more nucleophilic potassium aryloxide intermediates forming *via* reduction of **1** with a stoichiometric amount of potassium graphite (KC_8) in the presence of TIPSCl in refluxing THF (30% yield). The better choice is to activate sterically demanding silyl chlorides by addition of 1 eq. of imidazole, using zinc as a mild reducing agent at 80 °C: in this way *tert*-butyl-dimethylsilyl (TBDMS) ether **2f** was obtained in good yields (71%).

In contrast to **2a**, the yellow solids **2e** and **2f** are benchstable and do not suffer from hydrolysis and aerobic re-oxidation. In contrast to prior findings with diazadibenzoperylenes in our group,[45] we were not able to convert silyl ethers **2a**, **2e** and **2f** into triflate **2d**, and both strategies failed: desilylation of **2a** by *n*-BuLi followed by the addition of trifluoromethanesulfonic anhydride (Tf_2O), and alternatively treatment of **2a** with Tf_2O/4-dimethyl-aminopyridine (DMAP). Therefore, one-step synthesis of **2d** was developed involving the treatment of **1** with KC_8 at 80 °C in DME until a purple solution had formed, which is the most likely tetra potassium salt of reduced NTCDI, followed by slow addition of Tf_2O at −50 °C for 1 h. The use of DME is essential as cyclic ether dioxane or THF tends to ring open in the presence of Tf_2O even at −50 °C. After warming to room temperature, a blue fluorescent solution had formed. We were able to isolate air sensitive **2d** in 76% yield at a 3-gram scale as a beige solid. With this highly valuable and reactive platform chemical **2d** in hand we managed to synthesize tetra amino and 1-alkynyl derivatives not accessible by Miyake's pivaloates due to their weak leaving group ability compared to *ortho*-pyridinic triflate groups. Thus,

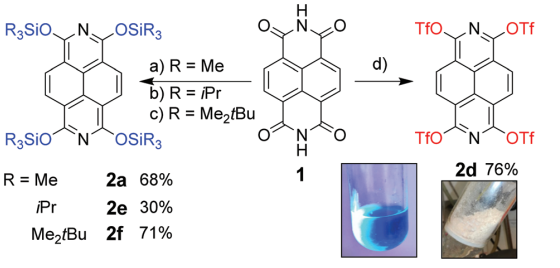

Scheme 2 Reductive synthesis of **2a**, **2d–2f** from NTCDI (**1**). (a) Zn, (8 eq.), TMSCl (8 eq.), dioxane, r.t. 6 h; (b) KC_8 (4.4 eq.), TIPSCl (5 eq.), THF, reflux, 16 h; (c) Zn, (8 eq.), TBDMSCl (8 eq.), imidazole (8 eq.) dioxane, 80 °C, 3 h; (d) 1. KC_8 (4.4 eq.), 80 °C, 3 h, 2. Tf_2O (4.4 eq.), −50 °C, 3 h, DME.

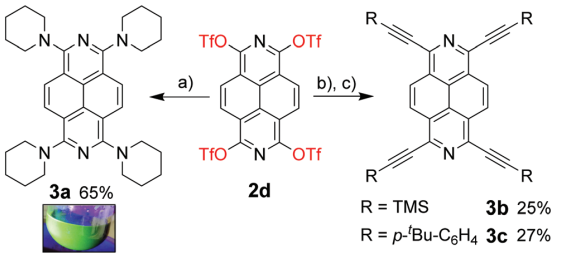

Scheme 3 Functionalisation of **2d** *via* nucleophilic aromatic substitution and Sonogashira coupling. (a) Piperidine (exc.), DMSO, 90 °C, 1 h; (b) trimethylsilyl acetylene (6 eq.), CuI (20 mol%), [Pd(dppf)Cl_2] (10 mol%), THF/NEt_3, 65 °C, 16 h; (c) *p-tert*-butylphenyl acetylene (6 eq.), NMe_4I, CuI (20 mol%), [Pd(dppf)Cl_2] (10 mol%), dioxane/NEt_3, 85 °C, 16 h.

tetra-1-piperidyl derivative **3a** is simply obtained by an uncatalyzed reaction of **2d** with excess piperidine in DMSO yielding a green fluorescent solution after 1 h at 90 °C (Scheme 3).

After removal of the solvent at 10^{-3} mbar, air-sensitive electron-rich tetra-amino-substituted **3a** could be extracted with dichloromethane in 65% yield. Other transformations not reported and probably not possible with pivaloate **2b** are Sonogashira cross-couplings. **2d** was reacted with trimethylsilyl acetylene in the presence of 10 mol% [Pd(dppf)Cl_2] and 20 mol% CuI under standard conditions,[47] resulting in the formation of tetra-alkyne **3b** in moderate yields (25%, av. 71% per C–C coupling step). **3b** turned to be air stable and purification *via* column chromatography was possible. Interestingly, larger 1-alkynes did not react with **2d** under these conditions, and only the decomposition of **2d** was confirmed. Therefore, 4 eq. of tetramethylammonium iodide were added in order to form better convertible, more selective iodide intermediates *in situ*. By using 1,4-dioxane instead of THF *p-tert*-butylphenyl acetylene could be coupled under these modified conditions to the corresponding tetraalkyne **3c** as a red, air stable solid in comparable yield. The assumption that triflate groups were completely substituted by iodide functionalities which are more selective in Sonogashira couplings was proven by a HR-EI(+) mass spectrum recorded directly from the reaction solution of **2d** and [NMe_4]I after 5 min of detection of tetraiodo-diazapyrene (**I1**) with an exact mass and correct isotopic pattern (see ESI, Fig. S12†).

X-ray crystallography

In order to study the solid-state arrangement of the synthesized diazapyrenes, single crystals of **2a**, **2f** and **3d** were studied by X-ray crystallography. **2a** and **3b** crystalized in the monoclinic space group $P2_1/n$ by layering a DCM solution with *n*-pentane. **2f** crystallized in the triclinic space group $P\bar{1}$ from 1,4-dioxane/methanol (Fig. 1). Altering the solid-state packing motive through functional groups plays an important role in modulating the fluorescence properties of pyrenes.[3] Here, we demonstrate that steric repulsion of the siloxy groups of diazapyrene **2a** with a Si–O···O–Si torsion angle of 23° prevents the

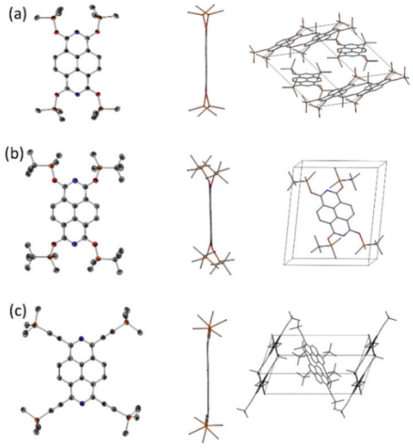

Fig. 1 Solid state structures (right: front view, center: side view and left: packing structure) of (a) **2a**; (b) **2f** and (c) **3b**. Hydrogen atoms are omitted for clarity and thermal ellipsoids are shown at the 50% probability level.

diazapyrene backbones of **2f** from forming π–π-stacking interactions. As expected, this tendency is even larger in the case of the bulkier **2f** showing a corresponding torsion angle of 47° and no π–π-stacking: the shortest distance between neighbouring π-systems is 5.81 Å. Contrastingly, the rather rigid in-plane alkyne substituents of **3b** display a torsion angle between the corresponding alkyne bonds C≡C···C≡C of only 5°. This lowers the intermolecular repulsion and allows molecules to form face to face π–π-stacked dimers with the shortest distance $d_{\pi-\pi}$ = 3.50 Å.

Scanning tunnelling microscopy (STM)

Since the device production of *e.g.* organic light emitting diodes requires sufficiently volatile and thermally stable organic chromophores, matrix and dopant molecules for high-vacuum deposition, we tested the volatility of **3b** not only in bulk sublimation but also in an ultra-high vacuum (UHV, $p < 10^{-9}$ mbar) setup. At 210 °C a sub-monolayer of **3b** was UHV-deposited on a single crystalline Cu(111) surface and characterized using scanning tunnelling microscopy (STM), a technique suitable to visualize single, planar aromatic molecules *via* the quantum tunnelling effect between the orbitals of the STM tip and the target molecules (Fig. 2).[48,49]

The single molecules are apparent on the metal surface as rectangular features with four bright protrusions, which are attributed to the four TMS groups.[50,51] TMS groups are protruding, because they are non-planar, unlike the diazapyrene backbone, leading to the increased apparent height in STM images. The Si–Si centroid-distances of **3b** measured from XRD (9.97 Å and 10.34 Å) are in good agreement with the distances between the centres of the bright spots (9.7 ± 0.5 Å) in Fig. 2(b), indicating that **3b** remains intact during deposition. Interestingly, despite a surface temperature of 100 K during

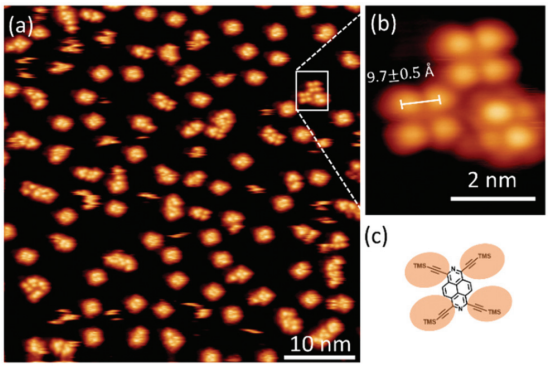

Fig. 2 Constant-current STM-images of **3b** on Cu(111) (recorded at 100 K). (a) Overview STM image of **3b** after deposition; (b) magnified view of three molecules **3b**; (c) the chemical structure of **3b** with four TMS groups marked by brown ovals, which corresponds to the four bright protrusions of **3b** in the STM image. Tunnelling parameters: (a), (b) $U = -1.7$ V, $I = 0.16$ nA.

the acquisition of STM images, single **3b** is mobile on the surface as shown by the fuzzy appearance of some molecules in Fig. 2(a). Only those **3b** molecules that have aggregated into small clusters are immobile enough for STM imaging as shown in Fig. 2(b). The high mobility can be explained by the bulky TMS groups reducing the adsorption interactions of the diazapyrene backbone with Cu(111).

Optical spectroscopy

In order to study the optoelectronic influence of the different introduced substituents, we recorded UV-Vis spectra in DCM (Fig. 3). Triflate **2d** and silyl ether **2f** show the most hypsochromic absorption maxima (350 nm and 378 nm), marking triflate groups as most electron-withdrawing substituents. The three silyl ethers **2a**, **2e** and **2f** show almost identical optical spectra, and therefore only **2f** is displayed.

In contrast to the UV-Vis spectra of the other compounds, the lowest energy bands of **2c** and **2f** do not represent the absorption maxima. According to TD-DFT calculations (PBE0-D3/def2-TZVPP level of theory, see Fig. S2, ESI†), the largest wavelength absorption can be assigned to a HOMO–LUMO+1 transition, whereas the HOMO–LUMO transition should be assigned to the highest peaks. In the case of tetraalkynes **3a** and **3b**, the HOMO–LUMO transition could be assigned to the absorption maximum that is the most bathochromically shifted peak. **3b** displays an absorption maximum of 435 nm meaning a bathochromic shift of 85 nm relative to **2d**.

3c with more electron-releasing alkynyl groups compared to **3b** leads to an absorption maximum of 480 nm. The ranges of the absorption maximum wavelengths of **3a–3c** are comparable to Miyake's aryl-diazapyrenes.[39] Neither silylether **2f** nor alkyne **3b** showed remarkable solvatochromic behaviour (see Fig. S6 and S7, ESI†). Due to the symmetric molecular structure with only a small permanent dipole momentum, the

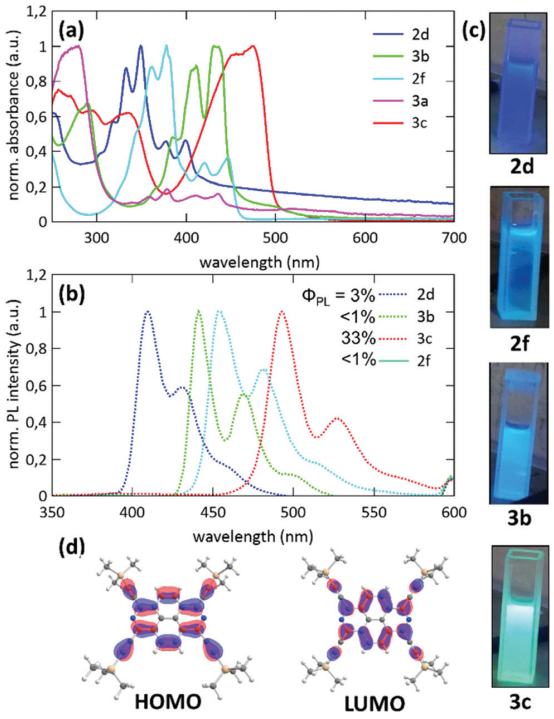

Fig. 3 (a) UV-Vis spectra of **2d**, **2f**, **3a**, **3d** and **3c**, recorded in DCM ($c \approx 10^{-5}$ M); (b) photoluminescence (PL) spectra of **2d**, **2f**, **3b** and **3c**, recorded in DCM ($c \approx 10^{-7}$ M, $\lambda_{ex.} = 350$ nm); (c) photographs of cuvettes containing **2d**, **2d**, **3d** and **3c** under UV-light ($\lambda = 366$ nm); (d) Kohn–Sham molecular orbitals of **3b** (def2-TZVPP/PBE level of theory).

absorption maxima of the recorded UV-Vis spectra deviate in a range below 10 nm in solvents of different polarities (cyclohexane to dimethyl-formamide).

The extinction coefficients range between 4.27×10^5 L mol^{-1} cm^{-1} for **3b** and a remarkably high 8.53×10^5 L mol^{-1} cm^{-1} for **2f** (see the ESI, Fig. S3–S5† for concentration-dependent UV-Vis spectra) which are higher than those in the case of tetraaryl substituted derivatives.[39] This shows that the use of 1-alkyne substituents at 1,3,6,8-positions is an effective way to tune the optical properties. This is supported by DFT-calculated Kohn–Sham frontier molecular orbitals of **3b** (see representative Fig. 3(d)). Fig. S1† displays the corresponding results for all other compounds calculated at the def2-TZVPP/PBE level of theory. The alkyne triple bond participates to a high extent in both the HOMO and LUMO since conjugation to the coplanar π-system is effectively possible and the π-system is enlarged. This is different from Miyake's derivatives displaying four aryl substituents preferentially in a non-conjugated conformation with respect to the central plane. Therefore, the aryl substituents do only contribute minorly to the HOMO and LUMO, resulting in larger HOMO–LUMO energy gaps and more hypsochromically shifted UV-Vis and PL maxima.[39]

TD-DFT also supports the observed trends of the absorption maximumy wavelengths (see Fig. S2, ESI†).

The fluorescence spectra of **2f**, **2d**, **3b** and **3c** (Fig. 3b) were recorded in dichloromethane. They are mirrored to the absorption spectra and show excitation maxima ranging from 410 nm (electron-deficient **2d**) to 493 nm (electron-rich **3c**) with only small Stokes shifts of 10–15 nm, indicating small reorganization energies during the fluorescence process due to the rigid diazapyrene scaffold. The particular rigid alkyne **3b** shows a remarkably narrow Stokes shift (5 nm, 0.03 eV), indicating a very low energy loss for geometry organization during the emission.[47,52] Tetraalkyne **3c** showed a remarkable fluorescence quantum yield (Φ_{PL} = 33%, determined by dilution method *vs.* fluorescein, see Fig. S8, ESI†) in a magnitude comparable to Miyake's aryl-substituted diazapyrenes,[39,40] whereas **3b**, **2f** and **2d** show only weak fluorescence (Φ_{PL} < 5%), possibly due to higher reorganization energy loss. Experimental optical HOMO–LUMO gap energies determined from the intersection wavelength of normalized absorption and emission spectra[47] or the onset wavelength of absorption spectra[53] show that chemical functionalization leads to HOMO–LUMO gaps varying from 2.36 eV (**3c**) to 3.05 eV (**2d**).

When an excess of trifluoroacetic acid (>100 eq.) was added to a toluene solution ($c = 10^{-5}$ M) of **2f** and **3b**, the pyridinic N-protonated species could be detected by UV-Vis spectrometry. Similar to the spectra of protonated tetraaryl diaza-

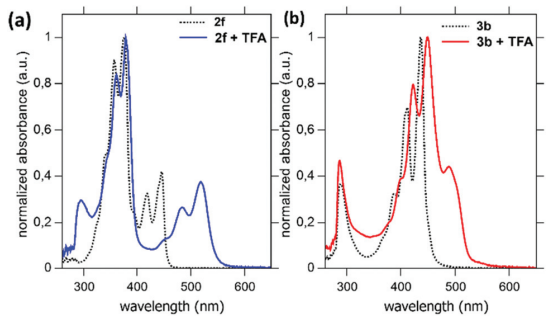

Fig. 4 Spectral change of the UV-Vis spectra of toluene ($c \approx 10^{-5}$ M) solutions of (a) **2f** and (b) **3b** after addition of excess TFA (>100 eq.).

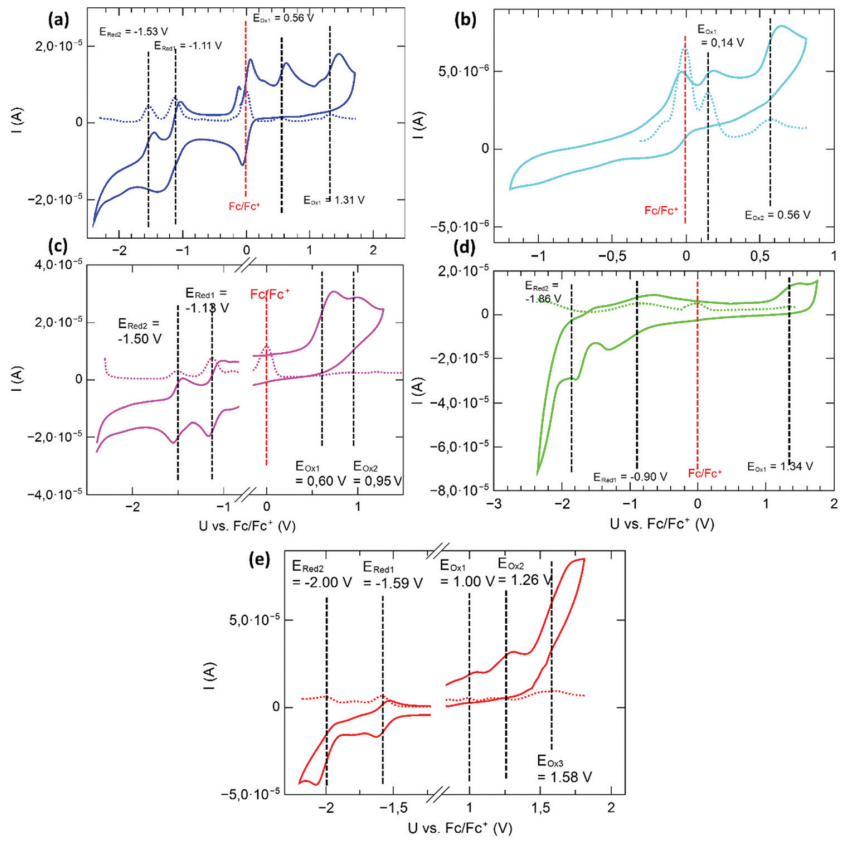

Fig. 5 Cyclic voltammograms (measured in CH_2Cl_2, 0.1 M n-Bu_4NPF_6, 50 mV s^{-1} scan rate, glassy carbon working electrode and Pt counter electrode) and their corresponding differential pulse voltammograms (DPV, dashed lines, 10 mV s^{-1} scan rate) for **2d** (a); **2f** (b); **3a** (c); **3b** (d) and **3c** (e).

pyrenes,[39] a bathocromic shift in the absorption spectra could be observed with an evolving novel band at 520 nm (**2f**) or 490 nm (**3b**) (Fig. 4).

Cyclovoltammetry

In order to characterize the electrochemical properties of the synthesized diazapyrenes, cyclovoltammetry (CV) and differential pulse voltammetry (DPV) were performed and referenced on the ferrocene/ferrocenium redox couple (E_{vac} = 4.8 eV (ref. 54)). The CV of triflate **2d**, piperidine-substituted **3a** and alkyne **3c** showed two reduction and two oxidation waves. Remarkably, the reduction waves of **3a** were nearly fully reversible, whereas **2d** shows only a reversible first reduction potential wave. The other compounds show rather irreversible redox behaviour, especially tetraalkyne **3b** which displays irreversible decomposition during CV measurement. The corresponding CVs (see Fig. 5) show first oxidation potentials of 0.14 V (**2f**) to 1.34 V (**3b**) *versus* ferrocene in agreement with the measured differential pulse voltammograms (DPVs). These correspond to experimental HOMO values ranging from −6.14 eV (**3b**) to −4.94 (**2f**). This proves that especially *O*-silyl substituted diazapyrenes show high lying HOMO levels. They can easily be oxidized, although their optical HOMO–LUMO energy gaps are large and their optical spectra are the most hypsochromically shifted ones. This trend is in agreement with the calculated frontier orbital energies (see Fig. S1, ESI†). Accordingly, silyl ether **2f** showed as the only congener with no reduction waves within the electrochemical window of DCM underlining its electron-rich character. Tetraalkyne **3b**, tetratriflate **2d** and remarkably tetraamine **3a** showed comparably high first reduction potentials (around −1 V) but also low first oxidation potentials. They can be classified as electron mediators, both electron donor and acceptor. Both alkyne and also amine functionalization leads to smaller optical HOMO–LUMO energy gaps than silyl ethers **2a**, **2e** and **2f** and also small electrochemical gaps due to energetically low first oxidation (electrochemical HOMO) and high first reduction (LUMO) waves. **3b** and **3c** show a higher first oxidation potential in comparison to silyl ethers **2a**, **2e** and **2f**. This is characteristic of the energetic stabilization of the LUMO of alkynes **3b** and **3c** in comparison to silyl ethers.

DFT and TD-DFT modelling of physical properties

Experimental physical properties of the reported molecules were modelled by DFT and TD-DFT calculations. Kohn–Sham frontier orbitals of the HOMO and LUMO and their energies as well as a comparison of normalized UV-Vis spectra and normalized electron transitions can be found in the ESI (Fig. S1, S2, S6 and Tables S1–S5†).

Conclusions

We reported a facile and scalable one-step reduction and functionalisation of commercially available naphthalene diimide (**1**) *via* a 1,3,6,8-tetratriflato-2,7-diazapyrene platform **2d**. The latter displayed superior reactivity and functionalization capabilities compared to the corresponding tetrapivaloates and made the synthesis and characterization of the corresponding tetra-1-alkynyl diazapyrenes **3b** and **3c** *via* a Sonogashira reaction and tetra-1-piperidinyl diazapyrene **3a** *via* non-catalyzed nucleophilic aromatic substitution possible. Furthermore, **1** was transformed into three electron-rich diazapyrene silyl ethers **2a**, **2e**, and **2f** employing chlorosilane activated zinc as a reducing agent. The obtained 2,7-diazapyrenes incorporating such electron-releasing and withdrawing 1,3,6,8-substituents were characterised in solution *via* UV-Vis and PL spectroscopy as well as CV and DPV. Previously non-accessible derivatives with absorption and emission maxima ranging in a large window of 100 nm and with HOMO–LUMO energy gaps between 2.36 eV and 3.05 eV teach how to precisely tune the optoelectronic properties by functionalisation of the reactive and versatile triflate **2d**, and how to predict physical properties by DFT and TD-DFT calculations. A sub monolayer of TMS-alkyne **3b** was deposited in an UHV onto a Cu(111) surface and investigated by STM. These experiments demonstrate an OMBE processability below the decomposition temperature of these functional molecules, surprising surface mobility even at 100 K and mostly repulsive intermolecular interactions in the adsorbed state.

Experimental section

Methods and devices

All preparative operations were conducted by using standard Schlenk techniques and solvents were dried according to common procedures[55] and passed through columns of aluminium oxide, 3 Å molecular sieves and an R3-11G-catalyst (BASF) or stored over molecular sieves (3 Å or 4 Å). Naphthalene diimide (NTCDI, **1**) was synthesized according to a literature method.[33]

The data collection for the single-crystal structure determination was performed on a Stoe Stadivari diffractometer or a Bruker D8 Quest diffractometer by the X-ray service of Fachbereich Chemie, Universität Marburg. Information concerning the used hardware, and software used for data collection, cell refinement and data reduction as well as structure refinement can be reviewed in the electronic supplementary tables and CCDC 2087066 (**2a**), 2087065 (**2f**), 2087067 (**3b**).† After solution (SHELXT)[56] and refinement process (SHELXL 2017/1)[57] the data were validated using Platon.[58] All graphic representations were created using Diamond 4.[59]

^{1}H and proton decoupled ^{13}C NMR spectra were recorded in automation or by the service department of Fachbereich Chemie with a Bruker Avance II 300, HD 300, DRX 400 or Avance III 500 spectrometer. All spectra were recorded at ambient temperature. ^{1}H and ^{13}C NMR spectra were calibrated using residual proton signals of the solvent (CD_2Cl_2: δ_H = 5.32 ppm, δ_C = 53.84 ppm, $CDCl_3$: δ_H = 7.26 ppm, δ_C = 77.16 ppm). Multiplicity is abbreviated as follows: s (singlet), d (doublet), t (triplet), q (quartet), qt (quintet), m (multiplet),

and br. HR-APCI mass spectra were acquired with an LTQ-FT Ultra mass spectrometer (Thermo Fischer Scientific). The resolution was set to 100.000. HR-EI mass spectra were acquired with an AccuTOF GCv 4G (JEOL) time of flight (TOF) mass spectrometer. An internal or external standard was used for drift time correction. The LIFDI ion source and FD-emitters were purchased from Linden ChroMasSpec GmbH (Bremen, Germany). IR spectra were recorded in a glovebox using a Bruker Alpha ATR-FT-IR spectrometer.

Absorption spectra were recorded with an Avance AvaSpect-2048 UV/Vis/NIR spectrophotometer in 10 mm cuvettes in dichloromethane with a concentration of 10 μM with a scan rate of 600 nm min^{-1}. Emission spectra were recorded with a Varian Cary Eclipse Spectrophotometer in 10 nm cuvettes in dichloromethane with a scan rate of 600 nm min^{-1}. Cyclic voltammetry (CV) and differential pulse voltammetry (DPV) measurements were carried out on an rhd instruments TSC 1600 closed electrochemical workstation (working electrode: glassy carbon; counter electrode: platinum crucible; reference electrode: platinum wire (pseudo reference electrode under a nitrogen atmosphere in a glovebox (Labmaster 130, MBraun))). The samples were measured in dichloromethane and calibrated using ferrocene as an internal standard after measurements. Dichloromethane was filtered through an aluminum oxide pad prior to use. Tetrabutylammonium hexafluorophosphate ($TBAPF_6$; >99.0%) was used as the electrolyte for electrochemical analysis. The measurements were carried out at a concentration of 100 mmol L^{-1} of the electrolyte.

Density functional theory (DFT) calculations using the PBE functional were performed. The def2-TZVPP[60–62] basis set was used with the RIJDX auxiliary base set,[63,64] employing the resolution-of-identity approximation.[65,66] A further D3-dispersion correction[67] was considered by applying Becke–Johnson damping.[68–71] Structural optimizations and TD-DFT calculations were performed using Orca 3.0.3.[72] The atomic coordinates for geometry optimization were taken from XRD structures, if possible. The structurally optimized molecules were used for TD-DFT calculations using the PBE[73,74] functional (PBE0-D3/def2-TZVPP), employing the resolution-of-identity approximation for both Coulomb integrals and HF exchange integrals.[66]

STM measurements were performed in an ultrahigh vacuum (UHV) system (base pressure below 1×10^{-10} mbar) equipped with a SPECS STM Aarhus 150 STM and photoelectron spectrometer system (SPECS). All bias voltages refer to the sample, and the images were recorded in constant current mode at around 100 K. Moderate filtering (Gaussian smooth, background subtraction) was applied for noise reduction. The Cu(111) single crystal with an alignment of better than 0.1° relative to the nominal orientation was purchased from MaTecK, Germany. Preparation of a clean and well-defined Cu(111) surface was achieved by cycles of bombardment with Ar^+ ions and annealing at 850 K. **3b** was evaporated in an UHV from a homebuilt Knudsen cell at 210 °C.

Synthesis of 2a. NTCDI (266 mg, 1.0 mmol, 1 eq.), zinc dust (392 mg, 8.0 mmol, 8.0 eq.) and trimethylsilyl chloride (TMSCl, 1.0 mL, 8.0 mmol, 8.0 eq.) were stirred at room temperature for 6 h in 20 mL of THF under an argon atmosphere, whilst the reaction mixture turned orange with intensive blue fluorescence. All volatilities were removed in a fine vacuum, the crude product was taken up in DCM (20 mL) and it was filtered. After the solvent was removed under vacuum, the solid was washed with *n*-pentane. 390 mg (0.68 mmol, 68%) of **2a** were obtained as a yellow solid. Single crystals suited for X-ray crystallography were obtained from a saturated solution of **2a** in *n*-pentane at −18 °C. ^{1}H NMR (300.1 MHz, $CDCl_3$): δ_H = 7.79 (s, 4H), 0.48 (s, 36H) ppm. ^{13}C NMR (75.1 MHz, $CDCl_3$): δ_C = 153.1, 133.1, 119.5, 111.7, 0.7 ppm. HR-FD(+) MS: found (clcd.) m/z = 556.20628 (556.20651) for $[C_{26}H_{40}N_2O_4Si_4]$. IR (ATR), $\tilde{\nu}$ = 2955 (w), 2898 (w), 1569 (s), 1473 (m), 1377 (s), 1339 (vs), 1249 (s), 1231 (m), 1185 (s), 1171 (m), 1123 (w), 1053 (w), 946 (w), 886 (vs), 837 (vs), 816 (s), 750 (m), 734 (m), 668 (w), 641 (w) cm^{-1}. M.p. = 153–156 °C.

Synthesis of 2e. NTCDI (266 mg, 1.0 mmol, 1.0 eq.), potassium graphite (KC_8, 616 mg, 4.4 mmol, 4.4 eq.) and triisopropylsilyl chloride (1.1 mL, 5.0 mmol, 5.0 eq.) were stirred under an argon atmosphere in 20 mL of THF at reflux for 16 h. All volatilities were removed in a fine vacuum and the crude product was dissolved in DCM and filtered over a pad neutral aluminum oxide. After removal of the solvent *in vacuo*, **2e** was recrystallized from *n*-pentane. 268 mg (0.30 mmol, 30%) of **2e** were obtained as a yellow solid. ^{1}H NMR (300.1 MHz, $CDCl_3$): δ_H = 7.87 (s, 4H), 0.47 (s, 36H), 1.73–1.52 (m, 2H), 1.15 (d, J = 7.4 Hz, 36H) ppm. ^{13}C NMR (75.1 MHz, $CDCl_3$): δ_C = 153.6, 133.7, 119.8, 112.0, 18.3, 13.6 ppm. HR-FD(+) MS: found (clcd.) m/z = 892.58231 (892.58211) for $[C_{50}H_{88}N_2O_4Si_4]^+$. IR (ATR), $\tilde{\nu}$ = 2940 (m), 2863 (m), 1700 (w), 1569 (s), 1474 (m), 1379 (s), 1343 (vs), 1228 (m), 1176 (m), 1122 (w), 1071 (m), 1012 (w), 917 (w), 819 (vs), 733 (w), 685 (m), 652 (m), 615 (m) cm^{-1}. M.p. = 145–148 °C.

Synthesis of 2f. NTCDI (1.06 g, 4.0 mmol, 1.0 eq.), zinc powder (2.09 g, 32.0 mmol, 8.0 eq.) and imidazole (2.17 g, 32.0 mmol, 8.0 eq.) were dissolved in 40 mL of 1,4-dioxane under an argon atmosphere. Then *tert*-butyldimethylsilyl chloride (4.82 g, 32.0 mmol, 8.0 eq.) was added to it and the reaction mixture was heated to 80 °C for 3 h. After cooling to room temperature, the orange-colored suspension was diluted with chloroform (50 mL) and filtered. The filtrate was washed with water and the organic layer was dried over magnesium sulphate. All volatilities were removed in a fine vacuum and the crude product was crystallized from the methanol/1,4-dioxane mixture at −20 °C. 2.04 g (2.81 mmol, 71%) of **2f** were obtained as a yellow solid. ^{1}H NMR (300.1 MHz, $CDCl_3$): δ_H = 7.82 (s, 4H), 1.12 (s, 36H), 0.45 (s, 24H) ppm. ^{13}C NMR (75.1 MHz, $CDCl_3$): δ_C = 135.3, 133.5, 119.6, 111.8, 67.1, 25.9, 18.3, −4.2 ppm. HR-FD(+) MS: found (clcd.) m/z = 724.39641 (724.39421) for $[C_{38}H_{64}N_2O_4Si_4]^+$. IR (ATR), $\tilde{\nu}$ = 2951 (w), 2929 (m), 2890 (w), 2856 (m), 1570 (s), 1469 (s), 1373 (s), 1335 (vs), 1245 (m), 1166 (m), 1119 (m), 943 (w), 888 (s), 823 (m), 780 (vs), 737 (m), 680 (m), 649 (w), 606 (w) cm^{-1}. M.p. = 170–173 °C.

Synthesis of 2d. NTCDI (1.33 g, 5.0 mmol, 1.0 eq.) and KC_8 (2.94 g, 21.0 mmol, 4.2 eq.) were stirred in 100 mL of DME under an argon atmosphere for 3 h at 80 °C whilst a purple suspension was formed. During a time period of 3h, 3.6 mL (21.0 mmol, 4.2 eq.) of trifluoromethyl sulfonic anhydride were added dropwise by cooling the reaction mixture to −50 °C (dry ice/*n*-octane cooling bath). The reaction mixture was warmed up to room temperature overnight and filtered under an inert gas atmosphere over a pad dried aluminum oxide and washed with DCM (100 mL). The pure product was precipitated from filtrate by the addition of 100 mL of *n*-pentane at −18 °C, filtered and dried *in vacuo*. 3.05 g (3.8 mmol, 76%) of **2d** were isolated as a beige solid. ^{1}H NMR (300.1 MHz, $CDCl_3$): δ_H = 8.56 (s, 4H) ppm. ^{13}C NMR (75.1 MHz, $CDCl_3$): δ_C = 163.2, 131.1, 126.8, 124.3, 118.8 ppm. ^{19}F NMR (250.1 MHz, $CDCl_3$): δ_F = 71.9 ppm. HR-FD(+) MS: found (clcd.) m/z = 795.85716 (795.85812) for $[C_{18}H_4F_{12}N_2O_{12}S_4]^+$. IR (ATR), $\tilde{\nu}$ = 1697 (w), 1652 (w), 1584 (w), 1460 (m), 1425 (w), 1370 (s), 1281 (m), 1215 (vs), 1173 (s), 1124 (s), 1083 (m), 915 (m), 860 (s), 791 (m), 758 (m), 730 (m), 663 (m), 619 (m) cm^{-1}. M.p. = 226–229 °C (dec.).

Synthesis of 3b. 2d (80 mg, 0.1 mmol, 1.0 eq.), copper iodide (4 mg, 0.02 mmol, 20 mol%) and $[Pd(dppf)Cl_2]$ (7 mg, 0.01 mmol, 10 mol%) were dissolved in THF (2 mL) and triethyl amine (2 mL) and degassed, subsequently. 0.1 mL (0.6 mmol, 6 eq.) of trimethylsilyl acetylene were added under an argon atmosphere and the reaction mixture was stirred for 16 h at 65 °C. After removal of all volatilities under vacuum by filtration, the crude product was purified *via* preparative thin layer chromatography (DCM). After removing the solvent *in vacuo*, 15 mg (0.025 mmol, 25%) of **3b** were obtained as an orange solid. X-ray suited single crystals were obtained by slow diffusion of layered *n*-pentane into a DCM solution of **3b** at −18 °C. ^{1}H NMR (300.1 MHz, $CDCl_3$): δ_H = 8.60 (s, 4H), 0.40 (s, 36H) ppm. ^{13}C NMR (75.1 MHz, $CDCl_3$): δ_C = 138.0, 127.4, 127.0, 126.0, 102.3, 101.3, 88.0, 85.9, −0.5 ppm. HR-FD(+) MS: found (clcd.) m/z = 588.22671 (588.22685) for $[C_{34}H_{40}N_2Si_4]^+$. IR (ATR), $\tilde{\nu}$ = 2958 (w), 2900 (w), 2157 (w), 2065 (w), 1571 (w), 1470 (m), 1342 (m), 1288 (m), 1246 (w), 1114 (m), 897 (w), 836 (w), 759 (vs), 701 (m), 640 (m), 553 (w) cm^{-1}. M.p. = 256–259 °C (dec.).

Synthesis of 3c. 2d (796 mg, 1.0 mmol, 1.0 eq.), tetramethylammonium iodide (804 mg, 4.0 mmol, 4.0 eq.), copper iodide (38 mg, 0.2 mmol, 20 mol%) and $[Pd(dppf)Cl_2]$ (71 mg, 0.1 mmol, 10 mol%) were dissolved in 30 mL of 1,4-dioxane and 10 mL of triethylamine and degassed. After 5 min, the formation of **I1** could be detected *via* EI-MS. To this mixture, 1.1 mL (6.0 mmol, 6 eq.) of 4-*tert*-butylphenylacetylene was added under an argon atmosphere and the reaction mixture was stirred for 16 h at 85 °C. After cooling to room temperature, the reaction mixture was filtered, the solvent was removed *in vacuo* and the crude product was purified *via* column chromatography on silica gel (*n*-pentane/DCM 1 : 1). After the solvent was removed, 225 mg (0.27 mmol, 27%) of **3c** were isolated as an orange solid. ^{1}H NMR (300.1 MHz, CD_2Cl_2): δ_H = 8.70 (s, 4H), 7.75 (d, J = 9.0 Hz, 8H), 7.50 (d, J = 9.0 Hz, 8H), 1.37 (s, 36H) ppm. ^{13}C NMR (125.8 MHz, $CDCl_3$): δ_C = 153.1, 138.7, 132.3, 127.2, 126.8, 125.7, 119.3, 96.6, 86.8, 35.1, 31.3 ppm. HR-EI(+) MS: found (clcd.) m/z = 707.65250 (707.65532) for $[C_{14}H_4{}^{127}I_4N_2]^+$ (**I1**) and HR-FD(+) MS: found (clcd.) m/z = 828.44049 (828.44435) for $[C_{62}H_{56}N_2]^+$ (**3c**). IR (ATR), $\tilde{\nu}$ = 2955 (m), 2901 (w), 2864 (w), 2202 (m), 1596 (m), 1534 (m), 1503 (m), 1476 (w), 1392 (s), 1360 (w), 1332 (m), 1263 (m), 1229 (m), 1200 (w), 1140 (w), 830 (vs), 737 (s), 559 (s) cm^{-1}. M.p. = 200–203 °C.

Synthesis of 3a. 2c (160 mg, 0.20 mmol, 1 eq.) was stirred in 4 mL of DMSO and 1 mL of piperidine (excess) at 90 °C for 1 h. The solvent was removed *in vacuo* and the residue was washed with water and dried *in vacuo*. 65 mg (0.12 mmol, 60%) of **3a** were isolated as a brown solid. ^{1}H NMR (300.1 MHz, $CDCl_3$): δ_H = 8.77 (s, 4H), 3.30–3.60 (m, 16H), 1.60–1.85 (m, 24 H) ppm. HR-EI(+) MS: found (clcd.) m/z = 536.36315 (536.36274) for $[C_{34}H_{44}N_6]^+$. IR (ATR), $\tilde{\nu}$ = 3355 (w), 3310 (m), 3196 (m), 3003 (w), 2956 (vs), 2924 (w), 2851 (m), 2810 (w), 1658 (s), 1633 (s), 1581 (w), 1529 (w), 1466 (w), 1410 (m), 1379 (m), 1244 (m), 1190 (m), 1152 (m), 1130 (w), 1091 (m), 1030 (m), 792 (m), 722 (m), 698 (w) cm^{-1}. M.p. = 218–221 °C (dec.).

Conflicts of interest

S.W. and J.S. declare a conflict of interest, since the above described compounds are part of the patent "Multi-functionalized [cd,ml]-annelated perylenes and their homologs" (WO2019/229134 A1).

Acknowledgements

Financial support from the LOEWE Program of Excellence of the Federal State of Hesse (LOEWE Focus Group PriOSS "Principles of On-Surface Synthesis") is gratefully acknowledged.

S. W. thanks Lei Zhang (group of Prof. Dr Olalla Vázquez) for the kind introduction in measuring fluorescence quantum yields.

Notes and references

1 J. Wu, W. Pisula and K. Müllen, Graphenes as potential material for electronics, *Chem. Rev.*, 2007, **107**, 718–747.
2 J. Mei, Y. Diao, A. L. Appleton, L. Fang and Z. Bao, Integrated materials design of organic semiconductors for field-effect transistors, *J. Am. Chem. Soc.*, 2013, **135**, 6724–6746.
3 T. M. Figueira-Duarte and K. Müllen, Pyrene-based materials for organic electronics, *Chem. Rev.*, 2011, **111**, 7260–7314.
4 M. Ball, Y. Zhong, Y. Wu, C. Schenck, F. Ng, M. Steigerwald, S. Xiao and C. Nuckolls, Contorted polycyclic aromatics, *Acc. Chem. Res.*, 2015, **48**, 267–276.

5 C. Zhang, Z. Wang, H. Li, J. Lu and Q. Zhang, Recent progress in the usage of tetrabromo-substituted naphthalene-tetracarboxylic dianhydride as a building block to construct organic semiconductors and their applications, *Org. Chem. Front.*, 2020, **7**, 3001–3026.

6 Y. Segawa, T. Maekawa and K. Itami, Synthesis of extended π-systems through C-H activation, *Angew. Chem.*, 2015, **127**, 68–83, (*Angew. Chem., Int. Ed.*, 2015, **54**, 66–81).

7 *Carbon-rich compounds. From molecules to materials*, ed. M. Haley and R. R. Tykwinski, John Wiley, Weinheim, Chichester, 2006.

8 R. G. Harvey, *Polycyclic aromatic hydrocarbons*, Wiley, New York, 1997.

9 K. Kalyanasundaram and J. K. Thomas, Solvent-dependent fluorescence of pyrene-3-carboxaldehyde and its applications in the estimation of polarity at micelle-water interfaces, *J. Phys. Chem.*, 1977, **81**, 2176–2180.

10 M. Sharnoff, Photophysics of aromatic molecules, *J. Lumin.*, 1971, **4**, 69–71.

11 K. K. T. Förster, Ein Konzentrationsumschlag der Fluoreszenz des Pyrens, *Z. Elektrochem.*, 1955, **59**, 976.

12 W.-L. Jia, T. McCormick, Q.-D. Liu, H. Fukutani, M. Motala, R.-Y. Wang, Y. Tao and S. Wang, Diarylamino functionalized pyrene derivatives for use in blue OLEDs and complex formation, *J. Mater. Chem.*, 2004, **14**, 3344–3350.

13 S. Bernhardt, M. Kastler, V. Enkelmann, M. Baumgarten and K. Müllen, Pyrene as chromophore and electrophore: encapsulation in a rigid polyphenylene shell, *Chem. – Eur. J.*, 2006, **12**, 6117–6128.

14 E. Tietze and O. Bayer, Die Sulfosäuren des Pyrens und ihre Abkömmlinge, *Justus Liebigs Ann. Chem.*, 1939, **540**, 189–210.

15 H. Zhang, Y. Wang, K. Shao, Y. Liu, S. Chen, W. Qiu, X. Sun, T. Qi, Y. Ma, G. Yu, Z. Su and D. Zhu, Novel butterfly pyrene-based organic semiconductors for field effect transistors, *Chem. Commun.*, 2006, 755–757.

16 T. Oyamada, S. Akiyama, M. Yahiro, M. Saigou, M. Shiro, H. Sasabe and C. Adachi, Unusual photoluminescence characteristics of tetraphenylpyrene (TPPy) in various aggregated morphologies, *Chem. Phys. Lett.*, 2006, **421**, 295–299.

17 H. Maeda, T. Maeda, K. Mizuno, K. Fujimoto, H. Shimizu and M. Inouye, Alkynylpyrenes as improved pyrene-based biomolecular probes with the advantages of high fluorescence quantum yields and long absorption/emission wavelengths, *Chem. – Eur. J.*, 2006, **12**, 824–831.

18 R. Muangpaisal, M.-C. Ho, T.-H. Huang, C.-H. Chen, J.-Y. Shen, J.-S. Ni, J. T. Lin, T.-H. Ke, L.-Y. Chen, C.-C. Wu and C. Tsai, Tetrasubstituted-pyrene derivatives for electroluminescent application, *Org. Electron.*, 2014, **15**, 2148–2157.

19 J.-Y. Hu, X. Feng, N. Seto, J.-H. Do, X. Zeng, Z. Tao and T. Yamato, Synthesis, structural and spectral properties of diarylamino-functionalized pyrene derivatives via Buchwald–Hartwig amination reaction, *J. Mol. Struct.*, 2013, **1035**, 19–26.

20 M. Gingras, V. Placide, J.-M. Raimundo, G. Bergamini, P. Ceroni and V. Balzani, Polysulfurated pyrene-cored dendrimers: luminescent and electrochromic properties, *Chem. – Eur. J.*, 2008, **14**, 10357–10363.

21 P. Sonar, M. S. Soh, Y. H. Cheng, J. T. Henssler and A. Sellinger, 1,3,6,8-tetrasubstituted pyrenes: solution-processable materials for application in organic electronics, *Org. Lett.*, 2010, **12**, 3292–3295.

22 T. Qin, W. Wiedemair, S. Nau, R. Trattnig, S. Sax, S. Winkler, A. Vollmer, N. Koch, M. Baumgarten, E. J. W. List and K. Müllen, Core, shell, and surface-optimized dendrimers for blue light-emitting diodes, *J. Am. Chem. Soc.*, 2011, **133**, 1301–1303.

23 D. N. Coventry, A. S. Batsanov, A. E. Goeta, J. A. K. Howard, T. B. Marder and R. N. Perutz, Selective Ir-catalysed borylation of polycyclic aromatic hydrocarbons: structures of naphthalene-2,6-bis(boronate), pyrene-2,7-bis(boronate) and perylene-2,5,8,11-tetra(boronate) esters, *Chem. Commun.*, 2005, 2172–2174.

24 A. G. Crawford, A. D. Dwyer, Z. Liu, A. Steffen, A. Beeby, L.-O. Pålsson, D. J. Tozer and T. B. Marder, Experimental and theoretical studies of the photophysical properties of 2- and 2,7-functionalized pyrene derivatives, *J. Am. Chem. Soc.*, 2011, **133**, 13349–13362.

25 L. Ji, A. Lorbach, R. M. Edkins and T. B. Marder, Synthesis and photophysics of a 2,7-disubstituted donor-acceptor pyrene derivative: an example of the application of sequential Ir-catalyzed C-H borylation and substitution chemistry, *J. Org. Chem.*, 2015, **80**, 5658–5665.

26 U. H. F. Bunz, The Larger Linear N-Heteroacenes, *Acc. Chem. Res.*, 2015, **48**, 1676–1686.

27 M. Stępień, E. Gońka, M. Żyła and N. Sprutta, Heterocyclic Nanographenes and Other Polycyclic Heteroaromatic Compounds: Synthetic Routes, Properties, and Applications, *Chem. Rev.*, 2017, **117**, 3479–3716.

28 M. Liebold, E. Sharikow, E. Seikel, L. Trombach, K. Harms, P. Zimcik, V. Novakova, R. Tonner and J. Sundermeyer, An experimental and computational study on isomerically pure, soluble azaphthalocyanines and their complexes and boron azasubphthalocyanines of a varying number of aza units, *Org. Biomol. Chem.*, 2018, **16**, 6586–6599.

29 S. Geib, S. C. Martens, U. Zschieschang, F. Lombeck, H. Wadepohl, H. Klauk and L. H. Gade, 1,3,6,8-Tetraazapyrenes: synthesis, solid-state structures, and properties as redox-active materials, *J. Org. Chem.*, 2012, **77**, 6107–6116.

30 R. Molenda, S. Boldt, A. Villinger, P. Ehlers and P. Langer, Synthesis of 2-Azapyrenes and Their Photophysical and Electrochemical Properties, *J. Org. Chem.*, 2020, **85**, 12823–12842.

31 S. V. Bhosale, C. H. Jani and S. J. Langford, Chemistry of naphthalene diimides, *Chem. Soc. Rev.*, 2008, **37**, 331–342.

32 M. A. Kobaisi, S. V. Bhosale, K. Latham, A. M. Raynor and S. V. Bhosale, Functional Naphthalene Diimides: Synthesis, Properties, and Applications, *Chem. Rev.*, 2016, **116**, 11685–11796.

33 C. Sotiriou-Leventis and Z. Mao, A facile synthesis of 2,7-diazapyrene, *J. Heterocycl. Chem.*, 2000, **37**, 1665–1667.

34 J. Toftered and U. Nilsson, Synthesis of Chiral Macrocycles by Cyclodimerization of Diamines with Stepwise Nucleophilic Aromatic Substitution of 1,5-Difluoro-2,4-dinitrobenzene, *Synlett*, 2004, 2517–2520.

35 P. H. Dinolfo, M. E. Williams, C. L. Stern and J. T. Hupp, Rhenium-based molecular rectangles as frameworks for ligand-centered mixed valency and optical electron transfer, *J. Am. Chem. Soc.*, 2004, **126**, 12989–13001.

36 G. H. Lee, L. Della Ciana and A. Haim, Intramolecular electron transfer from pentacyanoferrate(II) to pentaammineco-balt(III) with 3,3′-dimethyl-4,4′-bipyridine, 4,4′-bipyridylacetylene, 1,4-bis(4-pyridyl)butadiyne, 2,7-diazapyrene, and 3,8-phenanthroline as bridging ligands, *J. Am. Chem. Soc.*, 1989, **111**, 2535–2541.

37 P. J. Stang, D. H. Cao, S. Saito and A. M. Arif, Self-Assembly of Cationic, Tetranuclear, Pt(II) and Pd(II) Macrocyclic Squares. X-ray Crystal Structure of [Pt2+(dppp)(4,4′-bipyridyl).cntdot.2-OSO2CF3]4, *J. Am. Chem. Soc.*, 1995, **117**, 6273–6283.

38 H. Sachdev, Morylenes, a new class of modified rylenes, EP2390253A1, 2011.

39 T. Nakazato, T. Kamatsuka, J. Inoue, T. Sakurai, S. Seki, H. Shinokubo and Y. Miyake, The reductive aromatization of naphthalene diimide: a versatile platform for 2,7-diazapyrenes, *Chem. Commun.*, 2018, **54**, 5177–5180.

40 Y. Nakamura, T. Nakazato, T. Kamatsuka, H. Shinokubo and Y. Miyake, Soluble and Planar 2,9-Diazaperopyrenes through Reductive Aromatization of Perylene Diimides: Tunable Emission and Aggregation Behaviors, *Chem. – Eur. J.*, 2019, **25**, 10571–10574.

41 T. Nakazato, W. Matsuda, T. Sakurai, S. Seki, H. Shinokubo and Y. Miyake, Synthesis and Crystal Packing Structures of 2,7-Diazapyrenes with Various Alkyl Groups at 1,3,6,8-Positions, *Chem. Lett.*, 2020, **49**, 465–468.

42 T. Nakazato, H. Shinokubo and Y. Miyake, Complexation of 2,7-diazapyrene with boron for structural and electronic tuning, *Chem. Commun.*, 2021, **57**, 327–330.

43 S. Werner, T. Vollgraff and J. Sundermeyer, Access to functionalized Pyrenes, Peropyrenes, Terropyrenes and Quarterropyrenes via Reductive Aromatization, *Angew. Chem.*, 2021, **133**, 13743–13748, (*Angew. Chem.*, 2021, **60**, 13631–13635).

44 S. Werner, T. Vollgraff and J. Sundermeyer, Tetrasubstituted Peropyrenes Formed by Reductive Aromatization: Synthesis, Functionalization and Characterization, *Chem. – Eur. J.*, 2021, DOI: 10.1002/chem.202101101.

45 (*a*) J. Sundermeyer, E. Baal and S. Werner, Multi-functionalized [cd,ml]-annelated perylenes and their homologs, WO2019/229134A1, 2019; (*b*) E. Baal, M. Klein, K. Harms and J. Sundermeyer, 2,9-Diazadibenzoperylene- and 2,9-Dimethyldibenzoperylene-1,3,8,10-tetratriflates: Key to Functionalized 2,9-Diazaperopyrenes, *Chem. – Eur. J.*, 2021, DOI: 10.1002/chem.202101719.

46 J. Hinschberger, J.-P. Desvergne, H. Bouas-Laurent and P. Marsau, Synthesis and photophysical properties of fluorescent anthracenophanes incorporating two polyoxadioxoalkane chains, *J. Chem. Soc., Perkin Trans. 2*, 1990, 993–1000.

47 S. Geib, S. C. Martens, M. Märken, A. Rybina, H. Wadepohl and L. H. Gade, Tuning redox chemistry and photophysics in core-substituted tetraazaperopyrenes (TAPPs), *Chem. – Eur. J.*, 2013, **19**, 13811–13822.

48 T. Kudernac, N. Ruangsupapichat, M. Parschau, B. Maciá, N. Katsonis, S. R. Harutyunyan, K.-H. Ernst and B. L. Feringa, Electrically driven directional motion of a four-wheeled molecule on a metal surface, *Nature*, 2011, **479**, 208–211.

49 C. Bai, *Scanning tunneling microscopy and its applications*, Springer, Berlin, 2nd edn, 2000.

50 L. Zhang, Y.-Q. Zhang, Z. Chen, T. Lin, M. Paszkiewicz, R. Hellwig, T. Huang, M. Ruben, J. V. Barth and F. Klappenberger, On-Surface Activation of Trimethylsilyl-Terminated Alkynes on Coinage Metal Surfaces, *ChemPhysChem*, 2019, **20**, 2382–2393.

51 R. Hellwig, T. Paintner, Z. Chen, M. Ruben, A. P. Seitsonen, F. Klappenberger, H. Brune and J. V. Barth, Epitaxy-Induced Assembly and Enantiomeric Switching of an On-Surface Formed Dinuclear Organocobalt Complex, *ACS Nano*, 2017, **11**, 1347–1359.

52 J. R. Lakowicz, *Principles of fluorescence spectroscopy*, Springer, New York, NY, 4th edn, 2010.

53 Y.-C. Hung, J.-C. Jiang, C.-Y. Chao, W.-F. Su and S.-T. Lin, Theoretical study on the correlation between band gap, bandwidth, and oscillator strength in fluorene-based donor-acceptor conjugated copolymers, *J. Phys. Chem. B*, 2009, **113**, 8268–8277.

54 B. Dandrade, S. Datta, S. Forrest, P. Djurovich, E. Polikarpov and M. Thompson, Relationship between the ionization and oxidation potentials of molecular organic semiconductors, *Org. Electron.*, 2005, **6**, 11–20.

55 W. L. F. Armarego and D. D. Perrin, *Purification of laboratory chemicals*, Butterworth-Heinemann, Oxford, 4th edn, 2002.

56 G. M. Sheldrick, Crystal structure refinement with SHELXL, *Acta Crystallogr., Sect. C: Struct. Chem.*, 2015, **71**, 3–8.

57 C. B. Hübschle, G. M. Sheldrick and B. Dittrich, ShelXle: a Qt graphical user interface for SHELXL, *J. Appl. Crystallogr.*, 2011, **44**, 1281–1284.

58 A. L. Spek, Structure validation in chemical crystallography, *Acta Crystallogr., Sect. D: Biol. Crystallogr.*, 2009, **65**, 148–155.

59 H. P. K. Brandenburg, *Diamond*, Crystal Impact GbR, Bonn, 2012.

60 A. Schäfer, C. Huber and R. Ahlrichs, Fully optimized contracted Gaussian basis sets of triple zeta valence quality for atoms Li to Kr, *J. Chem. Phys.*, 1994, **100**, 5829–5835.

61 F. Weigend, Accurate Coulomb-fitting basis sets for H to Rn, *Phys. Chem. Chem. Phys.*, 2006, **8**, 1057–1065.

62 F. Weigend and R. Ahlrichs, Balanced basis sets of split valence, triple zeta valence and quadruple zeta valence quality for H to Rn: Design and assessment of accuracy, *Phys. Chem. Chem. Phys.*, 2005, **7**, 3297–3305.

63 F. Weigend, M. Häser, H. Patzelt and R. Ahlrichs, RI-MP2, *Chem. Phys. Lett.*, 1998, **294**, 143–152.

64 K. Eichkorn, O. Treutler, H. Öhm, M. Häser and R. Ahlrichs, Auxiliary basis sets to approximate Coulomb potentials, *Chem. Phys. Lett.*, 1995, **240**, 283–290.

65 M. von Arnim and R. Ahlrichs, Performance of parallel TURBOMOLE for density functional calculations, *J. Comput. Chem.*, 1998, **19**, 1746–1757.

66 F. Weigend, A fully direct RI-HF algorithm, *Phys. Chem. Chem. Phys.*, 2002, **4**, 4285–4291.

67 S. Grimme, J. Antony, S. Ehrlich and H. Krieg, A consistent and accurate ab initio parametrization of density functional dispersion correction (DFT-D) for the 94 elements H-Pu, *J. Chem. Phys.*, 2010, **132**, 154104.

68 A. D. Becke and E. R. Johnson, A density-functional model of the dispersion interaction, *J. Chem. Phys.*, 2005, **123**, 154101.

69 E. R. Johnson and A. D. Becke, A post-Hartree-Fock model of intermolecular interactions, *J. Chem. Phys.*, 2005, **123**, 24101.

70 E. R. Johnson and A. D. Becke, A post-Hartree-Fock model of intermolecular interactions: inclusion of higher-order corrections, *J. Chem. Phys.*, 2006, **124**, 174104.

71 S. Grimme, S. Ehrlich and L. Goerigk, Effect of the damping function in dispersion corrected density functional theory, *J. Comput. Chem.*, 2011, **32**, 1456–1465.

72 F. Neese, The ORCA program system, *Wiley Interdiscip. Rev.: Comput. Mol. Sci.*, 2011, **2**, 73–78.

73 J. P. Perdew, K. Burke and M. Ernzerhof, Generalized Gradient Approximation Made Simple, *Phys. Rev. Lett.*, 1996, **77**, 3865–3868.

74 J. P. Perdew, K. Burke and M. Ernzerhof, Generalized Gradient Approximation Made Simple, *Phys. Rev. Lett.*, 1997, **78**, 1396.

3.4 Publication 4: Rylene- and Diaza-rylene-derived Cobalt Clusters for the Solid-State Pyrolysis towards Undoped and N-doped Carbon Nanoparticles

Citation: S. Werner, T. Vollgraff, J. Sundermeyer, *Dalton Trans.* **2021**, *50*, 14374–14383.[D]

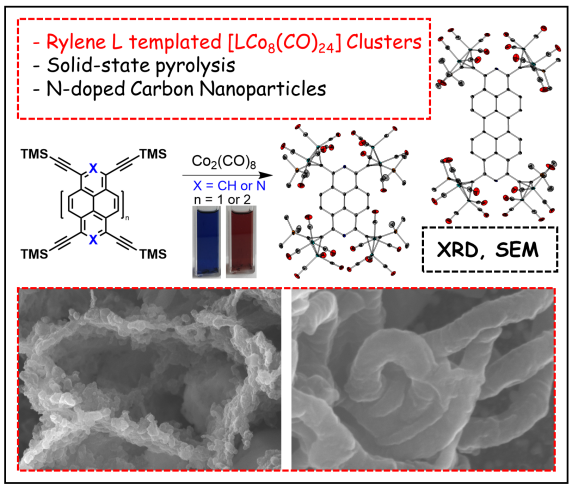

Summary: In this full paper, a material chemistry application of Co-carbonyl cluster complexes derived from (diaza)-pyrene and -peropyrene tetraalkynes (their synthesis is described in Publication 2 and 3 and by Eduard Baal) is presented. By complexation reaction of those four alkynes with $[Co_2(CO)_8]$, air- and moisture-stable (diaza-)ropyrenes containing four tetrahedral $[Co_2(CO)_6]$ units were obtained. The two diaza-complexes could be characterized by X-ray crystallography. All four complexes showed broad UV-Vis bands over the whole visible region. Their thermogravimetrical behaviour was characterized by TGA-DSC measurements, revealing a smooth one-or two-step decay of the $[Co_2(CO)_6]$ units via CO extrusion at temperatures over 200 °C, leading to fcc-Co and amorphous carbonaceous materials when heated to 850 °C. Solid-state vacuum pyrolysis of the four complexes at 850 °C followed by scanning electron microscopy (SEM) and elemental analysis of the obtained materials showed that in the case of nitrogen containing complexes N-containing porous carbon nanoparticles are formed, whereas the peropyrene-complex yielded multi-walled carbon nanotubes (CNTs). The study proofs that the solid-state pyrolysis products are highly dependent on the C/Co ratio of the complexes and the nitrogen content and not only on the shape and size of the aromatic backbone.

Own Contribution: All experimental work was done by myself as well as characterization by UV-Vis, IR spectrometry and DFT calculations. T. Vollgraff solved and refined the crystal structures. NMR, mass spectra and elemental analysis as well as RPD and TGA-DSC measurements were performed by service departments of the faculty. M. Hellwig (WZMW, Marburg) assisted in sample preparation and SEM/TEM measurements of the pyrolysis products. Prof. Dr. J. Sundermeyer initiated and supervised this study and was available as valuable discussion partner. The manuscript was written by myself with valuable feedback of Prof. Dr. J. Sundermeyer.

[D]Reproduced with permission of S. Werner, T. Vollgraff, J. Sundermeyer, *Dalton Trans.* **2021**, *50*, 14374–14383, Rights Managed by the Royal Society of Chemistry.

Dalton Transactions

ROYAL SOCIETY OF CHEMISTRY

PAPER

View Article Online
View Journal | View Issue

Cite this: *Dalton Trans.*, 2021, **50**, 14374

Rylene- and diaza-rylene-derived cobalt clusters for solid-state pyrolysis towards undoped and N-doped carbon nanoparticles†

Simon Werner, Tobias Vollgraff and Jörg Sundermeyer *

2,7-Diazapyrene and 2,9-diazaperopyrene tetraalkynes (**12** and **13**) as well as related non-N-doped pyrene and peropyrene tetraalkynes (**14** and **15**) of the same shape were used as polyaromatic templates in their metalation by $[Co_2(CO)_8]$. Isolated cobalt-rich [(**12**, **13**, **14**, **15**)$Co_8(CO)_{24}$] clusters were characterized by means of NMR, IR, UV–Vis spectroscopy and X-ray crystallography. Their thermogravimetric behaviour and products of solid-state pyrolysis (SSP) were investigated by TGA, DSC, and scanning electron microscopy (SEM). Despite the same precursor shape, different carbon nanoparticles and nanotubes were formed depending on the extension of the π-system and nitrogen content of the precursors. Diazapyrene and diazaperopyrene complexes formed cauliflower-shaped nanoparticles, and the pyrene complex formed spherical nanoparticles and the peropyrene complex led to multi-walled carbon nanotubes. These results elucidate that the carbon to cobalt ratio and the nitrogen dopant in the precursor have a significant impact on the products of the pyrolysis reaction.

Received 9th July 2021,
Accepted 1st September 2021

DOI: 10.1039/d1dt02276h

rsc.li/dalton

Introduction

Triggered by the discovery of carbon nanotubes (CNTs) by Iijima in 1991,[1] carbon nanoparticles (CNPs) in general attained tremendous research interest during the last three decades.[2–6] The unique thermal, mechanical and conducting properties[7–9] of CNTs made them promising candidates for many technological applications, such as for *e.g.* hydrogen storage,[10] data storage,[11] biomedical functions,[12] in chemical sensors and adsorbers[13,14,17] or in photovoltaics and light emitting diodes.[15,16] Besides this, also other CNPs, *e.g.* fullerenes[18] or carbon onions,[19] have been investigated.

The favorable syntheses (*i.e.* laser ablation,[20] arc discharge[21] or chemical vapor deposition (CVD)[22–24]) of CNPs and CNTs rely mostly on high temperature procedures or harsh conditions; but especially in the case of CVD, production volumes in ton scale are possible.[25,26]

Another facile approach for the synthesis of CNPs with tailored capabilities is the solid-state pyrolysis (SSP) of organometallic compounds, since the homogenously embedded metal atoms in a preformed molecular carbon matrix might allow high yields and selectivity. Earlier studies revealed ferrocene[27,28] or $[Fe(CO)_5]$[29] as an effective pre-catalyst and carbon source for the synthesis of CNPs and metal-encapsulated CNTs. Work by Vollhardt and Bunz demonstrated cobalt carbonyl complexes derived from diphenylethylene,[30] oligoalkyne[31] or organo-metallic dehydro-[18] annulenes[32] to be effective organometallic precursors for the SSP to synthesize CNPs in high yields with a controllable shape.

In systematic studies on various cobalt carbonyl precursors, Müllen *et al.*[33–35] and Bunz *et al.*[36] found that in the case of SSP, the organometallic precursor's shape is crucial for the morphology of the carbonaceous pyrolysis product (see Scheme 1 for selected examples).[37] Accordingly, the SSP of dicobalt-hexacarbonyl functionalized poly-*p*-phenylenethynylene (**1**) led to cobalt carbon spheres in the form of distributed cobalt NP in a carbon matrix.[36] In contrast, the use of a tetrakis(4-ethynylphenyl)-methane (**2**) derived cobalt complex led to one-dimensional square-shaped cobalt-carbon rod structural motifs.[33] Ill-defined larger particles were obtained, when non-planar hexaphenyl-benzene cobalt complex **3** was pyrolyzed.[34] High yields of CNTs with a bamboo shape (laminar built multi-walled CNTs with wall segments of an irregular length)[38,39] were only obtained in the case of cobalt complexes containing planar graphitic aromatic backbones (*e.g.* hexa-*peri*-hexabenzocoronenes **4** and **5**), illustrating the importance of the precursor's shape for the bottom-up synthesis of

Tobias Vollgraff, Simon Werner, Jörg Sundermeyer, Fachbereich Chemie and Material Science Center (WZMW), Philipps-Universität Marburg, Hans-Meerwein-Straße 4, 35043 Marburg, Germany. E-mail: JSU@staff.uni-marburg.de

†Electronic supplementary information (ESI) available: Additional experimental details, NMR spectra, Cartesian coordinates of the calculated structures (XYZ) and the XRD data. The CIF files of the presented structures are provided. CCDC 2087191 and 2087192. For ESI and crystallographic data in CIF or other electronic format see DOI: 10.1039/d1dt02276h

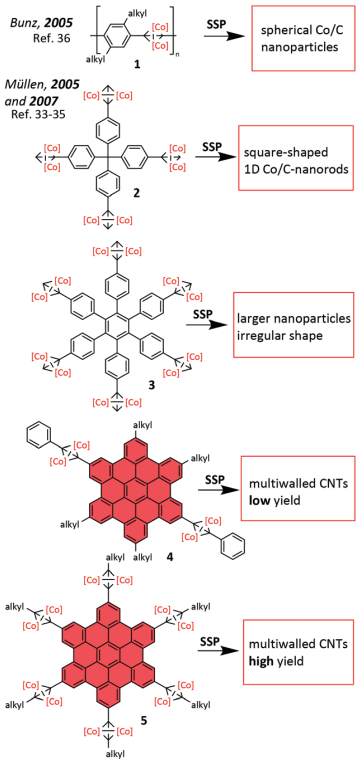

Scheme 1 Representative literature examples for aryl-cobalt carbonyl complexes (**1–5**) and their highly shape-dependent solid-state pyrolysis products. The $[Co(CO)_3]$ units are abbreviated with [Co]. Planar polyaromatic backbones are highlighted in red color.

nanostructures.[34,35] A second critical issue is a suitable Co to C ratio, since an optimum amount of catalytically active cobalt nanoparticles needs to be formed.[34]

To date, N-doped CNTs partly filled with iron carbide or nanofibers were synthesized by SSP of cobalt or iron phthalocyanines.[40] They are of particular interest, since nitrogen atoms in N-doped CNTs or NPs provide further electron density with narrowed energy band gaps[41] and give rise to metal-free electrocatalytic application (*e.g.* oxidative alkane dehydrogenations) of these nanostructures.[42–45] In contrast to their promising capabilities, there are only a few synthesis procedures to introduce defined amounts of nitrogen to CNTs or CNPs.

We were interested to investigate the influence of aza units incorporated into the scaffold of previously studied pure hydrocarbon precursors for SSP. Our approach is based on the cobalt carbonyl clusters of diazapyrene and diazaperopyrene tetraalkynes and a comparison with their purely carbon based pyrene and peropyrene analogues. We accessed tetra-alkynyl diazapyrene (**12**), diazaperopyrene (**13**) and peropyrene (**14**) *via* the Sonogashira cross-coupling of the corresponding tetratriflates with trimethylsilyl acetylene (TMSA) following our strategy of reductive aromatization and *O*-triflylation of naphthalene diimide (NTCDI, **6**),[46] perylene diimide (PTCDI, **7**)[47,48] and dihydroxy peropyrene quinone (**8**)[49,50] (Scheme 2). Here, we report the conversion of our tetraalkynes **12–14** and of literature-known tetratrimethylsilylethynyl-pyrene **15**[51,52] into their fully characterized octacobalt carbonyl clusters. We present a systematic SSP and SEM study in order to understand the role of the size of the (aza)aromatic backbone, in particular, the role of nitrogen doping for the evolving CNPs.

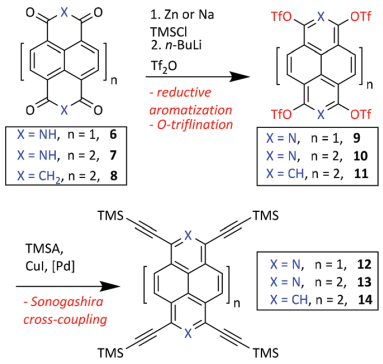

Scheme 2 Established synthesis route towards trimethylsilyl-acetylene ropyrenes **12**, **13** and **14** *via* reductive aromatization, *O*-triflination and Sonogashira cross coupling.

Results and discussion

Synthesis, NMR and XRD studies

The reactions of tetraalkynes **12–15** with a slight excess of $[Co_2(CO)_8]$ in dichloromethane at room temperature furnished air- and moisture-stable cobalt complexes **C1**, **C2**, **N1** and **N2** in almost quantitative yields after column chromatography (Scheme 3).

The reactions proceeded within 2 h at room temperature and gave black reaction solutions at high concentrations and partly precipitated microcrystalline product in the synthesis of C1 and N2, respectively. Archetypical photoluminescence of the non-metalated ligand templates is lost, and the products show no visible fluorescence. The larger congeners **C2** and **C1**, in particular, showed an improved solubility compared to their

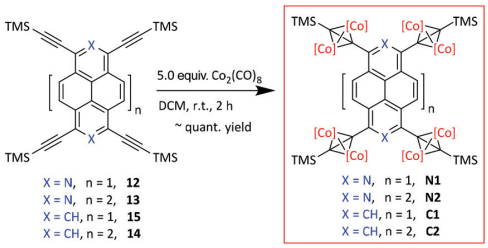

Scheme 3 Synthesis of ropyrene cobalt complexes **C1**, **C2**, **N1** and **N2**. The $[Co(CO)_3]$ units are abbreviated with [Co].

corresponding alkynes **13** and **14**. Recrystallization from dichloromethane/*n*-pentane mixtures furnished **C1**, **C2**, **N1** and **N2** in excellent purities. ^{1}H NMR spectroscopy revealed the covalent binding of $[Co_2(CO)_6]$ units symmetrically to all the alkynes by means of distinct downfield signal shifts of the aromatic protons observed as one singlet for **C1** and **N1** and two doublets for **C2** and **N2**. ^{13}C NMR spectra displayed well-resolved signals of the former alkynes, now metalated carbon atoms at 80 ppm and 100 ppm. Well-resolved ^{13}C NMR signals of even the inner carbon nuclei of the aromatic backbones were observed for all four complexes, next to the pronounced signal of the CO carbon atoms at 200 ppm (see Fig. 1 for the ^{1}H and ^{13}C NMR spectra). Furthermore, molecular structures of the nitrogen-containing complexes **N1** and **N2** were studied *via* X-ray crystallography. X-ray diffractive single crystals of **N1** and **N2** were grown by layering a saturated solution of **N1** or **N2** in dichloromethane at −20 °C with *n*-pentane. Fig. 2 displays the result of the structure analysis, and further details of the structure refinement and observed atom distances and angles are listed in the ESI (Tables S3 and S4†).

N1 crystallizes in the monoclinic space group $C2/c$ ($Z = 4$). In contrast to the X-ray structure of the corresponding alkyne **12**,[46] the protection of the alkyne groups of **12** as bulky tetrahedral clusters completely prevents any π-stacking in the case of **N1**. Intramolecular steric repulsion of these dicobalt–tetrahedrane units leads to a twist within the *meta*-C≡C bonds of the pyridine ring with a torsion angle of 4.5° with respect to each other, distorting the diazapyrene backbone. As expected, the former alkyne C–C triple bond is elongated to a double bond (observed av. d_{C-C} = 1.34 Å) in these archetypal $[C_2Co_2]$ tetrahedrane units. In contrast to **N1**, diazaperopyrene based **N2** crystallizes in the primitive space group $P\bar{1}$ ($Z = 1$), with a closest interatomic distance of 7.52 Å between two neighboring molecules, preventing any π-stacking. In the case of the larger π-system of **N2**, steric repulsion between the $[C_2Co_2]$ tetrahedrane units is decreased in comparison with **N1**, indicated by a smaller twist within the pyridine unit (torsion angle of the C–N bonds: 2.6° in comparison with 4.5° for **N1**). The diazapyrene backbone is only slightly distorted and nearly planar as marked by a splay angle of the backbone's bay area of only 1.9°. The bonding distances and angles within the $[C_2Co_2]$ units of **N2** and **N1** are identical within 3σ. Interestingly, **C1** and **C2** gave no X-ray diffractive single crystals under identical conditions. Their identity and purity were ensured by ^{1}H and ^{13}C NMR, FD-MS(+), and IR spectroscopy. In the case of elemental analysis, a systematic deviation of only the carbon content by *ca.* −1% is observed, most likely due to the cobalt carbide formation.

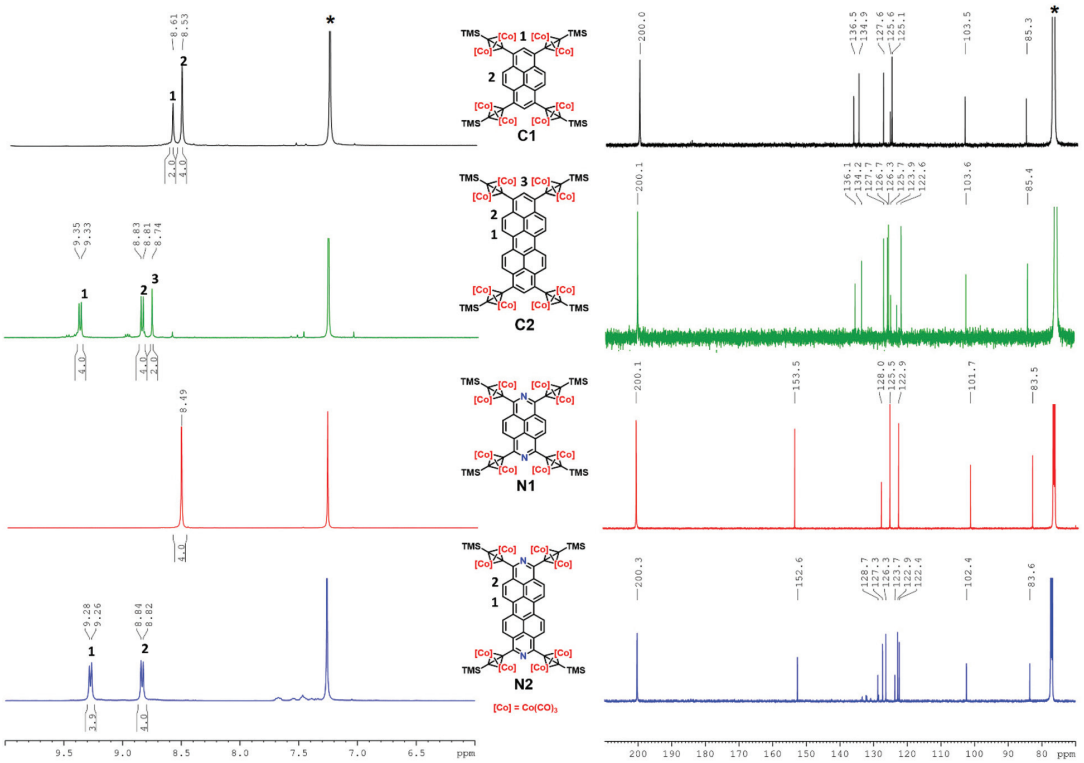

Fig. 1 Comparison of the ^{1}H NMR spectra (left side, 500 MHz, recorded in *$CDCl_3$) and ^{13}C NMR spectra (right side, 125 MHz, recorded in *$CDCl_3$) of **C1**, **C2**, **N1** and **N2** and the assignment of the protons of the complexes (center) to the aromatic signals.

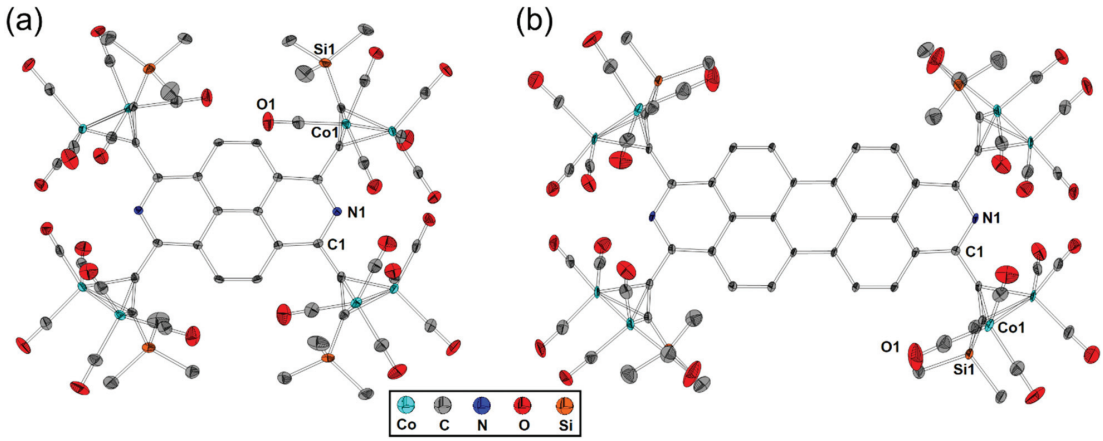

Fig. 2 Molecular XRD structures of **N1** (a) and **N2** (b). Hydrogen atoms are omitted for clarity. Thermal ellipsoids are shown at the 50% level.

UV–Vis and IR spectroscopy

As colors drastically changed during the reaction (see the photographs of **N1** and **N2** dissolved in dichloromethane in cuvettes in Fig. 3(b)), the UV–Vis spectra of the isolated complexes **C1**, **C2**, **N1** and **N2** were recorded in dichloromethane ($c \approx 10^{-5}$ M) to investigate the influence of the alkyne metalation on the absorption spectra (Fig. 3(a)). All four complexes showed broad absorption bands covering nearly the whole visible range of the absorption spectra associated with the charge transfer bands.[53] With an absorption maximum at 640 nm, blue **N2** shows the most bathochromic absorption maximum of the four investigated complexes. The absorption maximum of **C2** is shifted around 100 nm towards shorter wavelengths with respect to **N2**. **N1** and **C1** are also shifted towards shorter wavelengths in comparison with their π-extended homologs **N2** and **C2**. In comparison with the corresponding alkynes **12–15**,[46–50] the spectra show remarkable broadening and less structured absorption bands, indicating that the other transitions (*e.g.* vibronic transitions of the CO ligands) are excited simultaneously with the HOMO–LUMO electronic transitions.[54,55] Furthermore, the absorption maxima of **C1**, **C2**, **N1** and **N2** are bathochromically shifted by about 50–100 nm with respect to alkynes **12–15**, indicating the shrinking of the HOMO–LUMO energy gap in the case of the metal complexes.

The ATR–FTIR spectra of **C1**, **C2**, **N1** and **N2** of the C–O stretching vibration modes (Fig. 3(c)) showed three pronounced vibration modes at 2010 cm^{-1}, 2050 cm^{-1} and 2090 cm^{-1}, the latter one being the strongest vibration band. These are typical frequencies of the C–O stretching vibrations in such $[RR'C_2Co_2(CO)_6]$ tetrahedrane units.[33–36] The wavenumbers are shifted to higher numbers compared to the C–O stretching vibrations of $[Co_2(CO)_8]$ (*e.g.* 1857 cm^{-1} and 1886 cm^{-1}),[56] also indicating the quantitative formation of the pure complexes. Additionally, we performed DFT calculations (PBE/def2-TZVPP level of theory) of the vibrational spectra of

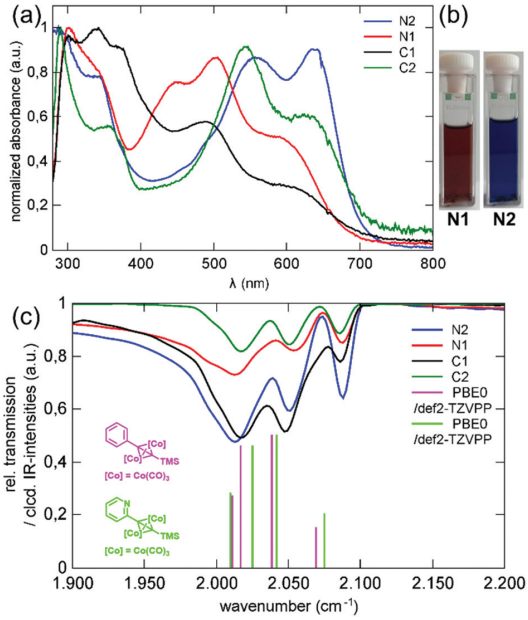

Fig. 3 (a) Normalized UV–Vis spectra of **C1**, **C2**, **N1** and **N2** recorded in dichloromethane ($c \approx 10^{-5}$ M); (b) the photographs of **N1** and **N2** in dichloromethane under ambient light; and (c) the FTIR spectra of the C–O stretching vibrations of **C1**, **C2**, **N1** and **N2** and the calculated IR intensities (normalized to the value 0.5) of the depicted model compounds. The $[Co(CO)_3]$ units are abbreviated with [Co].

phenyl- and 1-pyridinyl-dicobalthexacarbonyl model systems with the previously DFT-optimized geometries. The calculations predict four modes for the C–O stretching vibrations (intensities shown as vertical transitions in Fig. 3(c)) to be in good agreement with the experimental frequencies. According to the DFT-calculated spectra, the strongest frequency of **N1**,

N2, **C1** and **C2** at 2090 cm^{-1} as a broad band consists of two C–O stretching vibrations with similar energies, which could not be separated in the experimental spectra. The influence of the central nitrogen atom on the energy of the vibrational modes and therefore their wavenumbers seems to be negligible based on the experimental and calculated values.

Thermolysis of the precursor complexes

In order to study the thermochemistry of our precursors and to characterize the decomposition pathways, we performed thermogravimetric analysis (TGA) of **N1** and **C1**. In accordance with the previous findings for the hexabenzocoronene precursor **5**,[35] it was observed that the $[Co_2(CO)_6]$ units started to decompose below 200 °C. With a half point decay of **N1** at 204 °C and of **C1** at 191 °C, **N1** decomposes in one step, while **C1** decomposes in two steps (Fig. 4(a)) at a slightly lower temperature. The two-step decay is also indicated by two exothermic peaks in the corresponding differential scanning calorimetry (DSC) spectrum of **C1**. At 250 °C, the CO ligands of **N1** and **C1** were almost completely dissociated. Further heating led to a slow dissociation of the TMS groups of **C1** and **N1** between 300 °C and 900 °C. The total mass loss at 900 °C amounts to 55.5% in the case of **C1**, representing nearly exactly the calculated mass loss in the case of the dissociation of all CO ligands, all H atoms and all TMS groups for the remaining carbon and cobalt atoms (56.0%). To our surprise, the decomposition of related **N1** is rather incomplete under the same conditions (exp.: 50.1%, theory: 56.0% for the dissociation of CO ligands, H atoms and TMS groups). In the DSC spectrum, **N1** and **C1** show a small endothermic peak at ~800–850 °C.

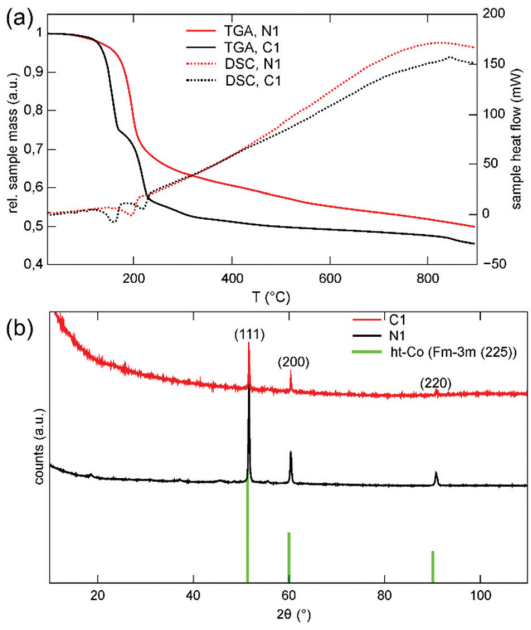

Fig. 4 (a) The TGA and DSC spectra of **C1** and **N1** (heating rate: 10 K min^{-1}). (b) PXRD of the thermolysis products of **C1** and **N1** and comparison to the literature reflexes of ht-Co (*Fm*-3*m* (225)).

The remaining black solid after thermolysis was investigated by X-ray powder diffraction (PXRD), showing three identical reflex peaks in the case of **C1** and **N1**. The observed reflexes are in agreement with the reported ones for a high temperature phase of cubic Co (phase prototype: Cu, cF4, (225), space group $Fm\bar{3}m$).[57] This proves the formation of elemental cobalt during pyrolysis (Fig. 4(b)).

Scanning electron microscopy of the products of SSP

With respect to the results of the TGA measurements, we pyrolyzed 5–20 mg of **C1**, **C2**, **N1** and **N2** controlled in vacuum-sealed (1×10^{-3} mbar) quartz glass ampoules in a muffle furnace. Thereby, we first heated the samples slowly (2 h) to 250 °C and held this temperature for 2 h to completely decompose the $[Co_2(CO)_6]$ units[35] and preform the active Co NP for CNP growth. Further slow heating to 850 °C within 10 h and maintaining 850 °C for 8 h was performed in order to carbonize the material *via* active cobalt carbide catalytic sites.[58] After slow cooling to room temperature, the obtained amorphous powders were investigated and analyzed *via* scanning electron microscopy. To enlarge the imaging contrast and for conducting reasons, the samples were previously sputtered with a 3 nm thick platinum layer.

The SSP of an amorphous sample of **C1** led to non-spherical NP with a dendritic growth mode starting from many nuclei, but no CNT formation was observed (Fig. 5(b)). The individual CNP exhibited typically diameters of less than 100 nm. This led to the conclusion that the aromatic backbone of **C1** is too small and the C to Co ratio is too small to provide enough carbon feed for successful CNT growth. Furthermore, the sample displayed the growth of cuboid microcrystalline particles rather than amorphous CNTs. The NPs were observed at the top (Fig. 5(a)).

According to the SEM images, no CNTs were formed upon pyrolysis of the two nitrogen containing complexes **N1** and **N2**. Instead, plate-like nanoparticles with sizes of 100–500 nm along with larger plates in the micrometer range were observed in the case of **N1**. In contrast to **C1**, the particles formed were less spherical and with more irregular shapes (Fig. 5(c)). In contrast, nanoparticles formed upon thermolysis of **N2** showed a cauliflower-like growth with a highly branched structure. The individual particles showed typically a smaller size (<100 nm) than that in the case of **N1** (Fig. 5(d)). The nanoparticles exhibited additionally a large surface due to their dendritic branched growth, which might make such N-doped CNPs suitable as anode materials for lithium ion batteries: porous structures and nitrogen doping in CNPs are known to lead to active sites for lithium insertion and to enhance their electrochemical performance.[59,60] According to the elemental combustion analysis of the pyrolysis products, the N content is 0.94% in the case of **N1** and 0.75% in the case of **N2**. Furthermore, larger graphitic plates with a thickness of up to 1 μm and interlayered with smaller nanoparticles could be

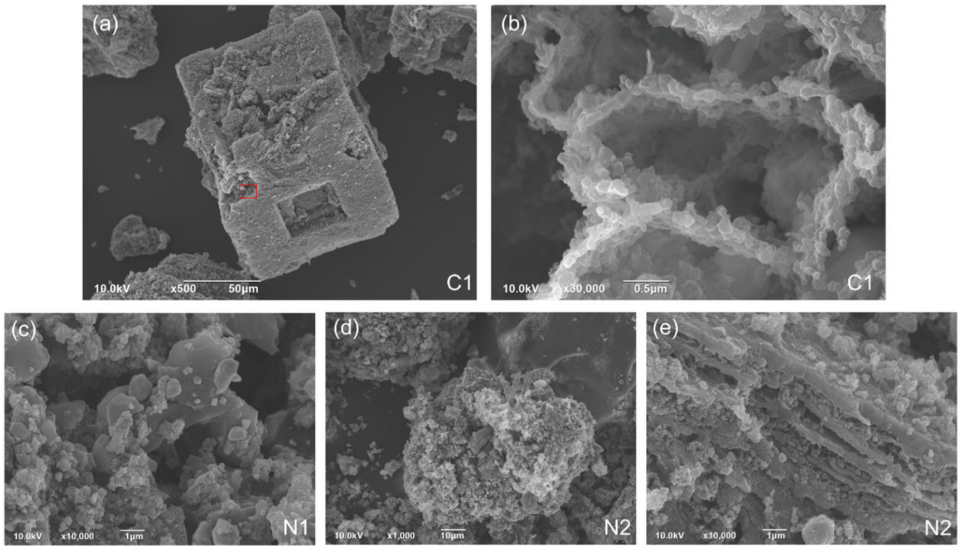

Fig. 5 (a) Overview SEM image of the pyrolysis product of **C1** shows microcrystalline particles; (b) the zoomed SEM image of a pyrolyzed amorphous sample of **C1** showing nanoparticles growing on the crystal surface; (c) the plate-like nanoparticles after the pyrolysis of **N1**; (d) the cauliflower-like nanoparticles as the pyrolysis product of **N2**; and (e) the intercalating nanoparticles between the graphitic sheets after the SSP of **N2**.

observed, indicating the higher carbon amount in the case of **N2** than in **N1** (Fig. 5(e)). Apparently, despite the higher carbon content in **N2**, nitrogen in the backbone of the precursor seems not to initiate or even inhibit the CNT growth. At this point, it only can be speculated whether this effect is due to the still intact pyridine rings at low temperatures and their coordinative inactivation of cobalt sites. A similar assumption was made by Müllen *et al.* in the case of the thermolysis of a dithienylethyne-dicobalthexacarbonyl, leading to the growth of micrometer-size particles. They assumed a coordinative inhibition of the Co catalyst due to the sulfur atoms.[34] In contrast to the pyrolysis of **C1**, **N1** and **N2**, the pyrolysis of carbon-rich and nitrogen-free **C2** produced CNTs (Fig. 6). According to the SEM measurements, the CNTs form bundles of highly aggregated tubes probably due to the strong non-covalent van der Waals interactions between the individual CNTs. With diameters estimated between 50 and 150 nm, they can be classified as multi-walled CNTs, which is in accordance with the previously synthesized CNTs from similar precursors by this methodology.[34,35]

Furthermore, also fibrous objects with larger diameters (around 500 nm to 1 µm) could be detected in the sample (see ESI, Fig. S6†). Due to the observed high aggregation grade and the tendency to form bundles, it can be estimated that CNTs grow initially from larger particles as the nucleus. The high aggregation tendency made it difficult to obtain the TEM images of the formed nanotubes (see ESI, Fig. S7† for the low-resolution TEM images of the CNT bundles), since the aggregates could not be separated by dispersion and high dilution in common organic solvents or the disaggregation agent *m*-cresol[61] and sonication. In the SEM images, the typical

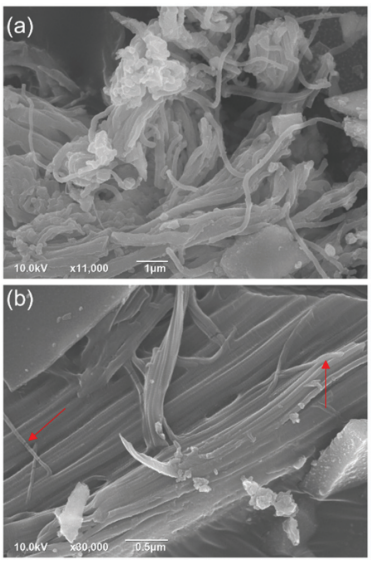

Fig. 6 (a) SEM image of a CNT bundle obtained by the SSP of **C2**. (b) Densely agglomerated and aligned CNTs from **C2** featuring the bamboo shape.

bamboo shape of the CNTs was observed, which was also reported for the pyrolysis of the hexabenzocoronene cobalt complex **5** upon pyrolysis.[35] Partly, the CNTs were aligned in a compressed layered fashion (see Fig. 6(b)), which made it difficult to distinguish the individual nanotubes; two individ-

ual nanotubes are marked with red arrows. The lengths of the CNTs ranged up to a micrometer scale in some cases, but also shorter CNTs were observed along with smaller nanoparticles. In this case, the ordered packing of the individual tubes is prevented, leading to agglomerations (Fig. 6(a) and ESI, Fig. S5†). It can be stated that the enhanced C to Co ratio in the case of **C2** is suitable for CNT growth. Nevertheless, the CNT yield is limited by the carbon amount that is lower as in the case of complex **5**.[34,35] The observed individual CNTs of **C2** showed a good quality with only a few defects and relatively uniform diameters and appearances.

Conclusions

Based on our recently published set of tetraalkynyl rylene and diaza-rylene templates L,[46,47,50] a set of four air- and moisture-stable tetraalkynyl rylene clusters of the type $[LCo_8(CO)_{24}]$, namely **C1** and **C2** and diaza-rylene clusters **N1** and **N2**, was synthesized. They were fully characterized in solution by NMR, UV–Vis and IR spectroscopy as well as in solid state *via* X-ray crystallography. Their thermogravimetric behavior was studied, showing a decomposition starting around 200 °C. Solid-state pyrolysis towards different carbon nanoparticles was performed at 850 °C under inert conditions. Thereby, the nature of the CNPs formed during the pyrolysis of the four planar precursor complexes of a similar molecular shape was found to be strongly dependent on (1) the complex size, namely the C to Co ratio and (2) the N-heteroatom dopant. It was found that nitrogen atoms in the case of **N1** and **N2** inhibited the CNT formation, instead leading to dendritic nanoparticles. This may be taken as an indicator that formal isoelectronic replacement of [C] by $[N^+]$ seems to be incompatible with a CNT structural architecture – the latter issue is also connected to the question of charge balance. Furthermore, peropyrene-based **C2** formed mainly multi-walled agglomerated bamboo-shaped CNTs, whereas smaller, carbon-deficient pyrene-based **C1** only formed smaller NPs. The study revealed that nanomaterials designed for distinct applications strongly rely on an appropriate architecture of the precursor complexes for solid-state pyrolysis.

Experimental section

Methods and devices

All preparative operations were conducted using standard Schlenk techniques and the solvents were dried according to the common procedures[62] and passed through columns of aluminium oxide, 3 Å molecular sieves and the R3-11G-catalyst (BASF) or stored over molecular sieves (3 Å or 4 Å).

The data collection for the single-crystal structure determination was performed on a Bruker D8 Quest diffractometer using the X-ray service of the Fachbereich Chemie, Universität Marburg. The information concerning the hardware and software used for data collection, cell refinement and data reduction as well as structure refinement are shown in the ESI tables and CCDC 2087192† (**N1**) and CCDC 2087191† (**N2**). After the solving (SHELXT)[63] and refinement processes (SHELXL 2017/1),[64] the data were validated by using PLATON.[65] All graphic representations were created using Diamond 4.[66]

The elemental analyses (C, H and N) were carried out by the service department for routine analysis using a Vario Micro Cube (Elementar) under standard conditions for easily combustible organic compounds.

The ^1H and proton decoupled ^{13}C NMR spectra were recorded in automation or by the service department of the Fachbereich Chemie using a Bruker Avance III 500 spectrometer. All spectra were recorded at ambient temperature. ^1H and ^{13}C NMR spectra were calibrated using residual proton signals of the solvent ($CDCl_3$: δ_H = 7.26 ppm, δ_C = 77.16 ppm). Multiplicity is abbreviated as follows: s (singlet), d (doublet), t (triplet), q (quartet), qt (quintet), m (multiplet) and br (broad). The FD mass spectra were recorded using an AccuTOF GCv 4G (JEOL) Time of Flight (TOF) mass spectrometer. An internal or external standard was used for the drift time correction. The LIFDI ion source and FD emitters were purchased from Linden ChroMasSpec GmbH (Bremen, Germany). The IR spectra were recorded in a glove box on a Bruker Alpha ATR-FT-IR spectrometer.

The absorption spectra were recorded using an Avantes AvaSpect 2048 UV/Vis/NIR spectrophotometer in 10 mm cuvettes in dichloromethane at concentrations of 10 μM with a scan rate of 600 nm min^{-1}.

The density functional theory (DFT) calculations were performed using the PBE[67–69] functional. The def2-TZVPP[70–72] basis set was used with the RIJDX auxiliary basis set,[73,74] employing the resolution-of-identity approximation.[75,76] Further D3-dispersion correction[77] was considered by applying Becke–Johnson damping.[78–81] The structural optimizations were performed using Orca 3.0.3.[82]

The scanning electron microscopy (SEM) measurements were performed using a JEOL JIB 4601F scanning electron microscope (operating at 10 kV) on solid samples, which were previously immobilized on an aluminium sheet with the help of double-sided Scotch tape and sputtered (Edwards Sputter Coater) with a 3 nm thick platinum layer in order to guarantee electronic conductivity.

Transmission electron microscopy (TEM) was performed using a TEM JEOL 2100 (operating at 200 kV) by drop-casting an ethanolic dispersion (~1 μg mL^{-1}) of the sample on a Cu TEM grid (manufactured by Plano).

The TGA and DSC measurements were performed on a Mettler Toledo TGA/DSC 3+ STAR device at a heating rate of 10 K min^{-1} between 25 and 900 °C under an inert atmosphere. The PXRD measurements were performed using a Philips/PANalytical X'Pert Pro PW3040/60 device, with a Co-Kα X-ray source.

General procedure for the complexation reaction

In a Schlenk flask, 1.0 equiv. of the corresponding tetraalkyne and 5.0 equiv. of $[Co_2(CO)_8]$ were evacuated and flushed with

argon. Anhydrous dichloromethane was added and the black reaction solution at high concentrations was stirred for 2 h, until gas evolution ceased. Thirty minutes after the detection of the complete conversion of the alkyne by TLC (*n*-hexane/dichloromethane 3 : 1), the reaction mixture was filtered over a plug of silica and the product was purified *via* column chromatography on silica (*n*-hexane/dichloromethane 3 : 1).

Synthesis of C1. Alkyne **15** (80 mg, 0.12 mmol, 1.0 equiv.) and $[Co_2(CO)_8]$ (239 mg, 0.70 mmol, 5.0 equiv.) were reacted as described in 10 mL DCM. Yield: 240 mg (0.14 mmol, ~quant.), black solid. ^{1}H NMR (500.1 MHz, $CDCl_3$): δ_H = 0.50 (s, 36H, Si(CH_3)$_3$), 8.53 (s, 4H, *H*2), 8.62 (s, 2H, *H*1) ppm. ^{13}C NMR (125.8 MHz, $CDCl_3$): δ_C = 2.0, 85.3, 103.5, 125.1, 125.6, 127.6, 134.9, 136.5, 200.0 ppm. FD-MS(+): *m*/*z* = 1729.58. Elemental analysis found (calcd) (%) for $C_{60}H_{42}Co_8O_{24}Si_4$: C 40.2 (41.6), H 2.5 (2.5), N 0.2 (0). IR (ATR), $\tilde{\nu}$ = 2957 (w), 2084 (m), 2045 (vs), 2015 (vs), 1852 (s), 1567 (w), 1471 (w), 1249 (w), 837 (m), 756 (w), 511 (m) cm^{-1}. UV–Vis: λ_{abs} = 301, 343, 372, 488, 604 nm (DCM).

Synthesis of C2. Alkyne **14** (5.0 mg, 7 μmol, 1.0 equiv.) and $[Co_2(CO)_8]$ (12.0 mg, 35 μmol, 5.0 equiv.) were reacted as described in 0.5 mL DCM. Yield: 6.5 mg (35 μmol, ~quant.), purple solid. ^{1}H NMR (500.1 MHz, $CDCl_3$): δ_H = 0.65 (s, 36H, Si(CH_3)$_3$), 8.74 (s, 2H, *H*1), 8.82 (d, 4H, ^3J = 9.3 Hz, *H*2), 9.34 (d, 4H, ^3J = 9.6 Hz, *H*3) ppm. ^{13}C NMR (125.8 MHz, $CDCl_3$): δ_C = 2.1, 85.4, 103.6, 122.6, 123.9, 125.7, 126.3, 126.7, 127.4, 134.2, 136.1, 200.1 ppm. Elemental analysis found (calcd) (%) for $C_{70}H_{46}Co_8O_{24}Si_4$: C 43.7 (45.3), H 2.3 (2.5), N 0.2 (0). IR (ATR), $\tilde{\nu}$ = 2957 (w), 2925 (w), 2085 (s), 2050 (vs), 2017 (vs), 1572 (w), 1416 (w), 1251 (w), 839 (m), 797 (w), 515 (w) cm^{-1}. UV–Vis: λ_{abs} = 292, 356, 545, 628 nm (DCM).

Synthesis of N1. Alkyne **12** (20 mg, 0.03 mmol, 1.0 equiv.) and $[Co_2(CO)_8]$ (51 mg, 0.15 mmol, 5.0 equiv.) were reacted as described in 3 mL DCM. Yield: 50 mg (0.03 mmol, ~quant.), dark brown solid. X-ray suitable single crystals were grown by slow diffusion of a layered *n*-pentane solution into a saturated solution of **N1** in DCM at −20 °C. ^{1}H NMR (500.1 MHz, $CDCl_3$): δ_H = 0.50 (s, 36H, Si(CH_3)$_3$), 8.46 (s, 4H, *H*1) ppm. ^{13}C NMR (125.8 MHz, $CDCl_3$): δ_C = 2.0, 83.5, 101.7, 122.9, 125.5, 128.0, 153.5, 200.1 ppm. FD-MS(+): *m*/*z* = 1732.50. Elemental analysis found (calcd) (%) for $C_{58}H_{40}Co_8N_2O_{24}Si_4$: C 39.0 (40.2), H 2.5 (2.3), N 1.6 (1.6). IR (ATR), $\tilde{\nu}$ = 2956 (w), 2087 (s), 2053 (s), 2012 (vs), 1563 (m), 1484 (w), 1376 (w), 1246 (w), 834 (m), 755 (w), 616 (w), 513 (m), 494 (m) cm^{-1}. UV–Vis: λ_{abs} = 303, 451, 505, 588 nm (DCM).

Synthesis of N2. Alkyne **13** (115 mg, 0.16 mmol, 1.0 equiv.) and $[Co_2(CO)_8]$ (276 mg, 0.81 mmol, 5.0 equiv.) were reacted as described in 15 mL DCM. Yield: 290 mg (0.16 mmol, ~quant.), dark blue solid. X-ray suitable single crystals were grown by slow diffusion of a layered *n*-pentane solution into a saturated solution of **N2** in DCM at −20 °C. ^{1}H NMR (500.1 MHz, $CDCl_3$): δ_H = 0.64 (s, 36H, Si(CH_3)$_3$), 8.83 (d, 4H, ^3J = 9.3 Hz, *H*1), 9.27 (d, 4H, ^3J = 9.5 Hz, *H*2) ppm. ^{13}C NMR (125.8 MHz, $CDCl_3$): δ_C = 2.1, 83.6, 102.4, 122.4, 122.9, 123.7, 126.3, 127.3, 128.7, 152.6, 200.3 ppm. FD-MS(+): *m*/*z* = 1854.80. Elemental analysis found (calcd) (%) for $C_{68}H_{44}Co_8N_2O_{24}Si_4$: C 42.5 (44.0), H 2.6 (2.4), N 1.2 (1.5). IR (ATR), $\tilde{\nu}$ = 2956 (w), 2087 (s), 2050 (s), 2012 (vs), 1570 (w), 1249 (w), 1158 (w), 836 (m), 798 (w), 512 (m), 494 (m) cm^{-1}. UV–Vis: λ_{abs} = 289, 343, 557, 640 nm (DCM).

Solid state pyrolysis procedure

Typically, 5–20 mg of the amorphous samples **C1**, **N1**, **C2** and **N2** were placed in a quartz glass ampoule and sealed under fine vacuum conditions (1 × 10^{-3} mbar). The ampoules were heated slowly in a muffle furnace for 2 h to 250 °C, and this temperature was maintained for a further 2 h. Subsequently, the temperature was increased to 850 °C within 10 h and maintained at 850 °C for 8 h. The samples in the oven were slowly cooled down to room temperature (approx. 2 K min^{-1}). After cooling down to room temperature, the resulting black powders were analyzed by SEM as obtained.

Author contributions

S. W.: synthesis, characterization, DFT calculations, writing and original draft preparation. T. V.: solving and refinement of XRD structures. J. S.: conceptualization, supervision, writing, reviewing and editing.

Conflicts of interest

There are no conflicts to declare.

Acknowledgements

The authors thank the technician Michael Hellwig (Material Science Center Marburg, WZMW) for his assistance in SEM and TEM imaging.

Notes and references

1 S. Iijima, *Nature*, 1991, **354**, 56–58.
2 *Handbook of Nanomaterials Properties*, ed. B. Bhushan, D. Luo, S. R. Schricker, W. Sigmund and S. Zauscher, Springer Berlin Heidelberg, 2014.
3 Y. Gogotsi and V. Presser, *Carbon nanomaterials*, CRC Press/Taylor & Francis Group, Boca Raton, 2014.
4 A. C. Power, B. Gorey, S. Chandra and J. Chapman, *Nanotechnol. Rev.*, 2018, **7**, 19–41.
5 R. Rao, C. L. Pint, A. E. Islam, R. S. Weatherup, S. Hofmann, E. R. Meshot, F. Wu, C. Zhou, N. Dee, P. B. Amama, J. Carpena-Nuñez, W. Shi, D. L. Plata, E. S. Penev, B. I. Yakobson, P. B. Balbuena, C. Bichara, D. N. Futaba, S. Noda, H. Shin, K. S. Kim, B. Simard, F. Mirri, M. Pasquali, F. Fornasiero, E. I. Kauppinen, M. Arnold, B. A. Cola, P. Nikolaev, S. Arepalli, H.-M. Cheng, D. N. Zakharov, E. A. Stach, J. Zhang, F. Wei, M. Terrones, D. B. Geohegan, B. Maruyama, S. Maruyama, Y. Li,

W. W. Adams and A. J. Hart, *ACS Nano*, 2018, **12**, 11756–11784.
6 K. Zhou, *Carbon Nanomaterials*, CRC Press/Taylor & Francis Group, Boca Raton, 2019.
7 M.-F. Yu, O. Lourie, M. J. Dyer, K. Moloni, T. F. Kelly and R. S. Ruoff, *Science*, 2000, **287**, 637–640.
8 C. T. White and T. N. Todorov, *Nature*, 1998, **393**, 240–242.
9 J. M. Schnorr and T. M. Swager, *Chem. Mater.*, 2011, **23**, 646–657.
10 A. C. Dillon, K. M. Jones, T. A. Bekkedahl, C. H. Kiang, D. S. Bethune and M. J. Heben, *Nature*, 1997, **386**, 377–379.
11 I. Hwang, W. Wang, S. K. Hwang, S. H. Cho, K. L. Kim, B. Jeong, J. Huh and C. Park, *Nanoscale*, 2016, **8**, 10273–10281.
12 S. Kumar, R. Rani, N. Dilbaghi, K. Tankeshwar and K.-H. Kim, *Chem. Soc. Rev.*, 2017, **46**, 158–196.
13 M. Meyyappan, *Small*, 2016, **12**, 2118–2129.
14 S. Zhang, T. Shao, H. S. Kose and T. Karanfil, *Environ. Sci. Technol.*, 2010, **44**, 6377–6383.
15 F. Wang, D. Kozawa, Y. Miyauchi, K. Hiraoka, S. Mouri, Y. Ohno and K. Matsuda, *Nat. Commun.*, 2015, **6**, 6305.
16 L. Wen, F. Li and H.-M. Cheng, *Adv. Mater.*, 2016, **28**, 4306–4337.
17 G. Lin, X. Liang, Z. Liu, J. Xie, B. Chen and H. Zhang, *Sci. China: Chem.*, 2015, **58**, 47–59.
18 H. W. Kroto, J. R. Heath, S. C. O'Brien, R. F. Curl and R. E. Smalley, *Nature*, 1985, **318**, 162–163.
19 H. W. Kroto, *Nature*, 1992, **359**, 670–671.
20 A. Thess, R. Lee, P. Nikolaev, H. Dai, P. Petit, J. Robert, C. Xu, Y. H. Lee, S. G. Kim, A. G. Rinzler, D. T. Colbert, G. E. Scuseria, D. Tomanek, J. E. Fischer and R. E. Smalley, *Science*, 1996, **273**, 483–487.
21 D. S. Bethune, C. H. Kiang, M. S. de Vries, G. Gorman, R. Savoy, J. Vazquez and R. Beyers, *Nature*, 1993, **363**, 605–607.
22 A. M. Cassell, J. A. Raymakers, J. Kong and H. Dai, *J. Phys. Chem. B*, 1999, **103**, 6484–6492.
23 *Carbon Nanotubes. Synthesis, Structure, Properties, and Applications*, ed. M. S. Dresselhaus, G. Dresselhaus and P. Avouris, Springer, Berlin, Heidelberg, 2001, vol. 80.
24 R. G. Lacerda, A. S. Teh, M. H. Yang, K. B. K. Teo, N. L. Rupesinghe, S. H. Dalal, K. K. K. Koziol, D. Roy, G. A. J. Amaratunga, W. I. Milne, M. Chhowalla, D. G. Hasko, F. Wyczisk and P. Legagneux, *Appl. Phys. Lett.*, 2004, **84**, 269–271.
25 M. F. L. De Volder, S. H. Tawfick, R. H. Baughman and A. J. Hart, *Science*, 2013, **339**, 535–539.
26 J. Huang, Q. Zhang, M. Zhao and F. Wei, *Chin. Sci. Bull.*, 2012, **57**, 157–166.
27 H. Hou, A. K. Schaper, F. Weller and A. Greiner, *Chem. Mater.*, 2002, **14**, 3990–3994.
28 C. N. R. Rao and R. Sen, *Chem. Commun.*, 1998, 1525–1526.
29 O. A. Nerushev, M. Sveningsson, L. K. L. Falk and F. Rohmund, *J. Mater. Chem.*, 2001, **11**, 1122–1132.
30 V. S. Iyer, K. P. C. Vollhardt and R. Wilhelm, *Angew. Chem.*, 2003, **115**, 4515–4519, (*Angew. Chem. Int. Ed.*, 2003, **42**, 4379–4383).
31 P. I. Dosa, C. Erben, V. S. Iyer, K. P. C. Vollhardt and I. M. Wasser, *J. Am. Chem. Soc.*, 1999, **121**, 10430–10431.
32 M. Laskoski, W. Steffen, J. G. M. Morton, M. D. Smith and U. H. F. Bunz, *J. Am. Chem. Soc.*, 2002, **124**, 13814–13818.
33 B. El Hamaoui, L. Zhi, J. Wu, U. Kolb and K. Müllen, *Adv. Mater.*, 2005, **17**, 2957–2960.
34 B. El Hamaoui, L. Zhi, J. Wu, J. Li, N. T. Lucas, Ž. Tomović, U. Kolb and K. Müllen, *Adv. Funct. Mater.*, 2007, **17**, 1179–1187.
35 J. Wu, B. El Hamaoui, J. Li, L. Zhi, U. Kolb and K. Müllen, *Small*, 2005, **1**, 210–212.
36 S. Scholz, P. J. Leech, B. C. Englert, W. Sommer, M. Weck and U. H. F. Bunz, *Adv. Mater.*, 2005, **17**, 1052–1055.
37 L. Zhi and K. Müllen, *J. Mater. Chem.*, 2008, **18**, 1472.
38 H. Dai, *Surf. Sci.*, 2002, **500**, 218–241.
39 S. Subramoney, *Adv. Mater.*, 1998, **10**, 1157–1171.
40 L. Zhi, T. Gorelik, R. Friedlein, J. Wu, U. Kolb, W. R. Salaneck and K. Müllen, *Small*, 2005, **1**, 798–801.
41 P. Ayala, R. Arenal, M. Rümmeli, A. Rubio and T. Pichler, *Carbon*, 2010, **48**, 575–586.
42 C. Chen, J. Zhang, B. Zhang, C. Yu, F. Peng and D. Su, *Chem. Commun.*, 2013, **49**, 8151–8153.
43 B. Frank, M. Morassutto, R. Schomäcker, R. Schlögl and D. S. Su, *ChemCatChem*, 2010, **2**, 644–648.
44 J. Zhang, X. Liu, R. Blume, A. Zhang, R. Schlögl and D. S. Su, *Science*, 2008, **322**, 73–77.
45 K. Gong, F. Du, Z. Xia, M. Durstock and L. Dai, *Science*, 2009, **323**, 760–764.
46 S. Werner, T. Vollgraff, Q. Fan, K. Bania, J. M. Gottfried and J. Sundermeyer, *Org. Chem. Front.*, 2021, **8**, 5013–5023.
47 E. Baal, M. Klein, K. Harms and J. Sundermeyer, *Chem. – Eur. J.*, 2021, **27**, 12610–12618.
48 J. Sundermeyer, E. Baal and S. Werner, WO*2019*/229134A1, 2019.
49 S. Werner, T. Vollgraff and J. Sundermeyer, *Angew. Chem.*, 2021, **133**, 13743–13748, (*Angew. Chem. Int. Ed.*, 2021, **60**, 13631–13635).
50 S. Werner, T. Vollgraff and J. Sundermeyer, *Chem. – Eur. J.*, 2021, **27**, 11065–11075.
51 A. Hayer, V. de Halleux, A. Köhler, A. El-Garoughy, E. W. Meijer, J. Barberá, J. Tant, J. Levin, M. Lehmann, J. Gierschner, J. Cornil and Y. H. Geerts, *J. Phys. Chem. B*, 2006, **110**, 7653–7659.
52 T. M. Figueira-Duarte and K. Müllen, *Chem. Rev.*, 2011, **111**, 7260–7314.
53 P. Chen and T. J. Meyer, *Chem. Rev.*, 1998, **98**, 1439–1478.
54 D. C. Harris and M. D. Bertolucci, *Symmetry and spectroscopy. An introduction to vibrational and electronic spectroscopy*, Dover, New York, 2014.
55 H.-H. Perkampus, *UV–VIS Spectroscopy and Its Applications*, Springer Berlin Heidelberg, 1992.
56 C. Elschenbroich, *Organometallchemie*, Vieweg + Teubner Verlag/GWV Fachverlage GmbH Wiesbaden, Wiesbaden, 6th edn, 2008.

57 A. W. Hull, *Trans. Am. Inst. Electr. Eng.*, 1919, **38**, 1445–1466.
58 Y. Wang, L. Qiu, L. Zhang, D.-M. Tang, R. Ma, Y. Wang, B. Zhang, F. Ding, C. Liu and H.-M. Cheng, *ACS Nano*, 2020, **14**, 16823–16831.
59 T. Chen, L. Pan, T. A. J. Loh, D. H. C. Chua, Y. Yao, Q. Chen, D. Li, W. Qin and Z. Sun, *Dalton Trans.*, 2014, **43**, 14931–14935.
60 S. Majeed, J. Zhao, L. Zhang, S. Anjum, Z. Liu and G. Xu, *Nanotechnol. Rev.*, 2013, **2**, 615–635.
61 K. Chiou, S. Byun, J. Kim and J. Huang, *Proc. Natl. Acad. Sci. U. S. A.*, 2018, **115**, 5703–5708.
62 W. L. F. Armarego and D. D. Perrin, *Purification of laboratory chemicals*, Butterworth-Heinemann, Oxford, 4th edn, 2002.
63 G. M. Sheldrick, *Acta Crystallogr., Sect. C: Struct. Chem.*, 2015, **71**, 3–8.
64 C. B. Hübschle, G. M. Sheldrick and B. Dittrich, *J. Appl. Crystallogr.*, 2011, **44**, 1281–1284.
65 A. L. Spek, *Acta Crystallogr., Sect. D: Biol. Crystallogr.*, 2009, **65**, 148–155.
66 H. P. K. Brandenburg, *Diamond*, Crystal Impact GbR, Bonn, 2012.
67 A. D. Becke, *J. Chem. Phys.*, 1993, **98**, 5648–5652.
68 C. Lee, W. Yang and R. G. Parr, *Phys. Rev. B: Condens. Matter Mater. Phys.*, 1988, **37**, 785–789.
69 P. J. Stephens, F. J. Devlin, C. S. Ashvar, C. F. Chabalowski and M. J. Frisch, *Faraday Discuss.*, 1994, **99**, 103.
70 A. Schäfer, C. Huber and R. Ahlrichs, *J. Chem. Phys.*, 1994, **100**, 5829–5835.
71 F. Weigend, *Phys. Chem. Chem. Phys.*, 2006, **8**, 1057–1065.
72 F. Weigend and R. Ahlrichs, *Phys. Chem. Chem. Phys.*, 2005, **7**, 3297–3305.
73 F. Weigend, M. Häser, H. Patzelt and R. Ahlrichs, *Chem. Phys. Lett.*, 1998, **294**, 143–152.
74 K. Eichkorn, O. Treutler, H. Öhm, M. Häser and R. Ahlrichs, *Chem. Phys. Lett.*, 1995, **240**, 283–290.
75 M. von Arnim and R. Ahlrichs, *J. Comput. Chem.*, 1998, **19**, 1746–1757.
76 F. Weigend, *Phys. Chem. Chem. Phys.*, 2002, **4**, 4285–4291.
77 S. Grimme, J. Antony, S. Ehrlich and H. Krieg, *J. Chem. Phys.*, 2010, **132**, 154104.
78 A. D. Becke and E. R. Johnson, *J. Chem. Phys.*, 2005, **123**, 154101.
79 E. R. Johnson and A. D. Becke, *J. Chem. Phys.*, 2005, **123**, 24101.
80 E. R. Johnson and A. D. Becke, *J. Chem. Phys.*, 2006, **124**, 174104.
81 S. Grimme, S. Ehrlich and L. Goerigk, *J. Comput. Chem.*, 2011, **32**, 1456–1465.
82 F. Neese, *Wiley Interdiscip. Rev.: Comput. Mol. Sci.*, 2011, **2**, 73–78.

3.5 Publication 5: Synthesis of Unsymmetrically Functionalized Violanthrenes by Reductive Aromatization of Violanthrone

Citation: S. Werner, J. Sundermeyer, *Synlett*, **2021**, *32*, 1855–1860.[E]

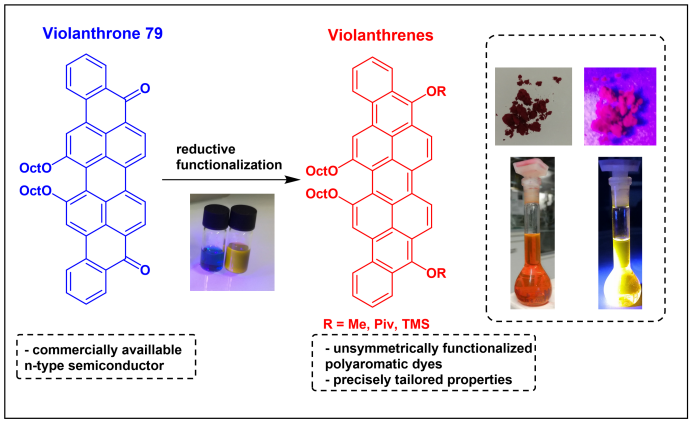

Summary: This communication presents an application for three different reductive functionalization approaches on the commercially available vat dye violanthrone 79. The two keto groups of violanthrone 79 could be successfully converted into siloxy- and pivaloxy groups with zinc as reducing agent in dioxane. Under biphasic reductive conditions ($Na_2S_2O_4$/KOH in water/toluene), two methoxy substituents could be attached. All three reactions proceeded with high yields (>75%) and yielded three highly soluble violanthrene dyes with yet unknown functionalization pattern. UV-Vis and PL measurements revealed a bathocromical shift of approx. 40 nm in comparison to comparable peropyrenes, characterizing the violanthrene system as more electron-rich system than the peropyrene scaffold with fine-tuning of optical spectra made possible via derivatization. This is verified by lower first oxidation potentials measured by cyclovoltammetry and supported by DFT calculated HOMO and LUMO energies. Each violanthrene derivative shows three oxidation waves and one or two reduction waves, demonstrating the high redox activity. Due to the excellent solubility even in *n*-hexane, these compounds could serve as solution processable organic fluorescence dyes.

Own Contribution: All experimental work was done by myself as well as characterization by spectroscopical (UV-Vis/PL) and electrochemical (CV/DPV) measurements and (TD-)DFT calculations. NMR and mass spectra were recorded by service departments of the faculty. Prof. Dr. J. Sundermeyer initiated and supervised this study and was available as valuable discussion partner. The manuscript was written by myself with valuable feedback of Prof. Dr. J. Sundermeyer.

[E]Reproduced with permission of S. Werner, J. Sundermeyer, *Synlett* **2021**, *32*, 1855–1860, Rights Managed by Thieme Stuttgard, New York.

Synlett S. Werner, J. Sundermeyer Letter

Synthesis of Unsymmetrically Functionalized Violanthrenes by Reductive Aromatization of Violanthrone 79

Simon Werner[a]
Jörg Sundermeyer*[b]

[a] Chemistry Department, Philipps-University of Marburg, Hans-Meerwein Straße 4, 35043 Marburg, Germany
werners4@staff.uni-marburg.de
[b] Chemistry Department and Materials Science Centre (WZMW), Philipps-University of Marburg, Hans-Meerwein Straße 4, 35043 Marburg, Germany
JSU@staff.uni-marburg.de

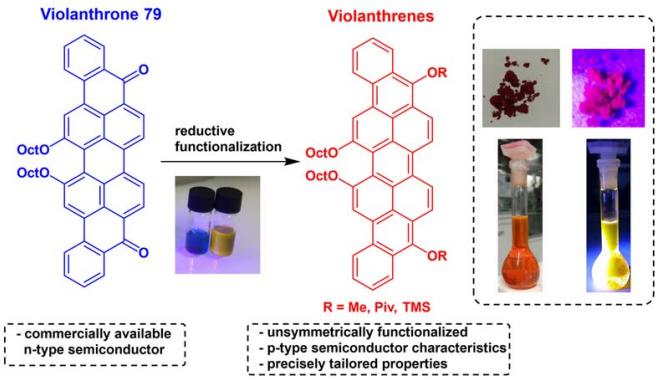

Received: 23.07.2021
Accepted after revision: 01.09.2021
Published online: 01.09.2021
DOI: 10.1055/a-1628-5664; Art ID: st-2021-b0264-l

Abstract The commercially available n-type semiconductive dye Violanthrone 79 was used as starting material to synthesize previously unexplored substituted violanthrenes through a reductive aromatization and functionalization strategy. By using the low-cost reducing agents zinc and sodium dithionite in combination with suitable electrophilic trapping reagents, three violanthrenes functionalized with two pivalyloxy, trimethylsiloxy, or methoxy groups were selectively obtained in high yields. Due to their octyl ether moieties, these new red dyes are highly soluble. They were characterized by means of UV/vis and fluorescence spectroscopy, and their redox properties were studied by cyclic voltammetry. The spectroscopically determined frontier molecular orbital energies are compared to those calculated by density functional theory and suggest that electron-deficient Violanthrone 79 was transformed into three electron-rich violanthrenes with molecular characteristics typically observed in molecular precursors for p-type organic semiconductors.

Key words arenes, violanthrenes, electron transfer, polycycles, reduction, dyes

Polycyclic aromatic hydrocarbons (PAHs), molecules consisting of fused aromatic carbon rings, have received much attention during recent years due to their broad variety of possible applications, for example, in organic light-emitting diodes, organic solar cells, and organic field-effect transistors.[1] For these technological applications, PAHs with high charge-transport mobilities via electrons or holes under an applied electrical field are crucial. Both a large delocalized π-system and the ability to undergo strong π–π stacking interactions between the molecules are desired.[2,3] In particular, perylene diimides (PDI) are well-studied electron-transporting (n-type) semiconductors with excellent electron mobilities (resulting from large π–π overlaps in the crystalline state) and tunable electronical properties.[4] The violanthrone system is also a candidate for n-type semiconductor applications, being red-shifted in contrast to the PDI system due to its larger π-system.[2] Early studies on violanthrone focused on its function as a model system for carbon black, and its conductivity was proven.[5] More recently, the commercially available soluble vat dye Violanthrone 79 (**VO79**) has been used as an electron acceptor in combination with poly(3-hexylthiophene) (P3HT) in a photoelectrochemical cell.[6] Chen and co-workers studied the π–π-aggregation behavior of various soluble violanthrone dyes in solution through concentration-dependent NMR spectroscopy and they found that dimer formation is responsible for the large hole mobilities.[2] Two-dimensional IR spectroscopy was also used to study the aggregation properties of the dyes.[7] Other groups studied violanthrones and their aggregation behavior as model systems for asphaltenes (polyaromatic compounds with aliphatic side chains).[8] Scheme 1 shows the synthesis of **VO79** starting from violanthrone by selective oxidation with manganese dioxide and etherification.[2]

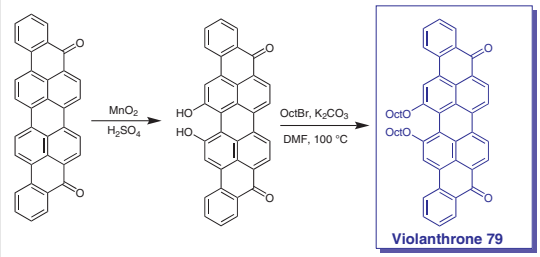

Scheme 1 Synthesis route to **VO79** through oxidation and etherification

Early attempts to reduce both carbonyl groups of violanthrone with zinc in a sodium chloride and zinc chloride molten salt flux at high temperatures led to violanthrene A, a poorly characterized insoluble PAH with nine fused benzene rings.[9] Patents describe a reduction of the carbonyl groups of violanthrone by using sodium dithionite in aqueous basic media to synthesize the corresponding leuco forms as ethers and esters.[10,11] The claims include two examples of the formation of an A_2B_2 functional-group pattern through reduction of bismethoxyviolanthrone and O-functionalization to form sulfates[10] or phosphates.[12] Recent work by Amsharov and co-workers focused on synthesis strategies toward violanthrene and other unfunctionalized PAHs through reductive acid-mediated intramolecular dehydrative π-extensive cyclizations of suitable arylaldehyde precursors.[13] This reaction furnishes unsubstituted violanthrene and isoviolanthrene through subsequent oxidative electrocyclization of diradicaloid intermediates.[14] To the best of our knowledge, there are no comparable studies on the commercially available vat dye **VO79** as a starting point for reductive functionalizations towards A_2B_2-type functionalized violanthrenes. The high solubility arising from the *O*-octyl chains promises reaction products with a low tendency to crystallize, designed for solution-based fabrication of films for their physical characterization. We therefore used **VO79** as a starting point for reductive aromatizations using cheap and bench-stable reducing agents such as zinc and sodium dithionite, aiming for selective high-yielding transformations performed at up to a 1 mmol scale (Scheme 2).

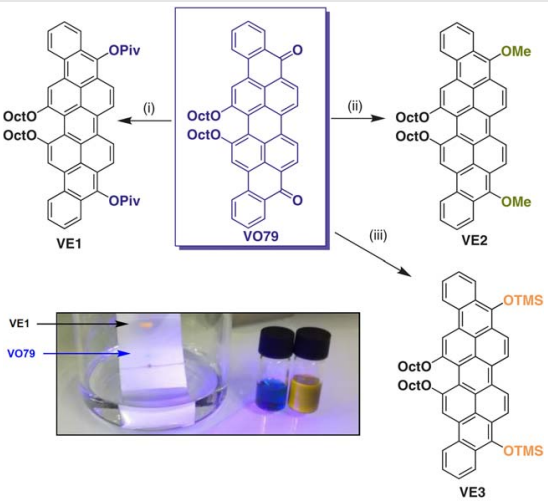

Scheme 2 Synthesis of violanthrenes **VE1**, **VE2**, and **VE3**. *Reagents and conditions*: (i) Zn (16 equiv), Piv_2O (16 equiv), 1,4-dioxane, reflux, 18 h, 85%; (ii) $Na_2S_2O_4$ (6 equiv), MeI (10 equiv), Aliquat 336, aq KOH/toluene, 90 °C, 3 h, 75%; (iii) Zn (16 equiv), TMSCl (16 equiv), 1,4-dioxane, 80 °C, 18 h, 80%.

Under conditions similar to those for the reductive silylation of anthracene-9,10-dione,[15] **VO79** was treated with an excess of zinc in the presence of trimethylsilyl chloride in 1,4-dioxane to yield the corresponding violanthrene **VE3**.[16] By applying conditions similar to those for the reductive pivaloylation of naphthalene diimide[17] or perylene diimide,[18] **VO79** could also be reductively pivaloylated with an excess of zinc in 1,4-dioxane to form **VE1**.[19] Reductive methylation of **VO79** to the corresponding methyl ether **VE2**[20] was accomplished by using sodium dithionite as a reducing agent and methyl iodide as a methylating agent under phase-transfer conditions in a basic water/toluene mixture. All transformations yielded violanthrenes **VE1–3** in good yields (>75%) and with excellent purity and selectivity. The reaction progress could be easily monitored by TLC of an evolving orange fluorescing spot (see inset in Scheme 1). Our attempts to transform **VO79** into the corresponding violanthrene bistriflate as a platform chemical for postfunctionalizations (e.g., C–C cross couplings) were unsuccessful. Following a recently established protocol[21] involving reducing a quinoid PAH with two equivalents KC_8 in DME and trapping of the reduced potassium aryloxide with (trifluoromethyl)sulfonic anhydride at –50 °C led to a product of intrinsic instability that decomposed under an argon atmosphere at –40 °C. In contrast, **VE1** and **VE2** were air and moisture stable, and could readily be purified by column chromatography, whereas the *O*-silylated leuco derivative **VE3** turned out to be sensitive to hydrolysis and reoxidation by air. Therefore, **VE3** was purified under an inert gas by extraction into hexane, filtration, and precipitation at –18 °C. In fact, all the PAHs **VE1–3** showed excellent solubilities in hydrocarbons at room temperature and low tendencies to crystallize, which are advantageous properties for thin-film applications and processing, for example by spin coating of dye layers.

To obtain insight into the effect of substituents on the electronic structures, the UV/vis and photoluminescence spectra of **VE1–3** were measured in dichloromethane ($c \approx 10^{-5}$ M and 10^{-7} M, respectively) and are shown in Figure 1.

Compared with the parent **VO79** ($\lambda_{max,abs}$ = 648 nm),[2] the absorption maxima of the corresponding violanthrenes were hypsochromically shifted by about 100 nm, with maxima ranging from 525 nm (**VE1**) to 540 nm (**VE3**), despite the larger aromatic system. This demonstrates that both the carbonyl groups in **VO79** exhibit a strong acceptor character. This push–pull effect is weakened upon reduction. The nature of the introduced functional groups on the violanthrene scaffold influences the electron density at the core, and the HOMO–LUMO gap explains the bathochromic shift (15 nm) due the electron-donating OTMS groups of **VE3** in comparison with the electron-withdrawing effect of the OPiv groups of **VE1**. Time-dependent density-functional-theory (DFT)-calculated absorption spectra [see the Supporting Information (SI); Figure S7] support this trend. The three congeners **VE1–3** show high molar attenuation coeffi-

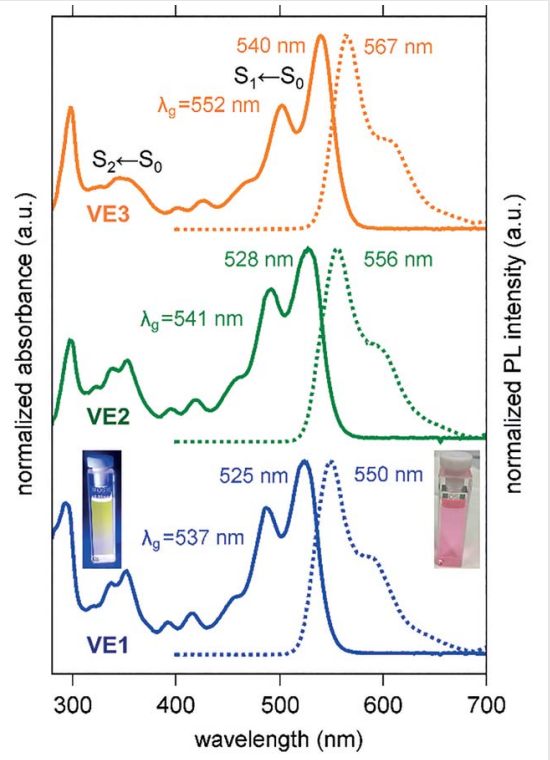

Figure 1 UV/vis absorption spectra (solid lines) and the corresponding emission spectra (dashed lines; excitation at 350 nm) of **VE1–3** recorded in dichloromethane

cients ($\varepsilon \approx 6.5 \times 10^{-4}$ L·mol^{-1}·cm^{-1}) with no significant concentration dependency of λ_{max} (see the SI, Figures S4 and S5 for the concentration-dependent UV/vis spectra). The emission spectra show the same trend, with moderate fluorescence quantum yields (Φ_{PL} = 27% for **VE1** and 22% for **VE2**; see SI, Figure S6). As typical for related peropyrene[22] or PDI systems,[23] these are also mirrored in the case of **VE1–3** with respect to the absorption spectra, and the Stokes shifts are also small in our case (25–30 nm, 0.11–0.12 eV). Both findings demonstrate that the molecular shapes in the excited and ground state are similar, and only a little energy is needed for reorganization of the geometry.[24] As typical for rigid systems,[24] **VE1–3** show vibronic progression fine structures in their absorption and emission spectra. Besides the $S_1 \leftarrow S_0$ absorption maxima, the UV/vis spectra also show weaker bands at 350–400 nm, indicating $S_2 \leftarrow S_0$ transitions into higher states.

To rationalize the electrochemical properties of **VE1–3**, their cyclic voltammograms (CVs) were measured. Redox half-wave potentials relative to an internal ferrocene/ferrocenium standard were determined by applying differential pulse voltammetry (see the SI for further information). Figure 2 shows the CV spectra of **VE1–3** and Table 1 summarizes the determined redox potentials.

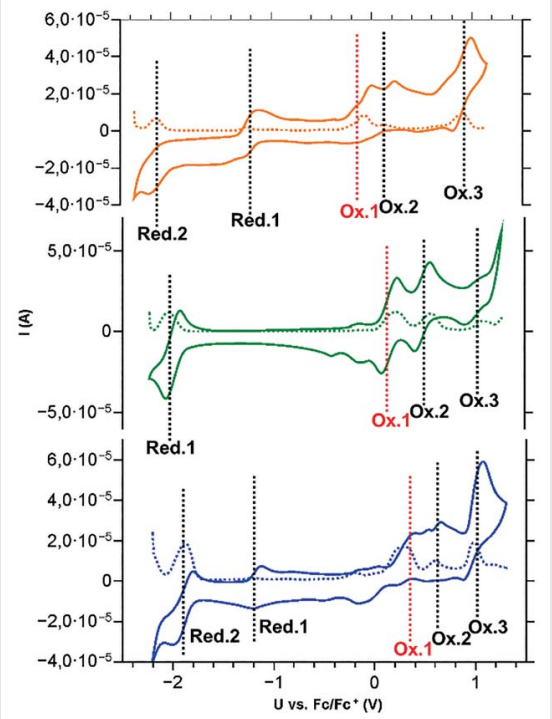

Figure 2 Cyclic voltammograms of **VE1–3** (measured in CH_2Cl_2, 0.1 M Bu_4NPF_6, 50 mV·s^{-1} scan rate, glassy carbon electrode) and the corresponding differential pulse voltammograms (DPVs, 10 mV·s^{-1} scan rate).

VE1 and **VE3** showed two reversible reduction potentials and three reversible oxidation potentials, whereas **VE2** showed only one reversible reduction wave. The first oxidation half-wave potentials [$E_{1/2}$(Ox1)] ranged from 0.28 V (**VE1**) to –0.07 V (**VE3**) vs. fc/fc$^+$ and the first reduction half-wave potentials ranged from –1.15 V (**VE1**) to –2.04 V (**VE2**), showing that **VE1–3** are generally electron-rich PAHs, more easily oxidized than reduced. With the help of the first oxidation half-wave potential, the experimental HOMO energies could be determined and the experimental LUMO energies were calculated with the help of the determined optical bandgap, estimated from the intersection wavelength between the normalized UV/vis and photoluminescence spectra (Figure 1).[25] These were compared with the frontier-orbital energies by DFT calculations DFT at the def2-TZVPP/B3LYP level of theory (Table 1; see also the SI for further information). Both, DFT and electrochemical measurements showed that the various substituents introduced into **VE1–3** enhanced both the absolute HOMO and LUMO energy levels of the frontier molecular orbitals with

Table 1 Calculated and Experimental (Opto)electronic Parameters of **VE1–3**

	UV/vis and PL spectra			Cyclic voltammetry				DFT calculations[a]		
	$\lambda_{max,abs.}$(nm) [ε (L·mol^{-1}·cm^{-1})]	$\lambda_{max,em.}$ (nm) [Φ_{PL}][b]	$E_{g,exp.}$(eV)[c] [nm]	$E_{1/2,Ox1.}$ (V)	$E_{1/2,Red1.}$ (V)	$E_{HOMO,exp}$[d] (eV)	$E_{LUMO,exp}$[e] (eV)		$E_{LUMO,DFT}$ (eV)	$E_{g,DFT.}$ (eV)
VE1	525 [6.70 × 10^{-4}]	550 [0.27]	2.31 [537]	0.28	−1.15	−5.08	−2.77	−4.83	−2.53	2.30
VE2	528 [6.45 × 10^{-4}]	556 [0.22]	2.29 [541]	0.23	−2.04	−5.03	−2.74	−4.64	−2.24	2.40
VE3	540 [6.76 × 10^{-4}]	567 [n.d.]	2.25 [552]	−0.07	−1.24	−4.73	−2.48	−4.49	−2.12	2.37

[a] At the def2-TZVPP/B3LYP level of theory.
[b] Determined by the dilution method[24] referenced to fluorescein (in 0.1 M aq NaOH),[24] (see the SI, Figure S6).
[c] Determined by reported methods using the intersection wavelength of the normalized absorption and emission spectra.[25]
[d] Determined by using reported methods with reference to Fc/Fc$^+$ as an internal standard [E_{HOMO} (fc) = −4.8 eV]; $E_{HOMO,exp}$ = −4.8 eV − $E_{1/2,ox1}$.[26]
[e] Determined with help of the optical bandgap: $E_{LUMO,exp} = E_{HOMO,exp} + E_{g,exp}$.

respect to electron-deficient **VO79**, which has calculated HOMO and LUMO levels lying about 1 eV lower (−5.22 and −3.16 eV, respectively) (see SI, Figure S8, for the Kohn–Sham frontier orbitals). The optical bandgap is a little bit narrower when the relatively electron-deficient **VE1** (DFT: 2.35 eV; experimental: 2.31 eV) is compared with the more electron-rich **VE3** (DFT: 2.35 eV; experimental: 2.25 eV). The theoretical values obtained by DFT calculations are in good agreement with the experimental ones. Surprisingly, both, experimental and theoretical results indicate that the HOMO and LUMO levels of the methoxy-substituted **VE2** lie between those of **VE1** and **VE3**. From the standpoint of better stabilization of negative charge at the position α to a silyl group through negative hyperconjugation (the α-effect) and the lower donor strength, basicity, and proton affinity of siloxy compared with alkoxy anions, one might have expected **VE2** to be the most-electron-rich PAH in this series. The HOMO and LUMO coefficients can be rationalized with the help of the DFT-calculated Kohn–Sham frontier molecular orbitals (Figure 3). The substituents participate only to a certain extent in both the HOMO and LUMO. Our interpretation is that conjugative effects with the aromatic π-system are much more effective in stabilizing and delocalizing negative charge at oxygen than are the competing negative hyperconjugative effects of the silyl substituents. The magnitude of the calculated HOMO and LUMO energies range from −4.83 eV (**VE1**) to −4.49 eV (**VE3**) for HOMO energies, and from −2.53 eV (**VE1**) to −2.12 eV (**VE3**) for LUMO energies (Table 1). This indicates lower-lying HOMO energies and better stabilization for **VE1** in comparison to **VE3** (and **VE2** in the midrange), whereas the LUMO energy for **VE1** is lower and, therefore, oxidation takes place more easily than in the case of **VE3** (and **VE2** in the midrange). This calculated trend is clearly supported by the absolute HOMO and LUMO energies determined experimentally from CV and optical measurements. The experimentally determined LUMO energies displayed in Table 1 range from −2.77 eV (**VE1**) through −2.77 eV (**VE2**) to −2.48 eV (**VE3**), and the experimental HOMO energies range from −5.08 eV (**VE1**) through −5.03 eV (**VE2**) to −4.73 eV (**VE3**).

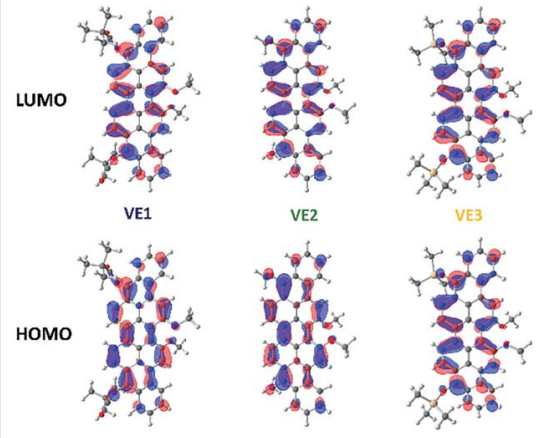

Figure 3 DFT-calculated Kohn–Sham frontier molecular orbitals of **VE1–3** (def2-TZVPP/B3LYP level of theory; octyl groups are simplified as methyl groups)

In conclusion, we transformed commercially available electron-deficient **VO79**, an n-type semiconducting dye, through a facile one-step high-yielding reductive functionalization, into the electron-rich dyes **VE1**, **VE2**, and **VE3**, whose molecular characteristics suggest that, after further studies on their collective physical properties, they might well lead to p-type semiconducting films. The optoelectronic and electrochemical properties of these violanthrenes are in accord with DFT-calculated frontier molecular orbital energies. The air-stable representatives **VE1** and **VE2** might find applications as solution-processable semiconducting dopants in thin-film coating technologies or as fluorescent dyes.

Conflict of Interest

The authors declare no conflict of interest.

Funding Information

Financial support by the LOEWE Program of Excellence of the Federal State of Hesse (LOEWE Focus Group PriOSS 'Principles of On-Surface Synthesis') is gratefully acknowledged.

Acknowledgment

We thank Lei Zhang and Prof. Dr. Olalla Vázquez for the kind introduction to the measurement of fluorescence quantum yields.

Supporting Information

Supporting information for this article is available online at https://doi.org/10.1055/a-1628-5664.

References and Notes

(1) (a) Ball, M.; Zhong, Y.; Wu, Y.; Schenck, C.; Ng, F.; Steigerwald, M.; Xiao, S.; Nuckolls, C. *Acc. Chem. Res.* **2015**, *48*, 267. (b) Rieger, R.; Müllen, K. *J. Phys. Org. Chem.* **2010**, *23*, 315. (c) Mei, J.; Diao, Y.; Appleton, A. L.; Fang, L.; Bao, Z. *J. Am. Chem. Soc.* **2013**, *135*, 6724. (d) Figueira-Duarte, T. M.; Müllen, K. *Chem. Rev.* **2011**, *111*, 7260.

(2) Shi, M.-M.; Chen, Y.; Nan, Y.-X.; Ling, J.; Zuo, L.-J.; Qiu, W.-M.; Wang, M.; Chen, H.-Z. *J. Phys. Chem. B* **2011**, *115*, 618.

(3) *Introduction to Organic Electronic and Optoelectronic Materials and Devices*; Sun, S.-S.; Dalton, L. R., Ed.; CRC Press: Boca Raton, **2008**.

(4) (a) Stepanenko, V.; Stocker, M.; Müller, P.; Büchner, M.; Würthner, F. *J. Mater. Chem.* **2009**, *19*, 6816. (b) Graser, F.; Hädicke, E. *Liebigs Ann. Chem.* **1980**, 1994. (c) Malenfant, P. R. L.; Dimitrakopoulos, C. D.; Gelorme, J. D.; Kosbar, L. L.; Graham, T. O.; Curioni, A.; Andreoni, W. *Appl. Phys. Lett.* **2002**, *80*, 2517.

(5) Akamatu, H.; Inokuchi, H. *J. Chem. Phys.* **1950**, *18*, 810.

(6) Chung, D. S.; Park, J. W.; Park, J.-H.; Moon, D.; Kim, G. H.; Lee, H.-S.; Lee, D. H.; Shim, H.-K.; Kwon, S.-K.; Park, C. E. *J. Mater. Chem.* **2010**, *20*, 524.

(7) Cyran, J. D.; Krummel, A. T. *J. Chem. Phys.* **2015**, *142*, 212435.

(8) (a) Orbulescu, J.; Mullins, O. C.; Leblanc, R. M. *Langmuir* **2010**, *26*, 15257. (b) Jian, C.; Tang, T.; Bhattacharjee, S. *Energy Fuels* **2014**, *28*, 3604.

(9) (a) Aoki, J. *Bull. Chem. Soc. Jpn.* **1961**, *34*, 1817. (b) Buu-Hoï, N. P.; Hoeffinger, J.-P.; Jacquignon, P. *Justus Liebigs Ann. Chem.* **1968**, *714*, 112.

(10) Stallmann, O.; Wentz, W. M. US 2148042, **1938**.

(11) Scottish Dyes Ltd. DE 601753, **1929**.

(12) Münster, W.; Müller, J. US 2249973, **1939**.

(13) (a) Feofanov, M.; Akhmetov, V.; Sharapa, D. I.; Amsharov, K. *Org. Lett.* **2020**, *22*, 1698. (b) Lungerich, D.; Papaianina, O.; Feofanov, M.; Liu, J.; Devarajulu, M.; Troyanov, S. I.; Maier, S.; Amsharov, K. *Nat. Commun.* **2018**, *9*, 4756.

(14) Feofanov, M.; Akhmetov, V.; Sharapa, D. I.; Amsharov, K. *Org. Lett.* **2020**, *22*, 5741.

(15) Castellan, A.; Daney, M.; Desvergne, J.-P.; Riffaud, M.-H.; Bouas-Laurent, H. *Tetrahedron Lett.* **1983**, *24*, 5215.

(16) **VE3**
Me_3SiCl (0.4 mL, 3.2 mmol, 16 equiv) was added to a mixture of **VO79** (142 mg, 0.20 mmol, 1.0 equiv) and Zn dust (209 mg, 3.20 mmol, 16 equiv) in 1,4-dioxane (10 mL), and the mixture was heated at 80 °C under argon for 18 h while the suspension turned red. When the reaction was complete (TLC), all volatilities were removed in vacuo and the residue was taken up in hexane (20 mL). The mixture was filtered and the product was precipitated at –80 °C then dried in a vacuum to give a red powder; yield: 137 mg (0.16 mmol, 80%). The reaction was also performed on a 1 mmol scale; yield: 660 mg (0.77 mmol, 77%).
IR (ATR): 3071 (w), 2925 (s), 2855 (m), 1578 (w), 1494 (w), 1462 (w), 1348 (s), 1314 (m), 1260 (w), 1033 (vs), 876 (vs), 756 (s), 628 (w) cm^{-1}. ^1H NMR (300.1 MHz, $CDCl_3$): δ = 0.44 [s, 18 H, $Si(CH_3)_3$], 0.82–0.85 (m, 6 H, H_{Oct}), 1.20–1.40 (m, 18 H, H_{Oct}), 1.50–1.55 (m, 4 H, H_{Oct}), 1.97 (quint, $^3J_{H,H}$ = 7.5 Hz, 4 H, H_{Oct}), 4.19–4.24 (m, 2 H, OCH_2), 4.53–4.58 (m, 2 H, OCH_2), 7.78–7.88 (m, 4 H, *H*3, *H*4), 8.37 (d, $^3J_{H,H}$ = 9.6 Hz, 2 H, *H*6), 8.41 (s, 2 H, *H*1), 8.56 (dd, $^3J_{H,H}$ = 9.4 Hz, $^4J_{H,H}$ = 2.6 Hz, 2 H, *H*2), 8.75 (d, $^3J_{H,H}$ = 9.7 Hz, 2 H, *H*7), 9.05 (dd, $^3J_{H,H}$ = 9.2, $^4J_{H,H}$ = 2.0 Hz, 2 H, *H*5). ^{13}C NMR (75.5 MHz, $CDCl_3$): δ = 1.2, 14.2, 22.8, 26.4, 29.5, 29.7, 29.9, 32.0, 69.0, 101.5, 117.8, 119.9, 120.0, 122.2, 123.0, 123.7, 123.8, 125.1, 125.4, 125.7, 125.8, 126.2, 126.6, 128.8, 144.8, 156.0. HRMS (LIFDI+): *m/z* [M⁺] calcd for $C_{56}H_{66}O_4Si_2$: 858.44996; found: 858.44898.

(17) Nakazato, T.; Kamatsuka, T.; Inoue, J.; Sakurai, T.; Seki, S.; Shinokubo, H.; Miyake, Y. *Chem. Commun.* **2018**, *54*, 5177.

(18) Nakamura, Y.; Nakazato, T.; Kamatsuka, T.; Shinokubo, H.; Miyake, Y. *Chem. Eur. J.* **2019**, *25*, 10571.

(19) **VE1**
Pivalic anhydride (0.4 mL, 3.5 mmol, 16 equiv) was added to a mixture of **VO79** (158 mg, 0.22 mmol, 1.0 equiv) and Zn dust (230 mg, 3.52mmol, 16 equiv) in 1,4-dioxane (15 mL), and the mixture was refluxed under argon for 18 h while the suspension turned brownish red. When the reaction was complete (TLC), the suspension was filtered, and all volatilities were removed in vacuo. The residue was taken up in CH_2Cl_2 (20 mL) and filtered over neutral alumina. The product was precipitated from hexane at –80 °C and dried in vacuo to give a red powder; yield: 163 mg (0.19 mmol, 85%).
IR (ATR): 2926 (m), 2858 (m), 1751 (s), 1582 (w), 1516 (w), 1430 (w), 1383 (w), 1215 (m), 1109 (vs), 1031 (w), 787 (w), 637 (w) cm^{-1}. ^1H NMR (300.1 MHz, $CDCl_3$): δ = 0.79–0.85 (m, 6 H, H_{Oct}), 1.20–1.43 (m, 18 H, H_{Oct}), 1.47–1.53 (m, 4 H, H_{Oct}), 1.74 [s, 18 H, $C(CH_3)_3$], 1.96 (quint, $^3J_{H,H}$ = 7.1 Hz, 4 H, H_{Oct}), 4.15–4.25 (m, 2 H, OCH_2), 4.50–4.62 (m, 2 H, OCH_2), 7.79–7.89 (m, 4 H, *H*3, *H*4), 7.99 (d, $^3J_{H,H}$ = 9.6 Hz, 2 H *H*6), 8.19 (dd, $^3J_{H,H}$ = 9.2, $^4J_{H,H}$ = 1.6 Hz, 2 H, *H*2), 8.42 (s, 2 H, *H*1), 8.71 (d, $^3J_{H,H}$ = 9.6 Hz, 2 H, *H*7), 9.07 (dd, $^3J_{H,H}$ = 8.6, $^4J_{H,H}$ = 1.1 Hz, 2 H, *H*5). ^{13}C NMR (75.5 MHz, $CDCl_3$): δ = 14.2, 22.8, 26.3, 26.7, 27.9, 29.5, 29.7, 29.8, 31.9, 40.0, 69.0, 101.7, 118.0, 118.9, 121.3, 121.5, 122.0, 123.9, 124.0, 125.6, 125.7, 125.7, 126.0, 126.9, 128.0, 128.5, 139.4, 156.8, 177.5. HRMS (APCI+): *m/z* [M + H]⁺ Calcd for $C_{60}H_{67}O_6$: 883.4932; found: 883.4953.

(20) **VE2**
VO79 (142 mg, 0.20 mmol, 1.0 equiv), KOH (400 mg; excess), and $Na_2S_2O_4$ (279 mg, 1.60 mmol, 8.0 equiv) were dissolved in toluene (10 mL) and H_2O (10 mL). Aliquat 336 (0.1 mL) was added, and the mixture was stirred for 1 h at 90 °C then cooled to r.t. MeI (0.12 mL, 2.0 mmol, 10 equiv) was added and the mixture was stirred for 30 min at 90 °C. When the reaction was complete (TLC), the organic phase was collected, dried ($MgSO_4$), filtered, and concentrated. The residue was taken up in CH_2Cl_2 (20 mL) and filtered over neutral alumina. The product was the precipitated at –80 °C from hexane and dried in vacuo to give a red powder; yield: 110 mg (0.15 mmol, 75%).
IR (ATR), 3069 (m), 2926 (vs), 2854 (s), 1581 (m), 1492 (m), 1426 (w), 1345 (m), 1211 (vs), 1068 (m), 973 (w), 790 (m), 632

(w) cm^{-1}. ^1H NMR (300.1 MHz, $CDCl_3$): δ = 0.75–0.90 (m, 6 H, H_{Oct}), 1.18–1.45 (m, 18 H, H_{Oct}), 1.45–1.55 (m, 4 H, *HOct*), 1.97 (quint, $^3J_{H,H}$ = 7.7 Hz, 4 H, *HOct*), 4.15–4.25 (m, 2 H, OC*H*2), 4.28 (s, 6 H, OC*H*3), 4.45–4.65 (m, 2 H, OC*H*2), 7.82–7.90 (m, 4 H, *H*3, *H*4), 8.43 (s, 2 H, *H*1), 8.48 (d, $^3J_{H,H}$ = 9.5 Hz, 2 H, *H*6), 8.62 (dd, $^3J_{H,H}$ = 9.5, $^4J_{H,H}$ = 4.2 Hz, 2 H, *H*2), 8.82 (d, $^3J_{H,H}$ = 9.7 Hz, 2 H, *H*7), 9.08 (dd, $^3J_{H,H}$ = 9.5, $^4J_{H,H}$ = 4.3 Hz, 2 H, *H*5). ^{13}C NMR (75.5 MHz, $CDCl_3$): δ = 14.2, 22.8, 26.4, 29.5, 29.7, 29.9, 31.7, 31.9, 63.7, 69.0, 101.6, 117.8, 119.5, 122.3, 123.0, 123.2, 124.0, 125.7, 125.9, 126.1, 126.4, 126.7, 128.9, 156.5. HRMS (LIFDI+): *m/z* [M⁺] Calcd for $C_{52}H_{54}O_4$: 742.40221; found: 742.40214.

(21) (a) Werner, S.; Vollgraff, T.; Sundermeyer, J. *Chem. Eur. J.* **2021**, *27*, 11065. (b) Werner, S.; Vollgraff, T.; Fan, Q.; Bania, K.; Gottfried, J. M.; Sundermeyer, J. *Org. Chem. Front.* **2021**, *8*, 5013. (c) Baal, E. *Klein M., Harms K., Sundermeyer J.* **2021**, *27*, 12610. (d) Sundermeyer, J.; Baal, E.; Werner, S. WO 2019229134, **2019**.

(22) Nichols, V. M.; Rodriguez, M. T.; Piland, G. B.; Tham, F.; Nesterov, V. N.; Youngblood, W. J.; Bardeen, C. J. *J. Phys. Chem. C* **2013**, *117*, 16802.

(23) Würthner, F.; Saha-Möller, C. R.; Fimmel, B.; Ogi, S.; Leowanawat, P.; Schmidt, D. *Chem. Rev.* **2016**, *116*, 962.

(24) Lakowicz, J. R. *Principles of Fluorescence Spectroscopy, 3rd ed*; Springer: Boston, **2006**.

(25) Klán, P.; Wirz, J. *Photochemistry of Organic Compounds: From Concepts to Practice*; Wiley: Chichester, **2009**.

(26) D'Andrade, B. W.; Datta, S.; Forrest, S. R.; Djurovich, P.; Polikarpov, E.; Thompson, M. E. *Org. Electron.* **2005**, *6*, 11.

3.6 Publication 6: On-Surface Synthesis and Characterization of a Cycloarene: C108 Graphene Ring

Citation: Q. Fan, D. Martin-Jimenez, S. Werner, D. Ebeling, T. Koehler, T. Vollgraff, J. Sundermeyer, W. Hieringer, A. Schirmeisen, J. M. Gottfried, *J. Am. Chem. Soc.* **2020**, *142*, 894-899.[F]

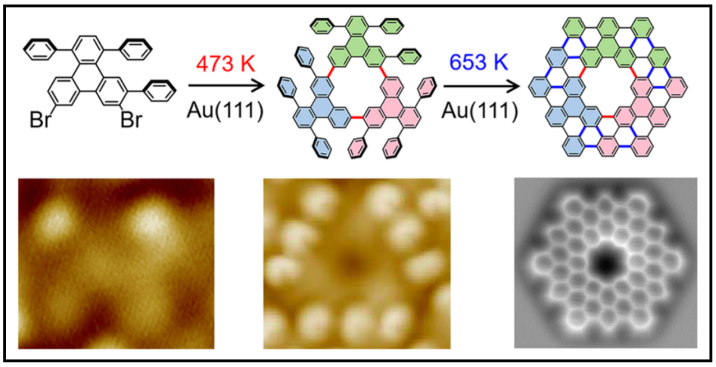

Summary: The topic of this article is the synthesis of a cyclic porous nanographene molecule containing 108 C atoms on Au(111) and the investigation of its electronical properties via scaning tunneling spectroscopy. The C108 nanographene was synthesized on Au(111) via hierarchical Ullmann trimerization at 200 °C followed by cyclodehydrogenation at 380 °C. A suitable bis-brominated precursor molecule was previously synthesized for this purose by a six-step synthesis protocol in solution starting with phenanthrene-dione followed by regioselective bromination and iodination, Knoevenagel reaction, Diels-Alder reaction, Suzuki-Miyaura coupling and TMS group deprotection (see supporting information). The final precursor DBTT was fully characterized via NMR, XRD and mass spectrometry and vacuum deposited on Au(111). The structure of C108 was investigated by STM and non-contact AFM at low temperatures. Although C108 was formed in high yields, unconventional side products such as phenyl ring extrusions via C-C ruptures or fusion of C108 molecules by intermolecular dehydrogenative couplings occuring at the cyclodehydrogenation step, could be investigated and characterized. The optical HOMO-LUMO gap was determined by scanning tunneling spectroscopy and supporting DFT calculation gave in-depth information about aromaticity and π-electron distribution within C108. The aromaticity of armchair-C108 can be described by Clar's electron-sextett rule.

Own Contribution: The precursor structure was designed by myself and Dr. Q. Fan in discussion with Prof. Dr. J. Sundermeyer. The retrosynthetical approach of the precursor DBTT, the chemical synthesis of precursor DBTT as well as in-solution characterization was performed by myself. T. Vollgraff solved and refined its crystal structure. Dr. Q. Fan performed STM measurements together with T. Koehler under supervision of Prof. Dr. J. M. Gottfried. Dr. D. Martin-Jimenez performed nc-AFM measurements under supervision of Dr. D. Ebeling and Prof. Dr. A. Schirmeisen. Dr. W. Hieringer performed DFT calculations. The manuscript was written by Dr. Q. Fan with input of all co-authors. The experimental part (synthesis of DBTT) was written by myself.

[F] Reproduced with permission of Q. Fan *et al.*, *J. Am. Chem. Soc.*, **2020**, *142*, 894-899. Copyright ©2020, Rights Managed by the American Chemical Society.

JACS
JOURNAL OF THE AMERICAN CHEMICAL SOCIETY
Article
Cite This: J. Am. Chem. Soc. 2020, 142, 894−899
pubs.acs.org/JACS

On-Surface Synthesis and Characterization of a Cycloarene: C108 Graphene Ring

Qitang Fan,[†,#] Daniel Martin-Jimenez,[‡,#] Simon Werner,[†,#] Daniel Ebeling,[*,‡] Tabea Koehler,[†] Tobias Vollgraff,[†] Jörg Sundermeyer,[*,†] Wolfgang Hieringer,[§] André Schirmeisen,[‡] and J. Michael Gottfried[*,†]

[†]Department of Chemistry and Material Sciences Center (WZMW), Philipps-Universität Marburg, Hans-Meerwein-Straße, 35032 Marburg, Germany

[‡]Institute of Applied Physics (IAP) and Center for Materials Research (LaMa), Justus-Liebig-Universität Gießen, Heinrich-Buff-Ring 16, 35392 Gießen, Germany

[§]Theoretical Chemistry and Computer-Chemistry-Center for Molecular Materials (ICMM), Department of Chemistry and Pharmacy, Friedrich-Alexander-Universität Erlangen-Nürnberg, Egerlandstraße 3, 91058 Erlangen, Germany

Supporting Information

ABSTRACT: The synthesis of cycloarenes in solution is challenging because of their low solubility and the often hindered cyclodehydrogenation reaction of their nonplanar precursors. Using an alternative on-surface synthesis protocol, we achieved an unprecedented double-stranded hexagonal cycloarene containing 108 sp^2 carbon atoms. Its synthesis is based on hierarchical Ullmann coupling and cyclodehydrogenation of a specially designed precursor on a Au(111) surface. The structure and other properties of the cycloarene are investigated by scanning tunneling microscopy/spectroscopy, atomic force microscopy, and density functional theory calculations.

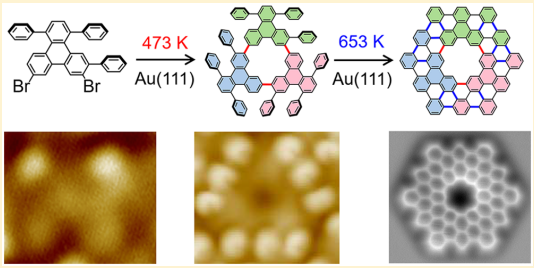

INTRODUCTION

Cycloarenes are polycyclic aromatic compounds with a central cavity surrounded by annulated benzene rings.[1] Only few cycloarenes have been synthesized in solution, including kekulene,[2] septulene,[3] cyclo[*d*,*e*,*d*,*e*,*e*,*d*,*e*,*d*,*e*,*e*]decakisbenzene,[4] and octulene[5] with a single strand of benzene rings. More recently, hexagonal **C216** cycloarene bearing three strands of benzene rings has been synthesized.[6] Solution-based cycloarene synthesis is challenging, because intramolecular cyclodehydrogenation reactions of the nonplanar precursor macrocycles, providing the planar cycloarenes, is often unsuccessful.[1] Additionally, their isolation and characterization remains difficult due to low solubility. Recently, a versatile alternative intramolecular cyclodehydrogenation reaction on metal surfaces has been widely used to planarize twisted organic molecules to form fully fused nanographenes.[7−16] The advantage of cyclodehydrogenation on metal surfaces is its reduced barrier and higher selectivity, compared to those of undesired intermolecular dehydrogenative coupling. In part, this is due to the release of torsion strain in the adsorbed nonplanar precursors.[12,13,17,18] This approach appears to be feasible for the synthesis of cycloarenes, which in an alternative view can be reckoned as nanorings cut out of graphene. Such carbon-based nanorings with delocalized π-electrons may serve as useful candidates for studying properties of quantum ring systems, e.g., the Aharonov−Bohm effect[19−21] and persistent ring currents (PRCs).[22−26] In particular, the much smaller sizes (diameter < 10 nm) of these graphene quantum rings, compared to those of the mesoscopic metal rings in previous work (diameters around 0.6−2 μm),[22,27] can lead to larger PRCs at a given low temperature or to PRCs persisting at higher temperatures.[27]

Here, we report the first successful on-surface synthesis of a cycloarene. Specifically, hexagonal cycloarene **C108** (**3**, Scheme 1), with two strands of annulated benzene rings containing 108 sp^2 carbons, was synthesized by Ullmann coupling and subsequent cyclodehydrogenation of 7,10-dibromo-1,4,11-triphenyl-triphenylene (DBTT **1**, Scheme 1) on a Au(111) surface. DBTT was designed to favor cyclotrimerization, resulting in nonplanar trimer macrocycle **2**, over polymerization into chain **4**. This selectivity is achieved by the weaker steric repulsion between the phenyl groups of two adjacent triphenyl-triphenylene building blocks in trimer macrocycle **2** compared to that in polymer chain **4**, as illustrated by the green and red ovals in Scheme 1. The identity of DBTT **1**, synthesized by a catalytic multistep metal−organic reaction protocol, was established as described in the

Received: September 25, 2019
Published: December 16, 2019

DOI: 10.1021/jacs.9b10151
J. Am. Chem. Soc. 2020, 142, 894−899

Journal of the American Chemical Society Article

Scheme 1. Reactions of 7,10-Dibromo-1,4,11-triphenyl-triphenylene (DBTT)[a]

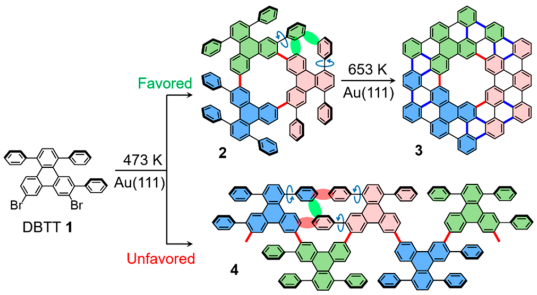

[a]1. Ullmann coupling of **1** leads to the formation of trimer macrocycle **2** (sterically favored) and polymer chain **3** (sterically unfavored). **C108** graphene ring **3** forms via **2** by cyclodehydrogenation. Green and red ovals mark the weak and strong steric repulsion between the phenyl groups, respectively.

Supporting Information. The structure and other properties of the **C108** ring were analyzed by scanning tunneling microscopy/spectroscopy (STM/STS), low-temperature atomic force microscopy (AFM) with CO-functionalized tips, and DFT calculations.

RESULTS AND DISCUSSION

In the first step, 0.8 monolayer (ML) of **1** was vapor-deposited onto the Au(111) surface held at 300 K. On the basis of previous work with other similarly sized precursors,[28] **1** is expected to adsorb on Au(111) as an intact molecule at 300 K. As shown by Figure 1a, **1** forms densely packed ordered domains, which consist of repeating motifs outlined by the red contours in Figure 1d. The distance between two bright dots in a single motif (Figure 1d) is measured to be 8.4 ± 0.3 Å, in agreement with the distance of 8.5770(4) Å between the centers of the two tilted phenyl groups (marked by orange spheres in Figure 1g) in the 3D crystalline state of DBTT (see the XRD analysis in the part d of the Supporting Information). Therefore, the STM features are attributed to intact DBTT **1**, as shown by the chemical structures in Figure 1g. Notably, prochiral **1** becomes chiral in the two-dimensional (2D)

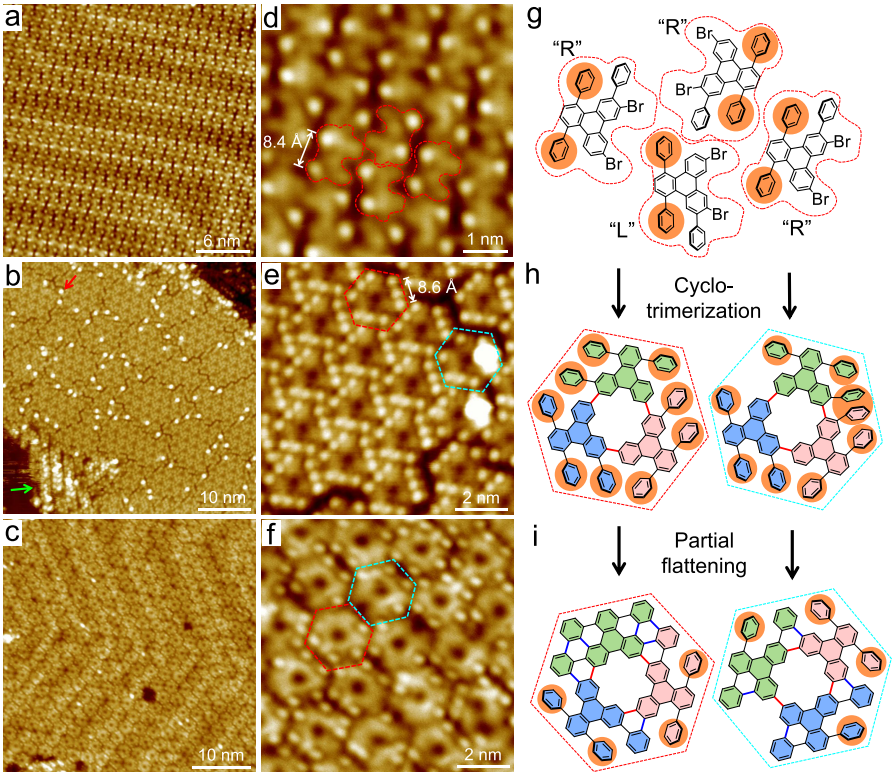

Figure 1. STM images of the structures formed from DBTT **1** at different temperatures. (a–c) Overview STM images taken after deposition of a submonolayer of **1** onto Au(111) held at (a) 300 K and (b) 473 K and (c) subsequent annealing to 593 K. (b) The green and red arrows mark the linear-chain side product and an ultrabright protrusion. (d–f) Zoom-in images of the species in panels (a–c), respectively. Tunneling parameters: (a) U = 1.7 V, I = 0.08 nA; (b) U = 2.4 V, I = 0.09 nA; (c),(f) U = −1.7 V, I = 0.16 nA; (d) U = 1.7 V, I = 0.11 nA; (e) U = 3.5 V, I = 0.13 nA. (g–i) Corresponding chemical structures of the species that are marked with contour lines in panels (d–f). The orange spheres mark the tilted phenyl groups. The three triphenyl-triphenylene units are colored differently for clarity. C–C bonds formed by Ullmann and cyclodehydrogenative coupling are red and blue, respectively.

DOI: 10.1021/jacs.9b10151
J. Am. Chem. Soc. 2020, 142, 894–899

confinement, forming two 2D enantiomers labeled by "L" and "R" in Figure 1g.

To trigger the C−C bond formation via Ullmann coupling, 0.8 ML of **1** was vapor-deposited onto the Au(111) surface held at 473 K. In addition to the cyclization-favoring precursor design (Scheme 1), we employed on-surface high dilution conditions[29,30] to maximize the yield of macrocycles. Therefore, a low deposition rate of 0.08 ML per minute (ML/min), was used during the coupling reaction. Figure 1b shows that an ordered structure with a densely packed hexagonal 2D lattice is formed by this procedure. Between the ordered domains, ultrabright protrusions (marked by red arrow) are occasionally observed at the domain boundaries. The magnified STM image (Figure 1e) of a typical domain shows two types of species with hexagonal shape, as outlined by the red and cyan dashed-line hexagons. The majority species (red hexagon) is assigned to the trimer macrocycle formed by C−C coupling of three molecules of DBTT **1** having the same 2D handedness (here "L"), as shown by the chemical structure in Figure 1h (left part). This is supported by the nine bright dots of the hexagon species, which are attributed to the nine tilted phenyl groups at the periphery (Figure 1h, left). Moreover, the distance between the two dots located at two adjacent corners is measured to be 8.6 ± 0.3 Å, in line with the expected distance (8.8 ± 0.4 Å) between two phenyl groups at two adjacent corners of the trimer macrocycle in Figure 1h (left). The ultrabright protrusions at the domain boundaries are related to the minority species; one example is marked by the cyan hexagonal contour. This minority species forms through C−C coupling of molecules of DBTT **1** with different 2D handedness. In the example illustrated by the chemical structure in Figure 1h (right), this trimer macrocycle contains two "L" handed and one "R" handed triphenyl-triphenylene moieties. This combination results in four phenyl groups located at one edge of the hexagon and only two phenyl groups at another edge. The missing phenyl ring can clearly be seen in Figure 1e (cyan hexagon). At the edge overloaded with four phenyl groups, steric hindrance leads to substantial out-of-plane deformation and thus to the ultrabright protrusion (Figure 1h, right). These "wrong" connections lead to the formation of defective trimer macrocycles, which represent only a minority species, because the steric repulsion between the colliding phenyl groups makes this product energetically and kinetically unfavorable.

Subsequent annealing of the sample in Figure 1b to 593 K leads to the formation of hexagonal macrocycles with reduced numbers (ranging from 3 to 6) of bright dots at their edges (Figure 1c), compared to trimer macrocycle **2** with nine bright dots (Figure 1b). This indicates that some of the tilted phenyl groups undergo cyclodehydrogenation reactions, resulting in a flat geometry. For instance, the hexagonal macrocycle outlined by the red dashed-line hexagon in Figure 1f (left) has four bright dots, i.e., four tilted phenyl groups. The other five formerly tilted phenyl groups have been flattened by cyclodehydrogenation as shown by the chemical structure in Figure 1i (left part). Noteworthy, the partially dehydrogenated defective macrocycles (containing a phenyl vacancy at one side) with four bright dots have also been observed, as enclosed by the cyan dashed-line hexagon in Figure 1f. The corresponding chemical structure is shown in Figure 1i (right). Unexpectedly, the partially flattened defective macrocycle (Figure 1f, cyan hexagon) does not show the ultrabright protrusion originating from the crowding of four phenyl groups at the same edge (as in Figure 1e, cyan hexagon). This finding indicates the loss of one of the four phenyl groups at the overloaded edge by C−C bond dissociation, in agreement with previous work.[31]

Further annealing of the sample in Figure 1c to 653 K leads to a higher degree of the surface-catalyzed cyclodehydrogenation of trimer macrocycles **2**, as shown by the overview and magnified STM images in Figure 2a,b, respectively. Hexagonal macrocycles again represent the major products. Rarely, short linear chains occur, as indicated by the green arrow in Figure 2a. As can be seen from Figure 2b, completely flat hexagonal rings (yellow arrow) and defective hexagonal rings (red arrow) are formed. STM images with submolecular resolution (Figure 2c) and AFM images (Figure 2e) of the intact hexagonal

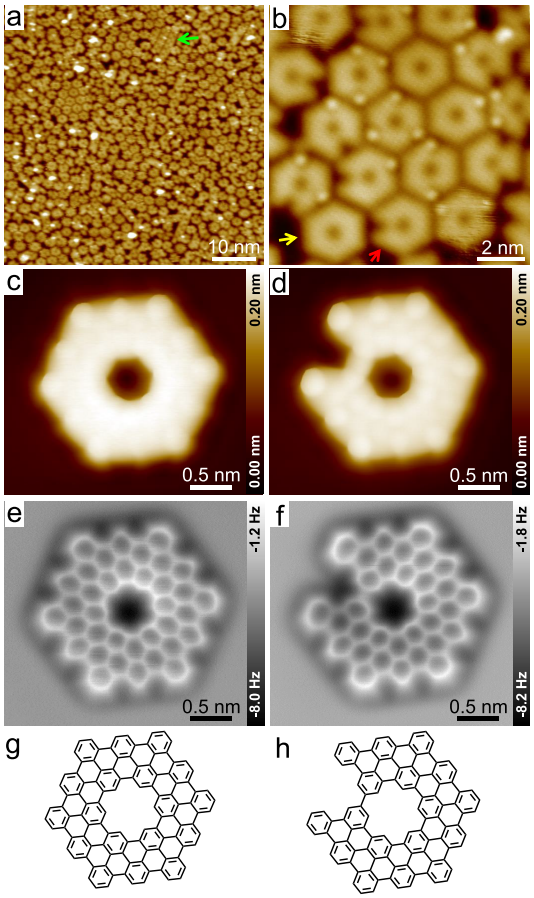

Figure 2. STM and AFM images of **C108** cycloarene **3** and defective **C102** graphene ring. (a) Overview and (b) zoom-in STM image taken after annealing the sample in Figure 1c to 653 K. (a) The green arrow marks the linear-chain side product. (b) The yellow and red arrows mark the completely flattened **C108** and **C102** macrocycles, respectively. (c−h) Submolecularly resolved (c, d) STM, (e, f) AFM images (measured with CO-functionalized tip) and (g, h) derived chemical structures of the **C108** and **C102** graphene ring, respectively. Tunneling parameters: (a, b) U = 2.2 V, I = 20 pA; (c) U = 10 mV, I = 80 pA; (d) U = 10 mV, I = 90 pA. Tip heights for AFM images: (e) z = −55 pm and (f) z = −50 pm from a STM set point of I = 10 pA with U = 100 mV on Au(111).

DOI: 10.1021/jacs.9b10151
J. Am. Chem. Soc. 2020, 142, 894−899

macrocycle reveal its **C108** cycloarene structure, **3**, consisting of 108 sp^2 carbon atoms as shown by the chemical structure in Figure 2g. Similarly, Figure 2d,f reveal that the defective hexagonal macrocycle is a **C102** graphene ring (Figure 2h), which can be reckoned as **C108** cycloarene with one missing benzene ring. **C102** graphene ring is therefore the final product of the reaction starting with the wrong connection of the monomers, followed by the detachment of a phenyl ring during planarization, as described above. Notably, not all of the hexagonal macrocycles are completely flattened by cyclodehydrogenation at 653 K. Some of them still contain between one and three tilted phenyl groups. Further increase of the annealing temperature to 693 K is sufficient to flatten all of the phenyl groups by completing the intramolecular cyclodehydrogenation reaction. However, the high temperature also increases the probability of intermolecular dehydrogenative coupling, which partly results in the formation of C−C bond linked graphene rings as shown by Figure 3.

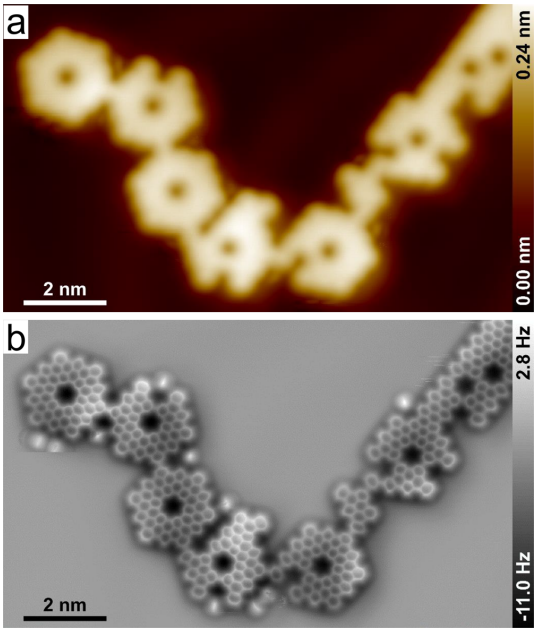

Figure 3. (a) STM topography and (b) constant-height frequency shift AFM images of chains of connected graphene rings obtained by annealing a submonolayer of DBTT molecules to 693 K. Tunneling parameters: (a) U = 50 V, I = 10 pA. Tip height for the AFM image: (b) z = 125 pm with respect to a STM set point of I = 30 pA and U = 7 mV above the Au(111) surface. In both images, the oscillation amplitude of the tuning fork sensor was set to 52.5 pm.

The electronic structure of adsorbed **C108** cycloarene **3** has been studied using STS. The six colored curves in Figure 4a show the voltage-dependent differential conductance spectra (dI/dV versus V) recorded at six different positions of the graphene ring (Figure 4a, inset, marked by the correspondingly colored dots). The gray curve is the reference dI/dV spectrum measured on the bare Au(111) surface. The bold red and blue spectra show the most prominent peaks located at −1.15 and +1.82 V, respectively. These two peaks are attributed to the positive and negative ion resonances (PIR and NIR) related to

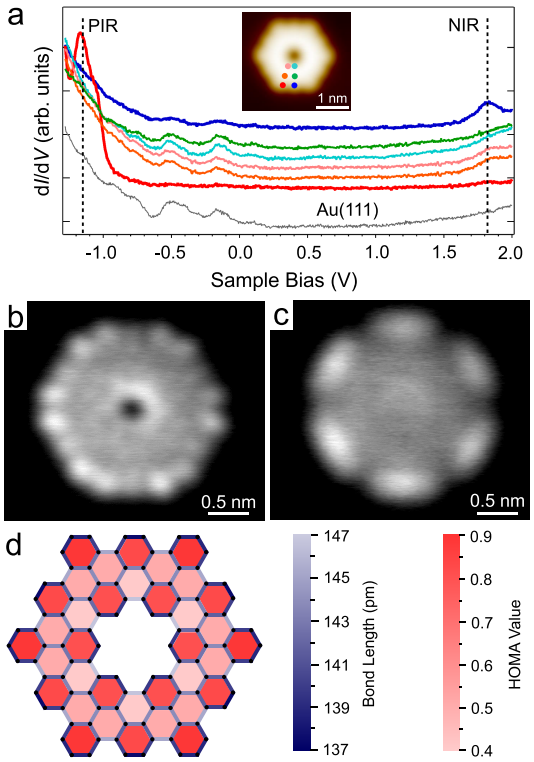

Figure 4. Electronic properties of the adsorbed **C108** cycloarene **3**. (a) dI/dV spectra acquired on **3** at the positions marked by differently colored dots in the inset. (b, c) Constant-height differential conductance (dI/dV) maps taken at bias voltages of (b) −1.15 V and (c) 1.82 V, corresponding to the PIR and NIR related to HOMO and LUMO. Tunneling parameters: inset in (a) U = 100 mV, I = 10 pA; (b) U = −1.15 V and (c) U = 1.82 V. (d) DFT-calculated C−C bonds lengths and harmonic oscillator model of aromaticity (HOMA) values of the **C108** cycloarene, represented by gradient colors as indicated.

the highest occupied and the lowest unoccupied molecular orbitals (HOMO and LUMO) of adsorbed **C108** cycloarene **3**. The constant-height dI/dV maps of **3** have been measured at the energies of the PIR and NIR peaks as shown by Figure 4b,c. These maps allow to visualize the spatial distribution of the electron density states related to HOMO and LUMO, which correlate to some extent with the DFT-calculated HOMO and LUMO shown in Figures S2 and S3.

C108 cycloarene **3** is an interesting case for aromaticity considerations, similar to the case of kekulene in recent work.[32] Accordingly, we have calculated the C−C bond lengths and derived the HOMA values (Figure 4d) for each benzene moiety.[33] A higher HOMA value is generally associated with higher degree of π-electron delocalization and increased aromatic stabilization. Benzene as the reference molecule has a HOMA value of 1.0.[33] Due to its D_{6h} symmetry, **C108** contains only five different types of benzene rings. Three of them show high HOMA values of 0.882, 0.825, and 0.807 and thus experience substantial aromatic stabilization. The other two benzene rings have HOMA values of only 0.509 and 0.400,

DOI: 10.1021/jacs.9b10151
J. Am. Chem. Soc. 2020, 142, 894−899

indicating less aromatic stabilization. These findings are in line with Clar's sextet formula of this molecule (Figure S1a). Additional aromatic stabilization may arise from conjugation along the [54]annulene path (Figure S1b, blue path) of the outer periphery (0.741), whereas the inner periphery (enclosing the central hole) with its [18]annulene path (Figure S1b, red path) has a lower HOMA value of only 0.498.

CONCLUSION

In conclusion, we have reported the successful synthesis of hexagonal **C108** cycloarene on a Au(111) surface by an eight-step sequence starting from phenanthren-9,10-dione: The first six steps toward novel precursor DBTT **1** involve catalytic C−C coupling reactions in solution; the final two steps toward title compound **C108** involve catalytic Ullmann and cyclodehydrogenative on-surface C−C coupling reactions. To optimize the macrocycle formation, the on-surface high-dilution principle is applied, and the DBTT precursor is specially designed to sterically favor cyclotrimerization over open-chain polymerization. The structure and electronic properties of the **C108** cycloarene have been characterized by STM, AFM, and DFT. HOMA values derived from DFT-calculated bond lengths suggest that the aromatic system is well-described by Clar's sextet formula.

METHODS

Synthesis. The synthetic details and characterization of DBTT are described in the Supporting Information (part d).

STM/AFM/STS. STM, AFM, and STS data were acquired with a commercial low-temperature STM/AFM (Scienta Omicron, Germany) at 5.2 K or a variable-temperature SPECS STM Arhus 150 STM and a base pressure below 1×10^{-10} mbar. An external lock-in amplifier and phase-locked loop electronics (MFLI, Zürich Instruments, Switzerland) was used to excite the Qplus tuning fork sensor.[34] The AFM tip was sharpened by indentations into the Au(111) surface and by voltage pulses. For the STM and AFM data, the tip was functionalized with a single CO molecule.[35] The Qplus sensor was operated in frequency modulation mode at constant amplitude (52.5 and 70 pm). The resonance frequency was about 26.970 kHz and the quality factor was in a range between 17000 and 33000. AFM images were measured on constant-height mode. The MFLI lock-in amplifier was also employed to acquire the STS data. dI/dV signal was extracted by adding a sinusoidal bias signal (alternatinc current bias: amplitude = 20 mV, frequency = 700 Hz) between the tip and the sample. STS spectra were measured with a metallic tip. Before acquiring the spectra, the tip was located at the corresponding position above the molecule and the Au surface with a tunneling set point of I = 200 pA and U = −1.3 V.

The DBTT molecules were evaporated using a lab-built evaporation device held at 517 K.[36] The Au(111) single crystals with an alignment of better than 0.1° relative to the nominal orientation were purchased from MaTecK, Germany. The Au(111) crystal was cleaned by Ar^+ sputtering (E = 1.5 kV, I = 1.4 μA, $p = 3 \times 10^{-6}$ mbar) and annealing (1000 K) cycles.

Computational Details. Density-functional theory (DFT) calculations of the isolated, planar cycloarene molecule were carried out in D_{6h} point group symmetry using the PBE[37] functional, augmented with the D3(BJ)[38−40] dispersion correction, and a TZVP[41] basis set. All DFT calculations were performed with the Turbomole program package, and images of molecular orbitals were generated using TmoleX18.[42]

ASSOCIATED CONTENT

Supporting Information

The Supporting Information is available free of charge at https://pubs.acs.org/doi/10.1021/jacs.9b10151.

Synthetic details and characterization of DBTT; illustrations of the conjugation pathways of the **C108** ring; calculated molecular orbitals and geometry of the cycloarene (PDF)

X-ray crystallographic data of DBT (CCDC 1946678T) (CIF)

AUTHOR INFORMATION

Corresponding Authors

*daniel.ebeling@ap.physik.uni-giessen.de
*jsu@staff.uni-marburg.de
*michael.gottfried@chemie.uni-marburg.de

ORCID

Daniel Ebeling: 0000-0001-5829-170X
Jörg Sundermeyer: 0000-0001-8244-8201
J. Michael Gottfried: 0000-0001-5579-2568

Author Contributions

#Q.F., D.M.-J., and S.W. contributed equally to this work.

Notes

The authors declare no competing financial interest.

ACKNOWLEDGMENTS

Financial support by the Deutsche Forschungsgemeinschaft via the grants GO 1812/2-1, 223848855-SFB 1083, the EXC 315, EB 535/1-1, SCHI 619/13, and the GRK 2204 is gratefully acknowledged. The RRZE of the University of Erlangen−Nürnberg is acknowledged for computational resources. Q.T.F. thanks the Alexander von Humboldt-Foundation for a Research Fellowship for Postdoctoral Researchers.

REFERENCES

(1) Buttrick, J. C.; King, B. T. Kekulenes, Cycloarenes, and Heterocycloarenes: Addressing Electronic Structure and Aromaticity Through Experiments and Calculations. *Chem. Soc. Rev.* **2017**, *46*, 7−20.

(2) Staab, H. A.; Diederich, F. Cycloarenes, a New Class of Aromatic Compounds, I., Synthesis of Kekulene. *Chem. Ber.* **1983**, *116*, 3487−3503.

(3) Kumar, B.; Viboh, R. L.; Bonifacio, M. C.; Thompson, W. B.; Buttrick, J. C.; Westlake, B. C.; Kim, M. S.; Zoellner, R. W.; Varganov, S. A.; Morschel, P.; Teteruk, J.; Schmidt, M. U.; King, B. T. Septulene: the Heptagonal Homologue of Kekulene. *Angew. Chem., Int. Ed.* **2012**, *51*, 12795−12800.

(4) Funhoff, D. J. H.; Staab, H. A. Cyclo[*d.e.d.e.e.d.e.d.e.e.*]-decakisbenzene, a New Cycloarene. *Angew. Chem., Int. Ed. Engl.* **1986**, *25*, 742−744.

(5) Majewski, M. A.; Hong, Y.; Lis, T.; Gregolinski, J.; Chmielewski, P. J.; Cybinska, J.; Kim, D.; Stepien, M. Octulene: A Hyperbolic Molecular Belt that Binds Chloride Anions. *Angew. Chem., Int. Ed.* **2016**, *55*, 14072−14076.

(6) Beser, U.; Kastler, M.; Maghsoumi, A.; Wagner, M.; Castiglioni, C.; Tommasini, M.; Narita, A.; Feng, X.; Müllen, K. A C216-Nanographene Molecule with Defined Cavity as Extended Coronoid. *J. Am. Chem. Soc.* **2016**, *138*, 4322−5.

(7) Jacobse, P. H.; van den Hoogenband, A.; Moret, M. E.; Klein Gebbink, R. J.; Swart, I. Aryl Radical Geometry Determines Nanographene Formation on Au(111). *Angew. Chem., Int. Ed.* **2016**, *55*, 13052−13055.

(8) Rogers, C.; Chen, C.; Pedramrazi, Z.; Omrani, A. A.; Tsai, H. Z.; Jung, H. S.; Lin, S.; Crommie, M. F.; Fischer, F. R. Closing the Nanographene Gap: Surface-Assisted Synthesis of Peripentacene from 6,6′-Bipentacene Precursors. *Angew. Chem., Int. Ed.* **2015**, *54*, 15143−6.

DOI: 10.1021/jacs.9b10151
J. Am. Chem. Soc. 2020, 142, 894−899

(9) Zuzak, R.; Castro-Esteban, J.; Brandimarte, P.; Engelund, M.; Cobas, A.; Piatkowski, P.; Kolmer, M.; Perez, D.; Guitian, E.; Szymonski, M.; Sanchez-Portal, D.; Godlewski, S.; Pena, D. Building a 22-Ring Nanographene by Combining In-Solution and On-Surface Syntheses. *Chem. Commun.* **2018**, *54*, 10256−10259.
(10) Xu, K.; Urgel, J. I.; Eimre, K.; Di Giovannantonio, M.; Keerthi, A.; Komber, H.; Wang, S.; Narita, A.; Berger, R.; Ruffieux, P.; Pignedoli, C. A.; Liu, J.; Müllen, K.; Fasel, R.; Feng, X. On-Surface Synthesis of a Nonplanar Porous Nanographene. *J. Am. Chem. Soc.* **2019**, *141*, 7726−7730.
(11) Hieulle, J.; Carbonell-Sanroma, E.; Vilas-Varela, M.; Garcia-Lekue, A.; Guitian, E.; Pena, D.; Pascual, J. I. On-Surface Route for Producing Planar Nanographenes with Azulene Moieties. *Nano Lett.* **2018**, *18*, 418−423.
(12) Treier, M.; Pignedoli, C. A.; Laino, T.; Rieger, R.; Müllen, K.; Passerone, D.; Fasel, R. Surface-Assisted Cyclodehydrogenation Provides a Synthetic Route Towards Easily Processable and Chemically Tailored Nanographenes. *Nat. Chem.* **2011**, *3*, 61−67.
(13) Fan, Q.; Werner, S.; Tschakert, J.; Ebeling, D.; Schirmeisen, A.; Hilt, G.; Hieringer, W.; Gottfried, J. M. Precise Monoselective Aromatic C-H Bond Activation by Chemisorption of Meta-Aryne on a Metal Surface. *J. Am. Chem. Soc.* **2018**, *140*, 7526−7532.
(14) Pozo, I.; Guitián, E.; Pérez, D.; Peña, D. Synthesis of Nanographenes, Starphenes, and Sterically Congested Polyarenes by Aryne Cyclotrimerization. *Acc. Chem. Res.* **2019**, *52*, 2472−2481.
(15) Mishra, S.; Beyer, D.; Eimre, K.; Liu, J.; Berger, R.; Gröning, O.; Pignedoli, C. A.; Müllen, K.; Fasel, R.; Feng, X.; Ruffieux, P. Synthesis and Characterization of π-Extended Triangulene. *J. Am. Chem. Soc.* **2019**, *141*, 10621−10625.
(16) Su, J.; Telychko, M.; Hu, P.; Macam, G.; Mutombo, P.; Zhang, H.; Bao, Y.; Cheng, F.; Huang, Z.-Q.; Qiu, Z.; Tan, S. J. R.; Lin, H.; Jelínek, P.; Chuang, F.-C.; Wu, J.; Lu, J. Atomically Precise Bottom-up Synthesis of π-Extended [5]Triangulene. *Sci. Adv.* **2019**, *5*, No. eaav7717.
(17) Björk, J.; Stafstrom, S.; Hanke, F. Zipping Up: Cooperativity Drives the Synthesis of Graphene Nanoribbons. *J. Am. Chem. Soc.* **2011**, *133*, 14884−14887.
(18) Zhong, Q.; Hu, Y.; Niu, K.; Zhang, H.; Yang, B.; Ebeling, D.; Tschakert, J.; Cheng, T.; Schirmeisen, A.; Narita, A.; Müllen, K.; Chi, L. Benzo-Fused Periacenes or Double Helicenes? Different Cyclodehydrogenation Pathways on Surface and in Solution. *J. Am. Chem. Soc.* **2019**, *141*, 7399−7406.
(19) Recher, P.; Trauzettel, B.; Rycerz, A.; Blanter, Y. M.; Beenakker, C. W. J.; Morpurgo, A. F. Aharonov-Bohm Effect and Broken Valley Degeneracy in Graphene Rings. *Phys. Rev. B: Condens. Matter Mater. Phys.* **2007**, *76*, 235404.
(20) Russo, S.; Oostinga, J. B.; Wehenkel, D.; Heersche, H. B.; Sobhani, S. S.; Vandersypen, L. M. K.; Morpurgo, A. F. Observation of Aharonov-Bohm Conductance Oscillations in a Graphene Ring. *Phys. Rev. B: Condens. Matter Mater. Phys.* **2008**, *77*, 085413.
(21) Smirnov, D.; Schmidt, H.; Haug, R. J. Aharonov-Bohm Effect in an Electron-Hole Graphene Ring System. *Appl. Phys. Lett.* **2012**, *100*, 203114.
(22) Bluhm, H.; Koshnick, N. C.; Bert, J. A.; Huber, M. E.; Moler, K. A. Persistent Currents in Normal Metal Rings. *Phys. Rev. Lett.* **2009**, *102*, 136802.
(23) Huang, B. L.; Chang, M. C.; Mou, C. Y. Persistent Currents in a Graphene Ring with Armchair Edges. *J. Phys.: Condens. Matter* **2012**, *24*, 245304.
(24) Bolívar, N.; Medina, E.; Berche, B. Persistent Charge and Spin Currents in the Long-Wavelength Regime for Graphene Rings. *Phys. Rev. B: Condens. Matter Mater. Phys.* **2014**, *89*, 125413.
(25) Peeks, M. D.; Claridge, T. D. W.; Anderson, H. L. Aromatic and Antiaromatic Ring Currents in a Molecular Nanoring. *Nature* **2017**, *541*, 200.
(26) Kaiser, K.; Scriven, L. M.; Schulz, F.; Gawel, P.; Gross, L.; Anderson, H. L. An sp-Hybridized Molecular Carbon Allotrope, Cyclo[18]Carbon. *Science* **2019**, *365*, 1299−1301.
(27) Bleszynski-Jayich, A. C.; Shanks, W. E.; Peaudecerf, B.; Ginossar, E.; von Oppen, F.; Glazman, L.; Harris, J. G. E. Persistent Currents in Normal Metal Rings. *Science* **2009**, *326*, 272.
(28) Talirz, L.; Ruffieux, P.; Fasel, R. On-Surface Synthesis of Atomically Precise Graphene Nanoribbons. *Adv. Mater.* **2016**, *28*, 6222−31.
(29) Fan, Q.; Wang, T.; Dai, J.; Kuttner, J.; Hilt, G.; Gottfried, J. M.; Zhu, J. On-Surface Pseudo-High-Dilution Synthesis of Macrocycles: Principle and Mechanism. *ACS Nano* **2017**, *11*, 5070−5079.
(30) Fan, Q.; Wang, C.; Han, Y.; Zhu, J.; Hieringer, W.; Kuttner, J.; Hilt, G.; Gottfried, J. M. Surface-Assisted Organic Synthesis of Hyperbenzene Nanotroughs. *Angew. Chem., Int. Ed.* **2013**, *52*, 4668−4672.
(31) Talirz, L.; Söde, H.; Dumslaff, T.; Wang, S.; Sanchez-Valencia, J. R.; Liu, J.; Shinde, P.; Pignedoli, C. A.; Liang, L.; Meunier, V.; Plumb, N. C.; Shi, M.; Feng, X.; Narita, A.; Müllen, K.; Fasel, R.; Ruffieux, P. On-Surface Synthesis and Characterization of 9-Atom Wide Armchair Graphene Nanoribbons. *ACS Nano* **2017**, *11*, 1380−1388.
(32) Pozo, I.; Majzik, Z.; Pavliček, N.; Melle-Franco, M.; Guitián, E.; Peña, D.; Gross, L.; Pérez, D. Revisiting Kekulene: Synthesis and Single-Molecule Imaging. *J. Am. Chem. Soc.* **2019**, *141*, 15488−15493.
(33) Setiawan, D.; Kraka, E.; Cremer, D. Quantitative Assessment of Aromaticity and Antiaromaticity Utilizing Vibrational Spectroscopy. *J. Org. Chem.* **2016**, *81*, 9669−9686.
(34) Giessibl, F. J. High-speed force sensor for force microscopy and profilometry utilizing a quartz tuning fork. *Appl. Phys. Lett.* **1998**, *73*, 3956−3958.
(35) Bartels, L.; Meyer, G.; Rieder, K. H. Controlled Vertical Manipulation of Single CO Molecules with the Scanning Tunneling Microscope: A Route to Chemical Contrast. *Appl. Phys. Lett.* **1997**, *71*, 213−215.
(36) Zint, S.; Ebeling, D.; Ahles, S.; Wegner, H. A.; Schirmeisen, A. Subsurface-Controlled Angular Rotation: Triphenylene Molecules on Au(111) Substrates. *J. Phys. Chem. C* **2016**, *120*, 1615−1622.
(37) Perdew, J. P.; Burke, K.; Ernzerhof, M. Generalized Gradient Approximation Made Simple. *Phys. Rev. Lett.* **1996**, *77*, 3865−3868.
(38) Grimme, S.; Antony, J.; Ehrlich, S.; Krieg, H. A Consistent and Accurate *ab initio* Parametrization of Density Functional Dispersion Correction (DFT-D) for the 94 Elements H-Pu. *J. Chem. Phys.* **2010**, *132*, 154104.
(39) Becke, A. D.; Johnson, E. R. A Density-Functional Model of the Dispersion Interaction. *J. Chem. Phys.* **2005**, *123*, 154101.
(40) Grimme, S.; Ehrlich, S.; Goerigk, L. Effect of the Damping Function in Dispersion Corrected Density Functional Theory. *J. Comput. Chem.* **2011**, *32*, 1456−1465.
(41) Weigend, F.; Ahlrichs, R. Balanced Basis Sets of Split Valence, Triple zeta Valence and Quadruple zeta Valence Quality for H to Rn: Design and Assessment of Accuracy. *Phys. Chem. Chem. Phys.* **2005**, *7*, 3297−3305.
(42) Furche, F.; Ahlrichs, R.; Hättig, C.; Klopper, W.; Sierka, M.; Weigend, F. Turbomole. *Wiley Interdiscip. Rev.: Comput. Mol. Sci.* **2014**, *4*, 91−100. www.turbomole.com.

DOI: 10.1021/jacs.9b10151
J. Am. Chem. Soc. 2020, 142, 894−899

Supporting Information for

On-Surface Synthesis and Characterization of a Cycloarene: C108 Graphene Ring

Qitang Fan,[1‡] Daniel Martin-Jimenez,[2‡] Simon Werner,[1‡] Daniel Ebeling,[2*] Tabea Koehler,[1] Tobias Vollgraff,[1] Jörg Sundermeyer,[1*] Wolfgang Hieringer,[3] André Schirmeisen,[2] J. Michael Gottfried[1*]

[1]Department of Chemistry and Material Sciences Center (WZMW), Philipps-Universität Marburg, Hans-Meerwein-Straße, 35032 Marburg, Germany

[2]Institute of Applied Physics (IAP) and Center for Materials Research (LaMa), Justus-Liebig-Universität Gießen, Heinrich-Buff-Ring 16, 35392 Gießen, Germany

[3]Theoretical Chemistry and Interdisciplinary Center for Molecular Materials (ICMM), Department of Chemistry and Pharmacy, Friedrich-Alexander-Universität Erlangen-Nürnberg, Egerlandstraße 3, 91058 Erlangen, Germany

[‡]Q.F., D.M.J, and S.W. contributed equally to this work.

(d1) General Information

All reactions were carried out under inert atmosphere (nitrogen) using Schlenk techniques if not mentioned otherwise. All reagents were purchased from commercial sources if not mentioned otherwise and were used without further purification. For thin-layer chromatography, TLC plates from Merck KGaA with silica gel 60 on aluminum with fluorescence-quenching F254 at room temperature were used. All solvents were dried and/or purified according to standard procedures and stored over 3 Å or 4 Å molecular sieves. NMR spectra were recorded in automation or by the service department (faculty of chemistry, Philipps University Marburg) with a Bruker Avance 300 or 500 spectrometer at 298 K using CD_2Cl_2 or $CDCl_3$ as solvent and for calibration (residual proton signals). HR-APCI mass spectra were acquired with a LTQ-FT Ultra mass spectrometer (Thermo Fischer Scientific). The resolution was set to 100.000. HR-EI mass spectra were acquired with a AccuTOF GCv 4G (JEOL) Time of Flight (TOF) mass spectrometer. An internal or external standard was used for drift time correction. The LIFDI ion source and FD-emitters were purchased from Linden ChroMasSpec GmbH (Bremen, Germany). The data collection for the single-crystal structure determination was performed on a Stoe Stadivari diffractometer or a Bruker D8 Quest diffractometer by the X-ray service department of the department of chemistry at the university of Marburg. Information concerning the used hardware, and software used for data collection, cell refinement and data reduction as well as structure solution and refinement can be reviewed in the attached CIF-files. After the solution (Shelxt)[1] and refinement process (Shelxl 2017/1)[2] the data was validated by using Platon.[3] All graphic representations were created with Diamond 4.[4] IR spectra are recorded with a Bruker Alpha FT-IR spectrometer with Platinum ATR sampling.

(d2) Experimental Procedures and Analytical Characterization

3,6-Dibromophenanthrene-9,10-dione (**2**)

According to a synthesis of Kobin[5] 2.98 g (14.4 mmol, 1.00 eq) phenanthrene-9,10-dione (**1**) and 0.60 g (2.3 mmol, 0.15 eq) dibenzoylperoxide were suspended in 18 mL nitrobenzene. To the stirred suspension, 1.5 mL (28.9 mmol, 2.05 eq) bromine were added dropwise. The dark reaction mixture was heated to 110 °C for 4 h and a yellow precipitate was formed. After detection of complete conversion by TLC, the reaction mixture was cooled to room temperature and 35 mL ethanol were added. The crude product was filtered and washed with ethanol, diethyl ether and *n*-pentane and dried in vacuo. 3.94 g (10.8 mmol, 75%) of the desired compound **2** were obtained as yellow solid.

^{1}H NMR: 300 MHz, 298 K, CD_2Cl_2, δ = 8.17 (d, 2H, ^4J = 1.74 Hz, *H* 3), 8.02 (d, 2H, ^3J = 8.34 Hz, *H* 1), 7.68 (dd, 2H, ^4J = 1.74 Hz, ^3J = 8.34 Hz, *H* 2) ppm.

^{13}C NMR: 75 MHz, 298 K, CD_2Cl_2, δ = 179.3, 136.4, 133.8, 132.3, 132.2, 130.4, 128.0 ppm.

The analytical data are in accordance with the literature.[13]

3,6-Dibromo-2-iodophenanthrene-9,10-dione (**3**)

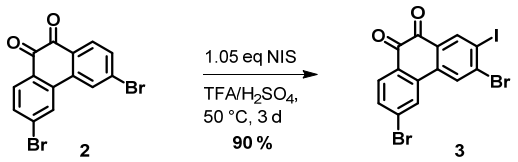

Adopting a synthesis protocol of Shirai *et al*.[6] 3.56 g (9.72 mmol, 1.00 eq) of **2** were suspended in 33 mL trifluoroacetic acid and cooled to 0 °C. 16 mL sulphuric acid were added dropwise. After 5 min 2.23 g (10.13 mmol, 1.05 eq) N-iodosuccinimide were added portionwise. The resulting dark brown suspension was heated to 50 °C and stirred for 3 d. After cooling to room temperature, the crude product was precipitated into a solution of 3 g sodium sulphate in 200 mL water. The crude product was filtered, washed with methanol, diethyl ether and *n*-pentane and dried in vacuo. 4.30 g (8.78 mmol, 90%) of compound **3** were obtained as orange-red solid and directly used for the next step without further purification.

^{1}H NMR: 300 MHz, $CDCl_3$, δ = 8.56 (s, 1H, *H* 1), 8.25 (s, 1H, *H* 2), 8.16 (dd, 1H, ^3J = 5.82 Hz, ^4J = 1.77 Hz, *H* 5), 8.03 (d, 1H, ^3J = 8.32 Hz, *H* 6), 7.71-7.66 (m, 1H, *H* 3) ppm.

^{13}C NMR: not recorded due to low solubility.

IR (ATR): $\tilde{\nu}$ = 3095 (w), 2058 (w), 2027 (w), 1989 (w), 1673 (vs), 1574 (s), 1523 (w), 1445 (m), 1353 (w), 1280 (m), 1224 (w), 1184 (w), 1109 (w), 1082 (w), 1024 (w), 910 (m), 837 (m), 703 (w), 635 (w) cm^{-1}.

m. p.: 225-228 °C dec.

6,9-Dibromo-5-iodo-1,3-diphenyl-2H-cyclopenta[l]phenanthren-2-one (**4**)

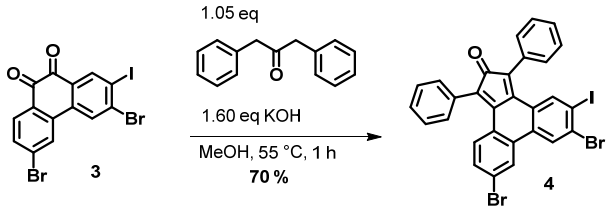

1.63 g (3.33 mmol, 1.00 eq) of compound **3** and 750 mg (3.57 mmol, 1.05 eq) diphenylpropan- 2-one were dissolved in 15 mL methanol. To the stirred solution, 300 mg (5.35 mmol, 1.60 eq) potassium hydroxide dissolved in 5 mL methanol were added dropwise. A color change towards a dark brownish solution occurred and the reaction mixture was stirred at 60°C for 1 h and a dark green precipitate was formed. After detection of complete conversion by TLC, the reaction mixture was cooled to room temperature and 20 mL methanol were added. The crude product was filtered and washed with cold methanol, diethyl ether and *n*-pentane and dried *in vacuo*. 1.55 g (2.34 mmol, 70%) of the desired compound **4** were obtained as dark green solid and directly used for the next step without further purification.

^{1}H NMR: 300 MHz, CD_2Cl_2, δ = 7.96 (d, 1H, ^{3}J = 10.38 Hz), 7.90 (dd, 1H, ^{4}J = 1.94 Hz, ^{3}J = 5.10 Hz), 7.46-7.32 (m, 12H), 7.12-7.08 (m, 1H) ppm.

^{13}C NMR: not recorded due to low solubility.

HRMS: *m/z* for $[C_{29}H_{16}O^{79}Br_2{}^{127}I]^+$ calc.: 666.8589, found: 666.8606 (APCI+).

IR (ATR): $\tilde{\nu}$ = 2311 (w), 2278 (w), 2223 (m), 2167 (w), 2109 (m), 2049 (w), 2006 (w),1937 (w), 1886 (w), 1702 (s), 1665 (w), 1445 (w), 1342 (m), 1240 (m), 1002 (s), 906 (w), 870 (w), 789 (m), 724 (w), 696 (m), 617 (vs), 571 (s), 440 (s) cm^{-1}.

m.p.: 264-267 °C (dec.)

(7,10-Dibromo-11-iodo-1,4-diphenyltriphenylen-2-yl)trimethylsilane (**5**)

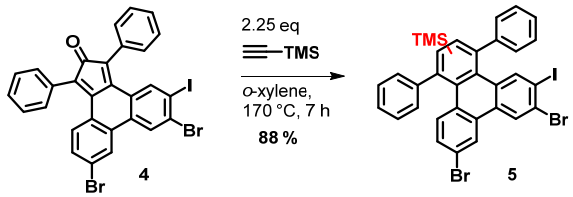

1.04 g (1.57 mmol, 1.00 eq) of compound **4** and 0.5 mL (3.51 mmol, 2.25 eq) trimethylsilyl acetylene were dissolved in 20 mL *o*-xylene and stirred for 7 h at 170°C. After this time, complete conversion could be detected by TLC and the reaction solution was cooled to room temperature. The solvent was removed in vacuo and the residue was purified via column chromatography over silica gel using *n*-pentane/DCM 9:1 as eluent. 1.01 g (1.38 mmol, 88%) of the desired compound **5** were obtained as beige solid, containing two inseparable constitutional isomers.

TLC: R_f = 0.40 (*n*-pentane/dichloromethane 9:1)

^{1}H NMR: 300 MHz, $CDCl_3$, δ = 8.53-8.43 (m, 2H), 8.15-8.07 (m, 1H), 7.85 (s, 1H, *H*3), 7.56-7.34 (m, 11H), 7.15-7.11 (m, 1H) ppm. (superimposed signals of two isomers)

^{13}C NMR: 75 MHz, $CDCl_3$, δ = 146.0, 146.0, 145.9, 145.9, 145.1, 145.0, 144.7, 144.6, 144.5, 144.4, 144.1, 144.0, 142.4, 142.3, 141.4, 141.1, 140.7, 140.5, 138.0, 137.9, 137.8, 137.7, 133.4, 132.0, 132.0, 131.9, 131.8, 131.8, 131.4, 131.4, 131.0, 129.9, 129.9, 129.8, 129.8, 129.7, 129.5, 129.5, 129.4, 129.3, 129.2, 129.1, 128.7, 128.6, 128.2, 128.1, 128.0, 127.8, 127.8, 127.7, 127.0, 126.9, 126.6, 126.5, 121.7, 121.7, 121.1, 121.1, 99.0, 99.0, 98.6, 98.6, 1.0, 1.0 ppm. (two sets of signals)

HRMS: *m/z* for $[C_{33}H_{25}{}^{81}Br^{79}Br^{127}I^{29}Si]^+$ calc.: 735.91165, found: 735.91175 (EI+).

IR (ATR): $\tilde{\nu}$ = 3055 (w), 3025 (w), 2951 (w), 2894 (w), 2187 (w), 1735 (w), 1591 (w), 1520 (w), 1489 (w), 1449 (m), 1410 (w), 1349 (w), 1247 (m), 1167 (m), 1075 (m), 1016 (w), 868 (m), 827 (vs), 760 (s), 697 (vs), 587 (m), 535 (w) cm^{-1}.

m.p.: 179-182 °C

(7,10-Dibromo-1,4,11-triphenyltriphenylen-2-yl)trimethylsilane (**6**)

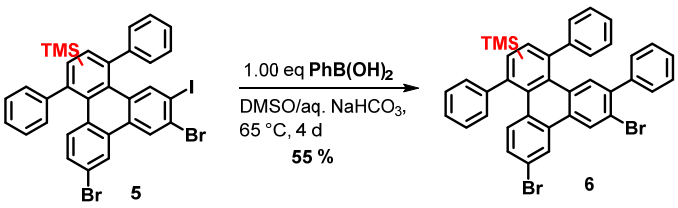

767 mg (1.05 mmol, 1.00 eq) of compound **5** and 128 mg (1.05 mmol, 1.00 eq) benzene boronic acid were dissolved in 35 mL DMSO and 3 mL saturated aqueous sodium hydrogencarbonate solution and degassed. 15 mg (0.02 mmol, 1.5 mol%) $Pd(dppf)Cl_2$ were added and the reaction mixture was stirred at 65°C under exclusion of light for 4 d. After this time, complete conversion could be detected by TLC and the reaction solution was cooled to room temperature and mixed with 20 mL ethyl acetate and 20 mL water. The organic layer was separated and washed three times with water and dried over magnesium sulphate. The solvent was removed in vacuo and the residue was purified via column chromatography over silica gel using *n*-pentane/DCM 9:1 as eluent. 400 mg (0.59 mmol, 55%) of the desired compound **6** were obtained as colorless solid, consisting of two inseparable constitutional isomers.

TLC: R_f = 0.35 (*n*-pentane/dichloromethane 9:1)

^{1}H NMR: 300 MHz, $CDCl_3$, δ = 8.64 (s, 1H, *H* 3), 8.53-8.51 (m, 1H), 7.80 (d, 1H, ^{4}J = 1.85 Hz, *H* 3), 7.72 (d, 1H, ^{4}J = 1.85 Hz, *H* 3) 7.60-7.08 (m, 14H), 7.18, 7.11 (2x dd, ^{3}J = 8.98 Hz, ^{4}J = 2.07 Hz, in sum 1H), 6.98-6.90 (m, 2H) ppm. (superimposed signals of two isomers)

^{13}C NMR: 75 MHz, $CDCl_3$, δ = 144.9, 144.5, 144.3, 144.1, 143.7, 139.6, 139.5, 137.0, 136.8, 136.5, 136.2, 132.6, 132.5, 131.1, 130.9, 130.8, 130.6, 130.1, 129.9, 129.9, 129.7, 129.6, 129.1, 129.1, 128.9, 128.9, 128.7, 128.6, 128.4, 128.2, 127.1, 127.1, 127.1, 127.0, 126.9, 126.9, 126.7, 126.6, 125.3, 120.7, 120.5, 120.3, 120.1, 0.0, 0.0 ppm. (two sets of signals)

HRMS: *m/z* for $[C_{33}H_{25}{}^{81}Br^{79}Br^{29}Si]^+$ calc.: 735.91165, found: 735.91175 (EI+).

IR (ATR): $\tilde{\nu}$ = 3053 (w), 2951 (w), 1948 (w), 1593 (w), 1520 (m), 1468 (w), 1441 (w),1398 (w), 1343 (m), 1246 (w), 1176 (w), 1097 (w), 1079 (w), 1021 (w), 864 (s), 828 (vs), 759 (s), 695 (vs), 628 (w), 564 (w), 471 (w) cm^{-1}.

m.p.: 170-173 °C

7,10-Dibromo-1,4,6-triphenyltriphenylene (**DBTT**)

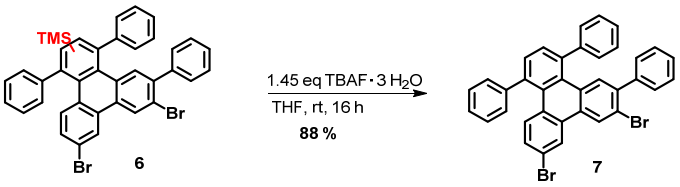

185 mg (0.27 mmol, 1.00 eq) **6** were dissolved in 12 mL THF. A solution of 125 mg (0.40 mmol, 1.45 eq) tetrabutylammonium fluoride trihydrate in 3 mL THF was added dropwise and the colorless reaction solution turned subsequently to an orange color. The reaction solution was stirred at room temperature for 18 h until complete conversion could be detected by TLC. The crude product was precipitated into water (20 mL), filtered and washed with *n*-pentane. Pure product was obtained after sublimation at HV-sublimation (240 °C at $5.5 \cdot 10^{-7}$ mbar). 145 mg (0.24 mmol, 88%) of the desired compound **DBTT** were obtained as colorless solid.

TLC: R_f = 0.25 (*n*-pentane/dichloromethane 10:1)

^{1}H NMR: 300 MHz, CD_2Cl_2, δ = 8.67 (s, 1H), 8.55 (d, 1H, ^4J = 1.79 Hz), 7.71 (s, 1H),

7.57-7.52 (m, 3H), 7.51-7.38 (m, 10H), 7.28-7.24 (m, 3H), 7.18 (dd, 1H, ^3J = 8.97 Hz, ^4J = 1.92 Hz), 6.98-6.95 (m, 2H) ppm.

^{13}C NMR: 75 MHz, CD_2Cl_2, δ = 144.3, 143.9, 140.1, 139.2, 139.2, 133.2, 131.6, 131.5, 130.5, 130.4, 130.3, 130.3, 130.2, 129.7, 129.6, 129.5, 129.4, 129.4, 129.2, 128.8, 127.6, 127.5, 127.5, 127.4, 127.3, 125.8, 121.1, 120.9 ppm.

HRMS: *m/z* for $[C_{36}H_{22}{}^{81}Br^{79}Br]^+$ calc.: 614.00678, found: 614.00957 (EI+).

IR (ATR): $\tilde{\nu}$ = 3054 (w), 3024 (w), 2953 (w), 1591 (w), 1519 (m), 1471 (w), 1441 (w), 1402 (w), 1349 (m), 1249 (w), 1079 (m), 1026 (w), 865 (w), 829 (s), 761 (s), 697 (vs), 631 (w). 564 (w), 526 (w) cm^{-1}.

m.p.: 240-243 °C

3.7 Publication 7: Kekulene: On-Surface Synthesis, Orbital Structure, and Aromatic Stabilization

Citation: A. Haags, A. Reichmann, Q. Fan, L. Egger, H. Kirschner, T. Naumann, S. Werner, T. Vollgraff, J. Sundermeyer, L. Eschmann, X. Yang, D. Brandstetter, F. C. Bocquet, G. Koller, A. Gottwald, M. Richter, M. G. Ramsey, M. Rohlfing, P. Puschnig, J. M. Gottfried, S. Soubatch, and F. S. Tautz, *ACS Nano* **2020**, *14*, 15766-15775.[G]

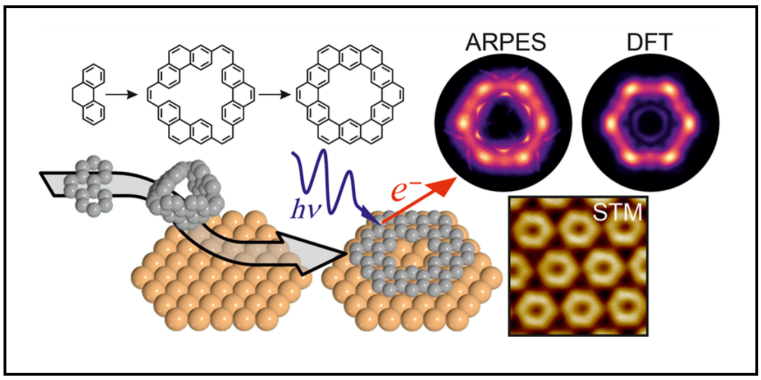

Summary: This article presents a fundamental in-depth study on the aromaticity of Kekulene as simplest and archetypical cycloarene. For this purpose, a strategy was developed to synthesize Kekulene in almost quantitative yields on Cu(111) at a temperature of 230 °C by threefold intramolecular cyclodehydrogenation of non-planar 1,4,7(2,7)-triphenanthrenacyclononaphane-2,5,8-triene as precursor. Its chemical synthesis involved the regioselective bromination and oxidative aromatization of dihydro phenanthrene. Corresponding dibromo-phenanthrene was converted into a bis-aldehyd, which could be trimerized applying McMurry reaction conditions. The final precursor was characterized unambiguously by NMR and XRD and after vacuum deposition onto Cu(111), it could be converted into well ordered hexagonally arranged Kekulene networks characterized by STM. Supported by DFT calculations, the symmetry and spatial structure of the charge distribution of Kekulene's HOMO was determined by photoemission tomography and angle-resolved photoemission spectroscopy (ARPES). In agreement with a recent aromaticity assessment of kekulene based solely on C-C bond lengths, it could be demonstrated that the π-conjugation of Kekulene is better described by the Clar model rather than a superaromatic model.

Own Contribution: The precursor structure was designed by myself together with Dr. Q. Fan. The design of the retrosynthetical approach of the precursor, the chemical synthesis of precursor DBTT as well as the in-solution characterization was performed by myself. T. Vollgraff solved and refined its crystal structure. The chemical synthesis part of the manuscript was written by myself. Prof. Dr. J. Sundermeyer supervised the chemical synthesis. All authors contributed in writing and approval of the manuscript
Note: The individual contributions of all co-authors can be taken from the original manuscript.

[G] Reproduced with permission of A. Haags *et al.*, *ACS Nano* **2020**, *14*, 15766-15775. Copyright ©2020, Rights Managed by the American Chemical Society.

ACSNANO

www.acsnano.org

ARTICLE

Kekulene: On-Surface Synthesis, Orbital Structure, and Aromatic Stabilization

Anja Haags,[@] Alexander Reichmann,[@] Qitang Fan,[@] Larissa Egger, Hans Kirschner, Tim Naumann, Simon Werner, Tobias Vollgraff, Jörg Sundermeyer, Lukas Eschmann, Xiaosheng Yang, Dominik Brandstetter, François C. Bocquet, Georg Koller, Alexander Gottwald, Mathias Richter, Michael G. Ramsey, Michael Rohlfing,* Peter Puschnig,* J. Michael Gottfried,* Serguei Soubatch,* and F. Stefan Tautz

Cite This: *ACS Nano* 2020, 14, 15766–15775

Read Online

ACCESS | Metrics & More | Article Recommendations | Supporting Information

ABSTRACT: **We revisit the question of kekulene's aromaticity by focusing on the electronic structure of its frontier orbitals as determined by angle-resolved photoemission spectroscopy. To this end, we have developed a specially designed precursor, 1,4,7(2,7)-triphenanthrenacyclononaphane-2,5,8-triene, which allows us to prepare sufficient quantities of kekulene of high purity directly on a Cu(111) surface, as confirmed by scanning tunneling microscopy. Supported by density functional calculations, we determine the orbital structure of kekulene's highest occupied molecular orbital by photoemission tomography. In agreement with a recent aromaticity assessment of kekulene based solely on C−C bond lengths, we conclude that the π-conjugation of kekulene is better described by the Clar model rather than a superaromatic model. Thus, by exploiting the capabilities of photoemission tomography, we shed light on the question which consequences aromaticity holds for the frontier electronic structure of a π-conjugated molecule.**

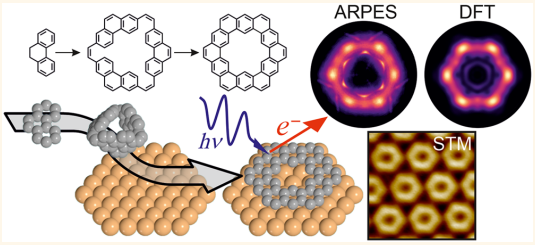

KEYWORDS: *kekulene, aromaticity, STM, photoemission, ARPES, DFT*

Aromaticity, a fundamental concept of organic chemistry used to explain the stabilization of cyclic conjugated π-electron systems, has been of special interest to chemists[1] ever since the cyclic structure of benzene has been proposed by Kekulé in 1865.[2] For kekulene ($C_{48}H_{24}$)—a prototypical cycloarene—a specific aromatic stabilization mechanism has been proposed, namely the π-conjugation in two concentric macrocyclic conjugation paths denoted as [18]annulene and [30]annulene.[3−13] This so-called "superaromaticity" has been debated extensively for many years.[4−9,12,14−16] In an alternative model, kekulene is thought to consist of six disjoint aromatic sextets, thus fulfilling Clar's rule[17] according to which in benzoid molecules the number of disjoint aromatic benzene rings should be maximized and the number of double bonds minimized.

Many attempts to assess kekulene's aromaticity theoretically were solely compared to the first, and until recently the only, experimental study by Staab et al.,[18−20] who developed a reliable synthesis of kekulene with 80% yield.[18] The authors analyzed the obtained kekulene microcrystals by mass spectrometry, infrared adsorption and electron spectroscopies, proton nuclear magnetic resonance (^{1}H NMR), X-ray diffraction (XRD), and optically detected magnetic resonance (ODMR).[20] However, all of these experiments were hindered by the extremely low solubility of the substance. XRD revealed a substantial variation in bond lengths, and ODMR results indicated a partial compartmentation of the π-system.[19] Based on ^{1}H NMR results[18] pointing at strong coupling between inner and outer annulene paths and thus suggesting against annulenoid ring currents, Krieger et al.[19] concluded that Clar's sextet model is the better representation of the bonding situation in kekulene.

Recently the synthesis of kekulene has been revisited.[21,22] Pozo et al.[21] deposited kekulene on the cold (10 K) Cu(111)

Received: August 13, 2020
Accepted: November 3, 2020
Published: November 13, 2020

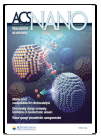

https://dx.doi.org/10.1021/acsnano.0c06798
ACS Nano 2020, 14, 15766–15775

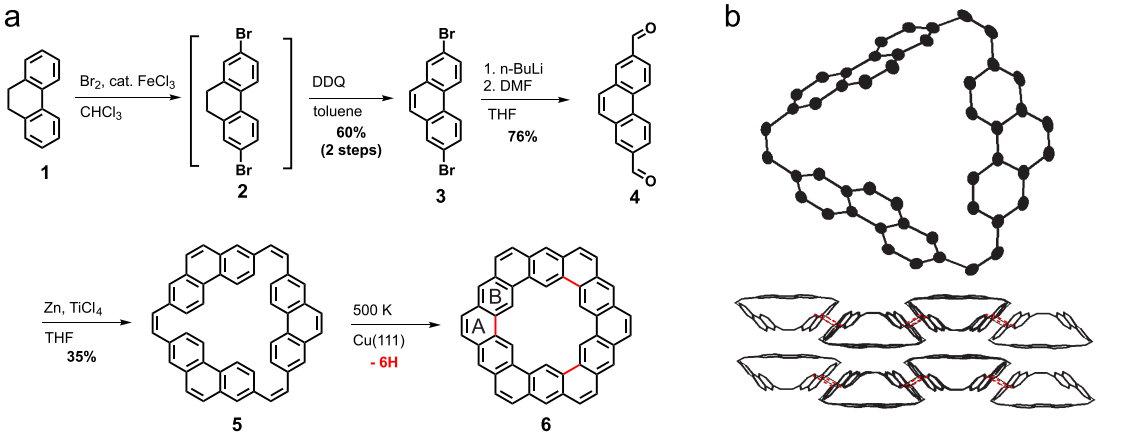

Figure 1. (a) Synthesis of the kekulene precursor 5 by a four-step reaction sequence starting with 9,10-dihydrophenanthrene (1), and the on-surface reaction of 5 leading to kekulene (6). C−C bonds of 6 formed upon cyclodehydrogenation are marked in red. The two nonequivalent benzene rings of 6 are labeled as A and B, respectively. (b) Molecular and lattice structure obtained from single-crystal XRD analysis of 5 (thermal ellipsoids are shown at the 50% probability level and hydrogen atoms are omitted for clarity). The red dashed lines in (b) represent the shortest intermolecular C−C distance (3.34 Å).

surface by rapid thermal evaporation in vacuum. Partial fragmentation due to the high sublimation temperature resulted in an adsorbate consisting of mostly small and often mobile molecules, while only few molecules with the expected hexagonal shape and size of kekulene were observed. Therefore, the investigation of kekulene has only been possible with locally resolved scanning probe methods. Using high-resolution noncontact atomic force microscopy (AFM), Pozo et al. have studied the geometric structure of single adsorbed molecules. By analyzing the contrast in their high-resolution AFM images and comparing with corresponding simulations, they could assess the bond-resolved bond order and hence provide insight into the aromaticity, letting the authors conclude that again the Clar model provides a better description of kekulene.[21]

In contrast to Pozo et al., who focused on structural properties to assess kekulene's aromaticity, in this study, we shed light directly on the electronic structure of kekulene's frontier molecular orbitals by employing angle-resolved photoemission spectroscopy (ARPES). It is important to note that, for such an area-averaging experimental technique, several requirements must be fulfilled: a sufficient number of molecules must be present on the surface, byproducts should be absent, and the majority of these molecules have to be oriented in the same way. To meet these requirements, we developed an on-surface synthesis route enabling the formation of a complete monolayer of well-oriented kekulene molecules, which would not have been possible via vapor deposition of kekulene. Combining density functional theory (DFT) calculations with scanning tunneling microscopy (STM) and photoemission tomography (PT)[23,24] experiments, we confirm the successful synthesis of a complete ordered kekulene monolayer and investigate the orbital structure of the highest occupied molecular orbital (HOMO). We argue that it can serve as an additional indicator of the type of aromatic bonding and give insight into the aromatic stabilization mechanism of a given molecule. By exploiting the capabilities of photoemission tomography to reveal an orbital-resolved spatial electron density,[23−32] we can unambiguously confirm the Clar model for the aromaticity of kekulene.

RESULTS AND DISCUSSION

Synthesis of Kekulene on Cu(111). The synthesis of the precursor **5** for the dehydrogenative formation of kekulene on Cu(111) proceeds in a four-step reaction sequence as summarized in Figure 1a and described in detail in the Methods section and the Supporting Information (SI). The molecular structure of **5** shown in Figure 1b was proven by X-ray crystallography, which reveals that **5** possesses a nonplanar, highly twisted conformation (cf. SI).

Figure 2a shows an STM image of the as-deposited precursor **5** on a Cu(111) surface. It reveals a number of asymmetric features that are attributed to intact precursor molecules. The bright protrusions in Figure 2a are assumed to represent phenanthrene moieties tilted out of the Cu(111) surface plane due to the nonplanar geometry of **5**. Annealing the sample at 500 K drastically changes the structure of the molecular layer. Figure 2b reveals a long-range ordered lattice (domain size up to 100 nm, cf. SI, Figure S1) of planar and aligned hexagonal species. With their central empty pores, they clearly resemble the structure of kekulene. Note that the free molecule belongs to the symmetry group D_{6h},[19] or, if the small alternating out-of-plane bending of the inner hydrogens is considered, D_{3d}.[21] Therefore, we infer that upon annealing **5** undergoes a cyclodehydrogenation reaction, resulting in a molecular layer of kekulene (**6**). The density of the molecular layer confirms the high reaction yield of our on-surface synthesis. Note that the formation of large ordered monolayer domains of kekulene on Cu(111) (or indeed any other surface) has not been reported to date.

Density Functional Calculations. We have performed van der Waals corrected density functional calculations for a monolayer of kekulene on Cu(111) by employing a repeated slab approach with six Cu-layers in order to determine the most favorable adsorption structure. As detailed in the SI, we find that the most preferable adsorption configuration is characterized by the *hcp* hollow site with kekulene's zigzag-

https://dx.doi.org/10.1021/acsnano.0c06798
ACS Nano 2020, 14, 15766−15775

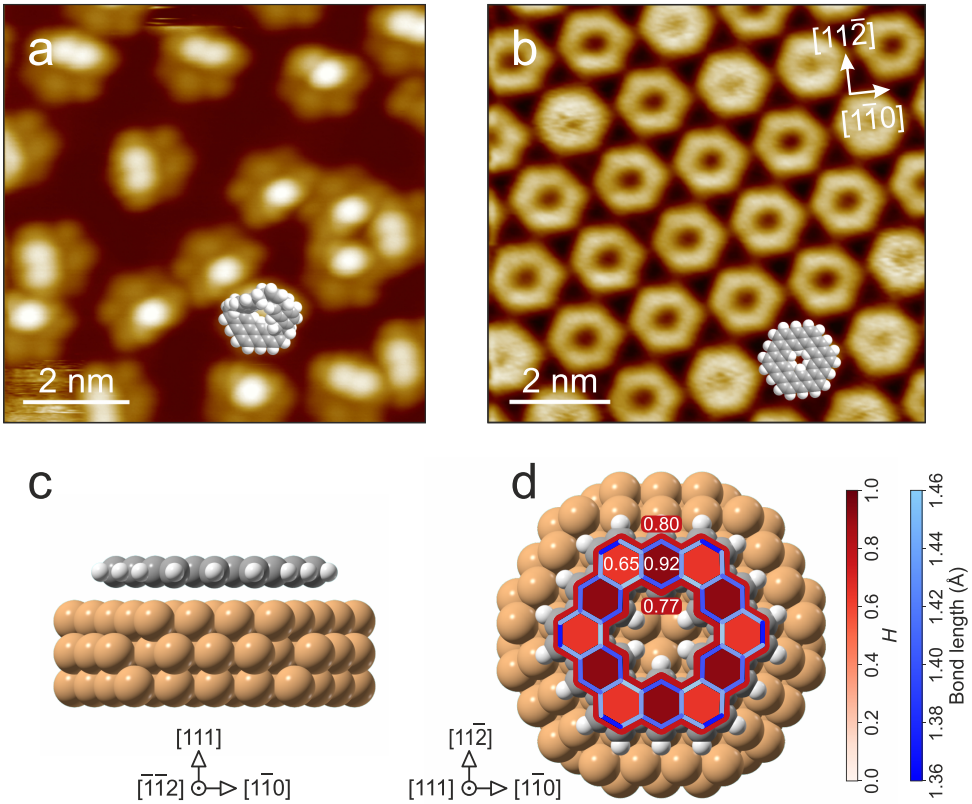

Figure 2. Structural information from STM and DFT. (a and b) STM micrographs of the precursor (5, U = −2.8 V, I = 0.11 nA) and kekulene (6, U = −2.9 V, I = 0.26 nA) on Cu(111), respectively, measured at 100 K. Space-filling molecular models are added to illustrate nonplanar and planar molecular conformations of 5 and 6, respectively. The two different appearances of kekulene in (b) are caused by a slight motion of some molecules, presumably induced by the STM tip. (c and d) Side and top views, respectively, of the relaxed adsorption geometry of kekulene/Cu(111) as obtained by DFT. HOMA values H and the bond lengths of adsorbed kekulene are color coded in red and blue, respectively.

edge oriented along the [1$\bar{1}$0] direction of Cu(111) (cf. the side and top views depicted in Figure 2c and 2d, respectively). Note that the predicted azimuthal orientation is in agreement with the STM data. The comparably large adsorption height ($\bar{h}_C$ = 3.05 Å), a relatively small adsorption energy (123 meV per C atom), and the flat geometry (vertical distortion Δh_C = 0.06 Å) indicate a rather weak interaction with Cu(111). This agrees with the large mobility of the molecules, reported in ref 21 and confirmed in our own STM experiments (cf. SI, Figure S2).

We have also analyzed the calculated internal geometric structure, i.e., the bond lengths of the relaxed adsorbed kekulene molecule as visualized by the blue color scale in Figure 2d. Moreover, we make use of the harmonic oscillator model of aromaticity (HOMA), which is a commonly applied, purely geometric measure to quantify the aromaticity of molecules.[33−36] The HOMA value H is defined as

$$H = 1 - \frac{\alpha(n)}{n}\sum_{i=1}^{n}(R_{opt} - R_i)^2 \quad (1)$$

H is related to the deformation energy of an aromatic system around its structural optimum, approximated as a harmonic potential around an optimum C−C bonding distance R_{opt}. R_{opt} itself follows from the minimization of the deformation energy and represents an ideal aromatic system. The original and fundamental idea is that each pair of carbon atoms can be involved in both a σ- and a π-bond, with $R_\sigma > R_\pi$. The actual bonding distance R_i represents a compression of R_σ and an extension of R_π. Both terms cost energy. While this energy penalty is minimized at R_{opt}, in any given molecule the R_i may deviate from R_{opt}, which is interpreted as a local dearomatization of the molecule. The HOMA value is a sum over n dearomatizing contributions in the relevant part of the molecule. Note that H = 1 signals perfect aromaticity, while smaller H values correspond to weaker aromatic stabilization. In our calculations, the normalization parameter $\alpha(n)$ is taken from ref 37 and R_{opt} is calculated as the average of single- and double-bond lengths of *trans*-1,3-butadiene as obtained by our DFT calculations, yielding R_{opt} = 1.403 Å (cf. SI for details).

We use the HOMA (red color scale and white numbers in Figure 2d) here as a reference for our orbital-based analysis of aromaticity to be introduced later. While the HOMA is not the only yardstick of aromaticity,[11] other suggested criteria of aromaticity based on geometric, energetic, magnetic, and

https://dx.doi.org/10.1021/acsnano.0c06798
ACS Nano 2020, 14, 15766−15775

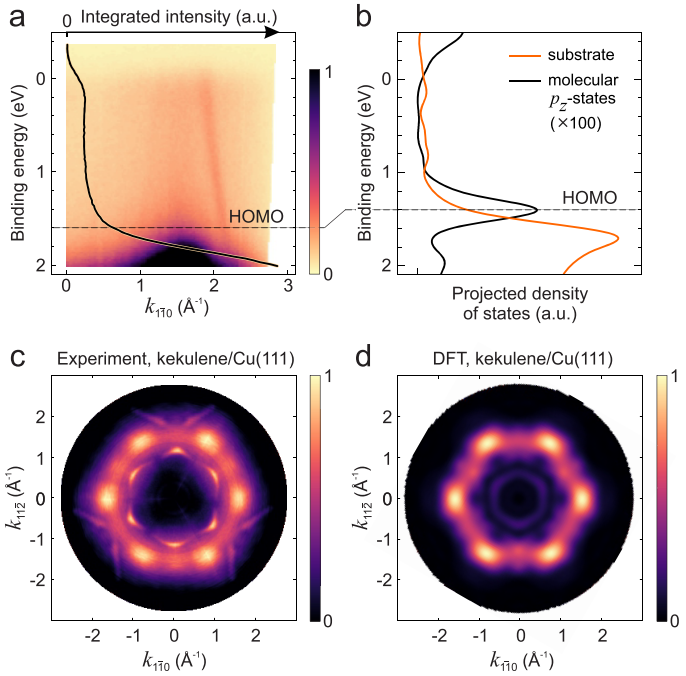

Figure 3. Angle-resolved photoemission data of kekulene/Cu(111) from experiment and theory. (a) ARPES band map along the [1$\bar{1}$0] direction in an energy range of about 2 eV below the Fermi edge. The black line shows an angle-integrated energy distribution curve. (b) Density of states projected onto substrate (orange) and molecular p_z states (black) from DFT. (c and d) Experimental and simulated momentum maps at the respective binding energies of the HOMO as indicated by the dashed lines in (a) and (b). Photoemission was excited by *p*-polarized light of 35 eV photon energy.

electronic properties of molecules are found to be in good correlation with the HOMA.[11,38,39] As an advantage of the HOMA concept, the partial equalization of bond lengths in aromatic systems, which is quantified by the HOMA value, can be easily obtained from DFT calculations. In addition, not only the aromaticity of the molecule as a whole but also the aromaticity of any cyclic conjugation path can be quantified, allowing, e.g., the separate description of local, peripheral and global aromaticities.[11] Here, we evaluate H for four conjugation paths of the surface-adsorbed kekulene molecule, namely for the two inequivalent sextets A (ring A in Figure 1a, H_A = 0.65) and B (ring B in Figure 1a, H_B = 0.92) as well as the [18]annulene and [30]annulene paths, respectively[40,41] ($H_{[18]}$ = 0.77 and $H_{[30]}$ = 0.80), each of which fulfills Hückel's $4n + 2$ condition of aromaticity and is therefore a possible candidate for affecting the aromatic stabilization of kekulene.

On the one hand, the HOMA values displayed in Figure 2d seem to indicate a propensity of kekulene toward Clar's limit as already noted by others,[3,5,11,19,21] because we observe that ring B exhibits the largest HOMA value (H_B = 0.92). On the other hand, this conclusion is not unambiguous, because with $H_{[30]}$ = 0.80, the [30]annulene path appears strongly aromatic as well. Also, the HOMA quite obviously exaggerates the peripheral aromaticity of kekulene, leading to the counter-intuitive result that the aromaticity of the larger [30]annulene path is predicted to be larger than the one of the smaller [18]annulene path, in contradiction to the Hückel rule, according to which π-systems with $4n + 2$ electrons are more stable for smaller n. Note, however, that such arguments, based on the Hückel molecular orbital method, might be oversimplified and neglect, for instance, the coupling between the two annulenes in kekulene. An overestimation of peripheral aromaticities is a well-known problem of the HOMA concept,[11] and it should be noted that there exist more sophisticated approaches to access the aromaticity of annulenes.[42] To conclude, from the purely structural deliberations, the relative importance of both postulated types of aromaticity in kekulene, Clar versus superaromatic model, cannot be inferred. Nevertheless, it is fair to state that the above findings regarding the HOMA assess the intrinsic aromaticity of kekulene, and in particular that the influence of the surface on the aromaticity of the adsorbed molecule is moderate (cf. SI, Table S4).

Photoemission Tomography. Up to this point, we solely concentrated on the analysis of aromaticity via bond lengths. However, aromaticity is an electronic stabilization of the molecule. To assess electronic properties of kekulene, we consult PT that can provide a complementary measure for aromaticity as we will show now.

In the experiment, a photoemission from a molecular state appears at the binding energy of 1.6 eV indicated by the dashed line in Figure 3a, i.e., only slightly above the onset of the Cu *d*-band, and is hence barely resolved in the energy distribution curve and band map. The computed projected density of states (pDOS) for kekulene/Cu(111) (Figure 3b) suggests that this emission can be assigned to the HOMO of kekulene, which, in the gas phase, belongs to the e_{1g} irreducible representation and is composed of a doubly degenerate state.

https://dx.doi.org/10.1021/acsnano.0c06798
ACS Nano 2020, 14, 15766−15775

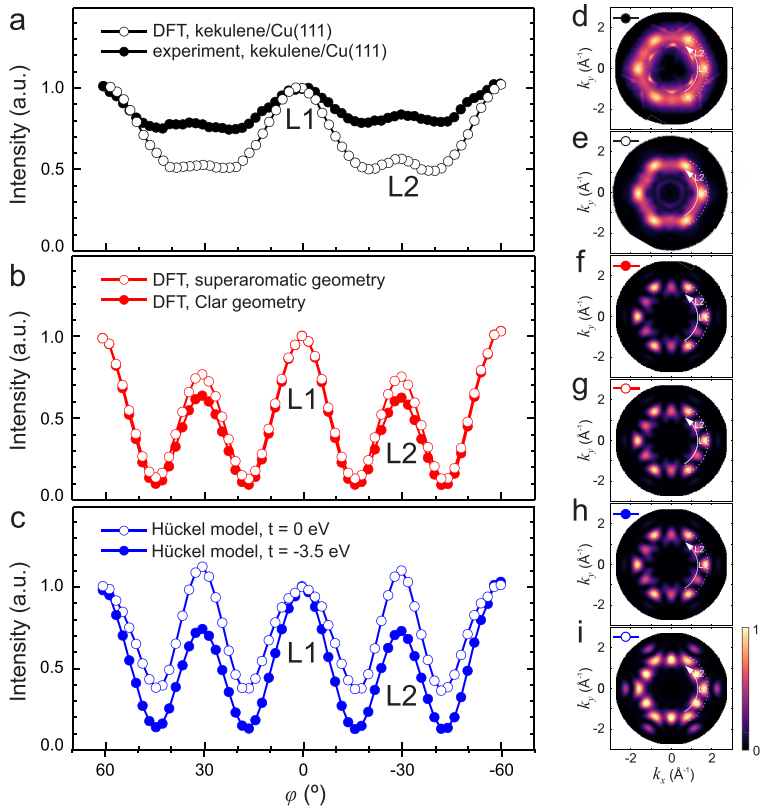

Figure 4. Comparison of experimental and simulated azimuthal ARPES intensity profiles of the kekulene HOMO. (a) Azimuthal profiles of the experiment (full symbols) and the DFT calculation of kekulene/Cu(111) (open symbols), extracted from the momentum maps shown in panels (d) and (e), respectively. (b) Simulated profiles from DFT gas-phase calculations of kekulene in the Clar geometry (full symbols) and superaromatic geometry (open symbols). The corresponding maps are shown in panels (f) and (g). (c) Simulated profiles from a Hückel model in which the coupling between inner and outer annulenes is set to $t = -3.5$ eV (full symbols) and to $t = 0$ (open symbols). The corresponding maps are shown in panels (h) and (i). Nonequivalent intensity lobes are labeled as L1 and L2. White lines in the momentum maps show the area used for intensity integration.

To confirm this assignment, we measure a momentum map of the photoemission intensity distribution at the respective constant binding energy. Figure 3c shows clear signatures of the molecule, namely six major lobes at $k_{\parallel} \approx 1.6$ Å^{-1} and six interjacent minor lobes at a slightly smaller $k_{\parallel} \approx 1.5$ Å^{-1}. In addition, the sharper features signal emissions from the copper *sp*-bands. The experimental momentum map is in excellent agreement with the simulated momentum map for the kekulene/Cu(111) HOMO at 1.4 eV depicted in Figure 3d. A number of conclusions can be drawn from this agreement: First, it unambiguously confirms the successful on-surface synthesis of kekulene on Cu(111) resulting in large (up to 100 nm, cf. SI, Figute S1) well-orientated domains. Second, the azimuthal alignment of the molecule, as already inferred from STM and DFT, is also confirmed by the photoemission data in which the sharp *sp*-band features indicate the substrate's orientation.

We now address the primary goal of our paper to demonstrate that PT, since it is directly related to the orbital structure of frontier molecular orbitals, provides substantial insights regarding the aromaticity of molecules. To this end, Figure 4 shows the experimental and various simulated HOMO momentum maps, and in particular, it compares azimuthal intensity profiles passing through the major (L1) and minor (L2) lobes of the HOMO momentum map. Panel (a) depicts the experimental intensity profile (filled symbols) and the corresponding simulation result for kekulene/Cu(111) (open symbols) extracted from the momentum maps already presented in Figure 3c and 3d, respectively, which are replicated here for convenience in Figure 4d and 4e. These intensity profiles confirm the qualitative agreement between theory and experiment. The barely comparable backgrounds of experimental and theoretical data for the states in the vicinity of the Cu *d*- and *sp*-bands prevent a full quantitative comparison of the intensity ratio between major and minor lobes.

In order to investigate how modifications in the geometry and/or electronic structure of kekulene are reflected in momentum maps of the HOMO emission, we next simulate momentum maps for the two idealized and extreme cases of the Clar and the superaromatic models of free kekulene, respectively. For the Clar model, we set $R_{sextet} = R_{opt}$, thus requiring maximal aromaticity of these sextets ($H_B = 1$). In contrast, for the superaromatic model we stipulate that all

https://dx.doi.org/10.1021/acsnano.0c06798
ACS Nano 2020, 14, 15766−15775

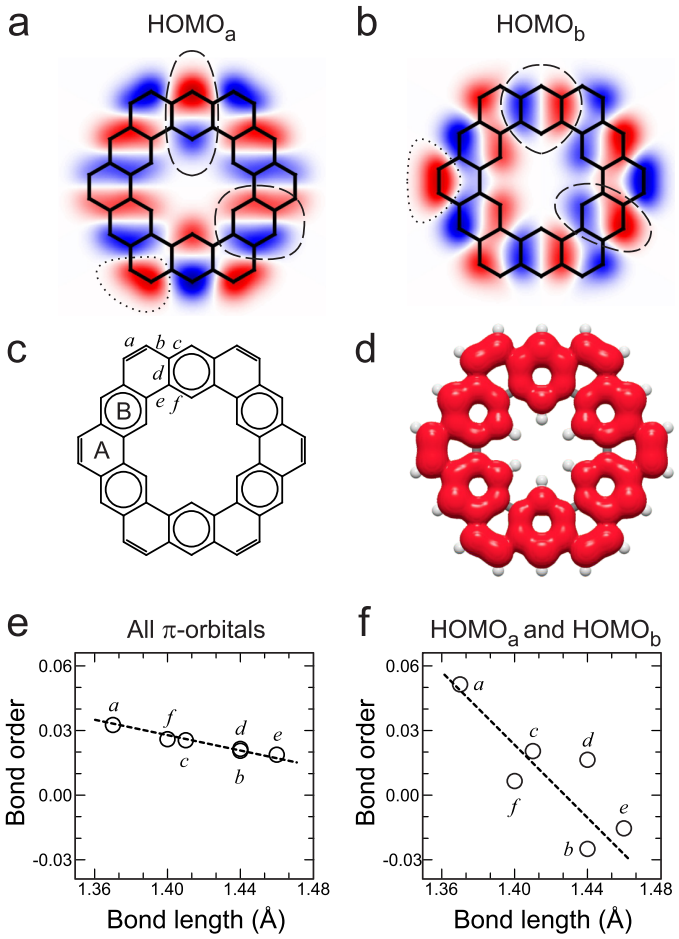

Figure 5. The frontier electronic structure of kekulene. (a and b) Nodal structure of the two degenerate orbitals comprising the HOMO, denoted HOMO$_a$ and HOMO$_b$, respectively, calculated with the Hückel model. (c) Chemical structure drawing of kekulene in the Clar model with six inequivalent C−C bonds labeled as *a* to *f*. (d) Charge density distribution of the HOMO (Hückel model). (e and f) Correlation between the C−C bond lengths of gas-phase kekulene as determined from DFT and a normalized bond order parameter from Hückel theory taking into account either all 24 occupied π-orbitals or only the degenerate HOMO (*m* = 23 to 24) orbital. Details are given in the text.

bonds in the annulene paths are identical, with $R_{[18]} = R_{[30]} = R_{opt} = 1.403$ Å to constrain that $H_{[18]} = H_{[30]} = 1$. Using these fixed geometries and neglecting the presence of the substrate, we employ DFT (cf. SI for details) to compute the orbital structure of the HOMO and the corresponding momentum maps for these two model geometries of free kekulene. Figure 4b displays the intensity profiles of these idealized Clar (full symbols) and superaromatic (open symbols) geometries, respectively. As is evident also from the corresponding momentum maps shown in Figure 4f and 4g, respectively, the overall symmetry and appearance of the momentum maps in Figure 4d and 4e as well as the fact that in Figure 4a the intensity of lobe L1 is considerably larger than that of lobe L2 are preserved in both model calculations. On the one hand, this can be taken as another indication that the interaction of kekulene with Cu(111) is rather weak and therefore neglecting the substrate completely when discussing the electronic structure of kekulene seems a reasonable approach (Yet, some discrepancies between the results of DFT simulations for the adsorbed and free kekulene exist, e.g., the background intensity in Figure 4a and b, and can be attributed to the effect of the substrate, namely a broadening of the molecular states due to the coupling to the metal states as well as additional emission from the substrate.) On the other hand, and more importantly, when changing from the Clar to the superaromatic geometry, we notice only moderate changes in the orbital structure of the HOMO observed as an ∼10% increase in the intensity of the minor lobe L2. It is important to note that this finding is insensitive to the choice for the exchange-correlation functional, even when incorporating a substantial fraction of Hartree−Fock exchange (cf. SI, Figure S3). Thus, from our DFT calculations it becomes evident that changing the geometry of the molecular backbone (bond lengths) from Clar-type to superaromatic does not affect the electronic

https://dx.doi.org/10.1021/acsnano.0c06798
ACS Nano 2020, 14, 15766−15775

system of kekulene profoundly. Generally speaking, this means that small variations in the geometric structure of the molecule, i.e., a system with an energy gap, does not change the nodal structure of the wave function. This noteworthy fact is illustrated in Figure S7 (cf. SI), where we compare the orbital structure of the kekulene's HOMO and HOMO−1 as obtained for the Clar and the superaromatic geometry.

Therefore, in order to impose the superaromatic stabilization by the annulene conjugation paths, we approximate the π-electron system of kekulene with a simple Hückel model.[43] This approach provides a way to tune the coupling between the inner [18]annulene path and the outer [30]annulene path by adjusting the hopping parameter t for corresponding bonds connecting them (see SI for details). In particular, a value of $t = -3.5$ eV leads to approximately the DFT result for free kekulene, as evidenced by the HOMO momentum map depicted in Figure 4h and the corresponding azimuthal intensity profile shown in Figure 4c (full symbols). If the coupling between the annulenes is completely suppressed ($t = 0$), the doubly degenerate HOMO is now concentrated exclusively around the outer [30]annulene path (cf. SI, Figure S7d,h) and could indeed be termed "superaromatic" from an electronic structure point of view. As can be seen from Figure 4i (cf. also SI, Figure S7l), the corresponding momentum map is also markedly different. The formerly minor lobe L2 is almost doubled in intensity and becomes the brightest feature. Also, there are six additional lobes at larger $k_{\parallel} \approx 2.1$ Å^{-1} which are a result of the confinement of the electrons to only the outer annulene path, leading to a larger spread in momentum space. None of these signatures are observed in the experimental momentum map of the HOMO (compare Figure 4d or 3c). Thus, we conclude that photoemission tomography indeed excludes a superaromatic state. Instead, all PT evidence points toward the Clar model also from an electronic structure perspective.

CONCLUSIONS

It remains to be clarified how exactly the orbital structure of the HOMO alone, as accessible via photoemission tomography, may serve as a sufficient measure for the aromaticity of kekulene, apparently not requiring the consideration of all π-electrons, i.e., including those in deeper-lying orbitals. To approach this question, we employ the Hückel model with $t = -3.5$ eV and analyze the orbital structures of the doubly degenerate HOMO of kekulene, denoted as HOMO$_a$ and HOMO$_b$ (Figure 5a and 5b). We observe that the electrons in the HOMO are confined to neither the inner nor the outer annulene path. Instead, the frontier electrons are delocalized over both annulene paths, and the pattern of this delocalization is already a portent of the Clar model, as a straightforward visual inspection of the electron distribution in HOMO$_a$ and HOMO$_b$ in Figure 5a and 5b shows: locally, the pair of kekulene HOMOs consists of benzene-like HOMOs (marked by the dashed lines in Figure 5a and 5b) which are located at exactly those carbon rings (ring B) where the Clar model predicts aromatic sextets (Figure 5c), while a pronounced double bond lobe appears at the corners of kekulene (marked by dotted lines in Figure 5a and 5b). The Clar structure also becomes clearly apparent when computing the charge density as a sum of HOMO$_a$ and HOMO$_b$ electron distributions (Figure 5d) and comparing it with a chemical structure drawing of the Clar model of kekulene (Figure 5c): the six disjoint aromatic sextets characteristic for the Clar model can be recognized in the charge distribution of the HOMO, as well as the isolated double bonds at the corners. The evolution of kekulene's HOMO from the doubly degenerate HOMO and HOMO−1 of concentric but initially electronically decoupled [18]-annulene and [30]annulene as the coupling is turned on, shown as a video in the SI, reveals that its Clar-like structure is in fact an immediate consequence of the interannulene coupling in kekulene and its effect on the frontier orbitals.

The significance of the HOMO for the aromaticity of kekulene is confirmed by considering its contribution to the bond order. In general, the bond order relates orbital structure to the bond lengths in a π-conjugated molecule, and thus also to structure-derived aromaticity parameters such as the HOMA values. We define a bond order parameter b_{ij}, which we normalize by the number of contributing π-electrons N, for a given bond between carbon atoms labeled i and j in the following way:[44]

$$b_{ij} = \frac{2}{N}\sum_{m=1}^{N} a_i(m)\, a_j(m) \tag{2}$$

Here, $a_i(m)$ is the contribution of the p_z orbital at carbon atom i to the molecular orbital m, as resulting from the solution of the Hückel model. If all 24 occupied π-orbitals of kekulene are included in the summation of eq 2, i.e., $m = 1$ to 24, plotting the bond order parameter against the DFT-optimized bond lengths for kekulene yields a clear and almost linear correlation (Figure 5e). This indicates that through the bond order parameter the nodal patterns of *all* occupied orbitals together determine the final bond lengths and thus also the HOMA-derived aromaticity in kekulene. For example, all occupied π-orbitals together lead to a large bond order for bond a (cf. Figure 5c,e), which therefore is short (DFT-calculated value of $d_a = 1.37$ Å) and can be interpreted as having a strong double bond character, while bond e with its smaller bond order is longer (DFT-calculated value of $d_e = 1.46$ Å) and thus appears to be more of single bond character. However, there is also a pronounced correlation if we only include the doubly degenerate HOMO$_a$ and HOMO$_b$ in the summation ($m =$ 23 to 24, Figure 5f). This reveals that the correct bond order pattern is already present in the occupied frontier orbital. It is therefore not surprising that the nodal patterns of the HOMO, which we measure in PT, are indicative of kekulene's aromaticity. Indeed, the shortest C−C bond (bond a) has a strong contribution of the HOMO charge density, while the longest C−C bond (bond e) does not (cf. Figure 5d). The disproportionate effect of the uppermost occupied π-orbitals to produce the final linear trend observed in Figure 5e also becomes apparent if only the lower half of the occupied π-states ($m = 1$ to 12) is included in the summation of eq 2, because then the trend is completely reversed (cf. SI, Figure S8a). Interestingly, if the interannulene coupling is switched off ($t = 0$), then the resulting bond order suggests all bonds to be of equal lengths, which is indeed the case if one was to optimize the structure of individual [18]annulene or individual [30]annulene paths.

In summary, we present an efficient on-surface synthesis route with a high reaction yield resulting in a well-oriented monolayer of kekulene on Cu(111). This allows us to apply the photoemission tomography technique to directly address the symmetry and spatial structure of the charge distribution of the frontier kekulene electronic level, its degenerate HOMO.

https://dx.doi.org/10.1021/acsnano.0c06798
ACS Nano 2020, 14, 15766−15775

By comparing the experimental momentum map of the HOMO with photoemission simulations for kekulene in various geometric and electronic states, we analyze the aromaticity of kekulene. We find that imposing either the Clar- or the superaromatic-type geometry influences the nodal structure of the two degenerate HOMO components only very slightly and, accordingly, leaves the simulated photoemission maps mainly unaffected. Only when suppressing the coupling of the π-electron system between two annulene paths, as we demonstrate within the Hückel molecular orbital model, a true superaromatic state characterized by a spatial confinement of the HOMO electron density to the outer annulene, accompanied by a pronounced change in the photoemission momentum map, can be mimicked (cf. SI, Figure S7). This comparison between measured and simulated momentum maps rules out a superaromatic state in kekulene but rather favors a Clar-type structure. Our work demonstrates that the spatial structure of occupied frontier orbitals can indeed be taken as a valid yardstick for the aromaticity of π-conjugated molecules and that photoemission tomography is a powerful complementary method to assess the role of aromatic stabilization in π-conjugated molecules.

METHODS AND EXPERIMENTAL DETAILS

The synthesis of the precursor **5** starts with commercially available 9,10-dihydrophenanthrene (**1**), which was regioselectively brominated to form 2,7-dibromo-9,10-dihydrophenanthrene (**2**) by applying a procedure of Wang et al.[45] using bromine in the absence of light. Compound **2** was oxidatively aromatized to the corresponding 2,7-dibromophen-anthrene (**3**). Subsequently, the latter was converted into bis-aldehyde (**4**) via Br−Li exchange at low temperature using *n*-butyl lithium and trapping the lithiated intermediate with dimethylformamide (DMF) and aqueous workup. Aldehyde **4** was coupled in the last step to kekulene precursor **5** using a McMurry reaction protocol established for related targets by Majewski et al.[22] This protocol requires dropwise addition of **4** to a diluted reaction solution of low-valent titanium reagent formed *in situ* from titanium tetrachloride and zinc.

The kekulene precursor **5** could be obtained as a beige crystalline solid in 35% yield next to higher oligomers of **4** via purification by column chromatography followed by recrystallization. The molecular structure and conformation of **5** were proven by X-ray crystallography (Figure 1b). X-ray diffractive single crystals of **5** were obtained by slow diffusion of *n*-pentane into a saturated solution of **5** in chloroform. Details of chemical synthesis and characterization of **5** are provided in the SI.

The preparation of kekulene/Cu(111), photoemission, and STM experiments were performed in an ultrahigh vacuum system with a base pressure in the 10^{-10} mbar range. Samples of Cu(111) were cleaned by repeating cycles of sputtering by Ar^+ ions (1.0 kV) and annealing (850 K). The molecular precursor **5** was deposited from a Knudsen-type effusion cell at 550 K onto the Cu(111) surface kept at room temperature. To trigger the reaction of cyclodehydrogenation resulting in kekulene, submonolayer films of **5** on Cu(111) were annealed at 500 K.

STM was performed with an STM Aarhus 150 microscope from SPECS GmbH. During measurements the samples were kept at 100 K.

ARPES and PT were conducted at the Metrology Light Source insertion device[46] beamline of the Physikalisch-Technische Bundesanstalt (PTB, Germany). *p*-Polarized ultraviolet light (35 eV photon energy) was used with the angle of incidence of 40°. Photoelectrons were collected with the toroidal electron spectrometer.[47] For the experimental spectrum, band map, and momentum map shown in Figure 3, the photoemission intensity in the emission angle range from 0° (sample normal) to +85° was used. Momentum maps were recorded by rotating the sample in the azimuthal direction in 2° steps and measuring the photoemission intensity at a constant kinetic energy of the electrons. This results in the full photoelectron distribution in the (k_x, k_y) plane perpendicular to the sample normal.

Details about the DFT calculations and the photoemission tomography simulations are given in the SI.

ASSOCIATED CONTENT

Supporting Information

The Supporting Information is available free of charge at https://pubs.acs.org/doi/10.1021/acsnano.0c06798.

Experimental details, details of chemical synthesis, kekulene/Cu(111) sample preparation, STM, ARPES and PT, details of computational analysis. (PDF)

video demonstrating the effect of electronic coupling between inner and outer annulene paths on the HOMO and HOMO−1 states of free kekulene (MP4)

SWP148.pdf and swp148loesen.cif: CIF check and CIF files for kekulene precursor 1,4,7(2,7)-triphenanthrenacyclononaphane-2,5,8-triene. (CIF)

AUTHOR INFORMATION

Corresponding Authors

Michael Rohlfing − *Institut für Festkörpertheorie, Westfälische Wilhelms-Universität Münster, 48149 Münster, Germany*; Email: michael.rohlfing@uni-muenster.de

Peter Puschnig − *Institut für Physik, Karl-Franzens-Universität Graz, NAWI Graz, 8010 Graz, Austria*; orcid.org/0000-0002-8057-7795; Email: peter.puschnig@uni-graz.at

J. Michael Gottfried − *Fachbereich Chemie, Philipps-Universität Marburg, 35032 Marburg, Germany*; orcid.org/0000-0001-5579-2568; Email: michael.gottfried@chemie.uni-marburg.de

Serguei Soubatch − *Peter Grünberg Institut (PGI-3), Forschungszentrum Jülich, 52425 Jülich, Germany; Jülich Aachen Research Alliance (JARA), Fundamentals of Future Information Technology, 52425 Jülich, Germany*; orcid.org/0000-0002-1455-0260; Email: s.subach@fz-juelich.de

Authors

Anja Haags − *Peter Grünberg Institut (PGI-3), Forschungszentrum Jülich, 52425 Jülich, Germany; Jülich Aachen Research Alliance (JARA), Fundamentals of Future Information Technology, 52425 Jülich, Germany; Experimentalphysik IV A, RWTH Aachen University, 52074 Aachen, Germany*

Alexander Reichmann − *Institut für Physik, Karl-Franzens-Universität Graz, NAWI Graz, 8010 Graz, Austria*

Qitang Fan − *Fachbereich Chemie, Philipps-Universität Marburg, 35032 Marburg, Germany*

Larissa Egger − *Institut für Physik, Karl-Franzens-Universität Graz, NAWI Graz, 8010 Graz, Austria*

Hans Kirschner − *Physikalisch-Technische Bundesanstalt (PTB), 10587 Berlin, Germany*

Tim Naumann − *Fachbereich Chemie, Philipps-Universität Marburg, 35032 Marburg, Germany*

Simon Werner − *Fachbereich Chemie, Philipps-Universität Marburg, 35032 Marburg, Germany*

Tobias Vollgraff − *Fachbereich Chemie, Philipps-Universität Marburg, 35032 Marburg, Germany*

Jörg Sundermeyer − *Fachbereich Chemie, Philipps-Universität Marburg, 35032 Marburg, Germany*

https://dx.doi.org/10.1021/acsnano.0c06798
ACS Nano 2020, 14, 15766−15775

Lukas Eschmann – *Institut für Festkörpertheorie, Westfälische Wilhelms-Universität Münster, 48149 Münster, Germany*
Xiaosheng Yang – *Peter Grünberg Institut (PGI-3), Forschungszentrum Jülich, 52425 Jülich, Germany; Jülich Aachen Research Alliance (JARA), Fundamentals of Future Information Technology, 52425 Jülich, Germany; Experimentalphysik IV A, RWTH Aachen University, 52074 Aachen, Germany;* orcid.org/0000-0002-7632-0401
Dominik Brandstetter – *Institut für Physik, Karl-Franzens-Universität Graz, NAWI Graz, 8010 Graz, Austria*
François C. Bocquet – *Peter Grünberg Institut (PGI-3), Forschungszentrum Jülich, 52425 Jülich, Germany; Jülich Aachen Research Alliance (JARA), Fundamentals of Future Information Technology, 52425 Jülich, Germany*
Georg Koller – *Institut für Physik, Karl-Franzens-Universität Graz, NAWI Graz, 8010 Graz, Austria;* orcid.org/0000-0001-7741-2394
Alexander Gottwald – *Physikalisch-Technische Bundesanstalt (PTB), 10587 Berlin, Germany*
Mathias Richter – *Physikalisch-Technische Bundesanstalt (PTB), 10587 Berlin, Germany*
Michael G. Ramsey – *Institut für Physik, Karl-Franzens-Universität Graz, NAWI Graz, 8010 Graz, Austria*
F. Stefan Tautz – *Peter Grünberg Institut (PGI-3), Forschungszentrum Jülich, 52425 Jülich, Germany; Jülich Aachen Research Alliance (JARA), Fundamentals of Future Information Technology, 52425 Jülich, Germany; Experimentalphysik IV A, RWTH Aachen University, 52074 Aachen, Germany*

Complete contact information is available at: https://pubs.acs.org/10.1021/acsnano.0c06798

Author Contributions

[@]A.H., A.R., and Q.F. contributed equally to this work.

Notes

The authors declare no competing financial interest.
The preprint version is available online.[48]
Raw data are available at the Jülich DATA public repository.[49]

ACKNOWLEDGMENTS

Financial support from the Deutsche Forschungsgemeinschaft (DFG) (Projects Po 2226/2-1, Ri 804/8-1, Go 1812/2-1, 223848855-SFB 1083 "Structure and Dynamics of Internal Interfaces") and the Austrian Science Fund (FWF) (Projects P27649-N20, P27427-N20, and I3731) is gratefully acknowledged. The computational results have been achieved using the computing facilities of the University of Graz and the Vienna Scientific Cluster (VSC3), as well as those of the John von Neumann Institute for Computing (NIC) on the GCS Supercomputer JUWELS at Jülich Supercomputing Centre (JSC). We thank Hendrik Kaser (PTB, Berlin) and John Riley (La Trobe University, Australia) for experimental support.

REFERENCES

(1) Balaban, A. T. Is Aromaticity Outmoded ? *Pure Appl. Chem.* **1980**, *52*, 1409–1429.
(2) Kekulé, M. A. Sur la Constitution des Substances Aromatique. *Bulletin mensuel de la Société chimique de Paris* **1865**, *3*, 98.
(3) Aihara, J.-i. On the Number of Aromatic Sextets in a Benzenoid Hydrocarbon. *Bull. Chem. Soc. Jpn.* **1976**, *49*, 1429–1430.
(4) Cioslowski, J.; Mixon, S. T.; Edwards, W. D. Weak Bonds in the Topological Theory of Atoms in Molecules. *J. Am. Chem. Soc.* **1991**, *113*, 1083–1085.
(5) Aihara, J.-i. Is Superaromaticity a Fact or an Artifact? The Kekulene Problem. *J. Am. Chem. Soc.* **1992**, *114*, 865–868.
(6) Jiao, H.; von Ragué Schleyer, P. Is Kekulene Really Superaromatic? *Angew. Chem., Int. Ed. Engl.* **1996**, *35*, 2383–2386.
(7) Zhou, Z. Are Kekulene, Coronene, and Corannulene Tetraanion Superaromatic? Theoretical Examination Using Hardness Indices. *J. Phys. Org. Chem.* **1995**, *8*, 103–107.
(8) Aihara, J.-i.; Makino, M.; Ishida, T.; Dias, J. R. Analytical Study of Superaromaticity in Cycloarenes and Related Coronoid Hydrocarbons. *J. Phys. Chem. A* **2013**, *117*, 4688–4697.
(9) Aihara, J.-i. A Simple Method for Estimating the Superaromatic Stabilization Energy of a Super-Ring Molecule. *J. Phys. Chem. A* **2008**, *112*, 4382–4385.
(10) Buttrick, J. C.; King, B. T. Kekulenes, Cycloarenes, and Heterocycloarenes: Addressing Electronic Structure and Aromaticity through Experiments and Calculations. *Chem. Soc. Rev.* **2017**, *46*, 7–20.
(11) Setiawan, D.; Kraka, E.; Cremer, D. Quantitative Assessment of Aromaticity and Antiaromaticity Utilizing Vibrational Spectroscopy. *J. Org. Chem.* **2016**, *81*, 9669–9686.
(12) Lahti, P. M. Localization of Aromaticity in Fused-Ring Cycloarene Systems. Prediction by an Effective Molecular Mechanics Model. *J. Org. Chem.* **1988**, *53*, 4590–4593.
(13) Allinger, N. L.; Li, F.; Yan, L.; Tai, J. C. Molecular Mechanics (MM3) Calculations on Conjugated Hydrocarbons. *J. Comput. Chem.* **1990**, *11*, 868–895.
(14) Liu, C.; Ni, Y.; Lu, X.; Li, G.; Wu, J. Global Aromaticity in Macrocyclic Polyradicaloids: Hückel's Rule or Baird's Rule? *Acc. Chem. Res.* **2019**, *52*, 2309–2321.
(15) Chen, Z.; King, R. B. Spherical Aromaticity: Recent Work on Fullerenes, Polyhedral Boranes, and Related Structures. *Chem. Rev.* **2005**, *105*, 3613–3642.
(16) Miyoshi, H.; Nobusue, S.; Shimizu, A.; Tobe, Y. Non-Alternant Non-Benzenoid Kekulenes: The Birth of a New Kekulene Family. *Chem. Soc. Rev.* **2015**, *44*, 6560–6577.
(17) Clar, E. *The Aromatic Sextet*; Wiley: London, 1972; p 74.
(18) Diederich, F.; Staab, H. A. Benzenoid *versus* Annulenoid Aromaticity: Synthesis and Properties of Kekulene. *Angew. Chem., Int. Ed. Engl.* **1978**, *17*, 372–374.
(19) Krieger, C.; Diederich, F.; Schweitzer, D.; Staab, H. A. Molecular Structure and Spectroscopic Properties of Kekulene. *Angew. Chem., Int. Ed. Engl.* **1979**, *18*, 699–701.
(20) Staab, H. A.; Diederich, F.; Krieger, C.; Schweitzer, D. Molecular Structure and Spectroscopic Properties of Kekulene. *Chem. Ber.* **1983**, *116*, 3504–3512.
(21) Pozo, I.; Majzik, Z.; Pavliček, N.; Melle-Franco, M.; Guitián, E.; Peña, D.; Gross, L.; Pérez, D. Revisiting Kekulene: Synthesis and Single-Molecule Imaging. *J. Am. Chem. Soc.* **2019**, *141*, 15488–15493.
(22) Majewski, M. A.; Hong, Y.; Lis, T.; Gregoliński, J.; Chmielewski, P. J.; Cybińska, J.; Kim, D.; Stępień, M. Octulene: A Hyperbolic Molecular Belt that Binds Chloride Anions. *Angew. Chem., Int. Ed.* **2016**, *55*, 14072–14076.
(23) Puschnig, P.; Berkebile, S.; Fleming, A. J.; Koller, G.; Emtsev, K.; Seyller, T.; Riley, J. D.; Ambrosch-Draxl, C.; Netzer, F. P.; Ramsey, M. G. Reconstruction of Molecular Orbital Densities from Photoemission Data. *Science* **2009**, *326*, 702–706.
(24) Puschnig, P.; Reinisch, E. M.; Ules, T.; Koller, G.; Soubatch, S.; Ostler, M.; Romaner, L.; Tautz, F. S.; Ambrosch-Draxl, C.; Ramsey, M. G. Orbital Tomography: Deconvoluting Photoemission Spectra of Organic Molecules. *Phys. Rev. B: Condens. Matter Mater. Phys.* **2011**, *84*, 235427.
(25) Puschnig, P.; Ramsey, M. G. In *Encyclopedia of Interfacial Chemistry: Surface Science and Electrochemistry*; Wandelt, K., Ed.; Elsevier Science: Oxford, 2018; pp 380–391.
(26) Lüftner, D.; Ules, T.; Reinisch, E. M.; Koller, G.; Soubatch, S.; Tautz, F. S.; Ramsey, M. G.; Puschnig, P. Imaging the Wave Functions of Adsorbed Molecules. *Proc. Natl. Acad. Sci. U. S. A.* **2014**, *111*, 605–610.

https://dx.doi.org/10.1021/acsnano.0c06798
ACS Nano 2020, 14, 15766–15775

(27) Lüftner, D.; Weiß, S.; Yang, X.; Hurdax, P.; Feyer, V.; Gottwald, A.; Koller, G.; Soubatch, S.; Puschnig, P.; Ramsey, M. G.; Tautz, F. S. Understanding the Photoemission Distribution of Strongly Interacting Two-Dimensional Overlayers. *Phys. Rev. B: Condens. Matter Mater. Phys.* **2017**, *96*, 125402.
(28) Wießner, M.; Hauschild, D.; Sauer, C.; Feyer, V.; Schöll, A.; Reinert, F. Complete Determination of Molecular Orbitals by Measurement of Phase Symmetry and Electron Density. *Nat. Commun.* **2014**, *5*, 4156.
(29) Weiß, S.; Lüftner, D.; Ules, T.; Reinisch, E. M.; Kaser, H.; Gottwald, A.; Richter, M.; Soubatch, S.; Koller, G.; Ramsey, M. G.; Tautz, F. S.; Puschnig, P. Exploring Three-Dimensional Orbital Imaging with Energy-Dependent Photoemission Tomography. *Nat. Commun.* **2015**, *6*, 8287.
(30) Yang, X.; Egger, L.; Hurdax, P.; Kaser, H.; Lüftner, D.; Bocquet, F. C.; Koller, G.; Gottwald, A.; Tegeder, P.; Richter, M.; Ramsey, M. G.; Puschnig, P.; Soubatch, S.; Tautz, F. S. Identifying Surface Reaction Intermediates with Photoemission Tomography. *Nat. Commun.* **2019**, *10*, 3189.
(31) Graus, M.; Grimm, M.; Metzger, C.; Dauth, M.; Tusche, C.; Kirschner, J.; Kümmel, S.; Schöll, A.; Reinert, F. Electron-Vibration Coupling in Molecular Materials: Assignment of Vibronic Modes from Photoelectron Momentum Mapping. *Phys. Rev. Lett.* **2016**, *116*, 1−5.
(32) Kliuiev, P.; Zamborlini, G.; Jugovac, M.; Gurdal, Y.; Arx, K. V.; Waltar, K.; Schnidrig, S.; Alberto, R.; Iannuzzi, M.; Feyer, V.; Hengsberger, M.; Osterwalder, J.; Castiglioni, L. Combined Orbital Tomography Study of Multi-Configurational Molecular Adsorbate Systems. *Nat. Commun.* **2019**, *10*, 5255.
(33) Kruszewski, J.; Krygowski, T. M. Definition of Aromaticity Basing on the Harmonic Oscillator Model. *Tetrahedron Lett.* **1972**, *13*, 3839−3842.
(34) Krygowski, T. M. Crystallographic Studies of Inter- and Intramolecular Interactions Reflected in Aromatic Character of π-Electron Systems. *J. Chem. Inf. Model.* **1993**, *33*, 70−78.
(35) Krygowski, T. M.; Cyrański, M. Separation of the Energetic and Geometric Contributions to the Aromaticity of π-Electron Carbocyclics. *Tetrahedron* **1996**, *52*, 1713−1722.
(36) Krygowski, T. M.; Cyrański, M. Separation of the Energetic and Geometric Contributions to the Aromaticity. Part IV. A General Model for the π-Electron Systems. *Tetrahedron* **1996**, *52*, 10255−10264.
(37) Setiawan, D.; Kraka, E.; Cremer, D. Hidden Bond Anomalies: The Peculiar Case of the Fluorinated Amine Chalcogenides. *J. Phys. Chem. A* **2015**, *119*, 9541−9556.
(38) Firme, C. L.; Galembeck, S. E.; Antunes, O. A.; Esteves, P. M. Density, Degeneracy, Delocalization-Based Index of Aromaticity (D_3BIA). *J. Braz. Chem. Soc.* **2007**, *18*, 1397−1404.
(39) Araújo, D. M.; da Costa, T. F.; Firme, C. L. Validation of the Recently Developed Aromaticity Index D3BIA for Benzenoid Systems. Case Study: Acenes. *J. Mol. Model.* **2015**, *21*, 248.
(40) Stępień, M. An Aromatic Riddle: Decoupling Annulene Conjugation in Coronoid Macrocycles. *Chem.* **2018**, *4*, 1481−1483.
(41) Aihara, J.-i. Validity and Limitations of the Annulene-Within-An-Annulene (AWA) Model for Macrocyclic π-Systems. *RSC Adv.* **2014**, *4*, 7256−7265.
(42) Casademont-Reig, I.; Ramos-Cordoba, E.; Torrent-Sucarrat, M.; Matito, E. How Do the Hückel and Baird Rules Fade Away in Annulenes? *Molecules* **2020**, *25*, 711.
(43) Hückel, E. Die freien Radikale der organischen Chemie. *Z. Physik* **1933**, *83*, 632−668.
(44) Coulson, C. A. The Electronic Structure of Some Polyenes and Aromatic Molecules VII. Bonds of Fractional Order by the Molecular Orbital Method. *Proc. R. Soc. London* **1939**, *169*, 413−428.
(45) Tian, H.; Shi, J.; Dong, S.; Yan, D.; Wang, L.; Geng, Y.; Wang, F. Novel Highly Stable Semiconductors Based on Phenanthrene for Organic Field-Effect Transistors. *Chem. Commun.* **2006**, 3498−3500.
(46) Gottwald, A.; Kaser, H.; Kolbe, M. The U125 Insertion Device Beamline at the Metrology Light Source. *J. Synchrotron Radiat.* **2019**, *26*, 535−542.
(47) Broekman, L.; Tadich, A.; Huwald, E.; Riley, J.; Leckey, R.; Seyller, T.; Emtsev, K.; Ley, L. First Results From a Second Generation Toroidal Electron Spectrometer. *J. Electron Spectrosc. Relat. Phenom.* **2005**, *144−147*, 1001−1004.
(48) Haags, A.; Reichmann, A.; Fan, Q.; Egger, L.; Kirschner, H.; Naumann, T.; Werner, S.; Vollgraff, T.; Sundermeyer, J.; Eschmann, L.; Yang, X.; Brandstetter, D.; Bocquet, F. C.; Koller, G.; Gottwald, A.; Richter, M.; Ramsey, M. G.; Rohlfing, M.; Puschnig, P.; Gottfried, J. M.; et al. *Kekulene: On-Surface Synthesis, Orbital Structure, and Aromatic Stabilization*, 2020, 12771254, ChemRxiv. https://doi.org/DOI: 10.26434/chemrxiv.12771254.v1, Accessed: August 07, 2020.
(49) Haags, A.; Reichmann, A.; Fan, Q.; Egger, L.; Kirschner, H.; Naumann, T.; Werner, S.; Vollgraff, T.; Sundermeyer, J.; Eschmann, L.; Yang, X.; Brandstetter, D.; Bocquet, F. C.; Koller, G.; Gottwald, A.; Richter, M.; Ramsey, M. G.; Rohlfing, M.; Puschnig, P.; Gottfried, J. M.; Soubatch, S.; Tautz, F. S. Data used in: "*Kekulene: On-Surface Synthesis, Orbital Structure, and Aromatic Stabilization*", 2020, Jülich DATA, https://doi.org/10.26165/JUELICH-DATA/UVHBRU.

https://dx.doi.org/10.1021/acsnano.0c06798
ACS Nano 2020, 14, 15766−15775

Supporting Information for

Kekulene: On-Surface Synthesis, Orbital Structure, and Aromatic Stabilization

Anja Haags[1,2,3‡], Alexander Reichmann[4‡], Qitang Fan[5‡], Larissa Egger[4], Hans Kirschner[6], Tim Naumann[5], Simon Werner[5], Tobias Vollgraff[5], Jörg Sundermeyer[5], Lukas Eschmann[7], Xiaosheng Yang[1,2,3], Dominik Brandstetter[4], François C. Bocquet[1,2], Georg Koller[4], Alexander Gottwald[6], Mathias Richter[6], Michael G. Ramsey[4], Michael Rohlfing[7], Peter Puschnig[4], J. Michael Gottfried[5], Serguei Soubatch[1,2], and F. Stefan Tautz[1,2,3]

[1] Peter Grünberg Institut (PGI-3), Forschungszentrum Jülich, 52425 Jülich, Germany
[2] Jülich Aachen Research Alliance (JARA), Fundamentals of Future Information Technology, 52425 Jülich, Germany
[3] Experimental Physics IV A, RWTH Aachen University, 52074 Aachen, Germany
[4] Institute of Physics, University of Graz, NAWI Graz, 8010 Graz, Austria
[5] Fachbereich Chemie, Philipps-Universität Marburg, Hans-Meerwein-Straße 4, 35032 Marburg, Germany
[6] Physikalisch-Technische Bundesanstalt (PTB), 10587 Berlin, Germany
[7] Institut für Festkörpertheorie, Westfälische Wilhelms-Universität Münster, 48149 Münster, Germany

[‡] A.H., A.R., and Q.F. contributed equally to this work.

S1. Details of the synthesis

S1.1. Synthesis route

The precursor for the dehydrogenative synthesis of kekulene on Cu(111) was obtained in four steps. Starting with 9,10-dihydrophenanthrene (**1**), a regioselective bromination to 2,7-dibromo-9,10-dihydrophenanthrene (**2**) was accomplished using a protocol of Tian *et al*.[S1.1]. This was oxidatively aromatized to the corresponding 2,7-dibromophenanthrene (**3**). **3** was subsequently converted into bis-aldehyde (**4**), which was oligomerized in the last step to the kekulene precursor **5** using a McMurry reaction protocol for similar reactions established by Majewski *et al*.[S1.2]. The synthesis strategy is shown in Figure 1a.

Single crystals of **5** appropriate for X-ray diffraction study were obtained by slow diffusion of *n*-pentane in a saturated solution of **5** in chloroform. The molecular structure of **5** derived from X-ray diffraction is shown in Figure 1b (top). In solid state, the three phenanthrene moieties of **5** are rotated out of the molecular plane made up by the double bonds. As a consequence, **5** has a highly distorted nonplanar geometry. The solid state packing of **5** (Figure 1b, bottom) is driven by π-stacking interactions of the phenanthrene moieties with intermolecular distances of 3.34 Å between the carbon atoms of neighbored molecules, which is only little larger than the interlayer distance in graphite (equilibrium interlayer distance is 3.231 Å [S1.3]).

S1.2. General Information

All reactions were carried out under inert atmosphere of nitrogen using Schlenk techniques, if not mentioned otherwise. All reagents were purchased from commercial sources, if not mentioned otherwise, and were used without further purification. For thin-layer chromatography (TLC), TLC plates from Merck KGaA with silica gel 60 on aluminum with fluorescence-quenching F254 at room temperature were used. All solvents were dried and/or purified according to standard procedures and stored over 3 Å or 4 Å molecular sieves. Nuclear magnetic resonance (NMR) spectra were recorded in automation or by the service department (Department of Chemistry, Philipps University Marburg, Germany) with a Bruker Avance 300 or 500 spectrometer at 298 K using CD_2Cl_2 or $CDCl_3$ as solvent and for calibration (residual proton signals). High-resolution atmospheric pressure chemical ionization (HR-APCI) mass spectra were acquired with a LTQ-FT Ultra mass spectrometer (Thermo Fischer Scientific). The resolution was set to 100000. High-resolution electron ionization (HR-EI) mass spectra were acquired with a AccuTOF GCv 4G (JEOL) time-of-flight (TOF) mass spectrometer. An internal or external standard was used for drift time correction. The liquid injection field desorption ionization (LIFDI) ion source and field desorption (FD) emitters were purchased from Linden ChroMasSpec GmbH (Bremen, Germany). The data collection for the single-crystal structure determination was performed on a Stoe Stadivari diffractometer or a Bruker D8 Quest diffractometer (X-ray Service Department, Philipps University Marburg, Germany). Information concerning the hardware and software used for data collection, cell refinement and data reduction as well as structure solution and refinement can be reviewed in the attached crystallographic information files (CIF). After the solution (Shelxt)[S1.4] and refinement process (Shelxl 2017/1)[S1.5] the data was validated by using Platon.[S1.6] All graphic representations were created with Diamond 4.[S1.7] Infrared (IR) spectra are recorded with a Bruker Alpha Fourier-transform infrared spectrometer (FT-IR) with platinum attenuated total reflectance (ATR) sampling.

S1.3. Experimental procedures and analytical characterization

*Scheme S1: Synthesis of 2,7-dibromophenanthrene **3**.*

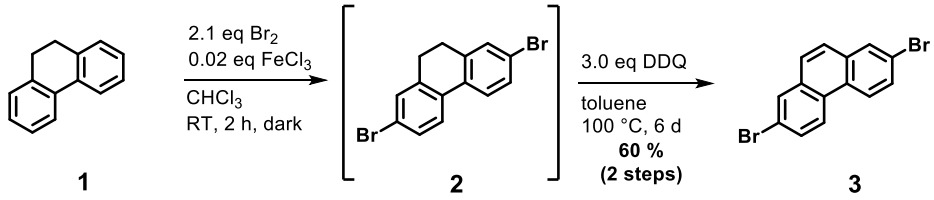

According to a synthesis of Tian *et al.*[S1.1], 2.50 g (13.9 mmol, 1.00 eq) 9,10-dihydrophenanthrene(**1**) and 30 mg (0.26 mmol, 2 mol%) iron(III)chloride were dissolved in 20 mL chloroform and cooled to 0 °C. To the stirred solution, 1.5 mL (29.3 mmol, 2.10 eq) bromine were added dropwise under exclusion of light and it was stirred for 2 h. After detection of complete conversion by TLC, 100 mL methanol were added to the reaction mixture and intermediate 2,7-dibromo-9,10-dihydrophenanthrene (**2**) was precipitated, collected by filtration and washed with methanol and *n*-pentane. The crude product **2** was dried in vacuum and dissolved in 60 mL toluene. To the solution, 9.46 g (41.7 mmol, 3.00 eq) 2,3-dichloro-5,6-dicyano-1,4-benzoquinone were added and the suspension was stirred for 4 days at 90 °C. The solvent was evaporated and the crude product was adsorbed on silica and purified *via* column chromatography (eluent: *n*-pentane). 2.77 g (8.34 mmol, 60 %) of product **3** were obtained as colorless solid.

TLC: R_f = 0.25 (*n*-pentane).

^{1}H - NMR: 300 MHz, 298 K, $CDCl_3$, δ = 8.47 (d, 2H, ^3J = 8.86 Hz, *H*4, *H*5), 8.03 (d, 2H, ^4J = 2.08 Hz, *H*1, *H*8), 7.74 (dd, 2H, ^4J = 2.08 Hz, ^3J = 8.86 Hz, *H*3, *H*6), 7.66 (s, *H*9, *H*10) ppm.

^{13}C NMR: 75 MHz, 298 K, $CDCl_3$, δ = 133.4, 131.0, 130.2, 128.7, 127.1, 124.4, 121.1 ppm.

The analytical data are in accordance with the literature.[S1.1]

*Scheme S2: Synthesis of phenanthrene-2,7-dicarbaldehyde **4**.*

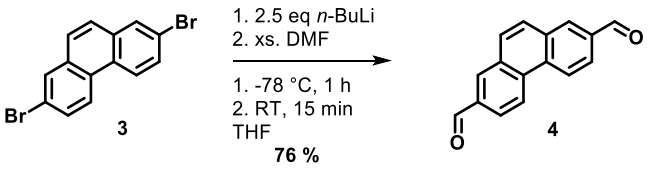

520 mg (1.55 mmol, 1.00 eq) 2,7-dibromophenanthrene (**3**) were dissolved in 20 mL tetrahydrofuran (THF) and cooled to -78 °C. 1.60 mL (3.87 mmol, 2.50 eq) of a 2.43 M solution of *n*-butyllithium in *n*-hexane were added dropwise over a time period of 30 min and then stirred for additional 1 h at this temperature. The reaction solution was warmed to room temperature within 2 h and 20 mL water were added to stop the reaction. The aqueous phase was separated and extracted twice with ethyl acetate (20 mL). The combined organic layers were dried over magnesium sulphate and filtered. The crude product was adsorbed on silica and purified *via* column chromatography (eluent: *n*-hexane/ethyl acetate 2:1). 275 mg (1.18 mmol, 76 %) of phenanthrene-2,7-dicarbaldehyde **4** were obtained as yellow solid.

TLC: R_f = 0.45 (*n*-hexane/ethyl acetate 2:1)

^{1}H - NMR: 300 MHz, 298 K, $CDCl_3$, δ = 10.26 (s, *H*2', *H*7'), 8.86 (d, 2H, ^3J = 8.62 Hz, *H*4, *H*5), 8.43 (d, 2H, ^4J = 1.56 Hz, *H*1, *H*8), 8.20 (dd, 2H, ^4J = 1.56 Hz, ^3J = 8.62 Hz, *H*3, *H*6), 7.97 (s, *H*9, *H*10) ppm.

^{13}C NMR: 75 MHz, 298 K, $CDCl_3$, δ = 192.0, 135.5, 133.8, 133.0, 132.9, 128.5, 125.4, 124.7 ppm.

The analytical data are in accordance with the literature.[S1.8]

*Scheme S3: Synthesis of 1,4,7(2,7)-triphenanthrenacyclononaphane-2,5,8-triene **5**.*

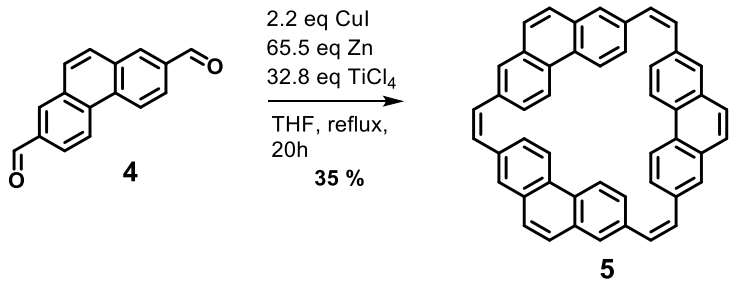

3.66 g (56.3 mmol, 65.5 eq) zinc and 360 mg copper(I)iodide (1.89 mmol, 2.20 eq) were suspended in 200 mL THF. 3.1 mL (28.2 mmol, 32.8 eq) titanium tetrachloride were added dropwise and the resulting black solution was heated to reflux for 2 h. Then, a solution of 200 mg (0.86 mmol, 1.00 eq) phenanthrene-2,7-dicarbaldehyde **4** (dissolved in 100 mL THF) were added dropwise over a time period of 90 min and then refluxed for additional 18 h. After cooling down to room temperature, 100 mL 10%-aqueous ammonia were added. The aqueous phase was separated and extracted twice with chloroform (100 mL). The combined organic layers were dried over magnesium sulphate and filtered. The crude product was adsorbed on silica and purified *via* column chromatography (eluent: *n*-pentane/dichloromethane 5:1). 60 mg (0.10 mmol, 35 %) of 1,4,7(2,7)-triphenanthrenacyclononaphane-2,5,8-triene **5** were obtained as colorless solid.

TLC: R_f = 0.55 (*n*-pentane/dichloromethane 5:1)

^{1}H - NMR: 300 MHz, 298 K, $CDCl_3$, δ = 8.14 (d, 2H, ^3J = 8.63 Hz, *H*4, *H*5), 7.58 (d, 2H, ^4J = 1.58 Hz, *H*1, *H*8), 8.74 (s, 2H, *H*2', *H*7') 7.18 (dd, 2H, ^4J = 1.58 Hz, ^3J = 8.63 Hz, *H*3, *H*6), 7.13 (s, *H*9, *H*10) ppm.

^{13}C NMR: 75 MHz, 298 K, $CDCl_3$, δ = 135.8, 132.7, 131.6, 129.0, 128.8, 128.2, 127.0, 122.3 ppm.

HRMS: *m/z* for $[C_{48}H_{30}]^+$ calc.: 606.23475, found: 606.23560 (EI+).

IR (ATR): $\tilde{\nu}$ = 3009 (m), 2925 (m), 2953 (w), 2033 (w), 1964 (w), 1921 (w), 1600 (m), 1476 (w), 1256 (m), 1160 (w), 960 (w), 902 (vs), 827 (s), 735 (w), 705 (vs), 660 (w), 427 (m) cm^{-1}.

m.p.: 326-329 °C.

3.8 Publication 8: Disentangling the Complex Electronic Structure of the Large Organic Adsorbate Cycloarene C108

Citation: J. Martinez-Castro, R. Bolat, Q. Fan, S. Werner, H. H. Arefi, T. Esat, J. Sundermeyer, C. Wagner, J. M. Gottfried, R. Temirov, M. Ternes, F. S. Tautz, *ACS Nano*, under Revision (submitted: 14.09.2021).

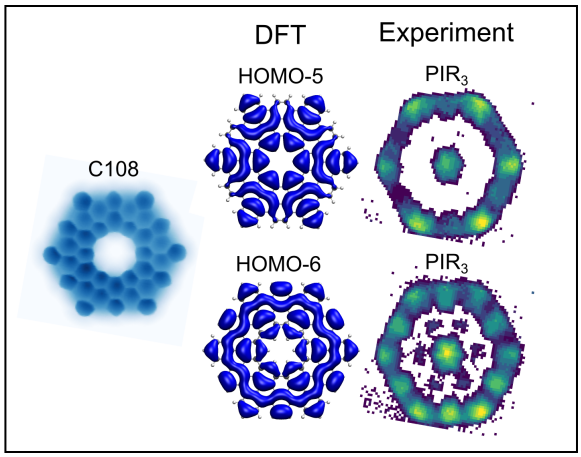

Summary: This article adresses the *on-Surface* investigation of the electronic structure of the cyclic nanographene C108. In contrast to the initial C108 surface synthesis described in Publication 6, an improved precursor was developed, which forms C108 in higher yields by a simple Ullmann dimerization followed by cyclodehydrogenation after deposition on Ag(111). The chemical synthesis and characterization of the precursor DBSP as well as solution-based approaches for the synthesis of C108 are described in chapter 3.10 of this thesis. Investigated by feature-detecting scaning tunneling spectroscopy (FD-STS) utilizing a CO-functionalized STM tip for better spatial and electronic resolution and statistical analysis, molecular resonances could be detected at an energy of 2 eV below the Fermi level. They could be resolved at 50 meV energetical resolution as three populated states of C108 and one unpopulated state. With the help of quantum chemical DFT calculations, this states could be interpret as partly degenerated LUMO, LUMO+1 and LUMO+2 levels of C108 for the unpopulated state (negative resonance signal, NIR). For the populated states (positive resonance signal, PIR), contributions of HOMO+HOMO-2 (first resonance), HOMO-3, HOMO-4 (second signal) and HOMO-5-HOMO-8 (third signal) could be assigned. This work marks a determination of a complex electronic structure by STS in yet unpresented resolution.

Own Contribution: The precursor structure was designed by myself together with Dr. Q. Fan. The design of the retrosynthetical approach of the precursor, the chemical synthesis of precursor DBSP as well as the in-solution characterization was performed by myself. The chemical synthesis part of the manuscript was written by myself. Prof. Dr. J. Sundermeyer supervised the chemical synthesis. All authors contributed in writing and approval of the manuscript.
Note: The individual contributions of all co-authors can be taken from the original manuscript.

Disentangling the Complex Electronic Structure of the Large Organic Adsorbate Cycloarene C108

Jose Martinez-Castro, Rustem Bolat, Qitang Fan, Simon Werner, Hadi H. Arefi, Taner Esat, Jörg Sundermeyer, Christian Wagner, J. Michael Gottfried, Ruslan Temirov, Markus Ternes, F. Stefan Tautz

KEYWORDS. Scanning tunneling microscopy, Molecular electronics, Macrocycles, Two dimensional materials,

We combine low-temperature scanning tunneling spectroscopy, CO-functionalized tips and algorithmic data analysis to investigate the electronic structure of the molecular cycloarene C108 (graphene nanoring) adsorbed on a Au(111) surface. We demonstrate that CO functionalized tips enhance the visibility of molecular resonances, both in differential conductance spectra (d*I*/d*V*) and in real-space topographic images without introducing spurious artifacts. Comparing our experimental data with ab-initio density functional theory reveals a remarkably precise agreement of the molecular orbitals and enables us to disentangle close-lying molecular states only separated by 50 meV at an energy of 2 eV below the Fermi level. We propose this combination of techniques as a promising new route for a precise characterization of complex molecules and other physical entities which have electronic resonances in the tip-sample junction.

INTRODUCTION

Molecular adsorbates are characterized by electronic resonances that can be spectroscopically detected[1]. Scanning tunneling microscopy (STM) with its sub-molecular imaging resolution and its ability to probe the local density of states (LDOS) by recording the differential conductance (d*I*/d*V*(*V*) or simply d*I*/d*V*) spectra yields spatially resolved images of molecular states[2,3]. Since scanning tunneling spectroscopy (STS) can access occupied as well as unoccupied molecular states, it has become a valuable tool for unveiling the electronic structure of molecular adsorbates[4,5].

So far, the spatial mapping of these molecular resonances has been conducted mostly in the following way: The tunneling bias of the junction is set to a value corresponding to the energy at which the resonance occurs and, while the molecule is scanned by the STM tip, the d*I*/d*V* signal is recorded. Such scanning can be performed in two distinct modes: constant-height or constant-current[6]. The obtained d*I*/d*V* map is commonly interpreted as a two-dimensional visualization of the molecular state. In some cases, this approach has been successfully employed and revealed a clear correspondence between calculated molecular orbitals and the measured electronic resonances. This has worked particularly well for model systems where there is little room for an ambiguous interpretation, e. g., molecules on which electronic resonances are well-separated from each other[3,7,8]. However, for the cases when the molecular resonance spectrum is denser and some electronic resonances have contributions from different molecular states,[9] the interpretation of the d*I*/d*V* data becomes a difficult problem which has in general not been solved yet.

In this work, we use a graphene nanoring, the cycloarene 108 (C108) adsorbed on Au(111), as a model system. Cycloarenes are considered as ideal test cases for studying electrons delocalization in extended aromatic systems[10]. The C108 possesses a rich energy spectrum in which several molecular states are only separated energetically by a few meV[11], making it particularly interesting for disentangling its molecular orbitals.

To access and map these states, we use an approach that aims to overcome the limitation of common d*I*/d*V* imaging. For that, **Error! Bookmark not defined.**we combine the use of CO functionalized tips which have been shown to provide sub-molecular resolution particularly on sp^2-hybridized carbon nanostructures[12], with feature-detection scanning tunneling spectroscopy (FD-STS)[13], a statistical analysis tool that allows the unbiased detection of electronic resonances. We find that this combination enables us to resolve and separate these close in energy lying orbitals, providing experimental information on the electronic structure of a cycloarene in unprecedented detail.

RESULTS AND DISCUSSION

We synthesize the cycloarene C108 on a Au(111) surface via Ullmann coupling followed by cyclodehydrogenation of a bromoarene precursor containing 9 phenyl moieties (5'''-([1,1'-biphenyl]-2-yl)-5'',5''''-dibromo-1,1':2',1'':3'',1''':3''',1'''':3'''',1''''':2''''',1'''''-septiphenyl) (Fig. 1a-c). The first step, on-surface Ullmann coupling, leads to the cyclodimerization of the precursor into the nonplanar macrocycle, which further forms C108. This new on-surface cyclodimerization reaction is more efficient than the on-surface cyclotrimerization used in previous work for the first synthesis of C108[11]. Details of the C108 precursor synthesis can be found in the supporting information.

We image the C108 at a base temperature of 10K using a tungsten tip at which the apex can be deliberately functionalized with a single CO molecule (CO tip), enabling sub-molecular resolution of the geometrical structure (Fig. 1d). Using the same tip, we also perform d*I*/d*V* spectroscopy revealing several electronic resonances in the energy range between -2eV and +2eV around the Fermi energy E_F (Fig. 1e). The CO tip impacts the

measured images and spectra compared to a bare metallic s-wave tip in two ways: first, at biases close to E_F it allows to achieve structural sub-molecular resolution, similar to previous reports[14–17] and, second, it enhances significantly the intensity of the electronic resonances. Point spectroscopy reveals four main features (gray dots) that we identify as positive (PIR) and negative ion resonances (NIR)[11] (Fig. 1e). Compared to previously published results, with the increased resolution of our CO functionalized tip, we additionally identify four secondary features shifted by approximately 150 mV from the main features to higher absolute bias (green dots in Fig. 1e).

To understand the origin of the peaks, we measure dI/dV spectra on a grid of 64 × 64 points covering an area of 2.4 × 2.4 nm^2 centered on an isolated C108 molecule with a metallic s-wave tip and with a CO tip. At each grid point we regulate the tip height prior to opening the feedback loop to a tunneling current of I_b = 80 pA at a bias of V_b = 200 mV. The bias lies inside the energy gap between PIR and NIR to avoid the influence of molecular orbitals on the tip height and thus the spectroscopic intensities. We then analyze the corresponding matrix of spectra using a recently developed FD-STS algorithm, which searches for peaks in the data set in an unbiased manner[13] (S1).

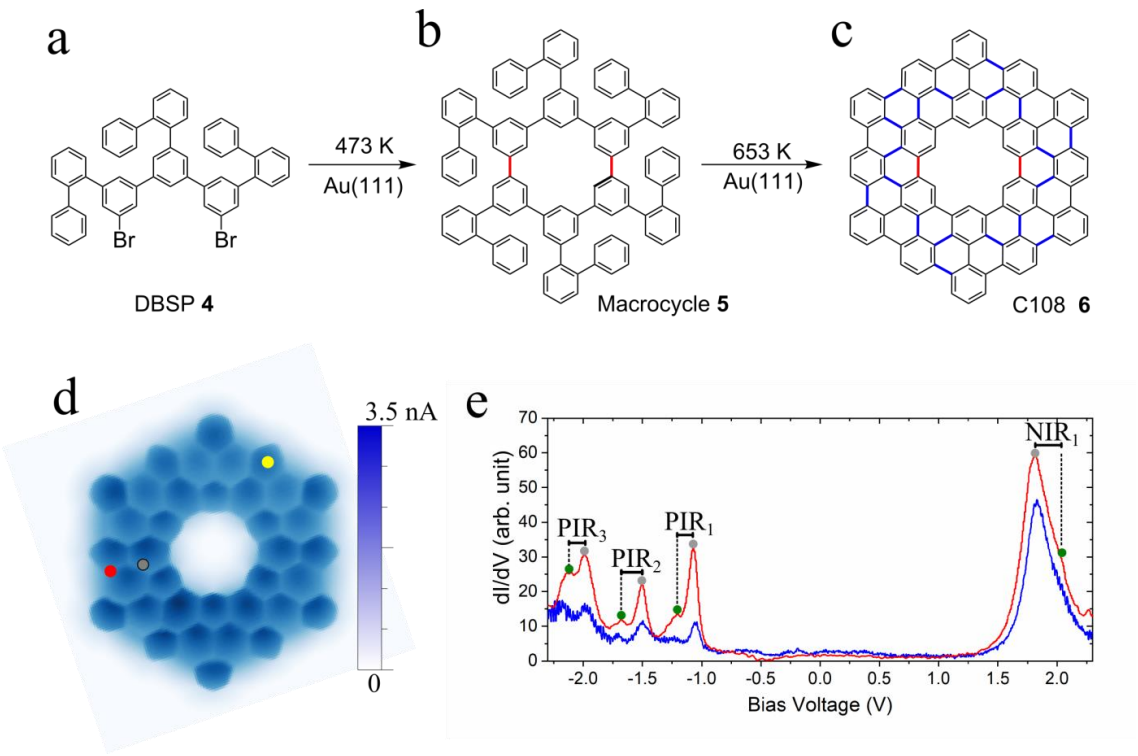

Figure 1. Synthesis, structural and electronic properties of C108. a-c) The precursor 5”’-([1,1’-biphenyl]-2-yl)-5”,5””-dibromo-1,1’:2’,1”:3”,1”’:3”’,1””:3””,1”””:2”””,1’””””-sepiphenyl (DBSP) (a) is vapor-deposited onto the surface. Subsequent annealing induces an Ullmann coupling, resulting in the nonplanar macrocycle (b)**.** Upon further annealing, the C108 macrocycle is formed by cyclodehydrogenation (c). The C-C bonds formed via Ullmann and dehydrogenative coupling are shown in red and blue, respectively. **d)** Constant-height STM image of the C108 nanoring (V_b = 20 mV, size 2.4 × 2.4 nm^2). The red and gray dots mark the locations at which the spectra in Fig. 2b were recorded. **e)** dI/dV spectrum taken with a metallic tip (blue) and a CO functionalized tip (red) measured over the yellow mark in (d). Main features (gray dots) and their replicas (green dots) are labeled with PIR_1, PIR_2, PIR_3 and NIR (V_b = 200 mV, I_{set} = 80 pA, V_{mod} = 20 mV).

We start by normalizing each individual spectrum to the intensity sum of the 3 PIRs that are the result of occupied molecular orbitals in the C108. This normalization compensates for the different tunneling probabilities occurring at different locations on the C108 (red and gray curves in Fig. 2b) assuming an approximately constant total electron density within the spatial extension of the molecule. The *energy distribution histogram* (EDH) of the weighted peak intensities shows the abundance of peak center energies E_p across the grid (Fig. 2a). This EDH reflects the PIR and NIR main energies and intensities and can be compared with density functional theory (DFT) calculations that use the B3LYP hybrid functional to calculate the density of states (DOS) (black curve in Fig. 2a).

From the DFT calculation, we find that the highest occupied molecule orbital (HOMO, H_0) at -1.094 eV, along with the orbitals HOMO-1 and HOMO-2 (H_{-1}, H_{-2}), situated both at -1.100 eV, are nearly degenerate and contribute to the measured resonance PIR_1, while the degenerate orbitals HOMO-3 and HOMO-4 (H_{-3}, H_{-4}), located both at -1.503 eV, contribute to the resonance PIR_2 and HOMO-5, HOMO-6 (H_{-5}, H_{-6}) at -1.964 eV and -2.019 eV contribute to the resonance PIR_3. On the unoccupied side, we observe a broad peak spanning through the energy range corresponding to the energy position of three different calculated orbitals: the lowest unoccupied molecular orbital (LUMO, L_0) at +1.830 eV and the degenerate LUMO+1 and LUMO+2 at +1.911 eV (L_{+1}, L_{+2}) contributing to the resonance NIR_1.

Additionally, we find a series of peaks (cyan in Fig. 2a) that are separated by about 150 meV from the main peaks. We attribute these peaks to vibronic replica[18–20] of the C108 electronic states. This conjecture is supported by a calculation of the vibrational spectrum based on a finite-difference approach at DFT-PBE level; the observed vibronic replica stem most likely from a family of vibrational modes found at frequencies of around 1200 cm^{-1} (S2), equivalent to approximately 150 meV.

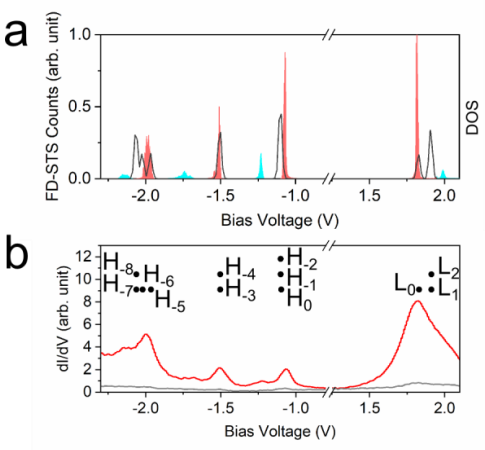

Figure 2. FD-STS histogram and DFT-calculated DOS and molecular orbital energy levels of the cycloarene C108. a) C108/Au(111) histogram of detected peaks (energy distribution histogram EDH, red) and vibronic replicas (cyan) produced by statistical analysis of a 64 × 64 grid of d*I*/d*V* spectra measured over the molecule. Simulated DOS of C108 in the gas phase (black curve). Peaks at negative bias are labeled as PIR_1 ($V \approx$ -1.06 V), PIR_2 ($V \approx$ -1.52 V), PIR_3 ($V \approx$ -1.98 V), while the peak found at positive bias is labeled as NIR_1 ($V \approx$ +1.8 V) **b)** Energetic positions of the gas-phase orbitals as found in the DFT calculation (black dots), overlaid with typical experimental d*I*/d*V* spectra, red and gray, taken at the positions of the red and gray dots, respectively, in Fig. 1d. Spectroscopy parameters: V_b = 200 V, I_{set} = 80 pA, V_{mod} = 20 mV. In both graphs, the region between -0.8 V and 1.2 V is omitted for a better visualization of the resonances.

The significant intensity variation between the NIR_1 and the $PIR_{1\text{-}3}$, which are not found in this extent in the calculated DOS, stems from the strongly varying tunneling probabilities for tunneling into or out of these resonances. At positive V_b, the tunneling barrier height is effectively reduced, leading to an increase of the NIR, while for increasingly negative V_b, the barrier for tunneling from these resonances into the tip is successively increased[6].

In order to investigate the spatial distribution of the molecular orbitals, we continue by performing constant current d*I*/d*V* maps at the energies of the resonances. In agreement with Fan et al.[11], we are able to reproduce the d*I*/d*V* maps of PIR_1 and NIR_1 and further investigate PIR_2 and PIR_3 (S3). Despite the enhanced resolution provided by the CO tip, we do not observe substantial differences between PIR_2 and PIR_3, pointing to the limitations of constant current d*I*/d*V* maps as a method to investigate molecular resonances.

FD-STS is a statistical tool that enables us to energetically classify the peaks and to analyze their spatial distributions. As we will show, *feature distribution maps* (FDM) and *energy distribution maps* (EDM) are particularly useful for the classification and visualization of molecular orbitals that are very close in energy and are present in different regions of the molecule. In combination with the enhanced spatial resolution of the CO tip's p-wave nature[21,22], this results in maps far more accurate than conventional d*I*/d*V* maps (Fig. 3), unveiling a finer electronic structure than the one detected with constant current d*I*/d*V* maps (S3) or metallic tips (S4). Note that the employed normalization allows us to observe features that could not be previously observed in d*I*/d*V* maps. We produce FDMs that, unlike previous work[13], use a linear scale to visualize the intensity variation of molecular orbitals within the molecule. In FDMs, we plot the intensity at the center of each detected peak of the normalized d*I*/d*V* spectra (Fig. 3d-f), while in EDMs we plot the energy of each detected peak within a defined energy range (Fig. 3g-i).

Next, we proceed to relate the spatial distribution of the detected features to molecular orbitals. To compare theory and experiment, we have to consider the electronic broadening due to the bias modulation of 20 mV (peak to peak) used for the lock-in detection in FD-STS, which limits our energy resolution. Therefore, we compute the absolute square of the molecular orbitals and add those which lie within the broadening range of the detection method (Fig. 3a-c). Comparison between the calculated molecular orbitals and the FDM shows similarities. For instance, the FDM obtained for PIR_1 (Fig. 3e) shows horseshoe features situated at the corners of the C108 molecule, in good agreement with the DFT calculations (Fig. 3b), on which the images are obtained by the addition of the calculated absolute square of H_0, H_{-1} and H_{-2}.

Additionally, by plotting the EDM (Fig. 3g-i), varying approximately only by the energy of the modulation broadening within the molecule, we find that the resonances are energetically monodisperse. In other words, we do not observe different resonances merged to a larger resonance. The corresponding EDH for the peaks (Fig. 3j-l) confirm a single resonance nature, even though they originate from combinations of different molecular orbitals.

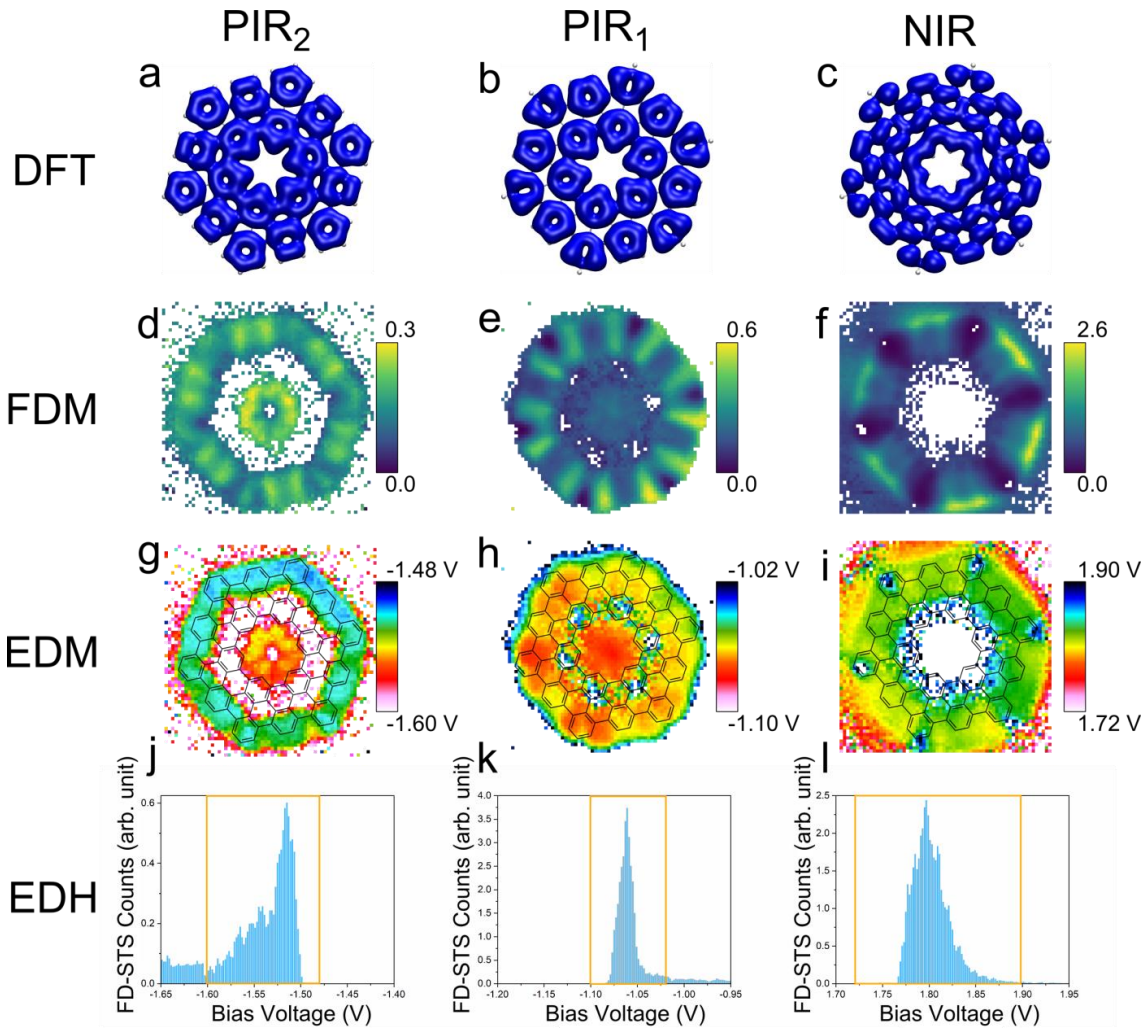

Figure 3. Calculated gas-phase molecular orbitals and FD-STS of C108. a-c) Visualization of the sum of the absolute squares of the molecular wavefunctions as calculated by DFT (isovalue 0.0005 a.u^2.) at the resonance energies $V_{PIR2} = -1.52$ V, $V_{PIR1} = -1.06$ V, and $V_{NIR1} = 1.8$ V. **d-f)** Feature distribution maps (FDM) of PIR_2, PIR_1 and NIR (from left to right), overlaid with the chemical structure of C108. **g-i)** Energy distribution maps (EDM) of PIR_2, PIR_1 and NIR (from left to right), overlaid with the chemical structure of C108. **j-l)** Energy distribution histograms (EDH) of PIR_2, PIR_1 and NIR (from left to right). The yellow box indicates the selected energy range chosen for the FDMs and EDMs in d-f and g-i, respectively. Image sizes 2.4 × 2.4 nm^2.

We note that the molecular resonances decay in their intensity as the tip moves towards the inner part of the ring to the point they cannot be detected, neither in the conventional dI/dV maps nor in the normalized spectra used for the FDM. This reveals the limits of not only our approach, similar to earlier experiments conducted on many different molecular systems probed both with metallic s-wave [8,23] and CO tips[24], in which the molecular states are observed extending beyond the atomic structure of the molecule, while the interior of the molecule tends to be electronically transparent. We observe in Fig. 3d-f and g-i that more negative bias voltages (i.e., larger tunneling barriers, see above) tend to concentrate the features closer to the periphery of the molecule.

Remarkably, and contrary to the DFT calculation, the FDM as well as constant current dI/dV maps using the CO tip (Fig. 3d-i and S3) show an increased intensity in the center of the C108 molecule which is not present in measurements using a bare metallic tip (see Fig. S4). At the center of the C108 nanoring, the tip is positioned above the Au(111) surface. Thus, we attribute the detection of these electronic resonances to a closer tip-sample distance caused by the directional sharper CO tip that is able to pick up tail electronic contributions from the molecular orbitals.

We now focus on the PIR_3. In contrast to the maps of Fig. 3g-i, the EDM shows a resonance that is composed of two separable regions with slightly different energies: Yellow/green areas with higher peak energy and red/orange areas with lower peak energy (Fig. 4a). A closer look at the EDH reveals that an at first glance single peak is a composition of two separate peaks whose energetic centers are located at −2.00 and −1.95 V (Fig 4b). The strong maximum in between the two peaks is an artifact of the FD-STS algorithm. If none of the two resonances

is dominant, the superposition of both will result in an apparent single peak close to the intermediate energy, artificially creating an extra peak in the histogram. Remarkably, our DFT calculations predict two non-degenerate molecular orbitals (H_{-5} and H_{-6}) at approximately −2 eV with a separation of only 50 meV (Fig. 4e,f).

To separate these two orbitals, we now fit this part of the d*I*/d*V* spectra with two Lorenzians with the fixed energies of −2.00 and −1.95 V as determined by the EDH. The resulting intensity maps (Fig. 4c,d) are in remarkable agreement with the DFT calculation (Fig. 4e,f), showing the potential of FD-STS to separate energetically overlapping molecular orbitals and to obtain a reliable image of the molecular orbitals.

Since also NIR_1 contains two orbitals, we follow the same procedure. In this case, the resonance is the contribution of L_0 and the degenerate L_{+1} and L_{+2} with an energy difference of 90 meV (Fig. 2b). We fix Lorentzian centers at an energy of 1.84 and 1.98 V, corresponding to the positions on which the central peak and the peak shoulders are found (Fig. 1b). In contrast to Fig. 4, however, we do not observe any significant difference in intensity (S5). This we relate to the lack of differences in the wavefunction intensities between the L_0 and the degenerate L_{+1} and L_{+2}.

.

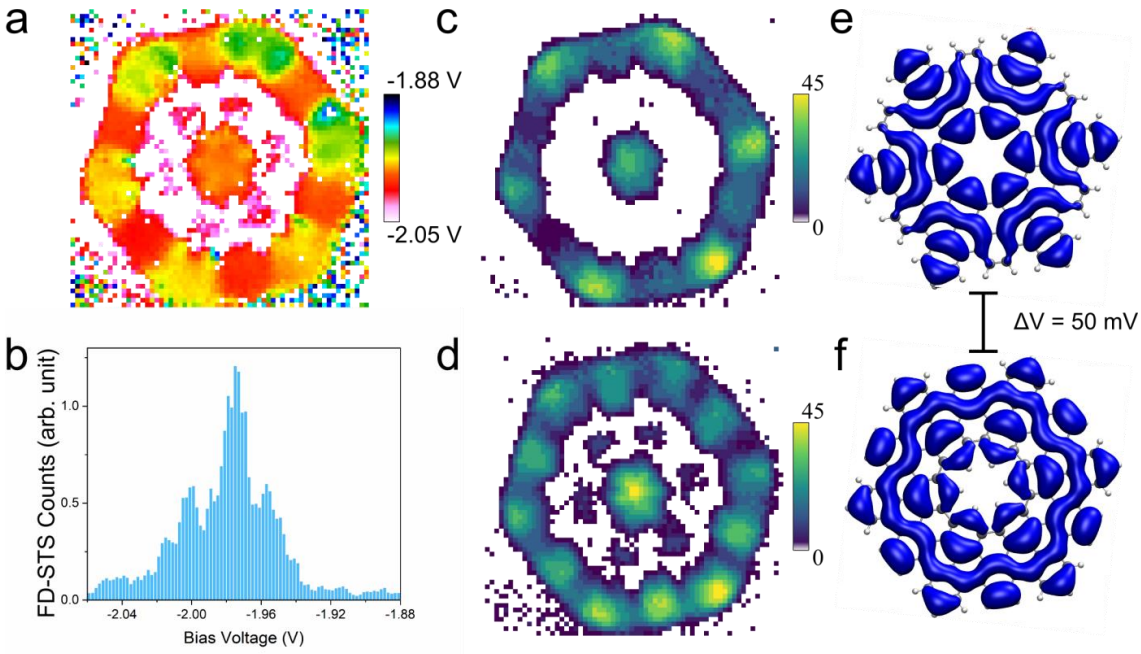

Figure 4. Feature distribution and peak fitting maps for PIR_3 and calculated molecular orbitals. a) Feature distribution map of PIR_3, showing two clearly differentiated regions which is also reflected in the energy distribution histogram in **b)**. **c-d)** Peak intensity maps, obtained by fitting PIR_3 with two Lorentzians whose centers have been fixed at -1.95 V and -2 V. **e-f)** Visualization of the molecular orbital wave functions as calculated by DFT (isovalue 0.0005^2 a.u.) at the resonance energies V_{PIR3},= −1.95 and −2 V. Image size 2.4 × 2.4 nm^2.

CONCLUSION

We have shown that the combination of CO tip and FD-STS is a powerful tool to identify and map the molecular states of the cycloarene C108 in good agreement with theoretical calculations. With this combination, we reach a level of detail that is neither achievable by constant current d*I*/d*V* maps nor by using a metallic tip and applying FD-STS. In particular, our method shows its potential by disentangling close-lying molecular states at -2 V only separated by an energy difference of 50 mV. We note that this method could also be applied to systems on which different types of electronic excitations are observed, e.g., superconductivity[25], spin excitations[26] or to molecular systems such as those incorporate transition metals or rare earth atoms[27], on which theoretical calculations are limited due to their complexity. Furthermore, we expect that the methodology presented here will make the studies of the complex electronic structure of larger nanostructures more efficient. In the case of C108, the unambiguous identification of molecular resonances may help in future experiments exploring the intriguing effects of high magnetic fields such as persistent ring currents[28,29] or the Aharonov-Bohm effect[30,31].

ASSOCIATED CONTENT

Details of the feature detection algorithm; DFT calculation details; schematic representation of the FD-STS algorithm; calculated IR spectrum for the isolated C108 molecule; constant current d*I*/d*V* maps of C108; feature and energy distribution maps of the C108 measured with a metallic s-wave tip; feature distribution and energy maps of C108 for PIR_3; resulting maps from peak fitting of NIR_1 and calculated molecular orbitals; synthetic details and characterization of DBT.
This material is available free of charge via the Internet at http://pubs.acs.org.

AUTHOR INFORMATION

Corresponding Authors

Jose Martinez-Castro – Peter Grünberg Institut (PGI-3), Forschungszentrum Jülich, 52425 Jülich, Germany.

orcid.org/0000-0001-7249-2567

Email: j.martinez@fz-juelich.de

Markus Ternes – Peter Grünberg Institut (PGI-3), Forschungszentrum Jülich, 52425 Jülich, Germany; II. Institute of Physics, RWTH Aachen University, D-52074 Aachen, Germany.

orcid.org/0000-0001-6800-4129

Email: ternes@physik.rwth-aachen.de

Authors

Rustem Bolat – Peter Grünberg Institut (PGI-3), Forschungszentrum Jülich, 52425 Jülich, Germany; Jülich Aachen Research Alliance (JARA), Fundamentals of Future Information Technology, 52425 Jülich, Germany; Experimentalphysik IV A, RWTH Aachen University, Otto-Blumenthal-Straße, 52074 Aachen, Germany.

Qitang Fan – Department of Chemistry, Philipps-Universität Marburg, 35032 Marburg, Germany.

Simon Werner – Department of Chemistry, Philipps-Universität Marburg, 35032 Marburg, Germany.

Hadi H. Aerfi – Peter Grünberg Institut (PGI-3), Forschungszentrum Jülich, 52425 Jülich, Germany; Jülich Aachen Research Alliance (JARA), Fundamentals of Future Information Technology, 52425 Jülich, Germany.

Taner Esat – Peter Grünberg Institut (PGI-3), Forschungszentrum Jülich, 52425 Jülich, Germany; Jülich Aachen Research Alliance (JARA), Fundamentals of Future Information Technology, 52425 Jülich, Germany.

orcid.org/0000-0003-1094-3718

Jörg Sundermeyer – Department of Chemistry, Philipps-Universität Marburg, 35032 Marburg, Germany.

Christian Wagner – Peter Grünberg Institut (PGI-3), Forschungszentrum Jülich, 52425 Jülich, Germany; Jülich Aachen Research Alliance (JARA), Fundamentals of Future Information Technology, 52425 Jülich, Germany.

orcid.org/0000-0002-2117-6289

J. Michael Gottfried – Department of Chemistry, Philipps-Universität Marburg, 35032 Marburg, Germany.

orcid.org/0000-0001-5579-2568

Ruslan Temirov – Peter Grünberg Institut (PGI-3), Forschungszentrum Jülich, 52425 Jülich, Germany; Jülich Aachen Research Alliance (JARA), Fundamentals of Future Information Technology, 52425 Jülich, Germany; II. Physikalisches Institut, Universität zu Köln, 50937 Köln, Germany.

orcid.org/0000-0001-8290-6831

F. Stefan Tautz – Peter Grünberg Institut (PGI-3), Forschungszentrum Jülich, 52425 Jülich, Germany; Jülich Aachen Research Alliance (JARA), Fundamentals of Future Information Technology, 52425 Jülich, Germany; Experimentalphysik IV A, RWTH Aachen University, Otto-Blumenthal-Straße, 52074 Aachen, Germany.

orcid.org/0000-0003-3583-2379

Author Contributions

J.M.-C., R.T. and F.S.T. conceived the project. J.M.-C. and R.B. performed the experiments. J.M.-C., R.B., T.E. and M.T evaluated the data. H.A. and C.W. performed the DFT calculations. S.W. and J.S. synthesized the C108 precursor. Q.F. and J.M.G. developed the on-surface synthesis protocol. All authors discussed the results. J.M.-C and M.T. wrote the paper with significant contributions from all authors.

Notes

The authors declare no competing financial interest.
The preprint version is available online.
Raw data are available at the Jülich DATA public repository.

ACKNOWLEDGMENTS

M.T. acknowledge funding by the Heisenberg Program (TE 833/2-1) of the Deutsche Forschungsgemeinschaft (DFG), J.M.C by the Humboldt Foundation, M.T. and J.M.C acknowledge funding by the Priority Program (SPP 2244) of the DFG. J.M.G. and F.S.T. acknowledge funding by the DFG through SFB 1083 “Structure and Dynamics of Internal Interfaces”. J.M.G. acknowledge funding by the DFG (GO1812/2) and by the LOEWE Program of Excellence of the Federal State of Hesse (LOEWE Focus Group PriOSS “Principles of On-Surface Synthesis”).

REFERENCES

(1) Niu, T.; Li, A. Exploring Single Molecules by Scanning Probe Microscopy: Porphyrin and Phthalocyanine. *J. Phys. Chem. Lett.* **2013**, *4*, 4095–4102.

(2) Pascual, J. I.; Gómez-Herrero, J.; Rogero, C.; Baró, A. M.; Sánchez-Portal, D.; Artacho, E.; Ordejón, P.; Soler, J. M. Seeing Molecular Orbitals. *Chem. Phys. Lett.* **2000**, *321*, 78–82.

(3) Repp, J.; Meyer, G.; Stojković, S.; Gourdon, A.; Joachim, C. Molecules on Insulating Films: Scanning-Tunneling Microscopy Imaging of Individual Molecular Orbitals. *Phys. Rev. Lett.* **2005**, *94*, 026803.

(4) Lu, X.; Grobis, M.; Khoo, K. H.; Louie, S. G.; Crommie, M. F. Spatially Mapping the Spectral Density of a Single C$_60$ Molecule. *Phys. Rev. Lett.* **2003**, *90*, 096802.

(5) Villagomez, C. J.; Zambelli, T.; Gauthier, S.; Gourdon, A.; Stojkovic, S.; Joachim, C. STM Images of a Large Organic Molecule Adsorbed on a Bare Metal Substrate or on a Thin Insulating Layer: Visualization of HOMO and LUMO. *Surf. Sci.* **2009**, *603*, 1526–1532.

(6) Chen, C. J. Introduction to Scanning Tunneling Microscopy. *Oxford Univ. Press* **1993**.

(7) Soe, W. H.; Manzano, C.; De Sarkar, A.; Chandrasekhar, N.; Joachim, C. Direct Observation of Molecular Orbitals of Pentacene Physisorbed on Au(111) by Scanning Tunneling Microscope. *Phys. Rev. Lett.* **2009**, *102* (17), 100–103.

(8) Villagomez, C. J.; Zambelli, T.; Gauthier, S.; Gourdon, A.; Barthes, C.; Stojkovic, S.; Joachim, C. A Local View on Hyperconjugation. *Chem. Phys. Lett.* **2007**, *450*, 107–111.

(9) Soe, W. H.; Wong, H. S.; Manzano, C.; Grisolia, M.; Hliwa, M.; Feng, X.; Müllen, K.; Joachim, C. Mapping the Excited States of Single Hexa- Peri -Benzocoronene Oligomers. *ACS Nano* **2012**, *6* (4), 3230–3235.

(10) Buttrick, J. C.; King, B. T. Kekulenes, Cycloarenes, and Heterocycloarenes: Addressing Electronic Structure and Aromaticity through Experiments and Calculations. *Chem. Soc. Rev.* **2017**, *46*, 7–20.

(11) Fan, Q.; Martin-Jimenez, D.; Werner, S.; Ebeling, D.; Koehler, T.; Vollgraff, T.; Sundermeyer, J.; Hieringer, W.; Schirmeisen, A.; Gottfried, J. M. On-Surface Synthesis and Characterization of a Cycloarene: C108 Graphene Ring. *J. Am. Chem. Soc.* **2020**, *142*, 894–899.

(12) Hapala, P.; Kichin, G.; Wagner, C.; Tautz, F. S.; Temirov, R.; Jelínek, P. Mechanism of High-Resolution STM/AFM Imaging with Functionalized Tips. *Phys. Rev. B* **2014**, *90*, 085421.

(13) Sabitova, A.; Temirov, R.; Tautz, F. S. Lateral Scattering Potential of the PTCDA/Ag(111) Interface State. *Phys. Rev. B* **2018**, *98* (20), 1–7.

(14) Temirov, R.; Soubatch, S.; Neucheva, O.; Lassise, A. C.; Tautz, F. S. A Novel Method Achieving Ultra-High Geometrical Resolution in Scanning Tunnelling Microscopy. *New J. Phys.* **2008**, *10*, 053012.

(15) Weiss, C.; Wagner, C.; Kleimann, C.; Rohlfing, M.; Tautz, F. S.; Temirov, R. Imaging Pauli Repulsion in Scanning Tunneling Microscopy. *Phys. Rev. Lett.* **2010**, *105*, 086103.

(16) Weiss, C.; Wagner, C.; Temirov, R.; Tautz, F. S. Direct Imaging of Intermolecular Bonds in Scanning Tunneling Microscopy. *J. Am. Chem. Soc.* **2010**, *132*, 11864–11865.

(17) Kichin, G.; Weiss, C.; Wagner, C.; Tautz, F. S.; Temirov, R. Single Molecule and Single Atom Sensors for Atomic Resolution Imaging of Chemically Complex Surfaces. *J. Am. Chem. Soc.* **2011**, *133*, 16847–16851.

(18) Wu, S. W.; Nazin, G. V.; Chen, X.; Qiu, X. H.; Ho, W. Control of Relative Tunneling Rates in Single Molecule Bipolar Electron Transport. *Phys. Rev. Lett.* **2004**, *93*, 236802.

(19) Matino, F.; Schull, G.; Köhler, F.; Gabutti, S.; Mayor, M.; Berndt, R. Electronic Decoupling of a Cyclophane from a Metal Surface. *Proc. Natl. Acad. Sci.* **2011**, *108*, 961–964.

(20) Qiu, X. H.; Nazin, G. V.; Ho, W. Vibronic States in Single Molecule Electron Transport. *Phys. Rev. Lett.* **2004**, *92*, 206102.

(21) Chen, C. J. Tunneling Matrix Elements in Three-Dimensional Space: The Derivative Rule and the Sum Rule. *Phys. Rev. B* **1990**, *42* (14), 8841–8857.

(22) Gross, L.; Moll, N.; Mohn, F.; Curioni, A.; Meyer, G.; Hanke, F.; Persson, M. High-Resolution Molecular Orbital Imaging Using a p-Wave STM Tip. *Phys. Rev. Lett.* **2011**, *107*, 086101.

(23) Rohlfing, M.; Temirov, R.; Tautz, F. S. Adsorption Structure and Scanning Tunneling Data of a Prototype Organic-Inorganic Interface: PTCDA on Ag(111). *Phys. Rev. B* **2007**, *76*, 115421.

(24) Lawrence, J.; Brandimarte, P.; Berdonces-Layunta, A.; Mohammed, M. S. G.; Grewal, A.; Leon, C. C.; Sánchez-Portal, D.; De Oteyza, D. G. Probing the Magnetism of Topological End States in 5-Armchair Graphene Nanoribbons. *ACS Nano* **2020**, *14*, 4499–4508.

(25) Pan, S. H.; O'Neal, J. P.; Badzey, R. L.; Chamon, C.; Ding, H.; Engelbrecht, J. R.; Wang, Z.; Eisaki, H.; Uchida, S.; Gupta, A. K.; Ng, K.-W.; Hudson, E. W.; Lang, K. M.; Davis, J. C. Microscopic Electronic Inhomogeneity in the High- T c Superconductor Bi 2 Sr 2 CaCu 2 O 8+ X. *Nature* **2001**, *413*, 282–285.

(26) Ternes, M. Spin Excitations and Correlations in Scanning Tunneling Spectroscopy. *New J. Phys.* **2015**, *17*, 063016.

(27) Warner, B.; El Hallak, F.; Atodiresei, N.; Seibt, P.; Prüser, H.; Caciuc, V.; Waters, M.; Fisher, A. J.; Blügel, S.; Van Slageren, J.; Hirjibehedin, C. F. Sub-Molecular Modulation of a 4f Driven Kondo Resonance by Surface-Induced Asymmetry. *Nat. Commun.* **2016**, *7*, 12785.

(28) Bolívar, N.; Medina, E.; Berche, B. Persistent Charge and Spin Currents in the Long-Wavelength Regime for Graphene Rings. *Phys. Rev. B - Condens. Matter Mater. Phys.* **2014**, *89* (12), 1–10.

(29) Huang, B. L.; Chang, M. C.; Mou, C. Y. Persistent Currents in a Graphene Ring with Armchair Edges. *J. Phys. Condens. Matter* **2012**, *24* (24).

(30) Russo, S.; Oostinga, J. B.; Wehenkel, D.; Heersche, H. B.; Sobhani, S. S.; Vandersypen, L. M. K.; Morpurgo, A. F. Observation of Aharonov-Bohm Conductance Oscillations in a Graphene Ring. *Phys. Rev. B - Condens. Matter Mater. Phys.* **2008**, *77* (8), 1–5.

(31) Smirnov, D.; Schmidt, H.; Haug, R. J. Aharonov-Bohm Effect in an Electron-Hole Graphene Ring System. *Appl. Phys. Lett.* **2012**, *100* (20), 1–4.

3.9 Publication 9: Porous Graphene Nanoribbon and Porous Nanographene by Precursor- and Substrate-Controlled On-Surface Synthesis

Citation: Q. Fan, S. Werner, T. Koehler, T. Vollgraff, J. Sundermeyer, W. Hieringer, J. M. Gottfried, *manuscript in preparation*, **2021**.

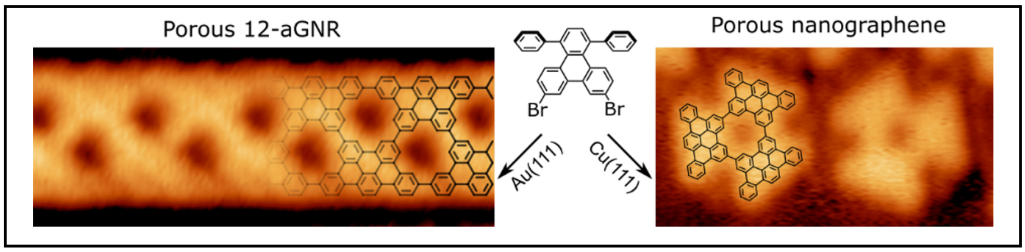

Summary: This communication adresses the question in how far effects of different surfaces determine the *on-Surface* reaction output of precursor DBDT. The C2-symmetric precursor was prepared in solution by a four step synthesis sequence starting from phenanthrene-dione, which was brominated and subsequently reacted in a Knoevenagel reaction followed by Diels-Alder reaction and desilylation described in supporting information. The final precursor was characterized by NMR, mass spectrometry and XRD. Deposited on the strongly interacting Cu(111) surface and heated to 200 °C, most exclusively cyclic trimers were formed by Ullmann reaction. The trimerization experiment was furthermore repeated in solution by Yamamoto reaction and the trimer was characterized in solution by optical spectroscopy, cyclovoltammetry, NMR, mass spectrometry and XRD (described in the supplement). The distances from XRD measurements could be well assigned to the features of the STM image of the non-planar trimer on Cu(111). Interestingly, on the weakly interacting Au(111) surface, porous polymer GNRs were predominantly formed. This could be explained by the decreased sterical repulsions hindering the polymerization on Cu(111). On Au(111), the molecules are weaker adsorbed and thus show higher sterical flexibility. The porous GNRs formed by Ullmann reaction and cyclodehydrogenation should show an increased band gap due to the regulary formed pores predicted by DFT calculations. These results demonstrate that not only the precursors shape determines the reaction outcome on surfaces, but also the strength of substrate-adsorbate interactions plays a crucial role.

Own Contribution: The precursor structure was designed by myself together with Dr. Q. Fan in discussion with Prof. Dr. J. Sundermeyer. The design of the retrosynthetical approach of the precursor DBTT, the chemical synthesis of precursor DBTT as well as the in-solution characterization was performed by myself. The in solution-based trimerization experiments and the full characterization (UV-Vis, PL, CV, NMR, mass spectrometry) were performed by myself. T. Vollgraff solved and refined the crystal structure of DBTT and the corresponding trimer. Dr. Q. Fan performed STM measurements together with T. Koehler under supervision of Prof. Dr. J. M. Gottfried. Dr. W. Hieringer performed DFT calculations. The manuscript was written by Dr. Q. Fan with input from all co-authors. The experimental part (chemical synthesis) was written by myself.

WILEY-VCH

COMMUNICATION

Porous Graphene Nanoribbon and Porous Nanographene by Precursor- and Substrate-Controlled On-Surface Synthesis

Qitang Fan,[a] Simon Werner,[a] Tabea Koehler,[a] Tobias Vollgraff,[a] Jörg Sundermeyer,*[a] Wolfgang Hieringer,*[b] J. Michael Gottfried*[a]

Abstract: Current methods for tuning the band gap of graphene nanoribbons (GNRs) use modifications of widths and edge topologies. Here, we report an additional approach, which relies on periodically arranged nanopores. The porous GNR was synthesized from a bromoarene precursor on a Au(111) surface via Ullmann coupling and cyclodehydrogenation. Additional control over the formation of the porous GNR or porous nanographene was achieved by using different metal surfaces. The structures of these products were elucidated by scanning tunneling microscopy (STM) and density functional theory (DFT) calculations.

The application of graphene derivatives in semiconductor devices such as field-effect transistors[1-6] requires band-gap tuning, which is typically achieved by chemical functionalization[7] or top-down modifications such as cutting[8, 9] and perforation.[10, 11] Although these methods have proven to open the band gap of graphene,[7, 8] they lack the atomic precision required for reproducible results.[9, 12] To account for the pronounced structure-sensitivity of the electronic properties,[13] bottom-up approaches have been introduced to synthesize graphene-related materials, including graphene nanoribbons (GNR),[12, 14-17] porous graphene[5, 18] and nanographenes.[19-23] They provide better control over widths and edge topologies as crucial structural properties of GNRs.[14, 15, 24] In particular, the solvent-free synthesis of graphene derivatives on metal surfaces has been widely used, because it works irrespective of the solubility of reactants and products.[12]

On the basis of haloarene precursors, various one-dimensional (1D) GNRs with well-defined widths and edge topologies have been prepared.[12] The influence of these two structural parameters on the electronic properties of GNRs has been elucidated by experimental and theoretical studies.[25] While remarkable structural control is achieved for 1D GNRs, attempts to synthesize 2D porous graphene nanomeshes typically result in small domain sizes and structural irregularities.[26] To date, only few examples of regular 2D porous graphene with extended domain sizes have been achieved by kinetic control[18] or hierarchical strategies.[5, 27] Due to this lack of a suitable well-defined model system, the understanding of the influence of nanopores on the band structure of graphene derivatives is limited.[28-31]

Here, we report the on-surface synthesis of a GNR with periodically arranged nanopores as an additional approach for band-gap engineering. Specifically, Ullmann coupling of 7,10-dibromo-1,4-diphenyl-triphenylene **1** (Scheme 1) on Au(111), followed by cyclodehydrogenation of the resulting polymer **3**, yields a porous armchair-edged GNR **4** with a width of 12 carbon atoms (12-aGNR). A different reaction is observed on Cu(111), where **1** forms the porous nanographene **2**. The product structures have been confirmed by STM and DFT. Both reported products **2** and **4** represent candidates for studying the influence of nanopores on the electronic properties of graphene derivatives. DFT-GGA calculations reveal an increased band gap of **4** compared to its nonporous counterpart.

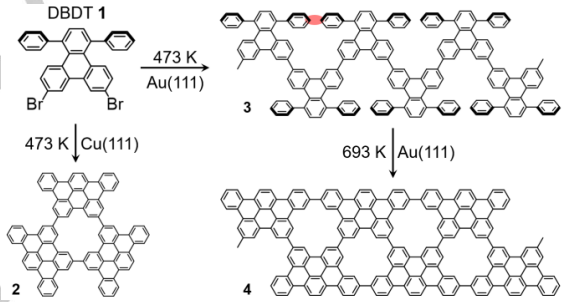

Scheme 1. Ullmann coupling and cyclodehydrogenation of 7,10-dibromo-1,4-diphenyl-triphenylene (DBDT) **1** on Cu(111) and Au(111) results in different products, i.e., porous nanographene **2** and porous graphene nanoribbon **4**, respectively.

Deposition of one monolayer of **1** onto Au(111) at 300 K, followed by annealing to 473 K, leads to the aligned polymer chains shown in Figure 1a. The magnified STM image in Figure 1c reveals periodically arranged protrusions at both sides of each chain. The repeat unit has a length of 13.0±0.2 Å, in agreement with the value of 12.8 Å[32] expected for **3**. As indicated by the chemical structure in Figure 1e, the protrusions are assigned to tilted phenyl groups, which are laterally displaced due to steric proximity effects.

Further annealing of the sample in Figure 1a to 693 K triggers cyclodehydrogenation and formation of the porous 12-aGNR **4** (Figure 1b). Its structure is confirmed by the uniform apparent height and a periodicity of 12.7±0.3 Å (Figure 1d), which compares well with the DFT-calculated value of 13.0 Å for free-standing **4**. The chemical structure, overlaid on an STM image, is displayed in Figure 1f. According to large-area STM images in Figure S1, the most probable length of **4** is approximately 35 nm, as shown by the inset in Figure 1d. Additionally, the influence of

[a] Dr. Q.T. Fan, S. Werner, T. Koehler, T. Vollgraff, Prof. J. Sundermeyer, Prof. J.M. Gottfried
Department of Chemistry, Philipps University Marburg
Hans-Meerwein-Straße 4, 35037 Marburg, Germany
E-mail: michael.gottfried@chemie.uni-marburg.de
[b] PD Dr. W. Hieringer
Theoretical Chemistry and Computer-Chemistry-Center, Department of Chemistry and Pharmacy, Friedrich-Alexander-Universität Erlangen-Nürnberg, Egerlandstraße 3, 91058 Erlangen, Germany

Supporting information for this article is given via a link at the end of the document.

the nanopores on the electronic properties of **4** was studied by calculations at the DFT-GGA level (PBE functional, see details in the SI). Figures 1g and 1h compare the band structures and densities of state (DOS) of the nonporous and porous 12-aGNR,[33] respectively. As demonstrated, the pores increase the band gap by 1.3 eV.

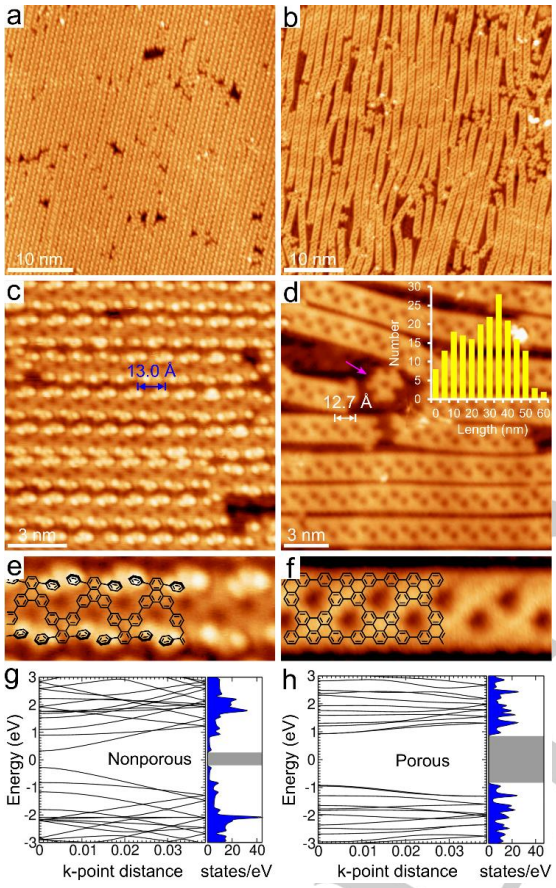

Figure 1. STM images (a) after deposition of **1** onto Au(111) at 473 K and (b) after annealing to 693 K. (c) and (d) show zoom-in STM images of the samples in (a) and (b), respectively. The inset in (d) shows the length distribution of **4**. Noteworthy, **2** appears as a minority species, as marked by the magenta arrow in (d). (e),(f) Chemical structures of **3** and **4** overlaid on STM images. Tunnelling parameters: (a) U = 2.9 V, I = 0.08 nA; (b) U = 1.0 V, I = 0.14 nA; (c) U = 2.5 V, I = 0.12 nA; (d) U = 1.0 V, I = 0.17 nA. (g),(h) Calculated band structures and DOS of the free-standing nonporous and porous 12-aGNR, with direct band gaps of 0.6 and 1.9 eV, respectively (periodic DFT calculations, PBE functional, see the SI for details).

On Cu(111), completely different products are obtained. As shown in Figure 2a, deposition of **1** onto Cu(111) at 300 K, followed by annealing to 373 K, leads to trimer macrocycles. Their structural details are shown by Figure 2c: Each macrocycle comprises six protrusions attributed to the six tilted phenyl groups from three diphenyl-triphenylene moieties. The measured distance between neighboring protrusions from adjacent diphenyl-triphenylene moieties is 11.1±0.3 Å (Figure 2c), which agrees with the center-to-center distance (10.9 Å) between C-Cu-C bonded triphenylenes.[34] We conclude that the diphenyl-triphenylene moieties are linked by C-Cu-C organometallic bonds, as illustrated in Figure 2e. Accordingly, the weak protrusions between each two adjacent diphenyl-triphenylene moieties are attributed to Cu atoms in C-Cu-C bridges. Further annealing to 473 K leads to planar trimer macrocycles and planar dimers (Figure 2b). In sharp contrast to the products obtained on Au(111) at 473 K (Figure 1a), no polymer chains are formed on Cu(111) at this temperature. The zoom-in STM image of a typical small island (Figure 2d) shows that the trimer macrocycles are planar and three-fold symmetric. The distance between two corners is 8.7±0.4 Å (Figure 2d, pink rectangle), indicating a reduced distance (-2.4 Å) compared to the organometallic macrocycle. This distance also agrees with the previously reported center-to-center distance (8.5 Å) between two C-C covalently bonded triphenylenes.[34] The product is therefore attributed to the nanographene **2**, formed by C-C covalent coupling and cyclodehydrogenation of diphenyl-triphenylene moieties. An enlarged STM image with overlaid structure is shown in Figure 2f. Noteworthy, the cyclodehydrogenation occurs already at 473 K on Cu(111), because this surface has a higher catalytic activity for C-H bond dissociation compared to Au(111).[35] Besides the trimer macrocycles, dimers consisting of two tribenzo[*b,n,pqr*]perylene moieties occur (green rectangle in Figure 2d). The measured distance of 15.5±0.4 Å between the outer peripheries of the two tribenzo[*b,n,pqr*]perylene moieties confirms their covalent linkage. An enlarged image with overlaid structure is shown in Figure 2g.

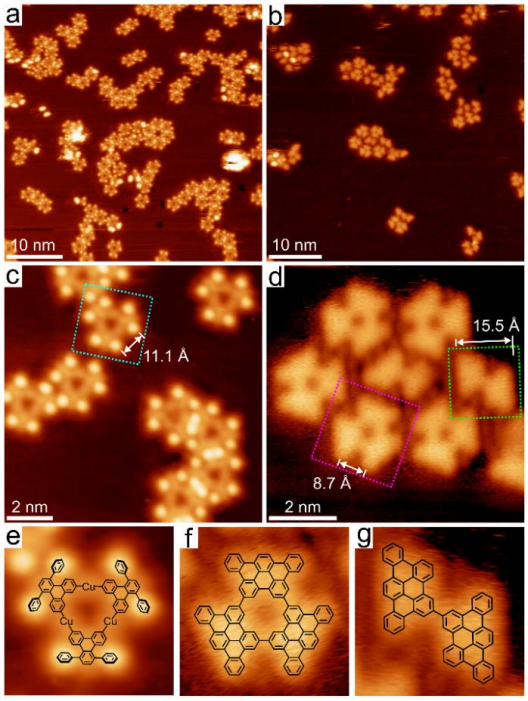

Figure 2. STM images taken after deposition of **1** onto Cu(111) at 300 K followed by annealing to (a) 373 K and (b) 473 K. (c) and (d) show zoom-in STM images of the samples in (a) and (b), respectively. (e-g) Chemical structures (overlaid on STM images) of the trimer macrocycle and dimer species marked by cyan, pink and green rectangles in (c) and (d). Tunnelling parameters: (a),(c) U = -1.8 V, I = 0.16 nA; (b) U = -1.9 V, I = 0.15 nA; (d) U = -1.9 V, I = 0.44 nA.

The formation of trimer macrocycle and dimer nanographenes, rather than porous graphene nanoribbons, on Cu(111) is attributed to previously reported stronger bonding of aromatic molecules to this surface, compared to Au(111).[36, 37] The increased interaction leads to a lower adsorption height and thus partial planarization of the precursor. As a result, its initial polymerization into linear chains is inhibited by steric hindrance between approaching diphenyl-triphenylene units (red oval in Scheme 1). Due to its weaker bond on Au(111), the precursor can more easily detach partly from the surface during bond formation to overcome such steric repulsion. This hypothesis is supported by the results for Ag(111), which represents the intermediate precursor-surface interaction (Cu > Ag > Au). As shown by Figure S2, annealing of **1** on Ag(111) to 473 K leads predominantly to covalently linked nonplanar dimers and trimer macrocycles, but not polymer chains, similar as on Cu(111). Note that the nonplanar trimer macrocycle was also synthesized in solution and was characterized by XRD analysis (see the SI).

In summary, by using different coinage metal surfaces, we achieved the selective synthesis of a porous 12-armchair edged graphene nanoribbon (12-aGNR) or porous nanographene from the same bromoarene precursor. The selectivity originates mainly from the special design of the precursor and the specific adsorbate-surface interactions, which cause surface-dependent different degrees of steric hindrance between the building blocks when forming polymer chains. DFT-GGA calculations predict that the nanopores substantially increase the band gap. This well-defined porous graphene nanoribbon may be a useful model system for further experimental studies of the influence of hexavacancy defects on the properties of graphene and its derivatives.

Acknowledgements

Financial support by the Deutsche Forschungsgemeinschaft (DFG, German Research Foundation) through project numbers 223848855-SFB1083 and GO1812/2-1 is acknowledged. Q.F. thanks the Alexander von Humboldt-Foundation for a Research Fellowship for Postdoctoral Researchers.

Keywords: porous graphene nanoribbon • porous nanographene • Ullmann coupling • cyclodehydrogenation • on-surface synthesis

[1] J. Wu, W. Pisula, K. Müllen, *Chem. Rev.* **2007**, *107*, 718-747.
[2] J. P. Llinas, A. Fairbrother, G. Borin Barin, W. Shi, K. Lee, S. Wu, B. Yong Choi, R. Braganza, J. Lear, N. Kau, W. Choi, C. Chen, Z. Pedramrazi, T. Dumslaff, A. Narita, X. Feng, K. Müllen, F. Fischer, A. Zettl, P. Ruffieux, E. Yablonovitch, M. Crommie, R. Fasel, J. Bokor, *Nat. Commun.* **2017**, *8*, 633.
[3] P. B. Bennett, Z. Pedramrazi, A. Madani, Y.-C. Chen, D. G. de Oteyza, C. Chen, F. R. Fischer, M. F. Crommie, J. Bokor, *Appl. Phys. Lett.* **2013**, *103*, 253114.
[4] V. Passi, A. Gahoi, B. V. Senkovskiy, D. Haberer, F. R. Fischer, A. Grüneis, M. C. Lemme, *ACS Appl. Mater. Inter.* **2018**, *10*, 9900-9903.
[5] C. Moreno, M. Vilas-Varela, B. Kretz, A. Garcia-Lekue, M. V. Costache, M. Paradinas, M. Panighel, G. Ceballos, S. O. Valenzuela, D. Peña, A. Mugarza, *Science* **2018**, *360*, 199.
[6] A. Celis, M. N. Nair, A. Taleb-Ibrahimi, E. H. Conrad, C. Berger, W. A. de Heer, A. Tejeda, *J. Phys. D: Appl. Phys.* **2016**, *49*, 143001.
[7] R. Balog, B. Jorgensen, L. Nilsson, M. Andersen, E. Rienks, M. Bianchi, M. Fanetti, E. Laegsgaard, A. Baraldi, S. Lizzit, Z. Sljivancanin, F. Besenbacher, B. Hammer, T. G. Pedersen, P. Hofmann, L. Hornekaer, *Nat. Mater.* **2010**, *9*, 315-319.
[8] C. Berger, Z. Song, X. Li, X. Wu, N. Brown, C. Naud, D. Mayou, T. Li, J. Hass, A. N. Marchenkov, E. H. Conrad, P. N. First, W. A. de Heer, *Science* **2006**, *312*, 1191.
[9] M. Y. Han, B. Özyilmaz, Y. Zhang, P. Kim, *Phys. Rev. Lett.* **2007**, *98*, 206805.
[10] J. Eroms, D. Weiss, *New J. Phys.* **2009**, *11*, 095021.
[11] W. Yuan, J. Chen, G. Shi, *Mater. Today* **2014**, *17*, 77-85.
[12] L. Talirz, P. Ruffieux, R. Fasel, *Adv. Mater.* **2016**, *28*, 6222-6231.
[13] O. V. Yazyev, *Acc. Chem. Res.* **2013**, *46*, 2319-2328.
[14] P. Ruffieux, S. Wang, B. Yang, C. Sánchez-Sánchez, J. Liu, T. Dienel, L. Talirz, P. Shinde, C. A. Pignedoli, D. Passerone, T. Dumslaff, X. Feng, K. Müllen, R. Fasel, *Nature* **2016**, *531*, 489-492.
[15] O. Gröning, S. Wang, X. Yao, C. A. Pignedoli, G. Borin Barin, C. Daniels, A. Cupo, V. Meunier, X. Feng, A. Narita, K. Müllen, P. Ruffieux, R. Fasel, *Nature* **2018**, *560*, 209-213.
[16] J. Cai, P. Ruffieux, R. Jaafar, M. Bieri, T. Braun, S. Blankenburg, M. Muoth, A. P. Seitsonen, M. Saleh, X. Feng, K. Müllen, R. Fasel, *Nature* **2010**, *466*, 470-473.
[17] J. Cai, C. A. Pignedoli, L. Talirz, P. Ruffieux, H. Sode, L. Liang, V. Meunier, R. Berger, R. Li, X. Feng, K. Müllen, R. Fasel, *Nat. Nanotechnol.* **2014**, *9*, 896-900.
[18] M. Bieri, M. Treier, J. Cai, K. Aït-Mansour, P. Ruffieux, O. Gröning, P. Gröning, M. Kastler, R. Rieger, X. Feng, K. Müllen, R. Fasel, *Chem. Commun.* **2009**, 6919-6921.
[19] A. Narita, X. Y. Wang, X. Feng, K. Müllen, *Chem. Soc. Rev.* **2015**, *44*, 6616-6643.
[20] N. Pavlicek, A. Mistry, Z. Majzik, N. Moll, G. Meyer, D. J. Fox, L. Gross, *Nat. Nanotechnol.* **2017**, *12*, 308-311.
[21] S. Mishra, D. Beyer, K. Eimre, J. Liu, R. Berger, O. Gröning, C. A. Pignedoli, K. Müllen, R. Fasel, X. Feng, P. Ruffieux, *J. Am. Chem. Soc.* **2019**, *141*, 10621-10625.
[22] J. Su, M. Telychko, P. Hu, G. Macam, P. Mutombo, H. Zhang, Y. Bao, F. Cheng, Z.-Q. Huang, Z. Qiu, S. J. R. Tan, H. Lin, P. Jelínek, F.-C. Chuang, J. Wu, J. Lu, *Sci. Adv.* **2019**, *5*, eaav7717.
[23] J. Hieulle, E. Carbonell-Sanroma, M. Vilas-Varela, A. Garcia-Lekue, E. Guitian, D. Pena, J. I. Pascual, *Nano lett.* **2018**, *18*, 418-423.
[24] D. J. Rizzo, G. Veber, T. Cao, C. Bronner, T. Chen, F. Zhao, H. Rodriguez, S. G. Louie, M. F. Crommie, F. R. Fischer, *Nature* **2018**, *560*, 204-208.
[25] L. Yang, C. H. Park, Y. W. Son, M. L. Cohen, S. G. Louie, *Phys. Rev. Lett.* **2007**, *99*, 186801.
[26] Q. Fan, J. M. Gottfried, J. Zhu, *Acc. Chem. Res.* **2015**, *48*, 2484-2494.
[27] J. Eichhorn, D. Nieckarz, O. Ochs, D. Samanta, M. Schmittel, P. J. Szabelski, M. Lackinger, *ACS Nano* **2014**, *8*, 7880-7889.
[28] J. J. Palacios, J. Fernández-Rossier, L. Brey, *Phys. Rev. B* **2008**, *77*, 195428.
[29] A. Baskin, P. Král, *Sci. Rep.* **2011**, *1*, 36.
[30] J. A. Fürst, J. G. Pedersen, C. Flindt, N. A. Mortensen, M. Brandbyge, T. G. Pedersen, A. P. Jauho, *New J. Phys.* **2009**, *11*, 095020.
[31] G. Calogero, I. Alcón, N. Papior, A.-P. Jauho, M. Brandbyge, *J. Am. Chem. Soc.* **2019**, *141*, 13081−13088.

[32] Q. Fan, J. M. Gottfried, *ChemPhysChem* **2019**, *20*, 2311-2316.
[33] Y.-W. Son, M. L. Cohen, S. G. Louie, *Phys. Rev. Lett.* **2006**, *97*, 216803.
[34] S. Zint, D. Ebeling, T. Schloder, S. Ahles, D. Mollenhauer, H. A. Wegner, A. Schirmeisen, *ACS Nano* **2017**, *11*, 4183−4190.
[35] Q. Fan, S. Werner, J. Tschakert, D. Ebeling, A. Schirmeisen, G. Hilt, W. Hieringer, J. M. Gottfried, *J. Am. Chem. Soc.* **2018**, *140*, 7526-7532.
[36] J. Björk, F. Hanke, S. Stafstrom, *J. Am. Chem. Soc.* **2013**, *135*, 5768-5775.
[37] W. Liu, F. Maaß, M. Willenbockel, C. Bronner, M. Schulze, S. Soubatch, F. S. Tautz, P. Tegeder, A. Tkatchenko, *Phys. Rev. Lett.* **2015**, *115*, 036104.

WILEY-VCH

Entry for the Table of Contents (Please choose one layout)

Layout 2:

COMMUNICATION

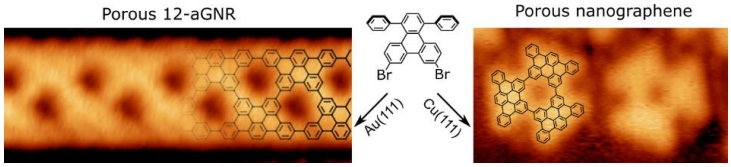

*Author(s), Corresponding Author(s)**

Page No. – Page No.

Title

By an on-surface synthetic approach, we have achieved the synthesis of two unprecedented graphene derivatives, i.e., a porous graphene nanoribbon and a porous nanographene, which can be used to study the influence of hexavacancy defects on the electronic properties of low-dimensional carbon-based materials.

WILEY-VCH

SUPPORTING INFORMATION

Supporting Information

Porous Graphene Nanoribbon and Porous Nanographene by Precursor- and Substrate-Controlled On-Surface Synthesis

Qitang Fan, Simon Werner, Tabea Koehler, Tobias Vollgraff, Jörg Sundermeyer,* Wolfgang Hieringer,* J. Michael Gottfried*

Table of contents

SUPPORTING INFORMATION

3. Synthetic details.

The precursor was synthesized in a four step synthesis starting with phenanthrene-9,10-dione (**M1**), which was brominated regioselectively in 3- and 6-position in the first step (**M2**) and subsequently reacted next in a Knoevenagel consensation resulting in diphenylketone **M3**. This was transfered into the silylated triphenylene **M4** via Diels-Alder reaction. The final step was accomplished via fluorid-mediated desilylation resulting in the final precursor (**DBDT**). This synthesis was adopted from the patent CN104447505A (B)[8] and is shown in scheme S1.

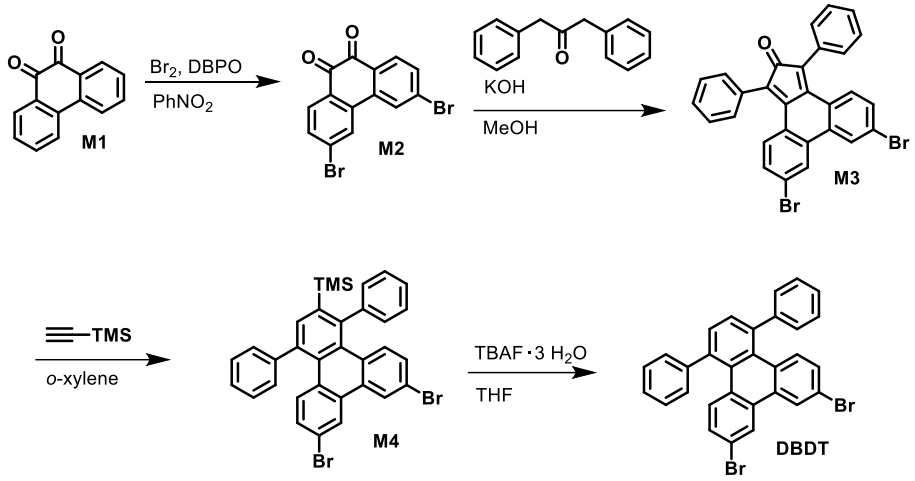

Scheme S1: Chemical synthesis of precursor **DBDT**.

In order to synthesize the trimerization product of precursor **DBDT** also in solution, the more soluble silylated triphenylene **M4** was trimerized in toluene/DMF solution using stoichiometric amounts of bis(cyclooctadiene)nickel(0) in a standard-Yamamoto reaction protocol, which was already applied in the trimerization of dibrominated triphenylenes by Müllen et al.[9] The blue fluorescent silylated trimeric reaction product was analogously desilylated to yield the trimeric macro- cyclization product which was also obtained via Ullmann reaction of precursor **DBDT** on Cu(111) described in the main text (see scheme S2 for the synthetical details).

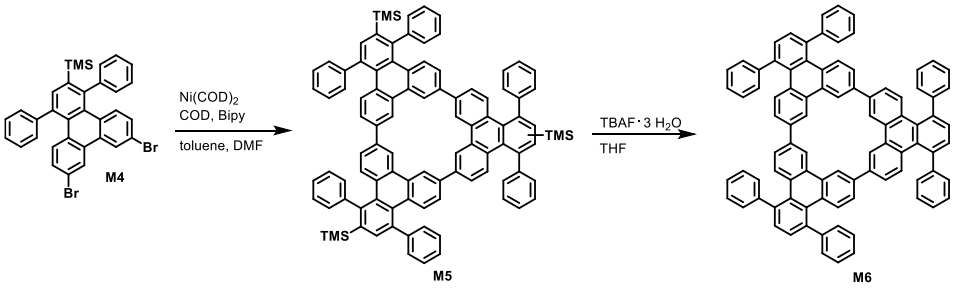

Scheme S2: In-solution approach for the trimerization of **M4** via Yamamoto cyclization and subsequent desilylation of **M5** to trimer **M6**.

The structure of trimer **M6** was unambiguously elucidated via standard solution characterization methods i.e. proton NMR spectroscopy and high resolution EI mass spectrometry. Furthermore, X-ray spectroscopy suited single crystals could be obtained by slow diffusion of *n*-pentane in a saturated solution of the trimer in THF. Trimer **M6** shows a high tendency for *π-stacking* in solid state with intermolecular distances of 3.20Å, which is close to the interlayer distance in graphite (equilibrium interlayer distance is 3.231 Å[10]). Furthermore, figure S1(a) shows the intramolecular centroid distance between two phenyl rings of neighbored triphenylene units (9.18 Å). This distance determined in the XRD structure is in agreement to the measured distance from the STM image (8.5 ± 0.4 Å, cf. figure S2f) of the covalent trimer. In the opposit of unsubstituted nanographene, trimer **M6** is slightly soluble in organic solvents like THF or dichloromethane because of the six phenyl side groups rotated out of the molecular plane as can be seen in the single crystal XRD-structure. This is consistent with the molecular shape of trimer **M6** on Cu(111) after Ullmann reaction, where the phenyl side groups appear as bright protrusions in the STM images. Figure S3 shows (a) a top view and (b) side view of the crystallographicaly determined molecular structure of **M6** and (c) the molecular arrangement in the crystal. The optoelectronical behaviour of trimer **M6** was also characterized in solution. From an approximately 10^{-5}M solution in dichloromethane, UV-Vis spectroscopy was performed (see figure S3 (e)). The adsorption maxima is located in the blue region of the visible light (346 nm). The corresponding emission spectrum (concentration 10^{-7}M) shows a photoluminescence (PL-) maximum at 423 nm (stokes-shift: 77 nm), making trimer **M6** also to a suitable candidate for application as a blue fluorescent dye in solution, what is illustrated in figure S3 (d) showing an photography of a solution of **M6** in dichloromethane irradiated with UV light (366 nm). The intersection wavelength of the normed UV-Vis and PL spectrum is a common approximation for estimating the bandgap energy.[11] For trimer **M6** this can be determined at a wavelength of λ=388 nm (3.80 eV). The cyclic voltammogram (figure S3 (f)) shows two oxidation waves: one reversible first oxidation potential ($E_{1/2}$ = 0.92 V vs. ferrocene/ferrocenium-cation) and one irreversible second oxidation potential at 2.20 V vs. ferrocene/ferrocenium.

SUPPORTING INFORMATION

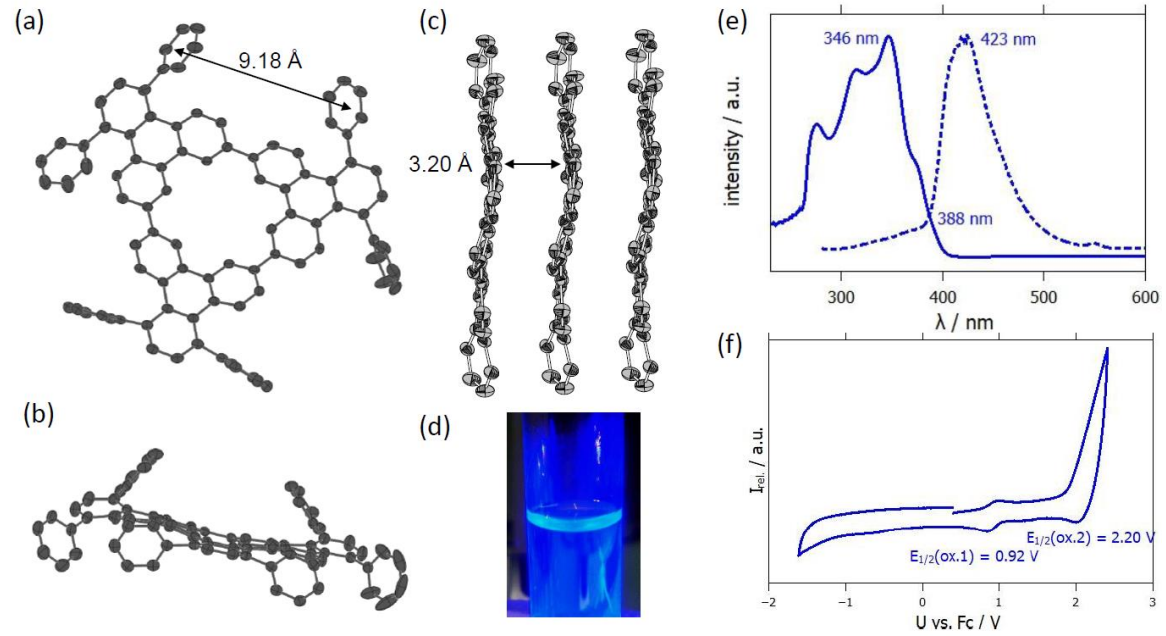

Figure S3: In-solution characterization of trimer **M6**: (a) and (b) single crystal X-ray structure; (c) solid state arrangement of the molecules driven by π-stacking; (d) sample of **M6** in dichloromethane under irradiation with UV light; (e) UV-Vis spectrum and photoluminescence (PL-) spectrum (dashed, λ_{ex}= 300 nm) of **M6** in dichloromethane; (f) cyclic voltammogram of **M6** in dichloromethane referenced with ferrocene.

General Information

All reactions were carried out under inert atmosphere (nitrogen) using Schlenk techniques if not mentioned otherwise. All reagents were purchased from commercial sources if not mentioned otherwise and were used without further purification. For thin-layer chromatography, TLC plates from Merck KGaA with silica gel 60 on aluminum with fluorescence-quenching F254 at room temperature were used. All solvents were dried and/or purified according to standard procedures and stored over 3 Å or 4 Å molecular sieves. NMR spectra were recorded in automation or by the service department (faculty of Chemistry, Philipps University Marburg) with a Bruker Avance 300 or 500 spectrometer at 298 K using CD_2Cl_2 or $CDCl_3$ as solvent and for calibration (residual proton signals). HR-APCI mass spectra were acquired with a LTQ-FT Ultra mass spectrometer (Thermo Fischer Scientific). The resolution was set to 100.000. HR-EI mass spectra were ac- quired with a AccuTOF GCv 4G (JEOL) Time of Flight (TOF) mass spectrometer. An internal or external standard was used for drift time correction. The LIFDI ion source and FD-emitters were purchased from Linden ChroMasSpec GmbH (Bremen, Germany). The data collection for the single-crystal structure determination was performed on a Stoe Stadivari diffractometer or a Bruker D8 Quest diffractometer by the X-ray service department of the department of chemistry at the university of Marburg. Information concerning the used hardware, and software used for data collection, cell refinement and data reduction as well as structure solution and refinement can be reviewed in the attached CIF-files. After the solution (Shelxt)[12] and refinement process (Shelxl 2017/1)[13] the data was validated by using Platon.[14] and SQUEEZE[15]. All graphic representations were created with Diamond 4.[16]. IR spectra are recorded with a Bruker Alpha FT-IR spectrometer with Platinum ATR sampling. Absorption spectra were recorded with a Varian Cary-5000 UV/Vis/NIR spectrophotometer in 10 mm cuvettes in dichloromethane with concentrations of 10 μM with a scan rate of 600 nm/min. Emission spectra were recorded with a Varian Cary Eclipse Spectrophotometer in 10 nm cuvettes in dichloromethane with a scan rate of 600 nm/min. Cyclic voltammetry and dif- ferential pulse voltammetry measurements are carried out on a rhd instruments TSC 1600 closed electrochemical workstation (working electrode: glassy carbon; counter electrode: platinum cru- cible; reference electrode: platinum wire (pseudo reference electrode under nitrogen atmosphere in a glovebox (Labmaster 130, mBraun). **7** was measured in dichloromethane and calibrated using ferrocene as internal standard after measurements. Dichloromethane was filtered through an aluminum oxide pad prior to use. Tetrabutylammonium hexafluorophosphate ($TBAPF_6$; >99.0 %) is used as electrolyte for electrochemical analysis. The measurements were carried out at a concentration of 100 mmol/L of electrolyte.

SUPPORTING INFORMATION

Chemical synthesis of Precursor DBDT and its macrocyclization

3,6-Dibromophenanthrene-9,10-dione (**M2**)

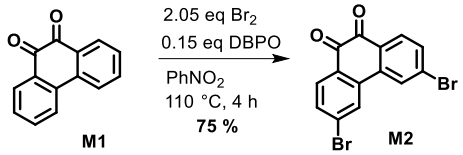

According to a synthesis of Hecht[17] 2.98 g (14.4 mmol, 1.00 eq) phenanthrene-9,10-dione (**M1**) and 0.60 g (2.3 mmol, 0.15 eq) dibenzoyl peroxide were suspended in 18 mL nitrobenzene. To the stirred suspension, 1.5 mL (28.9 mmol, 2.05 eq) bromine were added dropwise. The dark reaction mixture was heated to 110 °C for 4 h and a yellow precipitate was formed. After detection of complete conversion by TLC, the reaction mixture was cooled to room temperature and 35 mL ethanol were added. The crude product was filtered and washed with ethanol, diethyl ether and *n*-pentane and dried in vacuo. 3.94 g (10.8 mmol, 75%) of the desired compound **M2** were obtained as yellow solid.

^{1}H NMR: 300 MHz, 298 K, CD_2Cl_2, δ = 8.17 (d, 2H, ^4J = 1.74 Hz, *H* 3), 8.02 (d, 2H, ^3J = 8.34 Hz, *H* 1), 7.68 (dd, 2H, ^4J = 1.74 Hz, ^3J = 8.34 Hz, *H* 2) ppm.

^{13}C NMR: 75 MHz, 298 K, CD_2Cl_2, δ = 179.3, 136.4, 133.8, 132.2, 132.2, 130.4, 128.0 ppm.

The analytical data are in accordance with the literature.[17]

6,9-Dibromo-1,3-diphenyl-2*H*-cyclopenta[*l*]phenanthren-2-one (**M3**)

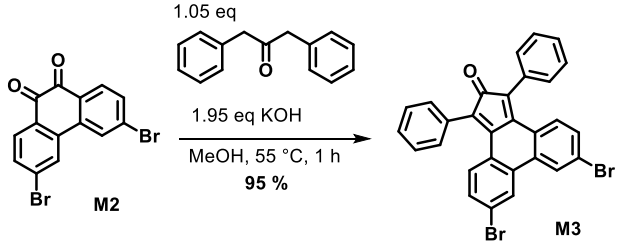

According to a synthesis of Förster and co-workers[18] 2.00 g (5.5 mmol, 1.00 eq) 3,6-dibromophenanthrene- 9,10-dione (**M2**) and 586 mg (10.4 mmol, 1.90 eq) potassium hydroxide were dissolved in 20 mL methanol. To the solution, 1.2 mL (5.8 mmol, 1.05 eq) 1,3-diphenylpropan-2-one were added dropwise. A color change towards a dark brownish solution occurred and the reaction mixture was stirred at 55 °C for 1 h and a dark green precipitate was formed. After detection of complete conversion by TLC, the reaction mixture was cooled to room temperature and 50 mL methanol were added. The crude product was filtered and washed with cold methanol, diethyl ether and *n*-pentane and dried *in vacuo*. 2.80 g (5.20 mmol, 95%) of the desired compound **M3** were obtained as dark green solid.

^{1}H NMR: 300 MHz, 298 K, CD_2Cl_2, δ = 7.93 (d, 2H, ^4J = 1.94 Hz, *H* 3), 7.46-7.33 (m, 12H), 7.11 (dd, 2H, ^4J = 1.94 Hz, ^3J = 8.65 Hz, *H* 2) ppm.

^{13}C NMR: 75 MHz, 298 K, CD_2Cl_2, δ = no signals resolved due to low solubility.

The analytical data are in accordance with the literature.[18]

(7,10-Dibromo-1,4-diphenyltriphenylen-2-yl)trimethylsilane (**M4**)

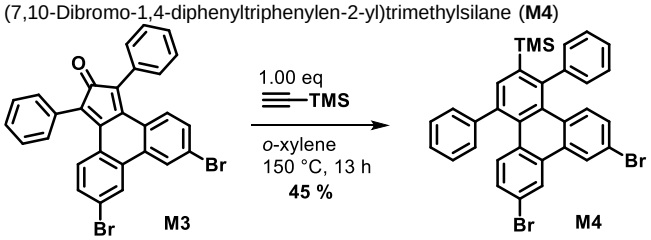

According to a described synthesis in the patent CN104447505A (B)[8] 1.50 g (2.80 mmol, 1.00 eq) **M3** and 0.4 mL (2.80 mmol, 1.00 eq) trimethylsilyl acetylene were dissolved in 18 mL *o*-xylene. The reaction solution was stirred at 150 °C for 13 h and after this complete conversion could be detected by TLC. silica gel was added to the reaction solution and the solvent was evaporated. The crude product was purified by column chromatography on silica gel (eluent: dichloromethane/*n*-pentane 3:4). 750 mg (1.20 mmol, 45%) of the desired compound **M4** were obtained as yellow solid.

TLC: R_f = 0.30 (*n*-pentane/dichloromethane 10:1)

SUPPORTING INFORMATION

^{1}H NMR: 300 MHz, 298 K, $CDCl_3$, δ = 8.43 (2d, 2H, ^4J = 2.00 Hz, *H*8, *H*9), 7.82 (s, 1H, *H*3), 7.56 (d, 1H, ^3J = 8.98 Hz, *H*5), 7.45-7.34 (m, 11H, *H*5, 10H_{Ph}), 7.18 (dd, 1H, ^4J = 2.04 Hz, ^3J = 8.98 Hz, *H*6 or *H*11), 7.12 (dd, 1H, ^4J = 2.11 Hz,^3J = 9.08 Hz, *H*6 or *H*11) ppm.

^{13}C NMR: 75 MHz, 298 K, $CDCl_3$, δ = 145.5, 144.9, 144.5, 140.1, 137.4, 137.0, 132.3, 132.0, 131.7, 131.6, 130.5, 130.3, 130.0, 129.7, 129.5, 129.4, 129.2, 129.1, 129.1, 127.9, 127.5, 126.0, 121.5, 121.0, 1.1 ppm.

^{29}Si NMR: 126 MHz, 298 K, $CDCl_3$, δ = -3.3 ppm.

HRMS: *m/z* for $[C_{33}H_{26}{}^{79}Br_2{}^{29}Si]^+$ calc.: 608.01705, found: 608.01682 (EI+).

IR (ATR): $\tilde{\nu}$ = 3054 (w), 2949 (w), 2896 (w), 1591 (m), 1530 (w), 1485 (w), 1442 (m), 1413 (w), 1382 (w), 1348 (w), 1308 (w), 1246 (w), 1173 (m), 1100 (w), 1076 (w), 1019 (m), 950 (s), 917 (w), 865 (w), 822 (s), 789 (vs), 759 (s), 699 (s), 626 (vs), 589 (w), 525 (w), 435 (w) cm^{-1}.

m. p.: 249-252 °C

7,10-Dibromo-1,4-diphenyltriphenylene (**DBDT**)

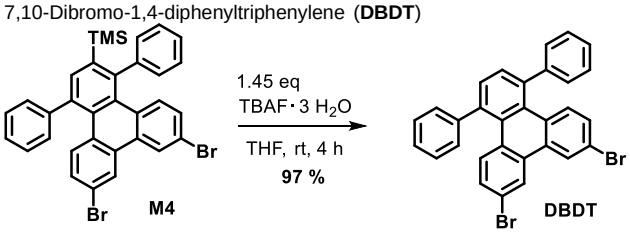

According to a described synthesis in the patent CN104447505A (B)[8] 500 mg (0.82 mmol, 1.00 eq) **M4** were dissolved in 18 mL THF. A solution of 380 mg (1.20 mmol, 1.45 eq) tetrabutylammonium fluoride trihydrate in 2.5 mL THF was added dropwise and the colorless reaction solution turned subsequently to an orange color. The reaction solution was stirred at room temperature for 4 h until complete conversion could be detected by TLC. The crude product was precipitated into water (20 mL), filtered and washed with *n*-pentane. Pure product was obtained after sublimation at HV-sublimation (205°C at $5.5 \cdot 10^{-7}$ mbar). 425 mg (0.79 mmol, 97%) of the desired compound **DBDT** were obtained as colorless solid.

TLC: R_f = 0.25 (*n*-pentane/dichloromethane 10:1)

^{1}H NMR: 300 MHz, 298 K, $CDCl_3$, δ = 8.46 (2d, 2H, ^4J = 1.96 Hz, *H*8, *H*9), 7.56-7.53 (m, 4H, *H*2, *H*3, *H*5, *H*12), 7.44-7.40 (m, 10H, H_{Ph}), 7.18 (dd, 2H, ^4J = 1.98 Hz, ^3J = 8.98 Hz, *H*6, *H*11) ppm.

^{13}C NMR: 75 MHz, 298 K, $CDCl_3$, δ = 144.2, 139.3, 132.0, 131.7, 130.6, 130.5, 129.7, 129.6, 129.4, 129.2, 127.6, 126.2, 121.4 ppm.

HRMS: *m/z* for $[C_{33}H_{18}{}^{79}Br_2]^+$ calc.: 535.97753, found: 535.97535 (EI+).

IR (ATR): $\tilde{\nu}$ = 3020 (w), 2015 (w), 1939 (w), 1877 (m), 1730 (w), 1676 (w), 1586 (m), 1523 (m), 1486 (w), 1441 (w), 1411 (w), 1362 (m), 1302 (w), 1257 (w), 1215 (m), 1170 (w), 1094 (w), 1018 (w), 950 (m), 911 (w), 858 (m), 807 (s), 792 (s), 757 (s), 693 (vs), 641 (m), 611 (m), 572 (w) cm^{-1}.

m. p.: 324-327 °C

(1^5,1^8,2^5,2^8,3^5,3^8-Hexaphenyl-1,2,3(2,11)-tritriphenylenacyclopropaphane-1^6,2^7,3^6-triyl)tris(trimethylsilane) (**M5**)

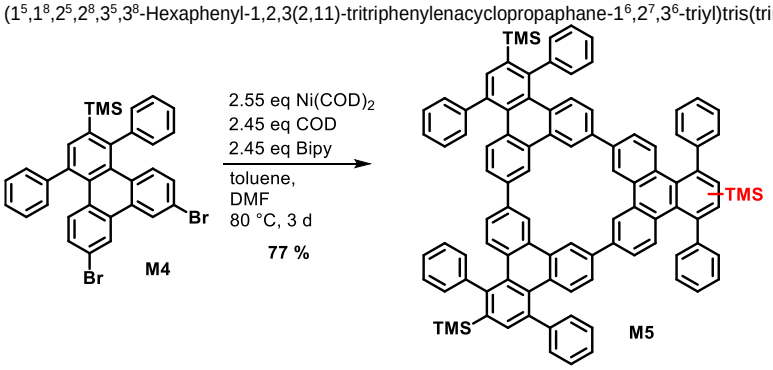

SUPPORTING INFORMATION

Adopting the synthesis protocol of Müllen et al. for Yamamoto-cyclotrimerizations of substituted triphenylenes[9], 565 mg (2.05 mmol, 2.55 eq) $Ni(COD)_2$, 315 mg (2.02 mmol, 2.45 eq) 2,2-bipyridyl and 0.25 mL cyclooctadiene (2.02 mmol, 2.45 eq) were dissolved in 8 mL DMF and 4 mL toluene under glovebox conditions and stirred under exclusion of light for 30 min at 60°C. A solution of 490 mg (0.81 mmol, 1.00 eq) **M4** in 40 mL toluene was added dropwise over a period of 30 min and the reaction mixture was stirred for 3 d at 80°C. After detection of complete conversion (TLC), the mixture was cooled to room temperature and 30 mL of 10 % HCL were added. After stirring for 1 h at room temperature, the organic layer was separated and the aqueous layer was extracted with ethyl acetate (3 x 20 mL) and the combined organic layers were dried over $MgSO_4$. The crude product was purified *via* column chromatography (*n*-pentane/dichloromethane 4:1). 280 mg (0.20 mmol, 77%) of the desired compound **M5** were obtained as colorless solid with a strong blue fluorescence. The product is an inseparable mixture of two constitutional isomers of the TMS-group ([1,1,2]- and [1,1,1]-substitution pattern).

TLC: R_f = 0.25 (*n*-pentane/dichloromethane 4:1).

^{1}H NMR: 300 MHz, 298 K, $CDCl_3$, δ = 9.54 (d, 6H, ^3J = 8.65 Hz, H_{cavity}), 7.88-7.78 (m, 6H), 7.68-7.40 (m, 39H), 0.14 and 0.18 (s, 9H and 18H, H_{TMS}) ppm.

^{13}C NMR: 75 MHz, 298 K, $CDCl_3$, δ = 145.8, 145.5, 145.1, 139.5, 139.5, 137.7, 136.8, 136.6, 136.4, 135.7, 135.7, 132.3, 132.2, 131.5, 131.1, 130.8, 130.7, 130.6, 130.2, 130.1, 129.8, 129.4, 129.0, 128.8, 127.8, 127.3, 123.0, 122.9, 120.4, 120.2, 1.2 ppm.

^{29}Si NMR: 126 MHz, 298 K, $CDCl_3$, δ = -3.5 ppm.

HRMS: *m/z* for $[C_{99}H_{78}{}^{29}Si_3]^+$ calc.: 1350.54113, found: 1350.54375 (EI+).

IR (ATR): $\tilde{\nu}$ = 2959 (w), 2920 (w), 2852 (w), 1603 (w), 1535 (w), 1492 (w), 1440 (m), 1311 (w), 1256 (w), 1080 (m), 1016 (s), 866 (w), 794 (vs), 696 (s), 629 (s), 588 (m), 531 (w) cm^{-1}.

m. p.: > 360 °C dec.

(1^5,1^8,2^5,2^8,3^5,3^8-Hexaphenyl-1,2,3(2,11)-tritriphenylenacyclopropaphane (**M6**)

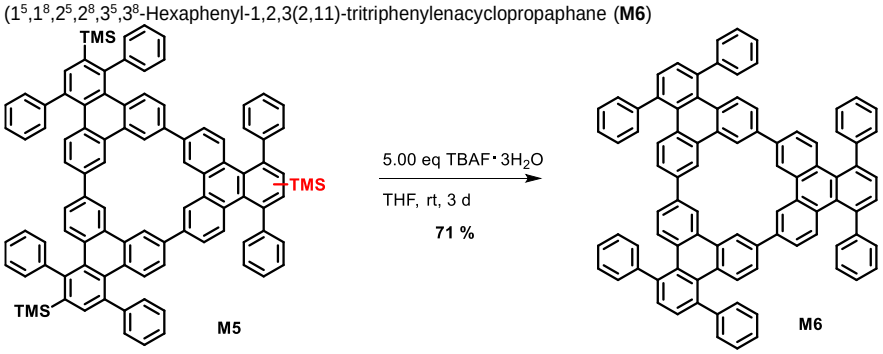

To a solution of **M5** (100 mg, 75 µmol, 1.00 eq) in 3 mL THF were added 0.38 mL (375 µmol, 5.00 eq) of a 1 M solution of TBAF·$3H_2O$. The resulting beige solution was stirred for 3 d at room temperature until complete conversion of **M5** could be monitored by TLC. The resulting suspension which contained precipitated product **M6** was diluted with 10 mL ethyl acetate and washed with 10 mL water. The aqueous layer was extracted with ethyl acetate (2 x 10 mL) and the combined organic layers were dried over magnesium sulphate. The crude product was purified via column chromatography (*n*-pentane/dichloromethane 4:1). 60 mg (53 µmol, 71%) of the desired compound **M6** were obtained as colorless solid with a strong blue fluorescence.

TLC: R_f = 0.20 (*n*-pentane/dichloromethane 4:1).

^{1}H NMR: 500 MHz, $CDCl_3$, δ = 9.56 (s, 6H, H_{cavity}), 7.76 (d, 6H, ^3J = 8.75 Hz), 7.61 (dd, 6H, ^3J = 8.75 Hz, ^4J = 1.45 Hz), 7.56-7.33 (m, 36H) ppm.

^{13}C NMR: not recorded due to low solubility.

HRMS: *m/z* for $[C_{90}H_{54}]^+$ calc.: 1134.42255, found: 1134.42331 (EI+).

IR (ATR): $\tilde{\nu}$ = 2959 (w), 2922 (w), 2853 (w), 1725 (w), 1600 (m), 1450 (w), 1258 (s), 1080 (vs), 1016 (vs), 869 (m), 795 (vs), 696 (s), 537 (w) cm^{-1}.

m. p.: > 360 °C dec.

3.10 Further work

Within this section, further preliminary experimental work is described that has not yet found entry in a scientific publication manuscript since further experimental work of cooperation partners in surface chemistry is in progress to the date of printing this thesis

3.10.1 Synthesis of Precursor DB9P for *on-Surface* Synthesis of C108

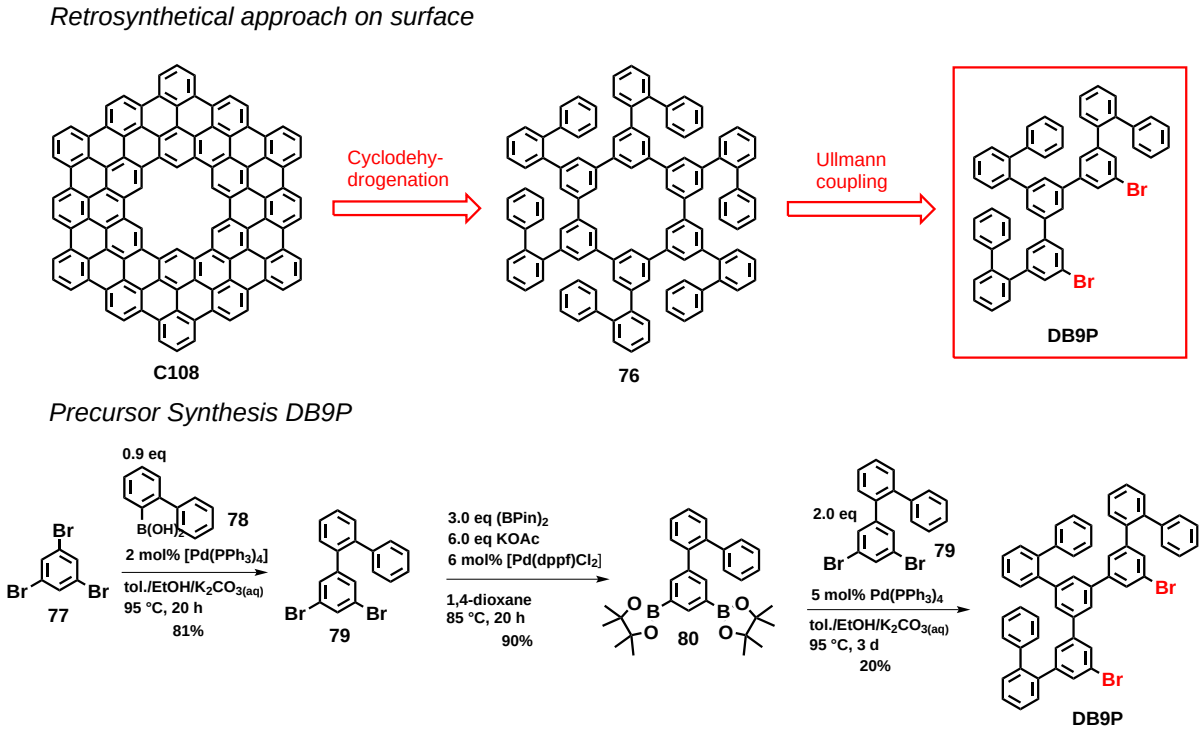

Scheme 3.1 Retrosynthetical approach for the *on-surface* synthesis of **C108** starting from **DB9P** and synthesis route towards **DB9P**.

Since the synthesis of **C108** on metal surfaces via trimerization of precursor **DBTT** led to several side products, a simpler approach via dimerization of a suitable precursor followed by cyclodehydrogenation was persued. For this purpose, the two-step *on-Surface* generation of **C108** was traced back to dibromo-terphenyl-based precursor **DB9P** (Scheme 3.1).

DB9P could be synthesized in a three-step sequence starting from commercially available tribromobenzene (**77**). This was reacted in a one-fold Suzuki-Miyaura coupling with 1-biphenylboronic acid (**78**) furnishing dibromo-*o*-terphenyl **79** in high yield (81%). **79** was bis-borylated to **80** via Miyaura borylation in excellent yields. Both terphenyls **79** and **80** were subsequently twofold coupled by use of a Suzuki-Miyaura cross coupling. Although the appropriate ratio between **79** and **80** was used, **DB9P** could only be obtained in low yield (20%). Higher oligomers had to be separated by column chromatography and multiple dissolution in chloroform and re-precipitation with *n*-pentane.

To achieve higher yields of **DB9P**, the bis-brominated reaction partner **79** should be reacted in excess (> 3 eq) with borylated compound **80**. Preliminary results of *on-Surface* dimerization

and subsequent planarization by Dr. FAN (group of Prof. Dr. GOTTFRIED) revealed a successful dimerization of **DB9P** on Au(111) at a temperature of 200 °C via ULLMANN reaction followed by cyclodehydrogenative planarization at 400 °C furnishing **C108** in high yields (see Scheme 3.2 for STM image of non-planar dimerization product **76**).

In order to test if bis-brominated *o*-terphenyl **79** is a suitable starting material to form a cyclic hexamer in solution, it was reacted in a YAMAMOTO cyclization.[253] Stoichiometric amounts of the coupling mediator system $[Ni(COD)_2]$/bipy were used and **79** was added dropwise to the catalyst solution at 80 °C under high dilution (10^{-4} M). After purification by column chromatography using a gradient of chloroform in *n*-hexane, fractions of different macrocycles could be separated, eluating one after another due to their increasing molecular mass. Although the geometrical angle of 120° between the bromine atoms should favor hexamer **76**, it was not the only macrocyclization product (Scheme 3.2). **76** could be isolated (14% yield) along with a smaller pentamer **81** (6%), a heptamer **82** (11%) and even an octamer **83** (5%) beside inseparable larger acyclic oligomers. The products could be detected and identified via EI(+) mass spectrometry. ^{1}H NMR proved not to be meaningful, since all congeners showed a broad multiplet in the aromatic region due to their high aggregation tendency.

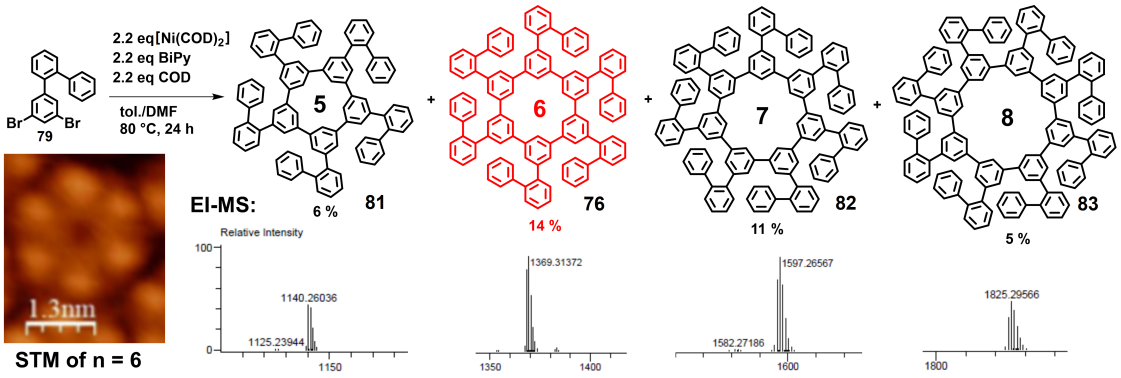

Scheme 3.2 YAMAMOTO reaction of terphenyl **79** and EI mass spectra of the corresponding macrocycles. Inset: STM image of hexamer **76** on Au(111), shown with the friendly permission of Prof. Dr. GOTTFRIED.

Encouraged by the successful *on-surface* planarization of the non-planar hexamer **76** by surface-assisted cyclodehydrogenation, attempts were performed to planarize pentamer **81** and hexamer **76** in solution via SCHOLL reaction using an excess (7.5 eq/H) of $FeCl_3$ as oxidant[249] in dichloromethane at room temperature. The reaction mixtures changed their color instantaneously to black and upon addition of methanol, a black solid could be precipitated. The obtained precipitates were completely insoluble in common organic solvents and identification via mass spectrometry (FD, EI, CI, APCI) did not give any evidence for the formation of the planarized reaction products. Unfortunately, suitable characterization methods for the completely planar and unsubstituted nanographenes such as MALDI-TOF mass spectrometry are not accessible at the faculty.

3.10.2 Synthesis of C108 Nanographene in Solution - Attempts

Parallel to the *on-surface* synthesis of C108 nanographene,[254] the porous macrocycle should also be synthesized and characterized by solution chemistry approaches. A suitable *in solution* approach for cyclic trimerization of bis-halogenated molecules derived from 3,6-dibromophenanthrene-9,10-dione (halogen atoms include ideal angle of 120°) are YAMAMOTO trimerization reactions under highly diluted conditions (10^{-4} M). Typical YAMAMOTO reaction conditions, as discussed above, should furnish the trimerization product of rigid 3,6-dibromophenanthrene scaffolds in high yield due to the ideal 120 ° angle of the bromine atoms. This was applyied to 84, the more soluble silylated derivative of precursor **DBTT** for *on-surface* synthesis of **C108**, which is discussed in Publication 6 (Scheme 3.3).

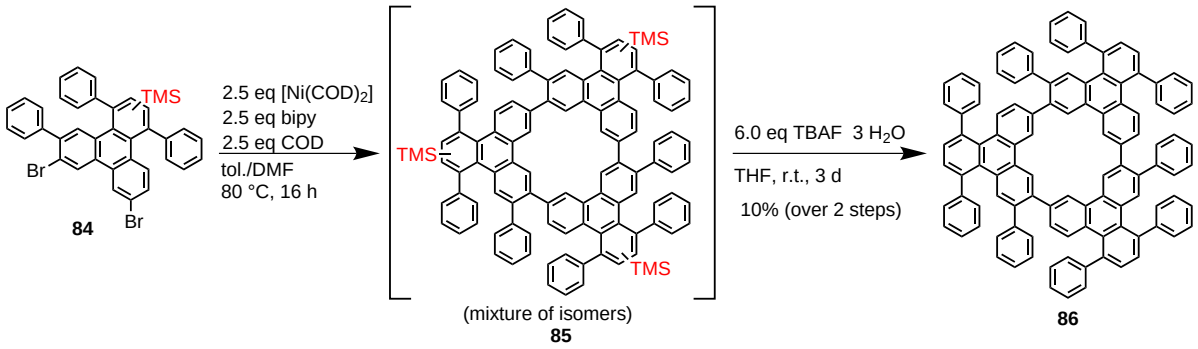

Scheme 3.3 *In solution* synthesis of macrocyclic trimer **86** for **C108** synthesis.

The obtained trimerization product **85** (along with larger oligomers) was directly reacted with TBAF trihydrate in order to remove the TMS groups. After column chromatography, the non-planar trimer **86** could be isolated as a beige powder. The large molecular weight accompanied with the low solubility made characterization via ^{1}H NMR spectroscopy difficult due to broadened signals resulting from molecular aggregation (Figure 3.1 (b)). Nevertheless, product formation could be verified with electron ionization (EI) mass spectrometry (Figure 3.1 (a)).

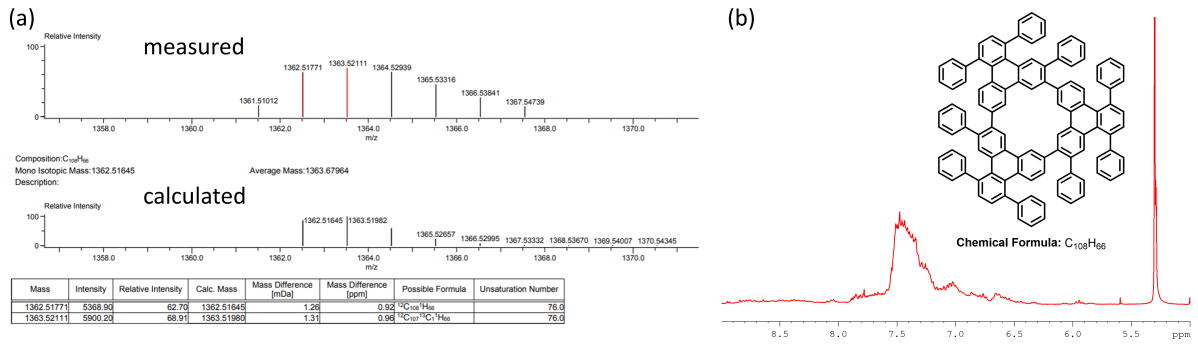

Fig. 3.1 (a) HR-EI(+) mass spectum of trimer **86**; (b) ^{1}H NMR spectrum (300 MHz, CD_2Cl_2) of trimer **86** sowing one broad, weakly resolved aromatic multiplet signal.

As reported previously for comparably large PAHs,[249] **86** was reacted in a SCHOLL reaction conditions (7.5 eq $FeCl_3$/H in DCM/MeCN at room temperature and continous argon flow), but after precipitation the black powder with MeOH and filtration, the formation of **C108** could not be verified by EI-MS.

Since the unsubstituted planar **C108** nanographene proofed to be to insoluble for characterization and even MS-detection in common organic solvents, substituted derivatives of the precursor **DBTT** were synthesized. A bis-hexyl substituted and a bis-hexylether substituted congener were synthesized, since long-chained alkyl and alkoxy groups are known to solubilize nanographenes without deactivating the SCHOLL reaction.[255] The alkoxy-substituted precursor **98** was synthesized analogously to our reported synthesis of **DBTT**[254] by use of bis(hexoxy)phenyl boronic acid[255] for the SUZUKI-MIYAURA coupling step (Scheme 3.4). The preceding steps to the mixed brominated and iodinated congener **96** were already published in the synthesis of **DBTT** and start with phenanthrenedione, which was regioselectively bisbrominated and iodinated to **93** and subsequently reacted with dibenzyl ketone in a KNOEVENAGEL reaction towards ketone **95**. **95** was used for a DIELS-ALDER reaction together with trimethylsilyl acetylene under CO extrusion to built up the final scaffold **96**. Under the chosen conditions, the cross coupling reaction with boronic acid **90**[255] showed incomplete conversion, delivering the hexylether-substituted, TMS protected congener **97** in moderate yield (44% borsm). In contrast to the reported synthesis of **DBTT**, the TMS deprotection in the last step also proceeded only with moderate yield and complete conversion of **97** to **98** was only achieved if TBAF trihydrate was used in excess (10 eq). The lower yields and conversions of the two last steps in comparison to the previously described synthesis of **DBTT** could be explained with the higher sterical demand of the additional hexylether groups.

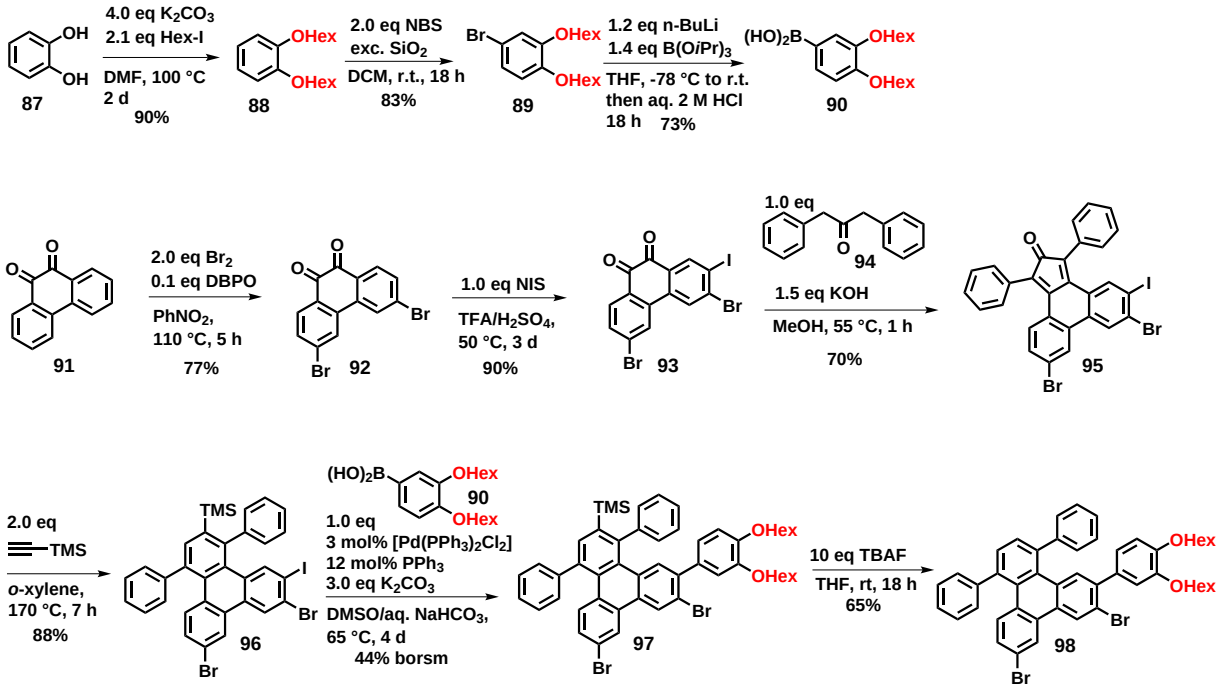

Scheme 3.4 Synthesis of bis-hexoxylated **C108** precursor **98**.

Nevertheless, precursor **98** could be obtained in high purity after column chromatography and each signal could be assigned to the corresponding protons in the ^{1}H NMR spectrum. The solubility is significantly improved in comparison to **DBTT**. Figure 3.2 shows the ^{1}H NMR spectrum of **98** and the assignment of the signals.

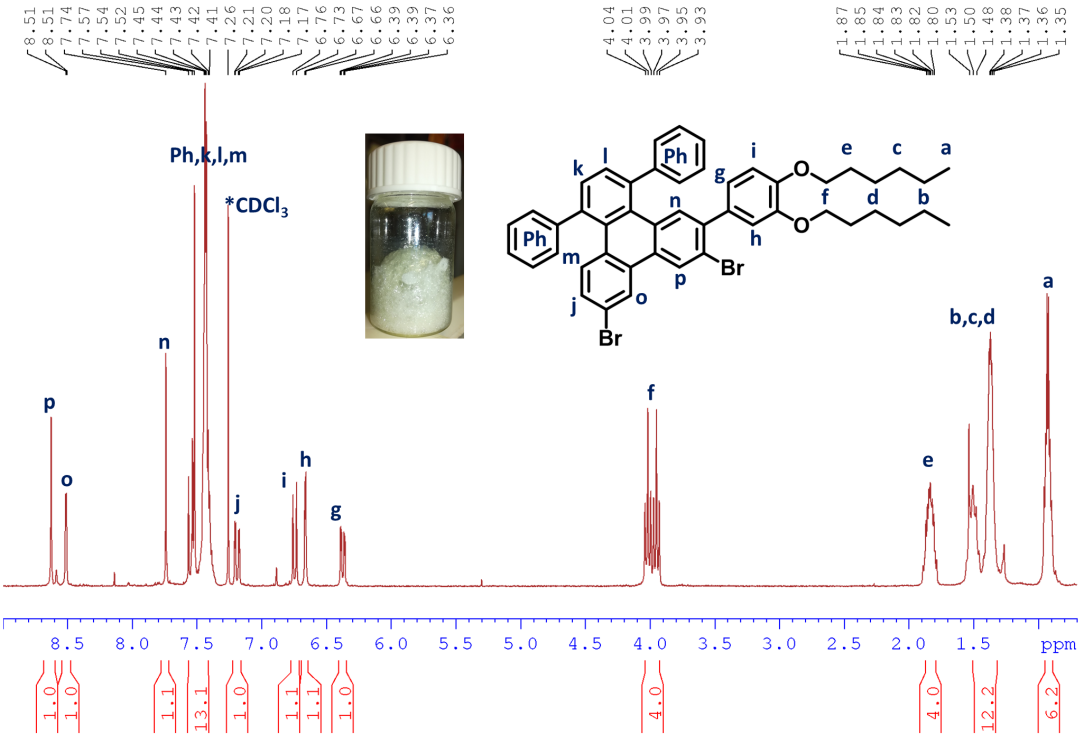

Fig. 3.2 ^{1}H NMR spectrum (300 MHz, $CDCl_3$) of **98** and assignment of the signals to the chemical structure.

When **98** was reacted under identical conditions as the TMS-substituted congener **84** (see Scheme 3.1) in a Ni-mediated YAMAMOTO reaction, only unselective conversion to higher molecular oligomers could be detected and no evidence for the formation of the corresponding cyclic trimer could be obtained from FD-mass spectra of the reaction mixture. The sterically demanding hexylether moieties in proximity to the C-Br bonds seem to hinder the YAMAMOTO trimerization.

Bulky TMS-groups at the backbone of the molecule as in case of **84** do not prevent the proceeding of the YAMAMOTO coupling, but nevertheless, C-Si bonds are not compatible with the strong oxidating conditions of the subsequent SCHOLL reaction. Therefore, instead of trimethylsilyl acetylene, tetradec-7-yne was used for the DIELS-ALDER reaction of **95** with the purpose to substitute the molecular backbone with two solubilizing *n*-hexyl groups. This reaction furnished the bis-hexylated congener **99** with satisfying yields (51%) under microwave radiation at 200 °C (Scheme 3.5). Nevertheless, **99** reacted only with low yield (27%) with phenylboronic acid in the subsequent SUZUKI-MIYAURA coupling to target compound **100**. A reason for this was the higher reaction temperature (100 °C), at which not exclusively C-I bonds, but also partly C-Br bonds were coupled.

Precursor **100** reacted smoothly under YAMAMOTO reaction conditions towards trimer **101**, but also higher oligomers and polymers were formed. Trimer **101** showed good solubility in chlorinated solvents and could be separated via column chromatography and was detected via FD mass spectrometry (Figure 3.3). The ^{1}H NMR signals were not evaluable due to overlapping multiplets.

The final SCHOLL reaction yielded trace amounts of a reddish-brown solid which could be purified by column chromatography on neutral aluminum oxide and dichloromethane as eluent. But no signals could be detected in the ^{1}H NMR spectrum. Also, no evidence for the formation of **102** could be gathered by various mass spectrometry methods (FD, APCI, EI, CI). Presumably, the only suitable method for detection of comparably large, non-volatile and unpolar molecules is MALDI-TOF mass spectrometry.

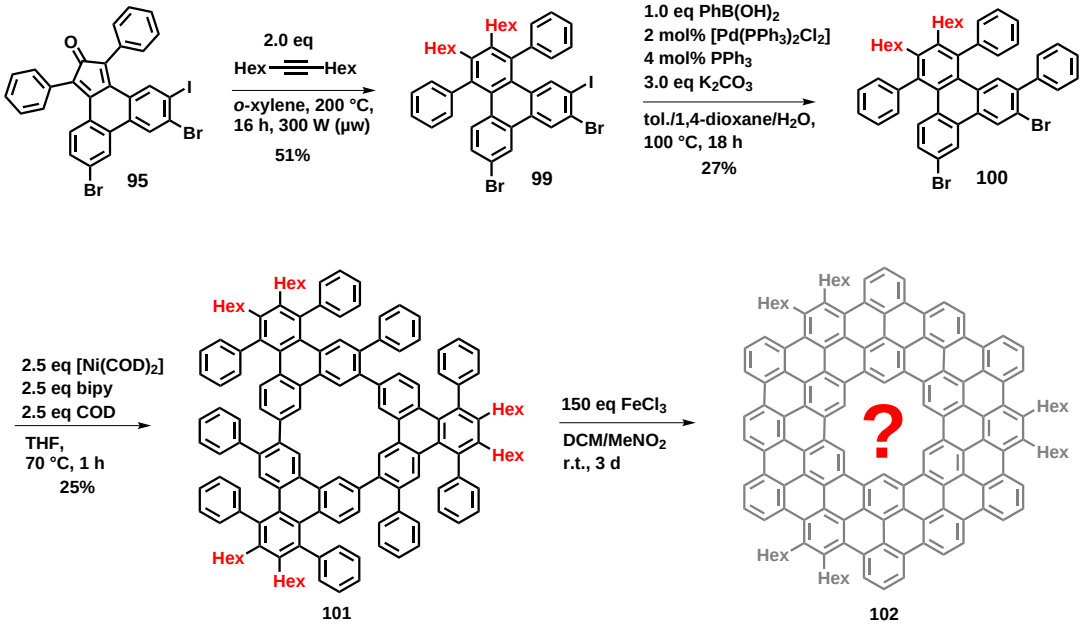

Scheme 3.5 Attempted synthesis of hexylated **C108** nanographene derivative **102**.

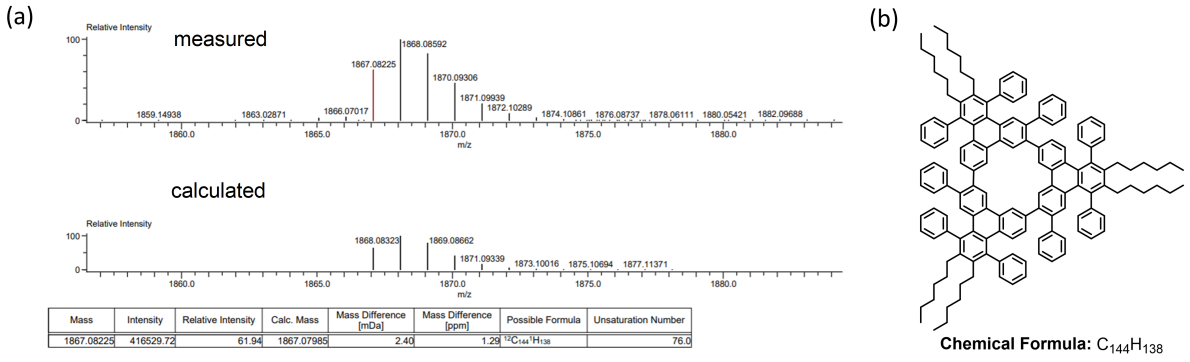

Mass	Intensity	Relative Intensity	Calc. Mass	Mass Difference [mDa]	Mass Difference [ppm]	Possible Formula	Unsaturation Number
1867.08225	416529.72	61.94	1867.07985	2.40	1.29	$^{12}C_{144}{}^{1}H_{138}$	76.0

Fig. 3.3 (a) High resolution FD(+) mass spectrum (measured and simulated) of **101**; (b) chemical structure and chemical formular of **101**.

Contemporaneously to our efforts for the synthesis of **C108** in solution, the group of TAN published in 2019 a synthesis strategy for a soluble hexa-mesityl substituted C108 derivative (**106**) shown in Figure 3.4.[256]H Their synthesis relies on a cross-coupling step of hexa-borylated compound **103** with the mesityl-substituted biphenyl building block **104**, followed by SCHOLL reaction of the coupling product to yield the planarized product **106**.[256] Since this synthesis approach does not rely on a YAMAMOTO cyclization step in the final stages, highly inseparable mixtures of higher homologue oligomeric macrocycles are not formed. Interestingly, in solution and in the crystalline state and even under MALDI ionization conditions, **106** formed a dimer of two π-stacked molecules, rotated by 30° towards each other due to repulsion of the mesityl substituents.[256] They also synthesized the congener of **C108** without cavity[257] in order to rationalize the effect of the cavity on optical spectra. The cavity leads to a blueshift in the absorption spectra of 150 nm (absorption maximum around 415 nm and yellowish green fluorescence).[256, 257] More recently, the group published a similar approach for the pentamer homologue of **106**, in order to synthesize a non-planar extended quintulene derivative that exhibited a lower tendency to form molecular bilayers due to the conical molecular shape and lowered π-stacking ability.[245]

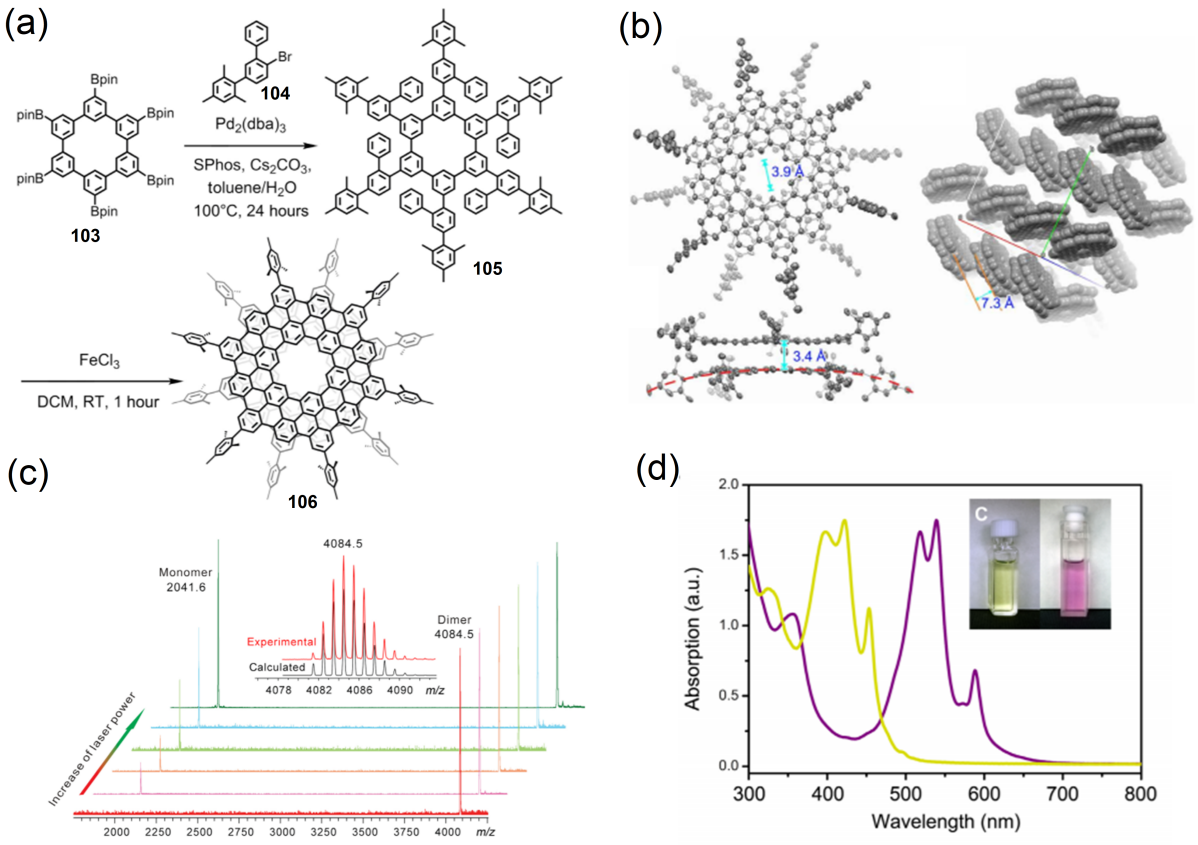

Fig. 3.4 (a) Synthesis of mesityl substituted **C108** dimer derivative **106** by TAN; (b) MALDI-TOF mass spectrum of **106** (dimer and monomer); (c) X-ray structure of dimeric **106**; (d) UV-Vis spectrum of dimer **106** (yellow) and congener without cavity (purple).[256]

As demonstrated by TAN in solution and by STS results on Au(111) by us,[254] **C108** pos-

sesses due to its cavity a comparably large HOMO-LUMO energy gap. In order to study the HOMO-LUMO energy gap of porous nanographene, DFT calculations (PBE0/def-TZVPP level of theory) were performed for **C108** and compared to the findings for a structurally closely related cyclic nanographene oxide containing partwise zig-zag edges (Figure 3.5).

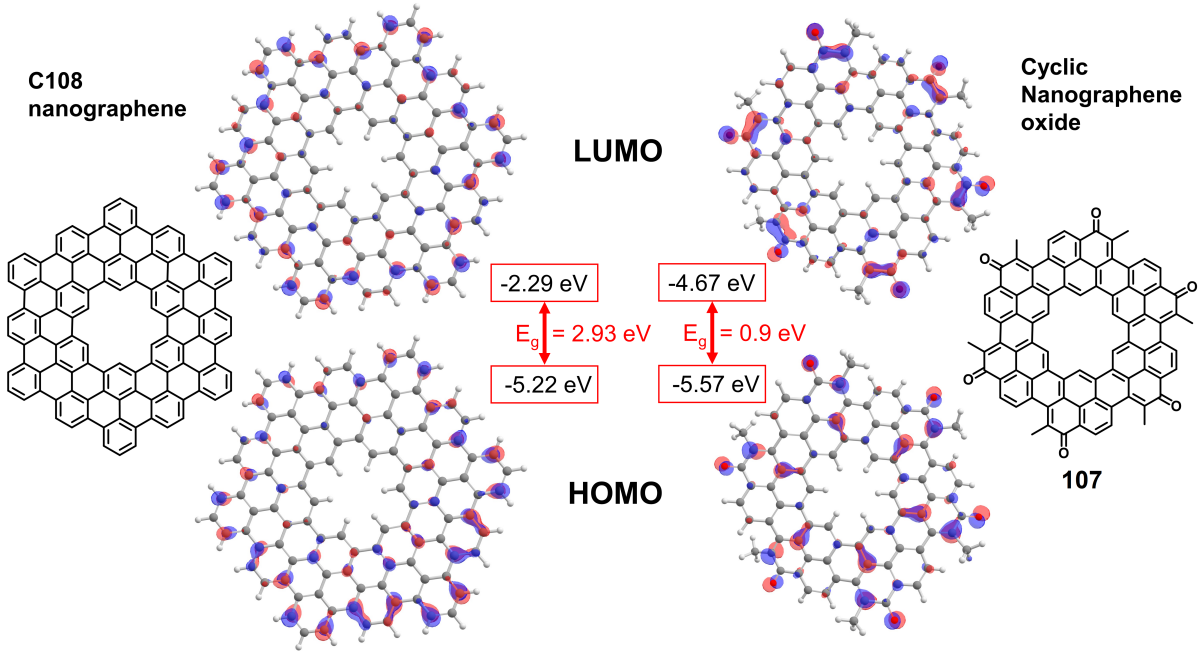

Fig. 3.5 Comparison of the chemical structures of **C108** and the related cyclic nanographene oxide **107** (alkyl groups simplified as methyl groups), their KOHN-SHAM frontier molecular orbitals and the corresponding MO energies.

The calculated KOHN-SHAM orbitals of **C108** show very homogenously and highly symmetric distributed nodes. The calculated molecular HOMO-LUMO energy gap (2.93 eV) is in agreement with experimental observations. In stark contrast to this, the KOHN-SHAM orbitals of the cyclic nanographene oxide modelsystem **107** show a pronounced localization at the carbonyl groups. Although the HOMO energies are comparable in both systems, especially the LUMO energy of **107** is dramatically lowered due to the oxide derivatization accompanied by partial zig-zag edges. This leads to a very narrow calculated HOMO-LUMO energy gap (0.9 eV), predicting UV-Vis absorption bands in the NIR region (1000 nm).

For the synthesis of the cyclic nanographene oxide a retrosynthetic plan was generated (see Scheme 3.6), in which the synthesis strategy relies on a SCHOLL reaction for planarization and the ring should be built up by a SUZUKI polycondensation[258] (hexamerization) of the molecular AB-type polymerization precursor **109**.

The synthesis of AB-type monomer **109** started with commercially available 4-bromo naphthalene anhydride (**110**), which was reacted in a condensation reaction with diethyl-*n*-butyl malonate to furnish **111**. In a subsequent step, it was further reacted in a MIYAURA borylation to furnish **112**, which could be converted into triflate **109** in moderate yields. The *n*-butyl group in terminal position should improve the solubility of the cyclic oligomers.

*Retrosynthesis towards cyclic nanographene oxide **107**:*

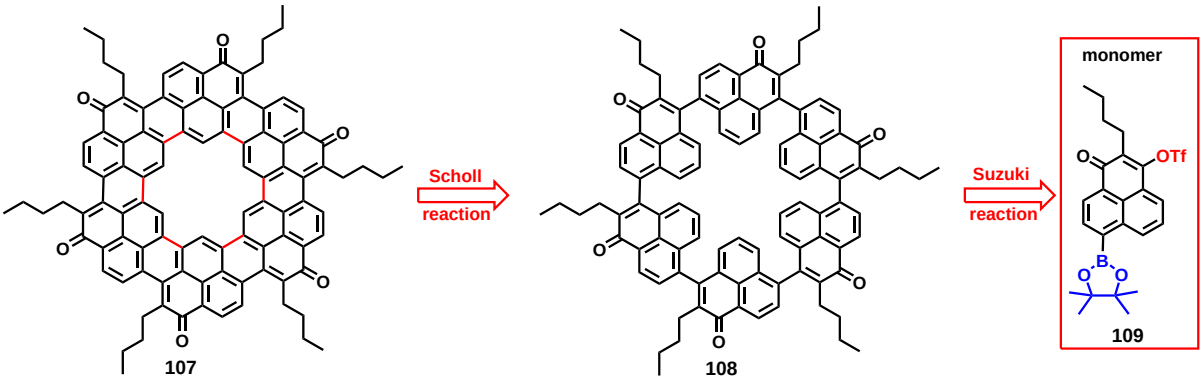

*Synthesis of AB-type monomer **109**:*

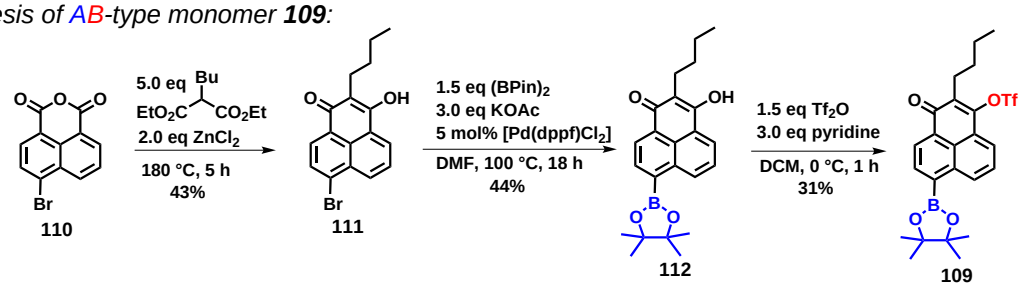

Scheme 3.6 Retrosynthetical approach for the synthesis of nanographene oxide **107** starting with AB-type synthon **109** and synthesis of monomer **109**.

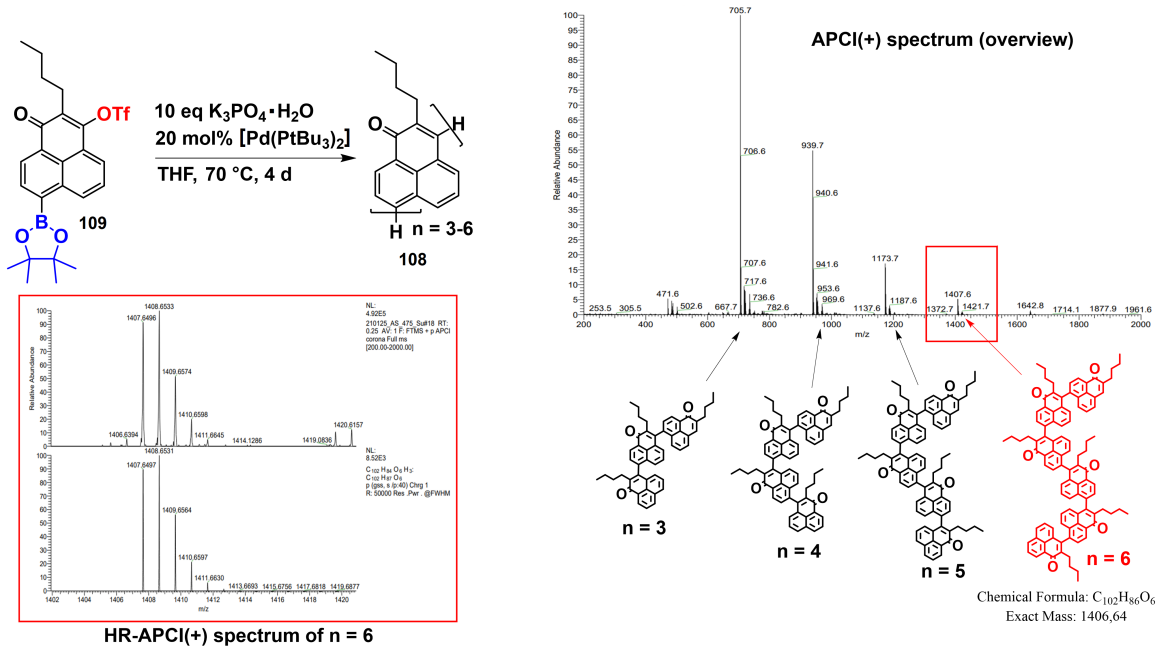

Scheme 3.7 Polycondensation of **109** led to linear oligomers according to HR-APCI(+) mass spectrometry. Inset: HR-APCI(+) spectrum of acyclic hexamer (measured and simulated).

AB-type monomer **109** could be obtained in high purity. To achieve selectivity for the formation of macrocycles instead of high molecular polymers, highly diluted conditions like in the case of YAMAMOTO reactions were chosen. For the first approach, $[Pd(PPh_3)_4]$ and K_2CO_3 as base

were used in 1,4-dioxane/H_2O. Despite high dilution (10^{-4} M), only rather insoluble polymers were obtained, whereas a second approach ([$Pd_2(dba)_3$]/SPhos, K_3PO_4 in toluene) showed no conversion, indicating that little amounts of water are imortant for the coupling. When typical SUZUKI-polycondensation reaction conditions were applied ([$Pd(PtBu_3)_2$], $K_3PO_4 \cdot H_2O$ as base in dry THF),[259] the main product was an inseparable mixture of acyclic oligomers with n = 3-6 repeting units according to APCI and FD mass spectrometry with trimeric **109** being the main product (see Scheme 3.7). This fraction could be separated via column chromatography using chloroform as eluent. Since protodeborylation instead of cross-coupling terminated the chain growth, anhydrous K_3PO_4 was used as base for comparison, but the result was similar. This indicates that the ring strain of the hypothetical macrocycle **108** is presumably too high for successfully proceeding macrocyclizations.

3.10.3 Synthesis of 114 as Precursor for zig-zag edged Nanographene

Since zig-zag edged nanographenes exhibit interesting electronic properties (*e.g.* spin-polarized edge states) deviating strongly from their armchair analogues,[260] synthetical strategies to build up zig-zag edged nanographene and graphene nanoribbons are highly demanded.[261, 262]

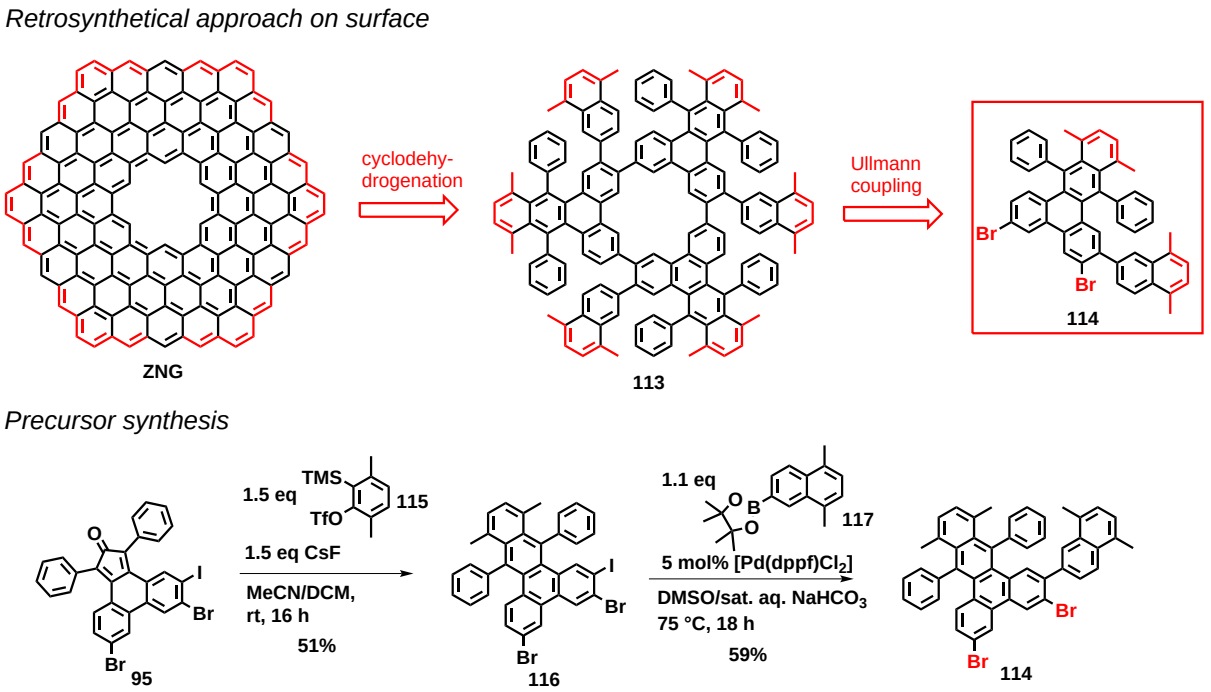

Scheme 3.8 Retrosynthetical approach for the synthesis of zig-zag nanographene **ZNG** starting from precursor **114** on metal surfaces and synthesis route towards **114**.

To date, there are only few *on-Surface* built up zig-zag edged nanographenes known as the zig-zag edged nanographene polymer by FASEL and MÜLLEN.[32] Their approach relied on the activation of methyl groups attached to the aromatic system in course of the cyclodehydrogenation reaction, which was later also realized for molecular nanographenes on Au(111). We decided to apply this strategy to precursor **DBTT**, which has proven to generate **C108** on

different surfaces in high yields. Therefore, methyl groups were added to the periphery of the precursor to give **114**, which should react after formation of **113** in an Ullmann trimerization in a cyclodehydrogenation step to form **ZNG** (Scheme 3.8). **ZNG** has already been studied *in silico* by Shigeta and others, predicting a comparably large open shell character of **ZNG** and related systems induced by the zig-zag edge structure,[263–265] which could be stabilized by noble metal surfaces.

The synthesis of precursor **114** starts with the bis-brominated and iodinated ketone **95**, an intermediate from the synthesis of **DBTT**. **95** was reacted with trimethylsilyl-triflate **115**[266] in the presence of CsF,[85] which formed an aryne species *in situ* reacting with **95** in a Diels-Alder reaction under extrusion of CO at moderate heating. Poorly soluble **116** was obtained as a product in acceptable yields (51%). The latter was then reacted with dimethyl-naphthalene boronic acid **117**[267] under cross-coupling conditions that should allow a selective activation of the C-I bonds. Due to the poor solubility of **116**, the conversion was rather unselective, but nevertheless **114** could be obtained as main product and it was possible to isolate **114** accompanied with small amounts of side products where also C-Br groups were additionaly coupled. These side products could also be only partly removed by several recrystallization attemps (in methanol and mixtures of chloroform/*n*-hexane) followed by high-vacuum sublimation (290 °C, at $1{\cdot}10^{-6}$ mbar). Interestingly, when heated shortly above the sublimation temperature of 320 °C, **114** decomposes slightly.

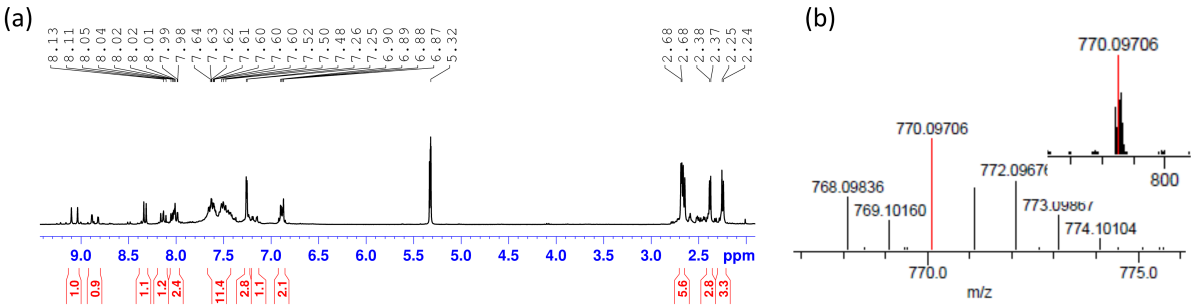

Fig. 3.6 (a) ^{1}H NMR spectrum (300 MHz, CD_2Cl_2) of precursor **114**; (b) HR-EI(+) mass spectrum of **114**.

The ^{1}H NMR spectrum (Figure 3.6 (a)) shows traces of two-fold cross-coupling products and the methyl group signals appear as doublets, since rotation of the bulky substituents is sterically hindered. Furthermore, the product identity could be identified via EI(+) mass spectrometry (Fig. 3.6 (b)). Unfortunally, all attempts to crystallize **114** failed, most likely due to the highly distorted and unsymmetrical molecular shape of **114**.

When deposited in ultrahigh vacuum and heated up to 200 °C in order to react **114** in an Ullmann reaction, no trimers (**113**) were obtained on Au(111). Most of the molecules aggregated into ill-defined cluster-like structures and only few of the molecules formed pairs that could be identified as Ullmann-coupled dimers. The absence of any cyclic trimers or higher molecular oligomeric structures (despite the occurrence of successful Ullmann couplings) gives rise to the assumption, that the high sterical demand of the methylated naphthalene substituents prevents

the formed dimer from undergoing coupling reactions with further precursor radicals.

3.10.4 *On-Surface* Synthesis of Sierpiński Triangle Fractals

The generation of self-similar fractals on metal surfaces gained large interest during the last years.[268] Especially the generation of Sierpiński triangles via non-covalent and reversible but stable arrangement of suitable molecular precursors (mostly based on *m*-terphenyl backbones, see Figure 3.7 (a) for selected precursor examples and Figure 3.7 (b) for examples of non-covalent fractals from dihydroxy-*m*-terphenyl of the 0. to 3. dimension)[269]I at low temperatures. Most of the published examples for Sierpiński triangles rely on hydrogen bonding motifs between thiols, alcohols,[269, 270] amines and carboxylic or boronic acids,[271, 272] coordination bondings *e.g.* between nitrile groups and metal ions[273] or halogen bondings[274].

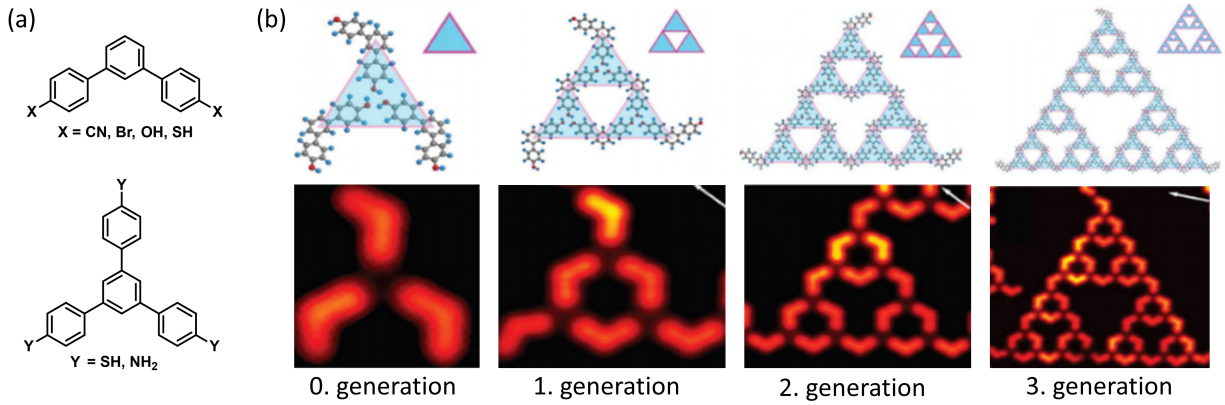

Fig. 3.7 (a) Suitable precursors for non-covalent generation of Sierpiński triangles; (b) hydrogen-bonded Sierpiński fractals built from dihydroxy-*m*-terphenyl of different generations.[269]

Since these assembled fractal networks are based on weak non-covalent interactions, only few examples of fractals are stable at room temperature,[271] therefore we intended to design suitably shaped halogenated precursors that are able to form fractal motifs via covalent bonding. Since the Ullmann reaction is to date the most versatile *on-Surface* coupling reaction, we focussed on appropriate halogenated precursors (Scheme 3.9).

Due to their molecular shape, we identified non C_3-symmetric threefold halogenated triphenylenes (**119** and **120**) as suitable precursors from the retrosynthetical point of view.[275] Especially the mixed bis-iodinated and brominated congener **119** should react on surfaces precisely via hierarchical Ullmann reactions, first by C-I bonds forming the cyclic trimer **118** that can in a second heating step form the fractals via C-Br bonds.

The tribrominated congener **120** was built up starting with 4-bromo-1,2-diiodobenzene (**122**), which was synthesized via aryne intermediate starting from amino carboxylic acid **121** (Scheme 3.10).[276] **122** reacted selectively with its C-I groups in a Suzuki-Miyaura reaction with 3-

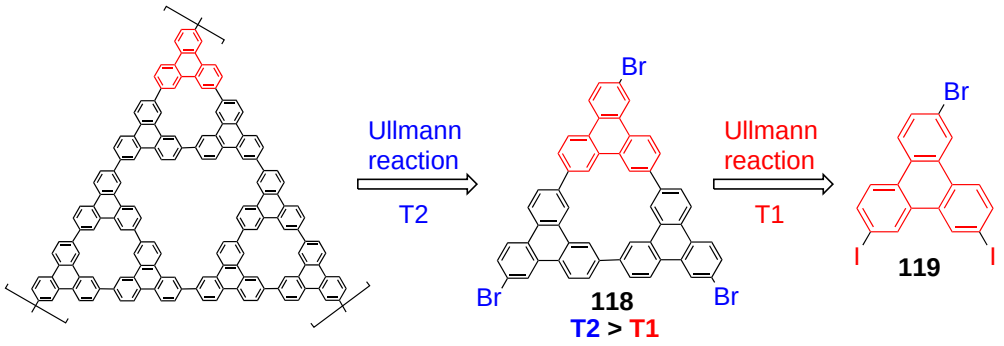

Scheme 3.9 Retrosynthetical approach for the synthesis of Sierpiński fractals on surfaces via hierarchical Ullmann reactions.

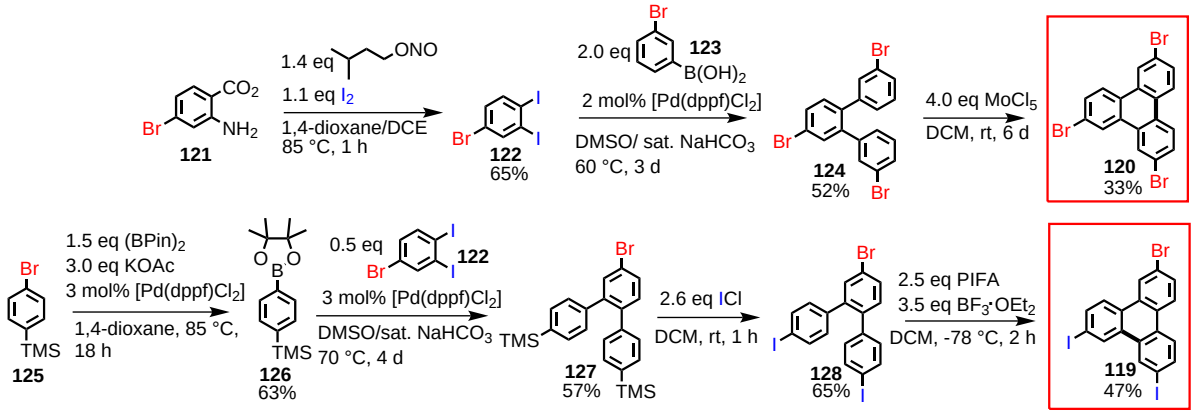

Scheme 3.10 Synthesis of two halogenated triphenylene precursors (**119** and **120**) for the *on-surface* synthesis of Sierpiński fractals.

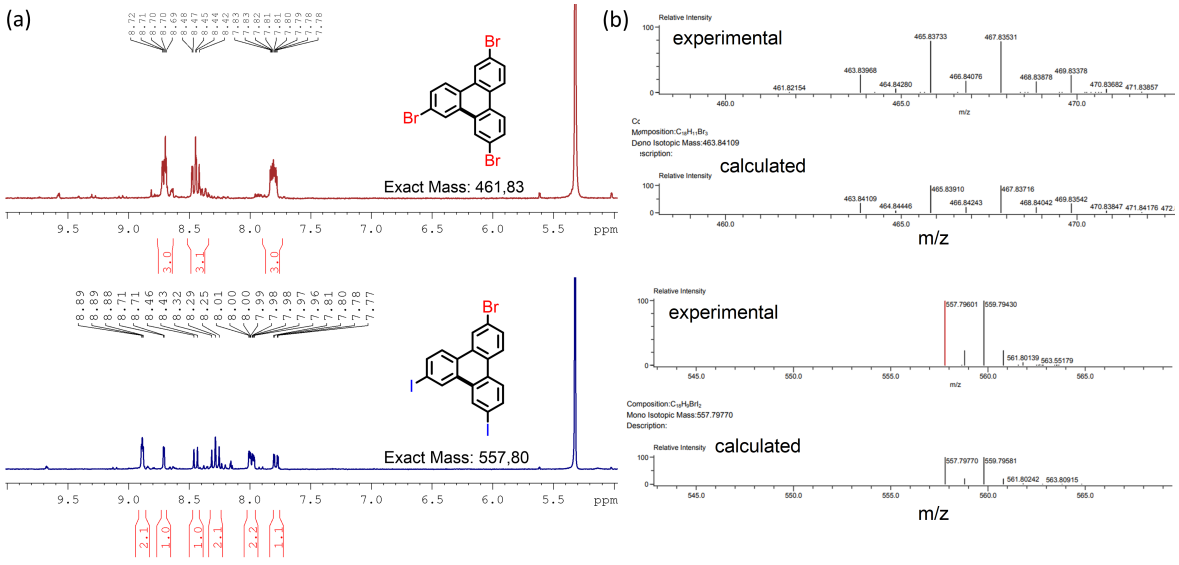

Fig. 3.8 (a) ^{1}H NMR spectra (300 MHz, CD_2Cl_2) of **119** and **120**; (b) HR-EI(+) mass spectra of **119** and **120**.

bromophenylboronic acid (**123**) in comparably good yields. Terphenyl **124** could be converted selectively into precursor **120** by Scholl reaction with $MoCl_5$ as oxidant.[277] However, yield

and conversion were not very satisfying (33% after 6 d reaction time), since **120** is due to its halogen substitution comparably electron poor, which is a problem for performing SCHOLL reactions.[277]

The second precursor is built up in a different way. Here, TMS-protected phenylboronic acid pinacolester **126** is reacted with **122** in a SUZUKI-MIYAURA cross-coupling to terphenyl **127**. Using iodine monochloride as iodination reagent, the TMS groups of **127** were converted to iodine substituents at room temperature in DCM with moderate yields (**128**). As a last step, mixed iodinated and brominated terphenyl **128** is converted to triphenylene precursor **119** by SCHOLL oxidation employing hypervalent (bis(trifluoroacetoxy)iodo)benzene (PIFA) as oxidant in combination with $BF_3{\cdot}OEt_2$ as Lewis acid at low temperatures (-78 °C) for 2 h.[278] Finally, **119** is obtained after column chromatography in acceptable yield (44%). Both precursors were purified via column chromatography, followed by recrystallization from methanol and high vacuum sublimation. Due to the limited solubility, NMR-characterization remained limited on ^{1}H NMR (Figure 3.8 (a)), but the product identity could be verified by HR-EI mass spectrometry (Figure 3.8 (b)). Smaller impurity signals in the NMR spectra indicate possible isomerizations in minor amounts during the SCHOLL reactions, which are known to occur.[277]

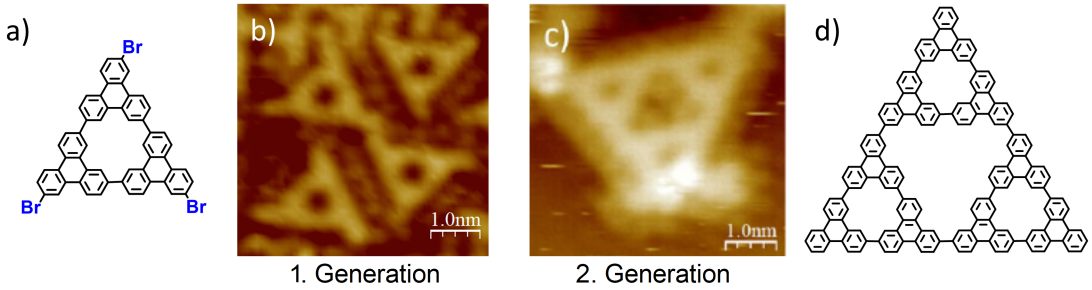

Fig. 3.9 (a) and (b) Formation of trimers (**118**) via ULLMANN reaction of precursor **119** on Au(111); (c) and (d) formation of second generation Sierpiński triangles by reaction of precursor **120** on Ag(111). Shown with friendly permission of Prof. Dr. GOTTFRIED.

First results from UHV deposition of precursor **119** on Au(111) show that at a reaction temperature of 400 °C, both C-I bonds are activated and trimers with intact C-Br bonds (**118**) are formed in high yield via ULLMANN reaction if the coverage of molecules on surface is low (see Figure 3.9 (a) and (b)) as first generation fractals). This indicates a high potential of precursor **119** to form higher order fractals upon reacting over C-Br bonds at higher temperature.

When tribrominated precursor **120** is reacted via ULLMANN coupling on Ag(111) at 270 °C, second generation Sierpiński triangles are formed at low precursor concentrations by direct assembly (see Figure 3.9 (c) and (d)). Apart from the presented first generation fractal, higher fractals are formed with defects. This can be explained by the irreversibility of the formation of the covalent network in contrast to self-assembled fractal structures, where defects can be healed by diffusion.[274] Interestingly, this finding could not be reproduced on Au(111) or Cu(111). At different precursor coverages, only randomly fused networks could be observed. For both precursors, further investigations are pending.

3.10.5 Synthesis of an alternative Kekulene Precursor

During a master's student internship, JAQUELINE BEPPLER synthesized an alternative precursor **130** for the *on-Surface* generation of Kekulene (**75**). In contrast to the published phenanthrene-based cyclophane **129** that forms Kekulene (**75**) in course of a threefold cyclodehydrogenation,[279] **130** can form **75** by only two cyclodehydrogenations (Scheme 3.11).

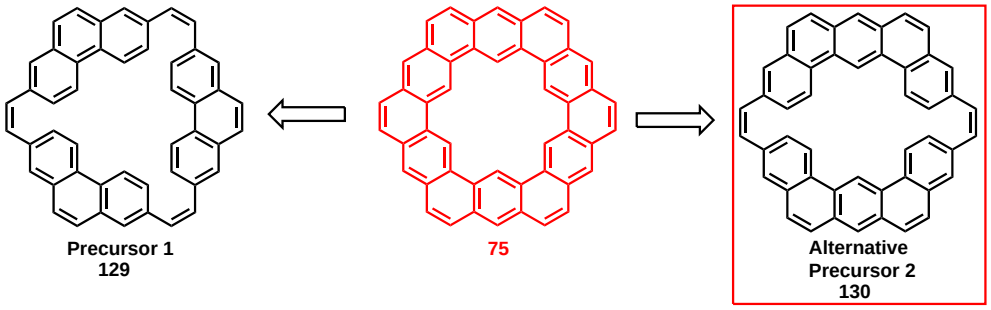

Scheme 3.11 Chemical structure of the two possible precursors **129** and **130** for cyclodehydrogenative formation of Kekulene (**75**).

The alternative precursor **130**[238] was synthesized by a five step synthesis procedure (Scheme 3.12) starting with diiodo-dibromobenzene (**131**)[280], which was selectively transferred into bis-alkyne **132** via SONOGASHIRA cross coupling over C-I functionalities at room temperature in good yields and selectivity (72%), followed by SUZUKI-MIYAURA cross coupling with **133** over C-Br bonds leading to bis-aldehyde **134** in good yield.

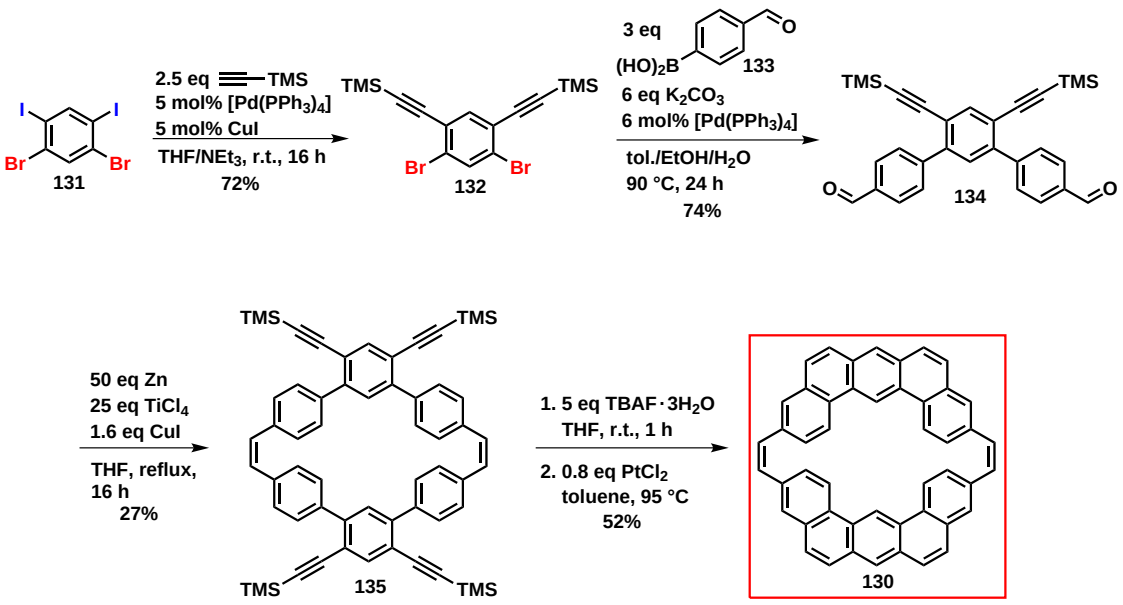

Scheme 3.12 Synthesis route towards Kekulene precursor **130**.

Bis-aldehyde **134** was subsequently dimerized under McMurry reaction conditions by slow addition of **134** to the system $Zn/TiCl_4$ that generates low-valent titanium species as reducing agent. Well soluble dimer **135** was obtained in 27% yield as beige solid which forms brightly blue fluorescent solutions in dichloromethane (Figure 3.10 (a)). The product identity was confirmed unambigously by X-ray crystallography (Figure 3.10 (b)) from a saturated dichloromethane solution showing clearly the highly distorted geometry of dimer **135** at the double bound (torsion angle at the double bond: 7.8°, dihedral angle of the Ph groups: 71.9°) enhancing the solubility of **135**.

In the second last synthesis step, deprotection of the trimethylsilyl groups of **135** was accomplished by dropwise addition of trihydrated TBAF to a THF solution. During the reaction, desilylated **135** precipitated from the reaction mixture. After termination of the reaction by protonation with methanol and filtration, the obtained yellow solid was directly cyclized by Fürstner's method using $PtCl_2$ as cyclization reagent.[281] After filtration over silica and recrystallization from methanol, hardly soluble precursor **130** was obtained as a beige solid and detected via EI mass spectrometry (Fig 3.10 (c)). Further spectroscopic analysis of the final precursor remained elusive, since the solubility of **130** in common organic solvents was too low for acquisition of NMR spectra. This is mainly due to enlarged π stacking ability of **130** compared to silylated and uncyclized **135**. Nevertheless, precursor **130** can be processed (and also further purified) by vacuum sublimation (at 290 °C and $1{\cdot}10^{-6}$ mbar) due to its excellent temperature stability. Therefore, **130** is a promising alternative precursor for *on-Surface* generation of Kekulene. In contrast, solution based approaches for the synthesis of kekulene (**75**) using **129** and **130** as starting materials for photocyclizations were not successful due to highly twisted geometries of the precursors.[238]

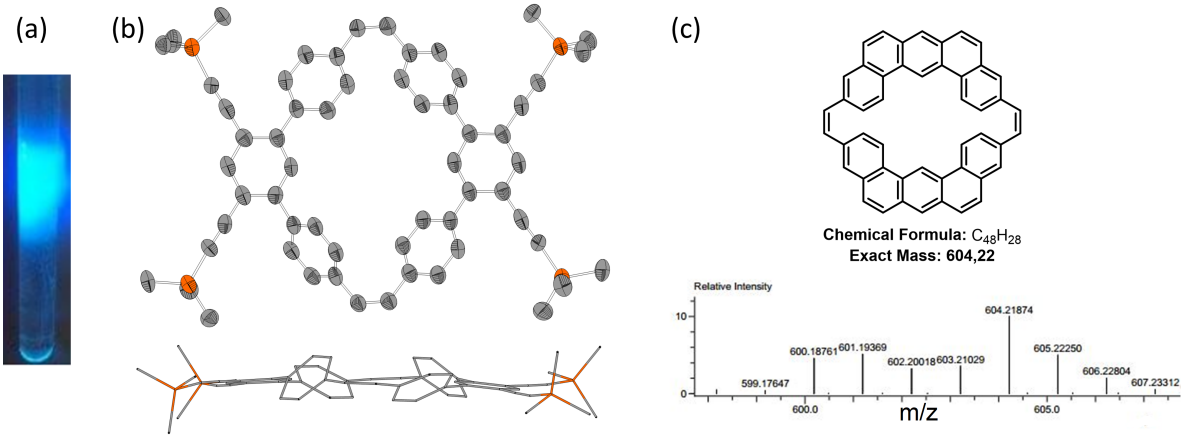

Fig. 3.10 (a) Blue fluorescence of alkyne **135** in DCM irradiated with UV light (366 nm); (b) X-ray structure of **135** (top, thermal ellipsoids shown at the 50% level and hydrogen atoms are omitted for clarity), bottom: side view (wire/sticks model); (c) chemical structure of precursor **130** and measured HR-EI(+) spectrum.

3.10.6 Synthesis of Octulene on Cu(111)

As published recently,[280] Kekulene (**75**) was synthesized on Cu(111) with high yields by a threefold cyclodehydrogenation of a phenanthrene-based cyclophane precursor **129**. The synthesis of the precursor by McMurry trimerization also afforded larger macrocyclic cyclophanes. In minor quantities (8% yield), a cyclophane based on a phenanthrene tetramer **140** could be isolated via column chromatography as a subsequent fraction (see Scheme 3.13). In contrast to Kekulene precursor **129**, the tetramer turned out to be more insoluble so that characterization by NMR or crystallography was not possible. But the product could be successfully detected via EI(+) mass spectrometry. Tetramer **140** is of high interest, since it may form Octulene[243] as higher homologue of Kekulene (**75**) via tetrafold intramolecular cyclodehydrogenation on surface.

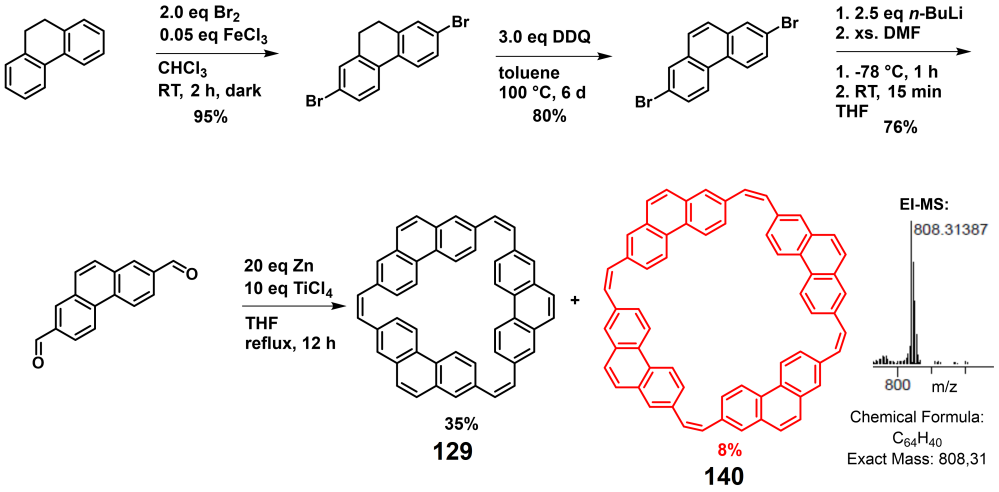

Scheme 3.13 Synthesis route towards Kekulene and Octulene precursors **129** and **140**.

Despite the high molecular weight of **140**, it could be sublimed successfully onto Cu(111), although harsch conditions needed to be applied (310 °C, p = 10^{-9} mbar). This led to partial decomposition of **140** in the course of sublimation, but the precursor could be identified according to its square shape via STM (Scheme 3.14 (b)). After identification of the correct shape of the molecular precursor via STM, the surface was heated to 225 °C in order to synthesize curved-shaped Octulene[243] via cyclodehydrogenation. Intringuingly, Octulene was not formed according to STM analysis (Scheme 3.14 (c)), but isooctulene. According to the molecular shape, it could be stated that one phenanthrene unit of isooctulene points inside the cavity and is therefore rotated via 180° before cyclodehydrogenation (*c.f.* reaction equation Scheme 3.14 (a)). This could be rationalized with a molecular model (Scheme 3.14 (d)). It shows that in the case of the defective Octulene, the phenanthrene unit pointing inside the cavity (highlighted in Scheme 3.14 (d)) may be able to adsorb planarly on the surface, leading to the observed STM representative. It can be assumed that these improved adsorbate-substrate interactions favour the formation of the observed isomeric Octulene. Interestingly, the same phenomenon could be observed when Kekulene precursor **129** was cyclodehydrogenated on Cu(110) instead of Cu(111), resulting in the formation of isokekulene. Further studies to characterize the Octulene isomer in more detail on metal surfaces are still ongoing.

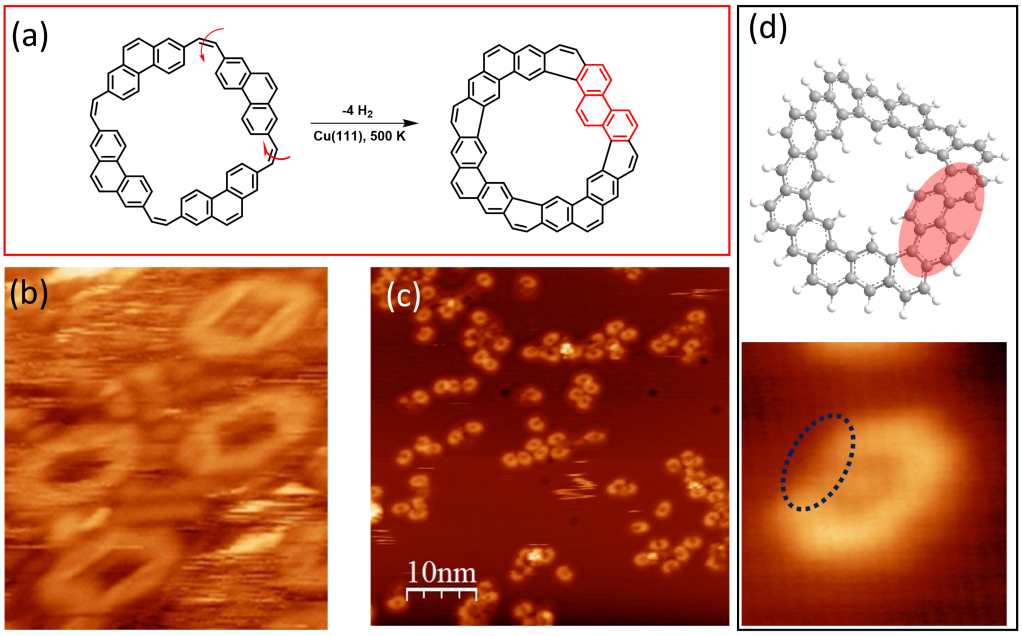

Scheme 3.14 (a) Reaction of precursor **140** on Cu(111) to isomeric Octulene; (b) STM image of precursor **140** on Cu(111); (c) STM image of defective Octulene on Cu(111) after cyclodehydrogenation; (d) detail STM image of defective Octulene and molecular model. STM images shown with friendly permission of Prof. Dr. Gottfried.

3.10.7 Synthesis of a Precursor for surface-mediated Alkyne Trimerizations

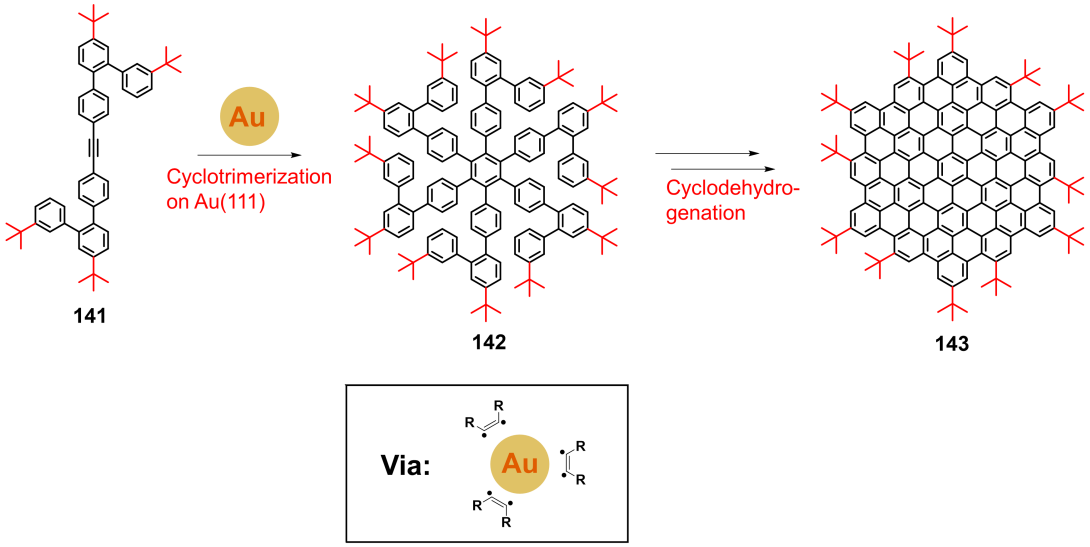

Scheme 3.15 Precursor **141** and its planned *on-surface* alkyne trimerization to **142** on Au(111) followed by cyclodehydrogenative formation of **143**.

In order to synthesize the non-porous counterpart **143** of **C108** nanographene, an alkyne cyclotrimerization was chosen as key step for the *on-Surface* synthesis of non-porous nanographene

143. In literature, this reaction is catalyzed by dicobalt octacarbonyl and shown for a similar system by former studies of the group of MÜLLEN.[282] On surface, Au adatoms diffusing on the single crystalline Au(111) surface are known to mediate alkyne trimerizations assumed to mechanistically proceed via *Z*-alkene diradicaloids coordinating to Au adatoms.[283] Due to the large aromatic systems that are generated, *tert*-butyl groups should be added to precursor **141** in order to enhance the surface mobility of the precursor which is important for the reactivity and also enhances the surface mobility of the formed large PAHs (Scheme 3.15). The planned surface reaction also consists of a cyclodehydrogenation step following the cyclotrimerization which will supposedly require higher reaction temperatures.

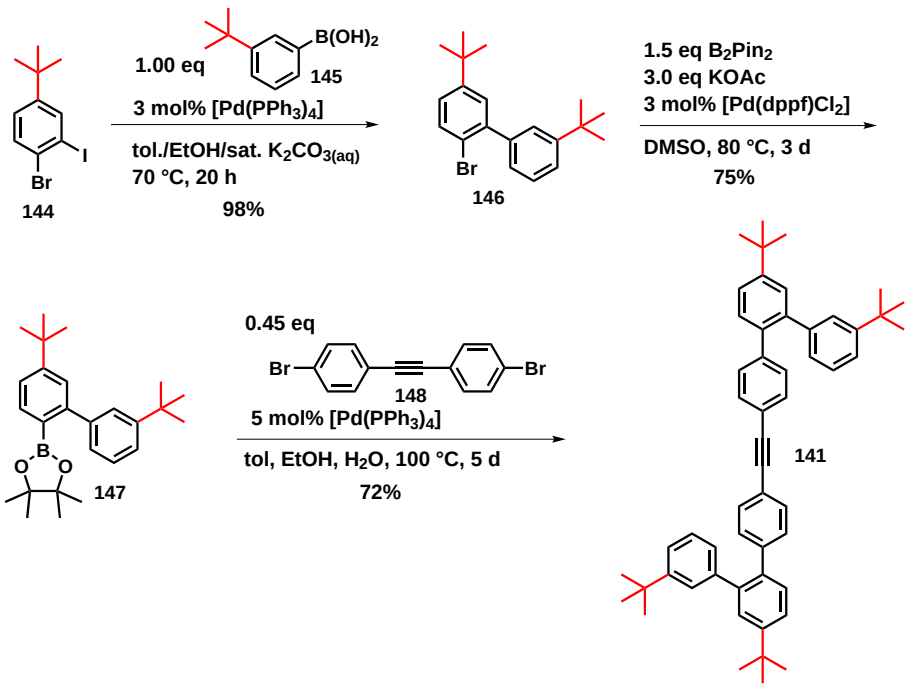

Scheme 3.16 Synthesis route towards cyclotrimerization precursor **141**.

The synthesis of precursor **141** started with 1-bromo-4-(*tert*-butyl)-2-iodobenzene (**144**)[284] that is reacted selectively with 3-*tert*-butylboronic acid (**145**) in a SUZUKI-MIYAURA cross coupling in almost quantitative yield (98%) (Scheme 3.16). The resulting brominated biphenyl **146** was subsequently borylated to **147** (MIYAURA borylation) in satisfying yields (75%). In the final SUZUKI-MIYAURA coupling step, borylated biphenyl **147**[285] was twofold reacted with 1,2-bis(4-bromophenyl)ethyne (**148**). After prolonged reaction times, precursor **141** was obtained in good yield (72%) after column chromatography. Further purification of the well soluble precursor **141** was achieved by crystallization of **141** in a mixture of dichloromethane and *n*-pentane.
The ^{1}H NMR (Figure 3.11 (a)) shows two signals for the *tert*-butyl groups with different chemical environment. In the aromatic region, complex overlapping multiplet signals are present, which makes signal assignments impossible. But the correct precursor geometry could be validated via X-ray crystallography (Figure 3.11 (b) and (c)). In the molecular structure, the non-planarity of **141** is visible: Substituting the linear triple bond (bonding angle: 178.4° around triple bond),

the phenyl groups of the *ortho*-terphenyl units describe torsion angles of 85.2° in perpendicular orientations. The *on-Surface* reaction and characterization of precursor **141** is currently in progress.

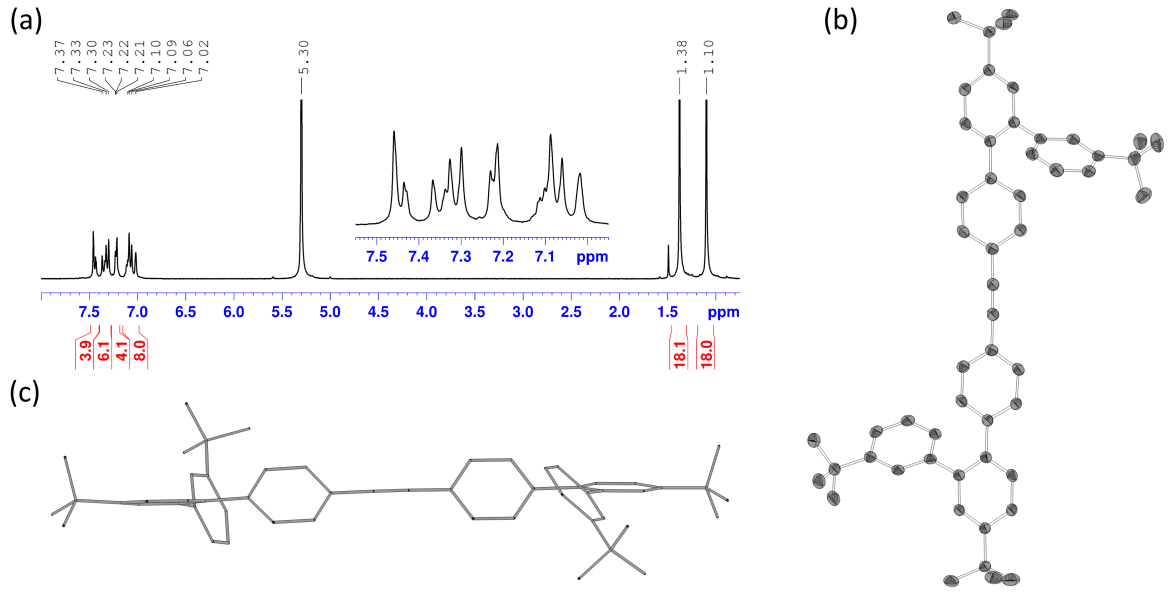

Fig. 3.11 (a) ^{1}H NMR (CD_2Cl_2, 300 MHz) of precursor **141**; (b) X-ray structure of **141** (thermal ellipsoids shown at the 50% level and hydrogen atoms are omitted for clarity); (c) side view (wire/sticks model)

3.10.8 Synthesis of a dipolar substituted Peropyrenequinone

Part of the published work of this thesis deals with reductive access towards symmetrically fourfold substituted peropyrenes and higher homologous compounds.[286] As starting materials for these reductions, easily synthetic available dihydroxy-ropyrenequinones were employed. Due to the used synthesis procedure and isomerization processes, they are obtained as inseparable mixture of *cis*- and *trans*-hydroxylated congeners.[287] The reduction always produces symmetric fourfold substitution patterns, so that an approach towards unsymmetric substitutions could be realized by a two-step approach. The first step would be a functionalization of the hydroxy groups with electrophiles[287] followed by reduction of the carbonyls and functionalization in a second step.

Attempts to functionalize the hydroxy groups of the weakly soluble dihydroxy-rylenequinones with chlorotrialkylsilanes, pivaloyl anhydride, *p*-tosylchloride and halogene alkanes with different bases (DBU, triethylamine, KHMDS or pyridine) showed no conversion. The only successful approach towards twofold functionalized ropyrenequinones was the reaction of 2,9-dibutyl-dihydroxy-peropyrenequinone (**151**) with 2.5 eq triflate anhydride in presence of pyridine as base in dichloromethane at 0 °C (Scheme 3.17). After 2 h at room temperature, a purple-blue solution was formed showing two different spots on a TLC plate. By use of preparative TLC, two fractions with a similar FD mass spectrum could be separated (Scheme 3.17). Both could be identified as bis-triflate diketones **152** (see Figure 3.12 (c) for HR-APCI(+) spectrum). The first

(unpolar) fraction was obtained along with inseparable impurities. The more polar second fraction could be obtained purely. Since the *cis*-disubstituted congener **152** exhibits a permanent dipole momentum and the *trans*-isomer **152** not, it can be concluded that the purely obtained second fraction should be ***cis*-152**.

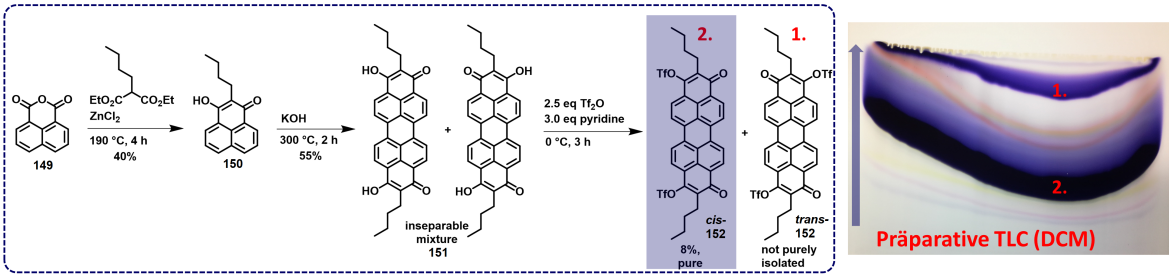

Scheme 3.17 Synthesis of *cis*- and *trans*-bistriflates **152** and their separation via preparative TLC with DCM as eluent (photograph).

Unfortunally, no single crystals in order to proof the substitution pattern by XRD could be obtained by different methods (layering, gas-phase diffusion, saturation methods with mixtures of DCM/*n*-pentane). The solubility of ***cis*-152** is very good, therefore ^{1}H and ^{13}C NMR spectra could be acquired. The ^{1}H NMR shows four aromatic doubletts, which belong to two different spin systems according to COSY NMR (Figure 3.12 (a)). This finding is an indicate for the assumed *cis*-substitution pattern of **152**. The ^{13}C NMR spectrum reveals clearly the presence of the carbonyl group with a signal at 183 ppm for the carbonyl-C atom (Fig. 3.12 (b)).

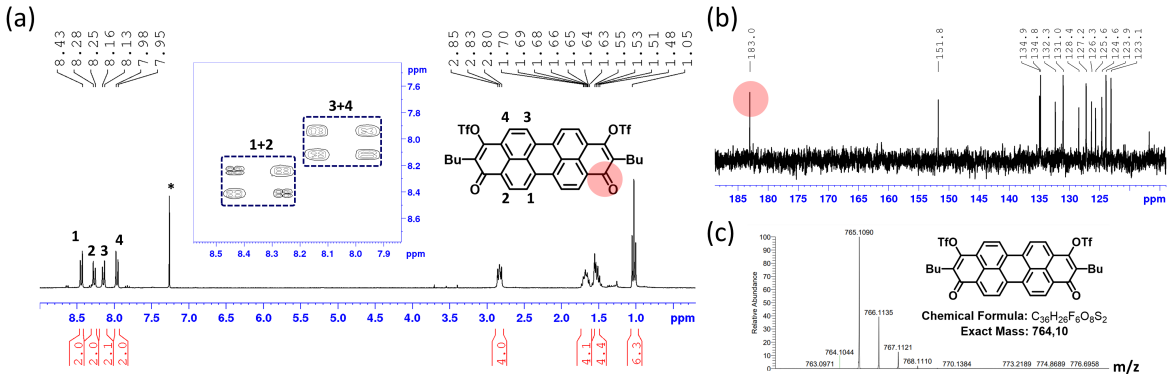

Fig. 3.12 (a) ^{1}H NMR spectrum (300 MHz, $CDCl_3$) of ***cis*-152** and COSY NMR spectrum of the aromatic region (inset); (b) ^{13}C NMR spectrum (75 MHz, $CDCl_3$) of the aromatic region of ***cis*-152**; (c) measured HR-APCI(+) mass spectrum of ***cis*-152**.

In order to rationalize the (opto-)electronical features of *cis*-bistriflate **152**, UV-Vis and CV measurements were performed and compared to symmetrical and reduced peropyrene tetratriflate (Figure 3.13).

As visually apparent, the purple colour of bis-triflate ***cis*-152** indicates a red-shift in the absorption in comparison to reduced tetratriflate **153**. The UV-Vis spectrum reveals an absorpion

maximum of ***cis*-152** at 600 nm, which is a bathocromic shift of 150 nm in comparison to tetratriflate **153** with a significantly higher extinction coefficient for ***cis*-152**. This bathochromical shift is supported by TD-DFT (Fig. 3.13 (b)). The higher extinction coefficient can be explained by the permanent dipole momentum of ***cis*-152** leading to more efficient HOMO-LUMO transitions. The bathochromic shift can be assigned to a narrower HOMO-LUMO energy gap for ***cis*-152**.

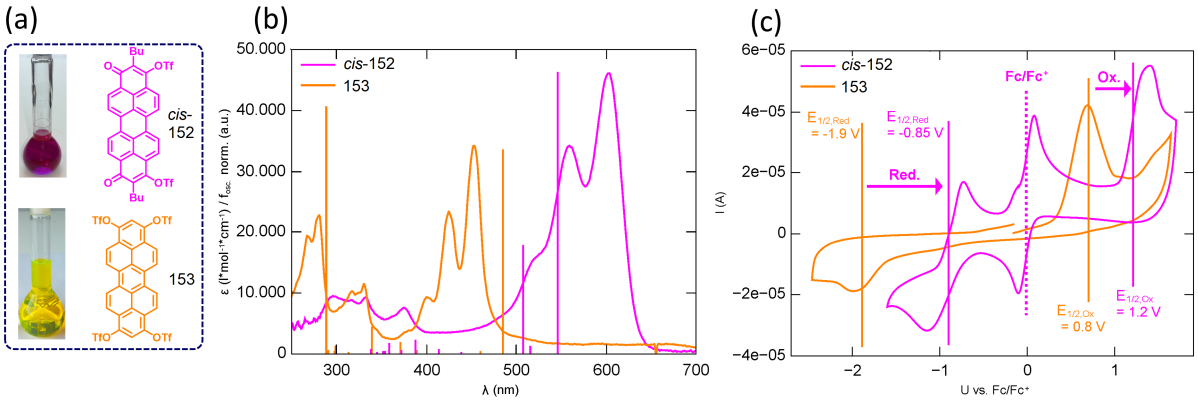

Fig. 3.13 (a) Photographs of ***cis*-152** and **153** in DCM solution and corresponding chemical structures; (b) UV-Vis spectra of ***cis*-152** and **153** in DCM and TD-DFT vertical transitions (def2-TZVPP/PBE, vertical lines); (c) cyclovoltamogramms of ***cis*-152** and **153** in DCM (scanrate: 50 mV/s, 100 mM NBu_4PF_6, vs. ferrocene).

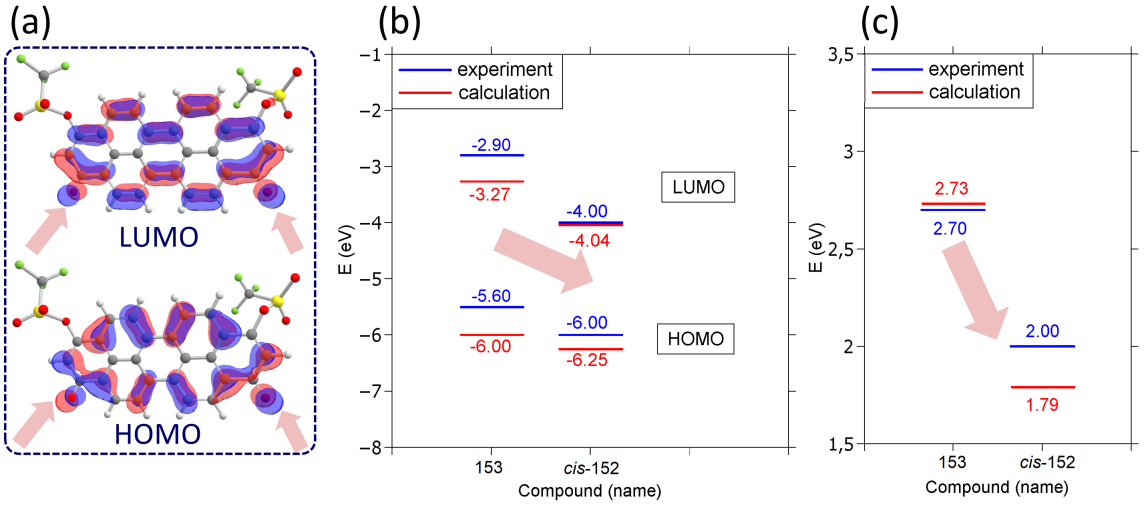

Fig. 3.14 (a) Kohn-Sham orbitals of HOMO and LUMO of ***cis*-152** (def2-TZVPP/B3LYP level of theory); (b) comparison of calculated and experimental HOMO and LUMO energies of ***cis*-152** and **153** and their HOMO-LUMO energy gaps (c).

In order to examine the influence of the unsymmetrical substitution on the electronic properties of ***cis*-152** in comparison to tetratriflate **153**, cyclovoltammetry measurements were performed. Both compounds show one reduction and one oxidation half wave potential. In the case of tetrasubstituted **153**, both were marked by irreversible processes, whereas electron-poor disubstituted ***cis*-152** shows a nearly full reversible reduction potential and a rather irreversible

oxidation potential wave. In the case of formally oxidized ***cis*-152**, the oxidation and reduction potential are both shifted to higher voltages, showing that ***cis*-152** is easier to be reduced and harder to be oxidized. But the electrochemical gap is similarly to the optical gap narrower in the case of ***cis*-152**. This is mostly due to a lowered LUMO value. The oxidation potential of tetrasubstituted **153** (0.8 V vs. Fc/Fc^+) refers to a HOMO level of -5.6 eV (refered to a vacuum energy level of ferrocene of -4.8 eV) and disubstituted ***cis*-152** shows a slightly lower HOMO value of -6.0 eV (first oxidation potential: 1.2 V). But due to the fact of a much lower optical HOMO-LUMO energy gap in the case of disubstituted ***cis*-152** in comparison to tetratriflate **153** (2.0 eV vs. 2.7 eV), the LUMO level is much lower (-4.0 eV vs. -2.87 eV) as depicted in Figure 3.13 (c).

A lower LUMO value means a higher oxidation stability and thus air stability. This is in accordance to DFT calculated frontier molecular orbital energies (def2-TZVPP/B3LYP level of theory, Figure 3.14). The calculated KOHN-SHAM orbitals of HOMO and LUMO show a large participation of the carbonyl group in the case of ***cis*-152**, illustrating the high impact of this functional groups on the frontier molecular orbitals (Figure 3.14).

Dipolar substituted bis-triflate ***cis*-152** should be a promising substrate for further reductive functionalizations of its keto-groups to form A_2B_2-substituted peropyrene push-pull systems. However, when the typical reductive silylation conditions described in Publication 1-3 (Zn, TIPSCl/imidazole in 1,4-dioxane at 80 °C were applied to ***cis*-152**, only decomposition of ***cis*-152** could be observed. A plausible explanation therefore could be the cleavage of the trilyl groups under this conditions. As a second functionalization approach, ***cis*-152** was reacted under typical SUZUKI-MIYAURA reaction conditions for phenalenone-triflates ($[Pd(PPh_3)_2Cl_2]$, Na_2CO_3 in 1,4-dioxane/H_2O at 100 °C) with 1-thienylboronic acid. But also here, only decomposition of ***cis*-152** was observable (Scheme 3.18). Presumably, the terminal butyl groups in *ortho*-position relative to the triflate groups prevent the oxidative addition step during the cross-coupling reaction due to sterical hindrance.

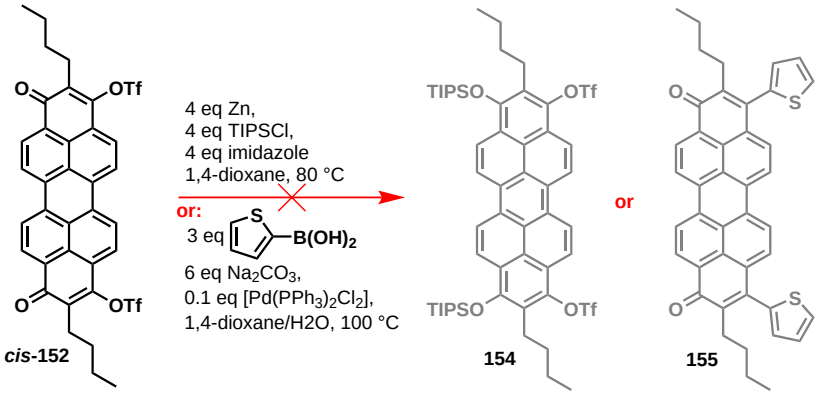

Scheme 3.18 Attempts to functionalize ***cis*-152** by reductive silylation or SUZUKI-MIYAURA cross-coupling.

3.10.9 Experimental Part

Synthesis of 3,5-dibromo-1,1':2',1"-terphenyl (79). 3.42 g (11.0 mmol, 1.00 eq) 1,3,5-tribromobenzene (**77**), 2.02 g (10.0 mmol, 0.90 eq) [1,1'-biphenyl]-2-ylboronic acid (**78**), 4.15 g (30.0 mmol, 3.00 eq) potassium carbonate and 300 mg (0.25 mmol, 2.5 mol%) $[Pd(PPh_3)_4]$ were dissolved in 70 mL toluene, 20 mL ethanol and 10 mL water and the mixture was degassed. The reaction solution was stirred at 95 °C for 20 h and after this complete conversion could be detected by TLC. The organic phase was separated after cooling to room temperature and the aqueous phase was extracted twice with ethyl acetate (20 mL). The combined organic phases were dried over magnesium sulphate. The crude product was purified by column chromatography on silica gel (eluent: *n*-hexane). 3.13 g (8.11 mmol, 81%) of the desired compound **79** were obtained as colorless solid.**TLC:** R_f = 0.45 (*n*-hexane). **^{1}H NMR:** 300 MHz, 298 K, $CDCl_3$, δ = 7.53 (t, 1H, ^4J = 1.66 Hz), 7.49-7.39 (m, 4H), 7.38-7.29 (m, 3H), 7.24 (d, 2H, ^4J = 1.66 Hz), 7.17-7.14 (m, 2H) ppm. **^{13}C NMR:** 75 MHz, 298 K, $CDCl_3$, δ = 145.6, 141.1, 140.9, 137.9, 132.3, 132.1, 131.1, 130.5, 130.2, 128.9, 128.5, 128.1, 127.3, 122.5 ppm. **EI-MS:** *m/z* for $[C_{18}H_{12}{}^{81}Br\ {}^{79}Br]^+$ calc.: 387.92853, found: 387.93066. **IR (ATR):** $\tilde{\nu}$ = 3061 (w), 3018 (m), 2955 (w), 2896 (w), 1960 (w), 1890 (w), 1591 (w), 1485 (w), 1591 (m), 1485 (w), 1465 (w), 1377 (w), 1250 (s), 1192 (m), 1112 (m), 1024 (w), 1003 (w), 844 (vs), 796 (m), 725 (m), 693 (w), 578 (w), 512 (w) cm^{-1}. **m.p.** = 104-107 °C.

Synthesis of 3,5-bis(4,4,5,5-tetramethyl-1,3,2-dioxaborolan-2-yl)-1,1':2',1"-terphenyl (80). 1.50 g (3.89 mmol, 1.00 eq) **79**, 2.98 g (11.67 mmol, 3.00 eq) bis(pinacolato)diboron, 2.30 g (23.34 mmol, 6.00 eq) water-free potassium acetate and 200 mg (0.26 mmol, 6 mol%) $[Pd(dppf)Cl_2]$ were dissolved in 20 mL 1,4-dioxane and stirred at 85 °C for 20 h. After this time, complete conversion could be detected by TLC. After cooling to room temperature, 50 mL water and 50 mL ethyl acetate were added and the aqueous phase was separated and extracted twice with ethyl acetate (20 mL). The combined organic layers were dried over magnesium sulphate and filtered. The crude product was purified by column chromatography on silica gel (eluent: *n*-hexane/ethyl acetate 5:1). 1.69 g (3.50 mmol, 90%) of the desired compound **80** were obtained as colorless solid. **TLC:** R_f = 0.50 *n*-hexane/ethyl acetate 5:1. **^{1}H NMR:** 300 MHz, 298 K, CD_2Cl_2, δ = 7.97 (t, 2H, ^4J = 1.09 Hz), 7.62 (d, 2H, ^4J = 1.09 Hz), 7.45-7.39 (m, 4H), 7.23-7.13 (m, 5H), 1.29 (s, 24H) ppm. **^{13}C NMR:** 75 MHz, 298 K, CD_2Cl_2, δ = 144.2, 142.0, 141.1, 140.9, 140.6, 139.6, 139.2, 130.8, 130.7, 130.3, 128.1, 127.7, 126.8, 84.1, 25.0 ppm. **EI-MS:** *m/z* for $[C_{20}H_{36}{}^{11}B_2O_4]^+$ calc.: 482.27997, found: 482.28049 . **IR (ATR):** $\tilde{\nu}$ = 32977 (m), 2928 (w), 2871 (w), 1699 (w), 1582 (w), 1557 (w), 1478 (w), 1441 (w), 1407 (w), 1370 (s), 1347 (vs), 1317 (s), 1269 (s), 1213 (w), 1112 (m), 1069 (vs), 1008 (m), 964 (m), 867 (m), 845 (w), 776 (m), 700 (s), 676 (w), 616 (w), 578 (w) 517 (w) cm^{-1}. **m.p.** = 105-108 °C.

Synthesis of 5"''-([1,1'-biphenyl]-2-yl)-5",5""-dibromo-1,1':2',1":3",1"':3"',1"":3"", 1""':2"",1"""-sepiphenyl (81). 794 mg (1.65 mmol, 0.50 eq) of terphenyl **79**, 1.27 g (3.30 mmol, 1.00 eq) boronic acid pinacol ester **80**, 1.37 g (9.90 mmol, 6.00 eq) potassium carbonate and 95 mg (0.08 mmol, 6 mol%) $[Pd(PPh_3)_4]$ were dissolved in 50 mL toluene, 20 mL ethanol and 10 mL water and the mixture was degassed. The reaction solution was stirred at 70 °C for 3 d and after this time, complete conversion could be detected by TLC. The organic phase was separated after cooling to room temperature and the aqueous phase was extracted twice with dichloromethane (20 mL). The combined organic phases were dried over magnesium sulphate. The crude product was purified for three times by column chromatography on silica gel (eluent: *n*-pentane/DCM 4:1). 280 mg (8.33 mmol, 20%) of the desired compound **81** were obtained as colorless solid. **TLC:** R_f = 0.30 (*n*-pentane/DCM 10:1). **^{1}H NMR:** 300 MHz, 298 K, CD_2Cl_2, δ = 7.55-6.97 (m, 36H) ppm. **^{13}C NMR:** 75 MHz, 298 K, CD_2Cl_2, δ = 144.2, 143.9, 143.5, 142.6, 142.4, 142.1, 141.9, 141.6, 141.5, 141.2, 140.2, 139.7, 139.6, 134.5, 131.8, 131.0, 130.9, 130.7, 130.7, 130.4, 130.4, 129.0, 128.8, 128.7, 128.7, 128.5, 128.5, 128.3, 128.1, 128.0, 128.0, 127.3, 125.7, 124.0, 122.7 ppm. **EI-MS:** *m/z* for $[C_{54}H_{36}{}^{81}Br\ {}^{79}Br]^+$ calc.: 844.11633, found: 844.11443. **IR (ATR):** $\tilde{\nu}$ = 3057 (w), 2925 (w), 2854 (w), 1733 (w), 1591 (m), 1564 (m), 1476 (m), 1444 (w), 1389 (m), 1295 (w), 1262 (w), 1159 (m), 1110 (w), 1071 (w), 1015 (w), 865 (m), 805 (w), 738 (vs), 700 (vs), 659 (m), 617 (m), 519 (w) cm^{-1}. **m.p.** = 120-123 °C.

Macrocyclization of terphenyl 79. In a flame-dryed Schlenk flask, 950 mg (3.45 mmol, 2.2 eq) $[Ni(COD)_2]$, 539 mg (3.45 mmol, 2.2 eq) 2,2'-bipyridine and 0.45 mL (3.45 mmol, 2.2 eq) 1,5-cyclooctadiene were dissolved in 20 mL dry toluene and 20 mL dry DMF and the mixture was stirred for 30 min at 80 °C under argon atmosphere under exclusion of light. In a droping funnel, 608 mg (1.59 mmol, 1.0 eq) of terphenyl **79** dissolved in 150 mL dry toluene were added dropwise to the catalyst solution within 1 h at 80 °C. The reaction mixture was further stirred for 18 h at 80 °C. After cooling to room temperature, 80 mL of diluted HCl (10%) were added and stirred for 30 min. The organic layer was separated and washed 2x with 50 mL LiCl solution (10%) and dryed over $MgSO_4$. The residue was purified via column chromatography (eluent: *n*-pentane/DCM 2:1). Different fractions of macrocycles were separated: 23 mg (16 μmol, 6%, R_f = 0.50) pentamer **81**, **EI-MS:** *m/z* for $[C_{90}H_{60}]^+$ calc.: 1140.46950, found: 1140.46974. 55 mg (40 μmol, 14%, R_f = 0.45) hexamer **76**, **EI-MS:** *m/z* for $[C_{108}H_{72}]^+$ calc.: 1368.56340, found: 1369.31372. 39 mg (31 μmol, 11%, R_f = 0.40) heptamer **82**, **EI-MS:** *m/z* for $[C_{126}H_{84}]^+$ calc.: 1596.65730, found: 1597.26567. 19 mg (14 μmol, 5%, R_f = 0.35) octamer **83**, **EI-MS:** *m/z* for $[C_{144}H_{96}]^+$ calc.: 1824.75120, found: 1825.29566. ^{1}H NMR analysis was not performed, since all macrocycles showed one broad ill-resolved multiplet between 7.5 and 9 ppm due to limited solubility.

Synthesis of macrocycle 86. In a flame-dryed Schlenk flask, 175 mg (0.64 mmol, 2.5 eq) $[Ni(COD)_2]$, 100 mg (0.64 mmol, 2.5 eq) 2,2'-bipyridine and 75 μL (0.64 mmol, 2.5 eq) 1,5-cyclooctadiene were dissolved in 2 mL dry toluene and 2 mL dry DMF and the mixture was

stirred for 30 min at 60 °C under argon atmosphere under exclusion of light. In a time period of 45 min, 175 mg (0.26 mmol, 1.0 eq) of compound **84** dissolved in 12 mL dry toluene were added dropwise to the catalyst solution at 60 °C. The resulting mixture was stirred for 16 h at 85 °C under exclusion of light. After cooling to room temperature, 10 ml of diluted HCl (10%) were added and stirred for 10 min. The aqueous phase was separated and extracted with ethyl acetate (2 x 20 mL). The combined organic layers were dried over $MgSO_4$ and the solvent was evaporated *in vacuo*. The crude intermediate **85** was dissolved in 2 mL THF under argon atmosphere and a solution of 2 mL of tetrabutylammonium fluoride trihydrate (1 M in THF, 3.1 eq) was added dropwise. The mixture was stirred at room temperature for 3 d. After complete conversion was monitored via TLC, the reaction mixture was poured in 10 mL water and was extracted with 20 mL DCM and the separated organic layer was subsequently dried over $MgSO_4$. The crude product was purified via column chromatography (eluent *n*-pentane/DCM 2:1) and the first, blue fluorescing band was separated. 27 mg (20 μmol, 10%) of the desired compound **86** were obtained as beige powder. **TLC:** R_f = 0.30 (*n*-pentane/DCM 10:1). **^{1}H NMR:** 300 MHz, 298 K, CD_2Cl_2, δ = 6.5-8.0 (m, 66H) ppm. **EI-MS:** *m/z* for $[^{13}C_1{}^{12}C_{107}H_{66}]^+$ calc.: 1363.51980, found: 1363.52111. **IR (ATR):** $\tilde{\nu}$ = 2960 (w), 1583 (w), 1478 (w), 1383 (w), 1260 (s), 1091 (m), 1019 (vs), 863 (m), 799 (vs), 760 (s), 742 (vs), 699 (vs), 614 (w) cm^{-1}.

Synthesis of (11-(3,4-bis(hexyloxy)phenyl)-7,10-dibromo-1,4-diphenyltriphenylen-2-yl)trimethylsilane (97). 2.52 g (3.43 mmol, 1.0 eq) of compound **96**[254] and boronic acid **90**[255] were dissolved in 40 mL DMSO and 5 mL sat. aqueous $NaHCO_3$ were added. The reaction mixture was subsequently degassed and 72 mg (0.1 mmol, 3 mol%) $[Pd(PPh_3)_2Cl_2]$ and 105 mg (0.4 mmol, 12 mol%) PPh_3 were added. The reaction mixture was heated for 4 d at a temperature of 65 °C under argon atmosphere. After cooling to room temperature, 100 mL water were added and the mixture was extracted with 50 mL EtOAc (3x). The combined organic layers were dried over $MgSO_4$ and the crude product was purified via column chromatography (eluent *n*-hexane/DCM 10:1 in order to separate unreacted **96** to 2:1 in order to elute the desired product **97**). 730 mg (0.82 mmol, 44% borsm.) of the yellow solid **97** could be isolated as a mixture of two regioisomers with respect to the position of the TMS group. **TLC:** R_f = 0.30 (*n*-hexane/DCM 2:1). **^{1}H NMR:** 300 MHz, 298 K, $CDCl_3$, δ = 8.55-8.62 (m, 1H), 7.53 (t, 1H, ^4J = 2.4 Hz), 7.82 (d, 1H, ^4J = 2.4 Hz), 7.74 (d, 1H, ^3J = 9.8 Hz), 7.32-7.55 (m, 11H), 7.18 (2x dd, 1H, ^3J = 9.0 Hz, ^4J = 2.0 Hz), 6.78 (t, 1H, ^4J = 8.2 Hz), 6.69 (2x d, 1H, ^4J = 2.1 Hz), 6.36 (2x d, 1H, ^4J = 2.1 Hz), 3.95-4.08 (m, 4H), 1.85-1.92 (m, 4H), 1.30-1.60 (m, 12H), 0.90-1.02 (m, 6H), 0.05 (2x s, 9H) ppm. **^{13}C NMR:** 75 MHz, 298 K, $CDCl_3$, δ = 149.1, 149.0, 148.0, 145.5, 145.2, 144.9, 144.5, 140.1, 139.6, 137.5, 137.4, 137.1, 136.9, 133.8, 133.2, 133.1, 132.1, 131.9, 131.7, 131.6, 131.5, 131.3, 130.5, 130.3, 129.9, 129.7, 129.5, 129.5, 129.4, 129.2, 129.1, 128.9, 128.8, 128.7, 128.6, 127.9, 127.8, 127.7, 127.6, 127.5, 127.4, 125.9, 122.7, 122.4, 121.8, 121.5, 121.3, 121.0, 116.1, 115.6, 112.8, 69.8, 69.7, 69.3, 31.8, 29.5, 25.9, 22.8, 14.2, 1.1, 1.0 (2 sets of isomers) ppm. **LIFDI-MS:** *m/z* for $[C_{51}H_{54}{}^{79}Br_2O_2Si]^+$ calc.: 884.22598, found: 884.22417. **IR (ATR):** $\tilde{\nu}$ = 2949 (w), 2925 (w), 2865 (w), 1630 (w), 1609 (w), 1550 (vs), 1507 (w), 1433 (m), 1411 (m), 1372 (m), 1280 (vs), 1211 (s), 1185 (s), 1150 (m), 1115 (s), 1018 (m),

933 (w), 843 (m), 746 (w) cm^{-1}. **m.p.** = 117-120 °C.

Synthesis of 6-(3,4-bis(hexyloxy)phenyl)-7,10-dibromo-1,4-diphenyltriphenylene (98). Under argon atmosphere, 530 mg (0.60 mmol, 1.0 eq) of compound **97** were dissolved in 20 mL dry THF. A solution of tetrabutyl ammoniumfluorid trihydrate (10 mL, 1 M in THF, 10 eq) was added dropwise and the resulting solution was stirred for 3 d at room temperature. After this time, 20 mL water were added and the mixture was extracted with DCM (2x 30 mL) and the combined organic layers were dried over $MgSO_4$. The crude product was purified by column chromatography (eluent: *n*-hexane/DCM 2:1). 317 mg (0.39 mmol, 65%) of compound **98** were obtained as colourless solid. **TLC:** R_f = 0.25 (*n*-hexane/DCM 2:1). **^{1}H NMR:** 300 MHz, 298 K, $CDCl_3$, δ = 8.62 (s, 1H), 8.51, (d, 1H, ^4J = 2.0 Hz), 7.74 (s, 1H), 7.35-7.58 (m, 13H), 7.19 (dd, 1H, ^3J = 9.0 Hz, ^4J = 2.0 Hz), 6.74 (d, 1H, ^3J = 8.3 Hz), 6.66 (d, 1H, ^4J = 2.1 Hz), 6.37 (dd, 1H, ^3J = 8.2 Hz, ^4J = 2.1 Hz), 3.98-4.06 (m, 4H), 1.80-1.90 (m, 4H), 1.30-1.55 (m, 12H), 0.85-1.00 (m, 6H) ppm. **^{13}C NMR:** 75 MHz, 298 K, $CDCl_3$, δ = 149.2, 148.0, 144.4, 144.1, 139.5, 139.1, 139.1, 133.2, 131.8, 131.7, 130.6, 130.4, 130.2, 129.8, 129.6, 129.5, 129.4, 129.1, 127.8, 127.6, 127.4, 126.0, 122.5, 121.6, 121.4, 115.7, 112.8, 69.7, 69.2, 31.8, 31.8, 29.5, 25.9, 14.2 ppm. **LIFDI-MS:** *m/z* for $[C_{48}H_{46}{}^{79}Br_2O_2]^+$ calc.: 812.18646, found: 812.18592. **IR (ATR):** $\tilde{\nu}$ = 3053 (w), 2952 (s), 2927 (vs), 2828 (m), 1596 (m), 1516 (w), 1468 (m), 1447 (m), 1404 (w), 1383 (w), 1352 (w), 1255 (m), 1140 (m), 1094 (s), 1024 (m), 907 (w), 829 (w), 804 (s), 730 (w), 684 (m) cm^{-1}. **m.p.** = 130-133 °C.

7,10-dibromo-2,3-dihexyl-6-iodo-1,4-diphenyltriphenylene (99). In a microwave vessel, 2.0 g (3.0 mmol, 1.0 eq) of compound **95**[254] and 1.45 mL (6.0 mmol, 2.0 eq) tetradec-7-yne were suspended in 10 mL *o*-xylene. The vessel was irradiated at 200 °C and 300 W for 14 h. After cooling to room temperature, the solvent was removed *in vacuo* and the residue was purified via column chromatography (eluent: *n*-hexane/DCM 10:1). The resulting oil was dissolved in *n*-pentane and precipitated at -80 °C overnight. After filtration and drying *in vacuo*, 850 mg (1.02 mmol, 51%) of the colourless solid **99** were obtained. **TLC:** R_f = 0.40 (*n*-hexane/DCM 10:1). **^{1}H NMR:** 300 MHz, 298 K, CD_2Cl_2, δ = 8.38-6.50 (m, 2H), 8.51, (d, 1H, ^4J = 3.5 Hz), 7.25-7.55 (m, 11H), 7.09 (dd, 1H, ^3J = 9.1 Hz, ^4J = 2.0 Hz), 2.84 (t, 4H, ^3J = 8.0 Hz), 1.00-1.32 (m, 16H), 0.78 (t, 6H, ^3J = 7.1 Hz) ppm. Due to low solubility, no ^{13}C NMR was recorded. **EI-MS:** *m/z* for $[C_{42}H_{41}{}^{79}Br_2{}^{127}I]^+$ calc.: 830.06197, found: 830.05949. **IR (ATR):** $\tilde{\nu}$ = 2945 (m), 2919 (s), 2849 (m), 1458 (w), 1440 (m), 1396 (w), 1373 (w), 1353 (m), 1073 (m), 885 (m), 871 (s), 858 (w), 822 (w), 801 (vs), 774 (w), 724 (w), 680 (m) cm^{-1}. **m.p.** = 142-145 °C.

Synthesis of 7,10-dibromo-2,3-dihexyl-1,4,6-triphenyltriphenylene (100). 730 mg (0.88 mmol, 1.0 eq) of compound **99**, benzene boronic acid (107 mg, 0.88 mmol, 1.0 eq) and potassium carbonate (365 mg, 2.64 mmol, 3.0 eq) were dissolved in 10 mL 1,4-dioxane, 5 mL toluene and 3 mL water. The reaction mixture was subsequently degassed and 12 mg (0.02 mmol, 2 mol%) $[Pd(PPh_3)_2Cl_2]$ and 10 mg (0.02 mmol, 4 mol%) PPh_3 were added. The reaction mix-

ture was heated for 18 h at a temperature of 100 °C under argon atmosphere. After cooling to room temperature, 10 mL water were added and the mixture was extracted with 20 mL EtOAc (2x). The combined organic layers were dried over $MgSO_4$ and the crude product was purified via column chromatography (eluent *n*-hexane/DCM 10:1 in order to separate unreacted **99** to 5:1 in order to collect the desired product **100**). 190 mg (0.23 mmol, 27%) of **100** could be isolated as colourless solid. **TLC:** R_f = 0.30 (*n*-hexane/DCM 10:1). **^{1}H NMR:** 300 MHz, 298 K, CD_2Cl_2, δ = 8.60 (s, 1H), 8.48, (d, 1H, ^4J = 2.0 Hz), 7.70 (s, 1H), 7.30-7.50 (m, 14H), 7.10 (dd, 1H, ^3J = 9.1 Hz, ^4J = 2.1 Hz), 6.94 (dd, 2H, ^3J = 7.5 Hz, ^4J = 2.0 Hz), 2.77-2.90 (m, 4H), 0.95-1.32 (m, 16H), 0.72-0.84 (m, 6H) ppm. **^{13}C NMR:** 75 MHz, 298 K, CD_2Cl_2, δ = 143.0, 142.7, 140.2, 140.0, 139.1, 137.9, 132.5, 131.5, 131.4, 131.3, 131.0, 130.1, 129.9, 129.5, 128.9, 128.7, 128.5, 128.4, 127.3, 127.2, 127.0, 126.9, 126.8, 125.3, 119.9, 30.9, 30.7, 30.0, 29.1, 22.1, 13.5 ppm. **EI-MS:** *m/z* for $[C_{48}H_{46}{}^{79}Br_2]^+$ calc.: 780.19663, found: 780.19621. **IR (ATR):** $\tilde{\nu}$ = 2949 (w), 2919 (m), 2849 (w), 1462 (w), 1440 (m), 1360 (w), 876 (m), 823 (w), 800 (w), 777 (m), 760 (vs), 692 (w), 570 (w), 537 (w) cm^{-1}. **m.p.** = 123-126 °C.

Macrocyclization of compound 100. In a flame-dryed Schlenk flask, 107 mg (0.39 mmol, 3.0 eq) $[Ni(COD)_2]$, 61 mg (0.39 mmol, 3.0 eq) 2,2'-bipyridine were dissolved in 20 mL dry THF and were stirred for 15 min at 60 °C under argon atmosphere under exclusion of light. In a time period of 30 min, 100 mg (0.13 mmol, 1.0 eq) of compound **100** dissolved in 20 mL dry THF were added dropwise to the catalyst solution at 60 °C. The resulting mixture was stirred for 1 h at 70 °C under exclusion of light. After cooling to room temperature, 10 ml diluted HCl (10%) were added and stirred for 10 min. The aqueous phase was separated and extracted with ethyl acetate (2 x 20 mL). The combined organic layers were dried over $MgSO_4$ and the solvent was evaporated *in vacuo*. The crude intermediate **101** was purified via column chromatography (eluent *n*-hexane/DCM 5:1) and the first, blue fluorescing band was separated. 19 mg (10 μmol, 25%) of the desired compound **101** along with impurities of larger oligomers were obtained as beige powder. **TLC:** R_f = 0.20 (*n*-hexane/DCM 5:1). **^{1}H NMR:** 300 MHz, 298 K, CD_2Cl_2, δ = 6.5-7.8 (m, 62H), 2.5-3.2 (m, 12H), 0.6-1.2 (m, 66H) ppm. Due to low solubility, no ^{13}C NMR was recorded. **LIFDI-MS:** *m/z* for $[C_{144}H_{138}]^+$ calc.: 1867.07985, found: 1867.08225. **IR (ATR):** $\tilde{\nu}$ = 2950 (w), 2918 (m), 2850 (w), 1596 (w), 1486 (w), 1460 (w), 1440 (m), 1365 (w), 1072 (w), 1024 (w), 896 (w), 876 (w), 804 (m), 753 (vs), 616 (m) cm^{-1}.

Synthesis of 2-butyl-3-hydroxy-7-(4,4,5,5-tetramethyl-1,3,2-dioxaborolan-2-yl)-1*H*-phenalen-1-one (112). In a Schlenk flask, potassium acetate (1.42 g, 14.5 mmol, 3.0 eq) was dried for 1 h at 100 °C under vacuum (1$\cdot$ 10^{-3}mbar). Subsequently, 1.60 g (4.83 mmol, 1.0 eq) hydroxy-phenalenone **111**,[286] 1.84 g (7.25 mmol, 1.5 eq) bis(pinacolato)diborone and $[Pd(dppf)Cl_2]$ (197 mg, 0.25 mmol, 5 mol%) were added and the mixture was dissolved in 25 mL dry DMF. The reaction mixture was stirred for 18 h under argon atmosphere at 100 °C. After cooling down to room temperature, the reaction mixture was diluted with 50 mL ethyl acetate and washed with 10% aqueous LiCl solution (4 x 100 mL). The organic layer was dried over sodium sulphite and the crude product was purified by column chromatography (eluent: *n*-

hexane/EtOAc 3:1 to 2:1). 810 mg (2.11 mmol, 44%) of compound **112** were obtained as brown solid. **TLC:** R_f = 0.25 (*n*-hexane/EtOAc 3:1). **^{1}H NMR:** 300 MHz, 298 K, DMSO-d_6, δ = 10.49 (br.s, 1H), 8.90 (d, 1H, ^3J = 8.3 Hz), 8.34 (t, 2H, ^3J = 7.4 Hz), 8.16 (d, 1H, ^3J = 7.3 Hz), 7.81 (t, 1H, ^3J = 8.2 Hz), 2.64 (t, 2H, ^3J = 7.4 Hz), 1.40 (s, 16H), 0.91 (t, 3H, ^3J = 7.1 Hz) ppm. **^{13}C NMR:** 75 MHz, 298 K, DMSO-d_6, δ = 135.4, 134.6, 126.9, 125.4, 118.6, 84.1, 30.6, 24.7, 22.3, 22.2, 14.0 ppm (C=O signal is missing). **APCI-MS:** *m/z* for $[C_{23}H_{26}{}^{11}BO_4]^-$ calc.: 377.1934, found: 377.1938. **IR (ATR):** $\tilde{\nu}$ = 3216 (br, w), 2975 (m), 2955 (m), 2928 (m), 2868 (w), 1623 (m), 1552 (vs), 1513 (w), 1470 (m), 1404 (vs), 1368 (s), 1343 (m), 1277 (s), 1205 (vs), 1145 (m), 1121 (m), 1105 (m), 1054 (w), 853 (m), 783 (m) cm^{-1}. **m.p.** = 76-79 °C.

Synthesis of 2-butyl-1-oxo-7-(4,4,5,5-tetramethyl-1,3,2-dioxaborolan-2-yl)-1H-phenalen-3-yl trifluoromethanesulfonate (109). Under argon atmosphere, 775 mg (2.05 mmol, 1.0 eq) of hydroxy-phenalenone **112** were dissolved in 100 mL dry dichloromethane and cooled down to 0 °C. Subsequently, 0.5 mL (6.3 mmol, 3.0 eq) pyridine were added. Over a time period of 1 h, 0.5 mL (3.2 mmol, 1.5 eq) of triflate anhydride were added. The resulting mixture was stirred for 1 h at 0 °C and then for 1 h at room temperature. The reaction mixture was filtered over neutral aluminum oxide and washed with DCM. 325 mg (0.64 mmol, 31%) of compound **109** were obtained as waxy yellow solid. R_f = 0.40 (DCM). **^{1}H NMR:** 300 MHz, 298 K, $CDCl_3$, δ = 9.19 (d, 1H, ^3J = 8.3 Hz), 8.66 (d, 2H, ^3J = 7.3 Hz), 8.26 (d, 1H, ^3J = 7.4 Hz), 8.06 (d, 1H, ^3J = 7.4 Hz), 7.84 (t, 1H, ^3J = 7.7 Hz), 2.81 (t, 2H, ^3J = 8.0 Hz), 1.53-1.68 (m, 2H), 1.45 (s, 14H), 0.96 (t, 3H, ^3J = 7.2 Hz) ppm. **^{19}F NMR:** 282 MHz, 298 K, $CDCl_3$, δ = -72.6 ppm. **^{13}C NMR:** 75 MHz, 298 K, $CDCl_3$, δ = 184.5, 152.8, 136.9, 135.8, 135.5, 135.0, 131.3, 128.3, 127.8, 126.0, 125.7, 125.6, 85.7, 30.6, 25.3, 25.1, 23.1, 13.9 ppm. **APCI-MS:** *m/z* for $[C_{24}H_{27}{}^{11}B^{32}S^{19}F_3O_6]^+$ calc.: 511.1572, found: 511.1572. **IR (ATR):** $\tilde{\nu}$ = 2965 (w), 2935 (w), 2870 (w), 1640 (m), 1574 (w), 1512 (w), 1463 (w), 1408 (m), 1366 (m), 1270 (s), 1242 (m), 1212 (w), 1135 (m), 1100 (s), 1051 (w), 983 (vs), 907 (s), 824 (s), 778 (s), 664 (m) cm^{-1}. **m.p.** = 125-128 °C

Macrocyclization of compound 109. Under argon atmosphere, 56 mg (0.11 mmol, 20 mol%) [Pd(P*t*Bu$_3$)$_2$] and 1.26 g (5.5 mmol, 10 eq) of monohydrated potassium phosphate were dissolved in 250 mL dry THF and heated for 30 min to 60 °C under argon atmosphere. Compound **109** (285 mg, 0.55 mmol, 1.0 eq) was dissolved in 10 mL dry THF and added dropwise. The reaction mixture was stirred for 4 d at 70 °C. After cooling to room temperature, 100 mL water and 100 mL ethyl acetate were added. The aqueous phase was separated and subsequently extracted with 100 mL ethyl acetate. The combined organic layers were dried over $MgSO_4$ and the crude product was purified by column chromatography (eluent: DCM to DCM/EtOAc 10:1). 60 mg of an inseparable mixture of acyclic oligomers (mostly tri- and tetramer, also acyclic hexamer) were obtained as yellow waxy solid and analyzed by APCI(+) mass spectrometry. **APCI-MS:** *m/z* for $[C_{102}H_{87}O_6]^+$ calc.: 1408.6531, found: 1408.6533 (acyclic hexamer).

Synthesis of 3,6-dibromo-2-iodo-10,13-dimethyl-9,14-diphenylbenzo[*f*]-tetraphene (116). In a Schlenk flask, 750 mg (1.13 mmol, 1.0 eq) of ketone **95**[254] and trimethylsilyl triflate **115**[266] (450 mg, 1.31 mmol, 1.15 eq) were dissolved in 40 mL DCM and 35 mL MeCN. 250 mg (1.63 mmol, 1.45 eq) caesium fluoride were suspended in 10 mL MeCN and added dropwise. The resulting suspension was heated for 6 h to 55 °C. After this time, complete conversion of **95** was detected by TLC. The reaction mixture was filtered and the solvent was removed in vacuo. The crude product was purified via column chromatography (*n*-pentane/DCM 1:2) in order to yield 430 mg (0.58 mmol, 51%) of the beige-grey solid **116**. R_f = 0.10 (*n*-pentane/DCM 1:2). **^{1}H NMR:** 300 MHz, 298 K, CD_2Cl_3, δ, δ = 8.88 (d, 1H, ^3J = 10.1 Hz), 8.80 (dd, 1H, ^3J = 9.7 Hz, ^4J = 1.7 Hz), 8.74 (d, 1H, ^4J = 2.0 Hz), 8.10 (d, 1H, ^3J = 8.9 Hz), 7.41-7.63 (m, 11H), 6.90 (d, 1H, ^4J = 1.9 Hz), 2.35 (m, 6H) ppm. Due to low solubility, no ^{13}C NMR was recorded. **EI-MS:** *m/z* for $[C_{36}H_{23}{}^{79}Br^{81}Br^{127}I]^+$ calc.: 741.91907, found: 741.92049. **IR (ATR):** $\tilde{\nu}$ = 1599 (w), 1492 (w), 1461 (w), 1445 (w), 1389 (m), 1262 (m), 1118 (s), 1036 (w), 932 (w), 887 (m), 814 (m), 797 (m), 708 (vs), 676 (m), 503 (w) cm^{-1}. **m.p.** = > 250 °C dec.

Synthesis of 3,6-dibromo-2-(5,8-dimethylnaphthalen-2-yl)-10,13-dimethyl-9,14-diphenylbenzo[*f*]tetraphene (114). 300 mg (0.41 mmol, 1.0 eq) of compound **116**[254] and 125 mg (0.44 mmol, 1.1 eq) dimethyl-naphthalene boronic acid pinacolester **117**[267] were dissolved in 14 mL DMSO and 2 mL sat. aqueous $NaHCO_3$ were added. The reaction mixture was subsequently degassed and 15 mg (0.02 mmol, 5 mol%) [Pd(dppf)Cl_2] were added. The reaction mixture was heated for 24 h at a temperature of 70 °C under argon atmosphere. After cooling to room temperature, 20 mL water were added and the mixture was extracted with 20 mL EtOAc (3x). The combined organic layers were dried over $MgSO_4$ and the crude product was purified via column chromatography (eluent *n*-pentane/DCM 10:4). 185 mg (0.24 mmol, 59%.) of the orange solid **97** could be isolated as a mixture of two regioisomers with respect to the position of the TMS group. **TLC:** R_f = 0.20 (*n*-pentane/DCM 10:4). **^{1}H NMR:** 500 MHz, 298 K, $CDCl_3$, δ = 8.55-8.62 (m, 1H), 9.01 (d, 1H, ^3J = 10.3 Hz, ^4J = 1.8 Hz), 8.34 (d, 1H, ^3J = 10.7 Hz), 8.15 (t, 1H, ^3J = 9.4 Hz), 7.95-8.04 (m, 2H), 7.40-7.80 (m, 13H), 6.83-6.90 (m, 2H), 2.69 (d, 3H, J = 4.9 Hz), 2.67 (d, 3H,J = 8.5 Hz), 2.40 (d, 3H, J = 4.5 Hz), 2.24 (d, 3H, J = 6.5 Hz) ppm. **^{13}C NMR:** 125 MHz, 298 K, $CDCl_3$, δ = 143.5, 143.3, 142.7, 142.4, 142.0, 141.0, 141.0, 137.5, 133.0, 132.5, 132.5, 132.0, 131.3, 131.2, 130.9, 130.8, 130.6, 130.1, 129.9, 129.6, 129.0, 128.6, 128.5, 128.2, 128.1, 127.9, 127.7, 127.2, 127.1, 126.9, 126.7, 126.5, 125.5, 124.3, 122.6, 121.7, 121.6, 22.3, 22.2, 19.8, 19.7, 19.5 ppm. **LIFDI-MS:** *m/z* for $[C_{48}H_{34}{}^{79}Br^{81}Br]^+$ calc.: 770.10068, found: 770.09706. **IR (ATR):** $\tilde{\nu}$ = 3076 (m), 3030 (w), 2962 (w), 2922 (m), 2860 (w), 1802 (vs), 1599 (m), 1555 (w), 1490 (m), 1473 (m), 1446 (s), 1413 (w), 1379 (w), 1263 (m), 1210 (m), 1183 (m), 1086 (m), 1022 (m), 915 (m), 812 (vs), 814 (w), 706 (w), 675 (w) cm^{-1}. **m.p.** = 296-299 °C dec.

Synthesis of 3,3",4'-tribromo-1,1':2',1"-terphenyl (124). 515 mg (1.25 mmol, 1.00 eq) of 4-bromo-1,2-diiodobenzene (**122**)[276] and 500 mg (2.50 mmol, 2.00 eq) 3-bromophenyl boronic acid (**123**) were dissolved in 20 mL DMSO and 2 mL saturated aqueous sodium hydrogen carbonate solution. The mixture was degassed and 15 mg (0.02 mmol, 1.5 mol%) [Pd(dppf)Cl_2] were added. The reaction mixture was stirred for 3 d at 60 °C under exclusion of light. After this, complete conversion could be detected by TLC. After cooling to room temperature, 50 mL of 2M HCl and 30 mL ethyl acetate were added and the aqueous phase was separated and extracted twice with chloroform (20 mL). The combined organic layers were dried over magnesium sulphate and filtered. The crude product was purified by column chromatography on silica gel (eluent: *n*-pentane/ethyl acetate 50:1). 298 mg (0.65 mmol, 52%) of the desired compound **124** were obtained as colorless oil. **TLC:** R_f = 0.50 (*n*-pentane/chloroform 50:1). **^{1}H NMR:** 300 MHz, 298 K, $CDCl_3$, δ = 6.92-6.98 (m, 2H), 7.08 (dt, 2H, ^3J = 7.8 Hz, ^4J = 3.6 Hz), 7.26-7.30 (m, 1H), 7.33-7.42 (m, 4H), 7.55-7.60 (m, 2H) ppm. **^{13}C NMR:** 75 MHz, 298 K, $CDCl_3$, δ = 122.2, 122.4, 128.4, 128.6, 128.6, 129.2, 129.7, 130.3, 130.5, 131.2, 132.1, 132.5, 132.5, 133.4, 138.1, 141.0, 141.8, 142.1 ppm. **EI-MS:** *m/z* for $[C_{18}H_{11}{}^{79}Br_3]^+$ calc.: 463.84109, found: 463.83968. **IR (ATR):** $\tilde{\nu}$ = 2979 (m), 2931 (w), 2871 (w), 1696 (w), 1557 (w), 1478 (w), 1441 (w), 1407 (w), 1370 (s), 1350 (s), 1317 (s), 1270 (s), 1211 (w), 1112 (m), 1066 (vs), 1008 (m), 964 (m), 869 (m), 783 (m), 700 (s), 676 (w), 618 (w), 578 (w) cm^{-1}.

Synthesis of 2,6,11-tribromotriphenylene (120). 295 mg (0.64 mmol, 1.00 eq) of compound **124** and 350 mg (1.28 mmol, 2.00 eq) molybdenum pentachloride were dissolved in 25 mL dichloromethane under argon atmosphere and stirred for 6 d at room temperature. After this time, complete conversion could be detected by TLC. 10 mL methanol were added and the reaction mixture was stirred for 30 min. Then, 20 mL water were added and the aqueous phase was separated and extracted with dichloromethane (20 mL) twice. The combined organic layers were dried over magnesium sulphate and filtered. The crude product was purified by column chromatography on silica gel (eluent: *n*-pentane/chloroform 100:1). 52 mg (0.11 mmol, 18%) of the desired compound **120** were obtained as colorless powder. For further purification, **120** was recrystallized (chloroform) and sublimed under high vacuum conditions (215 °C, $5{\cdot}10^{-6}$ mbar). **TLC:** R_f = 0.45 (*n*-pentane/chloroform 100:1). **^{1}H NMR:** 300 MHz, 298 K, CD_2Cl_2, δ = 8.64-8.75 (m, 3H), 8.35-8.47 (m, 3H), 7.76-7.84 (m, 3H) ppm. Due to limited solubility, no ^{13}C NMR was recorded. **EI-MS:** *m/z* for $[C_{18}H_9{}^{79}Br_3]^+$ calc.: 461.82650, found: 461.82544. **IR (ATR):** $\tilde{\nu}$ = 3060 (w), 2934 (w), 2866 (w), 1899 (w), 1731 (w), 1558 (s), 1469 (s), 1392 (s), 1236 (w), 1115 (m), 1035 (s), 1002 (m), 839 (m), 804 (w), 775 (s), 744 (vs), 720 (m), 701 (s), 678 (w), 549 (w), 537 (w) cm^{-1}. **m.p.** = 233-236 °C dec.

Synthesis of (4'-bromo-[1,1':2',1"-terphenyl]-4,4"-diyl)bis(trimethylsilane) (127). 326 mg (0.80 mmol, 1.0 eq) of compound **122**,[276] 442 mg (1.60 mmol, 2.0 eq) boronic acid pinacolester **126**[288] were dissolved in 20 mL DMSO and 5 mL saturated aqueous sodium hydrogen carbonate solution. The mixture was degassed and 23 mg (0.03 mmol, 3 mol%) [Pd(dppf)Cl_2] were added. The reaction mixture was stirred for 4 d at 70 °C under exclusion of light. After

this, complete conversion could be detected by TLC. After cooling to room temperature, 20 mL saturated NaCl solution and 40 mL DCM were added and the aqueous phase was separated. The organic phase was washed with saturated NaCl solution (3 x 20 mL). The combined organic layers were dried over magnesium sulphate and filtered. The crude product was purified by column chromatography on silica gel (eluent: *n*-hexane). 205 mg (0.45 mmol, 57%) of the desired compound **127** were obtained as colorless oil. **TLC:** R_f = 0.35 (*n*-hexane). **^{1}H NMR:** 300 MHz, 298 K, CD_2Cl_2, δ = 7.51-7.58 (m, 2H), 7.27 (d, 1H, ^3J = 8.0 Hz), 7.10 (dd, 4H, ^3J = 8.1 Hz, ^4J = 3.3 Hz), 0.23 (s, 9H) ppm. **^{13}C NMR:** 75 MHz, 298 K, CD_2Cl_2, δ = 142.1, 141.8, 141.0, 138.1, 133.4, 132.5, 132.5, 132.2, 131.1, 130.5, 130.3, 129.7, 129.2, 128.6, 128.6, 128.4, 122.4, 122.2 ppm. **EI-MS:** *m/z* for $[C_{24}H_{29}{}^{79}BrSi_2]^+$ calc.: 452.09912, found: 452.09950. **IR (ATR):** $\tilde{\nu}$ = 3061 (w), 3016 (w), 2955 (m), 2896 (w), 1960 (w), 1890 (w), 1591 (m), 1495 (m), 1456 (w), 1377 (w), 1250 (s), 1192 (m), 1112 (m), 1024 (w), 844 (vs), 756 (m), 726 (m), 693 (w), 578 (w) cm^{-1}.

Synthesis of 4'-bromo-4,4"-diiodo-1,1':2',1"-terphenyl (128). 180 mg (0.40 mmol, 1.0 eq) of **127** were dissolved in 10 mL DCM and cooled to 0 °C. A solution of 55 μL (1.04 mmol, 2.6 eq) iodine monochloride in 0.55 mL DCM was added dropwise. The mixture was stirred for 1 h under exclusion of light. After this time, complete conversion was detected by TLC. 20 mL of an 1M aqueous solution of sodium sulphite were added and the phases were separated. The aqueous layer was extracted with dichloromethane (20 mL). The combined organic layers were dried over magnesium sulphate and filtered. The crude product was purified by column chromatography on silica gel (eluent: *n*-hexane). 145 mg (0.26 mmol, 65%) of the desired compound **128** were obtained as a beige solid. **TLC:** R_f = 0.30 (*n*-hexane). **^{1}H NMR:** 300 MHz, 298 K, CD_2Cl_2, δ = 7.59 (dd, 4H, ^3J = 8.5 Hz, ^4J = 4.0 Hz), 7.54 (s, 2H), 7.26 (d, 1H, ^3J = 7.8 Hz), 6.86 (dd, 4H, ^3J = 8.4 Hz, ^4J = 4.0 Hz) ppm. **^{13}C NMR:** 75 MHz, 298 K, CD_2Cl_2, δ = 141.6, 140.1, 139.9, 138.7, 137.8, 137.8, 133.6, 132.5, 132.0, 131.1, 122.2, 93.4, 93.2 ppm. **EI-MS:** *m/z* for $[C_{12}H_{11}{}^{79}Br^{127}I_2]^+$ calc.: 559.81335, found: 559.81288. **IR (ATR):** $\tilde{\nu}$ = 33052 (w), 2921 (w), 2852 (w), 1901 (w), 1649 (w), 1551 (s), 1459 (m), 1373 (w), 1258 (m), 1185 (m), 1089 (vs), 997 (m), 880 (m), 805 (vs), 722 (s), 666 (w), 566 (w), 512 (m), 458 (m) cm^{-1}. **m.p.** = 164-166 °C.

Synthesis of 6-bromo-2,11-diiodotriphenylene (119). 140 mg (0.25 mmol, 1.0 eq) of **128** were dissolved in 10 mL dry DCM and cooled to -78 °C. A solution of 270 mg (0.62 mmol, 2.5 eq) [bis(trifluoroacetoxy)iodo]benzene (PIFA) and 0.11 mL (0.88 mmol, 3.5 eq) boron trifluoride diethyl etherate in 5 mL DCM was added dropwise to the solution of **128** in DCM at -78 °C. After stirring for 2 h at this temperature, complete conversion could be detected by TLC. The reaction solution was warmed to room temperature and adsorbed on neutral aluminum oxide. The crude product was purified by column chromatography on silica gel (eluent: *n*-hexane/chloroform 5:1). 65 mg (0.12 mmol, 47%) of the desired compound **119** were obtained as colorless solid. Further purification could be obtained via recrystallization in chloroform and fine vacuum sublimation (330 °C, 1 · 10^{-3} mbar). **TLC:** R_f = 0.25 (*n*-hexane). **^{1}H NMR:** 300 MHz, 298 K, $CDCl_3$, δ = 8.78 (t, 2H, ^4J = 2.0 Hz), 8.63 (d, 1H, ^4J = 1.9 Hz), 8.36 (d, 1H,

^3J = 8.9 Hz), 8.20 (t, 2H, ^3J = 8.8 Hz), 7.93 (dt, 2H, ^3J = 8.7 Hz, ^4J = 2.0 Hz), 7.73 (dd, 1H, ^3JH = 8.9 Hz, ^4J = 2.0 Hz) ppm. **^{13}C NMR:** 125 MHz, 298 K, $CDCl_3$, δ = 136.7, 136.7, 132.5, 131.0, 130.5, 130.1, 128.6, 128.0, 127.9, 126.1, 125.1, 124.9, 124.9, 122.5, 94.5, 94.0 ppm. **EI-MS:** *m/z* for $[C_{12}H_9{}^{79}Br^{127}I_2]^+$ calc.: 557.79601, found: 557.79770. **IR (ATR):** $\tilde{\nu}$ = 3064 (w), 2923 (m), 2863 (w), 1889 (w), 1736 (w), 1556 (s), 1545 (m), 1471 (s), 1388 (s), 1282 (w), 1236 (w), 1112 (m), 1034 (m), 999 (s), 832 (s), 772 (s), 742 (vs), 703 (s), 682 (w) cm^{-1}. **m.p.** = 209-212 °C.

Synthesis of 4',6'-bis((trimethylsilyl)ethynyl)-[1,1':3',1"-terphenyl]-4,4"-dicarbaldehyde (134) In a Schlenk tube, 474 mg (1.1 mmol, 1.0 eq) of brominated aryl alkyne **132**[289], K_2CO_3 (921 mg, 6.6 mmol, 6.0 eq) and 498 mg (3.3 mmol, 3.0 eq) of boronic acid **133** were dissolved in 20 mL toluene, 4 mL EtOH and 4 mL water and the mixture was degassed subsequently. Under argon atmosphere, 77 mg (0.07 mmol, 6 mol%) $[Pd(PPh_3)_4]$ were added and the reaction mixture was stirred for 24 h at 90 °C. After cooling to room temperature, 10 mL water were added and the aqueous phase was extracted with EtOAc (3x 20 mL). The combined organic layers were dried over $MgSO_4$. The crude product was purified by column chromatography (*n*-pentane/EtOAc 10:1). 394 mg (0.84 mmol, 74%) of compound **134** were obtained as colourless solid. **TLC:** R_f = 0.30 (*n*-pentane/EtOAc 10:1). **^{1}H NMR:** 300 MHz, 298 K, $CDCl_3$, δ = 8.78 (t, 2H, ^4J = 2.0 Hz) 10.08 (s, 2H), 7.95 (d, 4H, ^3J = 7.9 Hz), 7.84 (t, 5H, ^3J = 7.8 Hz), 7.44 (s, 1H), 0.15 (s, 18H) ppm. **^{13}C NMR:** 75 MHz, 298 K, $CDCl_3$, δ = 192.0, 145.5, 142.8, 135.9, 130.3, 130.1, 129.5, 121.6, 102.8, 100.4, -0.3 ppm. **IR (ATR):** $\tilde{\nu}$ = 2959 (s), 2899 (s), 2856 (s), 2151 (m), 2032 (s), 1687 (m), 1605 (m), 1566 (s), 1514 (s), 1479 (s), 1415 (s), 1392 (s), 1376 (s), 1310 (s), 1292 (s), 1249 (m), 1207 (m), 1170 (m), 1159 (m), 1106 (s), 1013 (s), 1004 (s), 971 (s), 929 (s), 899 (s), 825 (s), 751 (st), 698 (m), 654 (s), 633 (s), 615 (s) cm^{-1}. **m.p.** = 191-193 °C.

Synthesis of tetrakis((trimethylsilyl)ethynyl)-hexabenzenacyclodecaphan-4,9-diene (135). In a flame dried two-necked Schlenk flask equipped with a reflux condenser, 4.10 g (63 mmol, 50 eq) zinc and 380 mg (2.0 mmol, 1.6 eq) CuI were dissolved in 200 mL anhydrous THF. 3.4 mL (31 mmol, 25 eq) of $TiCl_4$ were added and the suspension was heated to reflux for 1.5 h. At reflux temperature, 600 mg (1.25 mmol, 1.0 eq) of compound **134** dissolved in 200 mL THF were added dropwise over a time period of 2 h. After complete addition of **134**, the resulting black suspension was refluxed for 16 h. After cooling to room temperature, 100 mL aqueous 2M K_2CO_3 solution were added and the mixture was stirred for 30 min. The resulting precipitate was separated by filtration and the filtrate was extracted with ethyl acetate (2x 50 mL). The combined organic layers were dried over $MgSO_4$. The crude product was purified via column chromatography (*n*-pentane/DCM 10:1) and the first blue fluorescing band was collected. 297 mg (0.33 mmol, 27%) of dimer **135** were obtained as beige solid. **TLC:** R_f = 0.50 (*n*-pentane/DCM 10:1). **^{1}H NMR:** 300 MHz, 298 K, $CDCl_3$, δ = 7.79 (s, 2H), 7.57 (d, 8H, ^3J = 7.6 Hz), 7.29 (s, 2H), 7.13 (d, 8H, ^3J = 7.14 Hz), 6.80 (s, 4H), 0.20 (s, 36H) ppm. **^{13}C NMR:** 75 MHz, 298 K, $CDCl_3$, δ = 143.3, 138.9, 138.3, 137.3, 132.4, 131.2, 129.0, 129.0, 119.6, 103.8, 98.8, -0.1 ppm. **EI-MS:** *m/z* for $[C_{60}H_{60}Si_4]^+$ calc.: 892.37721, found: 892.37825. **IR (ATR):** $\tilde{\nu}$ = 3017 (s), 2957 (s), 2895 (s), 2149 (s), 2022 (s), 1974 (s), 1907 (s), 1719 (s),

1480 (m), 1398 (s), 1373 (s), 1248 (m), 1198 (s), 1187 (s), 1169 (s), 1144 (s), 1114 (s), 1020 (s), 1006 (s), 975 (s), 912 (s), 839 (st), 757 (vs), 712 (s), 699 (s), 681 (s), 660 (s), 632 (s), 550 (s) cm^{-1}. **m.p.** = > 300 °C dec.

Synthesis of [2.2](3,11)dibenzo[*a,j*]anthracenophan-1,17-diene (130). 68 mg (0.08 mmol, 1.0 eq) of compound **135** were dissolved in 3 mL THF under argon atmosphere. A mixture of 120 mg (0.40 mmol, 5.0 eq) tetrabutyl ammoniumfluoride trihydrate in 2 mL THF was added dropwise. After stirring for 1 h at room temperature, 5 mL methanol were added. The precipitate was separated and dried *in vacuo*. 18 mg (0.06 mmol, 0.8 eq) of $PtCl_2$ and 5 mL anhydrous toluene were added and the suspension was heated for 24 h at 95 °C. After the solvent was removed *in vacuo*, the crude reaction mixture was purified by column chromatography (*n*-pentane/DCM/MeOH 3:1:0.01). 24 mg (0.04 mmol, 52%) of the yellow solid **130** were obatined. Further purification could be achieved by high vacuum sublimation (290 °C, p = 1 · 10^{-6} mbar). Due to its low solubility caused by high aggregation tendency, no NMR spectra of compound **130** could be recorded. **TLC:** R_f = 0.70 (*n*-pentane/DCM/MeOH 3:1:0.01). **EI-MS:** *m/z* for $[C_{48}H_{28}]^+$ calc.: 604.21920, found: 604.21874.

Synthesis of Octulene precursor 140. As described for the synthesis of Kekulene precursor **129**,[280] 3.66 g (56.3 mmol, 65.5 eq) zinc and 360 mg copper(I)iodide (1.89 mmol, 2.2 eq) were suspended in 200 mL THF. 3.1 mL (28.2 mmol, 32.8 eq) titanium tetrachloride were added dropwise and the resulting black solution was heated to reflux for 2 h. Subsequently, a solution of 200 mg (0.86 mmol, 1.00 eq) of phenanthrene-2,7-dicarbaldehyde **139** (dissolved in 100 mL THF) were added dropwise over a time period of 1.5 h and then refluxed for additional 18 h. After cooling down to room temperature, 100 mL 10%-aqueous ammonia were added. The aqueous phase was separated and extracted twice with chloroform (100 mL). The combined organic layers were dried over magnesium sulphate and filtered. The crude product was adsorbed on silica and purified via column chromatography (eluent: *n*-pentane/dichloromethane 5:1 to separate Kekulene precursor **129** as major product (60 mg, 0.10 mmol, 35%) to 5:2 to separate Octulene (5 mg, 0.03 mmol, 8%) as minor product. Due to its low solubility caused by high aggregation tendency, no NMR spectra could be acquired. **TLC:** R_f = 0.40 (*n*-pentane/DCM 5:2). **EI-MS:** *m/z* for $[C_{64}H_{40}]^+$ calc.: 808.31300, found: 808.31387.

Synthesis of 1,2-bis(3",4'-di-*tert*-butyl-[1,1':2',1"-terphenyl]-4-yl)ethyne (141). In a Schlenk flask, 113 mg (0.34 mmol, 1.0 eq) of alkyne **148**, 290 mg (0.74 mmol, 2.2 eq) of boronic acid pinacol ester **147** and 280 mg (2.02 mmol, 6.0 eq) K_2CO_3 were dissolved in 6 mL toluene, 2 mL ethanol and 2 mL water and degassed subsequently. Under argon atmosphere, 24 mg (0.02 mmol, 6 mol%) $[Pd(PPh_3)_4]$ were added and the reaction mixture was heated to reflux for 5 d. After cooling to room temperature, 10 mL EtOAc and 10 mL water were added. The aqueous phase was extracted with chloroform (2x 10 mL) and the combined organic layers were dried over $MgSO_4$. The crude product was purified by column chromatography (eluent: *n*-pentane/DCM 20:1). 170 mg (0.24 mmol, 72%) of the colourless solid **141** could be isolated.

TLC: R_f = 0.35 (*n*-pentane/DCM 20:1). **^{1}H NMR:** 300 MHz, 298 K, CD_2Cl_3, δ = 7.43-7.49 (m, 4H), 7.28-7.40 (m, 6H), 7.20-7.26 (m, 4H), 7.00-7.13 (m, 8H) ppm. Due to low solubility, no ^{13}C NMR was recorded. **EI-MS:** *m/z* for $[C_{54}H_{58}]^+$ calc.: 706.45385, found: 706.45599. **IR (ATR):** $\tilde{\nu}$ = 2954 (m), 2899 (w), 2863 (w), 1598 (w), 1481 (m), 1410 (w), 1390 (w), 1360 (w), 1260 (w), 1228 (w), 1105 (w), 1002 (w), 883 (m), 842 (m), 793 (vs), 702 (s), 554 (m) cm^{-1}. **m.p.** = >300 °C dec.

Synthesis of 2-butyl-3-hydroxy-1*H*-phenalen-1-one (150). 4.0 g (20 mmol, 1.0 eq) of 1,8-naphthalic anhydride (**149**) and 4.0 g (30 mmol, 1.5 eq) anhydrous zinc chloride were suspended in 20 mL diethyl butylmalonate and heated for 3 h at 190 °C under argon atmosphere until gas evolution ceased. after cooling to room temperature, the obtained red solid was dissolved in a mixture of 100 mL 2M aqueous KOH solution and 100 mL 2M ammonia and filtered. The crude product was precipitated upon addition of 2M acetic acid (300 mL) and it was collected by filtration. The obtained yellow solid was dried *in vacuo* and purified by column chromatography (eluent: chloroform/aceton 10:1). 2.05 g (8.1 mmol, 40%) of the yellow solid **150** could be isolated. **TLC:** R_f = 0.15 (chloroform).**^{1}H NMR:** 300 MHz, 298 K, DMSO-d_6, δ, δ = 10.41 (s, 1H), 8.34 (d, 2H, ^3J = 7.2 Hz), 8.28 (d, 2H, ^3J = 8.1 Hz), 7.77 (d, 1H, ^3J = 7.8 Hz), 2.65 (t, 2H, ^3J = 7.5 Hz), 1.33-1.48 (m, 4H), 0.96 (t, 3H, ^3J = 6.9 Hz) ppm. **^{13}C NMR:** 75 MHz, 298 K, DMSO-d_6, δ = 133.4, 132.1, 128.2, 127.3, 126.2, 119.1, 31.4, 23.0, 22.9, 14.7 ppm. **APCI-MS:** *m/z* for $[C_{17}H_{15}O_2]^-$ calc.: 252.1111, found: 252.1124. **IR (ATR):** $\tilde{\nu}$ = 3045 (br, w), 2947 (m), 2929 (m), 2864 (w), 1608 (w), 1550 (vs), 1434 (w), 1410 (m), 1376 (m), 1351 (m), 1212 (vs), 1149 (vs), 1076 (vs), 990 (m), 780 (vs), 724 (w), 669 (m), 638 (w) cm^{-1}. **m.p.** = 140-142 °C

Synthesis of dihydroxy-peropyrenequinone 151. In a Ni crucible, 1.90 g (7.5 mmol, 1.0 eq) of compound **150** were mixed with 15 g KOH and heated to 300 °C for 2 h. During this time, a purple foam is formed. After gas evolution ceased, the solidified mixture was cooled to room temperature. The mixture was taken up in water (300 mL), filtered and the filtrate was acidified with 200 mL 2M acetic acid. The formed precipitate was filtered and washed with water (200 mL). After drying at 120 °C for 6 h, 1.05 g (2.1 mmol, 55%) of compound **151** (inseparable mixture of *cis*- and *trans*-dihydroxy isomer) could be obtained as weakly soluble purple solid and directly used for the next step. Due to low solubility, no NMR spectra could be recorded. **APCI-MS:** *m/z* for $[C_{34}H_{27}O_4]^-$ calc.: 500.1949, found: 500.2010. **IR (ATR):** $\tilde{\nu}$ = 3040 (br, w), 2949 (m), 2924 (m), 2866 (w), 1630 (w), 1608 (vs), 1509 (m), 1433 (m), 1411 (w), 1371 (w), 1280 (vs), 1212 (s), 1185 (vs), 1115 (m), 1077 (m), 1013 (s), 977 (m), 843 (s), 781 (w), 726 (w) cm^{-1}.

Synthesis of bis-triflate *cis*-152. Under argon atmosphere, 1.45 g (3.74 mmol, 1.0 eq) of dihydroxy-peropyrenequinone **112** were dissolved in 150 mL dry dichloromethane and cooled down to 0 °C. Subsequently, 1.8 mL (22.4 mmol, 6.0 eq) of pyridine were added. Over a time period of 1 h, 1.8 mL (11.2 mmol, 3.0 eq) of triflate anhydride were added. The resulting mixture

was stirred for 1 h at 0 °C and then for 1 h at room temperature. The reaction mixture was filtered over neutral aluminum oxide and washed with DCM. The first second purple band was collected. 100 mg (0.30 mmol, 8%) of compound ***cis*-109** were obtained as waxy purple-blue solid. R_f = 0.30 (DCM). **^{1}H NMR:** 300 MHz, 298 K, $CDCl_3$, δ = 8.44 (d, 2H, ^3J = 8.1 Hz), 8.28 (d, 2H, ^3J = 8.2 Hz), 8.14 (d, 2H, ^3J = 8.3 Hz), 7.96 (d, 2H, ^3J = 8.2 Hz), 2.83 (t, 4H, ^3J = 8.1 Hz), 1.60-1.73 (m, 4H), 1.49-1.57 (m, 4H), 1.02 (t, 3H, ^3J = 7.3 Hz) ppm. **^{19}F NMR:** 282 MHz, 298 K, $CDCl_3$, δ = -72.5 ppm. **^{13}C NMR:** 75 MHz, 298 K, $CDCl_3$, δ = 183.0, 151.8, 134.9, 134.8, 132.3, 131.0, 128.4, 127.2, 126.3, 125.6, 124.6, 123.9, 123.0, 116.7, 30.6, 25.3, 23.2, 13.9 ppm. **APCI-MS:** *m/z* for $[C_{36}H_{27}S_2F_6O_8]^+$ calc.: 765.1046, found: 765.1090. **IR (ATR):** $\tilde{\nu}$ = 2960 (w), 2933 (w), 2870 (w), 1637 (s), 1583 (m), 1562 (m), 1387 (m), 1285 (w), 1216 (vs), 1134 (s), 1074 (m), 1029 (m), 1002 (w), 904 (w), 853 (s), 807 (m), 765 (m), 674 (w), 635 (w) cm^{-1}. **m.p.** = 183-185 °C

4 Summary

This work addresses two main topics concerning the synthesis and characterization of novel polyaromatic hydrocarbon (PAH) structures. Studies dealing with fundamental research on reductively synthesized and systematically functionalized (diaza-)ropyrenes in solution are presented, as well as research on the surface synthesis of novel porous nanographene structures from organic precursor molecules optimized for this purpose. For the second topic, the design of precursor molecules and their synthesis is investigated within this work, while the surface chemistry is performed in collaboration with the surface science groups of Prof. Dr. Gottfried (physical chemistry, Marburg), Prof. Dr. Schirmeisen (physics, Giessen) and the Forschungszentrum Jülich.

In the first part of this work, a new synthetic method was presented to prepare higher homologues of pyrene which are fourfold functionalized. In the first step, various (oligo-)naphthyls were prepared via iterative Suzuki-Miyaura couplings, which were converted to dihydroxyropyrene quinones via oxidative cyclodehydrogenations utilizing CsOH on air. These were converted to soluble tetrasiloxyropyrenes (precisely pyrene (n=1) to quarterropyrene (n=4)) using zinc in combination with trialkylsilyl chlorides (see Figure 4.1).

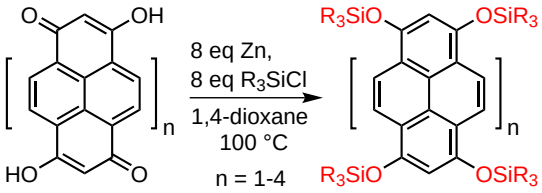

Fig. 4.1 Reductive silylation of ropyrenes with Zn as reducing agent (R = Me, *i*Pr).

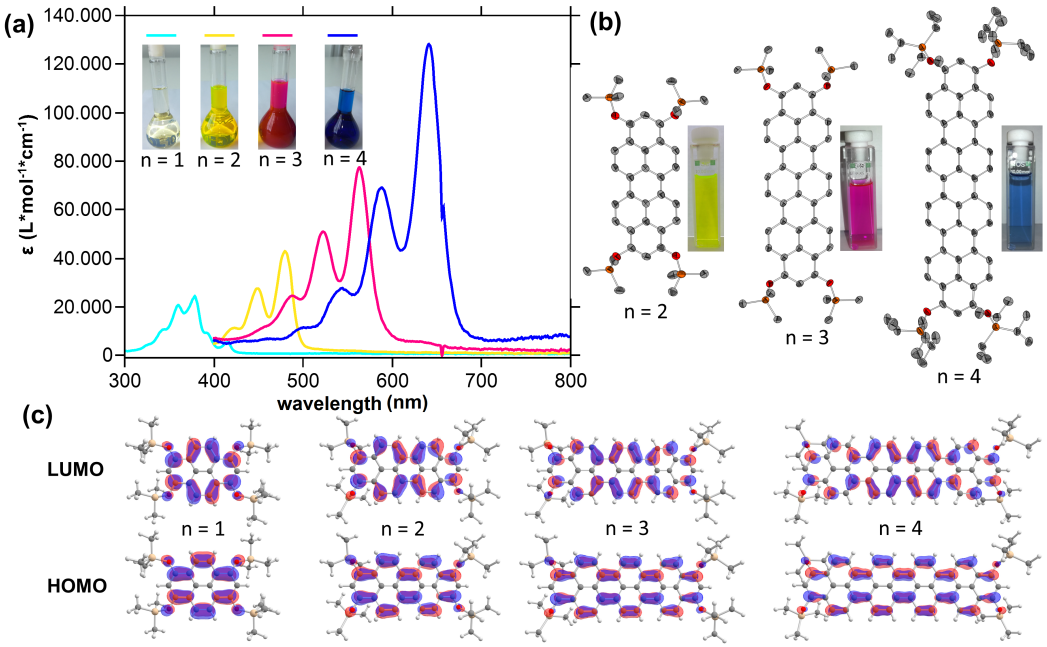

Fig. 4.2 Characterization of *O*-silylated ropyrenes (a) in solution by UV-Vis spectrometry; (b) in solid state by crystallography; and (c) *in silico* by DFT calculations.

In combination with sterically demanding triisopropylsilyl groups, the corresponding ropyrenes were found to be air stable. The following properties were modified as a function of increasing naphthyl groups from pyrene to quarterropyrene (see Figure 4.2):

- Increase in absorption maximum (UV-Vis) and emission maximum (PL) by 85 nm per additional naphthyl unit with linearly increasing extinction coefficients (ϵ) and band broadening.
- Decrease of optical and also electrochemical band gap (HOMO-LUMO gap).
- Lower oxidation potentials and higher reduction potentials.
- Increasing HOMO, decreasing LUMO (both experimentally (UV-Vis/PL, CV) and DFT-calculated).
- Increasing tendency to autoxidation in air to the detected radical cation.

A good predictability of the optoelectronical properties with the increase of the system size can be explained by the modular structure of the involved calculated KOHN-SHAM frontier orbitals as shown in figure 4.2 (c).

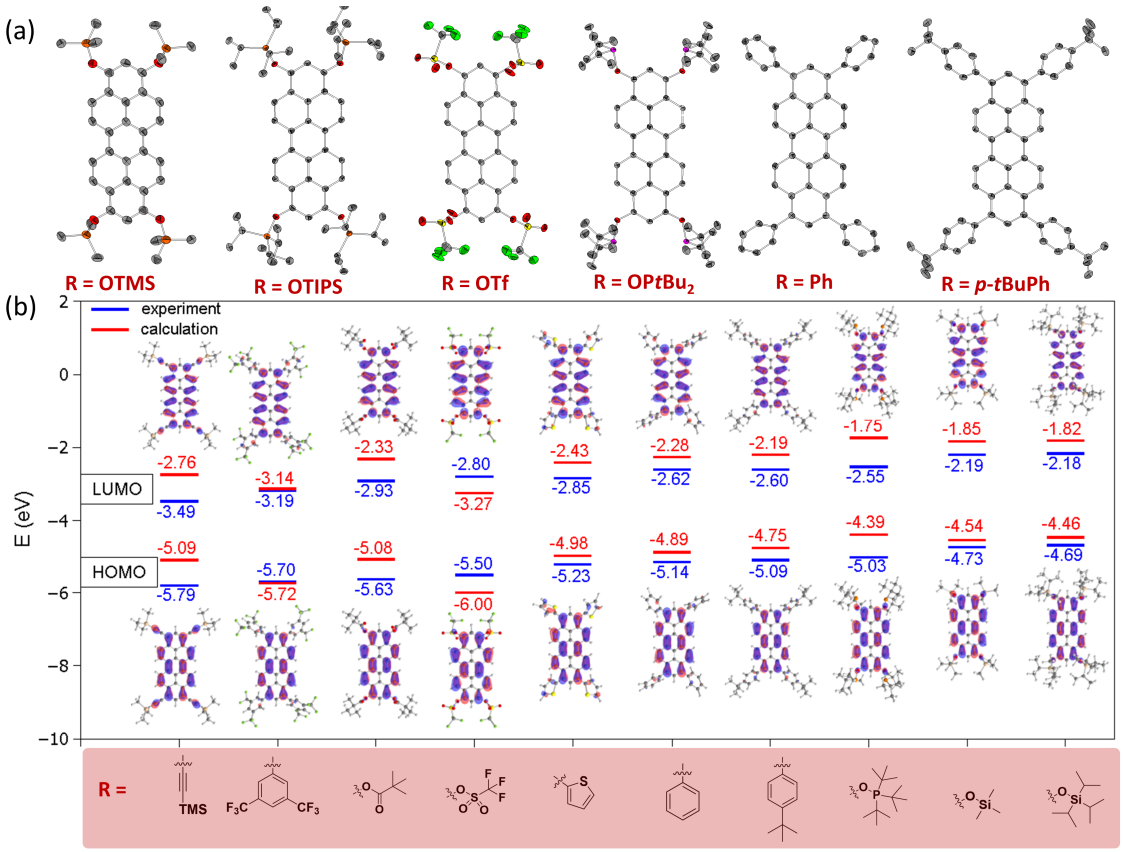

Fig. 4.3 (a) X-ray crystal structures of the different peropyrenes; (b) experimentally and theoretically calculated fine-tuned frontier orbital energies and DFT calculated KOHN-SHAM orbitals.

In the next step, the examplary class of peropyrenes (n=2) was used to investigate which alternative functionalizations in 1,3,8,10-position to silyl ethers or based on them are possible. Reductive functionalizations could be achieved by use of Zn resp. *n*-BuLi. Thereby, pivaloyl, triflyl or phosphinite groups could be introduced. The tetrapivaloate was successfully converted to a tetraphenyl derivative via Ni-catalyzed SUZUKI-MIYAURA cross-coupling. The tetratriflate showed improved reactivity and functional group tolerance in the SUZUKI-MIYAURA cross-coupling, even if trifluoromethylated phenyls and thienyl-substituted boronic acids were used. Using SONOGASHIRA cross-coupling conditions, four trimethylsilylethynyl groups were successfully attached.
The different residues provided various crystal structure packing motifs, which is valuable for an potential application in semiconductor devices. Derivatization made fine tuning of the frontier orbital energies precisely possible (Figure 4.3), which was also consistent to and predictable by DFT calculations. Thus, the HOMO energies could be experimentally varied from -5.79 eV to -4.89 eV and the HOMO-LUMO optical energy gaps modified in the range between 2.35 eV and 2.70 eV, just by variation of different functionalities.
In addition to peropyrenes and their higher homologues, other oxidized precursor molecules are also amenable to reductive functionalization approaches. Using the example of naphthalene diimide (NTCDI), it was shown that analogous functionalizations to peropyrenes are possible. In addition to a functionalization already described by MIYAKE *et al.*, who published the reductive pivaloation of NTCDI and SUZUKI-MIYAURA cross-couplings of the corresponding diazapyrene tetrapivaloate, a route for reductive silylations of NTCDI with zink as reducing agent was established in the course of this work. Furthermore, using potassium graphite (KC_8) and subsequently trapping the intermediately formed tetrapotassium salt with Tf_2O in DME, it was possible to prepare a diazapyrene tetratriflate from NTCDI in a one-pot procedure on a 3 gram scale. This compound could subsequently be reacted in a nucleophilic substitution with piperidine and was shown to be very reactive in SONOGASHIRA reactions (Scheme 4.1) in contrast to pivaloates.

Since the alkyne triple bond is in conjugation with the diazapyrene backbone, an effective way to vary the (opto)electronic properties could be achieved via alkynylation. For example, the *tert*-butylphenylacetyl derivative showed an absorption maximum of 490 nm, which is a bathochromic shift of over 100 nm compared to the electron-deficient tetratriflate. Using two silyl ethers and an alkyne, molecular and lattice structures were investigated by XRD analysis (Scheme 4.1).
In addition to NTCDI, various reductive functionalization reactions were also applied to the two keto groups of the commercially available dye violanthrone 79. For example, three different violanthrenes with additional trimethylsilyl groups, pivaloyl groups and methoxy groups were successfully prepared, which showed excellent solubility even in very nonpolar solvents such as *n*-hexane.

Furthermore, the tetra-trimethylsilylacetyl-substituted (diaza-)pyrenes and (diaza-)peropyrenes were successfully converted into Co-rich PAH complexes with four tetrahedral $[C_2Co_2(CO)_6]$-units via stoichiometric complexation reaction with $[Co_2(CO)_8]$. The air- and water-stable clus-

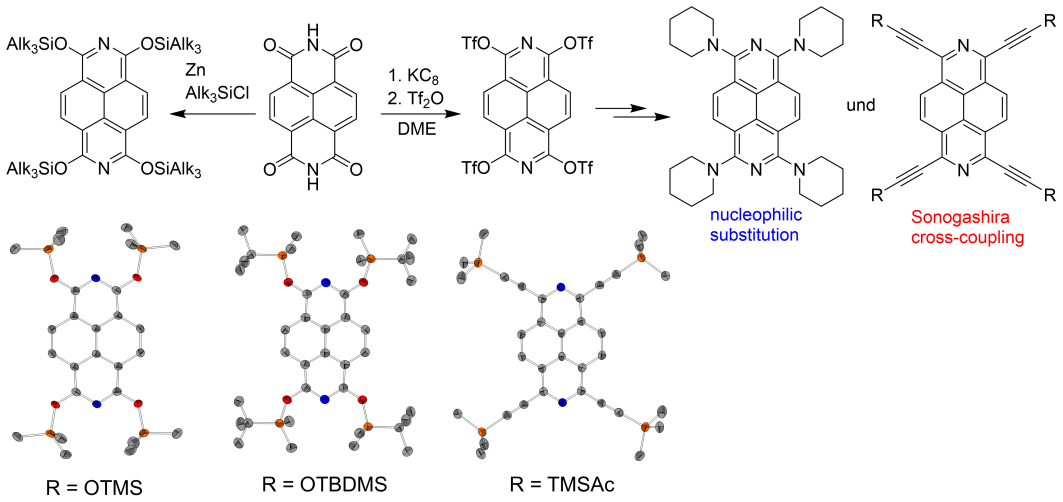

Scheme 4.1 Reductive *O*-triflination of NTCDI and conversion to alkynes or nucleophilic substitution with piperidine and X-ray crystal structures of two silyl ethers and a tetraalkyne.

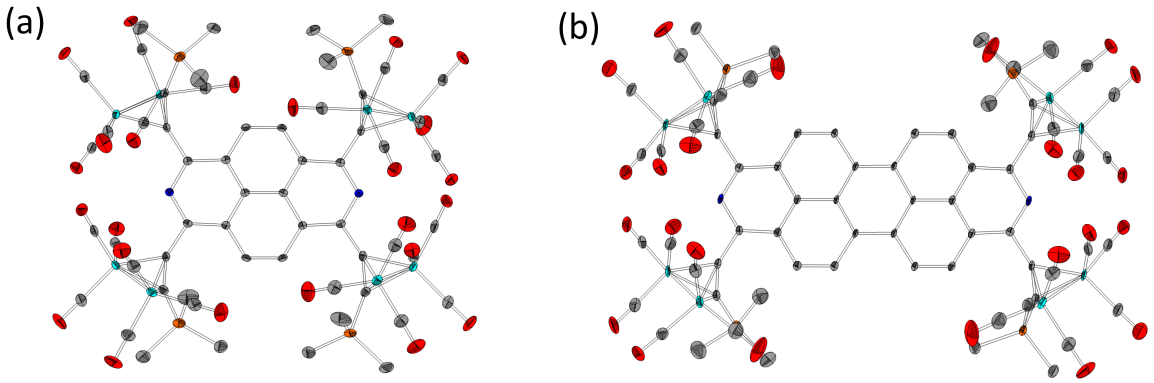

Fig. 4.4 X-ray crystal structures of Co-complexes with (a) diazapyrene backbone and (b) diazaperopyrene backbone.

ter complexes of the diaza derivatives could be characterized by X-ray crystallography (Figure 4.4). All four complexes were pyrolyzed in a vacuum sealed quartz tube at 850 °C to investigate the (N-doped) carbon nanomaterials formed. The pyrolysis products were characterized by elemental analysis, SEM and TEM. It was found that all four complexes gave different pyrolysis products due to their varying C/Co content or possible N-doping: In the case of the peropyrene-based complex, carbon nanotubes could be detected in good yield and quality, but in the case of the pyrene-based complex (lower C content), only nuclei of them could be detected as spherical, strongly intergrown nanoparticles. Nanotubes could not be detected in either of the two diaza analogs, only dendridic nanoparticles with large surface area and incorporated nitrogen.

In the second part of this work, various forms of porous (nano)graphene structures on coinage metal surfaces were realized in cooperation with other research groups. The precursors were prepared in solution in multistep syntheses and characterized by means of X-ray crystal structure analysis, as well as other methods.
The control over the selectivity of the respective surface reaction products in the step of the Ullmann-coupling could be controlled by the interaction strength of the surface with the aromatic system of the precursor in addition to the geometry of the precursors.

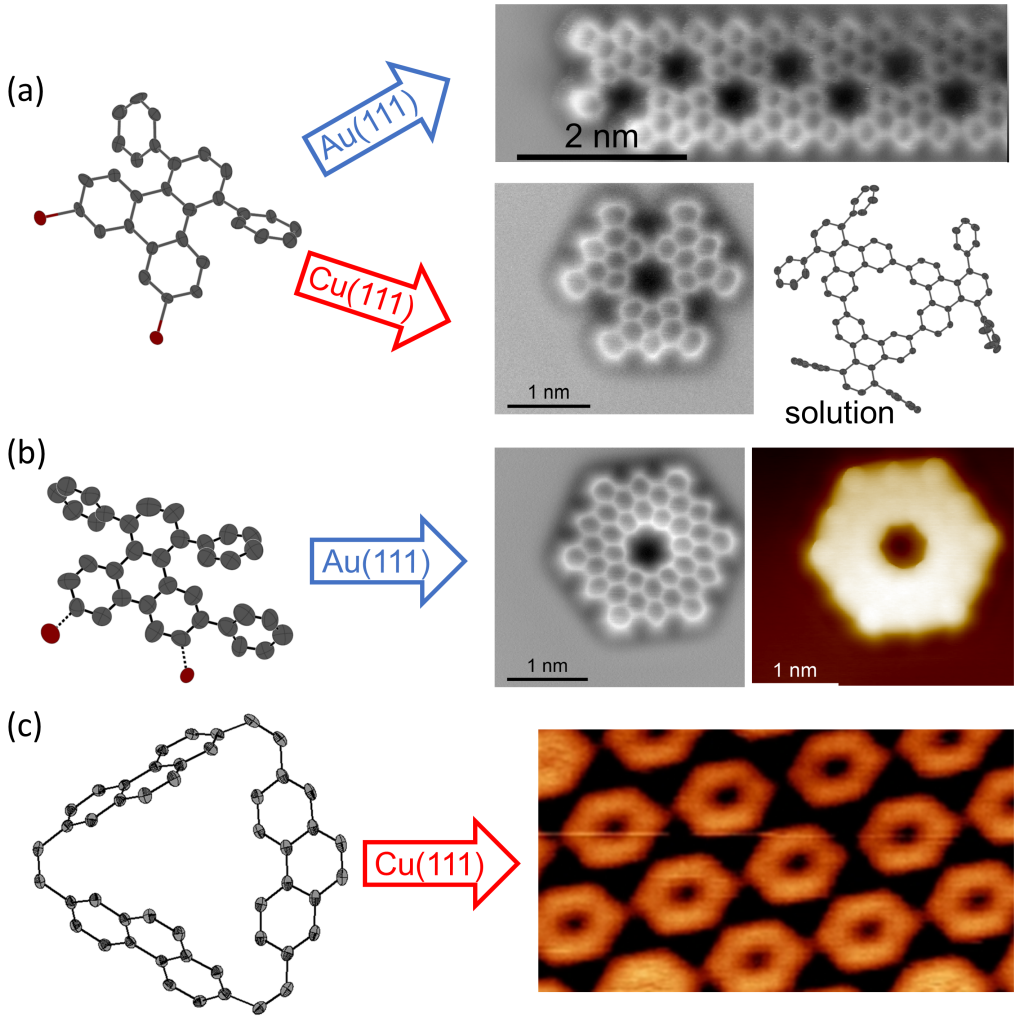

Fig. 4.5 (a) X-ray crystal structure of precursor DBDT and nc-AFM images of the reaction products on Au(111) and Cu(111), and crystal structure of the trimer synthesized from solution; (b) X-ray crystal structure of precursor DBTT and STM and nc-AFM image of reaction product C108 on Au(111); (c) X-ray crystal structure of cyclophane precursor and STM image of Kekulenes on Cu(111) after cyclodehydrogenation.

A C_2-symmetric triphenylene-based precursor DBDT (Figure 4.5 (a)) could be used on various single-crystalline M(111) surfaces (M = Cu, Ag and Au) to generate porous molecular nanographene structures via thermally induced dehalogenating Ullmann reactions followed by cyclodehydrogenations. In this context, different reaction products could be selectively syn-

thesized depending on the reactivity and catalytic activity of the surface and characterized by scanning tunneling microscopy (STM) and atomic force microscopy (nc-AFM): On the inert Au(111) surface, where the steric repulsion of phenyl rings of coupling precursors plays a minor role, the statistically more likely polymer (graphene nanoribbon) was formed (Fig. 4.5 (a)). On the Cu(111) surface showing stronger adsorption interaction, these steric repulsions were the reason for selective trimerization to minimize the repulsive interactions. Selectively, porous nanograph trimers were formed consistent with a macrocyclization experiment in solution via Yamamoto trimerization described in this context (Fig. 4.5 (a)).

A less symmetrical precursor molecule DBTT with an additionally attached phenyl group was also realized via a six-step synthesis route (4.5 (c)). The steric effect of the additional phenyl group prevented polymerization to a graphene nanoribbon at the precursor level, since an Ullmann reaction is only possible in a way that cyclic trimers are formed. Thus, a C_6-symmetric, planar and porous C108 nanographene were generated selectively on Au(111) and other surfaces after cyclodehydrogenation and detected by STM and nc-AFM by the surface science collaborations partners. The electronic properties were investigated by scanning tunneling spectroscopy (STS). It was shown that the pore contributes to the enlargement of the electronic band gap. The synthesis of C108 was also successfully reproduced and optimized using the larger precursor DBSP (Chapter 3.10, and Publication 8) via Ullmann dimerization and cyclodehydrogenation on the surface. All attempts to prepare C108 in solution based on precursors modified with solubilizing groups failed due to insufficient selectivity of the Yamamoto trimerization in solution or the presence of higher oligomers that could not be separated.

A third cyclophane-based precursor was synthesized for the synthesis of the simplest cycloarene representative, Kekulene. The highly twisted geometry of the precursor molecule (see XRD structure in Fig. 4.5 (c)) prevents planarization in solution via Scholl reaction, but however on the catalytically active and highly reactive Cu(111) surface, Kekulene could be synthesized in almost quantitative yield via selective sixfold intramolecular C-H activation (cyclodehydrogenation) and detected by STM. Angle-resolved photoelectron spectroscopy (ARPES) measurements showed that the aromaticity of Kekulene was consistent with the Clar sextet model. On Cu(110) surface, the same precursor molecule reacted selectively to isokekulene - an isomer of Kekulene with one inverted phenanthrene unit.

Further work on surface-assisted fabrication of porous nanographene structures based on Sierpiński fractal structures is currently underway in the Gottfried group. For this purpose, two different triple halogenated, non-C_2 symmetric precursors were prepared, which build fractal structures either via suitable assembly (triply brominated precursor) or hierarchical Ullmann reactions (doubly iodinated, brominated precursor). The challenge here is that control is only possible in the step of the organometallic intermediate in the Ullmann reaction, since the covalent C-C bond linkage is formed irreversible (described in Section 3.10).

5 Zusammenfassung

Diese Arbeit beschäftigt sich mit zwei Hauptthemen, die die Synthese und Charakterisierung neuartiger Polyaromatischer Kohlenwasserstoff (PAK)-Strukturen betreffen. Studien, die sich mit der Grundlagenforschung zu reduktiv synthetisierten und systematisch funktionalisierten (Diaza-)ropyrenen in Lösung befassen, werden ebenso vorgestellt wie Forschungsarbeiten zur Oberflächen-Synthese neuartiger poröser Nanographen-Strukturen aus für diesen Zweck optimierten organischen Vorläufermolekülen. Für das zweite Thema ist das Design von Vorläufermolekülen und deren Synthese eines der Forschungsthemen dieser Arbeit, während die Oberflächenreaktionen in Zusammenarbeit mit den Surface Science Gruppen von Prof. Dr. Gottfried (physikalische Chemie, Marburg), Prof. Dr. Schirmeisen (Physik, Gießen) und dem Forschungszentrum Jülich durchgeführt wurde.

Im ersten Teil der Arbeit wurde eine neue Synthesestrategie vorgestellt, um vierfach funktionalisierte höhere Homologe von Pyren darzustellen. Dabei wurden im ersten Schritt über iterative Suzuki-Miyaura-Kupplungen verschiedene (Oligo-)naphthyle hergestellt, welche über oxidative Cyclodehydrogenierungen CsOH-vermittelt an Luft zu Dihydroxyropyrenquinonen umgesetzt wurden. Diese wurden mit Zink in Kombination mit Trialkylsilylchloriden in lösliche Tetrasiloxyropyrene (explizit Pyren (n=1) bis Quarterropyren (n=4)) umgesetzt (siehe Abbildung 5.1).

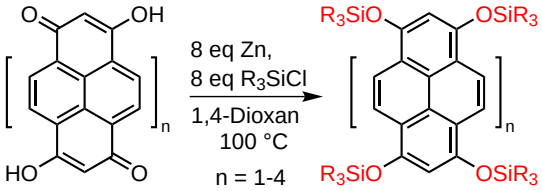

Fig. 5.1 Reduktive Silylierung von Ropyrenen mit Zn als Reduktionsmittel (R = Me, *i*Pr).

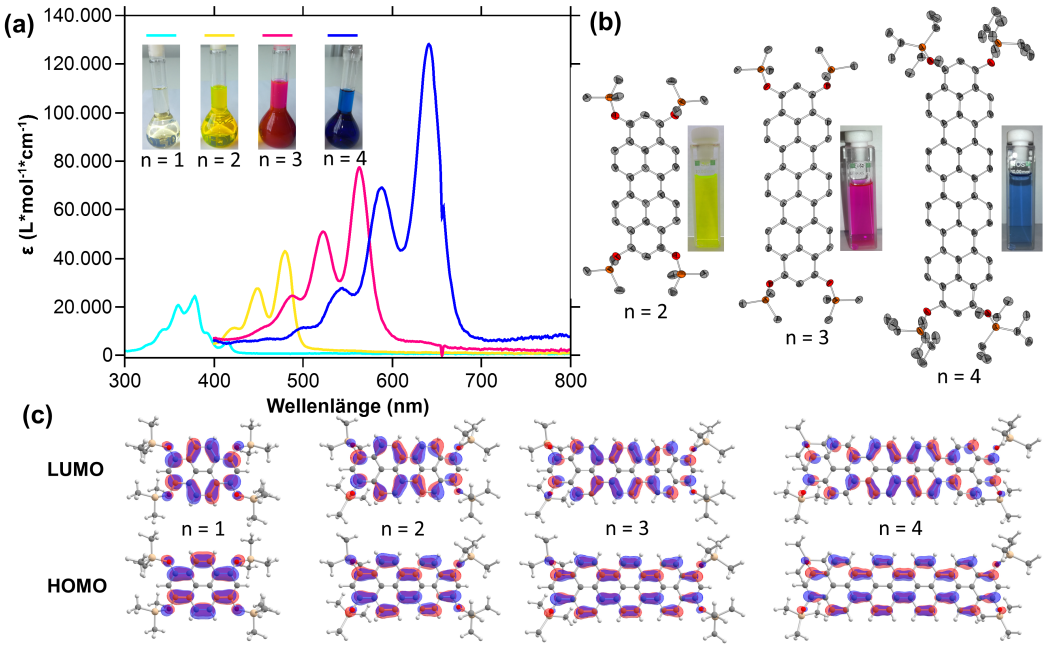

Fig. 5.2 Charakterisierung *O*-silylierter Ropyrene durch (a) UV-Vis Spektrometrie; (b) Kristallographie und (c) DFT-Rechnungen.

In Kombination mit sterisch anspruchsvollen Triisopropylsilylgruppen erwiesen sich die entsprechenden Ropyrene als luftstabil. Folgende Eigenschaften wurden in Abhängigkeit der zunehmender Anzahl an Naphthylgruppen von Pyren bis Quarterropyren modifiziert (Abbildung 5.2):

- Zunahme des Absorptionsmaximum (UV-Vis) und Emissionsmaximums (PL) um 85 nm pro hinzukommender Naphthyleinheit bei linear zunehmenden Extinktionskoeffizienten (ϵ) und Bandenverbreiterung.
- Abnahme der optischen und auch elektrochemischen Bandlücke (HOMO-LUMO Lücke).
- Niedriger liegende Oxidationspotentiale und höher liegende Reduktionspotentiale.
- Anhebung des HOMO, Absenkung des LUMO (sowohl experimentell (UV-Vis/PL, CV) wie auch DFT-berechnet).
- Zunehmende Tendenz zur Autoxidation an Luft zum nachgewiesenen Radikalkation.

Die gute Vorhersagbarkeit der optoelektronischen Eigenschaften mit der Vergrößerung des Systems kann mit einem modularen Aufbau der beteiligten berechneten Kohn-Sham Grenzorbitale begründet werden, wie in Abbildung 5.2 gezeigt.

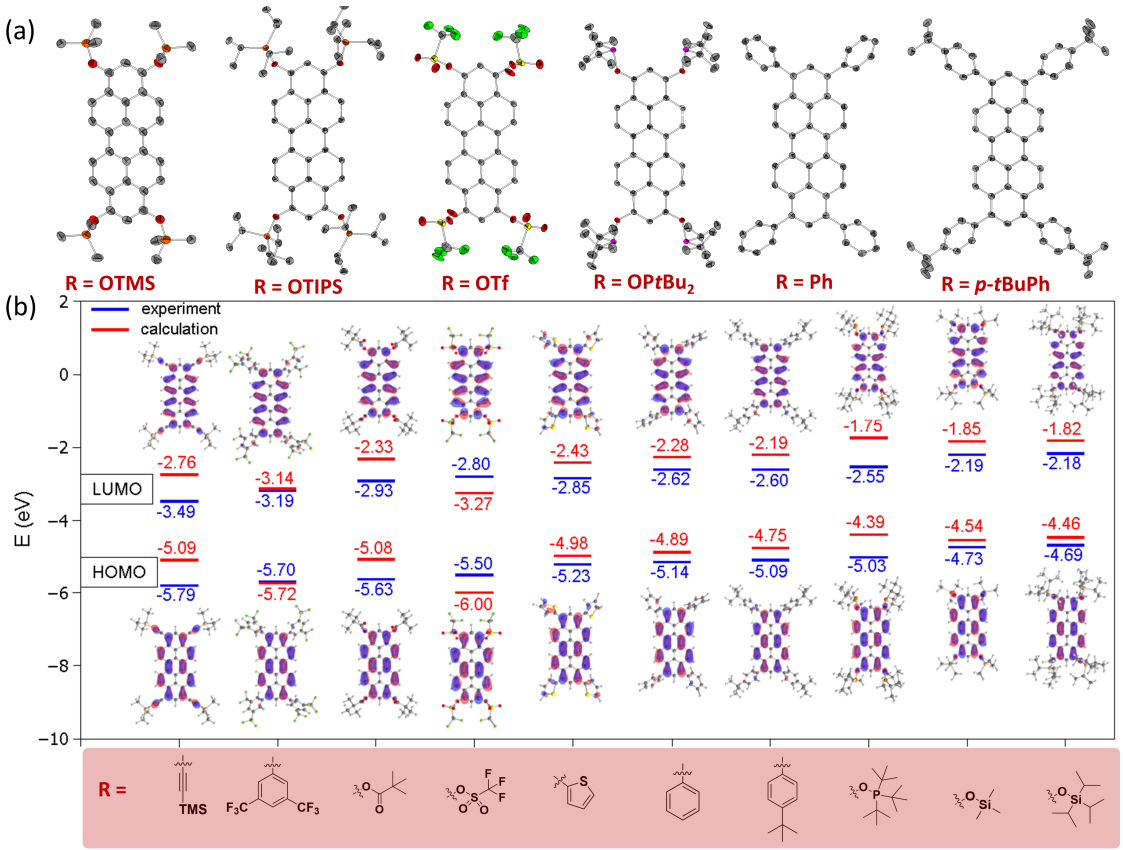

Fig. 5.3 (a) Röntgenkristallstrukturen der verschiedenen Peropyrene; (b) experimentelle und theoretisch berechnete Grenzorbitalenergien und DFT berechnete Kohn-Sham Orbitale.

Im nächsten Schritt wurde anhand der Beispielklasse der Peropyrene (n=2) untersucht, welche alternativen Funktionalisierungen in 1,3,8,10-Position basierend auf den Silylethern sind. So konnten reduktiv mittels Zn bzw. *n*-BuLi auch Pivaloyl-, Triflyl- oder Phosphinit-Gruppen eingeführt werden. Das Tetrapivaloat konnte erfolgreich mittels Ni-katalysierter Suzuki-Miyaura-Kreuzkupplung in ein Tetraphenyl-Derivat umgesetzt werden. Das Tetratriflat zeigte eine gegenüber den Pivaloaten verbesserte Reaktivität und funktionelle Gruppentoleranz in der Suzuki-Miyaura-Kreuzkupplung auch für fluorierte Aromaten bzw. Thienylreste. Mittels Sonogashira-Kreuzkupplung konnten erfolgreich vier Trimethylsilylethinyl Gruppen eingeführt werden.
Die unterschiedlichen Reste verursachten verschiedene Kristallstruktur-Packungsmotive, was wertvoll für den Einsatz in möglichen Halbleiterdevices ist. Die Derivatisierung machte desweiteren eine präzise Feineinstellung der Grenzorbitalenergien möglich (Abbildung 5.3), was ebenfalls mit DFT-Rechnungen im Einklang steht. So konnten die HOMO Energien experimentell von -5.79 eV bis -4.89 eV varriert werden und die optischen HOMO-LUMO Lücken zwischen 2.35 eV und 2.70 eV, allein durch Einführung verschiedene Funktionalitäten.

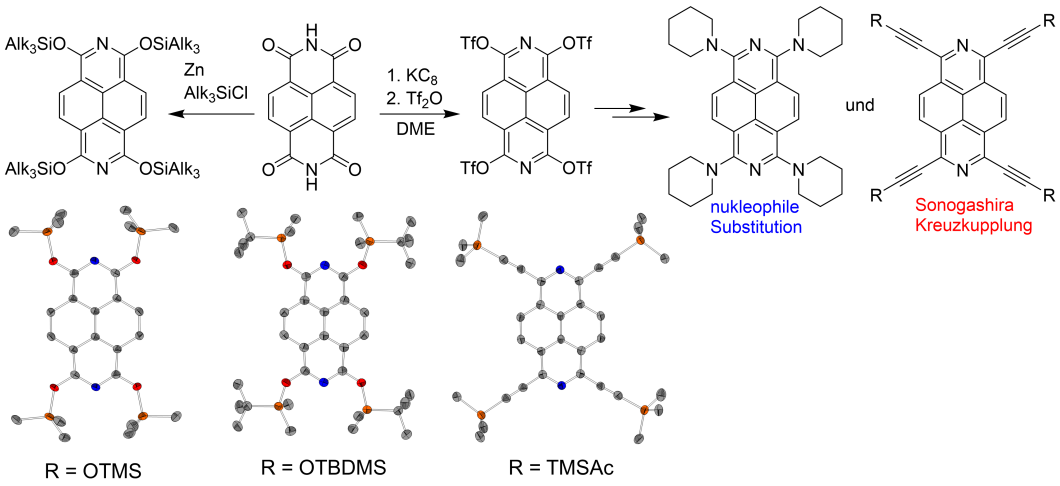

Scheme 5.1 Reduktive *O*-Triflierung von NTCDI und Umsetzung zu Alkinen bzw. nukleophile Substitution mit Piperidin und Röntgenkristallstrukturen zweier Silylether und eines Tetraalkins.

Neben Peropyrenen und ihren höheren Homologen sind auch weitere oxidativ generierte Vorläufermoleküle zugänglich für reduktive Funktionalisierungen. Am Beispiel von Naphthalin-Diimid (NTCDI) konnte gezeigt werden, dass auch hier analoge Derivatisierungen zu Peropyrenen möglich sind. Neben der bereits durch Miyake *et al.* publizierten reduktiven Pivaloierung von NTCDI und Suzuki-Miyaura-Kreuzkupplung des korrespondierenden Diazapyren Tetrapivaloats, konnte im Rahmen dieser Arbeit eine Route für reduktive Silylierungen von NTCDI mit Zink als Reduktionsmittel etabliert werden. Desweiteren war es möglich, unter Verwendung von Kaliumgraphit (KC_8) und anschließendem Abfangen des intermediär entstehenden Tetrakalium Salzes mit Tf_2O in DME aus NTCDI in einem Eintopfverfahren im 3 Gramm-Maßstab ein Diazapyren-Tetratriflat herzustellen. Dieses konnte anschließend in einer nukleophilen Substitution mit Piperidin umgesetzt werden und zeigte sich als sehr reaktiv in Sonogashira-Reaktionen (Schema 5.1), welche nicht auf Pivaloate anwendbar sind.

Da die Alkin-Dreifachbindung in Konjugation mit dem Diazapyren Rückgrat steht, konnte über die Alkinylierung ein effektiver Weg zur Variation der (opto-)elektronischen Eigenschaften erschlossen werden. So zeigte das *tert*-Butylphenylethinyl-Derivat ein Absorptionsmaximum von 490 nm, was eine bathochrome Verschiebung von über 100 nm im Vergleich zum elektronenarmen Tetratriflat bedeutet. Anhand von zwei Silylethern und einem Tetraalkin wurden Molekülstrukturen im Einkristall untersucht (Schema 5.1).
Neben NTCDI wurden verschiedene reduktive Funktionalisierungsreaktionen auch auf die beiden Ketogruppen des kommerziell erhältlichen Farbstoffs Violanthron 79 angewendet. So konnten beispielhaft drei verschiedene Violanthrene mit zusätzlichen Trimethylsilylgruppen, Pivaloylgruppen und Methoxygruppen erfolgreich dargestellt werden, welche eine hervorragende Löslichkeit auch in sehr unpolaren Lösemitteln wie *n*-Hexan zeigten.

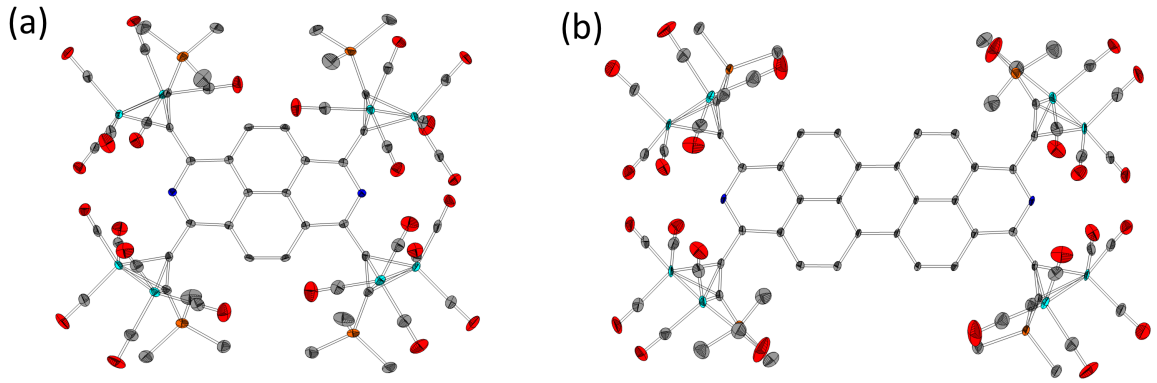

Fig. 5.4 Röntgenkristallstrukturen von Kobaltcluster-Verbindungen mit (a) Diazapyren-Grundgerüst und (b) Diazaperopyren-Grundgerüst.

Die dargestellten tetra-trimethylsilylethinyl-substituierten (Diaza-)pyrene und (Diaza-)peropyrene konnten desweiteren erfolgreich mittels stöchiometrischer Reaktion mit $[Co_2(CO)_8]$ über Komplexierung in Co-reiche PAK-Komplexe mit je vier tetraedrischen $[C_2Co_2(CO)_6]$-Einheiten überführt werden. Die luft-und wasserstabilen Komplexe der Diaza-Derivate konnten röntgenkristallographisch charakterisiert werden (Abbildung 5.4). Alle vier Komplexe wurden zur Analyse ihrer durch Pyrolyse zugänglichen (N-dotierten) Kohlenstoff Nanopartikel in unter Vakuum abgeschmolzenen Quartzglasampullen bei 850 °C pyrolysiert. Die Pyrolyseprodukte wurden mittels Elementaranalyse, SEM und TEM charakterisiert. Dabei zeigte sich, dass alle vier verschiedenen Komplexe aufgrund ihres variierenden C/Co-Gehaltes oder zum Teil beobachteter N-Dotierung unterschiedliche Pyrolyseprodukte lieferten: Im Fall des Peropyren-basierten Komplexes konnten Kohlenstoff-Nanoröhren in guter Ausbeute und Qualität nachgewiesen werden, im Fall des Pyren-basierten Komplexes (geringerer C-Anteil) jedoch nur Keime davon als sphärische, stark verwachsene Nanopartikel. Bei keinem der beiden Diaza-Analoga wurden Nanoröhren nachgewiesen, statt dessen dendritische Nanopartikel mit großer Oberfläche und eingebautem Stickstoff.

Im zweiten Teil der Arbeit wurden in Kooperation mit anderen Arbeitsgruppen verschiedene Formen poröser (Nano-)Graphen-Strukturen auf Münzmetalloberflächen dargestellt. Die Präkursoren konnten in mehrstufigen Synthesen in Lösung hergestellt und unter anderem mittels Röntgenkristallstrukturanalyse charakterisiert werden.
Die Kontrolle über die Selektivität der Ullmann-Kupplungsprodukte konnte neben der Geometrie der Präkursoren über die Interaktionsstärke der Oberfläche mit dem aromatischen System des Präkursoren gesteuert werden.

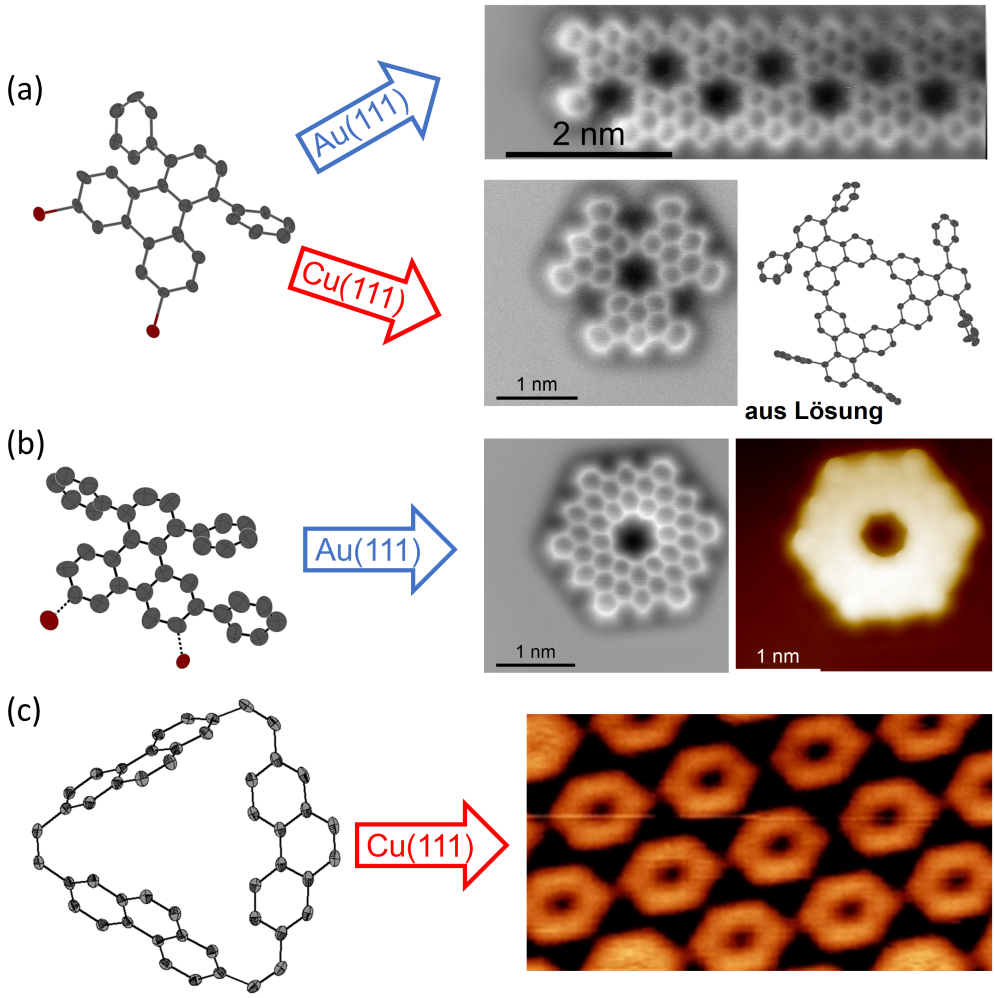

Fig. 5.5 (a) Röntgenkristallstruktur von Präkursor DBDT sowie nc-AFM Aufnahmen von den Reaktionsprodukten auf Au(111) und Cu(111), sowie Kristallstruktur des Trimers aus Lösung synthetisiert; (b) Röntgenkristallstruktur von Präkursor DBTT und STM sowie nc-AFM Aufnahme von Reaktionsprodukt C108 auf Au(111); (c) Röntgenkristallstruktur des Cyclophan Präkursors sowie STM Aufnahme von Kekulen auf Cu(111) nach Cyclodehydrogenierung.

Der C_2-symmetrische Präkursor DBDT auf Triphenylen Basis (Abbildung 5.5 (a)) konnte auf verschiedenen einkristallinen Edelmetalloberflächen dazu genutzt werden, um poröse molekulare Nanographen Strukturen über dehalogenierende Ullmann-Reaktionen gefolgt von Cyclodehydrogenierungen zu erzeugen. Dabei konnten in Abhängigkeit der Reaktivität der Oberfläche verschiedene Reaktionsprodukte selektiv synthetisiert und mittels Rastertunnelmikroskopie (STM)

und Rasterkraftmikroskopie (nc-AFM) durch Surface Science Kooperationspartner charakterisiert werden: auf der inerten Au(111) Oberfläche, auf der sterische Repulsion der Phenylringer kuppelnder Präkursoren eine untergeordnete Rolle spielen wurde das statistisch wahrscheinlichere Polymer (Graphennanoband) gebildet (Abb. 5.5 (a)). Auf der stärkere Adsorptionswechselwirkung zeigenden Cu(111) Oberfläche waren diese sterischen Repulsionen der Grund für eine selektive Trimerisierung zur Minimierung der repulsiven Wechselwirkungen. Selektiv wurden poröse Nanographen-Trimere gebildet, die im Einklang mit einem in dieser Arbeit durchgeführten Makrocyklisierungsexperiment in Lösung über Yamamoto-Trimerisierung stehen.
Das unsymmetrischere Präkursor Molekül DBTT (basierend auf dem in Abbildung 5.5 (a) gezeigten) mit zusätzlicher Phenylgruppe wurde ebenfalls über eine sechsstufige Syntheseroute dargestellt (siehe XRD-Struktur Abb. 5.5 (b)). Durch die sterische Wirkung der zusätzlichen Phenylgruppe konnte auf Präkursorebene eine Polymerisierung zu einem Graphen-Nanoband verhindert werden, da eine Ullmann-Reaktion nur in der Form möglich ist, dass cyclische Trimere gebildet werden. So konnte auf Au(111) und anderen Oberflächen selektiv nach erfolgter Cyclodehydrogenierung ein C_6-symmetrisches, planares und poröses C108-Nanographen erzeugt und mittels STM und nc-AFM durch die kooperierenden Surface Science Gruppen nachgewiesen werden. Die elektronischen Eigenschaften konnten mittels Rastertunnelspektroskopie (STS) untersucht werden. Dabei zeigte sich, dass die Pore zur Vergrößerung der elektronischen Bandlücke beiträgt. Die Synthese von C108 konnte auch über einen größeren Präkursor DBSP (Kapitel 3.10, weitere Arbeiten und Publikation 8) mittels Ullmann-Dimerisierung und Cyclodehydrogenierung auf der Oberfläche erfolgreich nachvollzogen werden. Alle Versuche, C108 in Lösung auf Grundlage löslichkeitsmodifizierter Prekursoren herzustellen scheiterten an einer nicht ausreichenden Selektivität der Yamamoto-Trimerisierung in Lösung bzw. dem Vorhandensein höherer, nicht abtrennbarer Oligomere.

Ein dritter Präkursor auf Cyclophan-Basis wurde zur Synthese des einfachsten Cycloaren-Vertreters Kekulen synthetisiert. Die stark verdrillte Geometrie des Präkursor Moleküls (siehe XRD-Struktur in Abb. 5.5 (c)) verhindert zwar eine Planarisierung in Lösung über die Scholl-Reaktion, aber auf der katalytisch aktiven und sehr reaktiven Cu(111)-Oberfläche konnte Kekulen in fast quantitativer Ausbeute über eine selektive, sechsfache intramolekulare C-H-Aktivierung (Cyclodehydrogenierung) dargestellt und mittels STM nachgewiesen werden. Winkelaufgelöste Photoelektronenspektroskopie (ARPES)-Messungen zeigten, dass die Aromatizität von Kekulen mit dem Clar-Sextett Modell übereinstimmt. Interessanterweise zeigten Cyclodehydrogenierungsexperimente auf Cu(110) die selektive Bildung eines Kekulen-Isomers mit einer nach innen rotierten Phenanthren-Einheit
Weitere Arbeiten zur oberflächengestützten Herstellung poröser Nanographenstrukturen auf Basis von Sierpiński Fraktal Strukturen sind gegenwärtig in der Arbeitsgruppe Gottfried in Arbeit. Hierzu wurden zwei verschiedene dreifach halogenierte, nicht C_2-symmetrische Präkursoren hergestellt, welche entweder über geeignete Assemblierung (dreifach bromierter Präkursor) oder hierarchische Ullmann-Reaktionen (zweifach iodierter, bromierter Präkursor) fraktale Strukturen aufbauen. Die Herausforderung hierbei liegt darin, dass eine Kontrolle nur während der organometallischen Zwischenstufe bei der Ullmann-Reaktion möglich ist, da die kovalente C-C-Bindungsknüpfung irreversibel erfolgt (beschrieben in Kapitel 3.10).

6 Bibliography

[1] A. K. Geim, K. S. Novoselov, *Nat. Mater.* **2007**, *6*, 183–191.

[2] K. S. Novoselov, A. K. Geim, S. V. Morozov, D. Jiang, Y. Zhang, S. V. Dubonos, I. V. Grigorieva, A. A. Firsov, *Science* **2004**, *306*, 666–669.

[3] L. Gao, J. R. Guest, N. P. Guisinger, *Nano Lett.* **2010**, *10*, 3512–3516.

[4] A. Basagni, F. Sedona, C. A. Pignedoli, M. Cattelan, L. Nicolas, M. Casarin, M. Sambi, *J. Am. Chem. Soc.* **2015**, *137*, 1802–1808.

[5] P. W. Sutter, J.-I. Flege, E. A. Sutter, *Nat. Mater.* **2008**, *7*, 406–411.

[6] K. Novoselov, *Nat. Mater.* **2007**, *6*, 720–721.

[7] J. Millman, C. C. Halkias, *Electronic devices and circuits*, McGraw-Hill, Auckland and Singapore, International student ed., **1976**.

[8] J. E. Lilienfeld, *U. S. Patent No. 1745175* **1930**.

[9] P. Horowitz, W. Hill, *The art of electronics*, Cambridge Univ. Press, Cambridge, 2nd ed., **1989**.

[10] X. Wang, H. Dai, *Nat. Chem.* **2010**, *2*, 661–665.

[11] M. Y. Han, B. Ozyilmaz, Y. Zhang, P. Kim, *Phys. Rev. Lett.* **2007**, *98*, 206805.

[12] Z. Chen, Y.-M. Lin, M. J. Rooks, P. Avouris, *Physica E* **2007**, *40*, 228–232.

[13] D. V. Kosynkin, A. L. Higginbotham, A. Sinitskii, J. R. Lomeda, A. Dimiev, B. K. Price, J. M. Tour, *Nature* **2009**, *458*, 872–876.

[14] K. Nakada, M. Fujita, G. Dresselhaus, M. S. Dresselhaus, *Phys. Rev. B* **1996**, *54*, 17954–17961.

[15] Y.-W. Son, M. L. Cohen, S. G. Louie, *Phys. Rev. Lett.* **2006**, *97*, 216803.

[16] C.-A. Palma, P. Samorì, *Nat. Chem.* **2011**, *3*, 431–436.

[17] J. Cai, P. Ruffieux, R. Jaafar, M. Bieri, T. Braun, S. Blankenburg, M. Muoth, A. P. Seitsonen, M. Saleh, X. Feng, K. Müllen, R. Fasel, *Nature* **2010**, *466*, 470–473.

[18] L. T. Canham, *Appl. Phys. Lett.* **1990**, *57*, 1046–1048.

[19] G. Vasseur, Y. Fagot-Revurat, M. Sicot, B. Kierren, L. Moreau, D. Malterre, L. Cardenas, G. Galeotti, J. Lipton-Duffin, F. Rosei, M. Di Giovannantonio, G. Contini, P. Le Fèvre, F. Bertran, L. Liang, V. Meunier, D. F. Perepichka, *Nat. Commun.* **2016**, *7*, 10235.

[20] H. Zhang, H. Lin, K. Sun, L. Chen, Y. Zagranyarski, N. Aghdassi, S. Duhm, Q. Li, D. Zhong, Y. Li, K. Müllen, H. Fuchs, L. Chi, *J. Am. Chem. Soc.* **2015**, *137*, 4022–4025.

[21] L. Talirz, H. Söde, T. Dumslaff, S. Wang, J. R. Sanchez-Valencia, J. Liu, P. Shinde, C. A. Pignedoli, L. Liang, V. Meunier, N. C. Plumb, M. Shi, X. Feng, A. Narita, K. Müllen, R. Fasel, P. Ruffieux, *ACS Nano* **2017**, *11*, 1380–1388.

[22] O. Deniz, C. Sánchez-Sánchez, T. Dumslaff, X. Feng, A. Narita, K. Müllen, N. Kharche, V. Meunier, R. Fasel, P. Ruffieux, *Nano Lett.* **2017**, *17*, 2197–2203.

[23] Y.-C. Chen, D. G. de Oteyza, Z. Pedramrazi, C. Chen, F. R. Fischer, M. F. Crommie, *ACS Nano* **2013**, *7*, 6123–6128.

[24] H. Huang, D. Wei, J. Sun, S. L. Wong, Y. P. Feng, A. H. C. Neto, A. T. S. Wee, *Sci. Rep.* **2012**, *2*, 983.

[25] J. Cai, C. A. Pignedoli, L. Talirz, P. Ruffieux, H. Söde, L. Liang, V. Meunier, R. Berger, R. Li, X. Feng, K. Müllen, R. Fasel, *Nat. Nanotech.* **2014**, *9*, 896–900.

[26] E. Carbonell-Sanromà, J. Hieulle, M. Vilas-Varela, P. Brandimarte, M. Iraola, A. Barragán, J. Li, M. Abadia, M. Corso, D. Sánchez-Portal, D. Peña, J. I. Pascual, *ACS Nano* **2017**, *11*, 7355–7361.

[27] S. Kawai, S. Saito, S. Osumi, S. Yamaguchi, A. S. Foster, P. Spijker, E. Meyer, *Nat. Commun.* **2015**, *6*, 8098.

[28] M. Liu, M. Liu, L. She, Z. Zha, J. Pan, S. Li, T. Li, Y. He, Z. Cai, J. Wang, Y. Zheng, X. Qiu, D. Zhong, *Nat. Commun.* **2017**, *8*, 14924.

[29] J. Liu, B.-W. Li, Y.-Z. Tan, A. Giannakopoulos, C. Sanchez-Sanchez, D. Beljonne, P. Ruffieux, R. Fasel, X. Feng, K. Müllen, *J. Am. Chem. Soc.* **2015**, *137*, 6097–6103.

[30] H. Sakaguchi, S. Song, T. Kojima, T. Nakae, *Nat. Chem.* **2017**, *9*, 57–63.

[31] M. Shekhirev, P. Zahl, A. Sinitskii, *ACS Nano* **2018**, *12*, 8662–8669.

[32] C. Moreno, M. Vilas-Varela, B. Kretz, A. Garcia-Lekue, M. V. Costache, M. Paradinas, M. Panighel, G. Ceballos, S. O. Valenzuela, D. Peña, A. Mugarza, *Science* **2018**, *360*, 199–203.

[33] P. Ruffieux, S. Wang, B. Yang, C. Sánchez-Sánchez, J. Liu, T. Dienel, L. Talirz, P. Shinde, C. A. Pignedoli, D. Passerone, T. Dumslaff, X. Feng, K. Müllen, R. Fasel, *Nature* **2016**, *531*, 489–492.

[34] W. Han, R. K. Kawakami, M. Gmitra, J. Fabian, *Nat. Nanotech.* **2014**, *9*, 794–807.

[35] P. Ruffieux, S. Wang, B. Yang, C. Sánchez-Sánchez, J. Liu, T. Dienel, L. Talirz, P. Shinde, C. A. Pignedoli, D. Passerone, T. Dumslaff, X. Feng, K. Müllen, R. Fasel, *Nature* **2016**, *531*, 489–492.

[36] X. Liang, Y.-S. Jung, S. Wu, A. Ismach, D. L. Olynick, S. Cabrini, J. Bokor, *Nano Lett.* **2010**, *10*, 2454–2460.

[37] J. Bai, X. Zhong, S. Jiang, Y. Huang, X. Duan, *Nat. Nanotech.* **2010**, *5*, 190–194.

[38] B. M. Venkatesan, R. Bashir, *Nat. Nanotech.* **2011**, *6*, 615–624.

[39] S. Garaj, W. Hubbard, A. Reina, J. Kong, D. Branton, J. A. Golovchenko, *Nature* **2010**, *467*, 190–193.

[40] K. Sint, B. Wang, P. Král, *J. Am. Chem. Soc.* **2008**, *130*, 16448–16449.

[41] R. C. Rollings, A. T. Kuan, J. A. Golovchenko, *Nat. Commun.* **2016**, *7*, 11408.

[42] D.-e. Jiang, V. R. Cooper, S. Dai, *Nano Lett.* **2009**, *9*, 4019–4024.

[43] S. Blankenburg, M. Bieri, R. Fasel, K. Müllen, C. A. Pignedoli, D. Passerone, *Small* **2010**, *6*, 2266–2271.

[44] S. P. Koenig, L. Wang, J. Pellegrino, J. S. Bunch, *Nat. Nanotech.* **2012**, *7*, 728–732.

[45] D. Cohen-Tanugi, J. C. Grossman, *Nano Lett.* **2012**, *12*, 3602–3608.

[46] S. P. Surwade, S. N. Smirnov, I. V. Vlassiouk, R. R. Unocic, G. M. Veith, S. Dai, S. M. Mahurin, *Nat. Nanotech.* **2015**, *10*, 459–464.

[47] K. Xu, J. I. Urgel, K. Eimre, M. Di Giovannantonio, A. Keerthi, H. Komber, S. Wang, A. Narita, R. Berger, P. Ruffieux, C. A. Pignedoli, J. Liu, K. Müllen, R. Fasel, X. Feng, *J. Am. Chem. Soc.* **2019**, *141*, 7726–7730.

[48] C. Fan, B. Sun, Z. Li, J. Shi, T. Lin, J. Fan, Z. Shi, *Angew. Chem. Int. Ed.* **2021**, *60*, 13896–13899.

[49] A. Gourdon, *On-Surface Synthesis*, Springer International Publishing, Cham, **2016**.

[50] Q. Shen, H.-Y. Gao, H. Fuchs, *Nano Today* **2017**, *13*, 77–96.

[51] P. A. Held, H. Fuchs, A. Studer, *Chem. Eur. J.* **2017**, *23*, 5874–5892.

[52] M. Di Giovannantonio, O. Deniz, J. I. Urgel, R. Widmer, T. Dienel, S. Stolz, C. Sánchez-Sánchez, M. Muntwiler, T. Dumslaff, R. Berger, A. Narita, X. Feng, K. Müllen, P. Ruffieux, R. Fasel, *ACS Nano* **2018**, *12*, 74–81.

[53] S. Clair, D. G. de Oteyza, *Chem. Rev.* **2019**, *119*, 4717–4776.

[54] S. Zint, D. Ebeling, T. Schlöder, S. Ahles, D. Mollenhauer, H. A. Wegner, A. Schirmeisen, *ACS Nano* **2017**, *11*, 4183–4190.

[55] J. B. F. Ullmann, *Ber. Dtsch. Chem. Ges.* **1901**, *34*, 2174–2185.

[56] S. A. Krasnikov, C. M. Doyle, N. N. Sergeeva, A. B. Preobrajenski, N. A. Vinogradov, Y. N. Sergeeva, A. A. Zakharov, M. O. Senge, A. A. Cafolla, *Nano Res.* **2011**, *4*, 376–384.

[57] S. W. Hla, L. Bartels, G. Meyer, K. H. Rieder, *Phys. Rev. Lett.* **2000**, *85*, 2777–2780.

[58] L. Grill, M. Dyer, L. Lafferentz, M. Persson, M. V. Peters, S. Hecht, *Nat. Nanotech.* **2007**, *2*, 687–691.

[59] L. Lafferentz, V. Eberhardt, C. Dri, C. Africh, G. Comelli, F. Esch, S. Hecht, L. Grill, *Nat. Chem.* **2012**, *4*, 215–220.

[60] K. J. Shi, D. W. Yuan, C. X. Wang, C. H. Shu, D. Y. Li, Z. L. Shi, X. Y. Wu, P. N. Liu, *Org. Lett.* **2016**, *18*, 1282–1285.

[61] P. H. Jacobse, A. van den Hoogenband, M.-E. Moret, R. J. M. Klein Gebbink, I. Swart, *Angew. Chem. Int. Ed.* **2016**, *55*, 13052–13055.

[62] A. Saywell, J. Schwarz, S. Hecht, L. Grill, *Angew. Chem. Int. Ed.* **2012**, *51*, 5096–5100.

[63] M. Koch, M. Gille, A. Viertel, S. Hecht, L. Grill, *Surf. Sci.* **2014**, *627*, 70–74.

[64] Q. Fan, T. Wang, J. Dai, J. Kuttner, G. Hilt, J. M. Gottfried, J. Zhu, *ACS Nano* **2017**, *11*, 5070–5079.

[65] Q. Fan, C. Wang, Y. Han, J. Zhu, W. Hieringer, J. Kuttner, G. Hilt, J. M. Gottfried, *Angew. Chem.* **2013**, *125*, 4766–4770.

[66] M. Kolmer, A.-K. Steiner, I. Izydorczyk, W. Ko, M. Engelund, M. Szymonski, A.-P. Li, K. Amsharov, *Science* **2020**, *369*, 571–575.

[67] V. K. Kanuru, G. Kyriakou, S. K. Beaumont, A. C. Papageorgiou, D. J. Watson, R. M. Lambert, *J. Am. Chem. Soc.* **2010**, *132*, 8081–8086.

[68] C. Sanchez-Sanchez, N. Orozco, J. P. Holgado, S. K. Beaumont, G. Kyriakou, D. J. Watson, A. R. Gonzalez-Elipe, L. Feria, J. Fernández Sanz, R. M. Lambert, *J. Am. Chem. Soc.* **2015**, *137*, 940–947.

[69] Q. Sun, L. Cai, H. Ma, C. Yuan, W. Xu, *Chem. Commun.* **2016**, *52*, 6009–6012.

[70] Q. Sun, L. Cai, Y. Ding, H. Ma, C. Yuan, W. Xu, *Phys. Chem. Chem. Phys.* **2016**, *18*, 2730–2735.

[71] H. Hayashi, J. Yamaguchi, H. Jippo, R. Hayashi, N. Aratani, M. Ohfuchi, S. Sato, H. Yamada, *ACS Nano* **2017**, *11*, 6204–6210.

[72] Q. Chen, J. R. Cramer, J. Liu, X. Jin, P. Liao, X. Shao, K. V. Gothelf, K. Wu, *Angew. Chem. Int. Ed.* **2017**, *56*, 5026–5030.

[73] Q. Fan, L. Yan, M. W. Tripp, O. Krejčí, S. Dimosthenous, S. R. Kachel, M. Chen, A. S. Foster, U. Koert, P. Liljeroth, J. M. Gottfried, *Science* **2021**, *372*, 852–856.

[74] R. Scholl, C. Seer, *Justus Liebig's Ann. Chem.* **1912**, *394*, 111–177.

[75] R. Scholl, C. Seer, R. Weitzenböck, *Ber. Dtsch. Chem. Ges.* **1910**, *43*, 2202–2209.

[76] P. Kovacic, C. Wu, *J. Polym. Sci.* **1960**, *47*, 45–54.

[77] P. Kovacic, A. Kyriakis, *Tetrahedron Lett.* **1962**, *3*, 467–469.

[78] P. Rempala, J. Kroulík, B. T. King, *J. Org. Chem.* **2006**, *71*, 5067–5081.

[79] P. Kovacic, M. B. Jones, *Chem. Rev.* **1987**, *87*, 357–379.

[80] O. Hammerich, V. D. Parker in *O. Hammerich, V. D. Parker*, *Vol. 20*, pp. 55–189.

[81] M. Treier, C. A. Pignedoli, T. Laino, R. Rieger, K. Müllen, D. Passerone, R. Fasel, *Nat. Chem.* **2011**, *3*, 61–67.

[82] Q. Sun, L. M. Mateo, R. Robles, P. Ruffieux, N. Lorente, G. Bottari, T. Torres, R. Fasel, *J. Am. Chem. Soc.* **2020**, *142*, 18109–18117.

[83] Q. Zhong, Y. Hu, K. Niu, H. Zhang, B. Yang, D. Ebeling, J. Tschakert, T. Cheng, A. Schirmeisen, A. Narita, K. Müllen, L. Chi, *J. Am. Chem. Soc.* **2019**, *141*, 7399–7406.

[84] T. G. Lohr, J. I. Urgel, K. Eimre, J. Liu, M. Di Giovannantonio, S. Mishra, R. Berger, P. Ruffieux, C. A. Pignedoli, R. Fasel, X. Feng, *J. Am. Chem. Soc.* **2020**, *142*, 13565–13572.

[85] J. Hieulle, E. Carbonell-Sanromà, M. Vilas-Varela, A. Garcia-Lekue, E. Guitián, D. Peña, J. I. Pascual, *Nano Lett.* **2018**, *18*, 418–423.

[86] Q. Fan, D. Martin-Jimenez, D. Ebeling, C. K. Krug, L. Brechmann, C. Kohlmeyer, G. Hilt, W. Hieringer, A. Schirmeisen, J. M. Gottfried, *J. Am. Chem. Soc.* **2019**, *141*, 17713–17720.

[87] D. Han, Q. Fan, J. Dai, T. Wang, J. Huang, Q. Xu, H. Ding, J. Hu, L. Feng, W. Zhang, Z. Zeng, J. M. Gottfried, J. Zhu, *J. Phys. Chem. C* **2020**, *124*, 5248–5256.

[88] C. Glaser, *Ber. Dtsch. Chem. Ges.* **1869**, *2*, 422–424.

[89] Y.-Q. Zhang, N. Kepčija, M. Kleinschrodt, K. Diller, S. Fischer, A. C. Papageorgiou, F. Allegretti, J. Björk, S. Klyatskaya, F. Klappenberger, M. Ruben, J. V. Barth, *Nat. Commun.* **2012**, *3*, 1286.

[90] H.-Y. Gao, H. Wagner, D. Zhong, J.-H. Franke, A. Studer, H. Fuchs, *Angew. Chem. Int. Ed.* **2013**, *52*, 4024–4028.

[91] H.-Y. Gao, J.-H. Franke, H. Wagner, D. Zhong, P.-A. Held, A. Studer, H. Fuchs, *J. Phys. Chem. C* **2013**, *117*, 18595–18602.

[92] Q. Sun, L. Cai, H. Ma, C. Yuan, W. Xu, *ACS Nano* **2016**, *10*, 7023–7030.

[93] K. Kaiser, L. M. Scriven, F. Schulz, P. Gawel, L. Gross, H. L. Anderson, *Science* **2019**, *365*, 1299–1301.

[94] R. Zhang, Y. Zhang, Q. Zhang, H. Xie, W. Qian, F. Wei, *ACS Nano* **2013**, *7*, 6156–6161.

[95] S. Iijima, T. Ichihashi, *Nature* **1993**, *363*, 603–605.

[96] D. S. Bethune, C. H. Kiang, M. S. de Vries, G. Gorman, R. Savoy, J. Vazquez, R. Beyers, *Nature* **1993**, *363*, 605–607.

[97] S. Iijima, *Nature* **1991**, *354*, 56–58.

[98] Hamada, Sawada, Oshiyama, *Phys. Rev. Lett.* **1992**, *68*, 1579–1581.

[99] S. B. Sinnott, R. Andrews, *Crit. Rev. Solid State Mater. Sci.* **2001**, *26*, 145–249.

[100] X. Lu, Z. Chen, *Chem. Rev.* **2005**, *105*, 3643–3696.

[101] S. Hong, S. Myung, *Nat. Nanotech.* **2007**, *2*, 207–208.

[102] C. T. White, T. N. Todorov, *Nature* **1998**, *393*, 240–242.

[103] E. A. Laird, F. Kuemmeth, G. A. Steele, K. Grove-Rasmussen, J. Nygård, K. Flensberg, L. P. Kouwenhoven, *Rev. Mod. Phys.* **2015**, *87*, 703–764.

[104] M. Endo, T. Hayashi, Y.-A. Kim, *Pure Appl. Chem.* **2006**, *78*, 1703–1713.

[105] Yu, Lourie, Dyer, Moloni, Kelly, Ruoff, *Science* **2000**, *287*, 637–640.

[106] B. Peng, M. Locascio, P. Zapol, S. Li, S. L. Mielke, G. C. Schatz, H. D. Espinosa, *Nat. Nanotech.* **2008**, *3*, 626–631.

[107] T. Tanaka, H. Jin, Y. Miyata, S. Fujii, H. Suga, Y. Naitoh, T. Minari, T. Miyadera, K. Tsukagoshi, H. Kataura, *Nano Lett.* **2009**, *9*, 1497–1500.

[108] M. Meyyappan, *Small* **2016**, *12*, 2118–2129.

[109] D.-M. Sun, C. Liu, W.-C. Ren, H.-M. Cheng, *Small* **2013**, *9*, 1188–1205.

[110] L. Wen, F. Li, H.-M. Cheng, *Adv. Mater.* **2016**, *28*, 4306–4337.

[111] I. Hwang, W. Wang, S. K. Hwang, S. H. Cho, K. L. Kim, B. Jeong, J. Huh, C. Park, *Nanoscale* **2016**, *8*, 10273–10281.

[112] F. Wang, D. Kozawa, Y. Miyauchi, K. Hiraoka, S. Mouri, Y. Ohno, K. Matsuda, *Nat. Commun.* **2015**, *6*, 6305.

[113] S. Kumar, R. Rani, N. Dilbaghi, K. Tankeshwar, K.-H. Kim, *Chem. Soc. Rev.* **2017**, *46*, 158–196.

[114] H. W. Kroto, J. R. Heath, S. C. O'Brien, R. F. Curl, R. E. Smalley, *Nature* **1985**, *318*, 162–163.

[115] T. W. Ebbesen, P. M. Ajayan, *Nature* **1992**, *358*, 220–222.

[116] J.-C. Liou, C.-C. Diao, J.-J. Lin, Y.-L. Chen, C.-F. Yang, *Nanoscale Res. Lett.* **2014**, *9*, 1.

[117] T. Guo, P. Nikolaev, A. G. Rinzler, D. Tomanek, D. T. Colbert, R. E. Smalley, *J. Phys. Chem.* **1995**, *99*, 10694–10697.

[118] T. Guo, P. Nikolaev, A. Thess, D. T. Colbert, R. E. Smalley, *Chem. Phys. Lett.* **1995**, *243*, 49–54.

[119] O. Smiljanic, B. L. Stansfield, J.-P. Dodelet, A. Serventi, S. Désilets, *Chem. Phys. Lett.* **2002**, *356*, 189–193.

[120] L. Yuan, K. Saito, W. Hu, Z. Chen, *Chem. Phys. Lett.* **2001**, *346*, 23–28.

[121] P.-X. Hou, C. Liu, H.-M. Cheng, *Carbon* **2008**, *46*, 2003–2025.

[122] M. José-Yacamán, M. Miki-Yoshida, L. Rendón, J. G. Santiesteban, *Appl. Phys. Lett.* **1993**, *62*, 657–659.

[123] M. Kumar, Y. Ando, *J. Nanosci. Nanotechnol.* **2010**, *10*, 3739–3758.

[124] N. Inami, M. A. Mohamed, E. Shikoh, A. Fujiwara, *Sci. Technol. Adv. Mater.* **2007**, *8*, 292–295.

[125] H. Reinhardt, C. Hellmann, P. Nürnberger, S. Kachel, N. Hampp, *Adv. Mater. Interfaces* **2017**, *4*, 1700508.

[126] N. Muradov, *Int. J. Hydrog. Energy* **2001**, *26*, 1165–1175.

[127] S. Naha, I. K. Puri, *J. Phys. D* **2008**, *41*, 065304.

[128] S. Banerjee, S. Naha, I. K. Puri, *Appl. Phys. Lett.* **2008**, *92*, 233121.

[129] A. Meyer-Plath, G. Orts-Gil, S. Petrov, F. Oleszak, H.-E. Maneck, I. Dörfel, O. Haase, S. Richter, R. Mach, *Carbon* **2012**, *50*, 3934–3942.

[130] Ren, Huang, Xu, Wang, Bush, Siegal, Provencio, *Science* **1998**, *282*, 1105–1107.

[131] T. Tanaka, Y. Urabe, D. Nishide, H. Kataura, *Appl. Phys. Express* **2009**, *2*, 125002.

[132] B. El Hamaoui, L. Zhi, J. Wu, U. Kolb, K. Müllen, *Adv. Mater.* **2005**, *17*, 2957–2960.

[133] B. El Hamaoui, L. Zhi, J. Wu, J. Li, N. T. Lucas, Ž. Tomović, U. Kolb, K. Müllen, *Adv. Funct. Mater.* **2007**, *17*, 1179–1187.

[134] J. Wu, B. El Hamaoui, J. Li, L. Zhi, U. Kolb, K. Müllen, *Small* **2005**, *1*, 210–212.

[135] S. Scholz, P. J. Leech, B. C. Englert, W. Sommer, M. Weck, U. H. F. Bunz, *Adv. Mater.* **2005**, *17*, 1052–1055.

[136] L. Zhi, K. Müllen, *J. Mater. Chem.* **2008**, *18*, 1472.

[137] H. Hou, A. K. Schaper, F. Weller, A. Greiner, *Chem. Mater.* **2002**, *14*, 3990–3994.

[138] C. N. R. Rao, R. Sen, *Chem. Commun.* **1998**, *15*, 1525–1526.

[139] O. A. Nerushev, M. Sveningsson, L. K. L. Falk, F. Rohmund, *J. Mater. Chem.* **2001**, *11*, 1122–1132.

[140] V. S. Iyer, K. P. C. Vollhardt, R. Wilhelm, *Angew. Chem.* **2003**, *115*, 4515–4519.

[141] P. I. Dosa, C. Erben, V. S. Iyer, K. P. C. Vollhardt, I. M. Wasser, *J. Am. Chem. Soc.* **1999**, *121*, 10430–10431.

[142] M. Laskoski, W. Steffen, J. G. M. Morton, M. D. Smith, U. H. F. Bunz, *J. Am. Chem. Soc.* **2002**, *124*, 13814–13818.

[143] M. Ball, Y. Zhong, Y. Wu, C. Schenck, F. Ng, M. Steigerwald, S. Xiao, C. Nuckolls, *Acc. Chem. Res.* **2015**, *48*, 267–276.

[144] S. Madayanad Suresh, D. Hall, D. Beljonne, Y. Olivier, E. Zysman-Colman, *Adv. Funct. Mater.* **2020**, *30*, 1908677.

[145] J. Gong, K. Sumathy, Q. Qiao, Z. Zhou, *Renew. Sustain. Energy Rev.* **2017**, *68*, 234–246.

[146] J. Mei, Y. Diao, A. L. Appleton, L. Fang, Z. Bao, *J. Am. Chem. Soc.* **2013**, *135*, 6724–6746.

[147] A. J. C. Kuehne, M. C. Gather, *Chem. Rev.* **2016**, *116*, 12823–12864.

[148] H. Kobayashi, M. Ogawa, R. Alford, P. L. Choyke, Y. Urano, *Chem. Rev.* **2010**, *110*, 2620–2640.

[149] F. Würthner, C. R. Saha-Möller, B. Fimmel, S. Ogi, P. Leowanawat, D. Schmidt, *Chem. Rev.* **2016**, *116*, 962–1052.

[150] T. M. Figueira-Duarte, K. Müllen, *Chem. Rev.* **2011**, *111*, 7260–7314.

[151] R. Thamatam, S. L. Skraba, R. P. Johnson, *Chem. Commun.* **2013**, *49*, 9122–9124.

[152] W. Yang, A. Lucotti, M. Tommasini, W. A. Chalifoux, *J. Am. Chem. Soc.* **2016**, *138*, 9137–9144.

[153] F. Röhrscheid in *Ullmann's Encyclopedia of Industrial Chemistry*, Wiley-VCH, Weinheim, **2000**.

[154] C. R. Newman, C. D. Frisbie, D. A. Da Silva Filho, J.-L. Brédas, P. C. Ewbank, K. R. Mann, *Chem. Mater.* **2004**, *16*, 4436–4451.

[155] S. V. Bhosale, C. H. Jani, S. J. Langford, *Chem. Soc. Rev.* **2008**, *37*, 331–342.

[156] A. Dodabalapur, H. E. Katz, L. Torsi, *Adv. Mater.* **1996**, *8*, 853–855.

[157] C. W. Tang, *Appl. Phys. Lett.* **1986**, *48*, 183–185.

[158] C. Huang, S. Barlow, S. R. Marder, *J. Org. Chem.* **2011**, *76*, 2386–2407.

[159] T. Weil, T. Vosch, J. Hofkens, K. Peneva, K. Müllen, *Angew. Chem. Int. Ed.* **2010**, *49*, 9068–9093.

[160] L. Chen, C. Li, K. Müllen, *J. Mater. Chem. C* **2014**, *2*, 1938–1956.

[161] Y. Avlasevich, S. Müller, P. Erk, K. Müllen, *Chem. Eur. J.* **2007**, *13*, 6555–6561.

[162] N. G. Pschirer, C. Kohl, F. Nolde, J. Qu, K. Müllen, *Angew. Chem. Int. Ed.* **2006**, *45*, 1401–1404.

[163] Z. Yuan, S.-L. Lee, L. Chen, C. Li, K. S. Mali, S. de Feyter, K. Müllen, *Chem. Eur. J.* **2013**, *19*, 11842–11846.

[164] S. Seifert, K. Shoyama, D. Schmidt, F. Würthner, *Angew. Chem. Int. Ed.* **2016**, *55*, 6390–6395.

[165] K. Shoyama, D. Schmidt, M. Mahl, F. Würthner, *Org. Lett.* **2017**, *19*, 5328–5331.

[166] K. Shoyama, M. Mahl, S. Seifert, F. Würthner, *J. Org. Chem.* **2018**, *83*, 5339–5346.

[167] K. Müllen, *ACS Nano* **2014**, *8*, 6531–6541.

[168] C. Liu, S. Zhang, J. Li, J. Wei, K. Müllen, M. Yin, *Angew. Chem. Int. Ed.* **2019**, *58*, 1638–1642.

[169] Z. Sun, Q. Ye, C. Chi, J. Wu, *Chem. Soc. Rev.* **2012**, *41*, 7857–7889.

[170] G. Qian, Y. Yang, Z. Wang, C. Yang, Z. Yang, M. Wang, *Chem. Phys. Lett.* **2003**, *368*, 555–560.

[171] A. Bohnen, K.-H. Koch, W. Lüttke, K. Müllen, *Angew. Chem. Int. Ed.* **1990**, *29*, 525–527.

[172] K.-H. Koch, K. Müllen, *Chem. Ber.* **1991**, *124*, 2091–2100.

[173] J. Li, K. Zhang, X. Zhang, K.-W. Huang, C. Chi, J. Wu, *J. Org. Chem.* **2010**, *75*, 856–863.

[174] E. Clar, *Chem. Ber.* **1948**, *81*, 52–63.

[175] S. Saïdi-Besbes, E. Grelet, H. Bock, *Angew. Chem. Int. Ed.* **2006**, *45*, 1783–1786.

[176] A. Konishi, Y. Hirao, M. Nakano, A. Shimizu, E. Botek, B. Champagne, D. Shiomi, K. Sato, T. Takui, K. Matsumoto, H. Kurata, T. Kubo, *J. Am. Chem. Soc.* **2010**, *132*, 11021–11023.

[177] A. Konishi, Y. Hirao, K. Matsumoto, H. Kurata, R. Kishi, Y. Shigeta, M. Nakano, K. Tokunaga, K. Kamada, T. Kubo, *J. Am. Chem. Soc.* **2013**, *135*, 1430–1437.

[178] E. Clar, *Ber. Dtsch. Chem. Ges.* **1943**, *76*, 458–466.

[179] E. Clar, *The aromatic sextet*, Wiley, London, **1972**.

[180] S. Pogodin, I. Agranat, *Org. Lett.* **1999**, *1*, 1387–1390.

[181] S. Pogodin, I. Agranat, *J. Am. Chem. Soc.* **2003**, *125*, 12829–12835.

[182] T. Umemoto, T. Kawashima, Y. Sakata, S. Misumi, *Tetrahedron Lett.* **1975**, *16*, 1005–1006.

[183] R. Rieger, K. Müllen, *J. Phys. Org. Chem.* **2010**, *23*, 315–325.

[184] S. Singh, W. J. Jones, W. Siebrand, B. P. Stoicheff, W. G. Schneider, *J. Chem. Phys.* **1965**, *42*, 330–342.

[185] M. B. Smith, J. Michl, *Chem. Rev.* **2010**, *110*, 6891–6936.

[186] I. Paci, J. C. Johnson, X. Chen, G. Rana, D. Popović, D. E. David, A. J. Nozik, M. A. Ratner, J. Michl, *J. Am. Chem. Soc.* **2006**, *128*, 16546–16553.

[187] W. G. Albrecht, M. E. Michel-Beyerle, V. Yakhot, *Chem. Phys.* **1978**, *35*, 193–200.

[188] A. Rao, M. W. B. Wilson, J. M. Hodgkiss, S. Albert-Seifried, H. Bässler, R. H. Friend, *J. Am. Chem. Soc.* **2010**, *132*, 12698–12703.

[189] W. E. Ford, P. V. Kamat, *J. Phys. Chem.* **1987**, *91*, 6373–6380.

[190] Y. Kamura, H. Inokuchi, J. Aoki, S. Fujisawa, *Chem. Phys. Lett.* **1977**, *46*, 356–359.

[191] U. Wenzel, H.-G. Löhmannsröben, *J. Photochem. Photobiol.* **1996**, *96*, 13–18.

[192] V. M. Nichols, M. T. Rodriguez, G. B. Piland, F. Tham, V. N. Nesterov, W. J. Youngblood, C. J. Bardeen, *J. Phys. Chem. C* **2013**, *117*, 16802–16810.

[193] K. Uchida, T. Kubo, D. Yamanaka, A. Furube, H. Matsuzaki, R. Nishii, Y. Sakagami, A. Abulikemu, K. Kamada, *Can. J. Chem.* **2017**, *95*, 432–444.

[194] W. Yang, J. H. S. K. Monteiro, A. de Bettencourt-Dias, V. J. Catalano, W. A. Chalifoux, *Angew. Chem. Int. Ed.* **2016**, *55*, 10427–10430.

[195] W. Yang, W. Chalifoux, *Synlett* **2017**, *28*, 625–632.

[196] W. Yang, R. R. Kazemi, N. Karunathilake, V. J. Catalano, M. A. Alpuche-Aviles, W. A. Chalifoux, *Org. Chem. Front.* **2018**, *5*, 2288–2295.

[197] Y. Yang, L. Yuan, B. Shan, Z. Liu, Q. Miao, *Chem. Eur. J.* **2016**, *22*, 18620–18627.

[198] Y. Hu, G. M. Paternò, X.-Y. Wang, X.-C. Wang, M. Guizzardi, Q. Chen, D. Schollmeyer, X.-Y. Cao, G. Cerullo, F. Scotognella, K. Müllen, A. Narita, *J. Am. Chem. Soc.* **2019**, *141*, 12797–12803.

[199] T. Riehm, G. de Paoli, A. E. Konradsson, L. de Cola, H. Wadepohl, L. H. Gade, *Chem. Eur. J.* **2007**, *13*, 7317–7329.

[200] S. Geib, S. C. Martens, U. Zschieschang, F. Lombeck, H. Wadepohl, H. Klauk, L. H. Gade, *J. Org. Chem.* **2012**, *77*, 6107–6116.

[201] S. C. Martens, T. Riehm, S. Geib, H. Wadepohl, L. H. Gade, *J. Org. Chem.* **2011**, *76*, 609–617.

[202] S. C. Martens, U. Zschieschang, H. Wadepohl, H. Klauk, L. H. Gade, *Chem. Eur. J.* **2012**, *18*, 3498–3509.

[203] S. Geib, U. Zschieschang, M. Gsänger, M. Stolte, F. Würthner, H. Wadepohl, H. Klauk, L. H. Gade, *Adv. Funct. Mater.* **2013**, *23*, 3866–3874.

[204] L. Hahn, F. Maass, T. Bleith, U. Zschieschang, H. Wadepohl, H. Klauk, P. Tegeder, L. H. Gade, *Chem. Eur. J.* **2015**, *21*, 17691–17700.

[205] S. Höfener, B. A. R. Günther, M. E. Harding, L. H. Gade, *J. Phys. Chem. A* **2019**, *123*, 3160–3169.

[206] S. Geib, S. C. Martens, M. Märken, A. Rybina, H. Wadepohl, L. H. Gade, *Chem. Eur. J.* **2013**, *19*, 13811–13822.

[207] S. Langbein, H. Wadepohl, L. H. Gade, *J. Org. Chem.* **2015**, *80*, 12620–12626.

[208] L. Hahn, H. Wadepohl, L. H. Gade, *Org. Lett.* **2015**, *17*, 2266–2269.

[209] L. Hahn, A. Hermannsdorfer, B. Günther, T. Wesp, B. Bühler, U. Zschieschang, H. Wadepohl, H. Klauk, L. H. Gade, *J. Org. Chem.* **2017**, *82*, 12492–12502.

[210] B. A. R. Günther, S. Höfener, U. Zschieschang, H. Wadepohl, H. Klauk, L. H. Gade, *Chem. Eur. J.* **2019**, *25*, 14669–14678.

[211] B. A. R. Günther, S. Höfener, R. Eichelmann, U. Zschieschang, H. Wadepohl, H. Klauk, L. H. Gade, *Org. Lett.* **2020**, *22*, 2298–2302.

[212] L. Hahn, S. Öz, H. Wadepohl, L. H. Gade, *Chem. Commun.* **2014**, *50*, 4941–4943.

[213] L. Hahn, N. J. Buurma, L. H. Gade, *Chem. Eur. J.* **2016**, *22*, 6314–6322.

[214] W. Yuan, J. Cheng, X. Li, M. Wu, Y. Han, C. Yan, G. Zou, K. Müllen, Y. Chen, *Angew. Chem. Int. Ed.* **2020**, *59*, 9940–9945.

[215] M. Stępień, E. Gońka, M. Żyła, N. Sprutta, *Chem. Rev.* **2017**, *117*, 3479–3716.

[216] U. H. F. Bunz, *Acc. Chem. Res.* **2015**, *48*, 1676–1686.

[217] M. A. Kobaisi, S. V. Bhosale, K. Latham, A. M. Raynor, S. V. Bhosale, *Chem. Rev.* **2016**, *116*, 11685–11796.

[218] F. Würthner, A. Sautter, J. Schilling, *J. Org. Chem.* **2002**, *67*, 3037–3044.

[219] C. Sotiriou-Leventis, Z. Mao, *J. Heterocycl. Chem.* **2000**, *37*, 1665–1667.

[220] A. Slama-Schwok, J. Jazwinski, A. Béré, T. Montenay-Garestier, M. Rougée, C. Hélène, J. M. Lehn, *Biochemistry* **1989**, *28*, 3227–3234.

[221] A. Aksenov, N. Aksenov, A. Lyakhovnenko, I. Aksenova, *Synthesis* **2009**, *20*, 3439–3442.

[222] P. H. Dinolfo, M. E. Williams, C. L. Stern, J. T. Hupp, *J. Am. Chem. Soc.* **2004**, *126*, 12989–13001.

[223] F. Würthner, A. Sautter, C. Thalacker, *Angew. Chem. Int. Ed.* **2000**, *39*, 1243–1245.

[224] A. N. Basuray, H.-P. Jacquot de Rouville, K. J. Hartlieb, T. Kikuchi, N. L. Strutt, C. J. Bruns, M. W. Ambrogio, A.-J. Avestro, S. T. Schneebeli, A. C. Fahrenbach, J. F. Stoddart, *Angew. Chem. Int. Ed.* **2012**, *51*, 11872–11877.

[225] S. Sampath, A. N. Basuray, K. J. Hartlieb, T. Aytun, S. I. Stupp, J. F. Stoddart, *Adv. Mater.* **2013**, *25*, 2740–2745.

[226] X. Gong, R. M. Young, K. J. Hartlieb, C. Miller, Y. Wu, H. Xiao, P. Li, N. Hafezi, J. Zhou, L. Ma, T. Cheng, W. A. Goddard, O. K. Farha, J. T. Hupp, M. R. Wasielewski, J. F. Stoddart, *J. Am. Chem. Soc.* **2017**, *139*, 4107–4116.

[227] H. Sachdev, *European Patent* **2011**, EP 390 253 A1.

[228] T. Nakazato, T. Kamatsuka, J. Inoue, T. Sakurai, S. Seki, H. Shinokubo, Y. Miyake, *Chem. Commun.* **2018**, *54*, 5177–5180.

[229] T. Nakazato, H. Takekoshi, T. Sakurai, H. Shinokubo, Y. Miyake, *Angew. Chem. Int. Ed.* **2021**.

[230] T. Nakazato, W. Matsuda, T. Sakurai, S. Seki, H. Shinokubo, Y. Miyake, *Chem. Lett.* **2020**, *49*, 465–468.

[231] B. M. Rosen, K. W. Quasdorf, D. A. Wilson, N. Zhang, A.-M. Resmerita, N. K. Garg, V. Percec, *Chem. Rev.* **2011**, *111*, 1346–1416.

[232] K. W. Quasdorf, X. Tian, N. K. Garg, *J. Am. Chem. Soc.* **2008**, *130*, 14422–14423.

[233] T. Nakazato, H. Shinokubo, Y. Miyake, *Chem. Commun.* **2021**, *57*, 327–330.

[234] Y. Nakamura, T. Nakazato, T. Kamatsuka, H. Shinokubo, Y. Miyake, *Chem. Eur. J.* **2019**, *25*, 10571–10574.

[235] T. Sakurai, T. Nakazato, H. Shinokubo, Y. Miyake, *Org. Lett.* **2021**, *23*, 2099–2103.

[236] J. Sundermeyer, E. Baal, S. Werner, *WO 2019/229134 A1* **2019**.

[237] E. Baal, *Dissertation*, **2018**.

[238] F. Diederich, H. A. Staab, *Angew. Chem. Int. Ed.* **1978**, *17*, 372–374.

[239] J. C. Buttrick, B. T. King, *Chem. Soc. Rev.* **2017**, *46*, 7–20.

[240] H. A. Staab, F. Diederich, C. Krieger, D. Schweitzer, *Chem. Ber.* **1983**, *116*, 3504–3512.

[241] W. Fan, Y. Han, S. Dong, G. Li, X. Lu, J. Wu, *CCS Chem.* **2020**, 1445–1452.

[242] B. Kumar, R. L. Viboh, M. C. Bonifacio, W. B. Thompson, J. C. Buttrick, B. C. Westlake, M.-S. Kim, R. W. Zoellner, S. A. Varganov, P. Mörschel, J. Teteruk, M. U. Schmidt, B. T. King, *Angew. Chem. Int. Ed.* **2012**, *51*, 12795–12800.

[243] M. A. Majewski, Y. Hong, T. Lis, J. Gregoliński, P. J. Chmielewski, J. Cybińska, D. Kim, M. Stępień, *Angew. Chem. Int. Ed.* **2016**, *55*, 14072–14076.

[244] W. Fan, Y. Han, X. Wang, X. Hou, J. Wu, *J. Am. Chem. Soc.* **2021**, *DOI: 10.1021/jacs.1c06757*, year.

[245] H. Hou, X.-J. Zhao, C. Tang, Y.-Y. Ju, Z.-Y. Deng, X.-R. Wang, L.-B. Feng, D.-H. Lin, X. Hou, A. Narita, K. Müllen, Y.-Z. Tan, *Nat. Commun.* **2020**, *11*, 3976.

[246] A. R. Katritzky, C. M. Marson, *J. Am. Chem. Soc.* **1983**, *105*, 3279–3283.

[247] J. E. Butler Ransohoff, H. A. Staab, *Tetrahedron Lett.* **1985**, *26*, 6179–6182.

[248] A. Tatibouët, R. Hancock, M. Demeunynck, J. Lhomme, *Angew. Chem. Int. Ed.* **1997**, *36*, 1190–1191.

[249] U. Beser, M. Kastler, A. Maghsoumi, M. Wagner, C. Castiglioni, M. Tommasini, A. Narita, X. Feng, K. Müllen, *J. Am. Chem. Soc.* **2016**, *138*, 4322–4325.

[250] J. Cioslowski, P. B. O'Connor, E. D. Fleischmann, *J. Am. Chem. Soc.* **1991**, *113*, 1086–1089.

[251] Z. Zhou, *J. Phys. Org. Chem.* **1995**, *8*, 103–107.

[252] J.-M. Gilles, J. F. M. Oth, F. Sondheimer, E. P. Woo, *J. Chem. Soc. B* **1971**, 2177.

[253] K. Ikemoto, A. Yoshii, T. Izumi, H. Taka, H. Kita, J. Y. Xue, R. Kobayashi, S. Sato, H. Isobe, *J. Org. Chem.* **2016**, *81*, 662–666.

[254] Q. Fan, D. Martin-Jimenez, S. Werner, D. Ebeling, T. Koehler, T. Vollgraff, J. Sundermeyer, W. Hieringer, A. Schirmeisen, J. M. Gottfried, *J. Am. Chem. Soc.* **2020**, *142*, 894–899.

[255] Q. Zhang, H. Peng, G. Zhang, Q. Lu, J. Chang, Y. Dong, X. Shi, J. Wei, *J. Am. Chem. Soc.* **2014**, *136*, 5057–5064.

[256] X.-J. Zhao, H. Hou, P.-P. Ding, Z.-Y. Deng, Y.-Y. Ju, S.-H. Liu, Y.-M. Liu, C. Tang, L.-B. Feng, Y.-Z. Tan, *Science Adv.* **2020**, *6*, eaay8541.

[257] X.-J. Zhao, H. Hou, X.-T. Fan, Y. Wang, Y.-M. Liu, C. Tang, S.-H. Liu, P.-P. Ding, J. Cheng, D.-H. Lin, C. Wang, Y. Yang, Y.-Z. Tan, *Nat. Commun.* **2019**, *10*, 3057.

[258] R. Kandre, K. Feldman, H. E. H. Meijer, P. Smith, A. D. Schlüter, *Angew. Chem.* **2007**, *119*, 5044–5047.

[259] J. R. Kuttner, G. Hilt, *Macromolecules* **2014**, *47*, 5532–5541.

[260] J. Kim, N. Lee, Y. H. Min, S. Noh, N.-K. Kim, S. Jung, M. Joo, Y. Yamada, *ACS Omega* **2018**, *3*, 17789–17796.

[261] S. Mishra, D. Beyer, K. Eimre, S. Kezilebieke, R. Berger, O. Gröning, C. A. Pignedoli, K. Müllen, P. Liljeroth, P. Ruffieux, X. Feng, R. Fasel, *Nat. Nanotech.* **2020**, *15*, 22–28.

[262] S. Mishra, D. Beyer, R. Berger, J. Liu, O. Gröning, J. I. Urgel, K. Müllen, P. Ruffieux, X. Feng, R. Fasel, *J. Am. Chem. Soc.* **2020**, *142*, 1147–1152.

[263] K. Yoneda, M. Nakano, Y. Inoue, T. Inui, K. Fukuda, Y. Shigeta, T. Kubo, B. Champagne, *J. Phys. Chem. C* **2012**, *116*, 17787–17795.

[264] J.-i. Aihara, M. Makino, T. Ishida, J. R. Dias, *J. Phys. Chem. A* **2013**, *117*, 4688–4697.

[265] B. Hajgató, K. Ohno, *Chem. Phys. Lett.* **2004**, *385*, 512–518.

[266] H. Yoon, A. Lossouarn, F. Landau, M. Lautens, *Org. Lett.* **2016**, *18*, 6324–6327.

[267] T. Yamamoto, A. Ishibashi, M. Koyanagi, H. Ihara, N. Eichenauer, M. Suginome, *Bull. Chem. Soc. Jpn.* **2017**, *90*, 604–606.

[268] Y. Wang, N. Xue, R. Li, T. Wu, N. Li, S. Hou, Y. Wang, *Chem. Phys. Chem.* **2019**, *20*, 2262–2270.

[269] X. Zhang, N. Li, G.-C. Gu, H. Wang, D. Nieckarz, P. Szabelski, Y. He, Y. Wang, C. Xie, Z.-Y. Shen, J.-T. Lü, H. Tang, L.-M. Peng, S.-M. Hou, K. Wu, Y.-F. Wang, *ACS Nano* **2015**, *9*, 11909–11915.

[270] X. Zhang, N. Li, L. Liu, G. Gu, C. Li, H. Tang, L. Peng, S. Hou, Y. Wang, *Chem. Commun.* **2016**, *52*, 10578–10581.

[271] G. Gu, N. Li, L. Liu, X. Zhang, Q. Wu, D. Nieckarz, P. Szabelski, L. Peng, B. K. Teo, S. Hou, Y. Wang, *RSC Adv.* **2016**, *6*, 66548–66552.

[272] G. Feng, Y. Shen, Y. Yu, Q. Liang, J. Dong, S. Lei, W. Hu, *Chem. Commun.* **2021**, *57*, 2065–2068.

[273] X. Zhang, G. Gu, N. Li, H. Wang, H. Tang, Y. Zhang, S. Hou, Y. Wang, *RSC Adv.* **2018**, *8*, 1852–1856.

[274] J. Shang, Y. Wang, M. Chen, J. Dai, X. Zhou, J. Kuttner, G. Hilt, X. Shao, J. M. Gottfried, K. Wu, *Nat. Chem.* **2015**, *7*, 389–393.

[275] D. J. Klein, M. J. Cravey, G. E. Hite, *Polycycl. Aromat. Comp.* **1991**, *2*, 163–182.

[276] Q. Fan, S. Werner, J. Tschakert, D. Ebeling, A. Schirmeisen, G. Hilt, W. Hieringer, J. M. Gottfried, *J. Am. Chem. Soc.* **2018**, *140*, 7526–7532.

[277] B. T. King, J. Kroulík, C. R. Robertson, P. Rempala, C. L. Hilton, J. D. Korinek, L. M. Gortari, *J. Org. Chem.* **2007**, *72*, 2279–2288.

[278] K. Morimoto, D. Koseki, T. Dohi, Y. Kita, *Synlett* **2017**, *28*, 2941–2945.

[279] A. Haags, A. Reichmann, Q. Fan, L. Egger, H. Kirschner, T. Naumann, S. Werner, T. Vollgraff, J. Sundermeyer, L. Eschmann, X. Yang, D. Brandstetter, F. C. Bocquet, G. Koller, A. Gottwald, M. Richter, M. G. Ramsey, M. Rohlfing, P. Puschnig, J. M. Gottfried, S. Soubatch, F. S. Tautz, *ACS Nano* **2020**, *14*, 15766–15775.

[280] M. B. Goldfinger, K. B. Crawford, T. M. Swager, *J. Am. Chem. Soc.* **1997**, *119*, 4578–4593.

[281] A. Fürstner, V. Mamane, *J. Org. Chem.* **2002**, *67*, 6264–6267.

[282] C. D. Simpson, J. D. Brand, A. J. Berresheim, L. Przybilla, H. J. Räder, K. Müllen, *Chem. Eur. J.* **2002**, *8*, 1424–1429.

[283] H. Zhou, J. Liu, S. Du, L. Zhang, G. Li, Y. Zhang, B. Z. Tang, H.-J. Gao, *J. Am. Chem. Soc.* **2014**, *136*, 5567–5570.

[284] H. A. Wegner, H. Reisch, K. Rauch, A. Demeter, K. A. Zachariasse, A. de Meijere, L. T. Scott, *J. Org. Chem.* **2006**, *71*, 9080–9087.

[285] S. Geng, J. Zhang, S. Chen, Z. Liu, X. Zeng, Y. He, Z. Feng, *Org. Lett.* **2020**, *22*, 5582–5588.

[286] S. Werner, T. Vollgraff, J. Sundermeyer, *Angew. Chem. Int. Ed.* **2021**, *60*, 13631–13635.

[287] N. Buffet, E. Grelet, H. Bock, *Chem. Eur. J.* **2010**, *16*, 5549–5553.

[288] Y. Sakamoto, T. Suzuki, *J. Am. Chem. Soc.* **2013**, *135*, 14074–14077.

[289] B. Song, Z. Zhang, K. Wang, C.-H. Hsu, O. Bolarinwa, J. Wang, Y. Li, G.-Q. Yin, E. Rivera, H.-B. Yang, C. Liu, B. Xu, X. Li, *Angew. Chem. Int. Ed.* **2017**, *56*, 5258–5262.

7 Appendix

In the appendix, NMR spectra as well as supplementary UV-Vis, PL and CV measurements of the corresponding publications and manuscripts is shown.
Only those parts of the supplementary informations are shown, which are part of my doctoral thesis and which were performed by myself within this thesis. Chapters of each supporting information, which have been contributed by co-authors are not shown within this context but described before each shown supporting information.

7.1 Supporting Information of Publication 1

The chapter *Single crystal X-ray structures* of the supporting information of Publication 1 is not shown in the following.
This was done by T. Vollgraff and is part of his doctoral thesis.
Also, the XYZ coordinates for DFT-optimized structures are not reprinted and can be retrieved from the online version of the supporting information.

Angewandte Chemie
Eine Zeitschrift der Gesellschaft Deutscher Chemiker

Supporting Information

Access to Functionalized Pyrenes, Peropyrenes, Terropyrenes, and Quarterropyrenes via Reductive Aromatization

*Simon Werner, Tobias Vollgraff, and Jörg Sundermeyer**

anie_202100686_sm_miscellaneous_information.pdf

Contents

Materials and Methods

All preparative operations were conducted by using standard Schlenk techniques and solvents were dried according to common procedures[1] and passed through columns of aluminium oxide, 3 Å molecular sieves and R3-11G-catalyst (BASF) or stored over molecular sieves (3 Å or 4 Å).
The data collection for the single-crystal structure determination was performed on a Stoe Stadivari by the X-ray service of Fachbereich Chemie, Universität Marburg. Information concerning the used hardware, and software used for data collection, cell refinement and data reduction as well as structure refinement can be reviewed in the electronic supplement tables and CCDC 2055267 – 2055269. After solution (SHELXT)[2] and refinement process (SHELXL 2017/1)[3] the data were validated by using Platon.[4] All graphic representations were created with Diamond 4.[5]
^{1}H and proton decoupled ^{13}C-NMR spectra were recorded in automation or by the service department of Fachbereich Chemie with a Bruker Avance II 300 spectrometer, a Bruker Avance II HD 300 or Avance III 500 spectrometer. All spectra were recorded at ambient temperature, if not mentioned otherwise. ^{1}H and ^{13}C NMR spectra were calibrated using residual proton signals of the solvent (CD_2Cl_2: δ_H = 5.32 ppm, δ_C = 53.84 ppm, $CDCl_3$: δ_H = 7.26 ppm, δ_C = 77.16 ppm). Multiplicity is abbreviated as follows: s (singlet), d (doublet), t (triplet), q (quartet), qt (quintet), m (multiplet), br. HR-APCI mass spectra were acquired with a LTQ-FT Ultra mass spectrometer (Thermo Fischer Scientific). The resolution was set to 100.000. HR-EI mass spectra were acquired with an AccuTOF GCv 4G (JEOL) Time of Flight (TOF) mass spectrometer. An internal or external standard was used for drift time correction. The LIFDI ion source and FD-emitters were purchased from Linden ChroMasSpec GmbH (Bremen, Germany). IR spectra were recorded in a glovebox on a Bruker Alpha ATR-FT-IR spectrometer.
Reverse Phase high-performance liquid chromatography coupled with mass spectrometry (HPLCMS) was used for estimation of product purity of Suzuki coupling products **9**, **10**, **S2** and **S7**. The spectra were recorded on a 1260 Infinity (Agilent) HPLC-system coupled with an Expression S CMS (Advion) mass spectrometer.
Absorption spectra were recorded with a Avance AvaSpect 2048 UV/Vis/NIR spectrophotometer in 10 mm cuvettes in dichloromethane in a nitrogen filled glovebox (Labmaster 130, mBraun) with a scan rate of 600 nm/min. Emission spectra were recorded with a Varian Cary Eclipse Spectrophotometer in 10 nm cuvettes in dichloromethane with a scan rate of 600 nm/min.
Fluorescence quantum yields (Φ_{PL}) were recorded by dilution method using a fluorescein solution (0.1 M in aqueous NaOH, Φ_{flu} = 0.95)[6] as reference. Both, the samples and the reference were measured at low concentrations in order to ensure a linear relationship between the intensity of emitted light and the concentration of the absorbing/emitting species. The quantum yields of the samples (Φ_s) were determined by the following equation 1.[6]

$$\Phi_{flu} = \frac{grad(s)}{grad(flu)} * \frac{n^2(s)}{n^2(flu)} * \Phi_{flu}$$

In equation 1, *grad* is the slope of the “emission versus absorbance” plot of the amples (s) and the standard fluorescein (flu). n is the refractive index of the used solvents.
Cyclic voltammetry (CV) and differential pulse voltammetry (DPV) measurements were carried out on a rhd instruments TSC 1600 closed electrochemical workstation (working electrode: glassy carbon; counter electrode: platinum crucible; reference electrode: platinum wire (pseudo reference electrode under nitrogen atmosphere in a glovebox (Labmaster 130, mBraun). The samples were measured in dichloromethane (concentration: 5 mmol/L) and calibrated using ferrocene as internal standard after measurements. Dichloromethane was filtered through an aluminum oxide pad prior to use. Tetrabutylammonium hexafluorophosphate ($TBAPF_6$; >99.0 %) was used as electrolyte for electrochemical analysis. The measurements were carried out at a concentration of 100 mmol/L of electrolyte.

Additional experimental data for synthesis

*Synthesis of a butyl-substituted quarteropyrene-trimethylsilyl ether (**S4**)*

As first attempt for the synthesis of a soluble quarteropyrene tetra-silylether, we synthesized a quarteropyrene trimethylsilylether (**S4**), terminal functionalized with *n*-butyl groups (see scheme S1). The synthesis route is analogous as discussed in the main text. As a first step, we reacted binaphthyl-bisboronic acid pinacolester with 6-bromo-2-butyl-3-hydroxy-1*H*-phenalen-1-one (**S1**) to form quarternaphthyl **S2** in moderate yields (37%). **S2** shows a slightly improved solubility in comparison with its non-butylated congener **10**, so a purification by column chromatography was possible. Nevertheless, the cyclodehydrogenated reaction product **S3** from the CsOH-melt air oxidation reaction of **S2**, was as insoluble as the non-butylated counterpart **12**. In a final step, **S3** was reacted with Zn and TMSCl to form silylether **S4**, proceeding with a yield (14% over 2 steps) comparable to the in the main text discussed reductive silylations of terropyrenequinone **11** and quarterropyrenequinone **12**. The solubility of **S4** in organic solvents as chloroform is moderate, so the acquisition of a proton NMR spectra was possible at elevated temperature (50 °C), but no 13C NMR or single crystals for XRD measurements could be obtained. It can be concluded that **S4** is less soluble than quarteropyrene triisopropylsilylether **15**, meaning that the TIPS groups prevent the quarteropyrene core much better from π-π-stacking interactions than butyl groups in combination with a TMS-substitution.

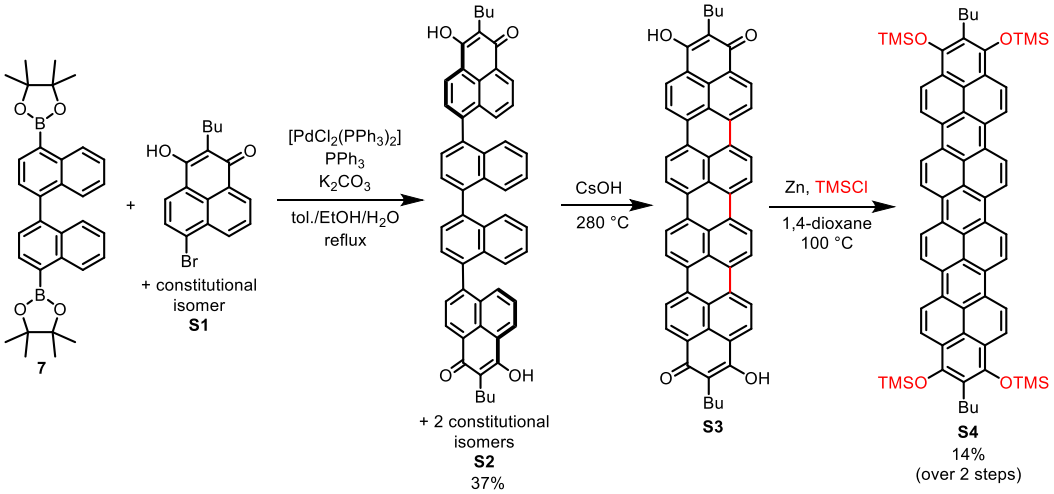

Scheme S1. Synthetic route towards butyl-substituted quarterropyrene trimethylsilyl ether **S4**.

S4 shows an absorption maximum at 634 nm in DCM with a nearly equal UV-Vis-NIR spectrum in comparison to **15**. The broadened bands in comparison to lighter homologue trimethylsilyl ethers indicate the weak solubility of **S4**. The cyclic voltammogram in DCM shows two reduction waves (-2.00 V and -1.82 V vs. Fc/Fc^+) and two oxidation waves (0.24 V and 1.24 V vs. Fc/Fc^+), none of them being fully reversible (figure S1).

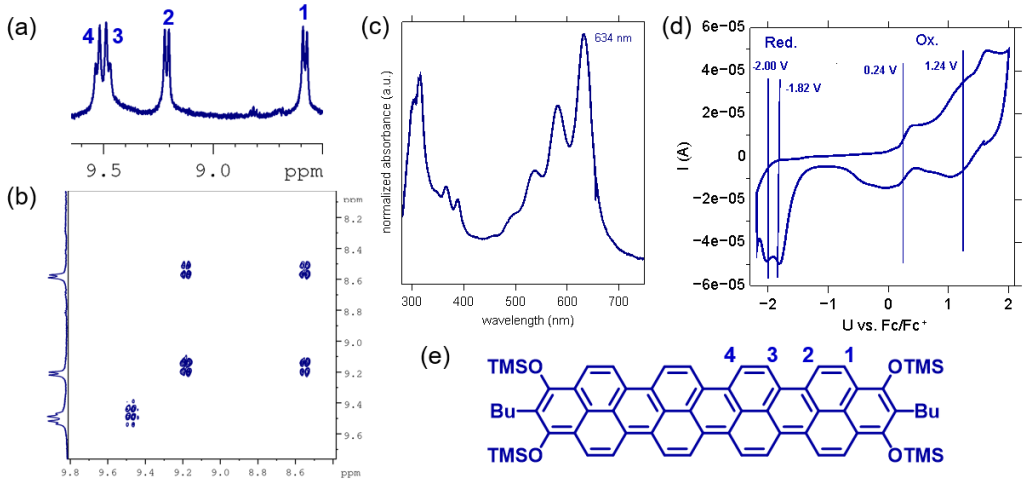

Figure S1. (a) Aromatic region of ^1H NMR spectrum of **S4** in $CDCl_3$ (323 K, 500 MHz); (b) COSY-NMR (500 MHz, $CDCl_3$) of the aromatic region of **S4**; (c) UV-Vis spectrum of **S4** measured in DCM; (d) cyclic voltammogram of **S4** in DCM (Scan rate 50 mV/s, electrolyte: $n Bu_4NPF_6$, vs. Fc/Fc^+); (e) chemical structure of **S4** with assigned aromatic protons from NMR.

Attempts for the reductive aromatization towards penteropyrenes

The strategy of terminal butyl functionalization was also applied in the case of the synthesis of a penteropyrene, the higher homologue of quarteropyrene (Scheme S2). Therefore, ternaphthyl-bis boronic acid pinacolester **S6** as central building block was synthesized by a Suzuki Miyaura cross coupling of 1,4-dibromonaphthalene (**S4**) in excess (3 eq) with naphthalene bis boronic acid pinacolester **6**, leading to dibromo-ternaphthyl **S5** in moderate yield (40%). **S5** was subsequently converted to **S6** by Miyaura borylation. **S6** could be analogously to the binaphthyl congener **7** reacted with hydroxy-phenalenone **S1** to the non-planar pentanaphthyl **S7**, which could be isolated in good yields (70%). The following cyclodehydrogenative oxidation led to the black powder **S8**. Suffering even more from insolubility than quarterropyrenequinone **S3**, the penterropyrenequinone-analogue **S8** did not react in silylation reactions, even treatment with Zn, TIPSCl in the presence of imidazole under reflux in dioxane did not lead to a detectable product formation by mass spectrometry. The only evidence for traces of conversion of **S8** was a slightly dark green colored DCM solution after extraction the residue and filtration, eventually indicating a red shifted absorption maximum with respect to the dark blue colored lighter homologue quarteropyrene.

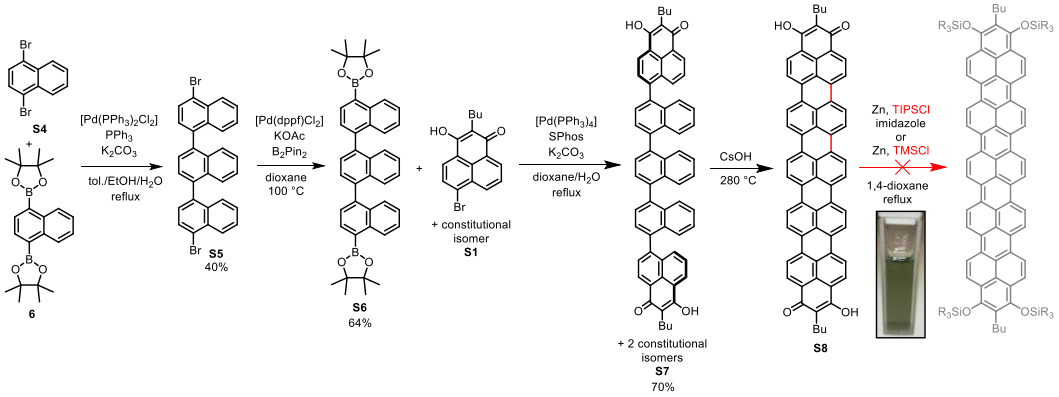

Scheme S2. Attempted synthetical route towards penterropyrenes**.**

Concentration-dependent UV-Vis-NIR spectra

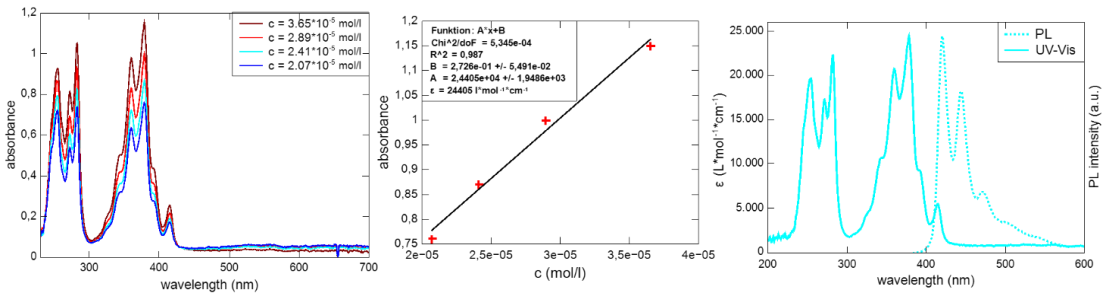

Figure S2. Left: UV-Vis-NIR spectra of pyrene **5** at four different concentration, recorded in CH_2Cl_2. Center: plot of the absorbance at λ_{max} versus the corresponding concentration to determine the molecular decadic attenuation coefficient ε from the slope (optical pass length = 1 cm). Right: UV-Vis-NIR and fluorescence spectrum shown in comparison.

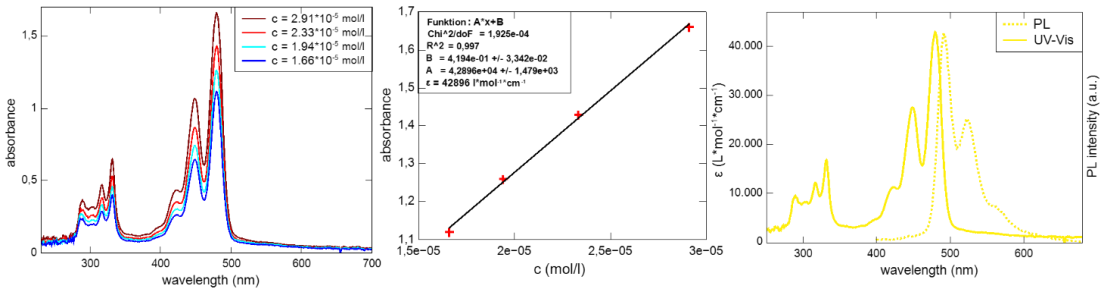

Figure S3. Left: UV-Vis-NIR spectra of peropyrene **4** at four different concentration, recorded in CH_2Cl_2. Center: plot of the absorbance at λ_{max} versus the corresponding concentration to determine the molecular decadic attenuation coefficient ε from the slope (optical pass length = 1 cm). Right: UV-Vis-NIR and fluorescence spectrum shown in comparison.

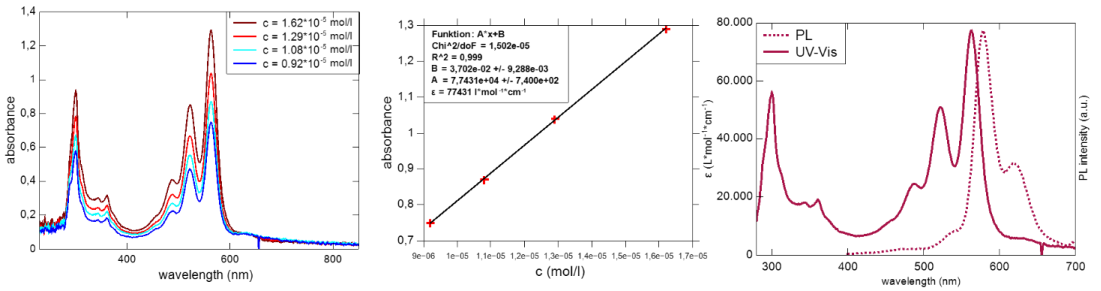

Figure S4. Left: UV-Vis-NIR spectra of terropyrene **13** at four different concentration, recorded in CH_2Cl_2. Center: plot of the absorbance at λ_{max} versus the corresponding concentration to determine the molecular decadic attenuation coefficient ε from the slope (optical pass length = 1 cm). Right: UV-Vis-NIR and fluorescence spectrum shown in comparison.

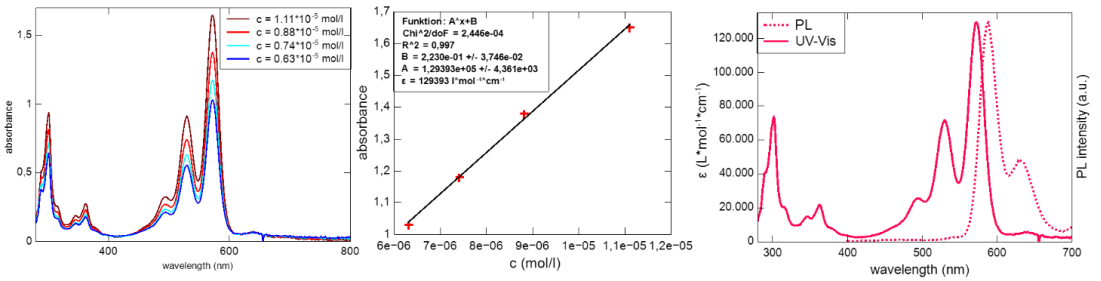

Figure S5. Left: UV-Vis-NIR spectra of terropyrene **14** at four different concentration, recorded in CH_2Cl_2. Center: plot of the absorbance at λ_{max} versus the corresponding concentration to determine the molecular decadic attenuation coefficient ε from the slope (optical pass length = 1 cm). Right: UV-Vis-NIR and fluorescence spectrum shown in comparison.

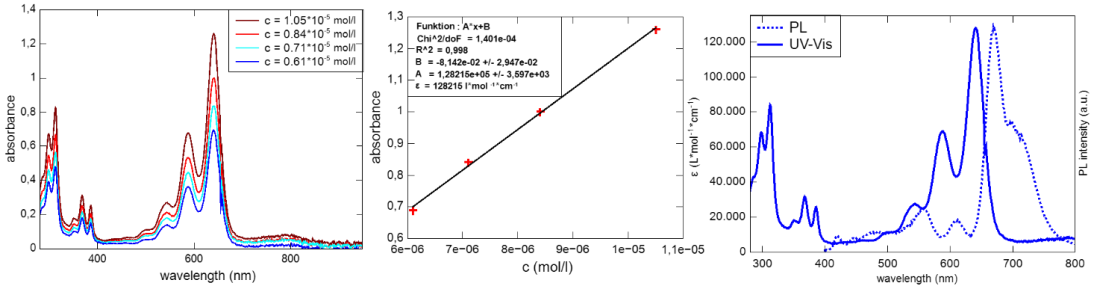

Figure S6. Left: UV-Vis-NIR spectra of quarterropyrene **15** at four different concentration, recorded in CH_2Cl_2. Center: plot of the absorbance at λ_{max} versus the corresponding concentration to determine the molecular decadic attenuation coefficient ε from the slope (optical pass length = 1 cm). Right: UV-Vis-NIR and fluorescence spectrum shown in comparison.

Determination of fluorescence quantum yields

In the following figure S7, the “emission versus absorbance” plots and the linear regression graphs for the determination of the fluorescence quantum yields of **4**, **13** and **14** as well as the standard fluorescein are shown. Note that in the case of triisopropylsilyl-substituted **5** and **15**, the emission values at suitable low concentrations were too low to determine fluorescence quantum yields.

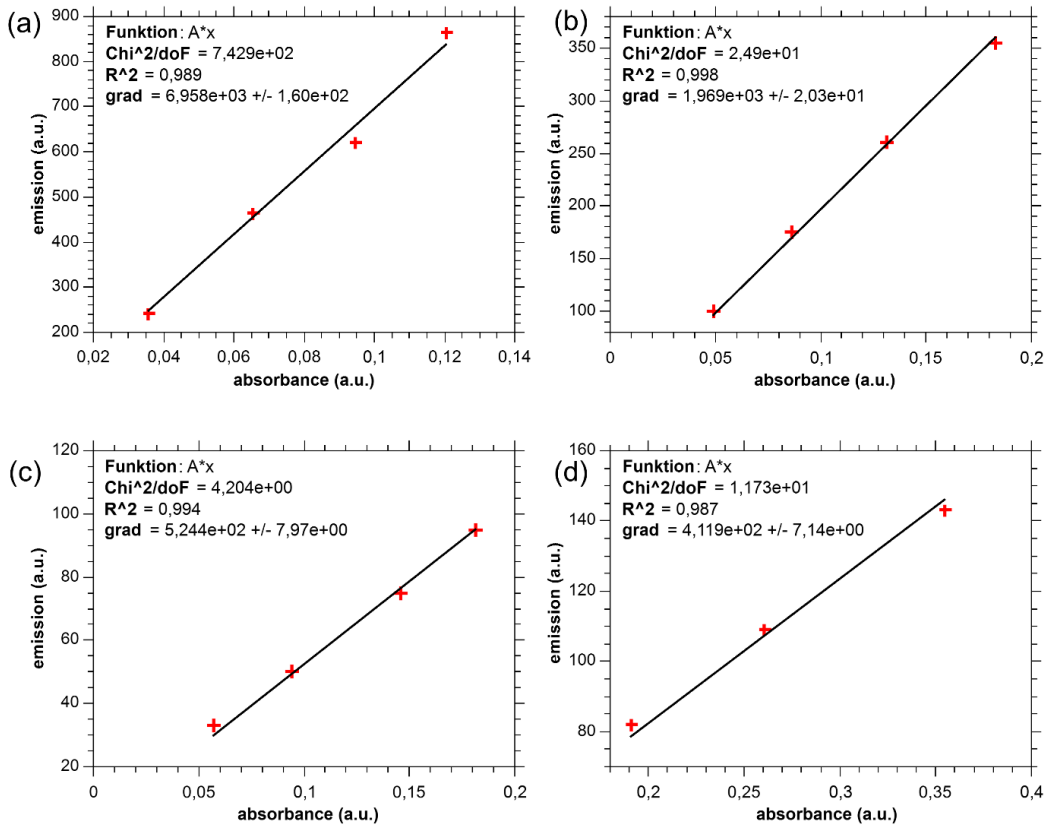

Figure S7. “emission versus absorption” plots of (a) reference fluorescein in 0.1 M NaOH solution; (b) compound **4** in dichloromethane; (c) compound **13** in dichloromethane and (d) compound **14** in dichloromethane. The concentrations were in the low 10^{-6} M range.

Comparison of TMS vs. TIPS substituted terropyrene

In order to verify whether a simplification of a TIPS-group by the smaller TMS-group is justified to simplify DFT calculations, we compared the optical and electrochemical properties of terropyrene trimethylsilyl ether **13** and terropyrene triisopropylsilyl ether **14** (figure S8). It can be clearly noted, that the UV-Vis and photoluminescence show only minor alterations. TIPS ether **14** is about 10 nm bathocromically shifted with respect to TMS ether **13**. This leads to an experimental error of only 0.03 eV for the optical bandgap determination from the intersection wavelength of the normalized UV-Vis and photoluminescence spectra. The cyclovoltammogramms of **13** and **14** show almost identical oxidation halfwave potential voltages. Whereas the two oxidation waves of **14** are almost reversible, the oxidation waves of **13** possess a more irreversible character. This indicates a possible decomposition of the more labile TMS ether groups of **13**. The first oxidation halfwave potential, which is crucial for the experimental determination of the HOMO energy, alters only about 0.02 V, leading to an experimentally small error of 0.02 eV for the HOMO energy due to the simplification.

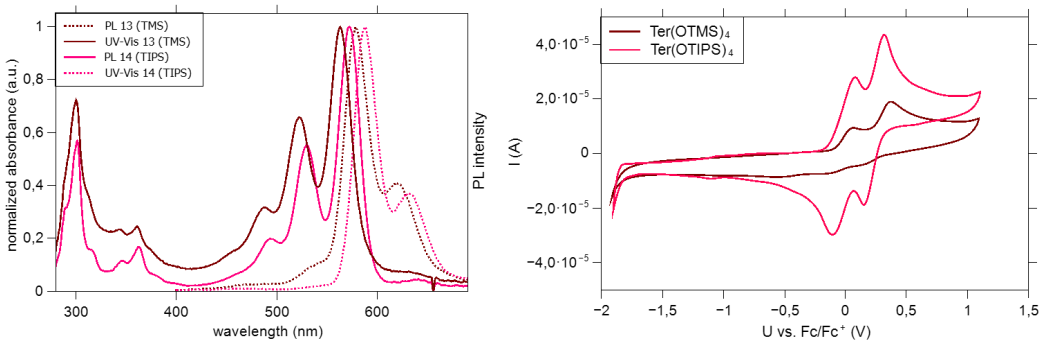

Figure S8. Left: Comparison of normalized UV-Vis-NIR spectra (solid lines) of **13** (red) and **14** (pink) and their corresponding photoluminescence spectra (dashed lines). Right: Comparison of the cyclovoltammogramms of **13** (red) and **14** (pink), referenced with ferrocene (measured in CH_2Cl_2, 0.1 M *n*-Bu_4NPF_6, 100 mV s^{-1} scan rate, glassy carbon working electrode, platinum reference electrode).

Cyclovoltammetry raw data and spectra referenced on ferrocene

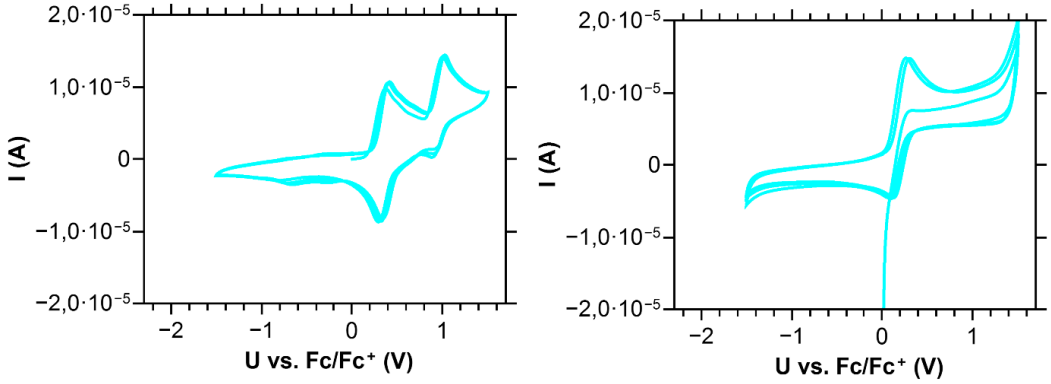

Figure S9. Left: Raw data of the cyclovoltammography of pyrene **5** (three scans were performed, the third one was used for analysis). Right: Cyclovoltammogramm of **5** after addition of 1 mM ferrocene (measured in CH_2Cl_2, 0.1 M *n*-Bu_4NPF_6, 100 mV s^{-1} scan rate, glassy carbon working electrode, platinum reference electrode).

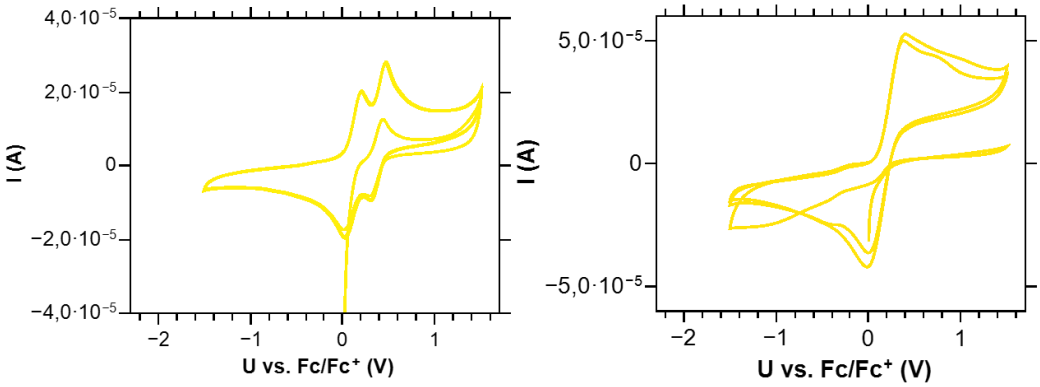

Figure S10. Left: Raw data of the cyclovoltammography of peropyrene **4** (three scans were performed, the third one was used for analysis). Right: Cyclovoltammogramm of **4** after addition of 1 mM ferrocene (measured in CH_2Cl_2, 0.1 M *n*-Bu_4NPF_6, 100 mV s^{-1} scan rate, glassy carbon working electrode, platinum reference electrode).

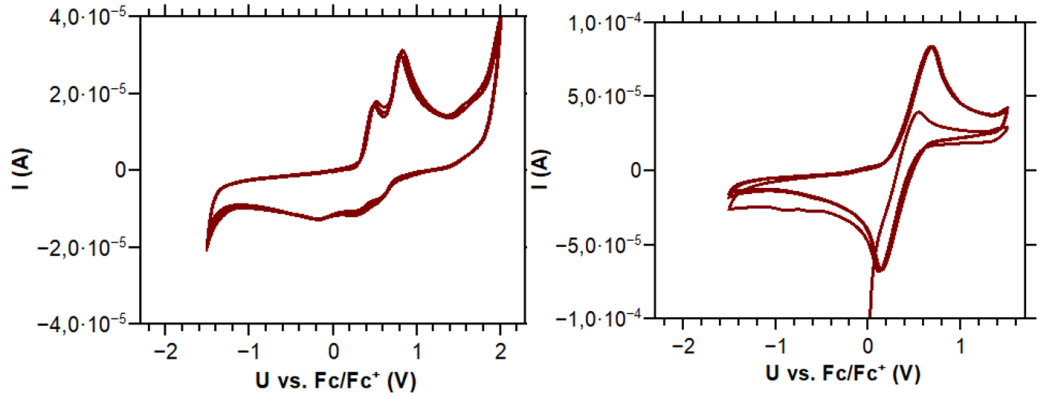

Figure S11. Left: Raw data of the cyclovoltammography of terropyrene **13** (three scans were performed, the third one was used for analysis). Right: Cyclovoltammogramm of **13** after addition of 1 mM ferrocene (measured in CH_2Cl_2, 0.1 M *n*-Bu_4NPF_6, 100 mV s^{-1} scan rate, glassy carbon working electrode, platinum reference electrode).

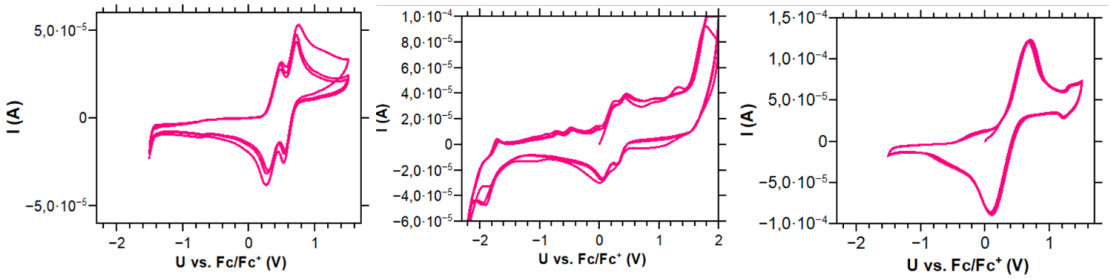

Figure S12. Left: Raw data of the cyclovoltammography of terropyrene **14** (three scans were performed, the third one was used for analysis). Center: Cyclovoltammogramm of **14** at larger voltage window to assign reduction potentials (note: this leads to decomposition of **14**). Right: Cyclovoltammogramm of **14** after addition of 1 mM ferrocene (measured in CH_2Cl_2, 0.1 M *n*-Bu_4NPF_6, 100 mV s^{-1} scan rate, glassy carbon working electrode, platinum reference electrode).

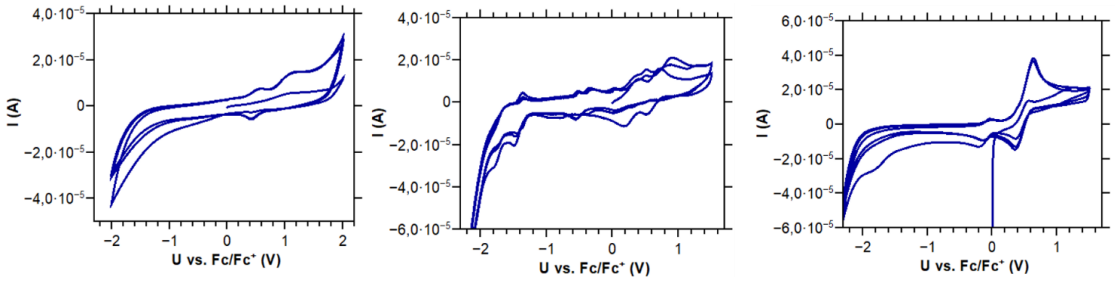

Figure S13. Left: Raw data of the cyclovoltammography of terropyrene **15** (three scans were performed, the third one was used for analysis). Center: Cyclovoltammogramm of **15** at larger voltage window to assign reduction potentials (note: this leads to decomposition of **15**). Right: Cyclovoltammogramm of **15** after addition of 1 mM ferrocene (measured in CH_2Cl_2, 0.1 M *n*-Bu_4NPF_6, 100 mV s^{-1} scan rate, glassy carbon working electrode, platinum reference electrode).

Density functional theory (DFT)

Density functional theory (DFT) calculations using the B3LYP[7] functional were performed. The def2-TZVPP[8,9] basis set was used with RIJCOSX auxiliary base set, employing the resolution-of-identity approximation.[9,10] For radical cation **[15-TMS]**$^+$, DFT calculations were performed using the CAM-B3LYP functional[11] with LANL2DZ base set.[12] Further D3-dispersion correction[13] was considered by applying Becke−Johnson damping.[14] Structural optimizations and TD-DFT calculations were performed using Orca 3.0.3.[15] The atomic coordinates for geometry optimization were taken from XRD structures, if possible. The structurally optimized molecules were used for TD-DFT calculations using the PBE functional[16] (PBE0-D3/def2-TZVPP), employing the resolution-of-identity approximation for both Coulomb integrals and HF exchange integrals.[17] For radical cation **[15-TMS]**$^+$, TD-DFT calculations were performed using the CAM-B3LYP functional with LANL2DZ base set.

Optimized geometries (XYZ-files)

Table S1. Cartesian coordinates (XYZ) of DFT optimized geometry of **5-TMS** (def-TZVPP/B3LYP).

C	-3.503569000	-0.056511000	-0.265835000
C	-2.796103000	-1.251619000	-0.355933000
C	-2.844943000	1.159476000	-0.109971000
C	-1.438855000	1.216686000	-0.092562000
C	-0.713071000	-0.010074000	-0.130621000
C	-1.392071000	-1.258853000	-0.234540000
C	0.717011000	0.013337000	-0.065335000
C	1.437840000	-1.215134000	-0.005917000
C	0.719113000	-2.449146000	-0.071848000
C	-0.632175000	-2.469578000	-0.204884000
C	-0.718399000	2.451127000	-0.048398000
C	0.639503000	2.474274000	-0.060533000
C	1.401176000	1.263917000	-0.061697000
C	2.809900000	1.256571000	-0.054724000
C	3.507929000	0.057302000	0.054022000
C	2.839878000	-1.161430000	0.105340000
O	-3.557155000	2.320582000	-0.020496000
Si	-4.742246000	2.785781000	1.069504000
C	-4.820507000	4.644403000	0.958564000
C	-4.301033000	2.237497000	2.802010000
C	-6.419968000	2.084209000	0.616569000
O	3.536889000	-2.328259000	0.221721000
Si	4.701968000	-2.799051000	1.330626000
C	4.735842000	-4.660458000	1.256844000
C	4.263527000	-2.214090000	3.052021000
C	6.399735000	-2.145937000	0.878740000
O	3.468781000	2.447030000	-0.119416000
Si	4.870960000	2.912841000	-0.908368000
C	4.861729000	4.774486000	-0.846201000
C	4.872332000	2.310350000	-2.678728000
C	6.406070000	2.283779000	-0.036951000
O	-3.435651000	-2.441527000	-0.526597000
Si	-4.813088000	-2.894332000	-1.363926000
C	-4.787935000	-4.757038000	-1.358240000
C	-4.781948000	-2.256255000	-3.121275000
C	-6.377530000	-2.301610000	-0.520557000

H	3.538467000	-13.381097000	-1.955125000
H	1.969260000	-12.733731000	-2.440611000
H	3.444697000	-11.793028000	-2.722753000
H	-0.336681000	-11.116153000	-0.691224000
H	0.459187000	11.045781000	0.238730000

TD-DFT calculations

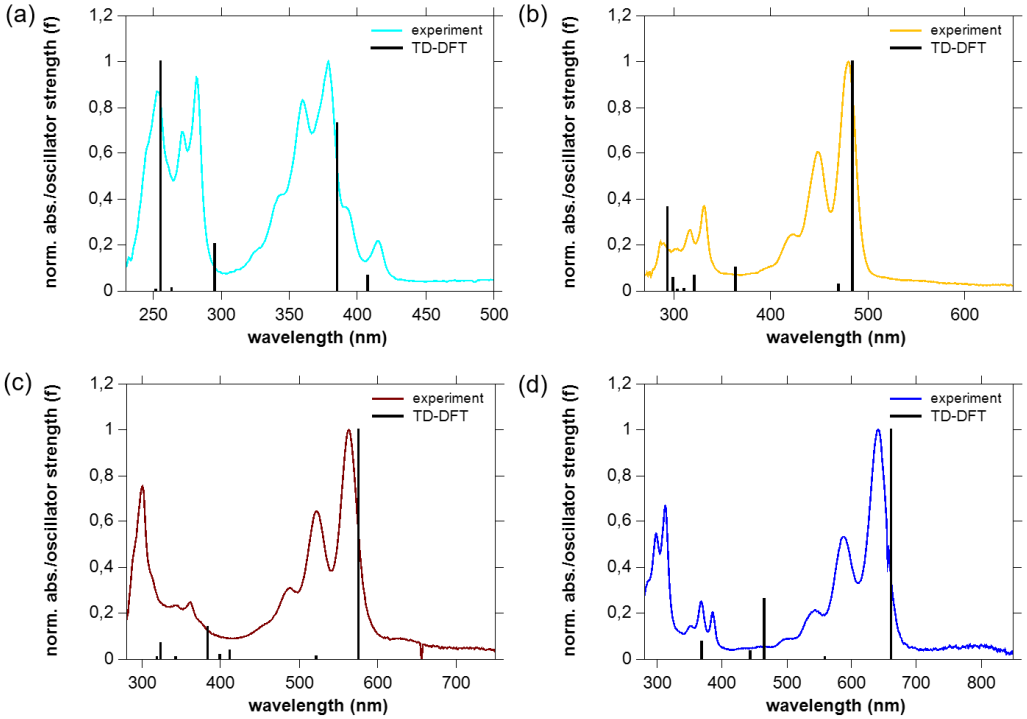

Figure S14. Comparison of normalized UV-Vis-NIR spectra (recorded in CH_2Cl_2) and normalized electron transitions calculated by TD-DFT (black bars, def-TZVPP/PBE level of theory) of a) pyrene **5-TMS**, b) peropyrene **4**, c) terropyrene **13** and d) quarterropyrene **15**.

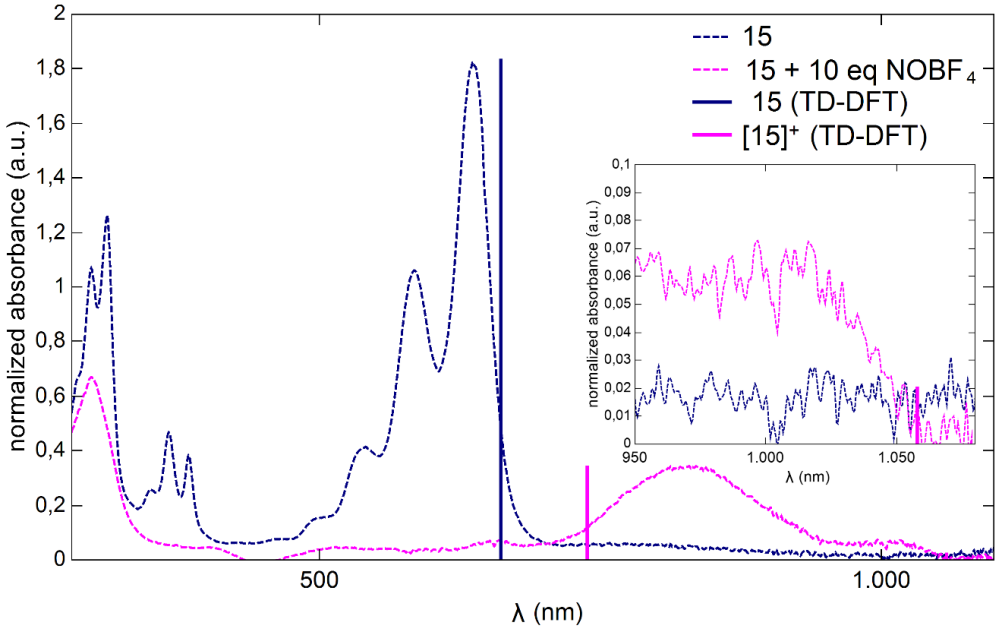

Figure S15. Comparison of normalized UV-Vis-NIR spectra of **15** (blue) and **15** after addition of 10 eq $NOBF_4$ (magenta), recorded in CH_2Cl_2/acetonitrile and main electron transitions calculated by TD-DFT (bars, normalized on absorption maxima) for **15-TMS** and radical cation **[15]**$^+$ (LANL2DZ/CAM-B3LYP level of theory).

Table S6. Characteristic main electron transition of **4**, **5**, **13** and **15**, calculated using TD-DFT (def2-TZVPP/PBE level of theory) and **[15]**$^+$ (LANL2DZ/CAM-B3LYP level of theory).

Compound	Transition energy (wavelength)	Oscillator strength	Description of main contributions
5-TMS	3.05 eV (407 nm)	0.054	HOMO→LUMO+1 (c = 0.915); 0.837 HOMO-1→LUMO (c = -0.368); 0.136 HOMO-2→LUMO+1 (c = 0.109); 0.012
	3.22 eV (385 nm)	0.626	HOMO→LUMO+1 (c = -0.916); 0.839 HOMO-1→LUMO+1 (c = -0.297); 0.088 HOMO-3→LUMO+2 (c = 0.160); 0.026 HOMO-2→LUMO+5 (c = 0.102); 0.011
4	2.56 eV (484 nm)	1.074	HOMO→LUMO (c = -0.929); 0.862 HOMO-2→LUMO+1 (c = -0.267); 0.071 HOMO-1→LUMO+3 (c = 0.115); 0.013 HOMO-4→LUMO+2 (c = -0.109); 0.012
13	2.15 eV (575 nm)	1.789	HOMO→LUMO (c = -0.937); 0.878 HOMO-3→LUMO (c = -0.140); 0.020 HOMO-2→LUMO (c = 0.219); 0.048 HOMO-1→LUMO+2 (c = -0.145); 0.021
15-TMS	1.85 eV (671 nm)	0.002	HOMO-1→LUMO (c = 0.735); 0.540 HOMO→LUMO+1 (c = -0.677); 0.459
	1.88 eV (661 nm)	2.458	HOMO→LUMO (c = -0.936); 0.875 HOMO-1→LUMO+1 (c = 0.179); 0.032 HOMO-3→LUMO (c = 0.179); 0.032 HOMO-2→LUMO+2 (c = -0.173); 0.030
[15]$^+$	1.17 eV (1057 nm)	0.110	SOMOβ→LUMOβ (c = -0.833), 0.693 SOMO-1β→LUMO+1β (c = -0.144), 0.021 SOMOα→LUMOα (c = -0.509), 0.259
	1.68 eV (739 nm)	2.729	SOMOβ→LUMOβ (c = -0.474), 0.225 SOMO-1β→LUMO+1β (c = -0.139), 0.019 SOMOα→LUMOα (c = 0.797), 0.635 SOMO-1α→LUMO+1α (c = 0.198), 0.039 SOMO-3α→LUMO+2α (c = 0.107), 0.012

NMR spectra

*1,4-bis(4,4,5,5-tetramethyl-1,3,2-dioxaborolan-2-yl)naphthalene (**6**)*

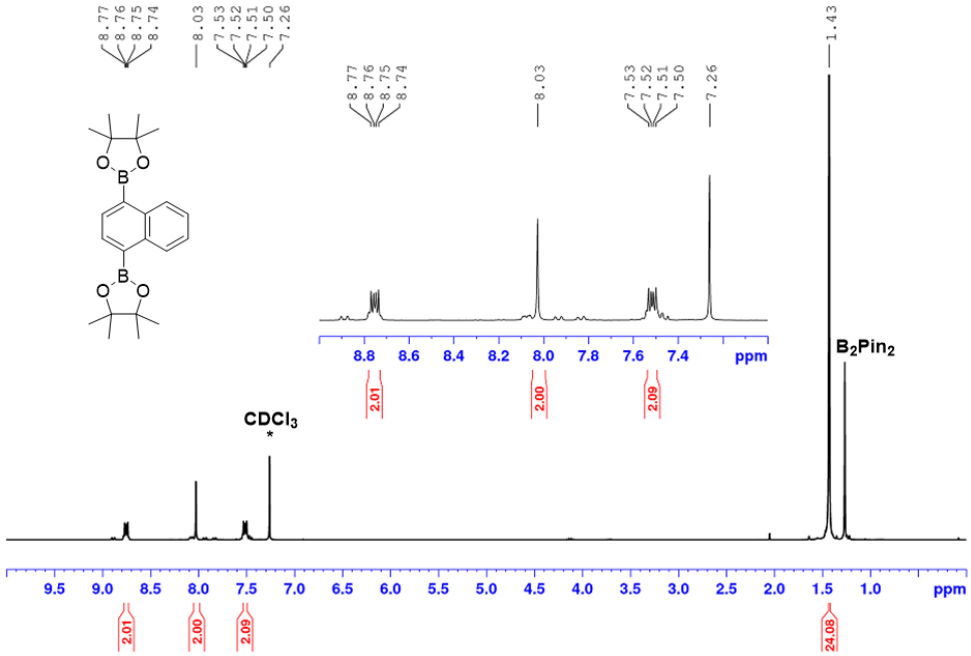

Figure S19. ^{1}H-NMR (300.1 MHz, 298K, $CDCl_3$*) of **6**, contains trace amounts (ca. 5%) of single borylated species.

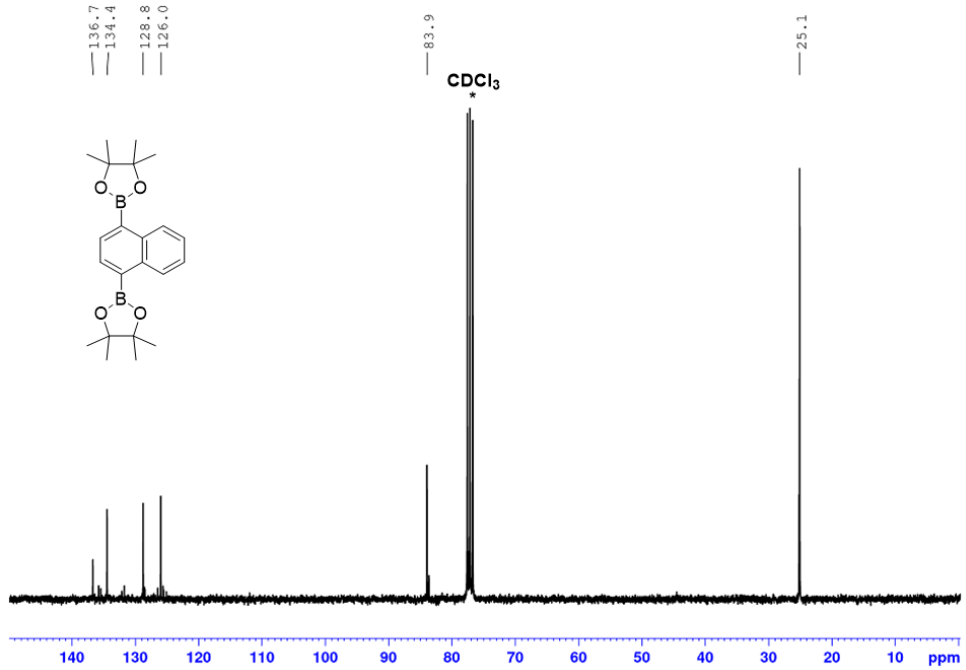

Figure S20. ^{13}C-NMR (75.5 MHz, 298K, $CDCl_3$*) of **6**, contains trace amounts (ca. 5%) of single borylated species.

*4,4'-dibromo-1,1'-binaphthyl (**S10**)*

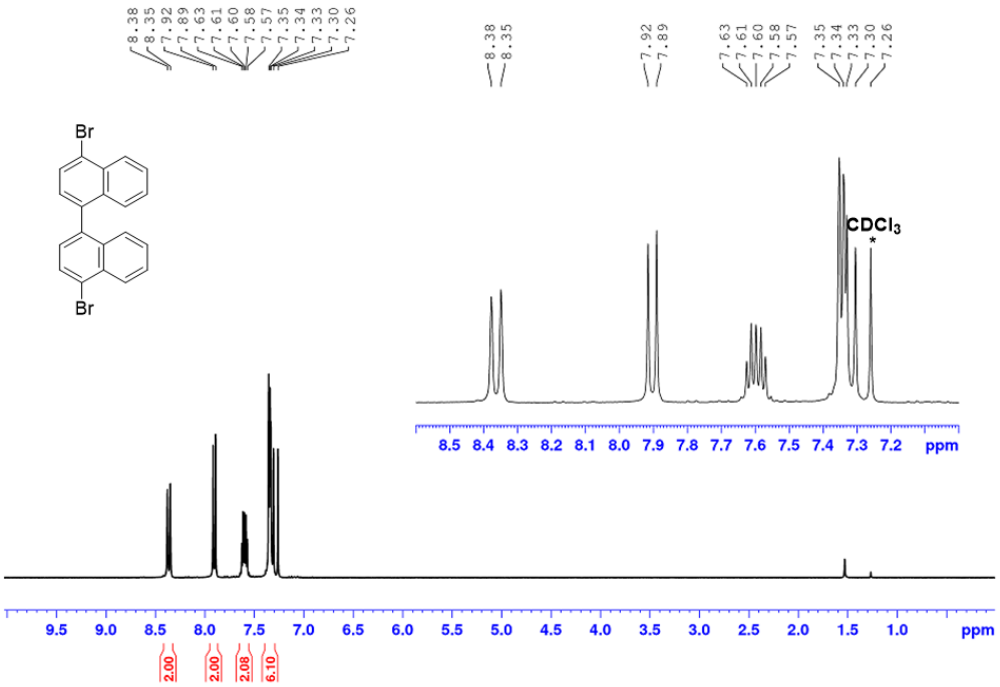

Figure S21. ^{1}H-NMR (300.1 MHz, 298K, $CDCl_3$*) of **S10**.

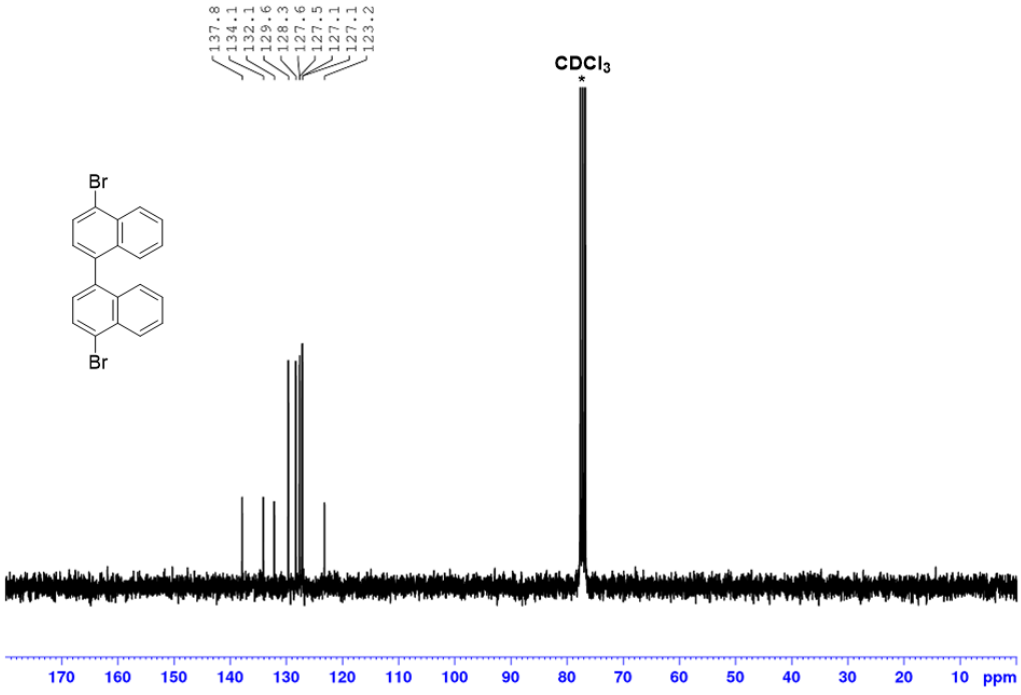

Figure S22. ^{13}C-NMR (75.5 MHz, 298K, $CDCl_3$*) of **S10**.

*4,4'-bis(4,4,5,5-tetramethyl-1,3,2-dioxaborolan-2-yl)-1,1'-binaphthalene (**7**)*

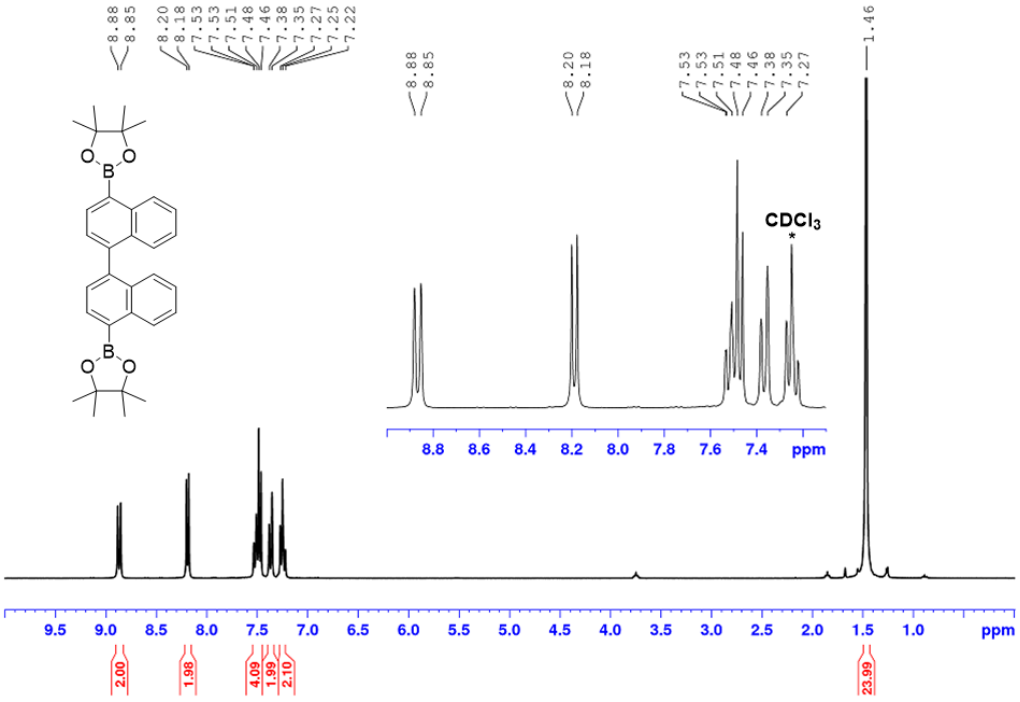

Figure S23. ^{1}H-NMR (300.1 MHz, 298K, $CDCl_3$*) of **7**.

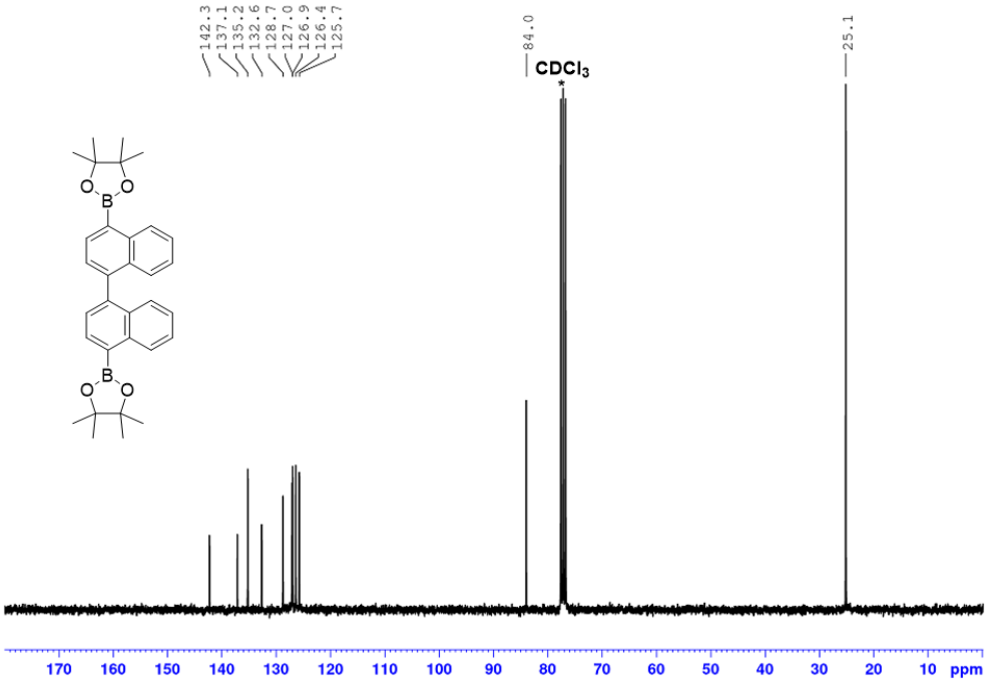

Figure S24. ^{13}C-NMR (75.5 MHz, 298K, $CDCl_3$*) of **7**.

*4,4''-dibromo-1,1':4',1''-ternaphthalene (**S5**)*

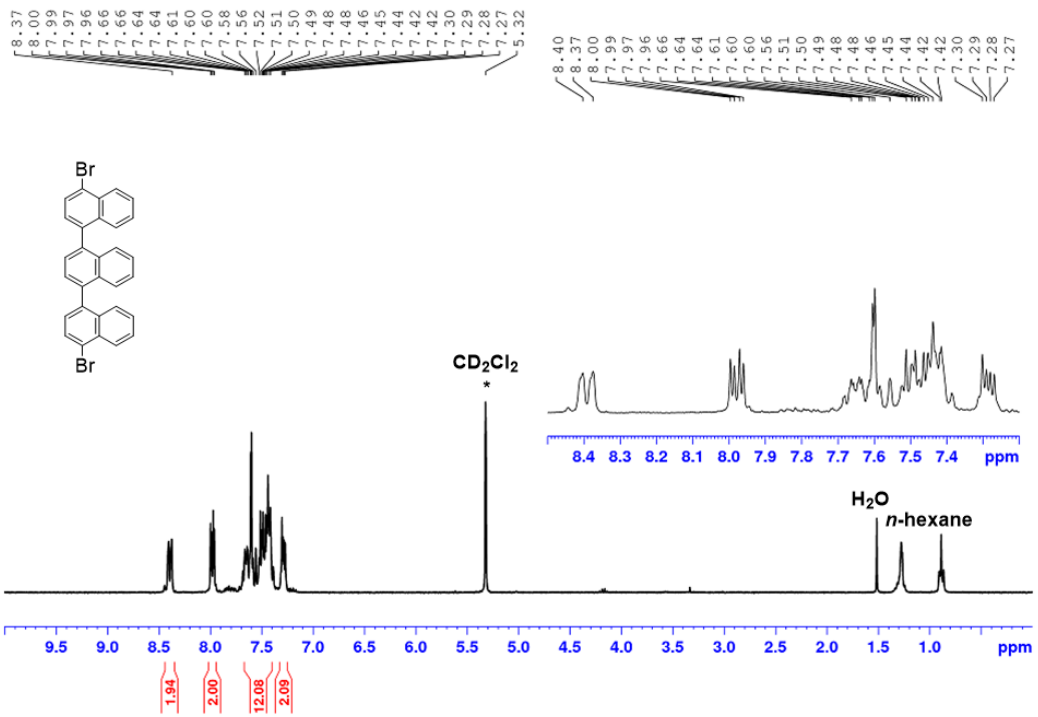

Figure S25. ^{1}H-NMR (300.1 MHz, 298K, CD_2Cl_2*) of **S5**.

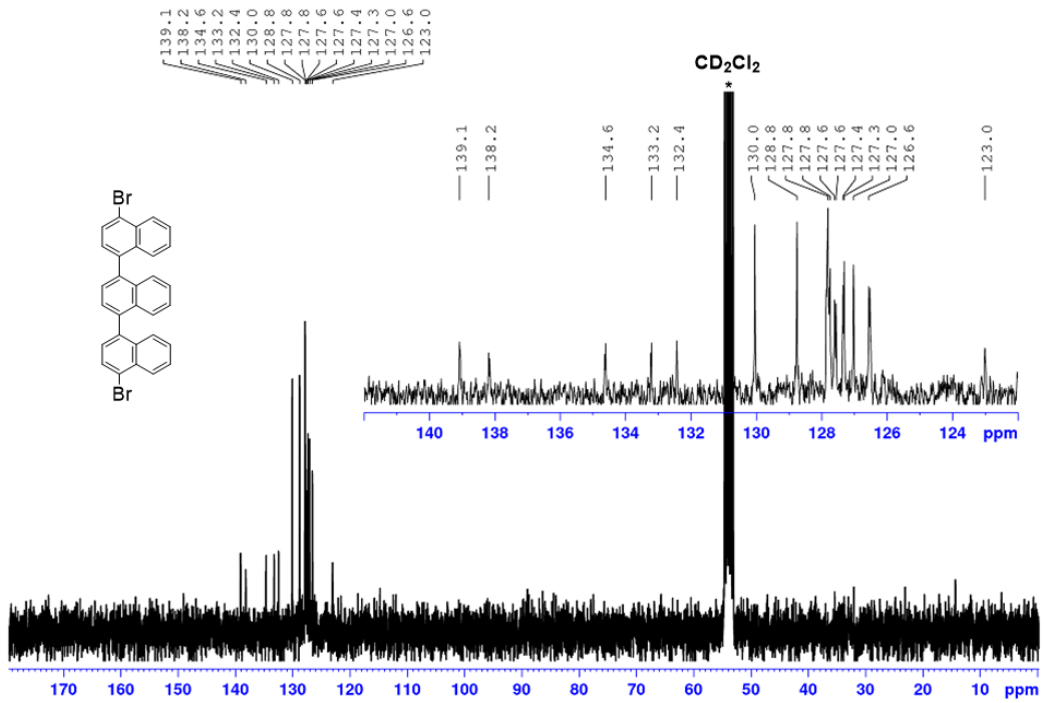

Figure S26. ^{13}C-NMR (75.5 MHz, 298K, $CDCl_3$*) of **S5**.

*4,4''-bis(4,4,5,5-tetramethyl-1,3,2-dioxaborolan-2-yl)-1,1':4',1''-ternaphthalene (**S6**)*

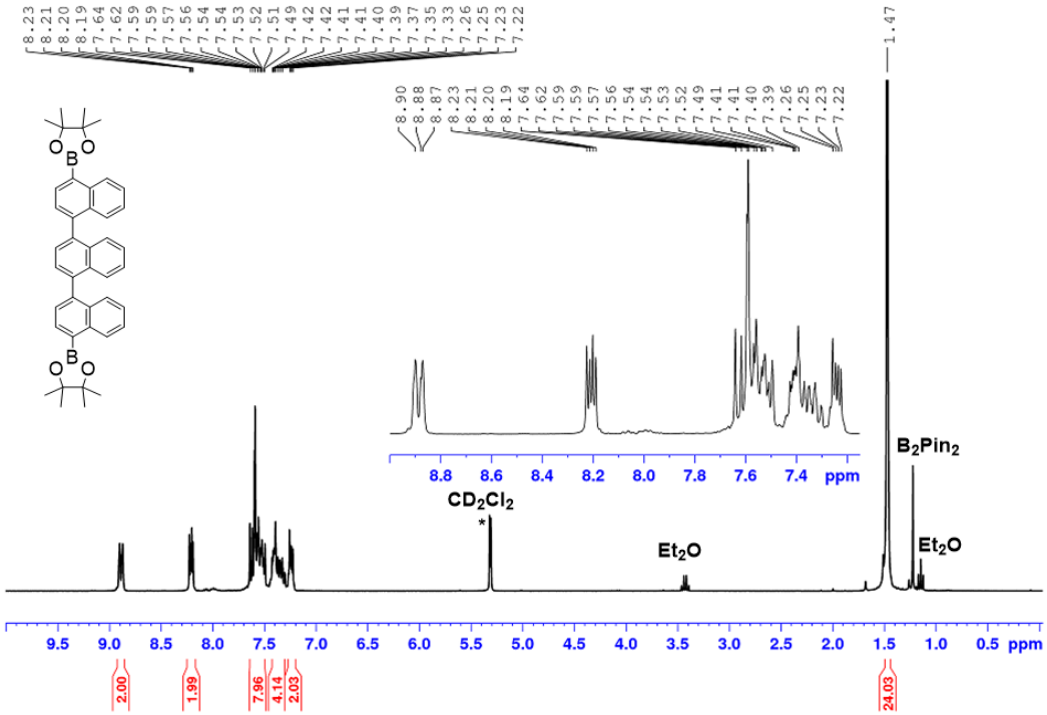

Figure S27. ^{1}H-NMR (300.1 MHz, 298K, CD_2Cl_2*) of **S6**.

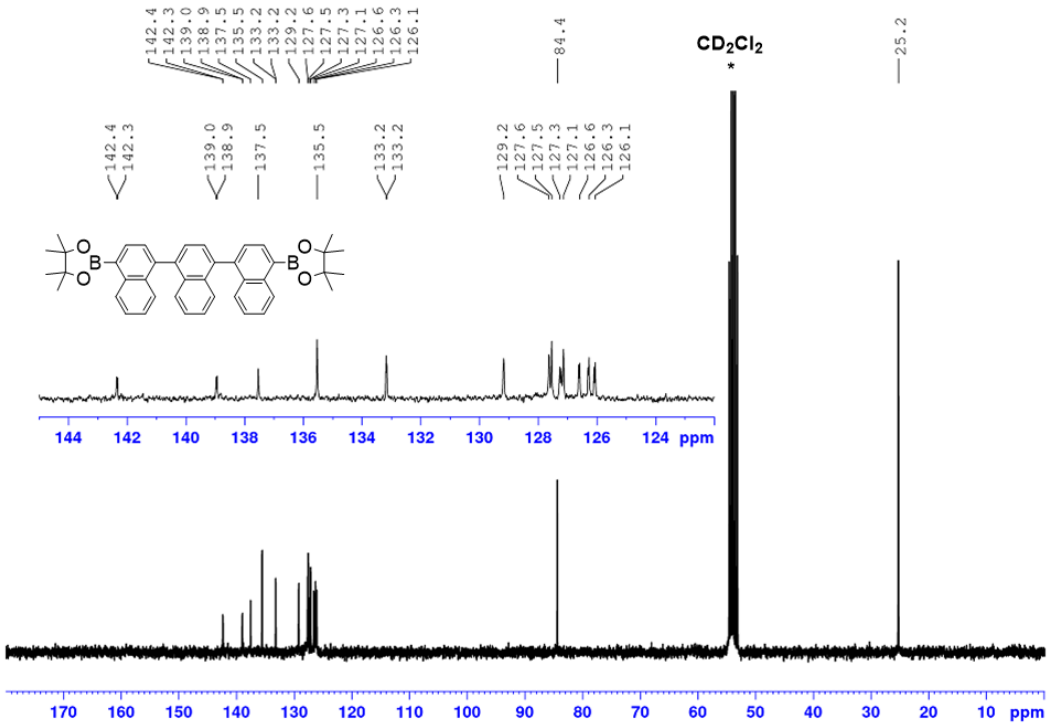

Figure S28. ^{13}C-NMR (75.5 MHz, 298K, $CDCl_3$*) of **S6**.

*6-bromo-3-hydroxy-1H-phenalen-1-one (**8**)*

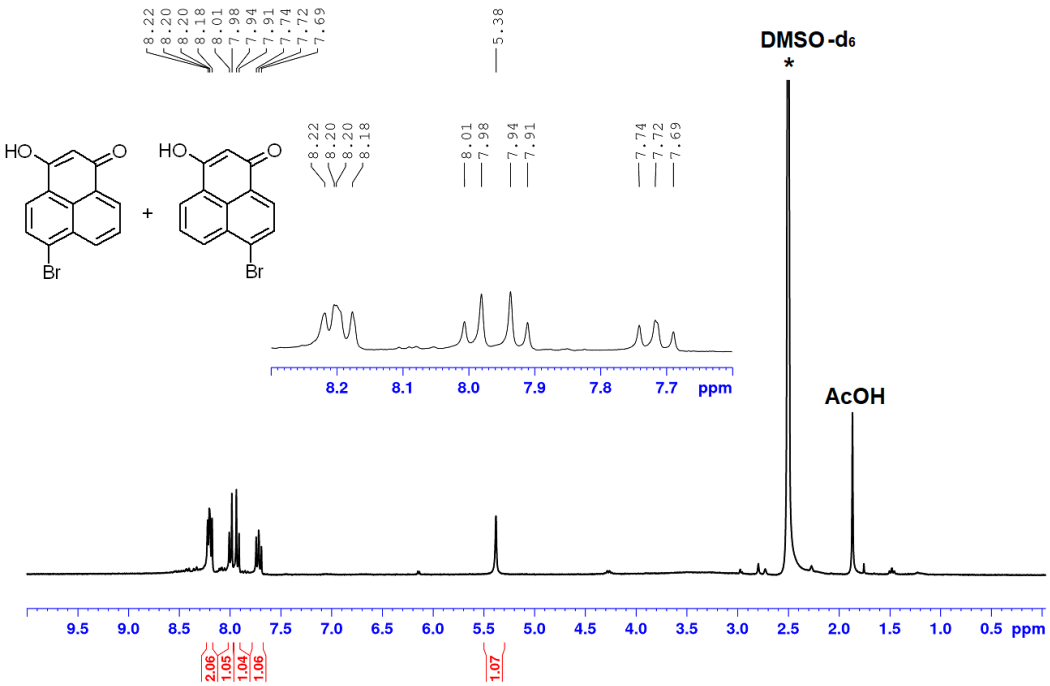

Figure S29. ^{1}H-NMR (300.1 MHz, 298K, DMSO-d_6*) of **8** (isomer mixture). Contains traces of acetic acid.

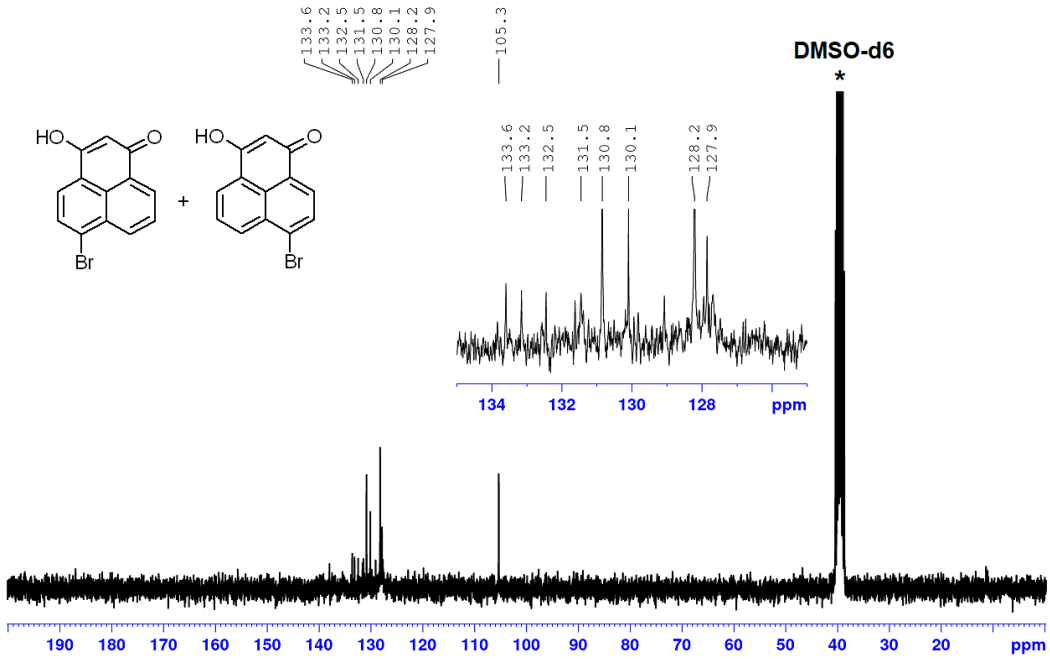

Figure S30. ^{13}C-NMR (75.5 MHz, 298K, DMSO-d_6*) of **8** (isomer mixture).

*6-bromo-2-butyl-3-hydroxy-1H-phenalen-1-one (**S1**)*

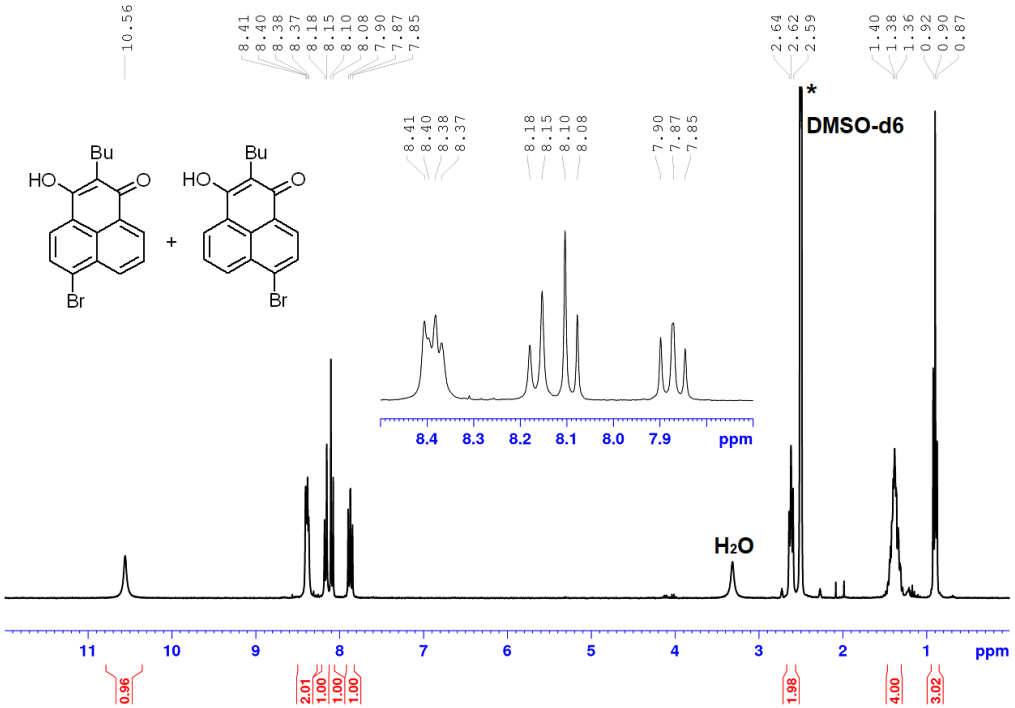

Figure S31. ^{1}H-NMR (300.1 MHz, 298K, DMSO-d_6*) of **S1** (isomer mixture).

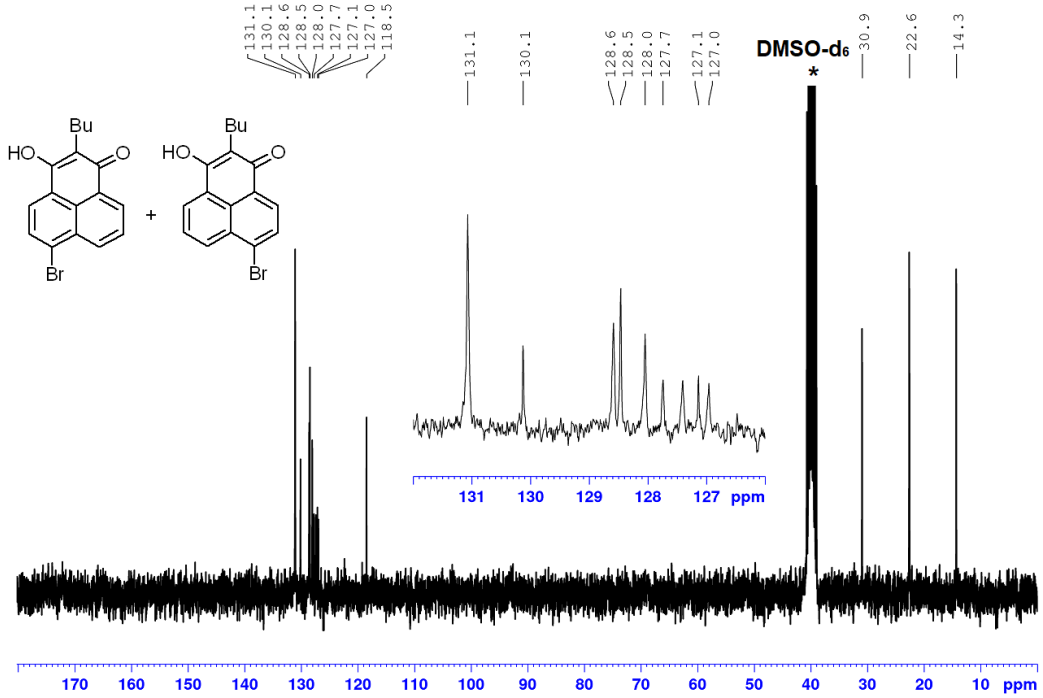

Figure S32. ^{13}C-NMR (75.5 MHz, 298K, DMSO-d_6*) of **S1** (isomer mixture).

*3-hydroxy-7-(4-(3-hydroxy-1-oxo-1H-phenalen-6-yl)naphthalen-1-yl)-1H-phenalen-1-one (**9**)*

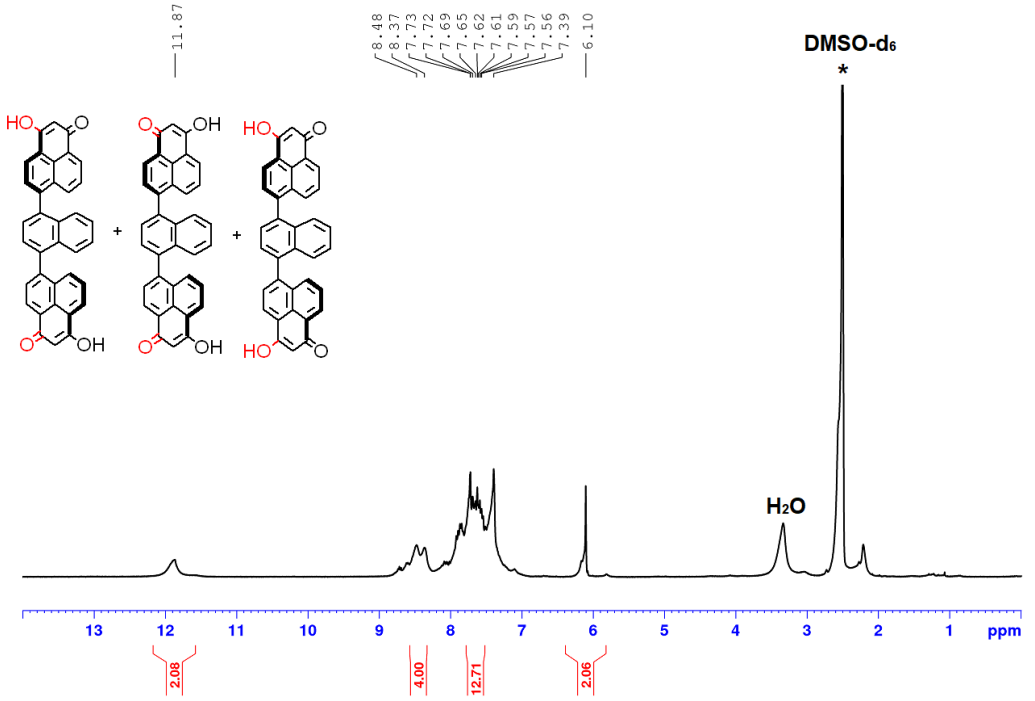

Figure S33. ^{1}H-NMR (300.1 MHz, 298K, DMSO-d_6*) of **9** (isomer mixture). Contains inseparable aromatic by-products.

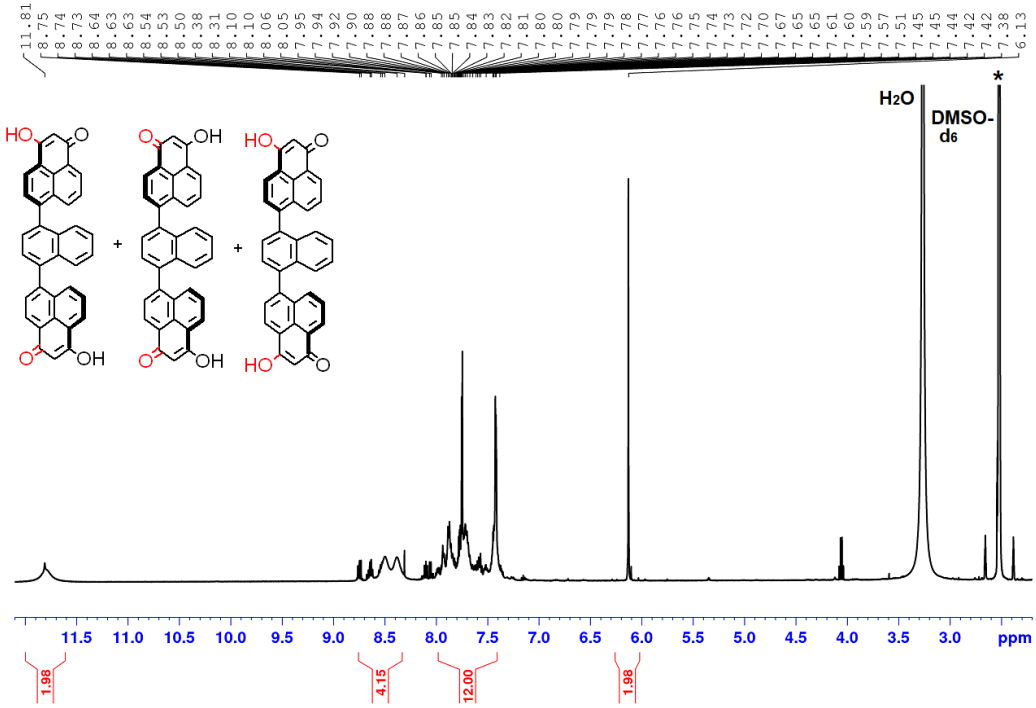

Figure S34. HT ^{1}H-NMR (500.1 MHz, 323K, DMSO-d_6*) of **9** (isomer mixture). Contains inseparable aromatic by-products.

*3-hydroxy-7-(4'-(3-hydroxy-1-oxo-1H-phenalen-6-yl)-[1,1'-binaphthalen]-4-yl)-1H-phenalen-1-one (**10**)*

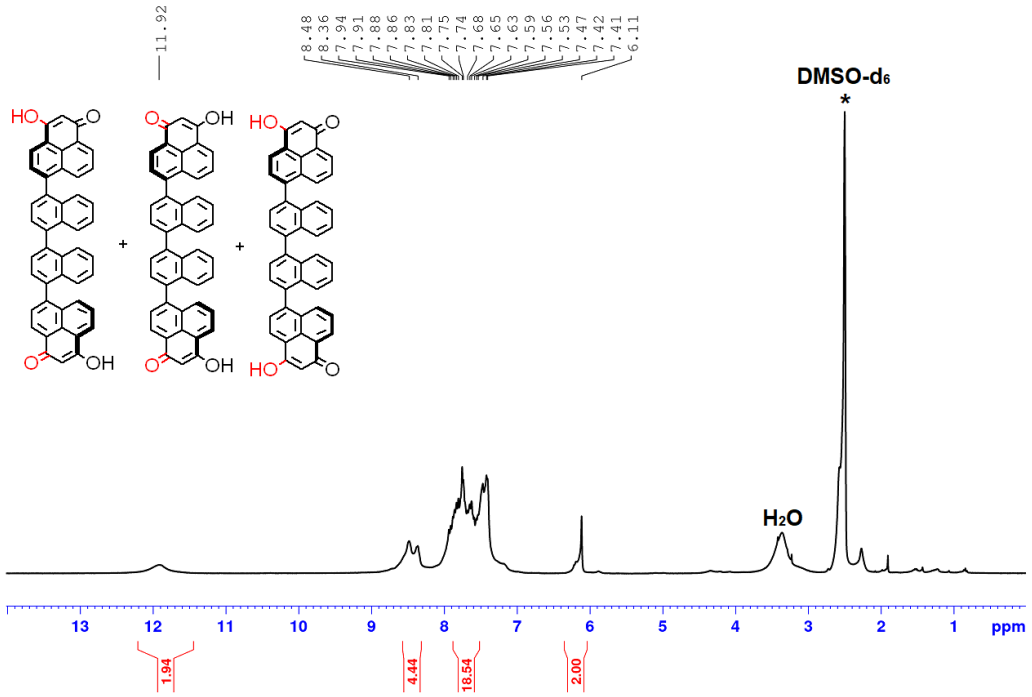

Figure S35. ^{1}H-NMR (300.1 MHz, 298K, DMSO-d$_6$*) of **10** (isomer mixture). Contains inseparable aromatic by-products.

*2-butyl-7-(4'-(2-butyl-3-hydroxy-1-oxo-1H-phenalen-6-yl)-[1,1'-binaphthalen]-4-yl)-3-hydroxy-1H-phenalen-1-one (**S2**)*

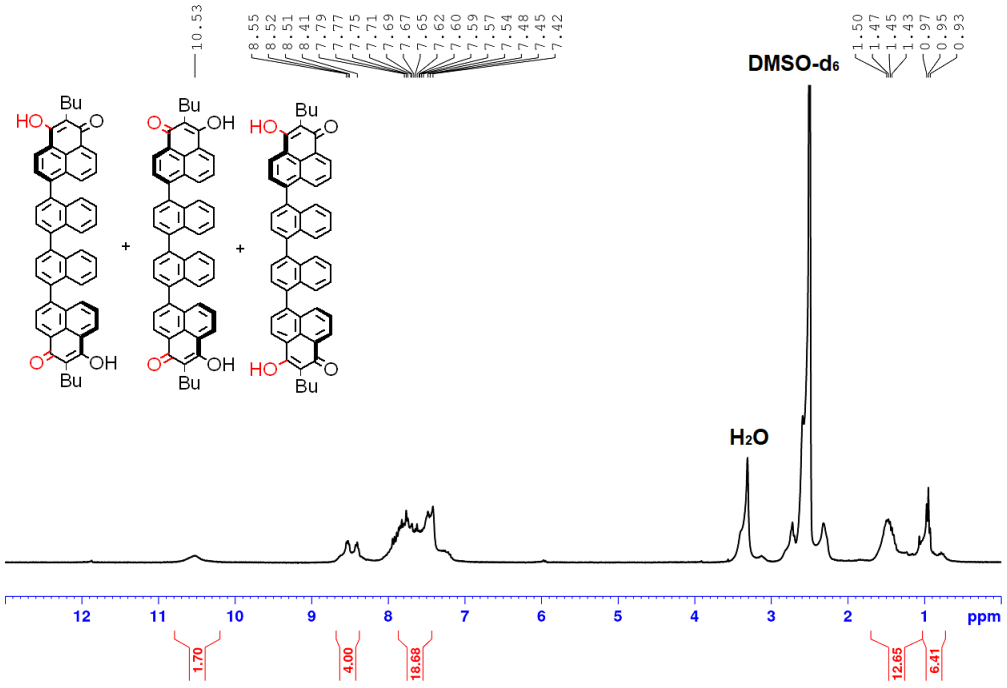

Figure S36. ^{1}H-NMR (300.1 MHz, 298K, DMSO-d$_6$*) of **S2** (isomer mixture). Contains inseparable aromatic by-products.

*2-butyl-7-(4'-(2-butyl-3-hydroxy-1-oxo-1H-phenalen-6-yl)-[1,1'-binaphthalen]-4-yl)-3-hydroxy-1H-phenalen-1-one (**S7**)*

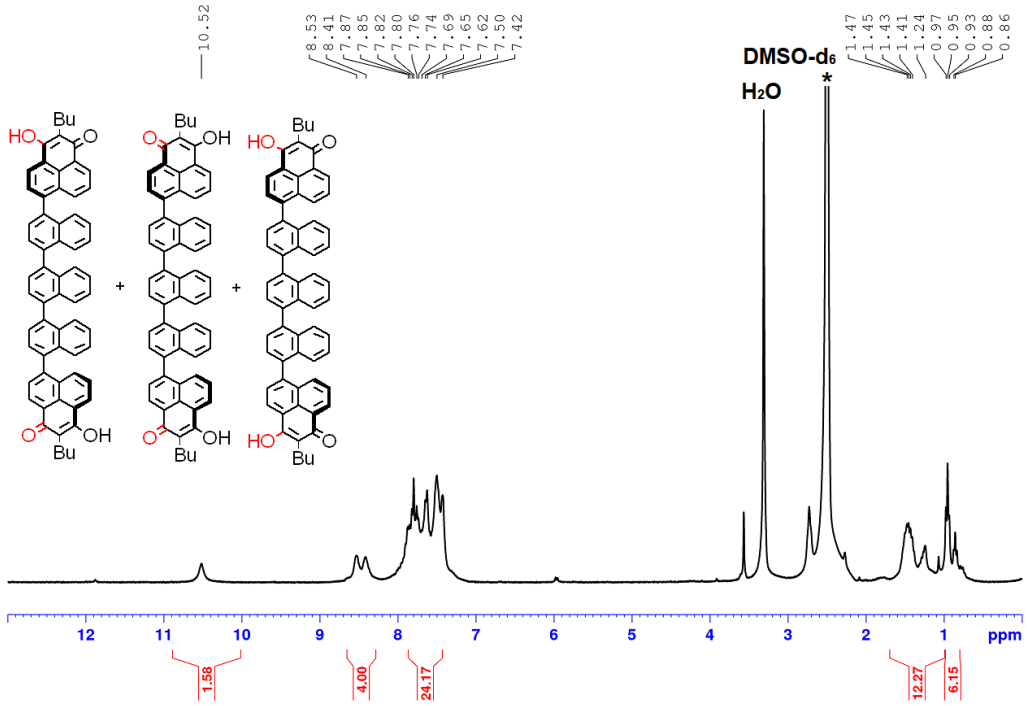

Figure S37. ^{1}H-NMR (300.1 MHz, 298K, DMSO-d_6*) of **S7** (isomer mixture). Contains inseparable aromatic by-products.

*1,3,6,8-tetrakis((triisopropylsilyl)oxy)pyrene (**5**)*

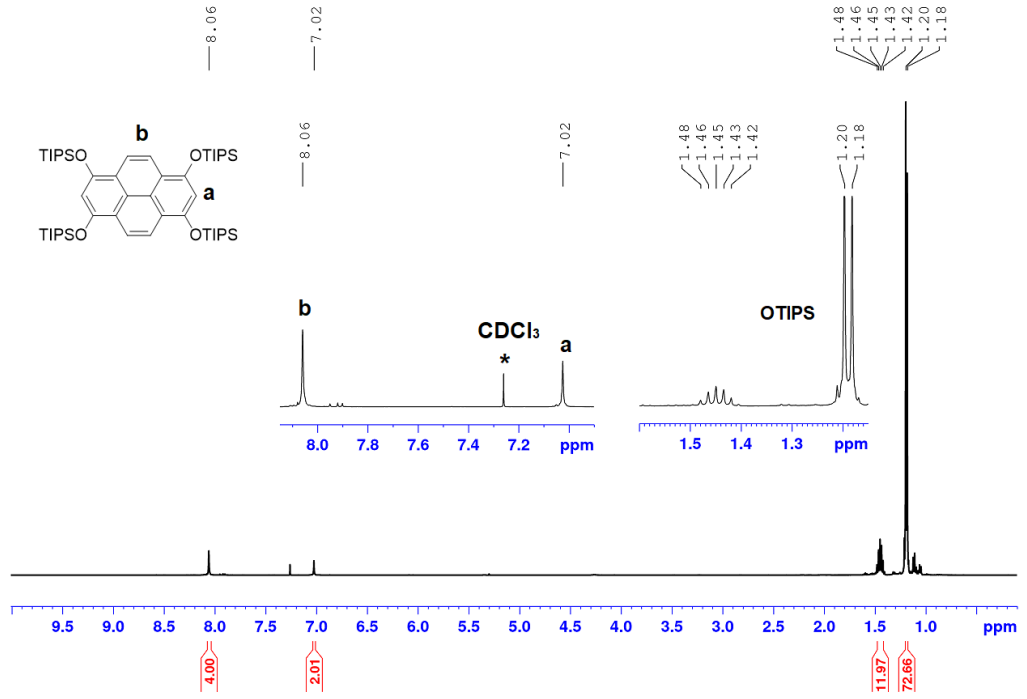

Figure S38. ^{1}H-NMR (500.1 MHz, 298K, $CDCl_3$*) of **5**.

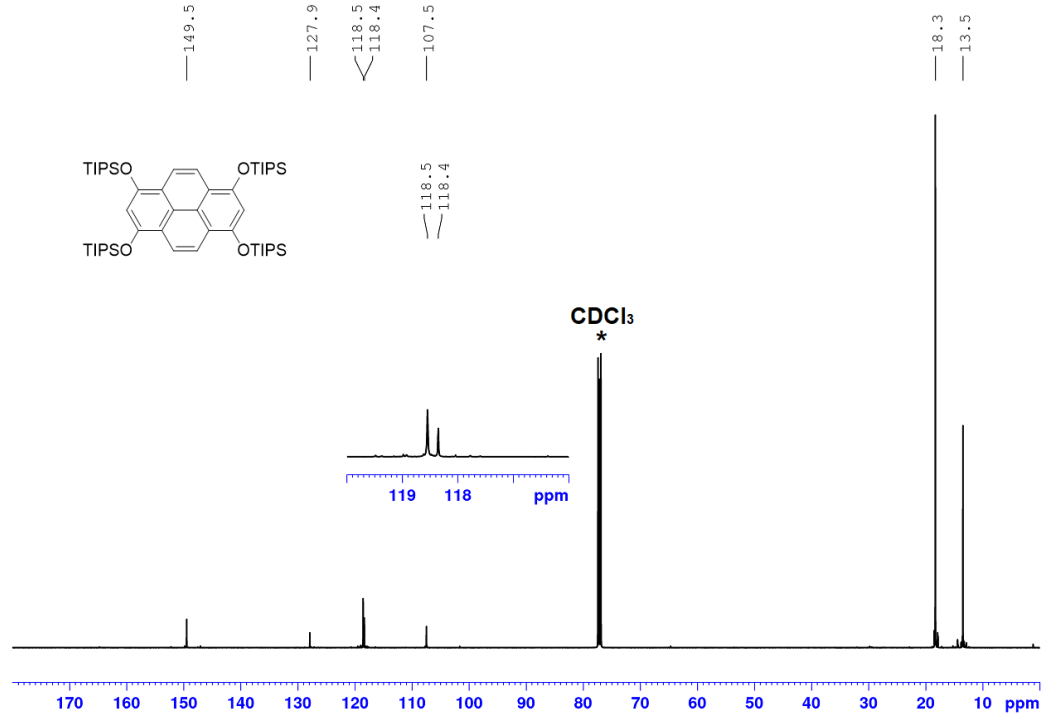

Figure S39. ^{13}C-NMR (125.8 MHz, 298K, $CDCl_3$*) of **5**.

*1,3,8,10-tetrakis((trimethylsilyl)oxydibenzo[cd,lm]-perylene (**4**)*

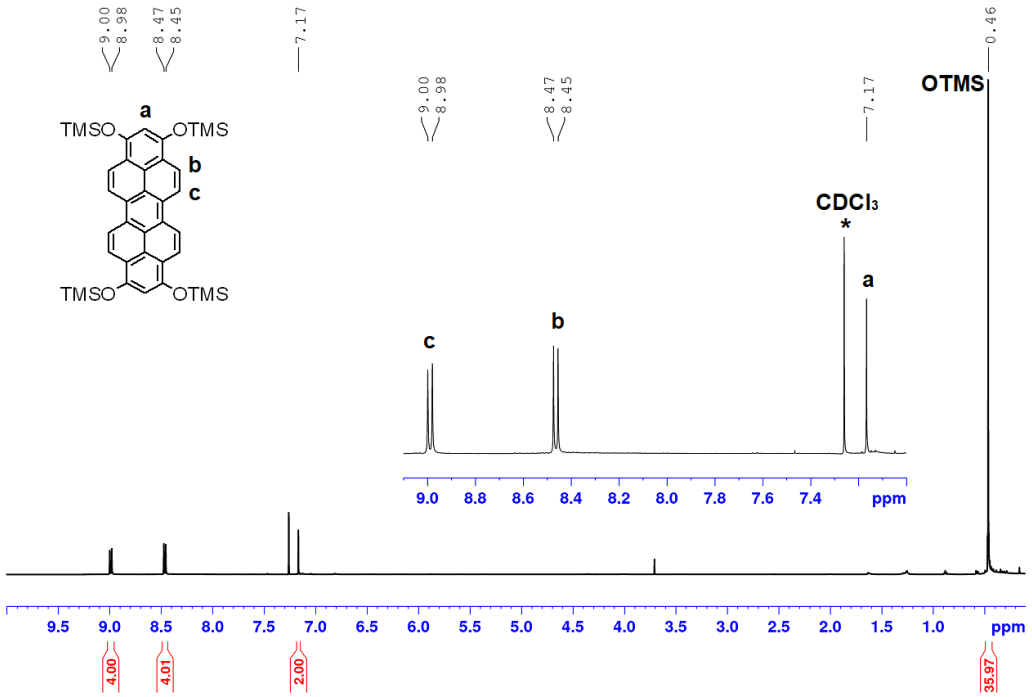

Figure S40. ^{1}H-NMR (500.1 MHz, 298K, $CDCl_3$*) of **4**.

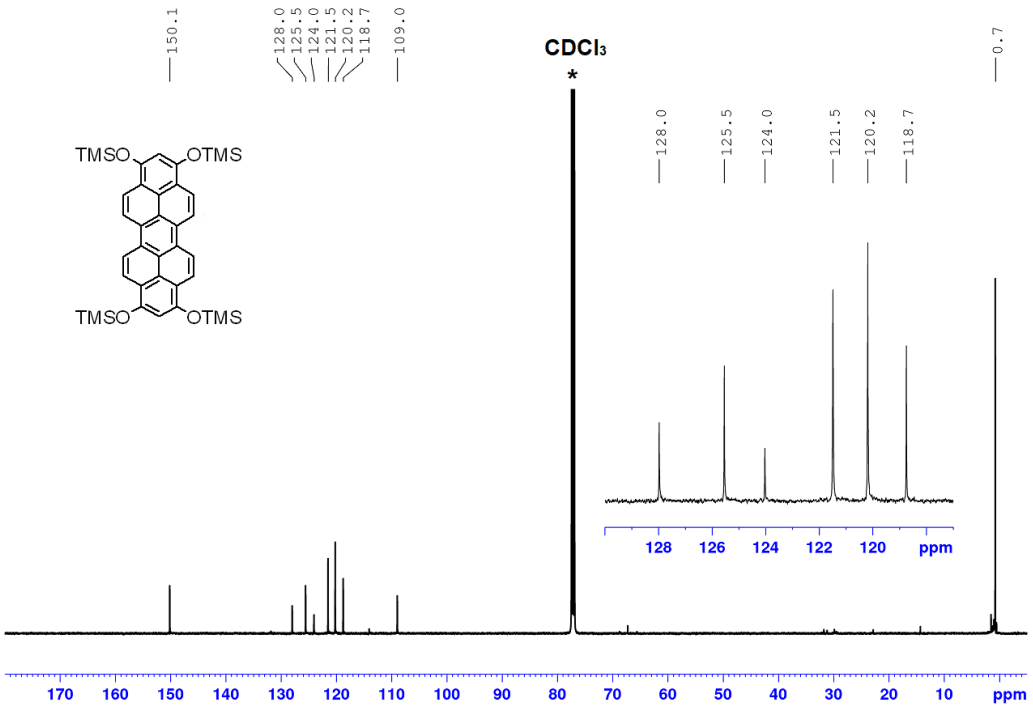

Figure S41. ^{13}C-NMR (125.8 MHz, 298K, $CDCl_3$*) of **4**.

*1,3,10,12-tetrakis((trimethylsilyl)oxy)benzo[rst]dinaphtho[8,1,2-cde:2',1',8'-klm]pentaphene (**13**)*

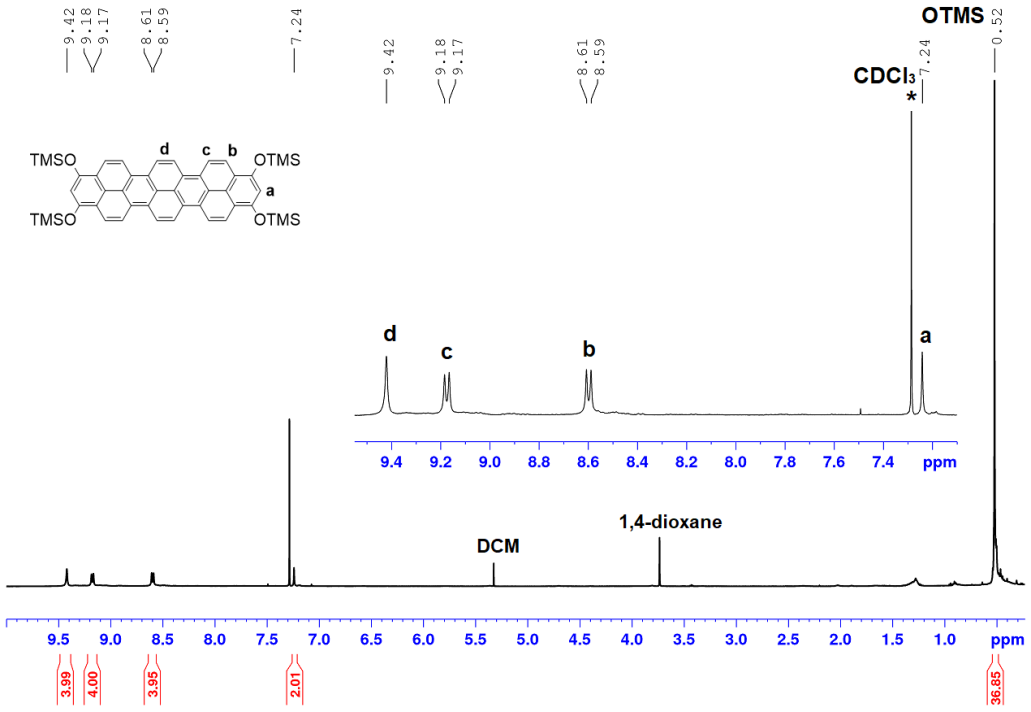

Figure S42. ^{1}H-NMR (500.1 MHz, 298K, $CDCl_3$*) of **13**.

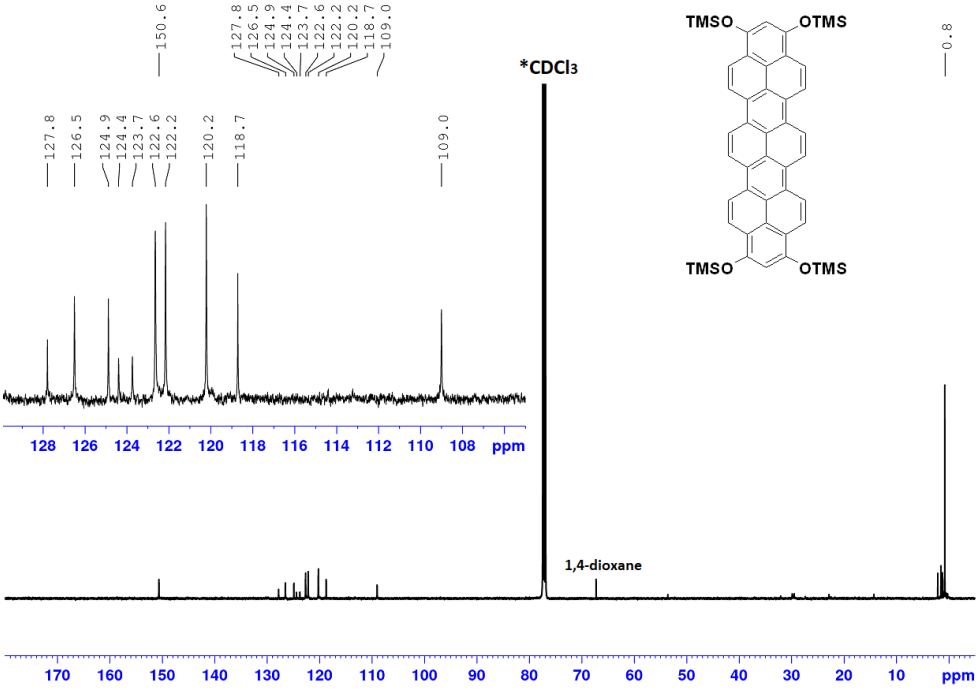

Figure S43. ^{13}C-NMR (125.8 MHz, 298K, $CDCl_3$*) of **13**.

*1,3,10,12-tetrakis((triisopropylsilyl)oxy)benzo[rst]dinaphtho[8,1,2-cde:2',1',8'-klm]pentaphene (**14**)*

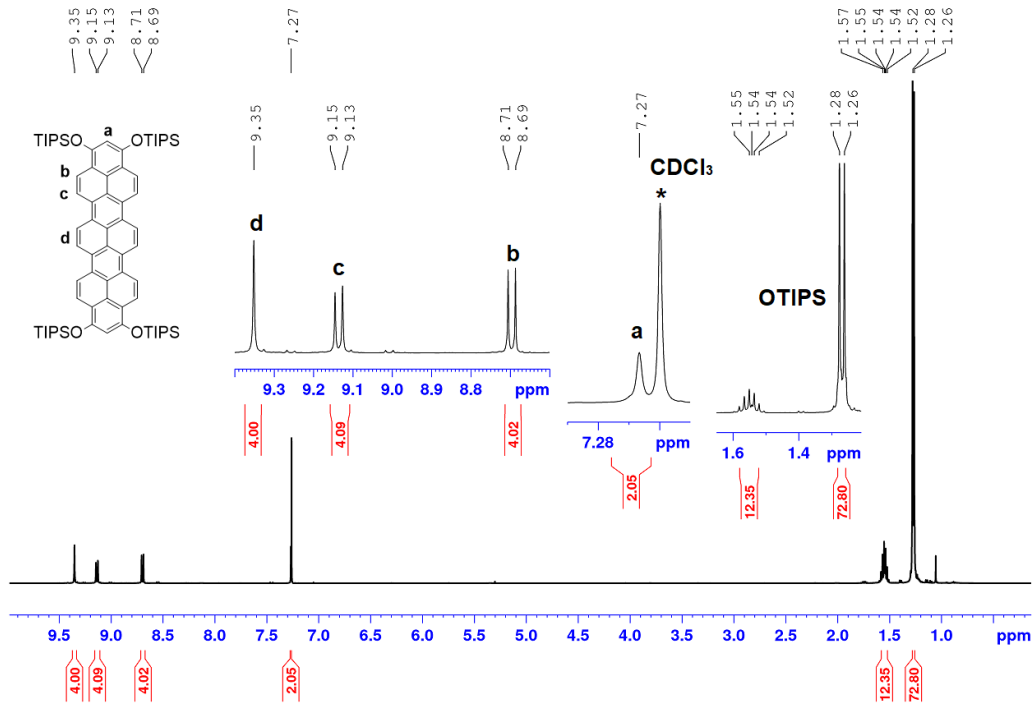

Figure S44. ^{1}H-NMR (500.1 MHz, 298K, $CDCl_3$*) of **14**.

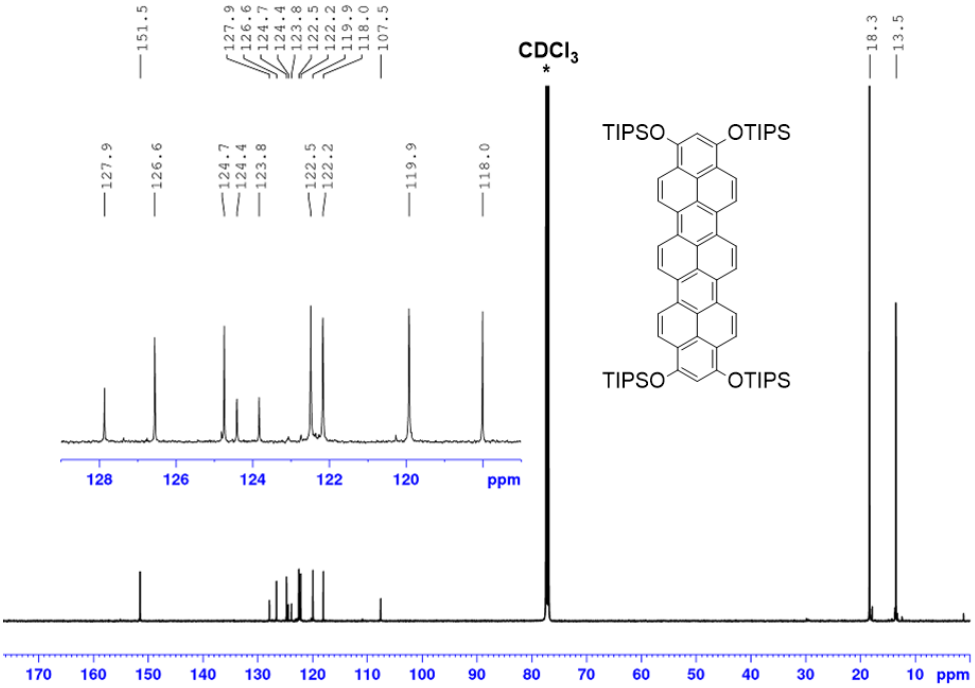

Figure S45. ^{13}C-NMR (125.8 MHz, 298K, $CDCl_3$*) of **14**.

*((2,13-dibutylbenzo[rst]benzo[12,1]tetrapheno[7,8,9-cde]naphtho[2,1,8-klm]pentaphene-1,3,12,14-tetrayl)tetrakis(oxy))-tetrakis(trimethylsilane) (**S4**)*

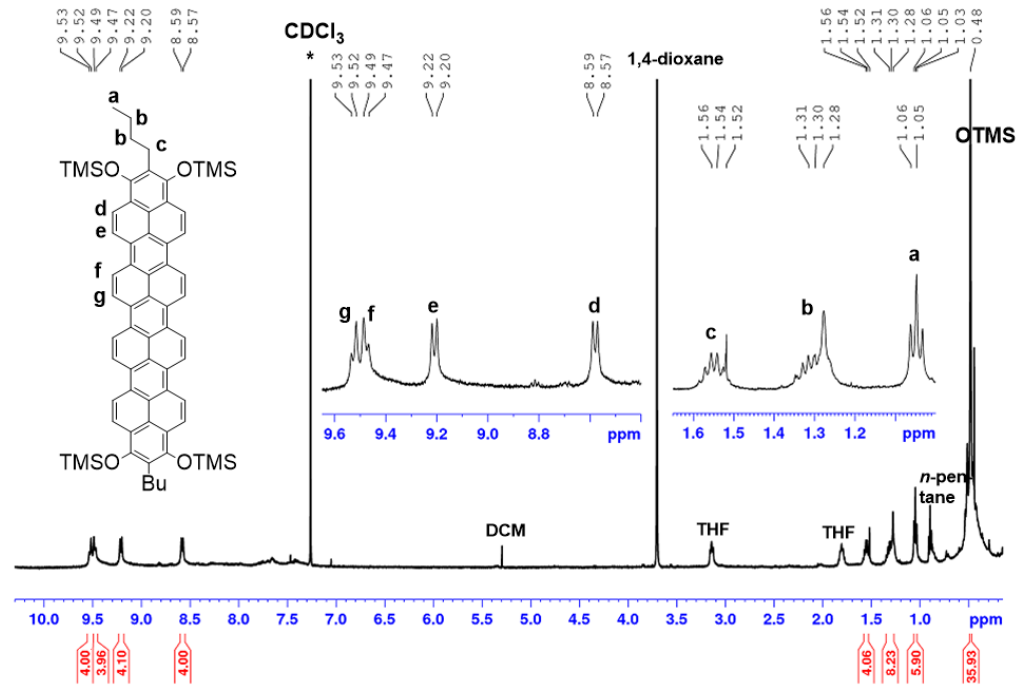

Figure S46. ^{1}H-NMR (500.1 MHz, 323K, $CDCl_3$*) of **S4**.

*1,3,10,12-tetrakis((triisopropylsilyl)oxy)benzo[rst]dinaphtho[8,1,2-cde:2',1',8'-klm]pentaphene (**15**)*

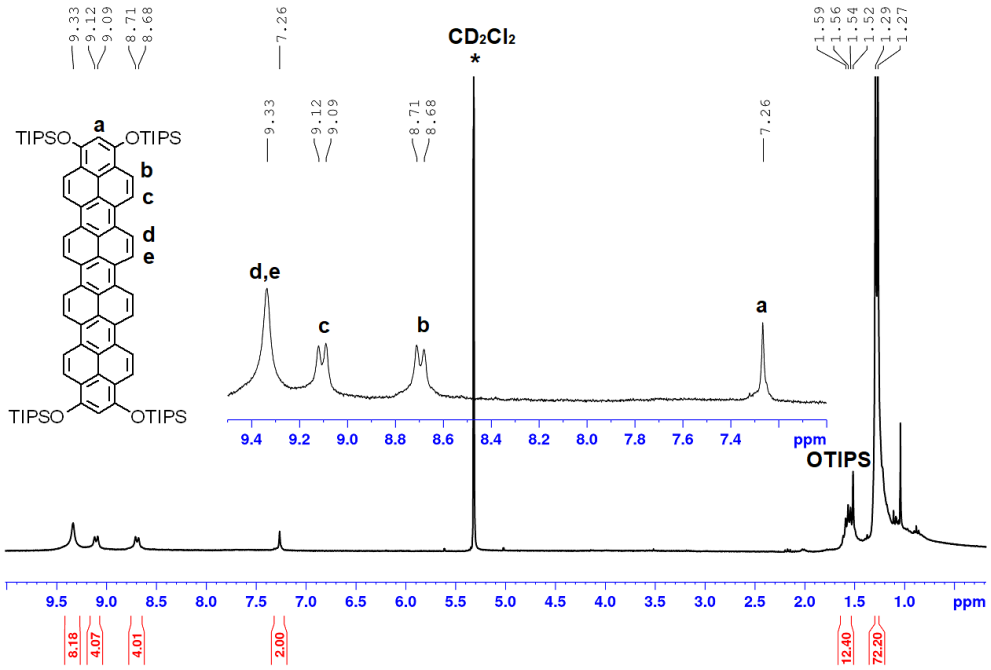

Figure S47. ^{1}H-NMR (300.1 MHz, 298K, CD_2Cl_2*) of **15**.

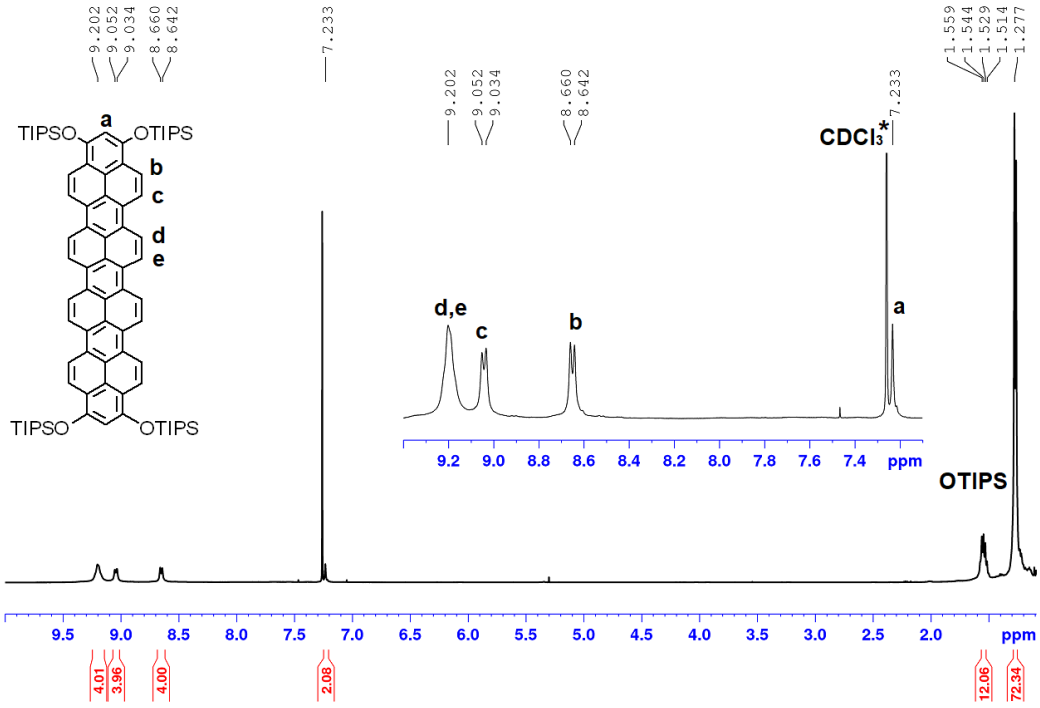

Figure S48. ^{1}H-NMR (500.1 MHz, 298K, $CDCl_3$*) of **15**.

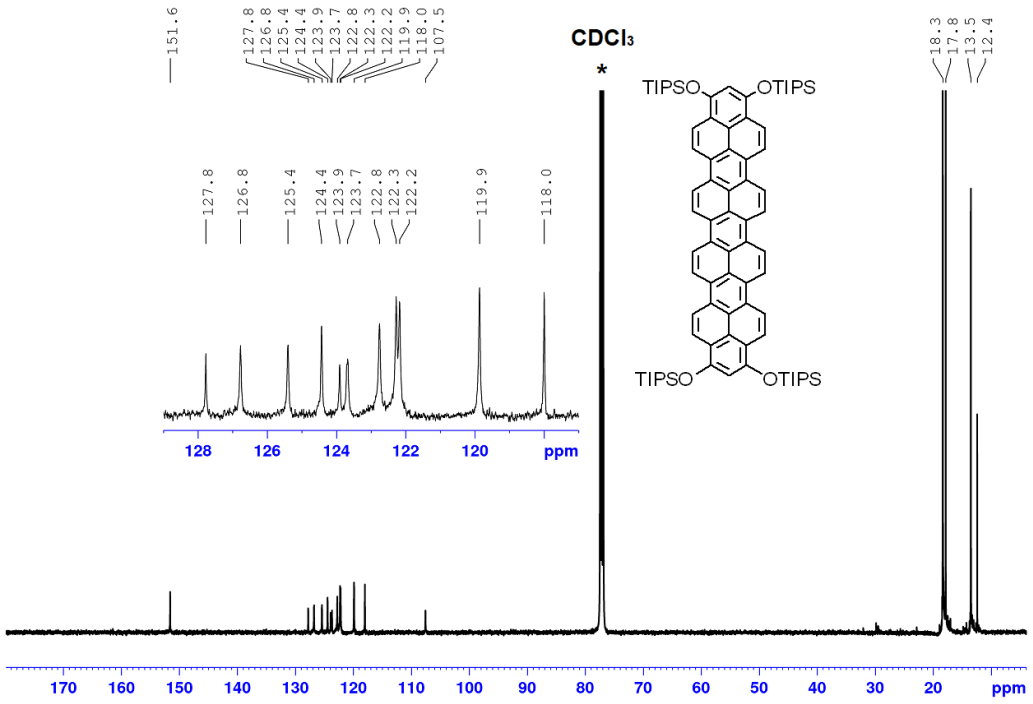

Figure S49. ^{13}C-NMR (125.8 MHz, 298K, $CDCl_3$*) of **15**.

APCI(-) Mass spectra of Suzuki coupling products

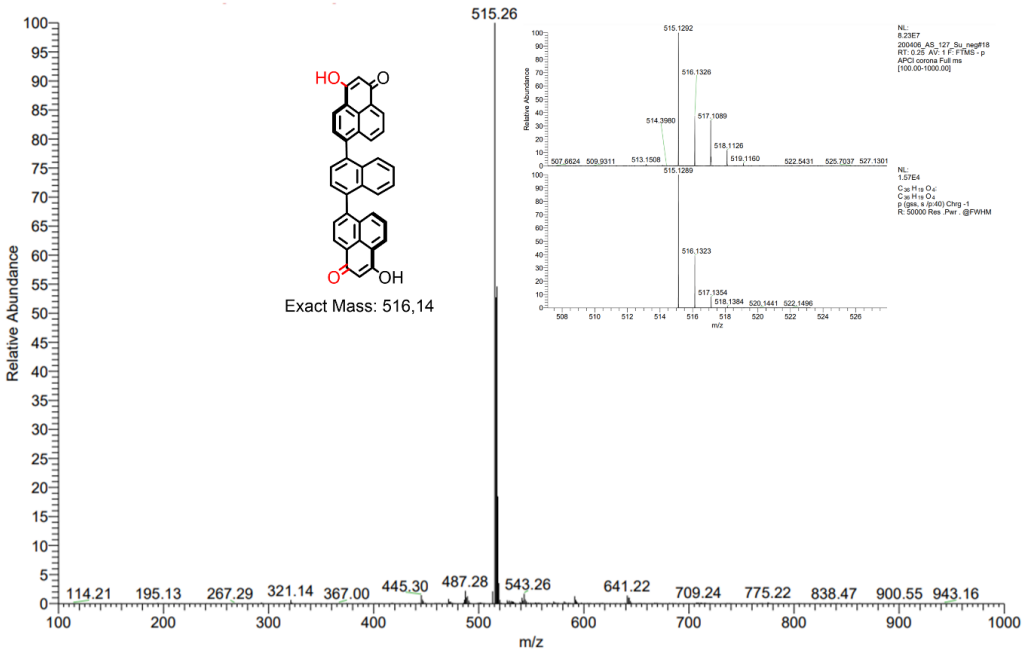

Figure S50. APCI(-) spectrum of **9**. Inset: high resolution spectrum and simulation of the product peak.

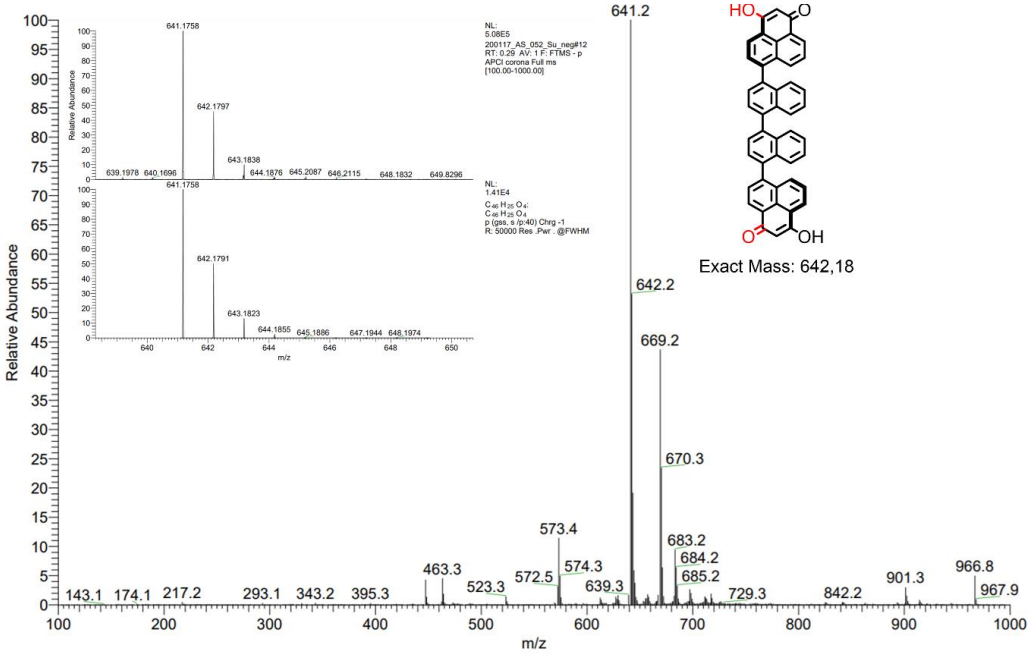

Figure S51. APCI(-) spectrum of **10**. Inset: high resolution spectrum and simulation of the product peak.

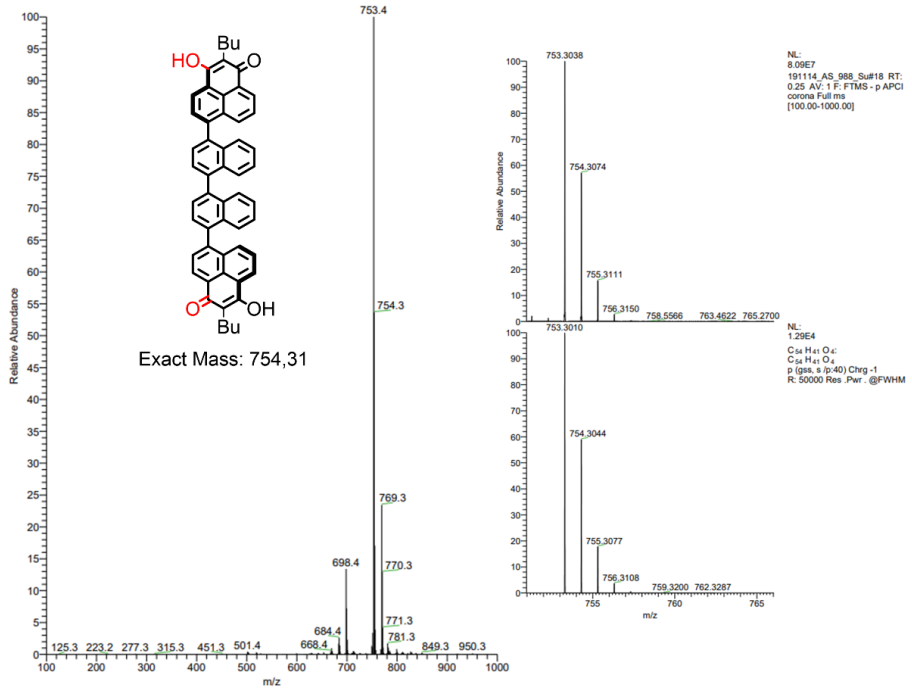

Figure S52. APCI(-) spectrum of **S2**. Inset: high resolution spectrum and simulation of the product peak.

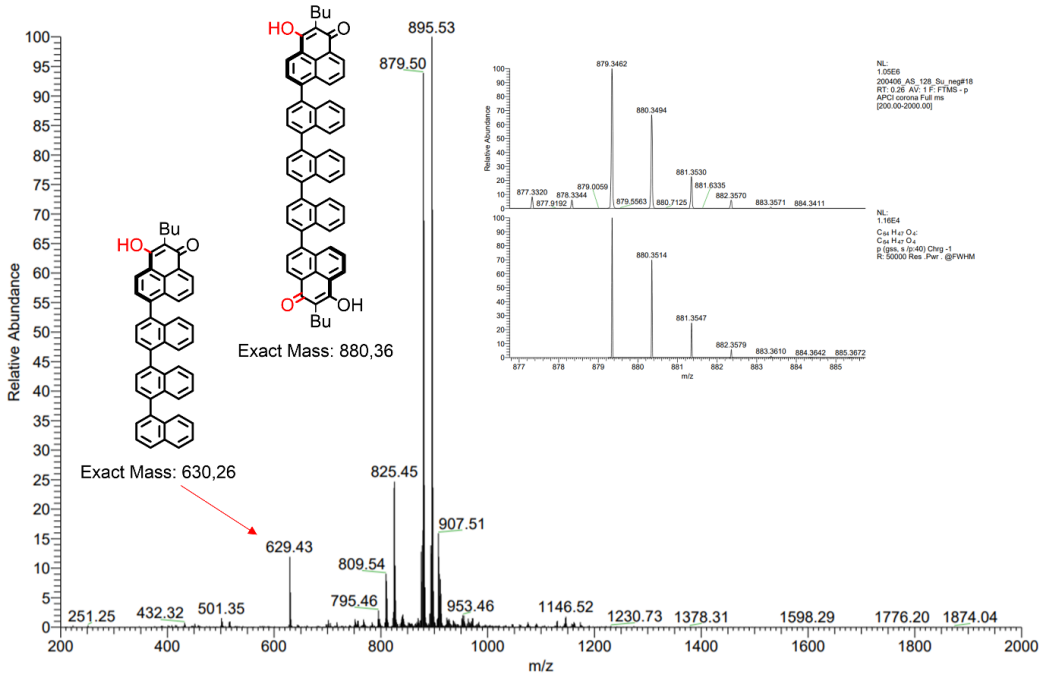

Figure S53. APCI(-) spectrum of **S7**. Inset: high resolution spectrum and simulation of the product peak.

Reverse Phase HPLC traces of Suzuki coupling products

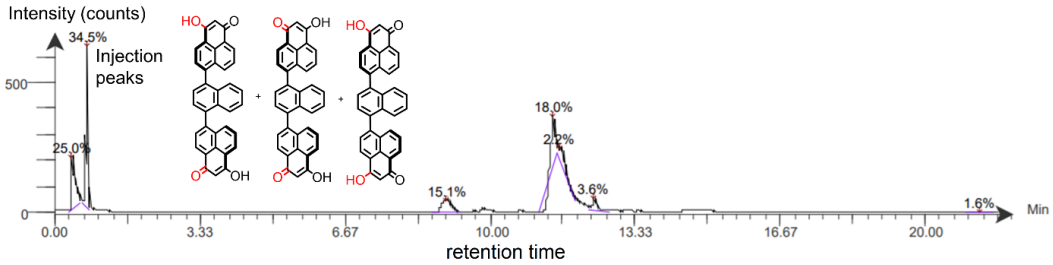

Figure S54. HPLC elution trace of **9** deprotonated with diluted aqueous NaOH (1 M), eluent: H_2O/acetonitrile, 95:5→5:95.

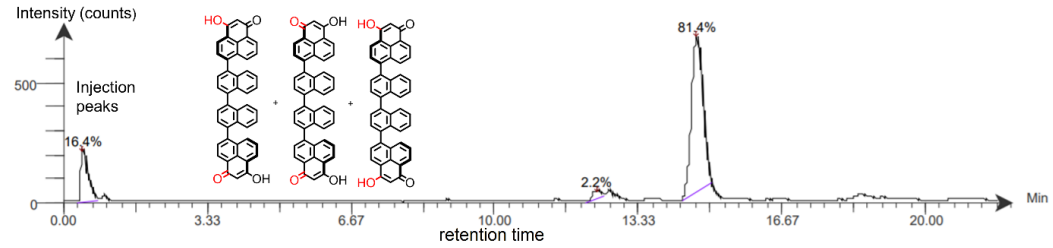

Figure S55. HPLC elution trace of **10** deprotonated with diluted aqueous NaOH (1 M), eluent: H_2O/acetonitrile, 95:5→5:95.

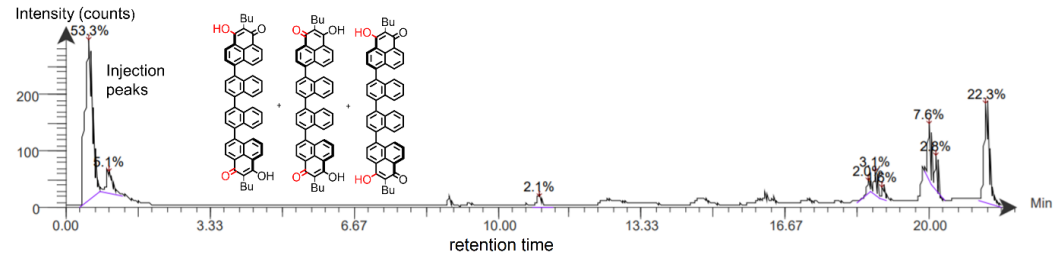

Figure S56. HPLC elution trace of **S2** deprotonated with diluted aqueous NaOH (1 M), eluent: H_2O/acetonitrile, 95:5→5:95.

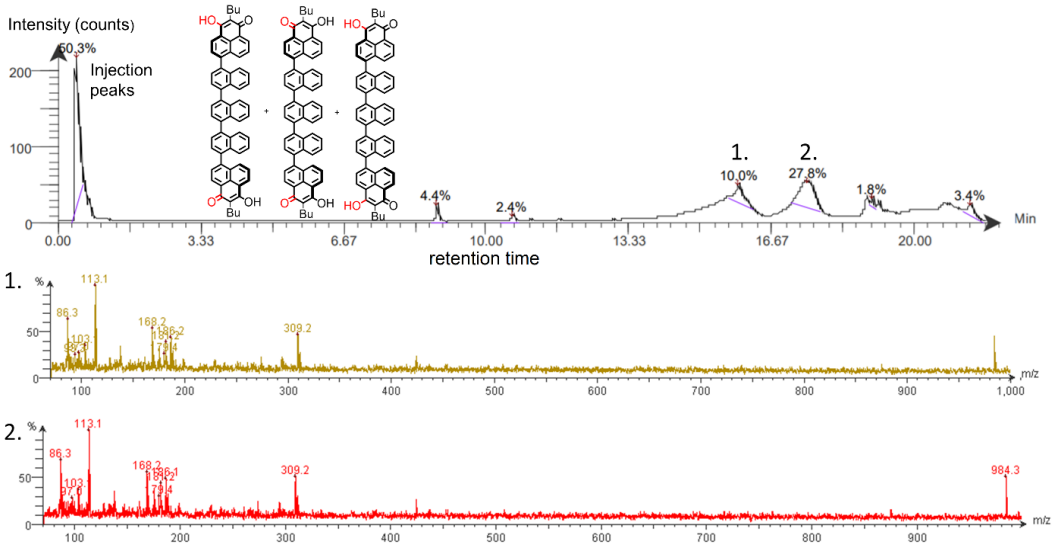

Figure S57. HPLC elution trace of **S7** deprotonated with diluted aqueous NaOH (1 M), eluent: H_2O/acetonitrile, 95:5→5:95 and ESI(-) mass spectra of fractions 1 and 2.

References

[1] W. L. F. Armarego, D. D. Perrin, *Purification of laboratory chemicals*, Butterworth-Heinemann, Oxford, **2002**.
[2] G. M. Sheldrick, *Acta Cryst. C* **2015**, *71*, 3–8.
[3] C. B. Hübschle, G. M. Sheldrick, B. Dittrich, *J. Appl. Cryst.* **2011**, *44*, 1281–1284.
[4] A. L. Spek, *Acta Cryst. D* **2009**, *65*, 148–155.
[5] H. P. K. Brandenburg, *Diamond*, Crystal Impact GbR, Bonn, **2012**.
[6] J. R. Lakowicz, *Principles of fluorescence spectroscopy*, Springer, New York, **2010**.
[7] a) Lee, Yang, Parr, *Phys. Rev. B* **1988**, *37*, 785–789; b) P. J. Stephens, F. J. Devlin, C. S. Ashvar, C. F. Chabalowski, M. J. Frisch, *Faraday Disc.* **1994**, *99*, 103; c) A. D. Becke, *J. Chem. Phys.* **1993**, *98*, 5648–5652.
[8] a) A. Schäfer, C. Huber, R. Ahlrichs, *J. Chem. Phys.* **1994**, *100*, 5829–5835; b) F. Weigend, *Phys. Chem. Chem. Phys.* **2006**, *8*, 1057–1065.
[9] F. Weigend, R. Ahlrichs, *Phys. Chem. Chem. Phys.* **2005**, *7*, 3297–3305.
[10] a) K. Eichkorn, O. Treutler, H. Öhm, M. Häser, R. Ahlrichs, *Chem. Phys. Lett.* **1995**, *240*, 283–290; b) M. von Arnim, R. Ahlrichs, *J. Comput. Chem.* **1998**, *19*, 1746–1757; c) F. Weigend, M. Häser, H. Patzelt, R. Ahlrichs, *Chem. Phys. Lett.* **1998**, *294*, 143–152.
[11] T. Yanai, D. P. Tew, N. C. Handy, *Chem. Phys. Lett.* **2004**, *393*, 51–57.
[12] a) R. Krishnan, J. S. Binkley, R. Seeger, J. A. Pople, *J. Chem. Phys.* **1980**, *72*, 650–654; b) A. D. McLean, G. S. Chandler, *J. Chem. Phys.* **1980**, *72*, 5639–5648.
[13] S. Grimme, J. Antony, S. Ehrlich, H. Krieg, *J. Chem. Phys.* **2010**, *132*, 154104.
[14] a) A. D. Becke, E. R. Johnson, *J. Chem. Phys.* **2005**, *123*, 154101; b) S. Grimme, S. Ehrlich, L. Goerigk, *J. Comput. Chem.* **2011**, *32*, 1456–1465; c) E. R. Johnson, A. D. Becke, *J. Chem. Phys.* **2006**, *124*, 174104; d) E. R. Johnson, A. D. Becke, *J. Chem. Phys.* **2005**, *123*, 24101.
[15] F. Neese, *WIREs Comput Mol Sci* **2011**, *2*, 73–78.
[16] a) Perdew, Burke, Ernzerhof, *Phys. Rev. Lett.* **1996**, *77*, 3865–3868; b) J. P. Perdew, K. Burke, M. Ernzerhof, *Phys. Rev. Lett.* **1997**, *78*, 1396.
[17] F. Weigend, *Phys. Chem. Chem. Phys.* **2002**, *4*, 4285–4291.
[18] D. Alezi, Y. Belmabkhout, M. Suyetin, P. M. Bhatt, Ł. J. Weseliński, V. Solovyeva, K. Adil, I. Spanopoulos, P. N. Trikalitis, A.-H. Emwas et al., *J. Am. Chem. Soc.* **2015**, *137*, 13308–13318.
[19] H. Jia, Y. Gao, Q. Huang, S. Cui, P. Du, *Chem. Commun.* **2018**, *54*, 988–991.
[20] N. Buffet, E. Grelet, H. Bock, *Chem. Eur. J.* **2010**, *16*, 5549–5553.

7.2 Supporting Information of Publication 2

The chapter *Single crystal X-ray structures* of the supporting information of Publication 2 is not shown in the following.
This was done by T. Vollgraff and is part of his doctoral thesis.
Also, the XYZ coordinates for DFT-optimized structures are not reprinted and can be retrieved from the online version of the supporting information.

Supporting Information

Tetrasubstituted Peropyrenes formed by reductive aromatization: Synthesis, Functionalization and Characterization

Simon Werner [a],Tobias Vollgraff [a], and Jörg Sundermeyer*[a]

[a] S. Werner, T. Vollgraff, Prof. Dr. J. Sundermeyer
Fachbereich Chemie and Materials Science Center
Philipps-Universität Marburg, Hans-Meerwein-Straße 4
35043 Marburg (Germany)
E-Mail: JSU@staff.uni-marburg.de

Contents

Concentration-dependent UV-Vis spectroscopy

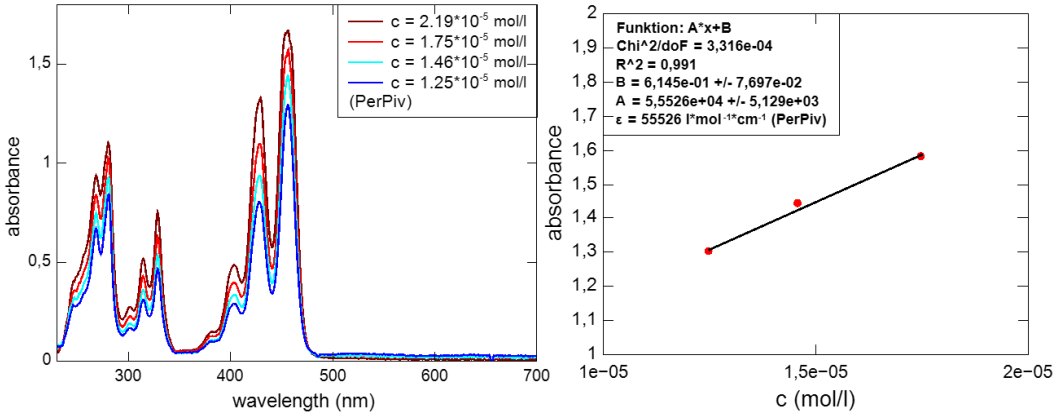

Figure S1. Left: UV-Vis spectra of **4** at four different concentration, recorded in CH_2Cl_2. Center: plot of the absorbance at λ_{max} versus the corresponding concentration to determine the molecular decadic attenuation coefficient ε from the slope (optical pass length = 1 cm).

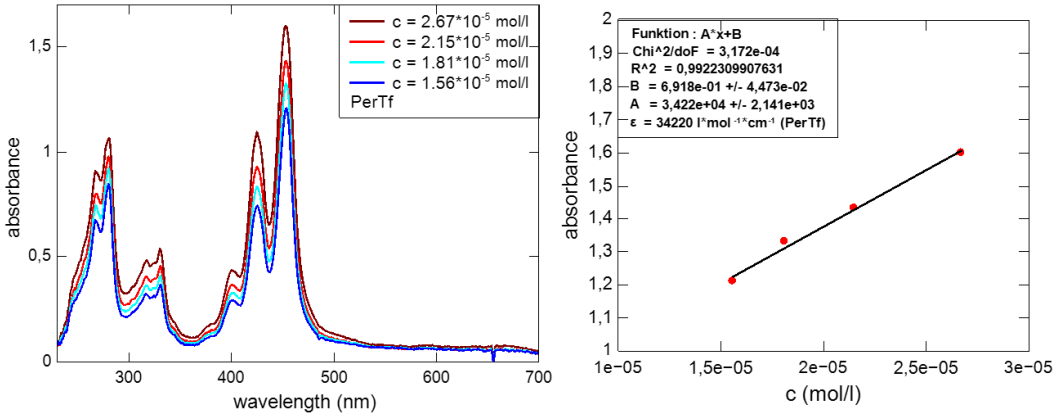

Figure S2. Left: UV-Vis spectra of **5** at four different concentration, recorded in CH_2Cl_2. Center: plot of the absorbance at λ_{max} versus the corresponding concentration to determine the molecular decadic attenuation coefficient ε from the slope (optical pass length = 1 cm).

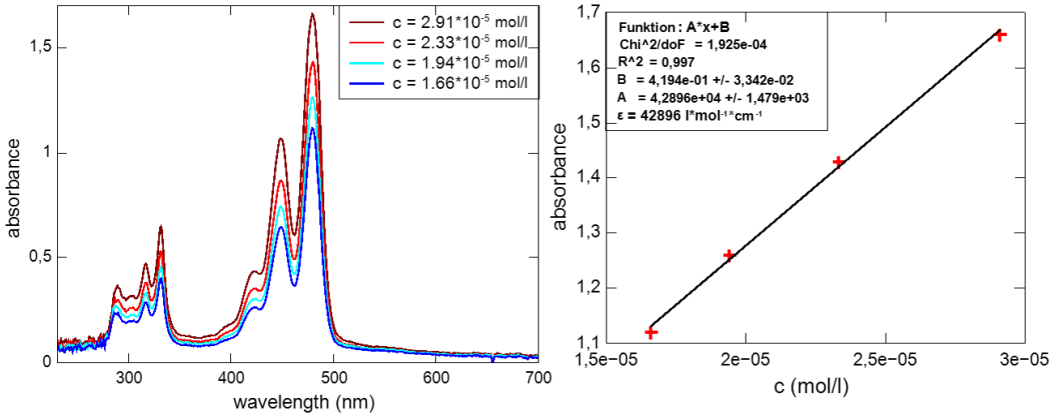

Figure S3. Left: UV-Vis spectra of **2** at four different concentration, recorded in CH_2Cl_2. Center: plot of the absorbance at λ_{max} versus the corresponding concentration to determine the molecular decadic attenuation coefficient ε from the slope (optical pass length = 1 cm).

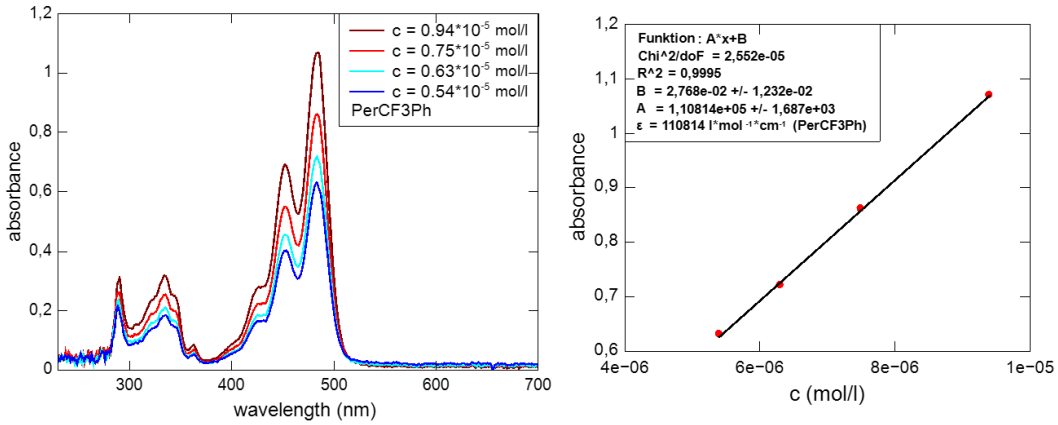

Figure S4. Left: UV-Vis spectra of **8** at four different concentration, recorded in CH_2Cl_2. Center: plot of the absorbance at λ_{max} versus the corresponding concentration to determine the molecular decadic attenuation coefficient ε from the slope (optical pass length = 1 cm).

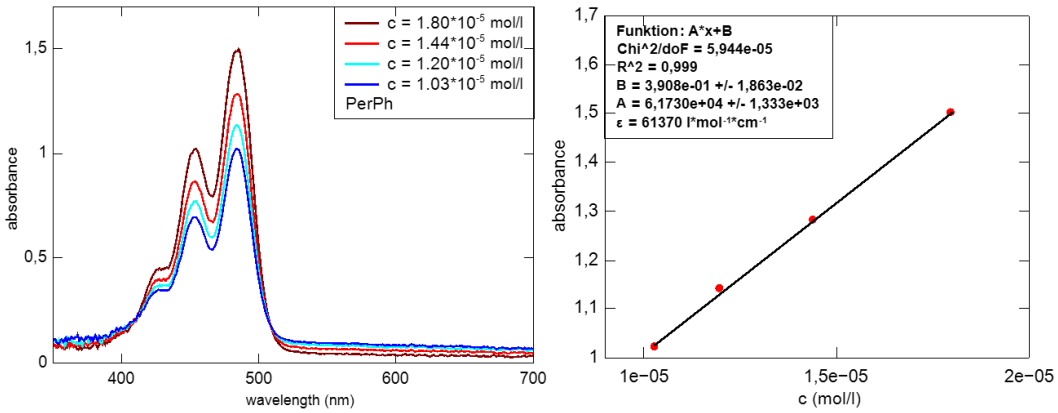

Figure S5. Left: UV-Vis spectra of **10** at four different concentration, recorded in CH_2Cl_2. Center: plot of the absorbance at λ_{max} versus the corresponding concentration to determine the molecular decadic attenuation coefficient ε from the slope (optical pass length = 1 cm).

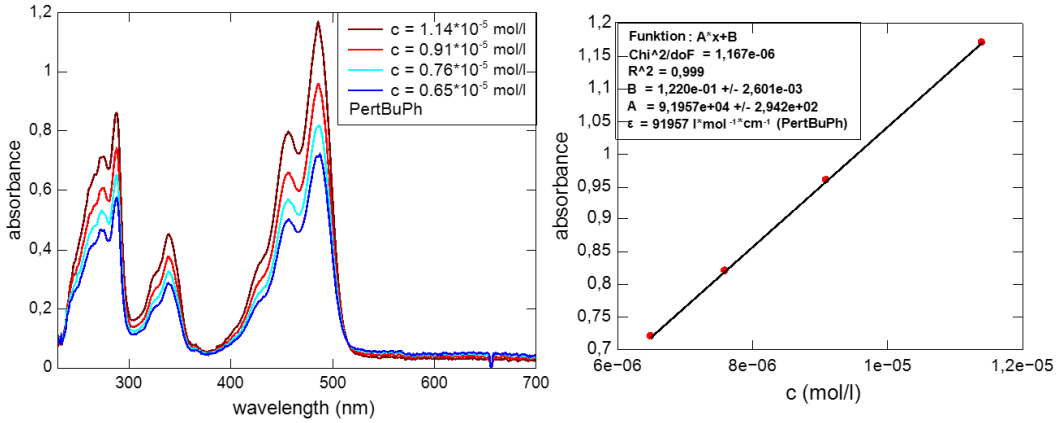

Figure S6. Left: UV-Vis spectra of **11** at four different concentration, recorded in CH_2Cl_2. Center: plot of the absorbance at λ_{max} versus the corresponding concentration to determine the molecular decadic attenuation coefficient ε from the slope (optical pass length = 1 cm).

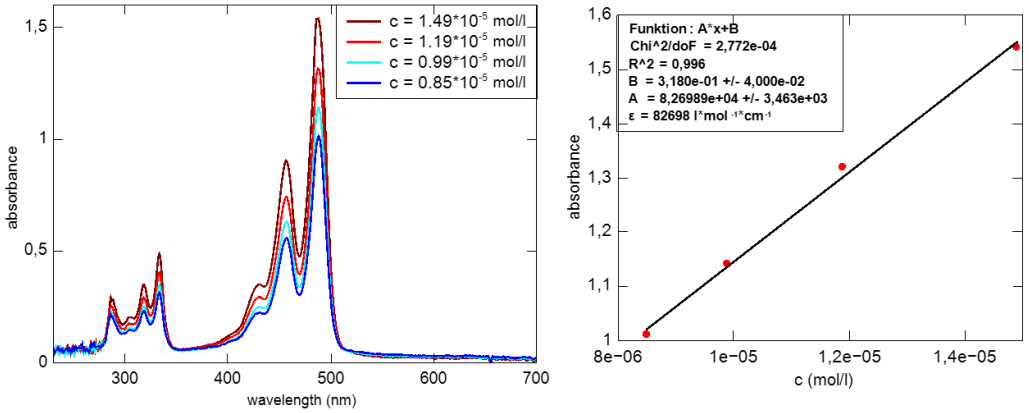

Figure S7. Left: UV-Vis spectra of **3** at four different concentration, recorded in CH_2Cl_2. Center: plot of the absorbance at λ_{max} versus the corresponding concentration to determine the molecular decadic attenuation coefficient ε from the slope (optical pass length = 1 cm).

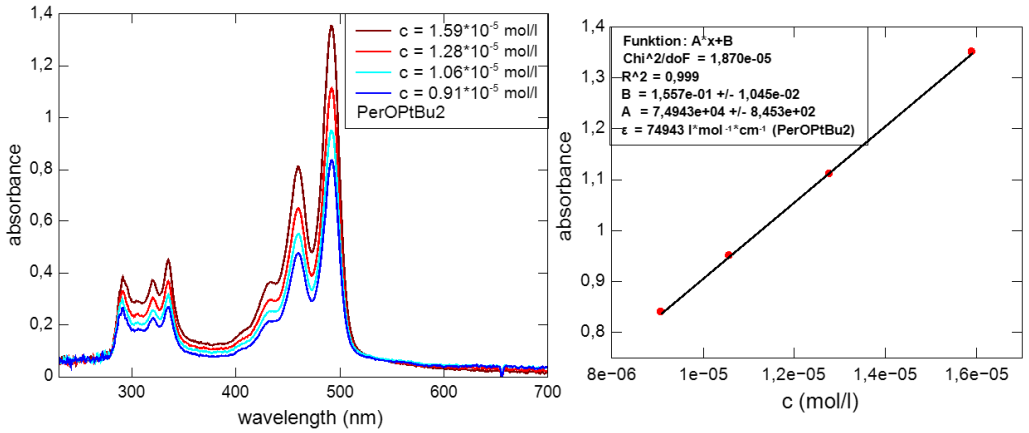

Figure S8. Left: UV-Vis spectra of **6** at four different concentration, recorded in CH_2Cl_2. Center: plot of the absorbance at λ_{max} versus the corresponding concentration to determine the molecular decadic attenuation coefficient ε from the slope (optical pass length = 1 cm).

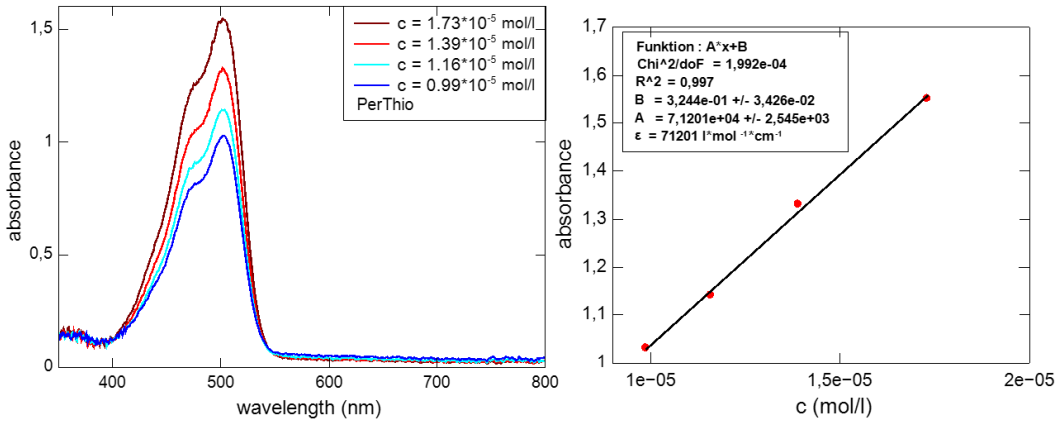

Figure S9. Left: UV-Vis spectra of **9** at four different concentration, recorded in CH_2Cl_2. Center: plot of the absorbance at λ_{max} versus the corresponding concentration to determine the molecular decadic attenuation coefficient ε from the slope (optical pass length = 1 cm).

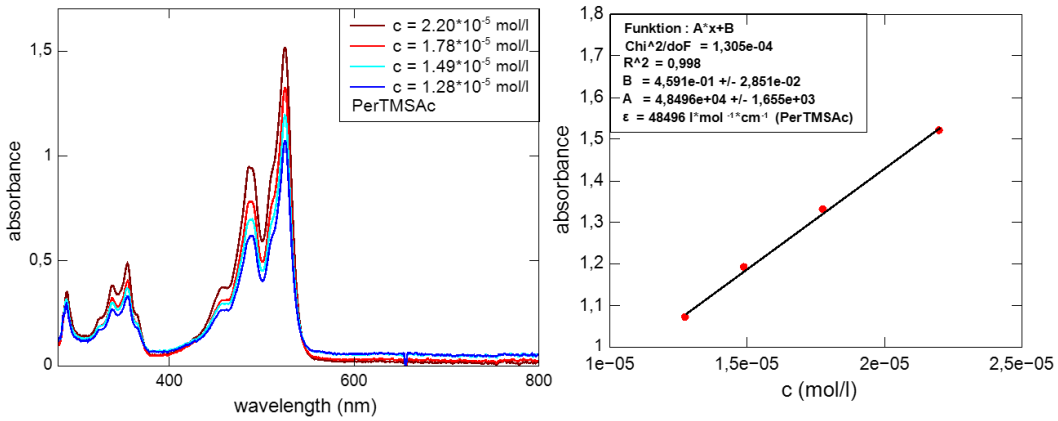

Figure S10. Left: UV-Vis spectra of **7** at four different concentration, recorded in CH_2Cl_2. Center: plot of the absorbance at λ_{max} versus the corresponding concentration to determine the molecular decadic attenuation coefficient ε from the slope (optical pass length = 1 cm).

Determination of fluorescence quantum yields

Fluorescence quantum yields (Φ_{PL}) were recorded by dilution method using a fluorescein solution (0.1 M in aqueous NaOH, Φ_{flu} = 0.95) [27] as reference. Both, the samples and the reference were measured at low concentrations in order to ensure a linear relationship between the intensity of emitted light and the concentration of the absorbing/emitting species.
The quantum yields of the samples (Φ_s) were determined by the following equation 1.[6]

$$\Phi_{flu} = \frac{grad(s)}{grad(flu)} * \frac{n^2(s)}{n^2(flu)} * \Phi_{flu}$$

In equation 1, *grad* is the slope of the "emission versus absorbance" plot of the samples (s) and the standard fluorescein (flu). n is the refractive index of the used solvents.
In the following figures S11 and S12, the "emission versus absorbance" plots and the linear regression graphs for the determination of the fluorescence quantum yields of **3**-**11** are shown. The plot of the most efficient fluorescence dye **3** was calibrated against fluorescein in order to calculate the fluorescence quantum yields. The fluorescence quantum yield of trimethylsilyl ether **2** has been determined previously.[28] Note that in the case of phenyl-substituted congeners **13** and **14**, the emission values at suitable low concentrations were too low to determine fluorescence quantum yields.

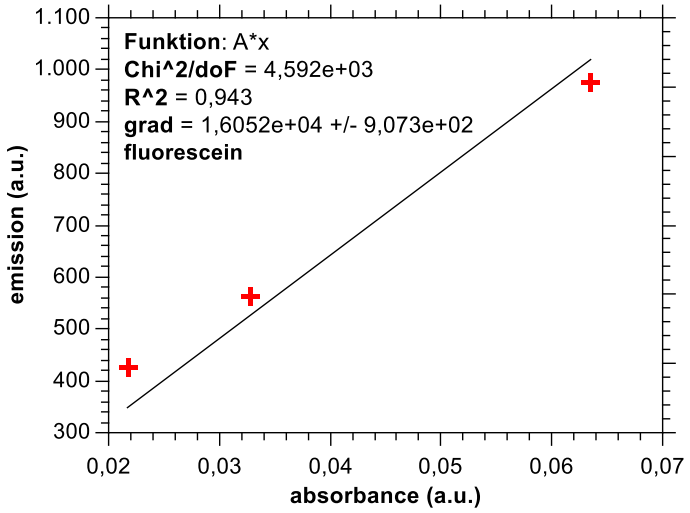

Figure S11. "emission versus absorption" plots fluorescein as 0.1 M solution in aqueous NaOH for direct referencing.

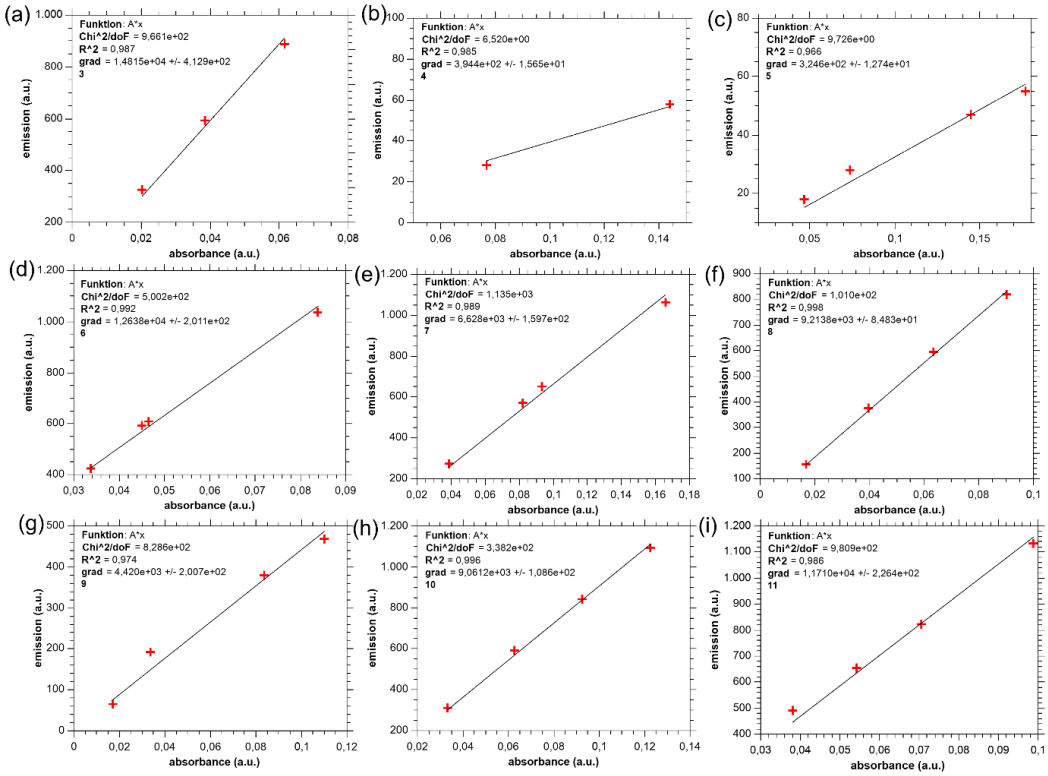

Figure S12. "emission versus absorption" plots of (a) **3**; (b) **4**; (c) **5**; (d) **6**; (e) **7**; (f) **8**; (g) **9**; (h) **10**; (i) **11** recorded in dichloromethane. The concentrations were in the low 10^{-6} M range.

Additional CV spectra

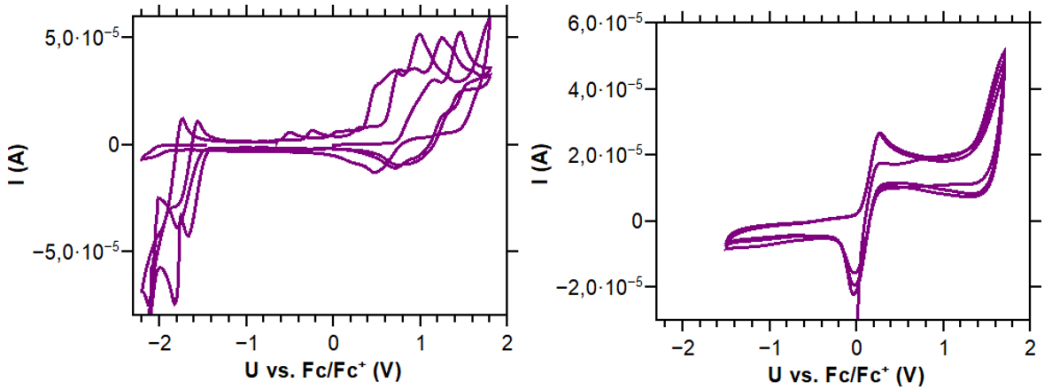

Figure S13. Left: Raw data of the cyclovoltammography of **4** (three scans were performed, only the first scan was usable for analysis, since **4** decomposes during CV measurement). Right: Cyclovoltammogramm of **4** after addition of 1 mM ferrocene (measured in CH_2Cl_2, 0.1 M *n*-Bu_4NPF_6, 100 mV s^{-1} scan rate, glassy carbon working electrode, platinum reference electrode).

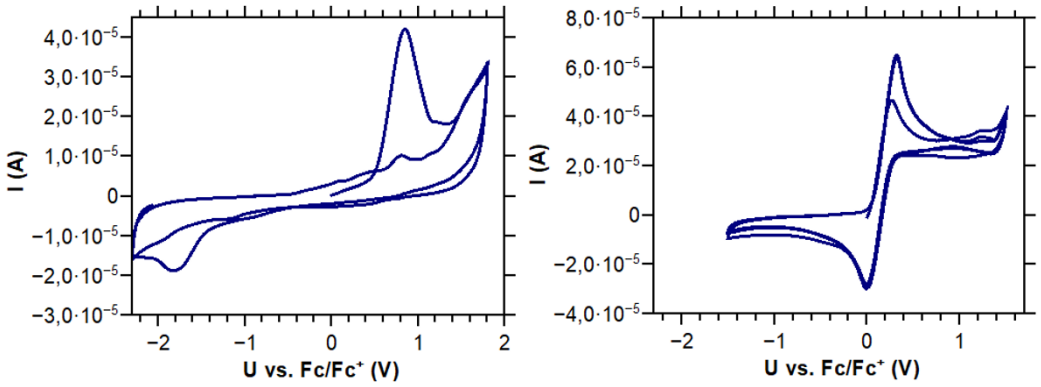

Figure S14. Left: Raw data of the cyclovoltammography of **5** (three scans were performed, only the first scan was usable for analysis, since **5** decomposes during CV measurement). Right: Cyclovoltammogramm of **5** after addition of 1 mM ferrocene (measured in CH_2Cl_2, 0.1 M *n*-Bu_4NPF_6, 100 mV s^{-1} scan rate, glassy carbon working electrode, platinum reference electrode).

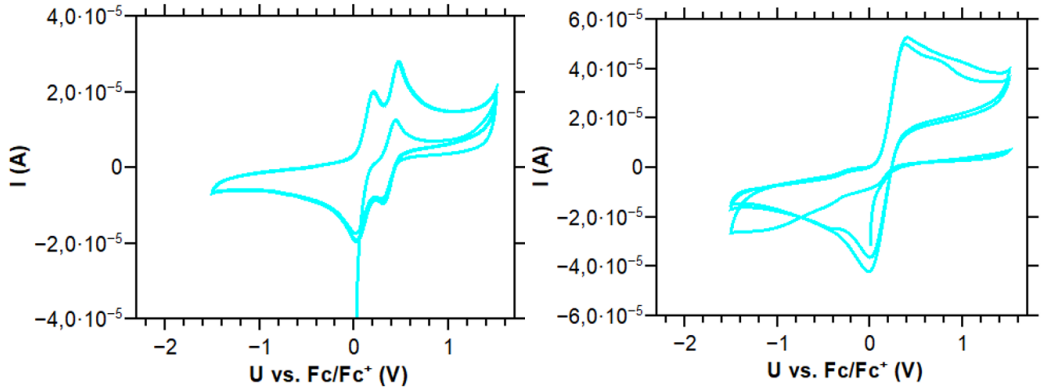

Figure S15. Left: Raw data of the cyclovoltammography of **2** (three scans were performed, the third one was used for analysis). Right: Cyclovoltammogramm of **2** after addition of 1 mM ferrocene (measured in CH_2Cl_2, 0.1 M *n*-Bu_4NPF_6, 100 mV s^{-1} scan rate, glassy carbon working electrode, platinum reference electrode).

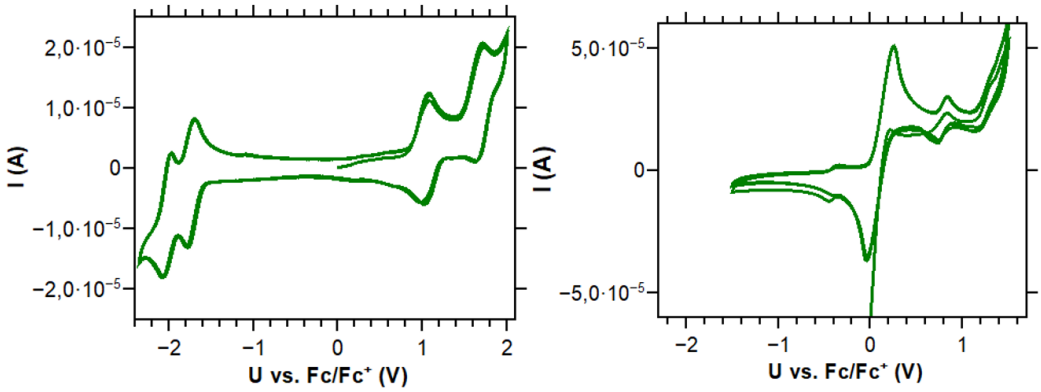

Figure S16. Left: Raw data of the cyclovoltammography of **8** (three scans were performed, the third one was used for analysis). Right: Cyclovoltammogramm of **8** after addition of 1 mM ferrocene (measured in CH_2Cl_2, 0.1 M *n*-Bu_4NPF_6, 100 mV s^{-1} scan rate, glassy carbon working electrode, platinum reference electrode).

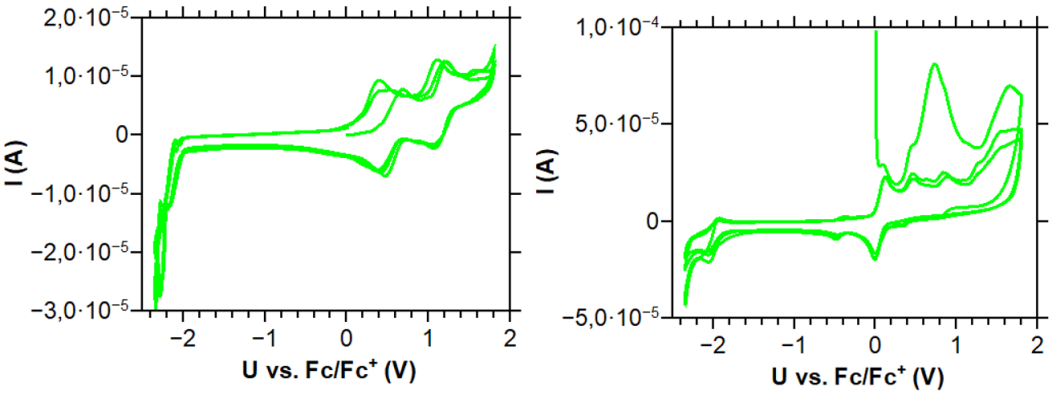

Figure S17. Left: Raw data of the cyclovoltammography of **10** (three scans were performed, the third one was used for analysis). Right: Cyclovoltammogramm of **10** after addition of 1 mM ferrocene (measured in CH_2Cl_2, 0.1 M *n*-Bu_4NPF_6, 100 mV s^{-1} scan rate, glassy carbon working electrode, platinum reference electrode).

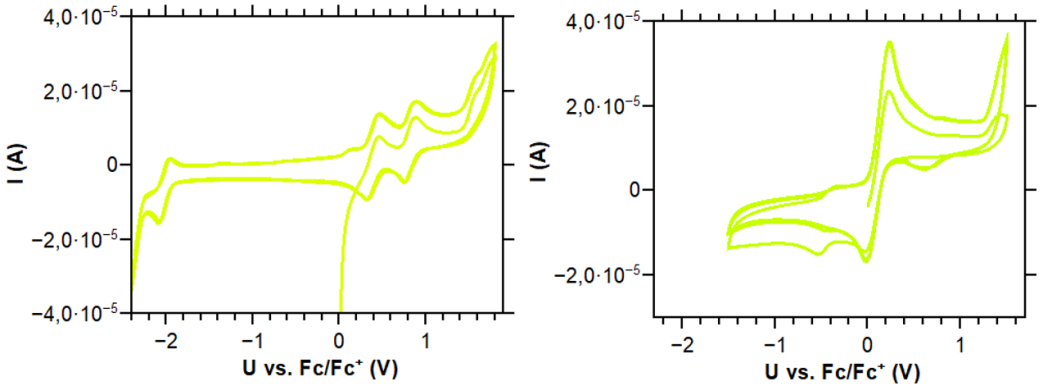

Figure S18. Left: Raw data of the cyclovoltammography of **11** (three scans were performed, the third one was used for analysis). Right: Cyclovoltammogramm of **11** after addition of 1 mM ferrocene (measured in CH_2Cl_2, 0.1 M *n*-Bu_4NPF_6, 100 mV s^{-1} scan rate, glassy carbon working electrode, platinum reference electrode).

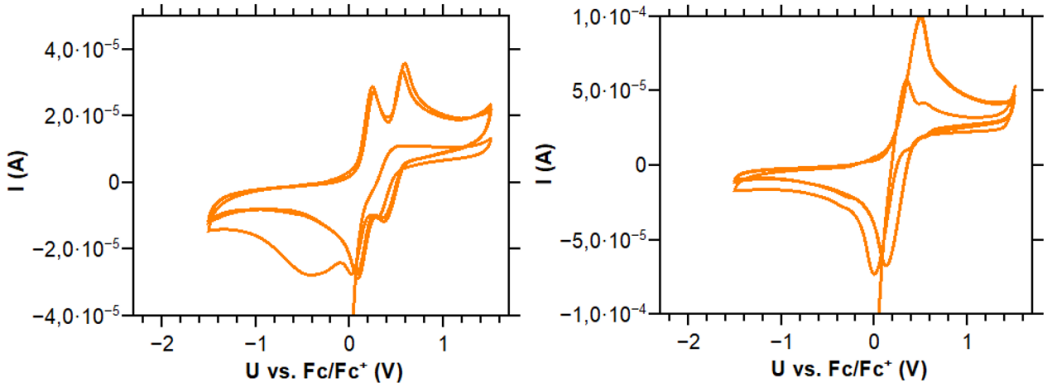

Figure S19. Left: Raw data of the cyclovoltammography of **3** (three scans were performed, the third one was used for analysis). Right: Cyclovoltammogramm of **3** after addition of 1 mM ferrocene (measured in CH_2Cl_2, 0.1 M *n*-Bu_4NPF_6, 100 mV s^{-1} scan rate, glassy carbon working electrode, platinum reference electrode).

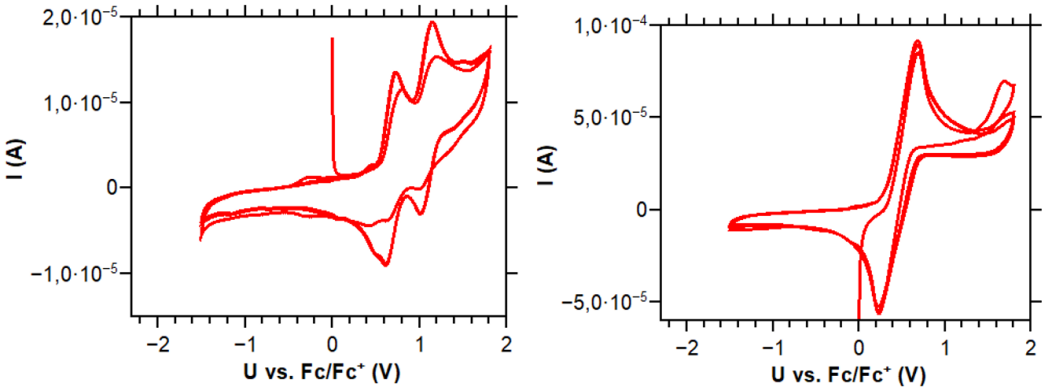

Figure S20. Left: Raw data of the cyclovoltammography of **6** (three scans were performed, the third one was used for analysis). Right: Cyclovoltammogramm of **6** after addition of 1 mM ferrocene (measured in CH_2Cl_2, 0.1 M *n*-Bu_4NPF_6, 100 mV s^{-1} scan rate, glassy carbon working electrode, platinum reference electrode).

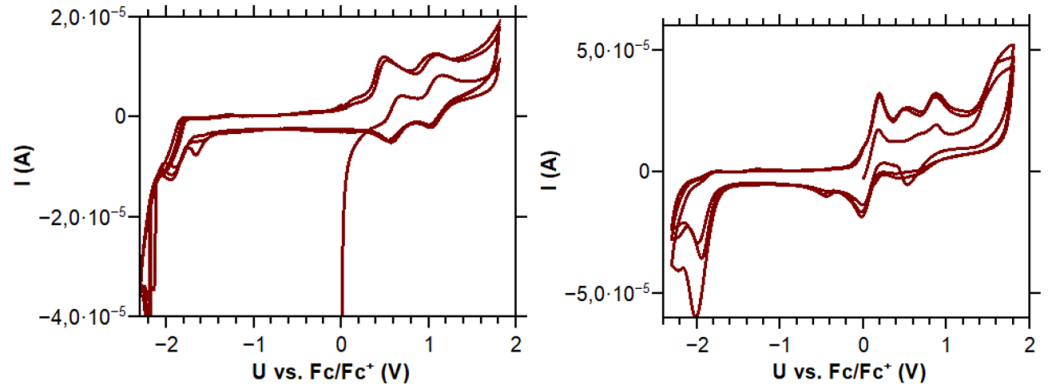

Figure S21. Left: Raw data of the cyclovoltammography of **9** (three scans were performed, the third one was used for analysis). Right: Cyclovoltammogramm of **9** after addition of 1 mM ferrocene (measured in CH_2Cl_2, 0.1 M *n*-Bu_4NPF_6, 100 mV s^{-1} scan rate, glassy carbon working electrode, platinum reference electrode).

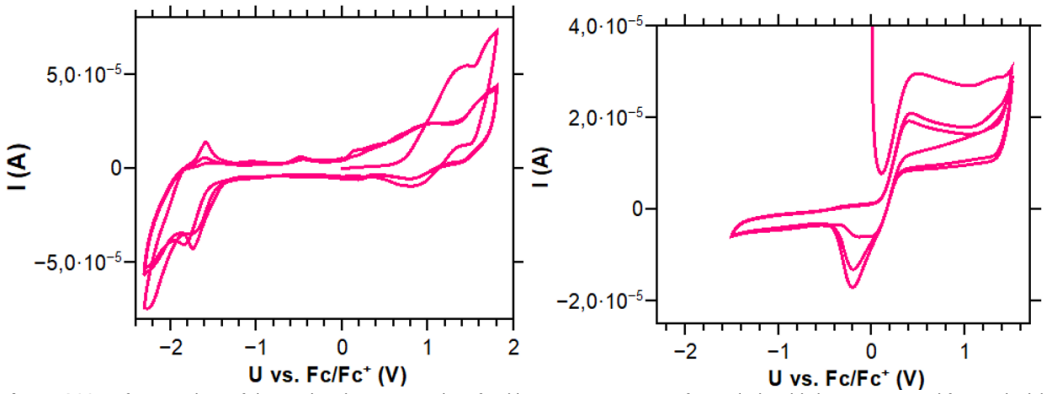

Figure S22. Left: Raw data of the cyclovoltammography of **7** (three scans were performed, the third one was used for analysis). Right: Cyclovoltammogramm of **7** after addition of 1 mM ferrocene (measured in CH_2Cl_2, 0.1 M *n*-Bu_4NPF_6, 100 mV s^{-1} scan rate, glassy carbon working electrode, platinum reference electrode).

TD-DFT results

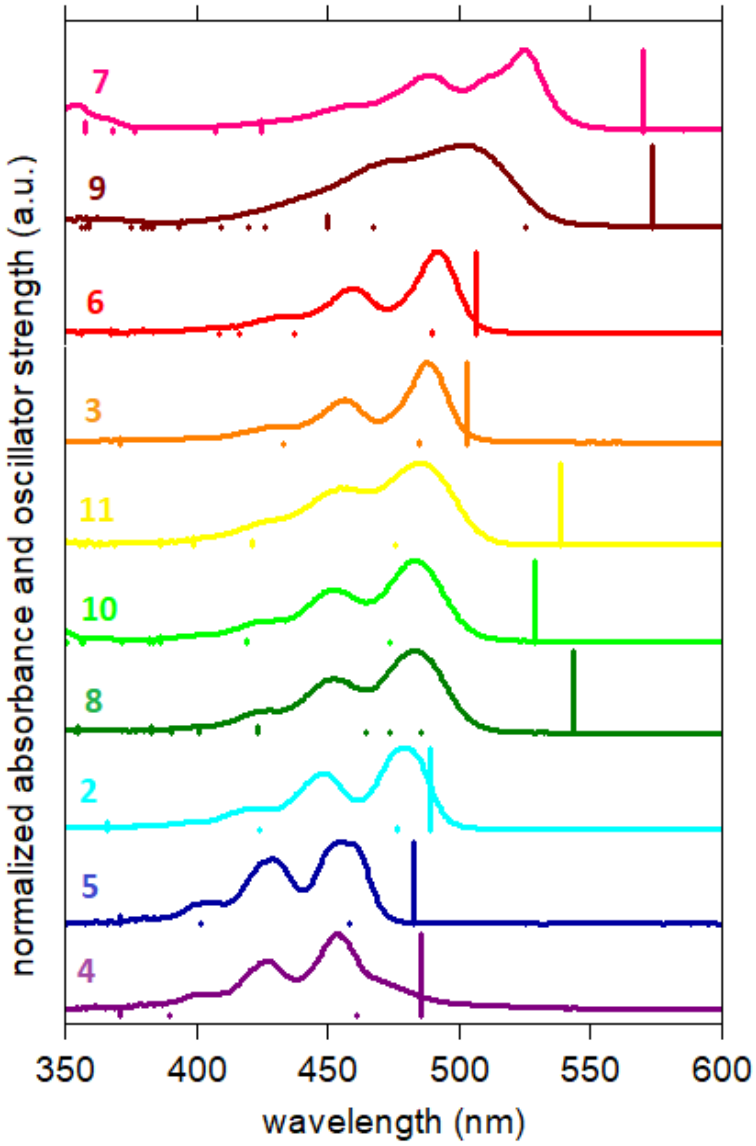

Figure S23. Comparison of normalized absorption spectra and TD-DFT results (vertical lines) of **2**-**11**.

Table S1. Characteristic main electron transition of **2**-**11**, calculated using TD-DFT (def2-TZVPP/PBE level of theory).

Compound	Transition energy (wavelength)	Oscillator strength	Description of main contributions
4	2.57 eV (482 nm)	1.139	HOMO→LUMO (c = -0.924), 0.853 HOMO-2→LUMO+2 (c = -0.268), 0.072 HOMO-1→LUMO+2 (c = 0.101), 0.010 HOMO-5→LUMO+3 (c = 0.107), 0.011
5	2.56 eV (485 nm)	1.163	HOMO→LUMO (c = -0.928), 0.862 HOMO-2→LUMO+1 (c = 0.274), 0.075 HOMO-3→LUMO+3 (c = 0.112), 0.012 HOMO-2→LUMO+2 (c = -0.112), 0.012
2	2.56 eV (485 nm)	1.074	HOMO→LUMO (c = -0.929); 0.862 HOMO-2→LUMO+1 (c = -0.267); 0.071 HOMO-1→LUMO+3 (c = 0.115); 0.013 HOMO-4→LUMO+2 (c = -0.109); 0.012
8	2.28 eV (543 nm)	1.478	HOMO→LUMO (c = 0.921), 0.849 HOMO→LUMO+9 (c = 0.272), 0.074 HOMO-1→LUMO+2 (c = -0.151), 0.023
10	2.35 eV (529 nm)	1.499	HOMO→LUMO (c = 0.933), 0.870 HOMO-2→LUMO+1 (c = -0.197), 0.039 HOMO→LUMO+5 (c = -0.135), 0.018 HOMO→LUMO+9 (c = 0.105), 0.011 HOMO-5→LUMO (c = -0.138), 0.018
11	2.30 eV (539 nm)	1.642	HOMO→LUMO (c = -0.933), 0.870 HOMO-2→LUMO+1 (c = -0.180), 0.032 HOMO-4→LUMO (c = -0.175), 0.031 HOMO→LUMO+7 (c = 0.146), 0.021
3	2.46 eV (503 nm)	1.642	HOMO→LUMO (c = 0.933), 0.870 HOMO-2→LUMO+1 (c = -0.238), 0.057 HOMO-1→LUMO+3 (c = -0.100), 0.010
6	2.45 eV (506 nm)	1.431	HOMO→LUMO (c = -0.930), 0.865 HOMO-2→LUMO+1 (c = 0.149), 0.022 HOMO-4→LUMO (c = -0.164), 0.027 HOMO-9→LUMO (c = -0.112), 0.013
9	2.16 eV (574 nm)	1.597	HOMO→LUMO (c = -0.936), 0.876 HOMO-4→LUMO (c = 0.191), 0.036 HOMO→LUMO+5 (c = 0.133), 0.018 HOMO-5→LUMO+2 (c = -0.108), 0.011 HOMO-2→LUMO+2 (c = 0.113), 0.013
7	2.17 eV (570 nm)	1.642	HOMO→LUMO (c = 0.947), 0.897 HOMO-2→LUMO+1 (c = -0.160), 0.026 HOMO-7→LUMO (c = -0.138), 0.019 HOMO-1→LUMO+1 (c = 0.103), 0.010

NMR Spectra

*1,3,8,10-tetrakis((trimethylsilyl)oxydibenzo[cd,lm]-perylene (**2**)*

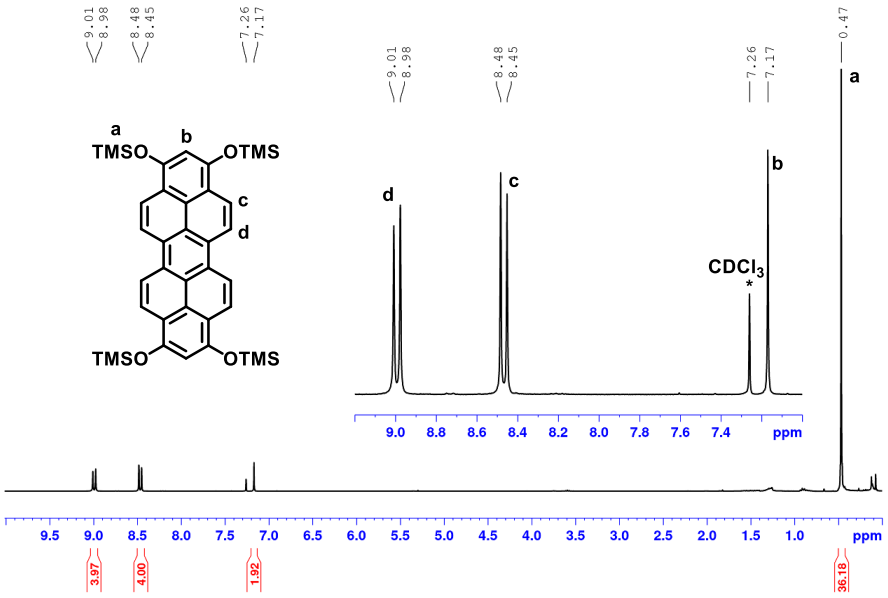

Figure S24. ^{1}H-NMR (300.1 MHz, 298K, $CDCl_3$*) of **2**.

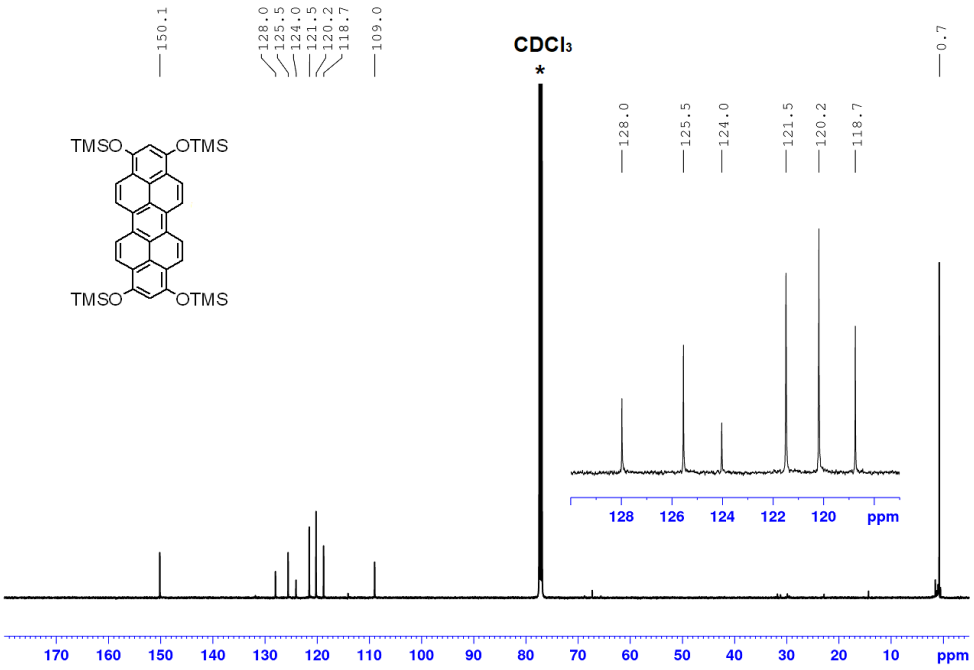

Figure S25. ^{13}C-NMR (125.8 MHz, 298K, $CDCl_3$*) of **2**.

*1,3,8,10-tetrakis((triisopropylsilyl)oxy)dibenzo[cd,lm]-perylene (**3**)*

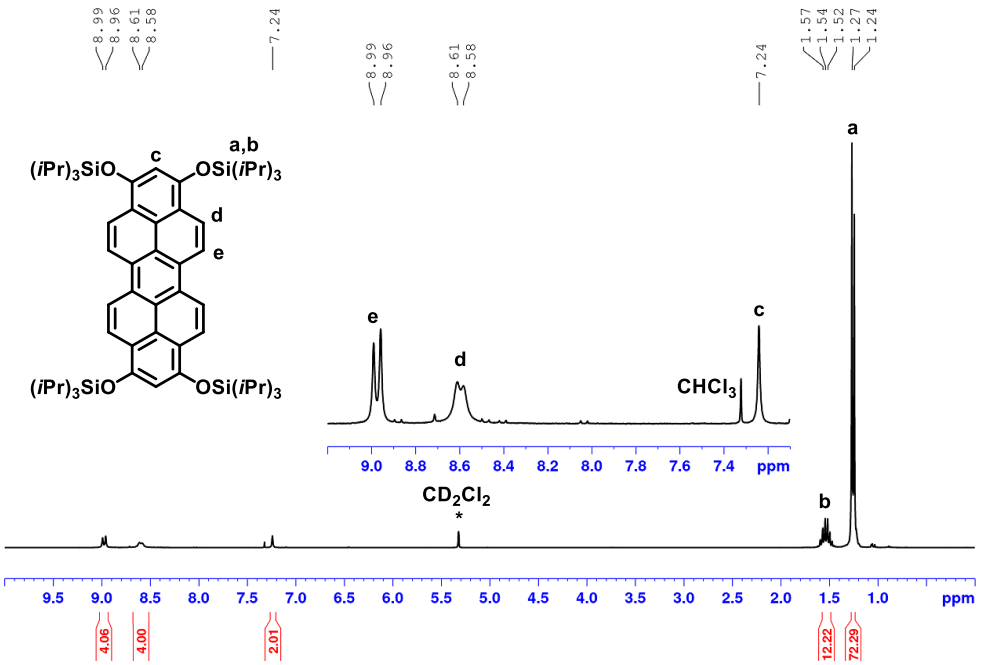

Figure S26. ^{1}H-NMR (300.1 MHz, 298K, CD_2Cl_2*) of **3**.

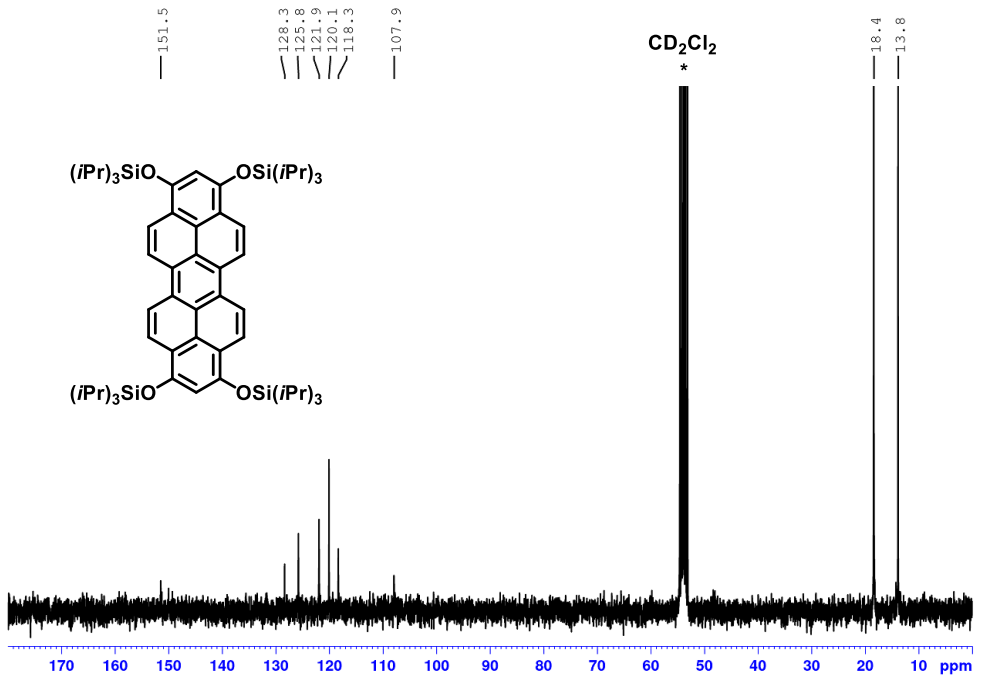

Figure S27. ^{13}C-NMR (75.5 MHz, 298K, $CDCl_3$*) of **4**.

*Dibenzo[cd,lm]perylene-1,3,8,10-tetrayltetrakis(2,2-dimethyl-propanoate) (**4**)*

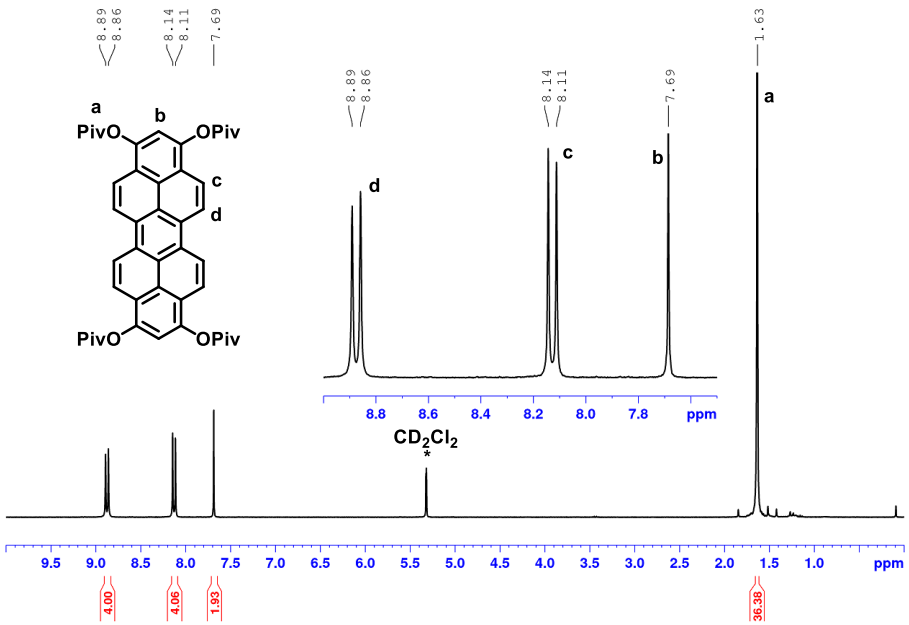

Figure S28. ^{1}H-NMR (300.1 MHz, 298K, CD_2Cl_2*) of **4**.

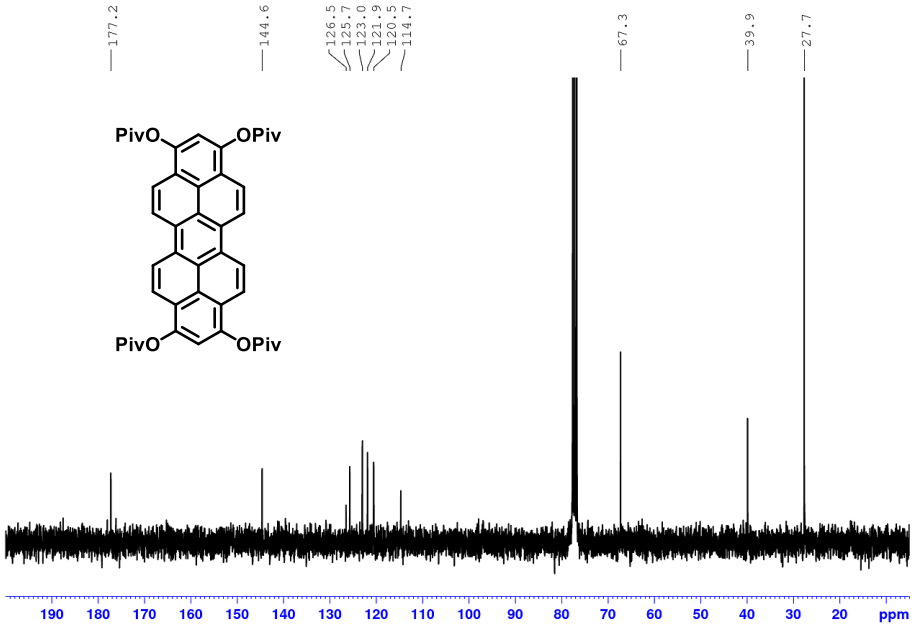

Figure S29. ^{13}C-NMR (75.5 MHz, 298K, $CDCl_3$*) of **4**.

*Dibenzo[cd,lm]perylene-1,3,8,10-tetrayl tetrakis-(trifluoromethanesulfonate) (**5**)*

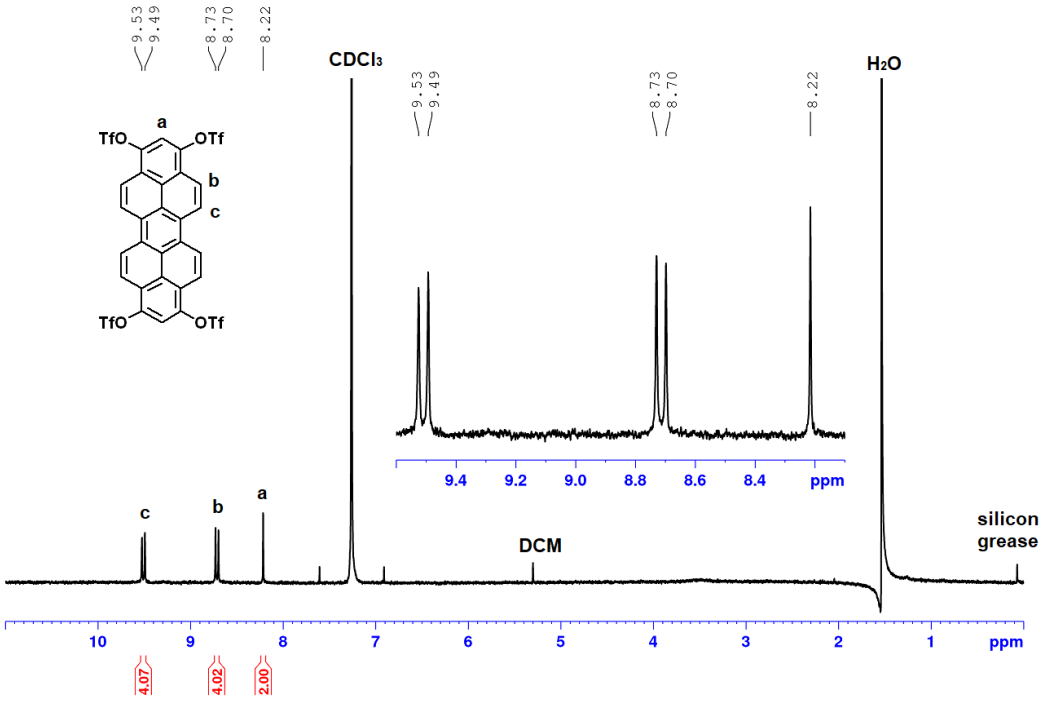

Figure S30. ^{1}H-NMR (300.1 MHz, 298K, $CDCl_3$*) of **5**.

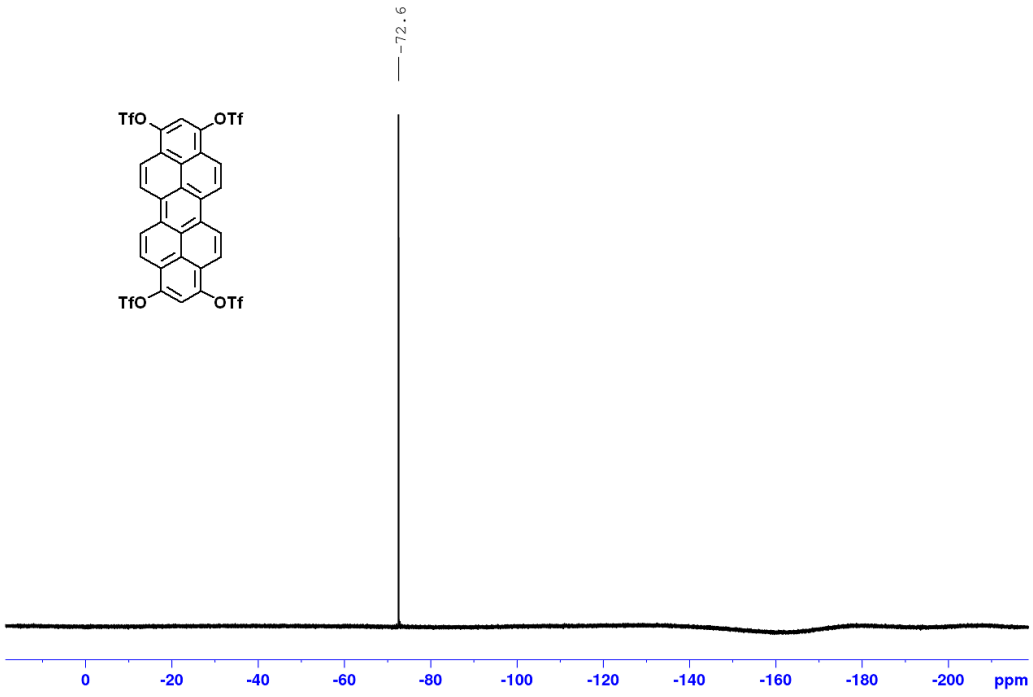

Figure S31. ^{19}F-NMR (235.3 MHz, 298K, $CDCl_3$*) of **5**.

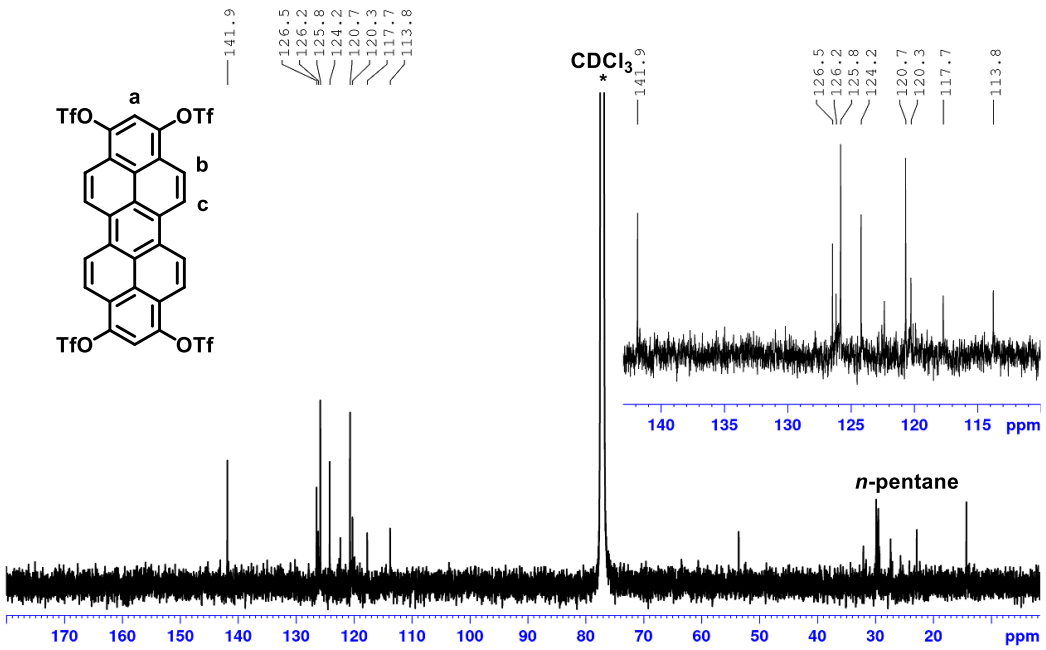

Figure S32. ^{13}C-NMR (125.8 MHz, 298K, $CDCl_3$*) of **5** with residual *n*-pentane.

*Dibenzo[cd,lm]perylene-1,3,8,10-tetrayl tetrakis-(trifluoromethanesulfonate) (**6**)*

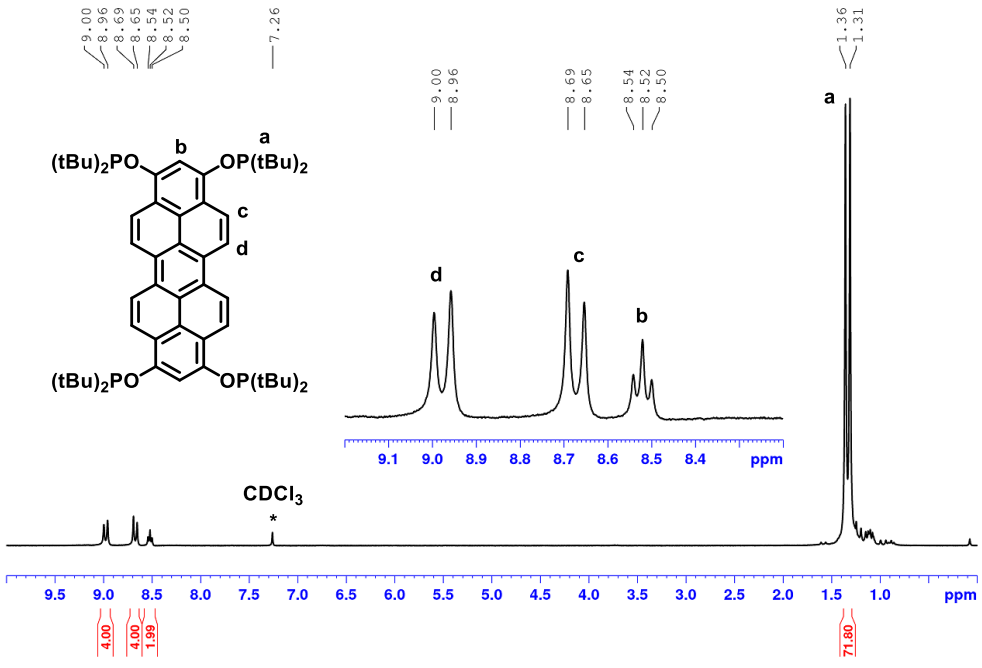

Figure S33. ^{1}H-NMR (300.1 MHz, 298K, $CDCl_3$*) of **6**.

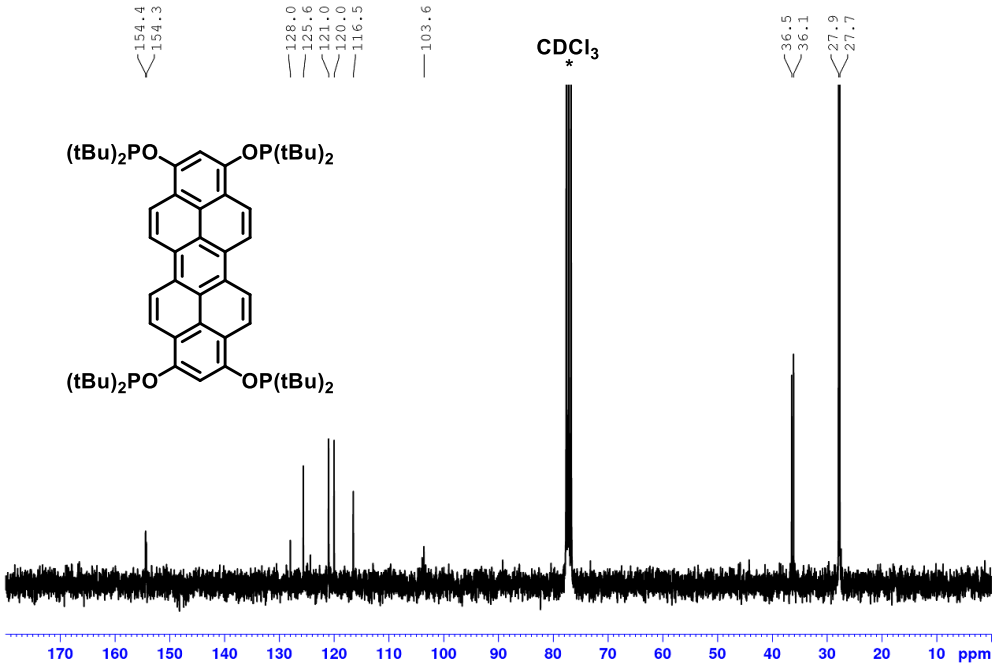

Figure S34. ^{13}C-NMR (75.5 MHz, 298K, $CDCl_3$*) of **6**.

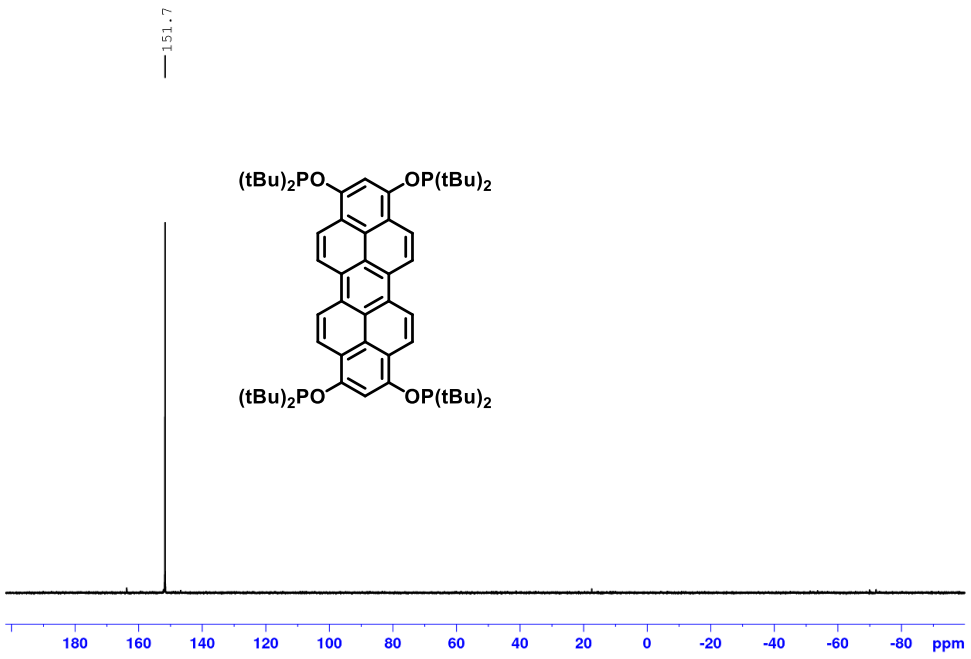

Figure S35. ^{31}P-NMR (101 MHz, 298K, $CDCl_3$*) of **6**.

*1,3,8,10-tetrakis((trimethylsilyl)ethynyl)dibenzo[cd,lm]-perylene (**7**)*

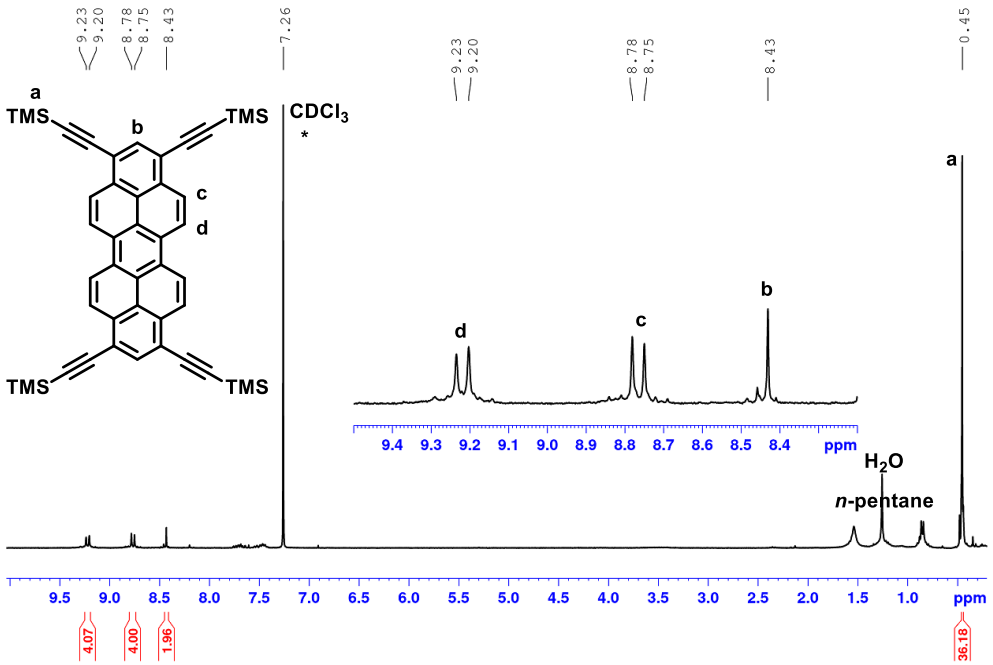

Figure S36. ^{1}H-NMR (300.1 MHz, 298K, $CDCl_3$*) of **7** with residual *n*-pentane.

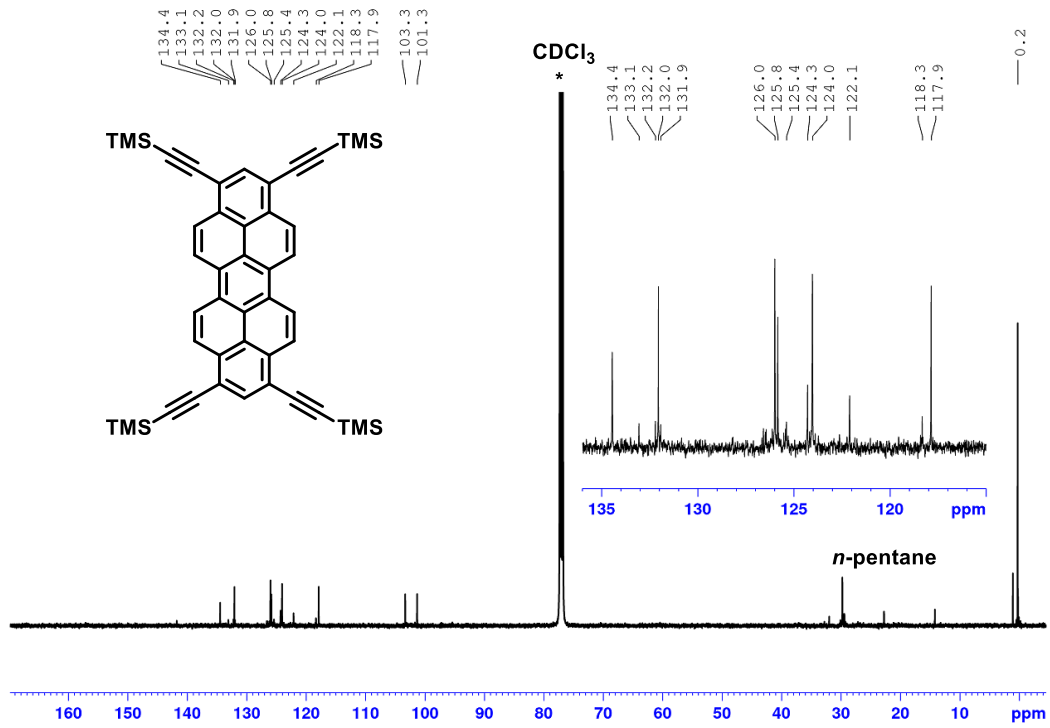

Figure S37. ^{13}C-NMR (125.8 MHz, 298K, $CDCl_3$*) of **7** with residual *n*-pentane.

*1,3,8,10-tetrakis(3,5-bis(trifluoromethyl)phenyl)dibenzo-[cd,lm]perylene (**8**)*

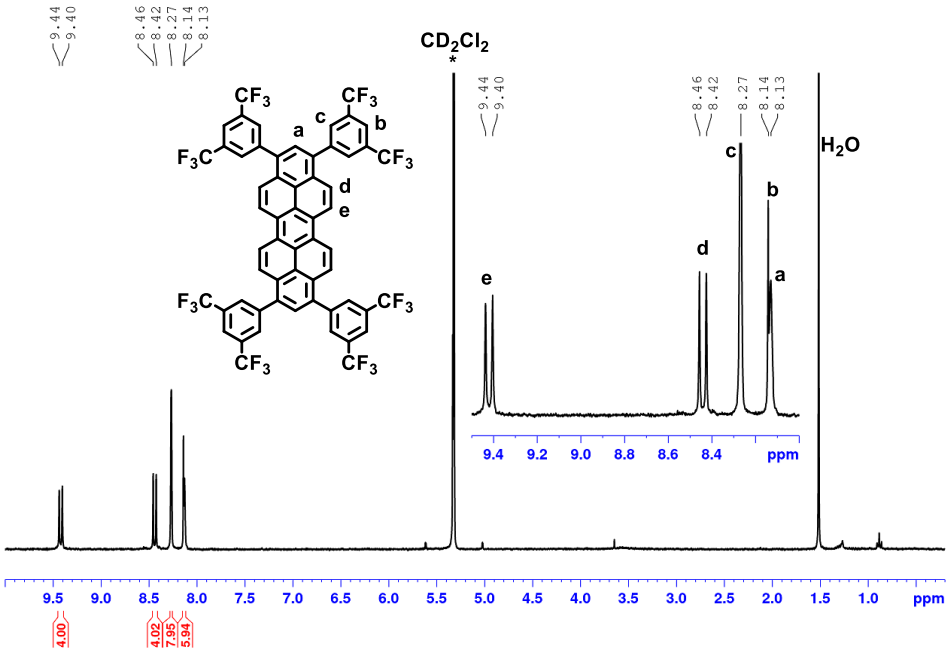

Figure S38. ^{1}H-NMR (300.1 MHz, 298K, CD_2Cl_2*) of **8**.

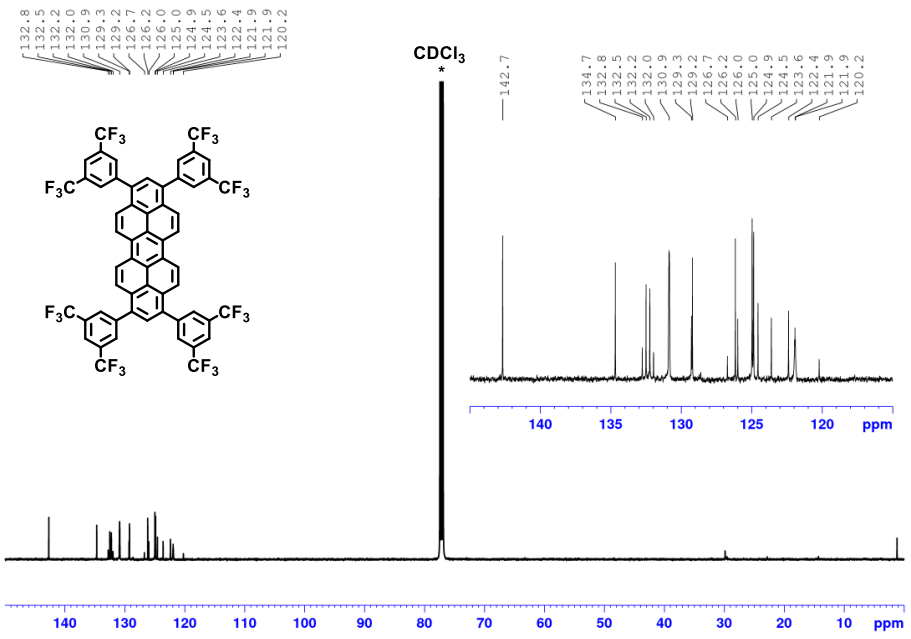

Figure S39. ^{13}C-NMR (125.8 MHz, 298K, $CDCl_3$*) of **8**.

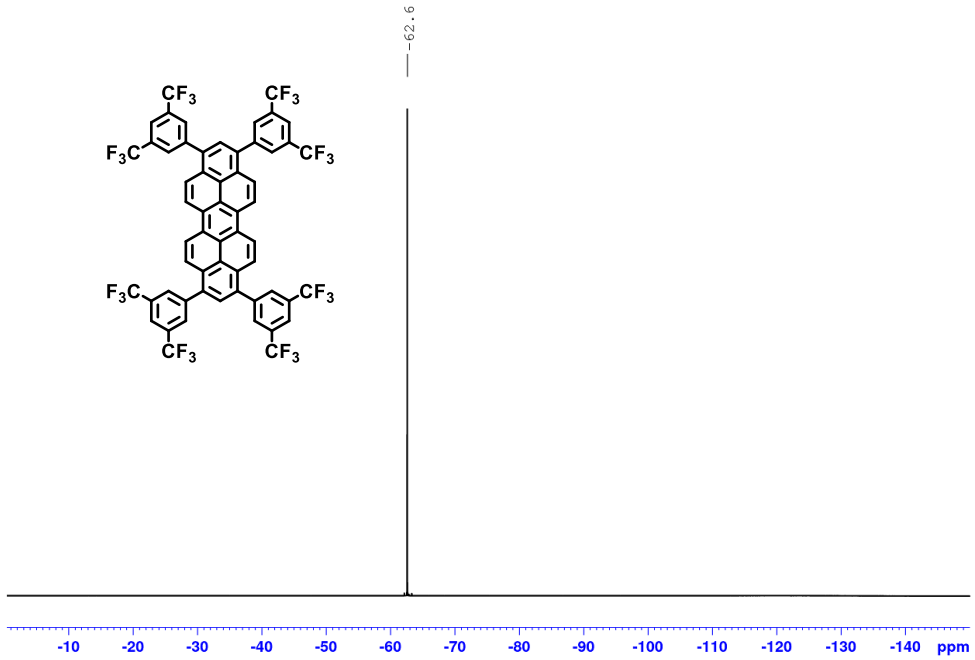

Figure S40. ^{19}F-NMR (235.3 MHz, 298K, $CDCl_3$*) of **8**.

*1,3,8,10-tetra(thiophen-2-yl)dibenzo[cd,lm]perylene (**9**)*

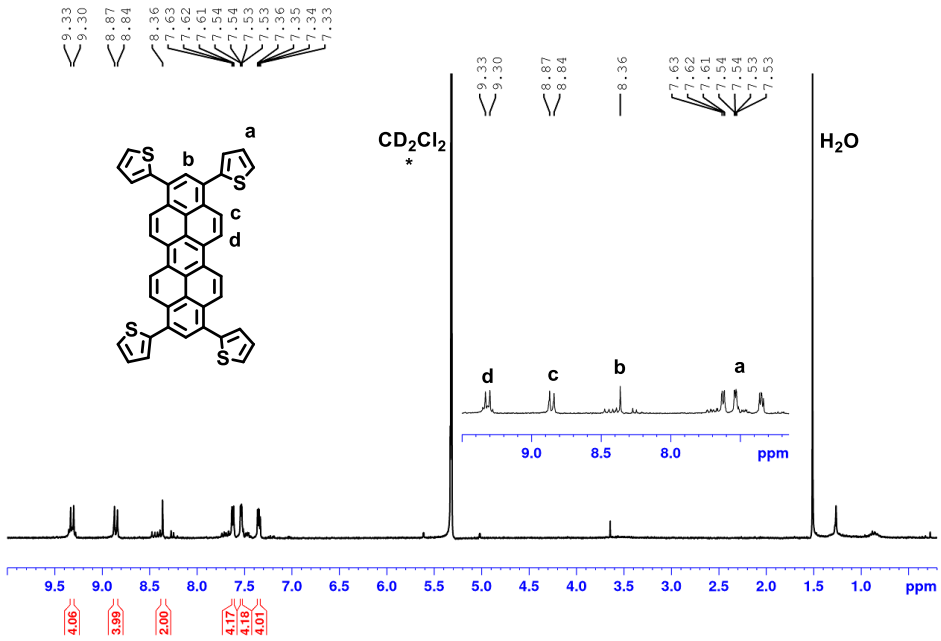

Figure S41. ^{1}H-NMR (300.1 MHz, 298K, CD_2Cl_2*) of **9**.

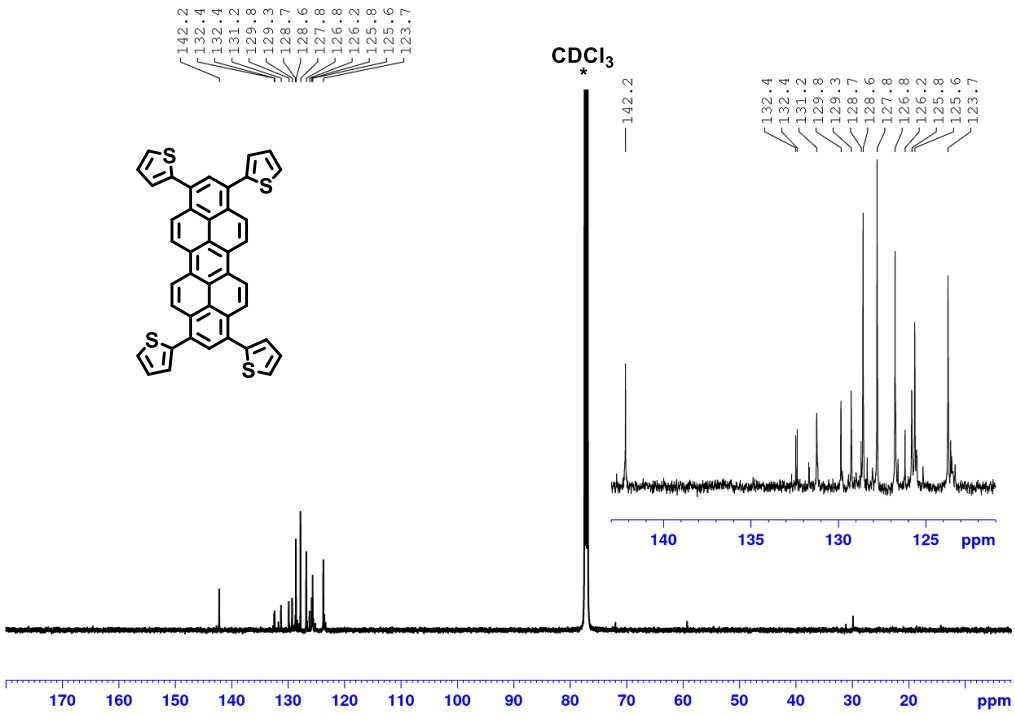

Figure S42. ^{13}C-NMR (125.8 MHz, 298K, $CDCl_3$*) of **9**.

*1,3,8,10-tetraphenyldibenzo[cd,lm]perylene (**10**)*

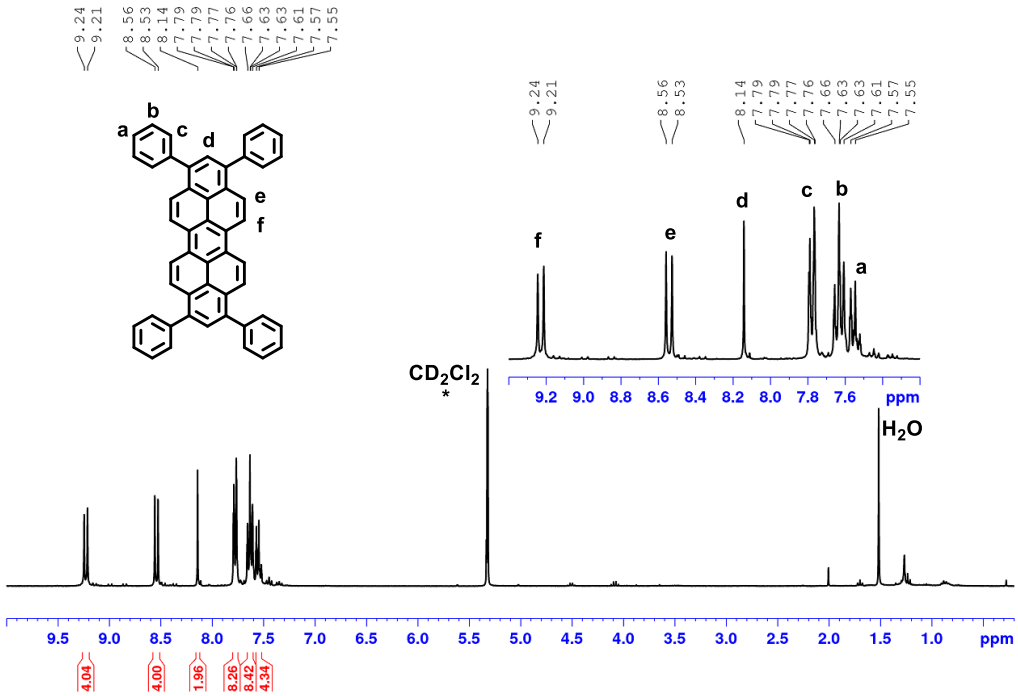

Figure S43. ^{1}H-NMR (300.1 MHz, 298K, CD_2Cl_2*) of **10**.

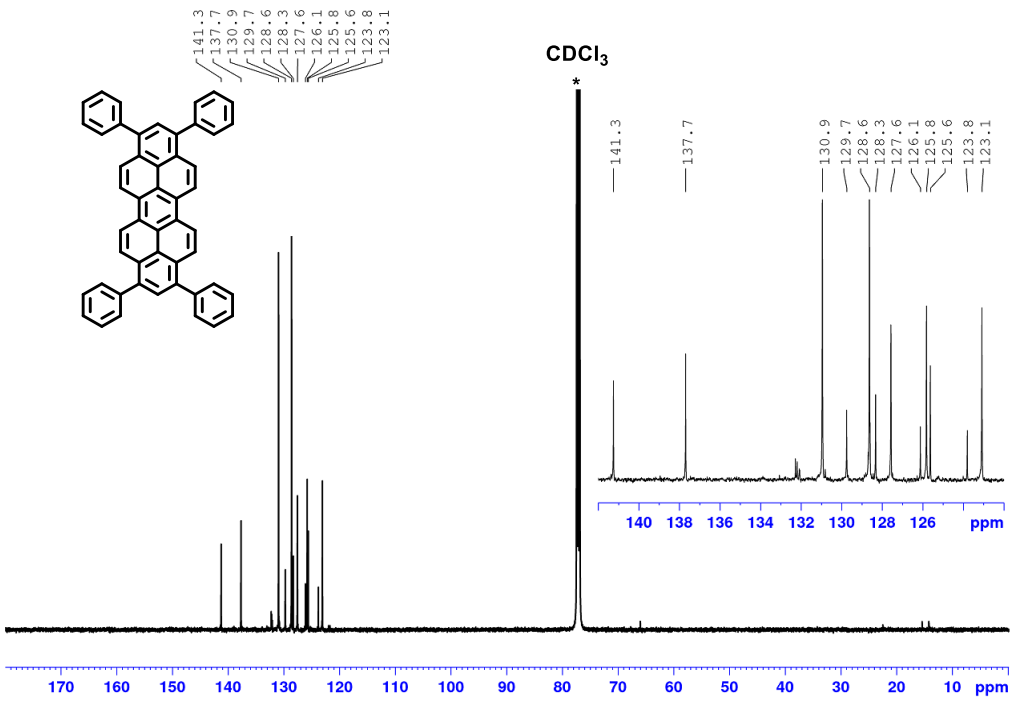

Figure S44. ^{13}C-NMR (125.8 MHz, 298K, $CDCl_3$*) of **10**.

*1,3,8,10-tetraphenyldibenzo[cd,lm]perylene (**11**)*

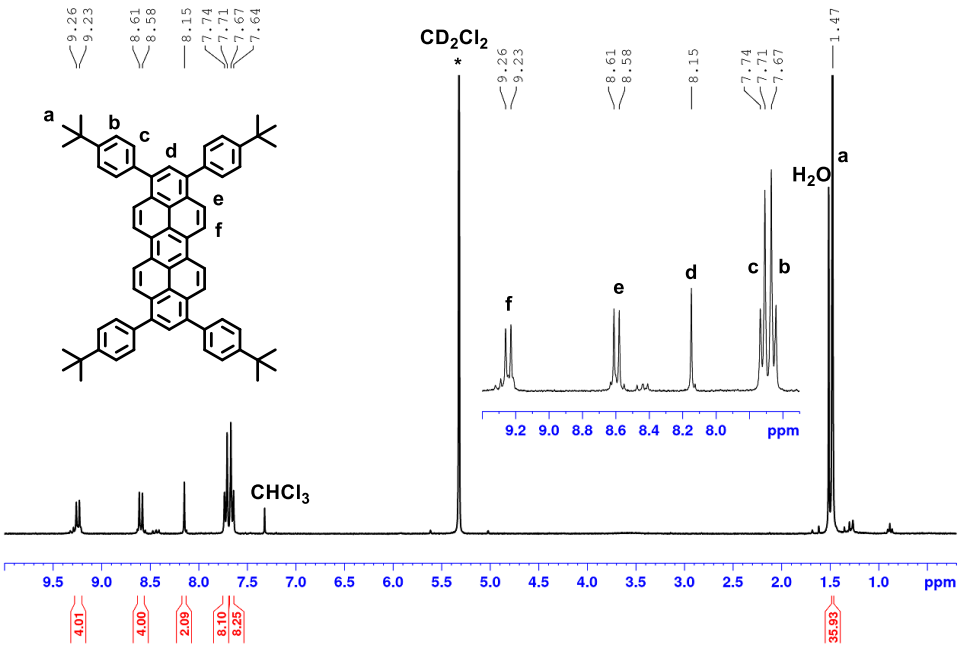

Figure S45. ^{1}H-NMR (300.1 MHz, 298K, CD_2Cl_2*) of **11**.

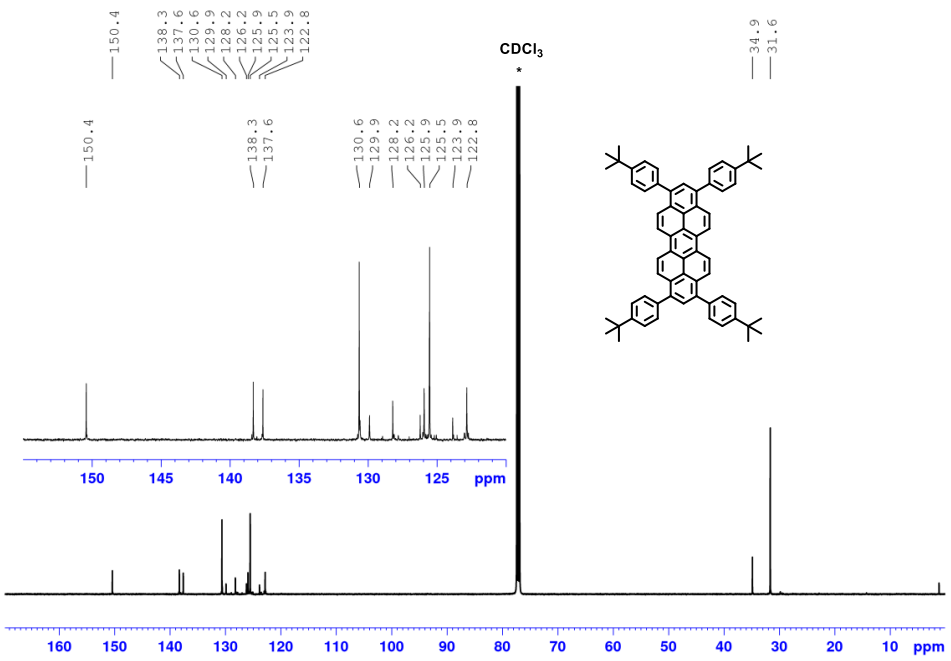

Figure S46. ^{13}C-NMR (125.8 MHz, 298K, $CDCl_3$*) of **11**.

*((2,9-diphenyldibenzo[cd,lm]perylene-1,3,8,10-tetrayl)tetrakis(oxy))tetrakis(trimethylsilane) (**13**)*

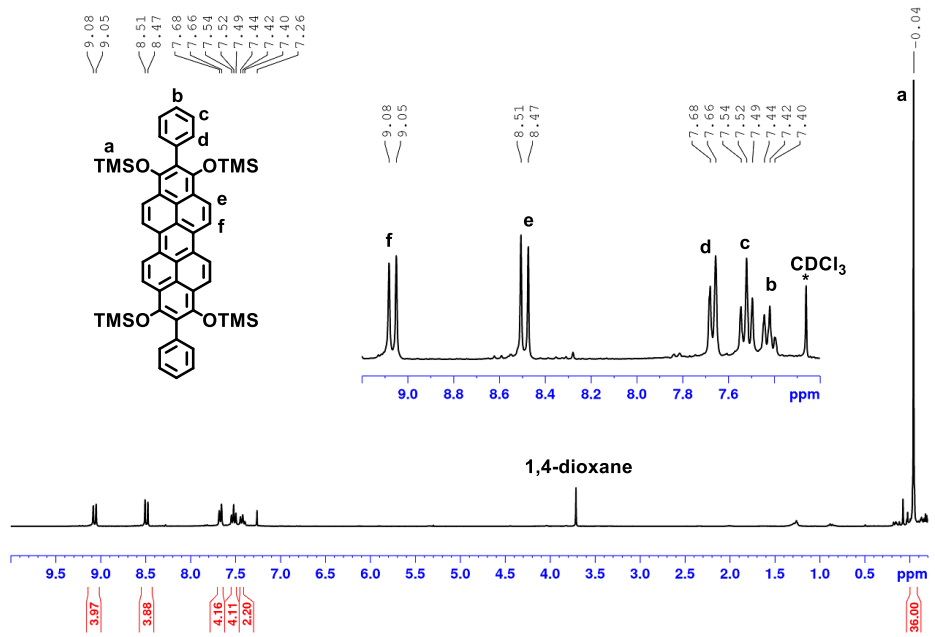

Figure S47. ^{1}H-NMR (300.1 MHz, 298K, $CDCl_3$*) of **13**.

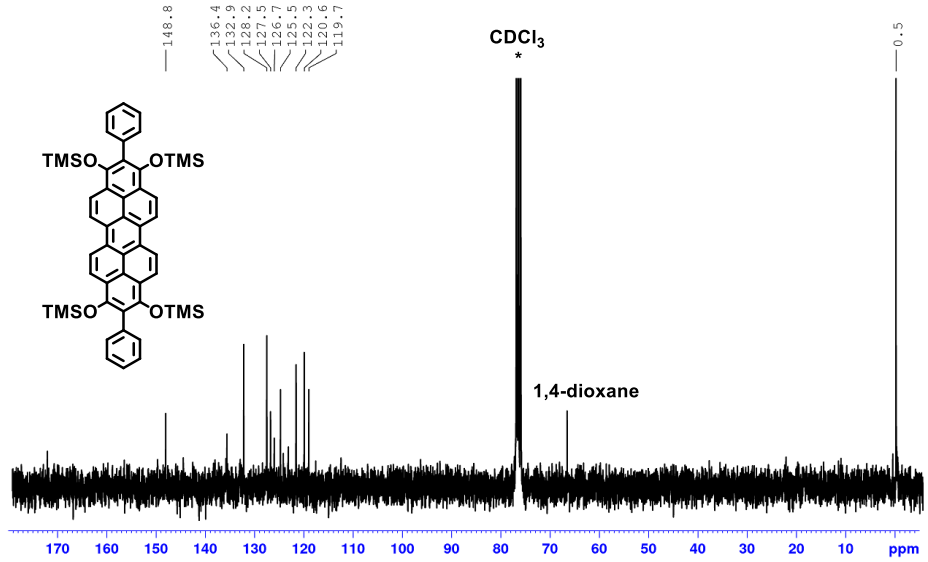

Figure S48. ^{13}C-NMR (75.5 MHz, 298K, $CDCl_3$*) of **13**.

2,9-diphenyldibenzo[cd,lm]perylene-1,3,8,10-tetrayl tetrakis(2,2-dimethylpropanoate) (**14**)

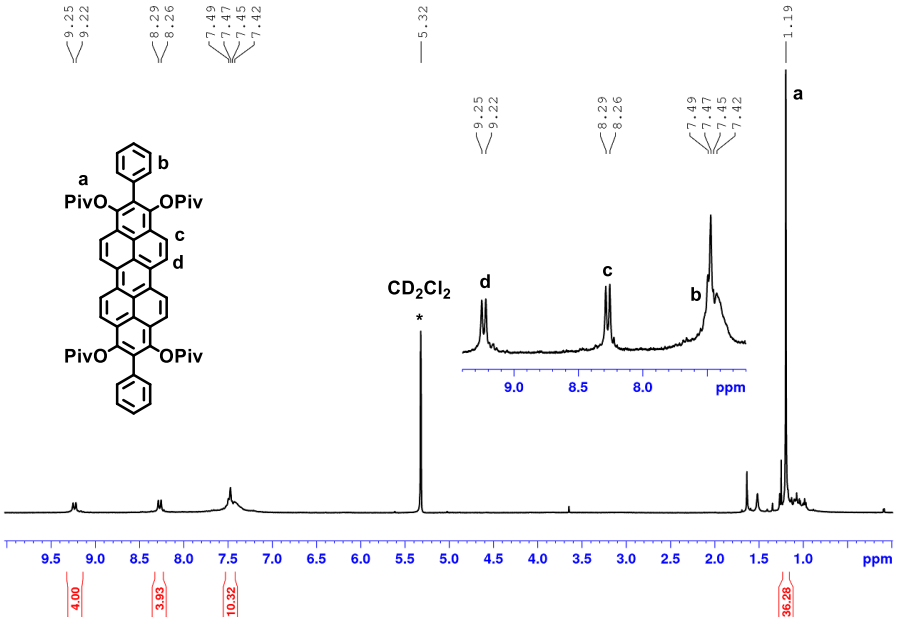

Figure S49. ^{1}H-NMR (300.1 MHz, 298K, CD_2Cl_2*) of **14**.

References

[1] W. L. F. Armarego, D. D. Perrin, *Purification of laboratory chemicals*, Butterworth-Heinemann, Oxford, **2002**.
[2] B. Eistert, W. Eifler, O. Ganster, *Chem. Ber.* **1969**, *102*, 1988–2002.
[3] N. Buffet, E. Grelet, H. Bock, *Chem. Eur. J.* **2010**, *16*, 5549–5553.
[4] D. T. W. van Stadlbauer, *Molecules* **1997**, *1*, 201–206.
[5] G. M. Sheldrick, *Acta Cryst. C Section C* **2015**, *71*, 3–8.
[6] C. B. Hübschle, G. M. Sheldrick, B. Dittrich, *J. Appl. Cryst.* **2011**, *44*, 1281–1284.
[7] A. L. Spek, *Acta Cryst. D* **2009**, *65*, 148–155.
[8] H. P. K. Brandenburg, *Diamond*, Crystal Impact GbR, Bonn, **2012**.
[9] A. D. Becke, *J. Chem. Phys.* **1993**, *98*, 5648–5652.
[10] Lee, Yang, Parr, *Phys. Rev. B* **1988**, *37*, 785–789.
[11] P. J. Stephens, F. J. Devlin, C. S. Ashvar, C. F. Chabalowski, M. J. Frisch, *Faraday Disc.* **1994**, *99*, 103.
[12] A. Schäfer, C. Huber, R. Ahlrichs, *J. Chem. Phys.* **1994**, *100*, 5829–5835.
[13] F. Weigend, *Phys. Chem. Chem. Phys.* **2006**, *8*, 1057–1065.
[14] F. Weigend, R. Ahlrichs, *Phys. Chem. Chem. Phys.* **2005**, *7*, 3297–3305.
[15] F. Weigend, M. Häser, H. Patzelt, R. Ahlrichs, *Chem. Phys. Lett.* **1998**, *294*, 143–152.
[16] K. Eichkorn, O. Treutler, H. Öhm, M. Häser, R. Ahlrichs, *Chem. Phys. Lett.* **1995**, *240*, 283–290.
[17] M. von Arnim, R. Ahlrichs, *J. Comput. Chem.* **1998**, *19*, 1746–1757.
[18] F. Weigend, *Phys. Chem. Chem. Phys.* **2002**, *4*, 4285–4291.
[19] S. Grimme, J. Antony, S. Ehrlich, H. Krieg, *J. Chem. Phys.* **2010**, *132*, 154104.
[20] A. D. Becke, E. R. Johnson, *J. Chem. Phys.* **2005**, *123*, 154101.
[21] E. R. Johnson, A. D. Becke, *J. Chem. Phys.* **2005**, *123*, 24101.
[22] E. R. Johnson, A. D. Becke, *J. Chem. Phys.* **2006**, *124*, 174104.
[23] S. Grimme, S. Ehrlich, L. Goerigk, *J. Comput. Chem.* **2011**, *32*, 1456–1465.
[24] F. Neese, *WIREs Comput Mol Sci* **2011**, *2*, 73–78.
[25] Perdew, Burke, Ernzerhof, *Phys. Rev. Lett.* **1996**, *77*, 3865–3868.
[26] J. P. Perdew, K. Burke, M. Ernzerhof, *Phys. Rev. Lett.* **1997**, *78*, 1396.
[27] J. R. Lakowicz, *Principles of fluorescence spectroscopy*, Springer, New York, **2010**.
[28] S. Werner, T. Vollgraff, J. Sundermeyer, *Angew. Chem.* **2021**. DOI: 10.1002/ange.202100686; *Angew. Chem. Int. Ed.* **2021**, DOI: 10.1002/anie.202100686.

7.3 Supporting Information of Publication 3

The chapter *Single crystal X-ray structures* of the supporting information of Publication 3 is not shown in the following.
This was done by T. Vollgraff and is part of his doctoral thesis.
Also, the XYZ coordinates for DFT-optimized structures are not reprinted and can be retrieved from the online version of the supporting information.

Electronic Supplementary Material (ESI) for Organic Chemistry Frontiers.

Supporting Information

Reductive O-Triflylation of Naphthalene Diimide: Access to Alkyne- and Amine-functionalized 2,7-Diazapyrenes

Simon Werner, [a] Tobias Vollgraff, [a] Qitang Fan, [a] Kevin Bania, [a] J. Michael Gottfried, [a] and Jörg Sundermeyer*[a]

Contents

Density functional theory (DFT)

Kohn-Sham frontier molecular orbitals and optimized geometries

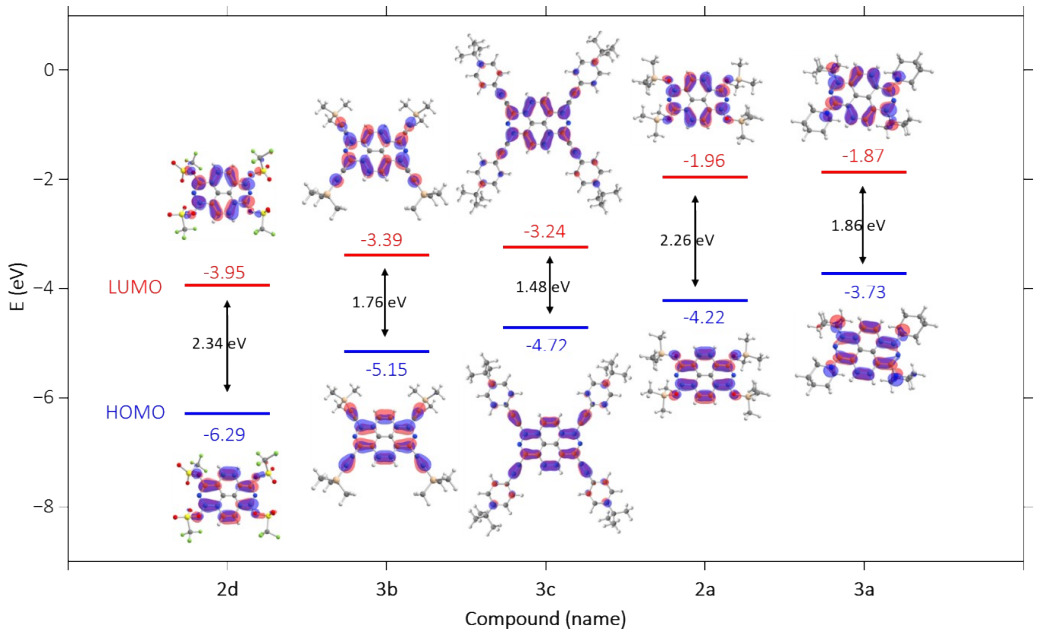

Figure S1. Kohn-Sham orbitals of HOMO and LUMO of **2a**, **2d**, **3a**, **3b** and **3c**, and their energies calculated by DFT (def2-TZVPP/PBE level of theory).

Table S1. Cartesian coordinates (XYZ) of DFT optimized geometry of **2d** (def2-TZVPP/PBE).

C	-2.759505000	1.260306000	0.603317000
C	-1.391672000	1.372323000	0.286771000
C	-0.698449000	0.137576000	0.124201000
C	-1.376063000	-1.106231000	0.275932000
C	-2.738411000	-1.012287000	0.620135000
N	-3.399768000	0.119167000	0.786372000
C	-0.683868000	2.605966000	0.136278000
C	0.650423000	2.613908000	-0.163585000
C	1.366657000	1.388846000	-0.341810000
C	0.681902000	0.146029000	-0.207203000
C	1.367983000	-1.089357000	-0.386981000
C	0.665179000	-2.324298000	-0.229518000
C	-0.664816000	-2.332461000	0.090682000
C	2.735180000	1.293376000	-0.660791000
N	3.383206000	0.161072000	-0.869599000
C	2.729619000	-0.978342000	-0.728953000
O	-3.470644000	2.434788000	0.835115000
S	-4.828543000	2.801207000	-0.031497000
O	-5.680020000	3.515782000	0.874340000
O	-5.239999000	1.695077000	-0.849845000
C	-4.046896000	4.075545000	-1.181327000
F	-3.466544000	5.052868000	-0.469745000
F	-5.010107000	4.591488000	-1.951518000
F	-3.122907000	3.480631000	-1.953650000
O	-3.420179000	-2.194536000	0.863175000
S	-4.921959000	-2.406175000	0.187370000
O	-4.978770000	-1.748873000	-1.090624000
O	-5.924401000	-2.280865000	1.206533000
C	-4.651980000	-4.249184000	-0.118454000

TD-DFT calculations

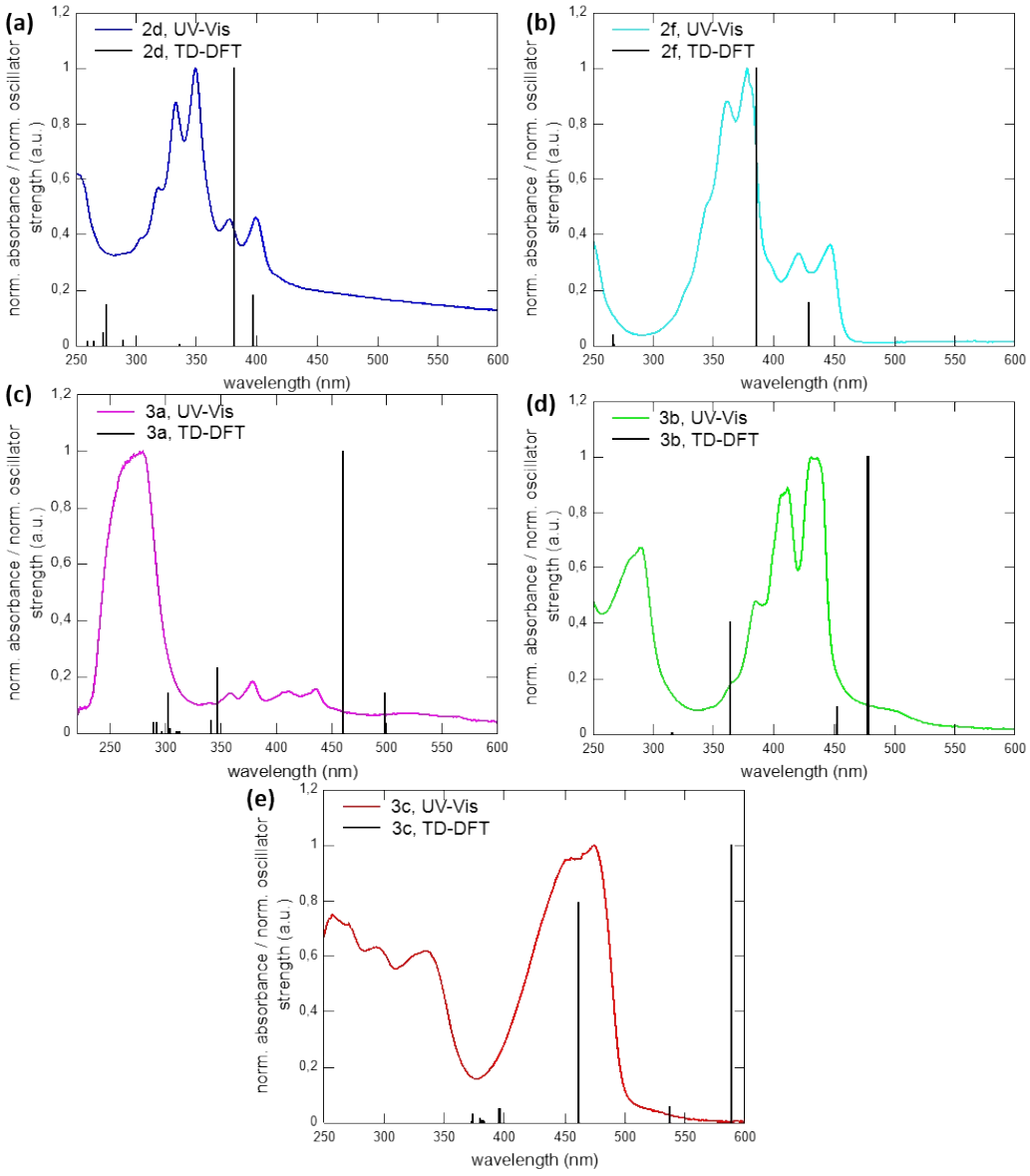

Figure S2. Comparison of normalized UV-Vis spectra (recorded in CH_2Cl_2) and normalized electron transitions calculated by TD-DFT (black bars, def2-TZVPP/PBE level of theory) of a) **2d** (calculation for silyl ether **2a**); b) of **2f**; c) of **3a**; d) of **3b**; e) of **3c**.

Table S6. Characteristic main electron transition of **2a**, **2f**, **3a**, **3b** and **3c** calculated using TD-DFT (def2-TZVPP/PBE level of theory).

Compound	Transition energy (wavelength)	Oscillator strength	Description of main contributions
2a	2.88 eV (429 nm)	0.119	HOMO→LUMO+1 (c = -0.950); 0.903 HOMO-1→LUMO+2 (c = -0.152); 0.023 HOMO-4→LUMO (c = -0.210 0.045
	3.22 eV (385 nm)	0.768	HOMO→LUMO (c = 0.927); 0.859 HOMO-1→LUMO+3 (c = -0.105); 0.011 HOMO-2→LUMO+2 (c = 0.177); 0.031 HOMO-4→LUMO+1 (c = -0.241); 0.058
2d	3.13 eV (397 nm)	0.119	HOMO→LUMO+1 (c = -0.937); 0.877 HOMO-3→LUMO+1 (c = -0.107); 0.011 HOMO-5→LUMO (c = -0.282); 0.080
	3.26 eV (381 nm)	0.652	HOMO→LUMO (c = 0.922); 0.849 HOMO-2→LUMO+2 (c = -0.165); 0.027 HOMO-5→LUMO+1 (c = -0.266); 0.071
3a	2.49 eV (498 nm)	0.115	HOMO→LUMO (c = 0.246); 0.059 HOMO→LUMO+1 (c = 0.916); 0.839 HOMO-1→LUMO+2 (c = -0.134); 0.018 HOMO-3→LUMO (c = 0.196); 0.038 HOMO-8→LUMO (c = 0.112); 0.012
	2.69 eV (460 nm)	0.818	HOMO→LUMO (c = -0.913); 0.833 HOMO→LUMO+1 (c = 0.239); 0.057 HOMO-7→LUMO+2 (c = -0.114); 0.013 HOMO-8→LUMO (c = -0.114); 0.020 HOMO-9→LUMO+1 (c = -0.168); 0.028
3b	2.59 eV (478 nm)	1.115	HOMO→LUMO (c = -0.959); 0.902 HOMO-11→LUMO+1 (c = 0.149); 0.022 HOMO-12→LUMO (c = 0.149); 0.022
3c	2.14 eV (579 nm)	1.632	HOMO→LUMO (c = -0.960); 0.921 HOMO-6→LUMO (c = 0.170); 0.028

Concentration-dependent UV-Vis spectroscopy

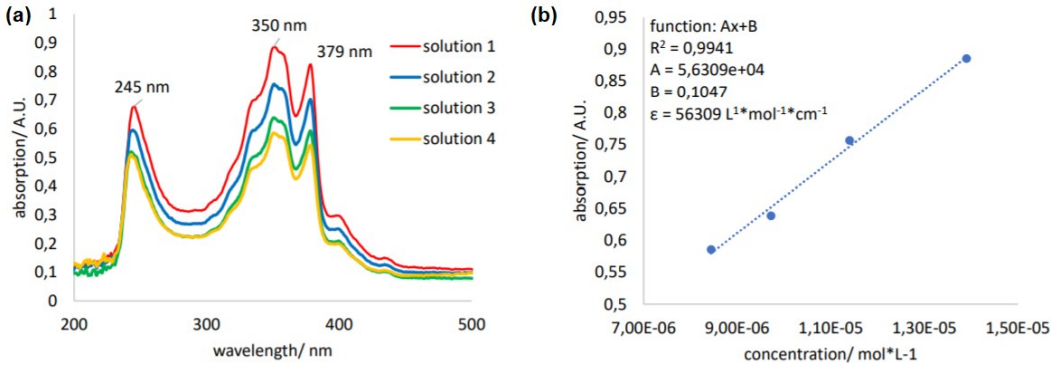

Figure S3. a) UV-Vis spectra of **2d** in dichloromethane in four different concentrations; b) corresponding linear regression of the absorbances for the determination of the molar decadic attenuation coefficient (ε).

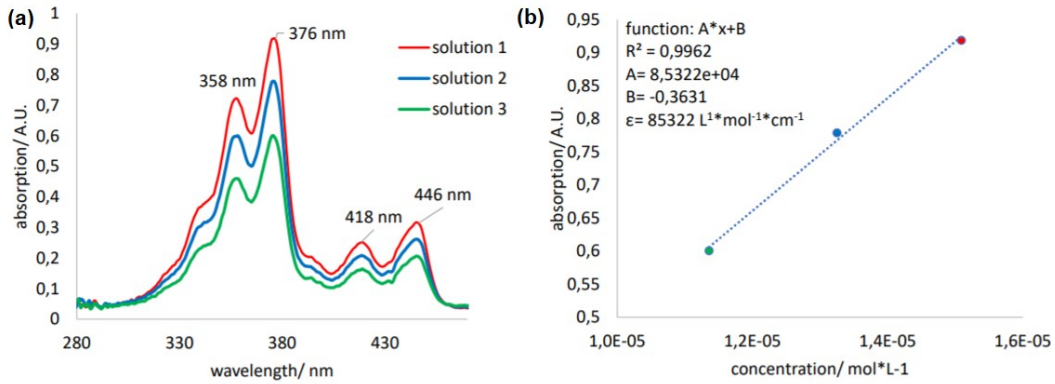

Figure S4. a) UV-Vis spectra of **2f** in dichloromethane in four different concentrations; b) corresponding linear regression of the absorbances for the determination of the molar decadic attenuation coefficient (ε).

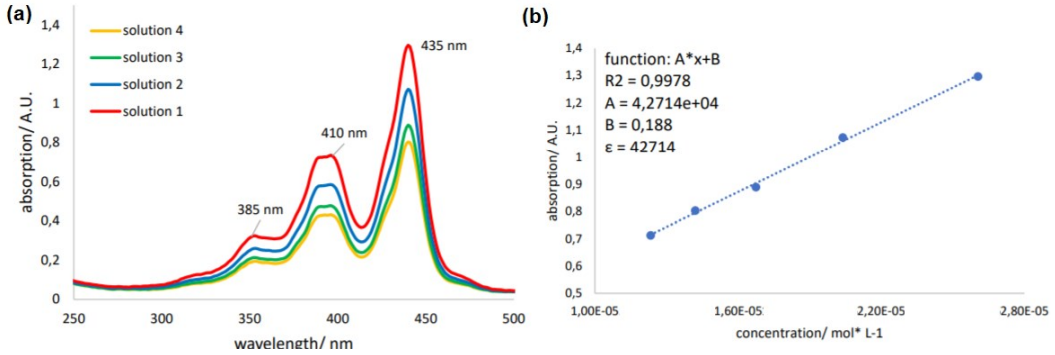

Figure S5. a) UV-Vis spectra of **3b** in dichloromethane in four different concentrations; b) corresponding linear regression of the absorbances for the determination of the molar decadic attenuation coefficient (ε).

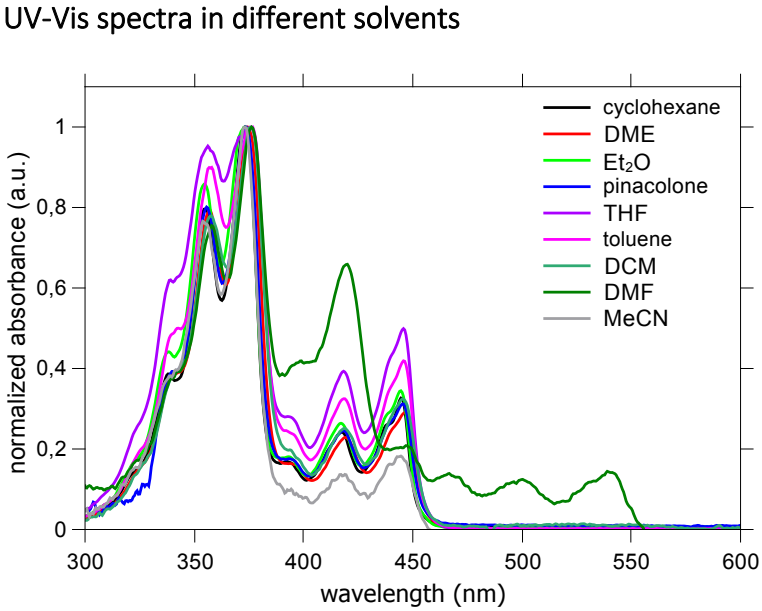

Figure S6. a) Normalized UV-Vis spectra of **2f** recorded in different solvents (c ≈ 10^{-5} M). Note that **2f** decomposes in DMF.

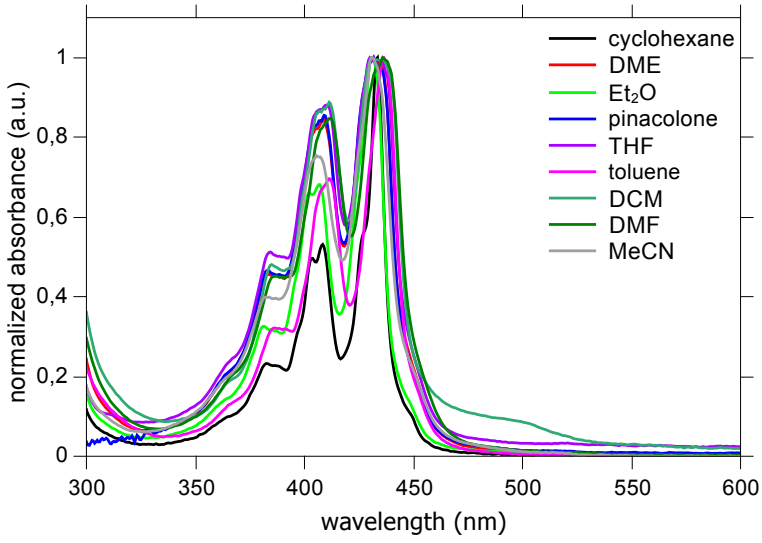

Figure S7. a) Normalized UV-Vis spectra of **3b** recorded in different solvents (c ≈ 10^{-5} M).

Determination of fluorescence quantum yields

Fluorescence quantum yields (Φ_{PL}) were recorded by dilution method using a fluorescein solution (0.1 M in aqueous NaOH, Φ_{flu} = 0.95[1]) as reference. Both, the samples and the reference were measured at low concentrations in order to ensure a linear relationship between the intensity of emitted light and the concentration of the absorbing/emitting species.
The quantum yields of the samples (Φ_s) were determined by the following equation 1.[1]

$$\Phi_{flu} = \frac{grad(s)}{grad(flu)} * \frac{n^2(s)}{n^2(flu)} * \Phi_{flu}$$

In equation 1, *grad* is the slope of the "emission versus absorbance" plot of the samples (s) and the standard fluorescein (flu). n is the refractive index of the used solvents.
In the following Figure S7, the "emission versus absorbance" plots and the linear regression graphs for the determination of the fluorescence quantum yields of **2d**, **2f**, **3b**, **3c** as well as the reference fluorescein are shown.

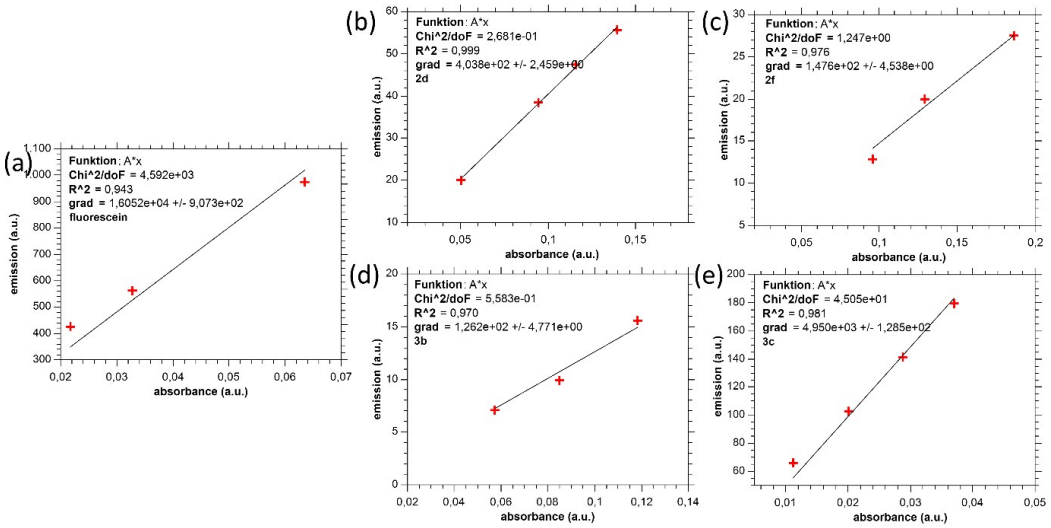

Figure S8. "Emission versus absorption" plots of (a) fluorescein (in 0.1 M NaOH solution); (b) **2d**; (c) **2f**; (d) **3b**; (e) **3c** recorded in dichloromethane. The concentrations were in the low 10^{-6} M range.

1 J. R. Lakowicz, *Principles of fluorescence spectroscopy*, Springer, New York, NY, 4th edn., 2010.

EI-MS spectrum of 1,3,6,8-tetraiodobenzo[lmn][3,8]phenanthroline (I1)

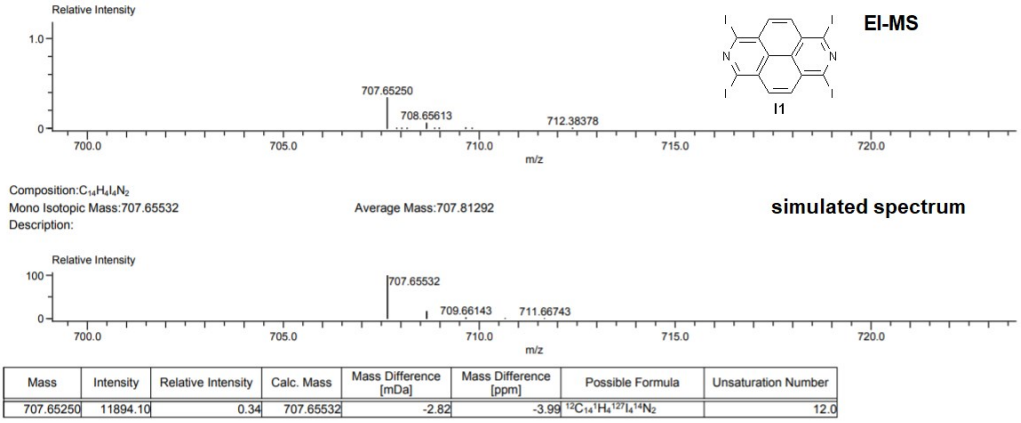

Composition:$C_{14}H_4I_4N_2$
Mono Isotopic Mass:707.65532
Average Mass:707.81292
Description:

simulated spectrum

Mass	Intensity	Relative Intensity	Calc. Mass	Mass Difference [mDa]	Mass Difference [ppm]	Possible Formula	Unsaturation Number
707.65250	11894.10	0.34	707.65532	-2.82	-3.99	$^{12}C_{14}{}^{1}H_4{}^{127}I_4{}^{14}N_2$	12.0

Figure S12. High-resolution electron ionization (EI) mass spectrum (top) of **I1** and simulated spectrum (below).

NMR spectra

*1,3,6,8-Tetrakis((trimethylsilyl)oxy)benzo[lmn][3,8]phenanthroline (**2a**)*

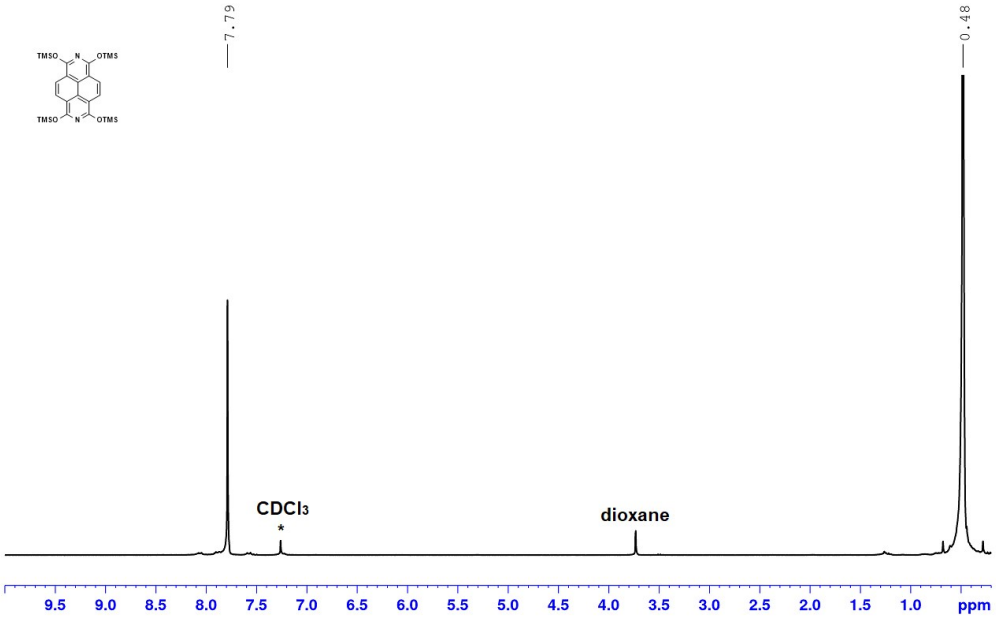

Figure S13. ^{1}H-NMR (300.1 MHz, 298K, $CDCl_3$*) of **2a**.

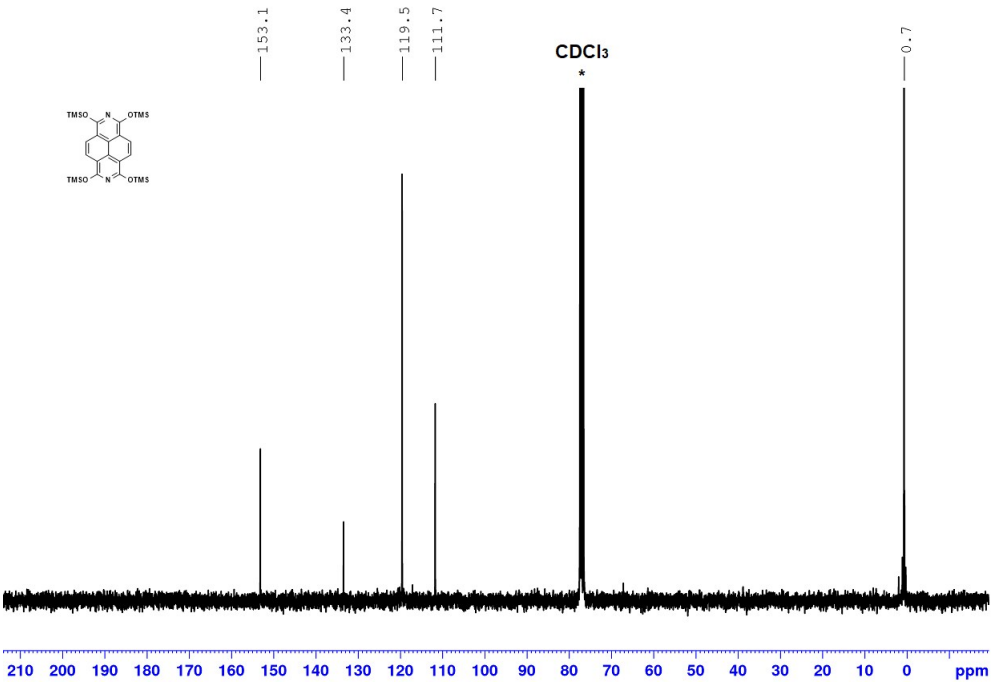

Figure S14. ^{13}C-NMR (75.1 MHz, 298K, $CDCl_3$*) of **2a**.

*1,3,6,8-Tetrakis((triisopropylsilyl)oxy)benzo[lmn][3,8]phenanthroline (**2e**)*

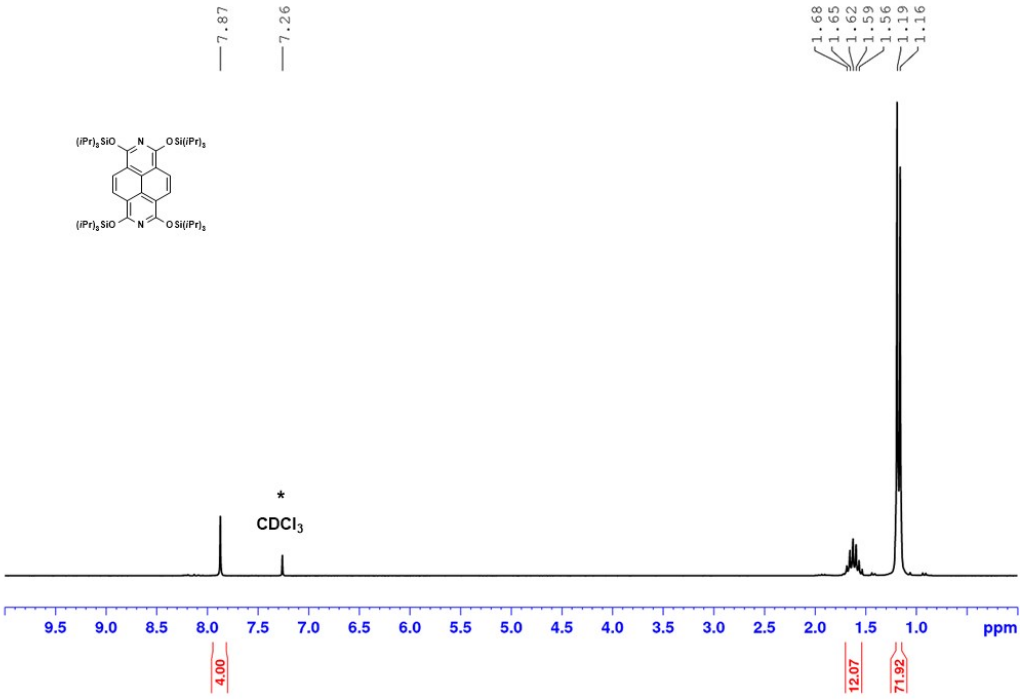

Figure S15. ^{1}H-NMR (300.1 MHz, 298K, $CDCl_3$*) of **2e**.

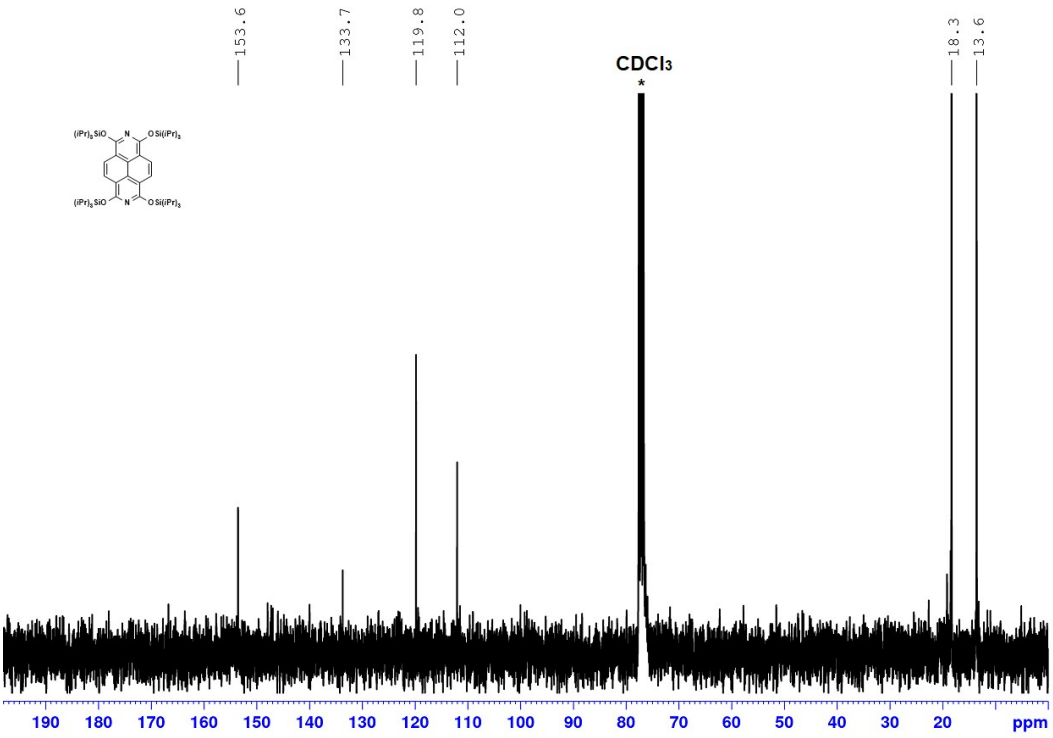

Figure S16. ^{13}C-NMR (75.1 MHz, 298K, $CDCl_3$*) of **2e**.

*1,3,6,8-Tetrakis((tert-butyldimethylsilyl)oxy)benzo[lmn][3,8]phenanthroline (**2f**)*

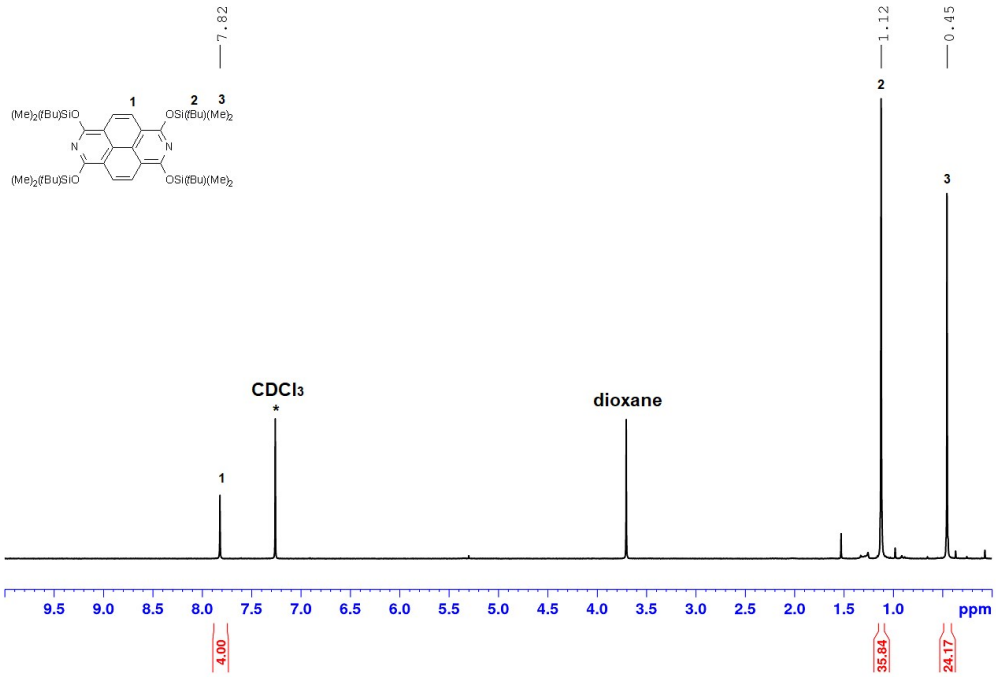

Figure S17. ^{1}H-NMR (300.1 MHz, 298K, $CDCl_3$*) of **2f**. Contains residual 1,4-dioxane.

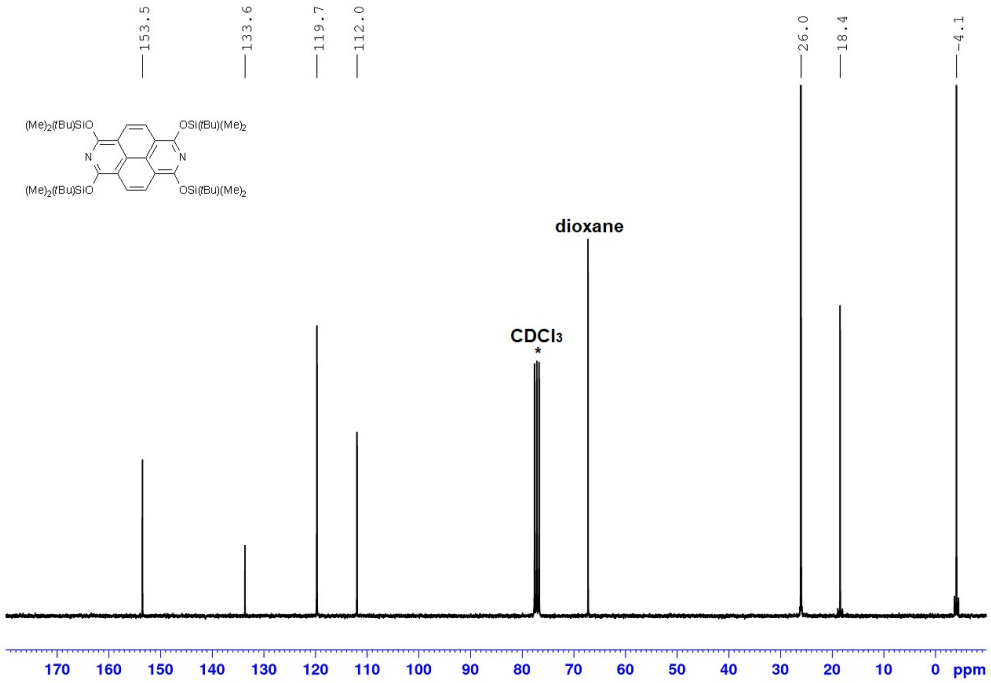

Figure S18. ^{13}C-NMR (75.1 MHz, 298K, $CDCl_3$*) of **2f**. Contains residual 1,4-dioxane.

*Benzo[lmn][3,8]phenanthroline-1,3,6,8-tetrayltetrakis(trifluoromethanesulfonate) (**2d**)*

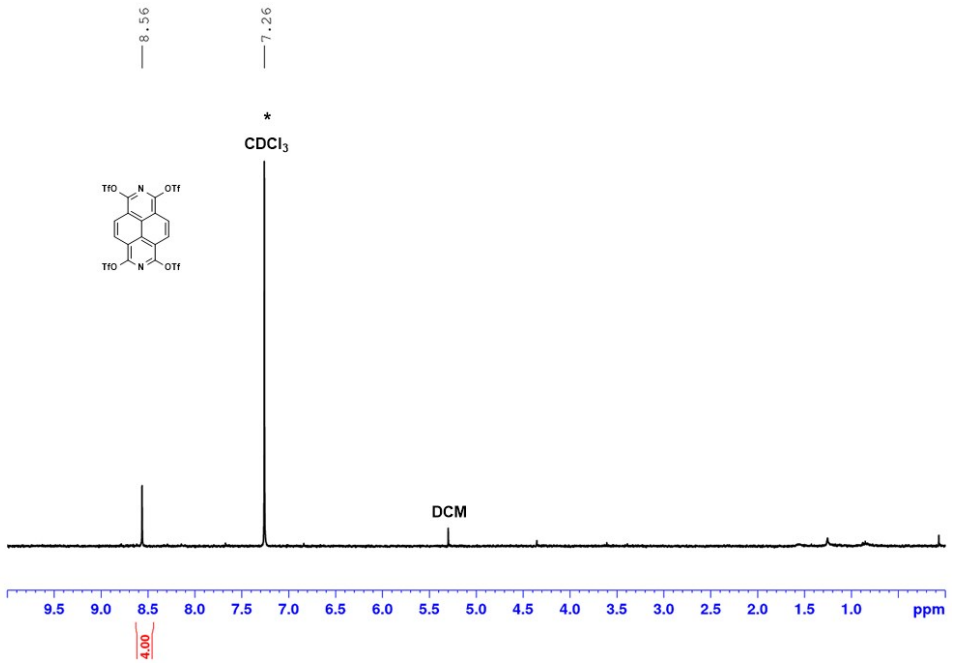

Figure S19. ^{1}H-NMR (300.1 MHz, 298K, $CDCl_3$*) of **2d**. Contains residual dichloromethane.

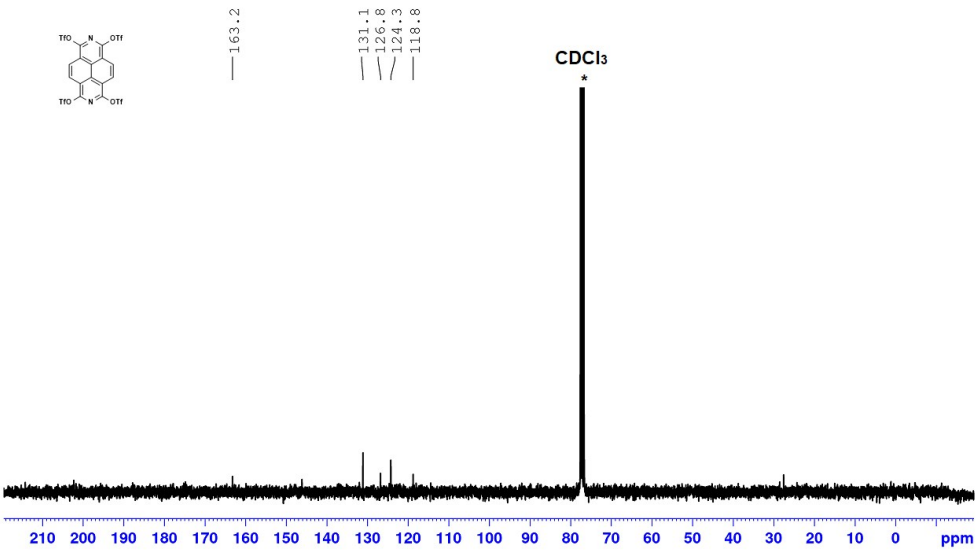

Figure S20. ^{13}C-NMR (75.1 MHz, 298K, $CDCl_3$*) of **2d**.

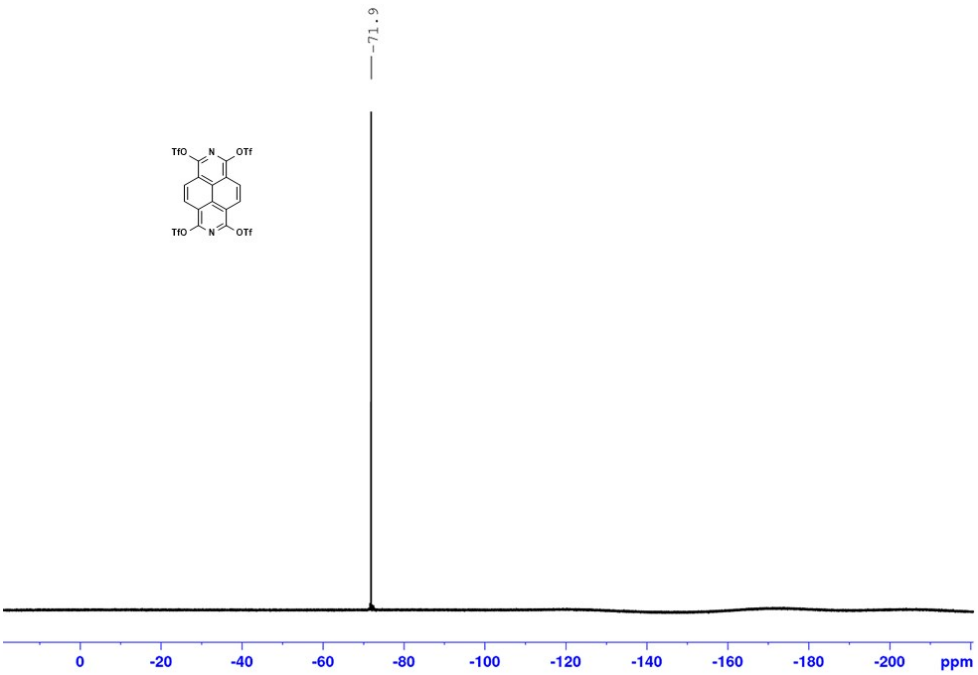

Figure S21. ^{19}F-NMR (235.3 MHz, 298K, $CDCl_3$*) of **2d**.

*1,3,6,8-Tetrakis((trimethylsilyl)ethynyl)benzo[lmn][3,8]phenanthroline (**3b**)*

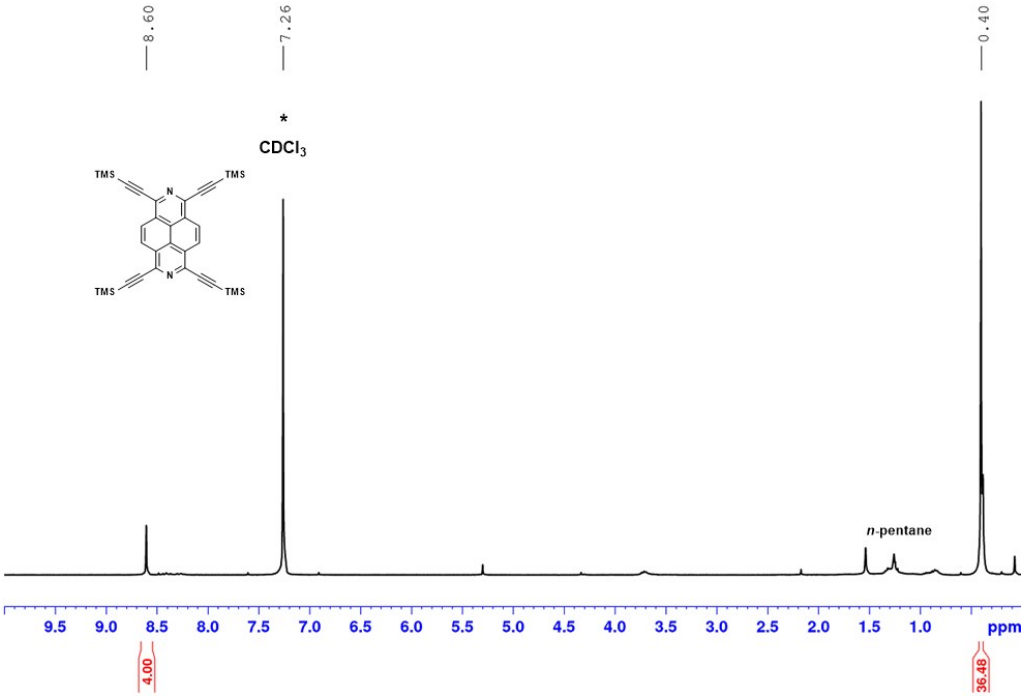

Figure S22. ^{1}H-NMR (300.1 MHz, 298K, $CDCl_3$*) of **3b**. Contains residual *n*-pentane and silicon grease.

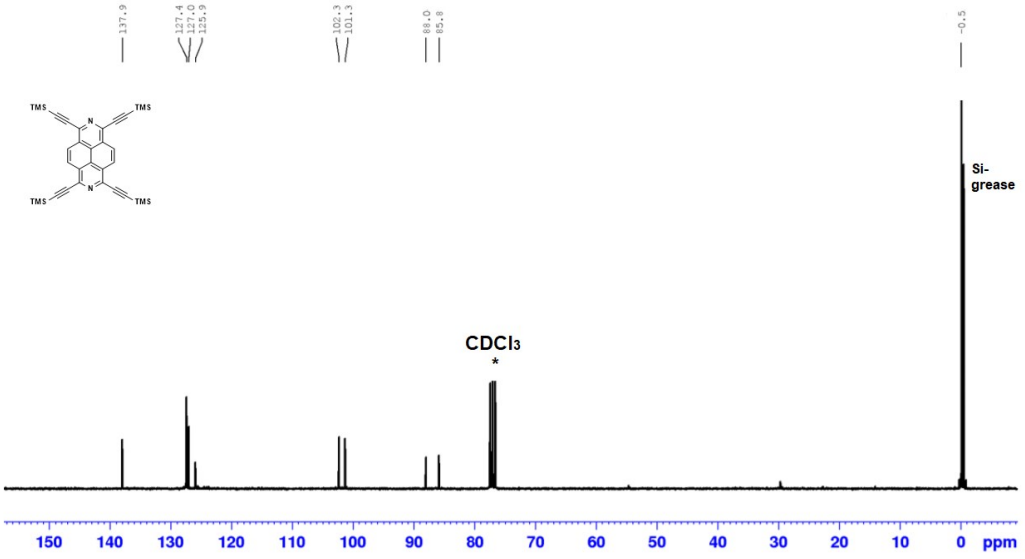

Figure S23. ^{13}C-NMR (75.1 MHz, 298K, $CDCl_3$*) of **3b**.

*1,3,6,8-Tetrakis((4-(tert-butyl)phenyl)ethynyl)benzo[lmn][3,8]phenanthroline (**3d**)*

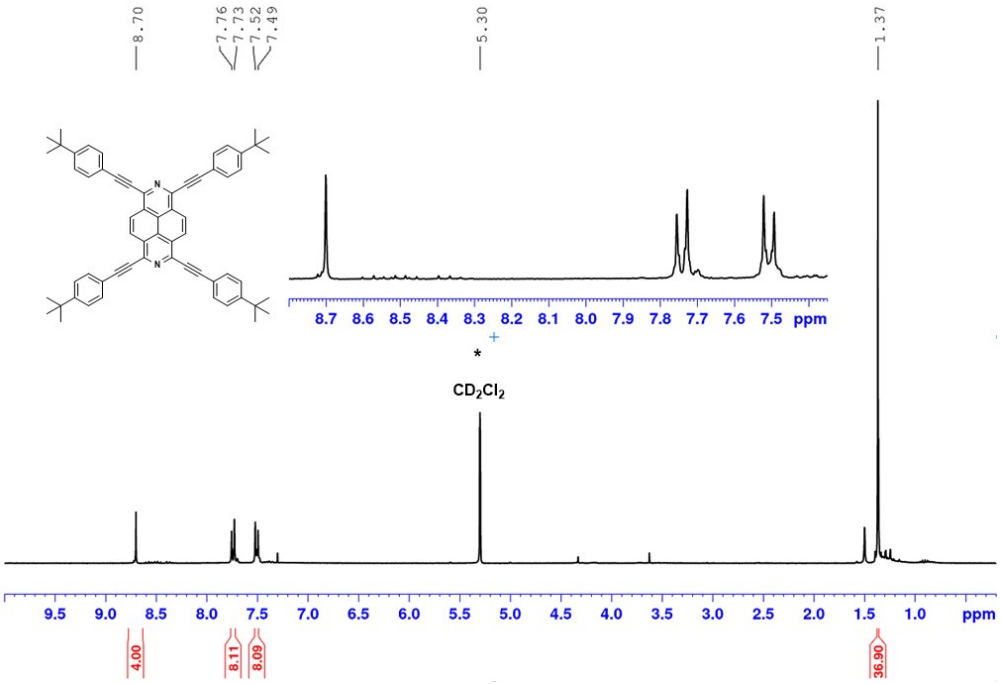

Figure S24. ^{1}H-NMR (300.1 MHz, 298K, CD_2Cl_2*) of **3c**.

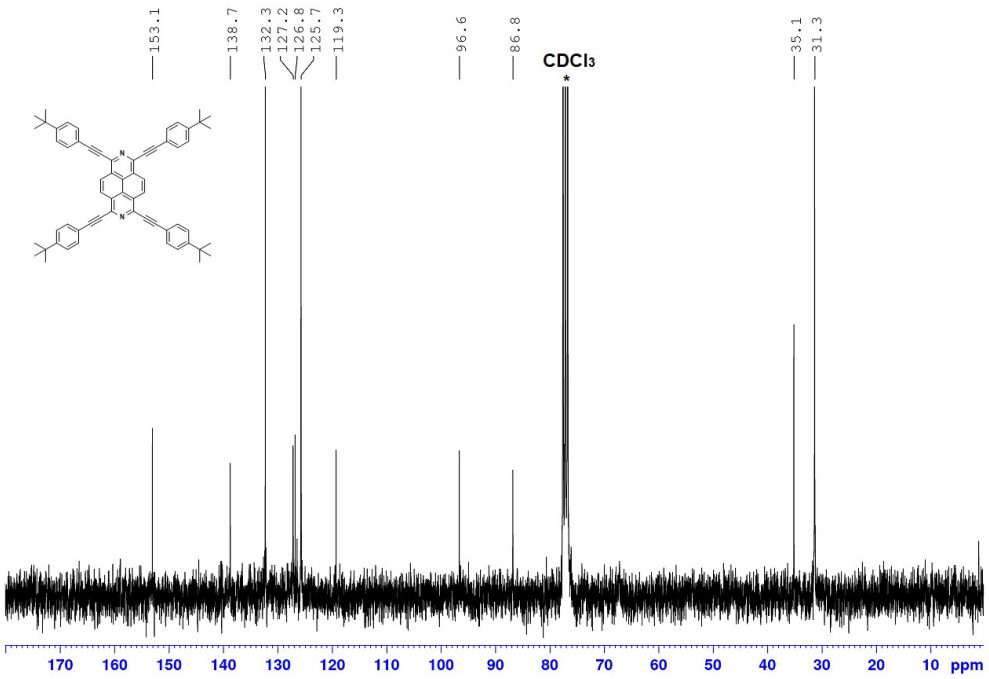

Figure S25. ^{13}C-NMR (75.1 MHz, 298K, $CDCl_3$*) of **3b**.

7.4 Supporting Information of Publication 4

The chapter *Single crystal X-ray structures* of the supporting information of Publication 4 is not shown in the following.
This was done by T. Vollgraff and is part of his doctoral thesis.

Supporting Information

Oligo-(diaza)rylene type cobalt complexes for the solid-state pyrolysis towards (N-doped) carbon nanoparticles

Simon Werner [a],Tobias Vollgraff [a], and Jörg Sundermeyer*[a]

[a] S. Werner, T. Vollgraff, Prof. Dr. J. Sundermeyer
Fachbereich Chemie and Materials Science Center
Philipps-Universität Marburg, Hans-Meerwein-Straße 4
35043 Marburg (Germany)
E-Mail: JSU@staff.uni-marburg.de

Contents

IR Spectra

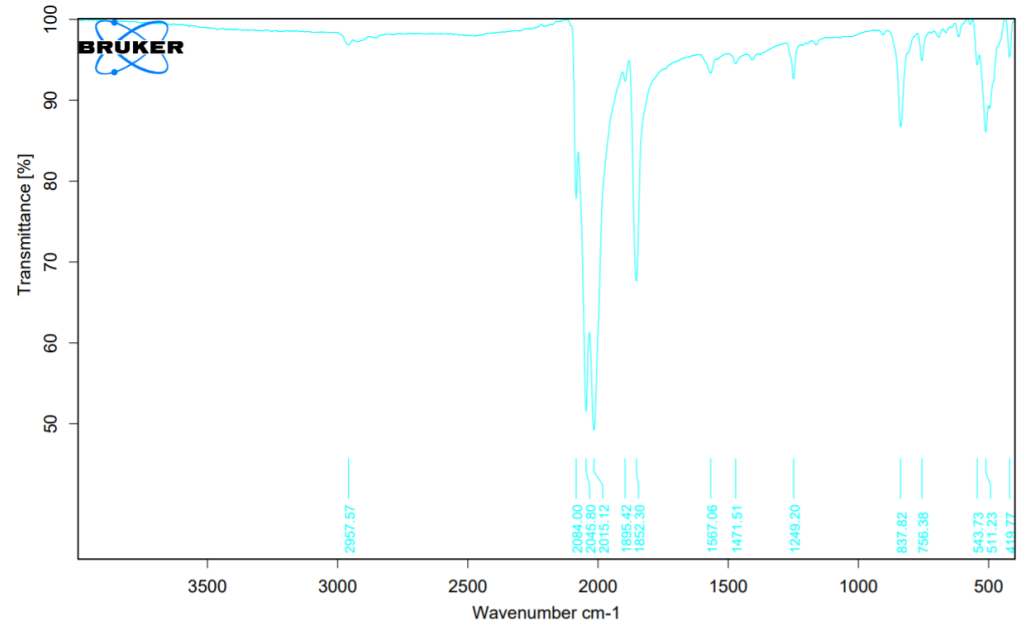

Figure S12. Measured FT-IR-spectrum of compound **C1**.

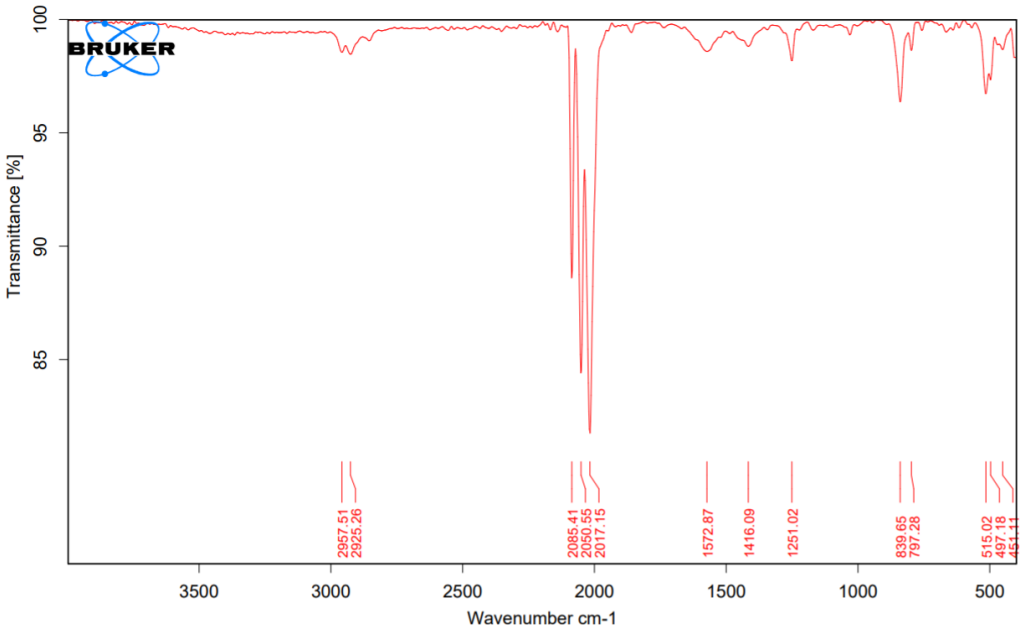

Figure S13. Measured FT-IR-spectrum of compound **C2**.

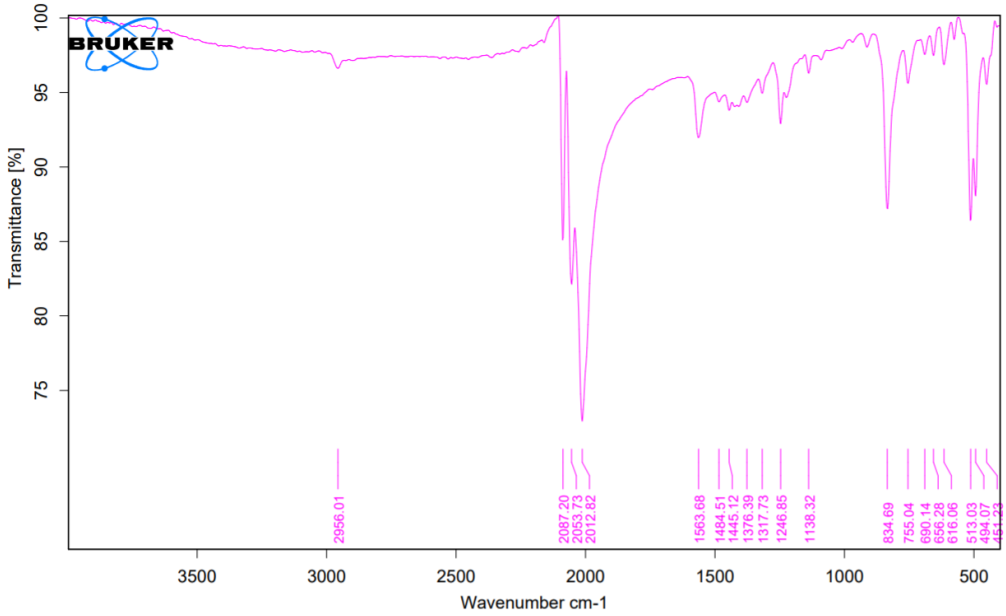

Figure S14. Measured FT-IR-spectrum of compound **N1**.

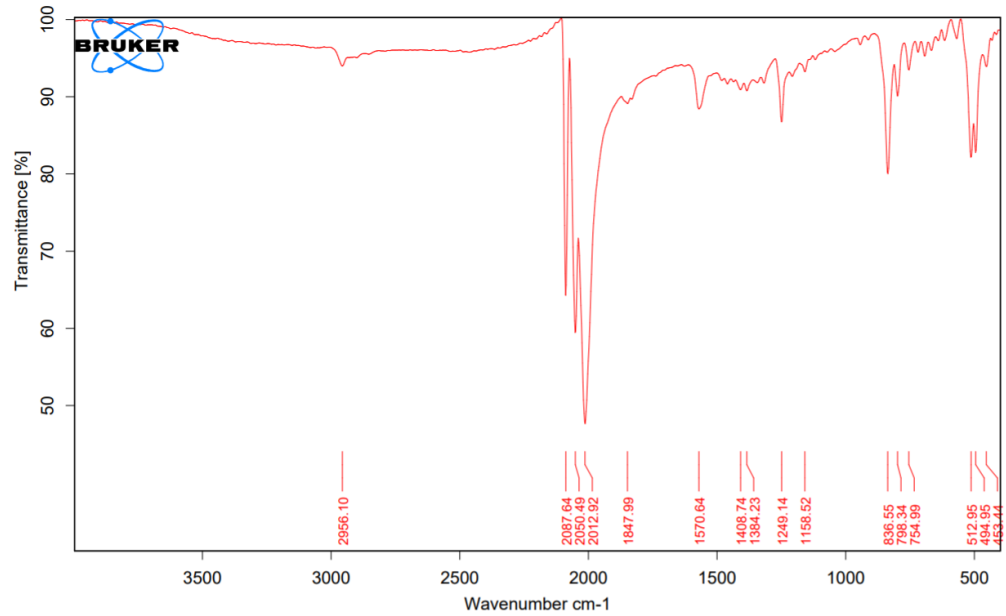

Figure S15. Measured FT-IR-spectrum of compound **N2**.

Optimized geometries (DFT)

Table S2. Cartesian coordinates (XYZ) of DFT optimized geometry of the phenyl-model complex (def2-TZVPP/PBE).

C	3.184006000	0.515229000	1.788314000
C	3.852976000	-0.587923000	1.247346000
C	3.173378000	-1.461591000	0.395568000
C	1.833553000	-1.235832000	0.084804000
C	1.151289000	-0.128500000	0.624025000
C	1.846321000	0.743276000	1.480424000
C	-0.244419000	0.089127000	0.289101000
Co	-1.237174000	1.578188000	-0.550029000
C	-1.264981000	-0.414010000	-0.444859000
Co	-1.909949000	0.147192000	1.356203000
C	-3.704520000	0.195148000	1.155254000
C	-1.720759000	-1.377076000	2.229436000
C	-1.525790000	1.280841000	2.698072000
C	-2.871279000	1.982589000	-1.205252000
C	-0.244867000	1.784427000	-1.997100000
C	-0.701029000	3.032341000	0.361829000
O	-1.582505000	-2.372724000	2.795188000
O	-4.851271000	0.210880000	1.039699000
O	-1.272832000	1.989980000	3.571170000
O	0.412858000	1.911028000	-2.936221000
O	-3.906471000	2.250544000	-1.635364000
O	-0.343605000	3.970794000	0.928312000
Si	-1.823806000	-1.730282000	-1.636870000
C	-3.614772000	-1.455061000	-2.121890000
C	-1.632020000	-3.400694000	-0.787055000
C	-0.717899000	-1.636980000	-3.159074000
H	3.710089000	1.200401000	2.453531000
H	4.901107000	-0.764707000	1.489727000
H	3.689065000	-2.323320000	-0.029498000
H	1.300218000	-1.915609000	-0.579717000
H	1.325095000	1.603030000	1.901442000
H	-3.753998000	-0.490164000	-2.626961000
H	-3.938896000	-2.245518000	-2.814360000
H	-4.280800000	-1.480751000	-1.249445000
H	-0.604865000	-3.565491000	-0.433617000
H	-1.882220000	-4.210413000	-1.488071000
H	-2.302755000	-3.485866000	0.078460000
H	-0.963073000	-2.453472000	-3.853986000
H	-0.856297000	-0.687587000	-3.693476000
H	0.345698000	-1.723646000	-2.897662000

Table S3. Cartesian coordinates (XYZ) of DFT optimized geometry of the 1-pyridinyl-model complex (def2-TZVPP/PBE)

C	3.004925000	0.597290000	1.782018000
C	3.796615000	-0.462854000	1.326038000
C	3.215996000	-1.399159000	0.471835000
C	1.880274000	-1.240161000	0.110932000
C	1.164751000	-0.141912000	0.620638000
N	1.723845000	0.765528000	1.447188000
C	-0.231831000	0.045982000	0.261287000
Co	-1.203895000	1.540815000	-0.556558000
C	-1.252816000	-0.455254000	-0.470529000
Co	-1.873217000	0.102609000	1.343323000
C	-3.666145000	0.209997000	1.185659000
C	-1.730188000	-1.435318000	2.198189000
C	-1.401070000	1.209161000	2.690264000
C	-2.840908000	2.020168000	-1.139316000
C	-0.278651000	1.747244000	-2.045153000
C	-0.553130000	2.949222000	0.370890000
O	-1.622605000	-2.441549000	2.753002000

O	-4.814389000	0.261247000	1.094419000
O	-1.104853000	1.891589000	3.567764000
O	0.335529000	1.874972000	-3.013926000
O	-3.881634000	2.332283000	-1.525024000
O	-0.129603000	3.859908000	0.931390000
Si	-1.846784000	-1.751851000	-1.664227000
C	-3.631880000	-1.422068000	-2.135076000
C	-1.690320000	-3.431128000	-0.824455000
C	-0.745030000	-1.686011000	-3.191241000
H	3.425435000	1.351513000	2.452864000
H	4.838120000	-0.545814000	1.635478000
H	3.793907000	-2.241819000	0.090735000
H	1.384890000	-1.946999000	-0.554236000
H	-3.743885000	-0.446911000	-2.627400000
H	-3.986560000	-2.194024000	-2.833230000
H	-4.290519000	-1.435544000	-1.256619000
H	-0.664377000	-3.620675000	-0.479262000
H	-1.962776000	-4.231545000	-1.527858000
H	-2.356486000	-3.505908000	0.045391000
H	-1.021944000	-2.488305000	-3.890802000
H	-0.849403000	-0.728630000	-3.718842000
H	0.315616000	-1.814589000	-2.934250000

Additional SEM images of pyrolysis products of C2

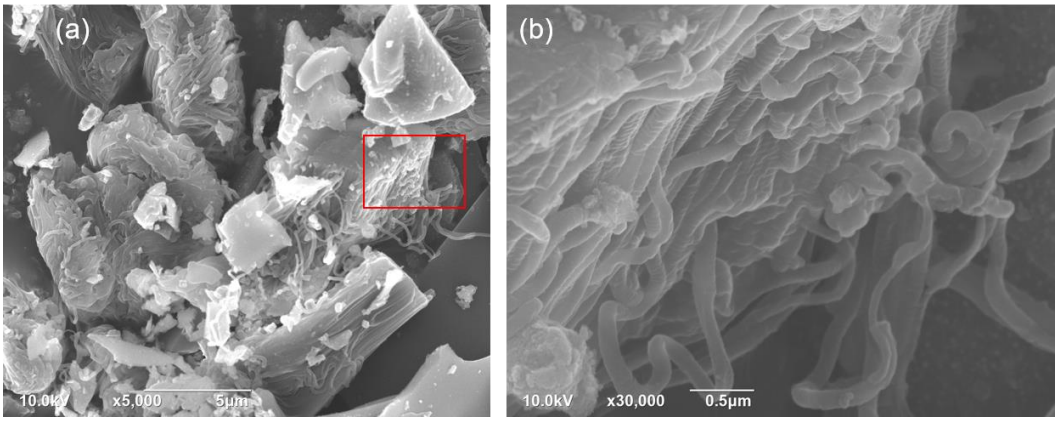

Figure S12. (a) and (b) Bundles of agglomerated carbon nanotubes obtained after SSP of **C2**.

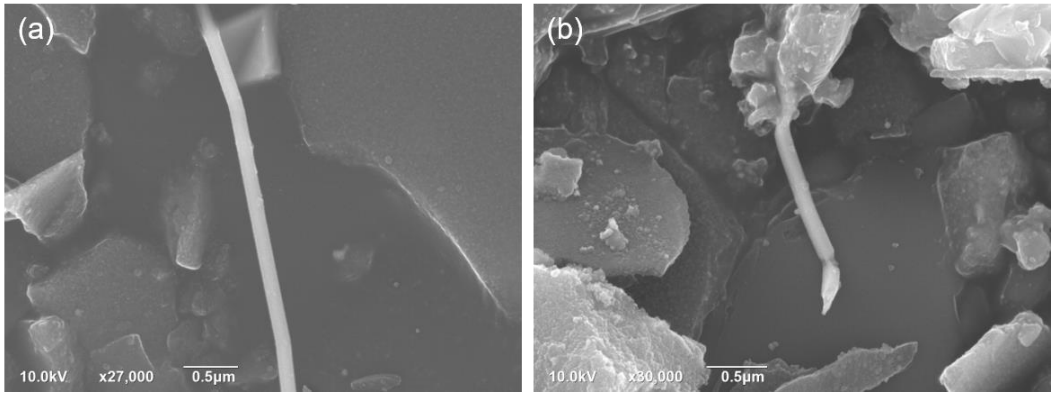

Figure S12. (a) and (b) Isolated larger fibrous-type carbon nanotubes after SSP of **C2**.

Low resolution TEM images of pyrolysis products of C2

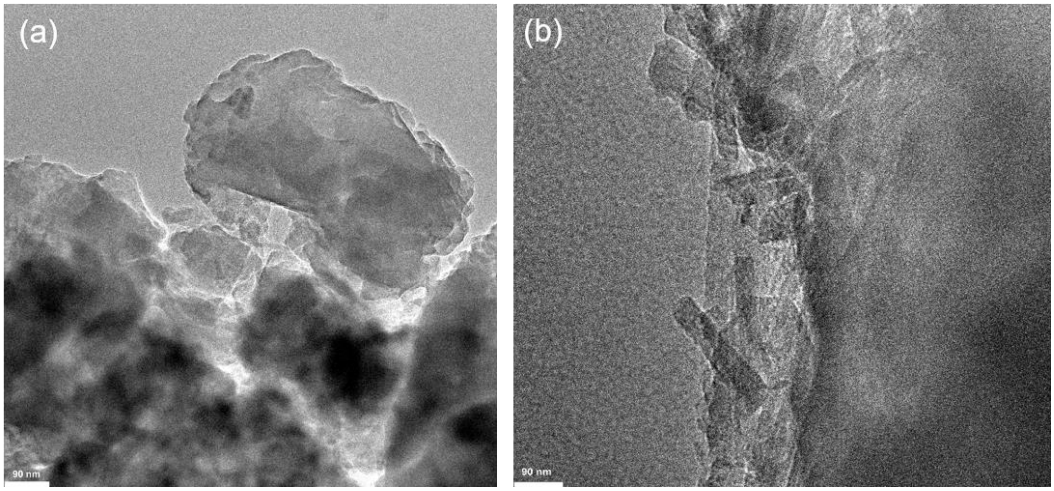

Figure S12. (a) and (b) Low resolution bright field TEM images of agglomerated carbon nanotubes and nanoparticlesobtained after SSP of **C2**.

FD mass spectra

*Co-complex **N1***

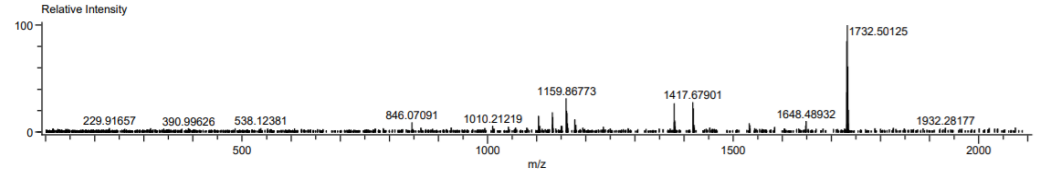

Figure S12. FD(+)-MS spectrum of **N1**.

*Co-complex **N2***

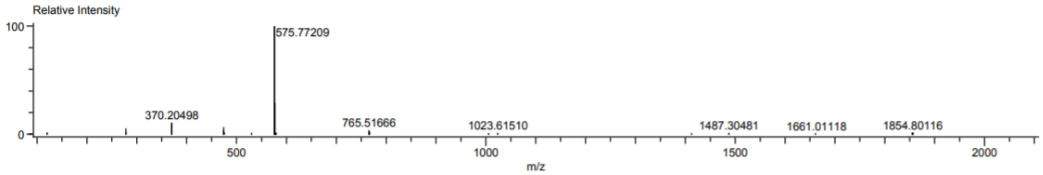

Figure S12. FD(+)-MS spectrum of **N2**.

NMR Spectra

*Co-complex **C1***

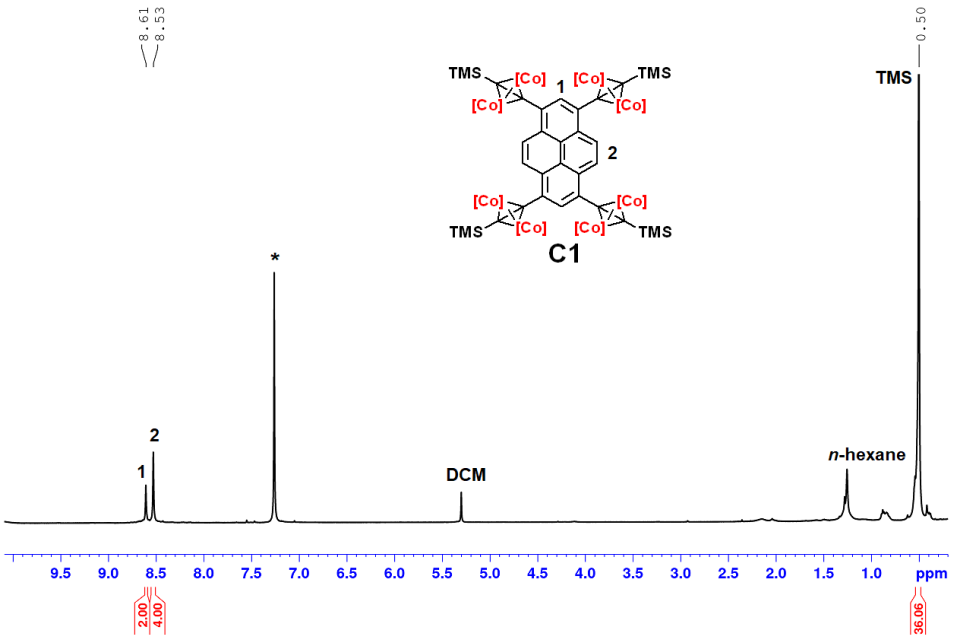

Figure S23. ^{1}H-NMR (500.1 MHz, 298K, $CDCl_3$*) of **C1**. Contains solvent residues. The $[Co(CO)_3]$-units are abbreviated with [Co].

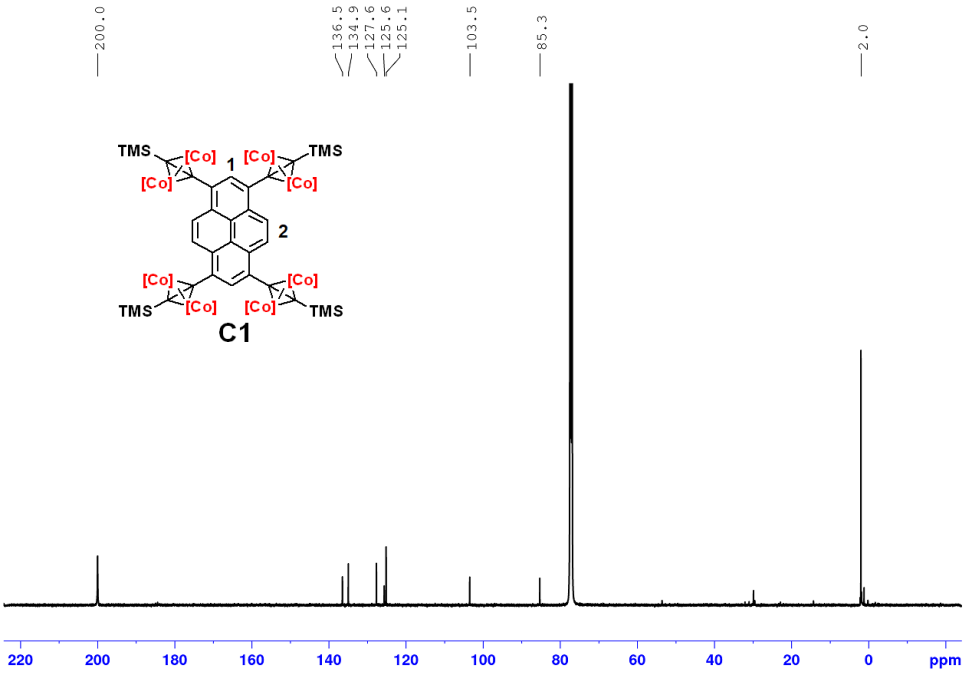

Figure S24. ^{13}C-NMR (125.8 MHz, 298K, $CDCl_3$*) of **C1**. Contains solvent residues. The $[Co(CO)_3]$-units are abbreviated with [Co].

*Co-complex **C2***

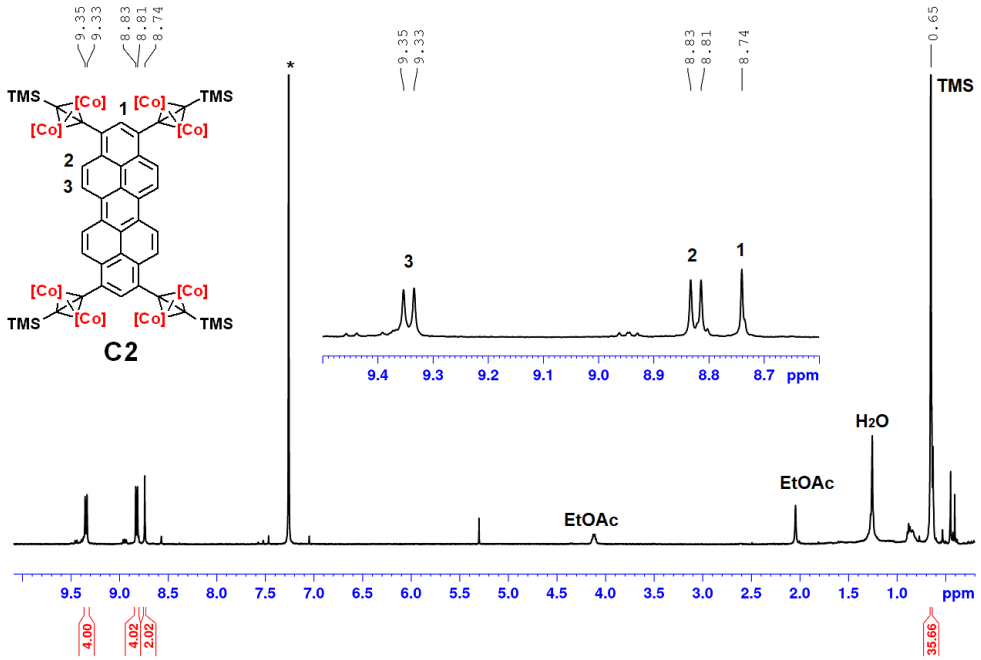

Figure S25. ^{1}H-NMR (500.1 MHz, 298K, $CDCl_3$*) of **C2**. Contains solvent residues. The $[Co(CO)_3]$-units are abbreviated with [Co].

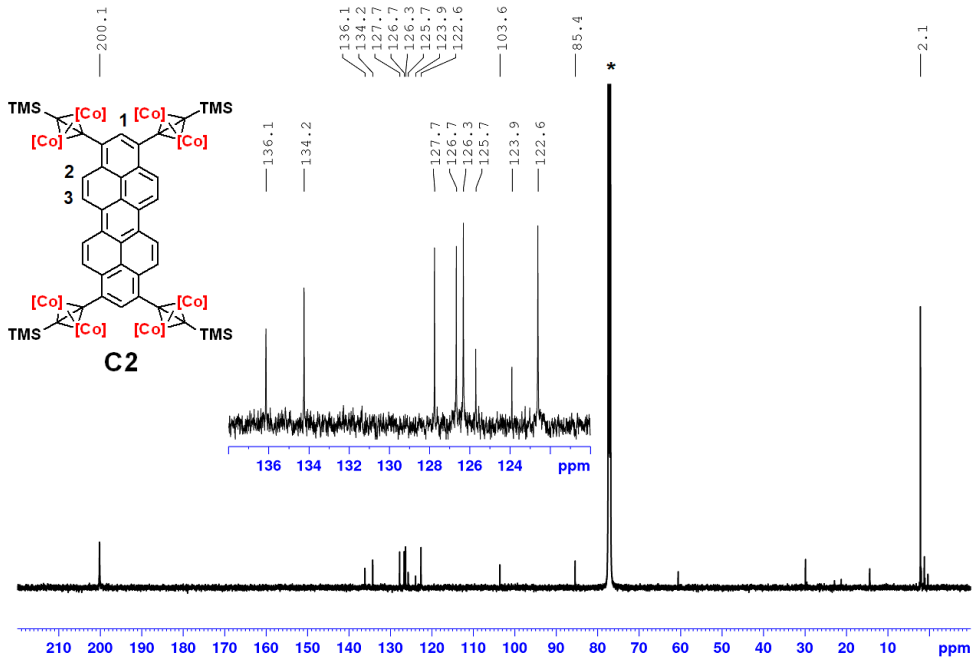

Figure S26. ^{13}C-NMR (125.8 MHz, 298K, $CDCl_3$*) of **C2**. Contains solvent residues. The $[Co(CO)_3]$-units are abbreviated with [Co].

*Co-complex **N1***

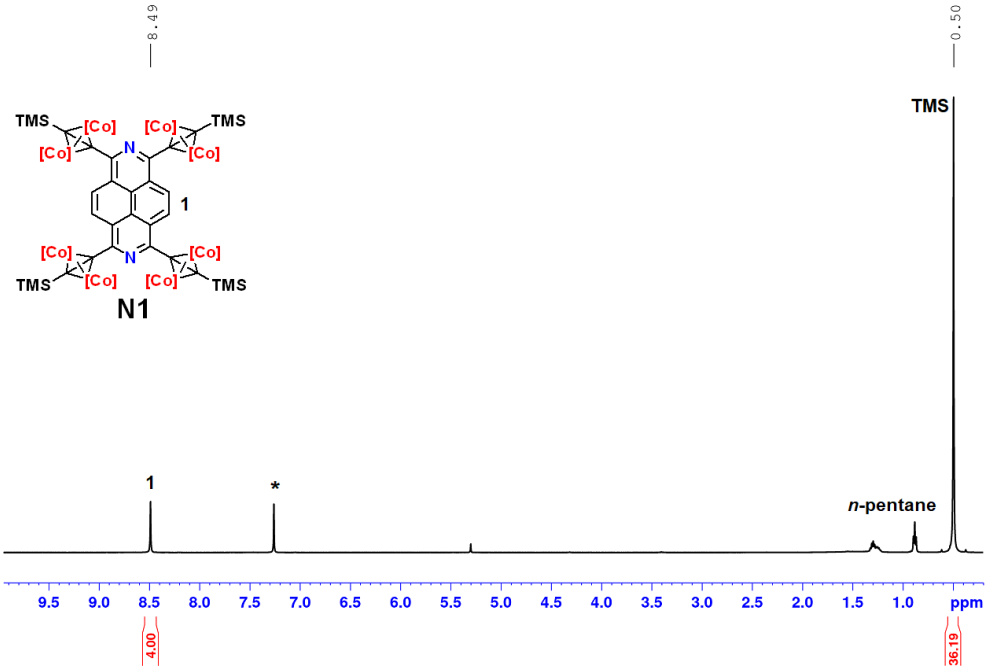

Figure S25. ^{1}H-NMR (500.1 MHz, 298K, $CDCl_3$*) of **N1**. Contains solvent residues. The $[Co(CO)_3]$-units are abbreviated with [Co].

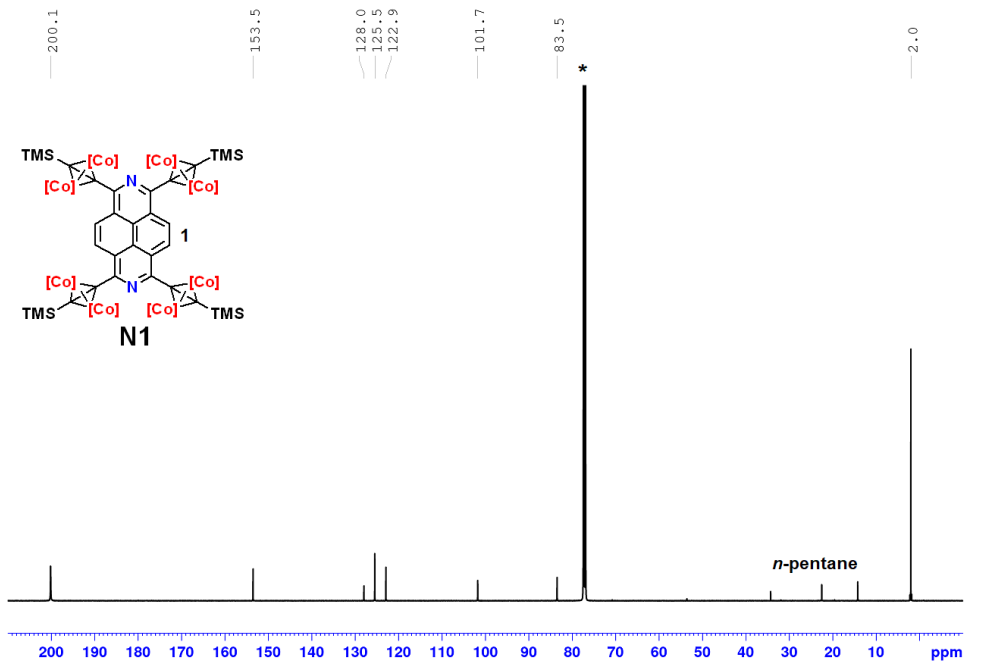

Figure S26. ^{13}C-NMR (125.8 MHz, 298K, $CDCl_3$*) of **N1**. Contains solvent residues. The $[Co(CO)_3]$-units are abbreviated with [Co].

*Co-complex **N2***

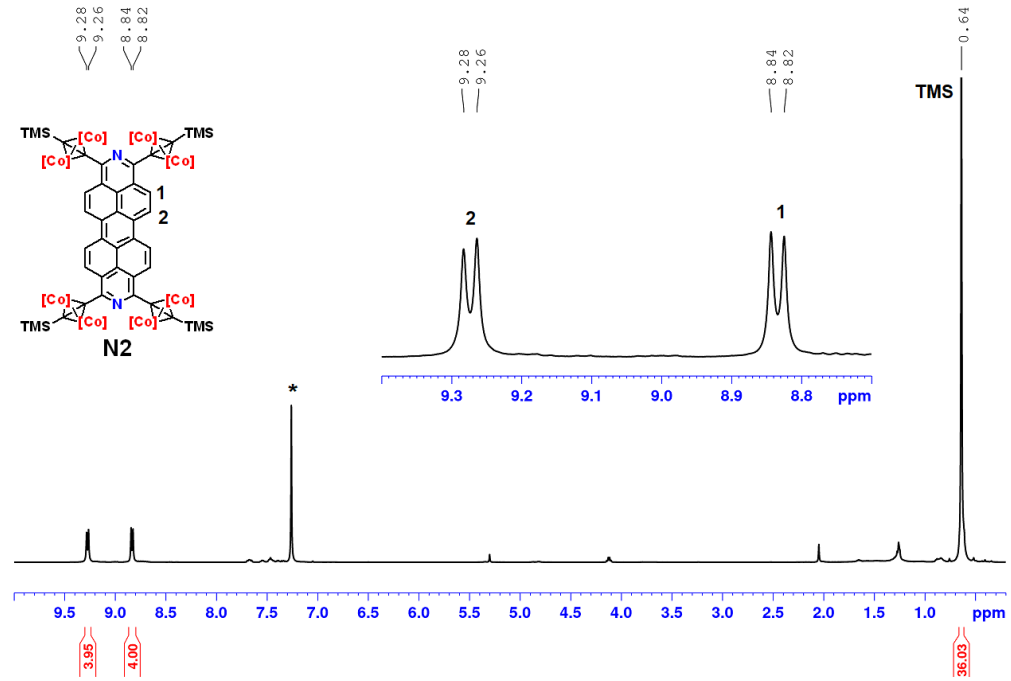

Figure S25. ^{1}H-NMR (500.1 MHz, 298K, $CDCl_3$*) of **N2**. Contains solvent residues. The $[Co(CO)_3]$-units are abbreviated with [Co].

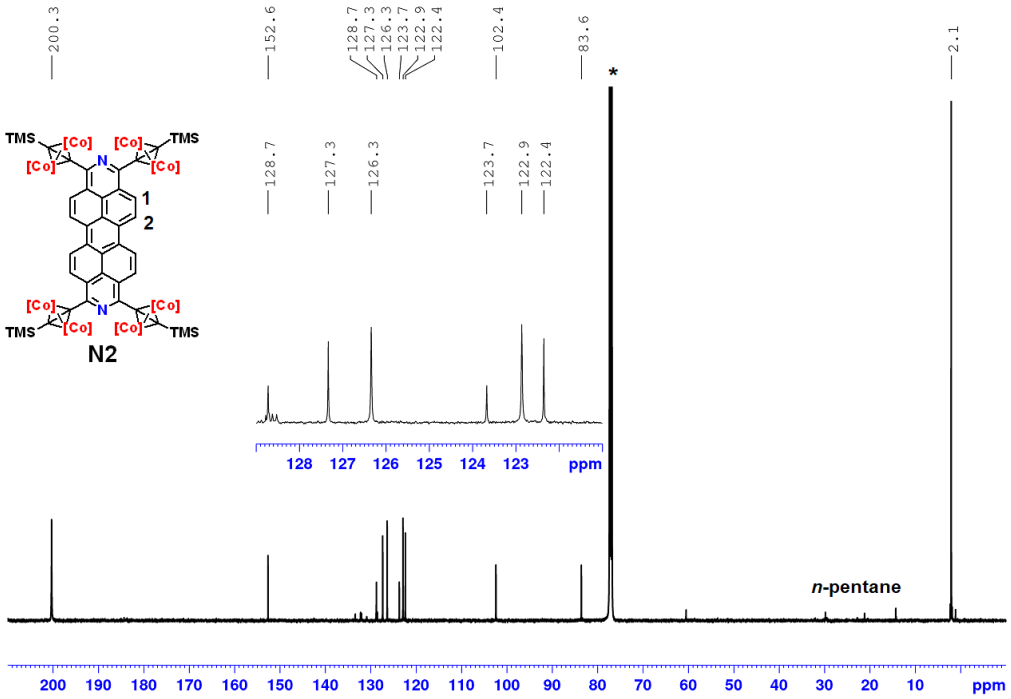

Figure S26. ^{13}C-NMR (125.8 MHz, 298K, $CDCl_3$*) of **N2**. Contains solvent residues. The $[Co(CO)_3]$-units are abbreviated with [Co].

7.5 Supporting Information of Publication 5

Supporting Information

Synthesis of unsymmetrically functionalized Violanthrenes by Reductive Functionalization of Violanthrone 79

Simon Werner [a], and Jörg Sundermeyer*[a]

[a] S. Werner, Prof. Dr. J. Sundermeyer
Fachbereich Chemie and Materials Science Center
Philipps-Universität Marburg, Hans-Meerwein-Straße 4
35043 Marburg (Germany)
E-Mail: JSU@staff.uni-marburg.de

Contents

Materials, Methods and Devices

All reactions were carried out under inert atmosphere (nitrogen) using Schlenk techniques if not mentioned otherwise. Violanthrone 79 was bought from ChemPur (manufactured by BLD Pharma). For thin-layer chromatography, TLC plates from Merck KGaA with silica gel 60 on aluminum with fluorescence-quenching F254 at room temperature were used. All solvents were dried and/or purified according to standard procedures and stored over 3 Å or 4 Å molecular sieves. NMR spectra were recorded in automation or by the service department (faculty of Chemistry, Philipps University Marburg) with a Bruker Avance 300 spectrometer at 298 K using $CDCl_3$ as solvent and for calibration (residual proton signals). HR-APCI mass spectra were acquired with a LTQ-FT Ultra mass spectrometer (Thermo Fischer Scientific). The resolution was set to 100.000. HR-EI mass spectra were acquired with a AccuTOF GCv 4G (JEOL) Time of Flight (TOF) mass spectrometer. An internal or external standard was used for drift time correction. The LIFDI ion source and FD-emitters were purchased from Linden ChroMasSpec GmbH (Bremen, Germany). IR spectra are recorded with a Bruker Alpha FT-IR spectrometer with Platinum ATR sampling. Absorption spectra were recorded with a Varian Cary-5000 UV/Vis/NIR spectrophotometer in 10 mm cuvettes in dichloromethane with concentrations of 10 μM with a scan rate of 600 nm/min. Emission spectra were recorded with a Varian Cary Eclipse Spectrophotometer in 10 nm cuvettes in dichloromethane with a scan rate of 600 nm/min. Cyclic voltammetry and differential pulse voltammetry measurements are carried out on a rhd instruments TSC 1600 closed electrochemical workstation (working electrode: glassy carbon; counter electrode: platinum crucible; reference electrode: platinum wire (pseudo reference electrode under nitrogen atmosphere in a glovebox (Labmaster 130, mBraun). **7** was measured in dichloromethane and calibrated using ferrocene as internal standard after measurements. Dichloromethane was filtered through an aluminum oxide pad prior to use. Tetrabutylammonium hexafluorophosphate ($TBAPF_6$; >99.0 %) is used as electrolyte for electrochemical analysis. The measurements were carried out at a concentration of 100 mmol/L of electrolyte.

Additional CV spectra

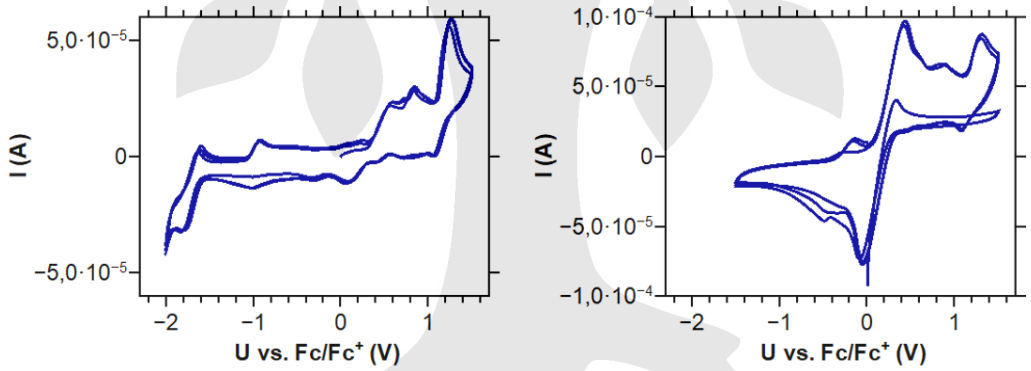

Figure S1. CV spectra (raw data, three scans) of **VE1** (left) and with ferrocene added for calibration (right), measured in CH_2Cl_2, 0.1 M *n*-Bu_4NPF_6, 50 mV s^{-1} scan rate, glassy carbon electrode.

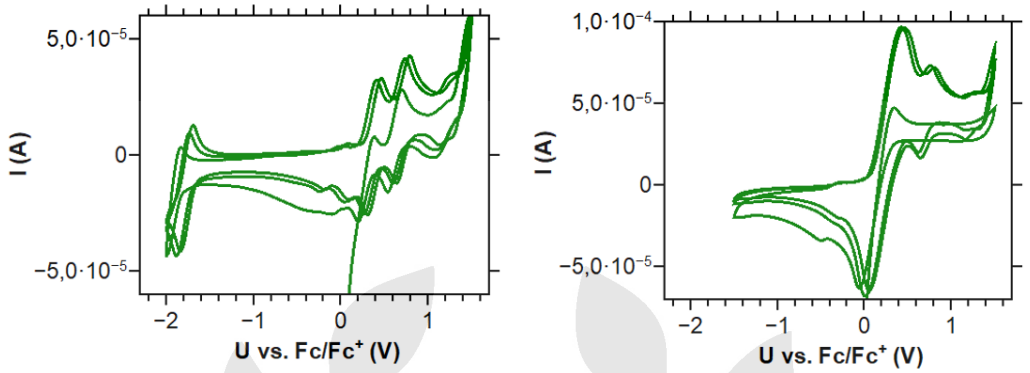

Figure S2. CV spectra (raw data, three scans) of **VE2** (left) and with ferrocene added for calibration (right), measured in CH_2Cl_2, 0.1 M *n*-Bu_4NPF_6, 50 mV s^{-1} scan rate, glassy carbon electrode.

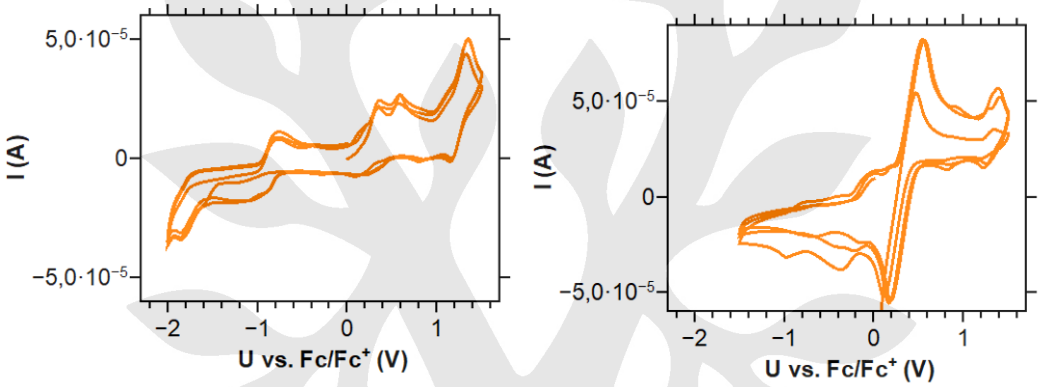

Figure S3. CV spectra (raw data, three scans) of **VE2** (left) and with ferrocene added for calibration (right), measured in CH_2Cl_2, 0.1 M *n*-Bu_4NPF_6, 50 mV s^{-1} scan rate, glassy carbon electrode.

Concentration-dependent UV-Vis spectra

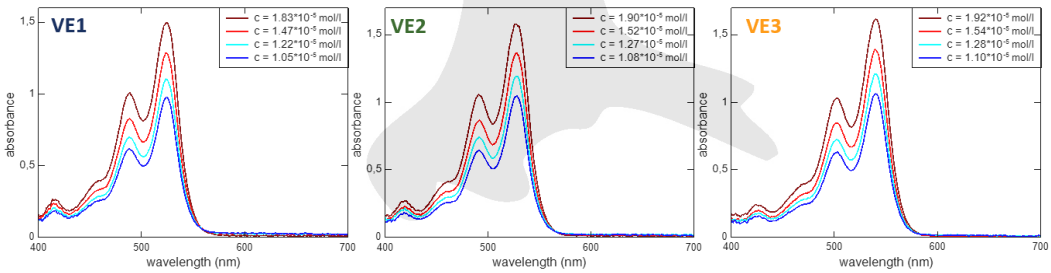

Figure S4. UV-Vis spectra of **VE1**-**VE3** recorded at four different concentrations in CH_2Cl_2.

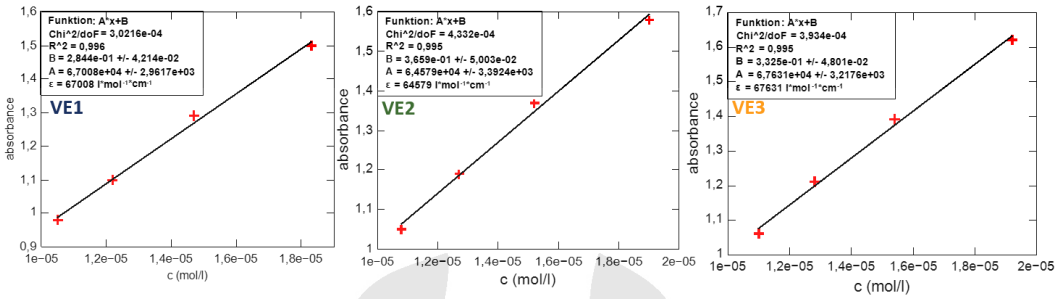

Figure S5. Plot of the absorbance at λ_{max} versus concentration of **VE1**-**VE3**. The slope of the linear regression marks the molar decadic attenuation coefficient ε (optical pass length = 1 cm).

Determination of fluorescence quantum yields

Fluorescence quantum yields (Φ_{PL}) were recorded by dilution method using a fluorescein solution (0.1 M in aqueous NaOH, Φ_{flu} = 0.95)[1] as reference. Both, the samples and the reference were measured at low concentrations in order to ensure a linear relationship between the intensity of emitted light and the concentration of the absorbing/emitting species.
The quantum yields of the samples (Φ_s) were determined by the following equation 1.[1]

$$\Phi_{flu} = \frac{grad(s)}{grad(flu)} * \frac{n^2(s)}{n^2(flu)} * \Phi_{flu}$$

In equation 1, *grad* is the slope of the "emission versus absorbance" plot of the samples (s) and the standard fluorescein. n is the refractive index of the used solvents.
In the following Figure S4, the "emission versus absorbance" plots and the linear regression graphs for the determination of the fluorescence quantum yields of **VE1 and VE2** and the reference fluorescein. Note that the fluorescence quantum yield of congener **VE3** was not determined due since **VE3** decomposes too fast under air exposure.

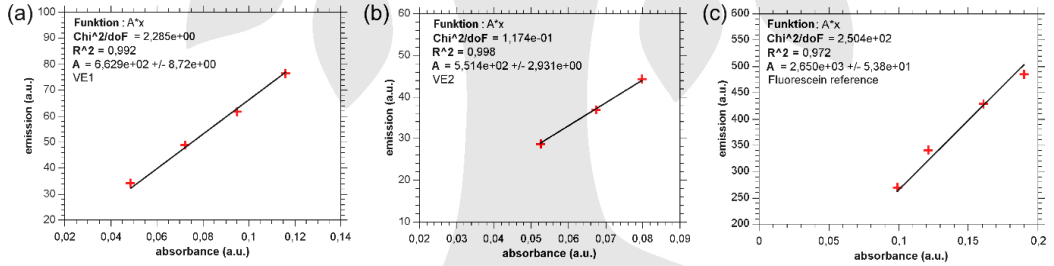

Figure S6. "emission versus absorption" plots of (a) **VE1**; (b) **VE2**; recorded in dichloromethane and (c) fluorescein as 0.1 M solution in aqueous NaOH for direct referencing. The concentrations were in the low 10^{-6} M range.

DFT and TD-DFT results

Density functional theory (DFT) calculations using the B3LYP [2] functional were performed. The def2-TZVPP[3] basis set was used with RIJDX or RIJCOSX auxiliary base set[4], employing the resolution-of-identity approximation.[5,6] Further D3-dispersion correction[7] was considered by applying Becke−Johnson damping.[8] Structural optimizations and TD-DFT calculations were performed using Orca 3.0.3.[9] The atomic coordinates for geometry optimization were taken from XRD structures, if possible. The structurally optimized molecules were used for TD-DFT calculations using the PBE[10] functional (PBE0-D3/def2-TZVPP), employing the resolution-of-identity approximation for both Coulomb integrals and HF exchange integrals.[6]

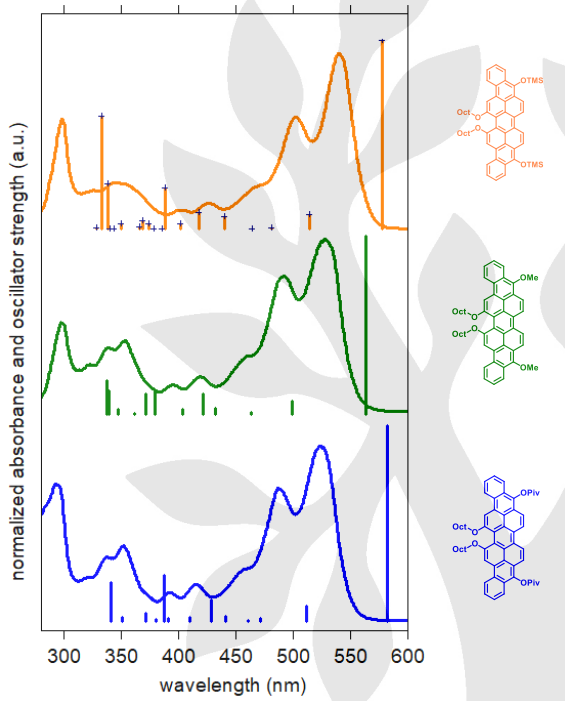

Figure S7. Comparison of normalized absorption spectra and TD-DFT results (vertical lines) of **VE1**-**VE3**

Table S1. Characteristic main electron transition of **VE1**-**VE3**, calculated using TD-DFT (def2-TZVPP/PBE level of theory).

Compound	Transition energy (wavelength)	Oscillator strength	Description of main contributions
VE1	2.13 eV (582 nm)	1.139	HOMO→LUMO (c = 0.920); 0.846 HOMO-2→LUMO (c = 0.192); 0.037 HOMO-1→LUMO+2 (c = -0.159); 0.025 HOMO-3→LUMO+1 (c = 0.128); 0.016
VE2	2.20 eV (564 nm)	1.013	HOMO→LUMO (c = 0.914); 0.835 HOMO-2→LUMO (c = 0.192); 0.037 HOMO-1→LUMO+2 (c = 0.167); 0.028 HOMO-3→LUMO+1 (c = -0.142); 0.020
VE3	2.15 eV (577 nm)	1.076	HOMO→LUMO (-0.918); 0.842 HOMO-2→LUMO (-0.175); 0.030 HOMO-1→LUMO+2 (0.161); 0.026 HOMO-3→LUMO+1 (0.135); 0.018 HOMO→LUMO+5 (-0.101); 0.010

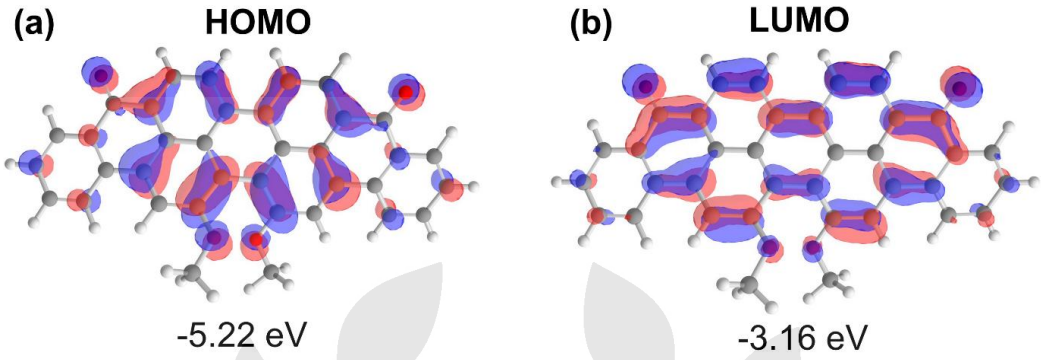

Figure S8. DFT-Calculated Kohn-Sham frontier molecular orbitals (B3LYP/def-TZVPP) of **VO79**.

NMR Spectra

*16,17-Bis(octyloxy)anthra[9,1,2-cde]benzo[rst]pentaphene-5,10-bis(oxy-trimethylsilane) (**VE3**)*

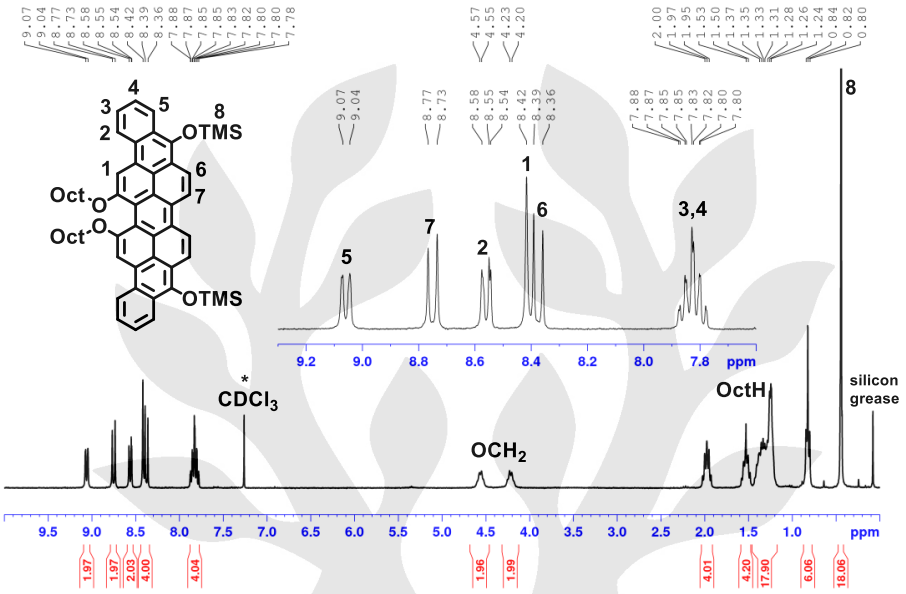

Figure S9. ^{1}H NMR (300.1 MHz, 298K, $CDCl_3$*) of **VE3**.

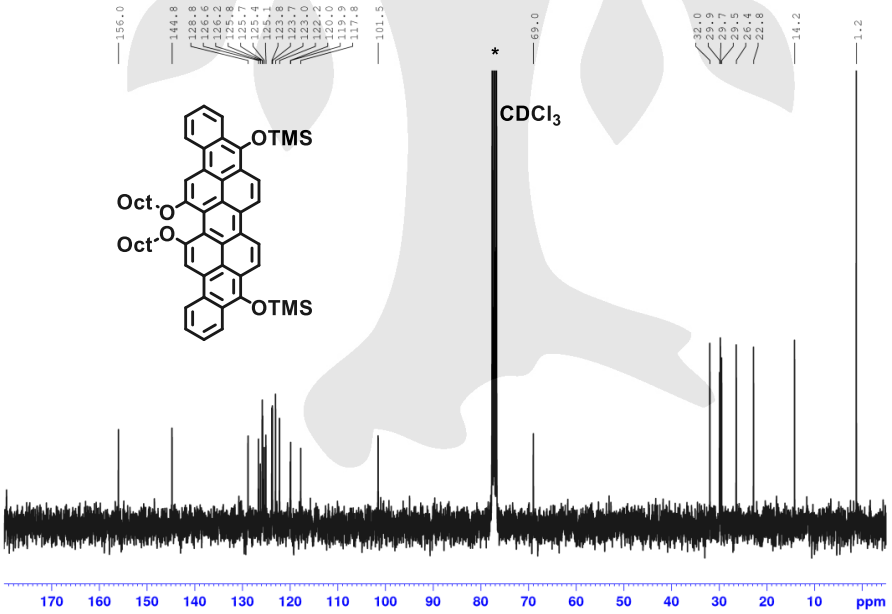

Figure S10. ^{13}C NMR (75.5 MHz, 298K, $CDCl_3$*) of **VE3**.

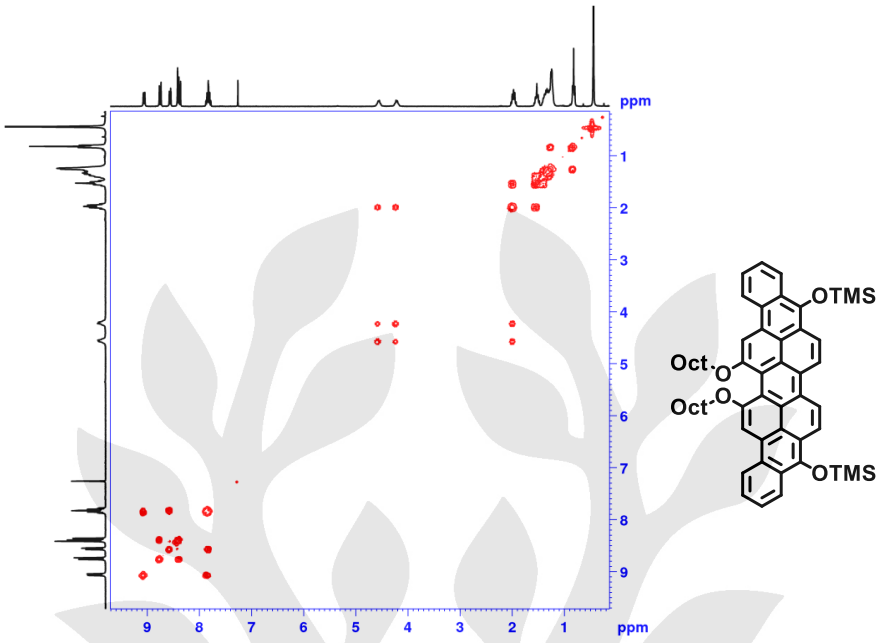

Figure S11. COSY NMR (300.1 MHz, 298K, $CDCl_3$*) of **VE3**.

*5,10-Dimethoxy-16,17-bis(octyloxy)anthra[9,1,2-cde]benzo[rst]pentaphene (**VE2**)*

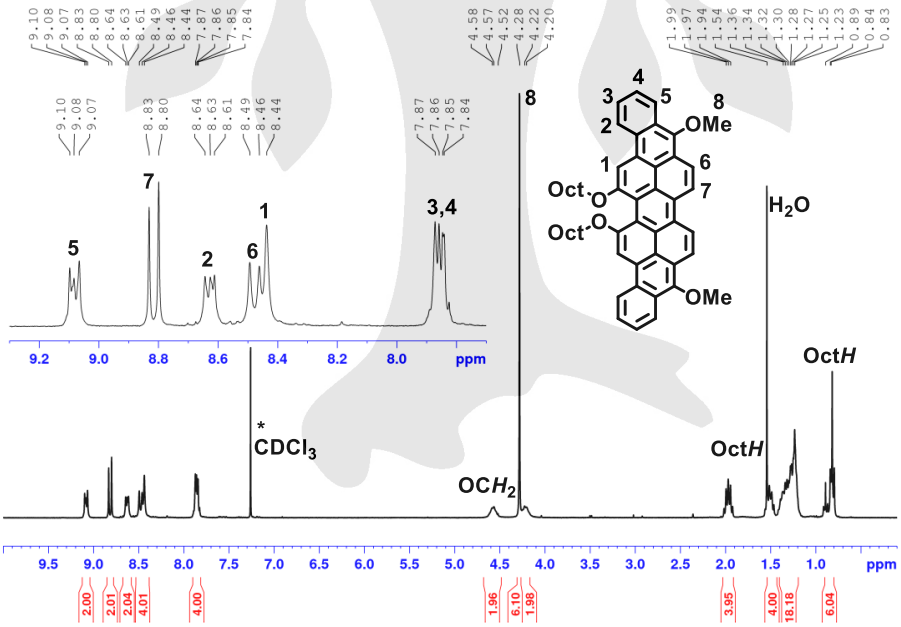

Figure S12. ^1H NMR (300.1 MHz, 298K, $CDCl_3$*) of **VE2**.

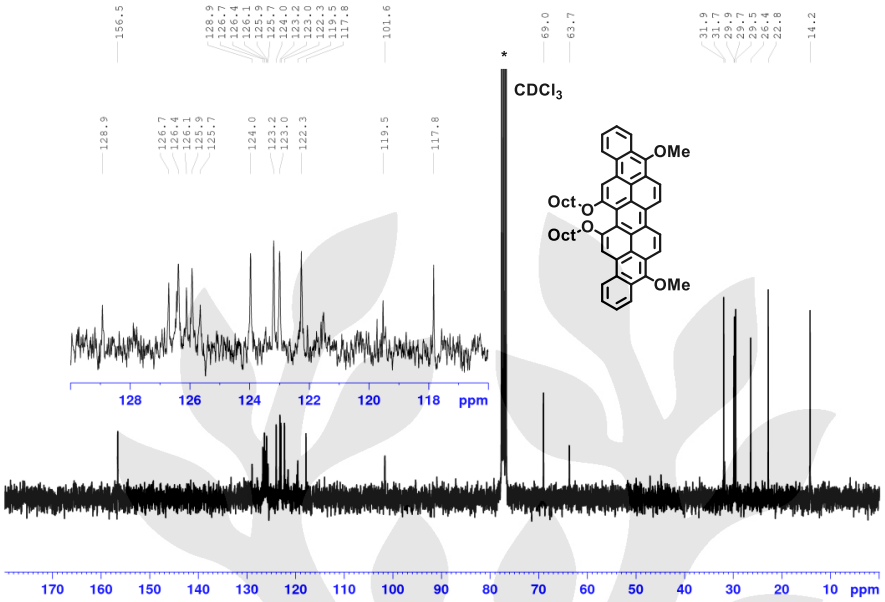

Figure S13. ^{13}C NMR (75.5 MHz, 298K, $CDCl_3$*) of **VE2**.

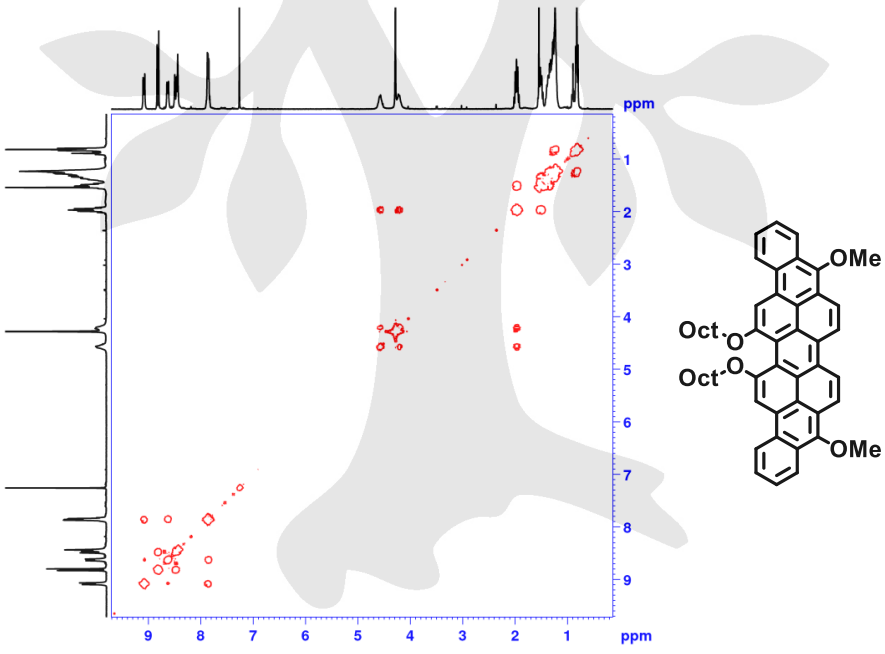

Figure S14. COSY NMR (300.1 MHz, 298K, $CDCl_3$*) of **VE2**.

*16,17-Bis(octyloxy)anthra[9,1,2-cde]benzo[rst]pentaphene-5,10-bis(2,2-dimethylpropanoate) (**VE1**)*

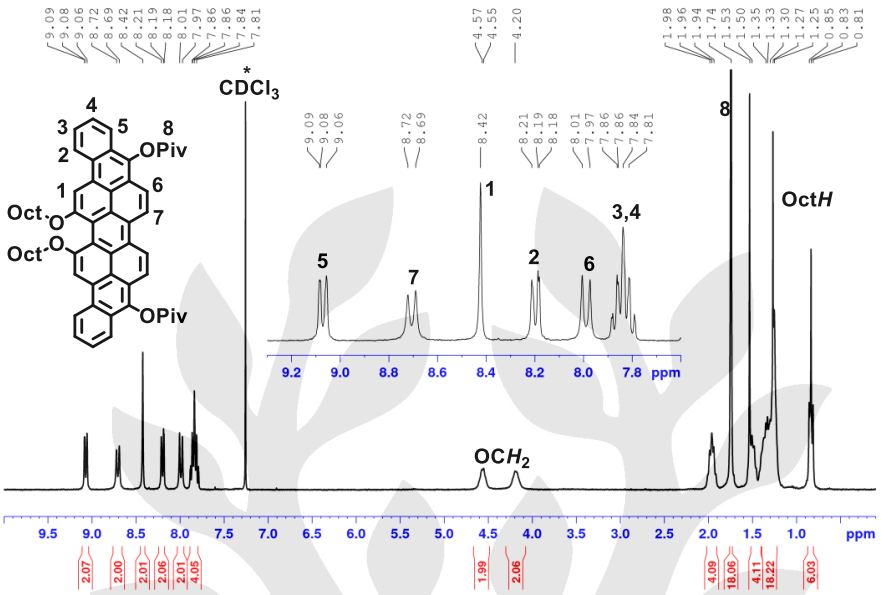

Figure S15. ^{1}H NMR (300.1 MHz, 298K, $CDCl_3$*) of **VE1**.

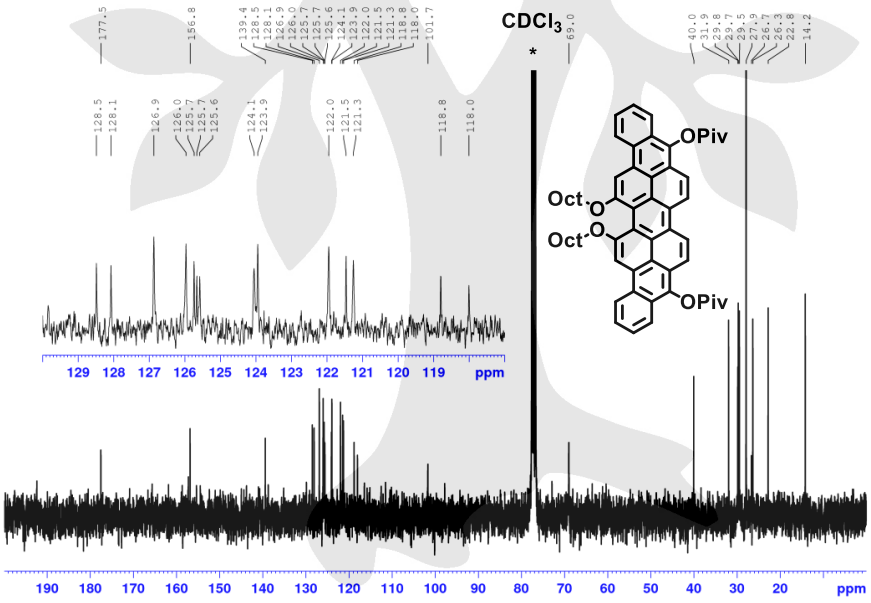

Figure S16. ^{13}C NMR (75.5 MHz, 298K, $CDCl_3$*) of **VE1**.

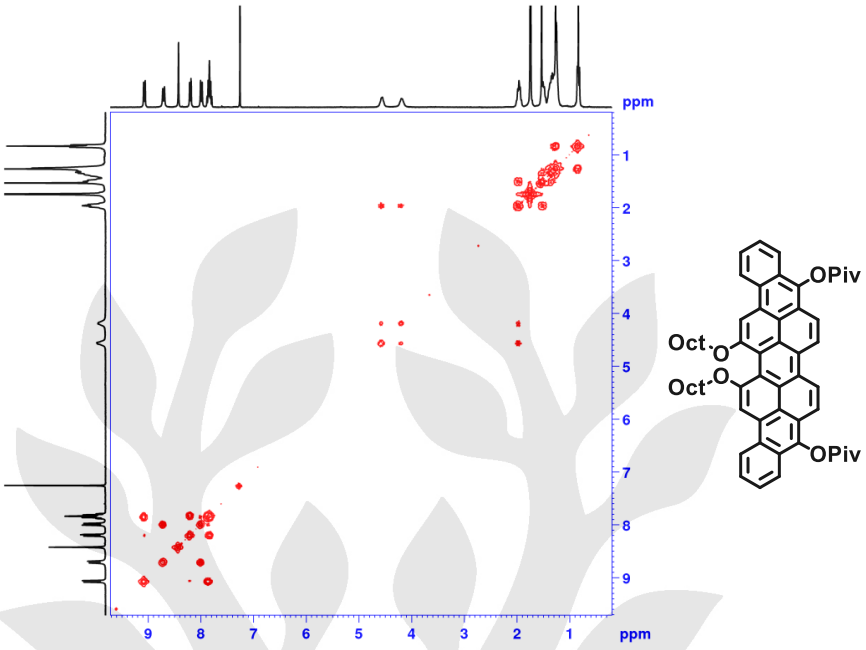

Figure S17. COSY NMR (300.1 MHz, 298K, $CDCl_3$*) of **VE1**.

Literature

[1] J. R. Lakowicz, *Principles of fluorescence spectroscopy*, Springer, New York, NY, **2010**.

[2] a) Lee, Yang, Parr, *Phys. Rev. B* **1988**, *37*, 785–789; b) P. J. Stephens, F. J. Devlin, C. S. Ashvar, C. F. Chabalowski, M. J. Frisch, *Faraday Disc.* **1994**, *99*, 103; c) A. D. Becke, *J. Chem. Phys.* **1993**, *98*, 5648–5652.

[3] a) A. Schäfer, C. Huber, R. Ahlrichs, *J. Chem. Phys.* **1994**, *100*, 5829–5835; b) F. Weigend, *Phys. Chem. Chem. Phys.* **2006**, *8*, 1057–1065; c) F. Weigend, R. Ahlrichs, *Phys. Chem. Chem. Phys.* **2005**, *7*, 3297–3305.

[4] a) F. Weigend, M. Häser, H. Patzelt, R. Ahlrichs, *Chem. Phys. Lett.* **1998**, *294*, 143–152; b) K. Eichkorn, O. Treutler, H. Öhm, M. Häser, R. Ahlrichs, *Chem. Phys. Lett.* **1995**, *240*, 283–290.

[5] M. von Arnim, R. Ahlrichs, *J. Comput. Chem.* **1998**, *19*, 1746–1757.

[6] F. Weigend, *Phys. Chem. Chem. Phys.* **2002**, *4*, 4285–4291.

[7] S. Grimme, J. Antony, S. Ehrlich, H. Krieg, *J. Chem. Phys.* **2010**, *132*, 154104.

[8] a) A. D. Becke, E. R. Johnson, *J. Chem. Phys.* **2005**, *123*, 154101; b) E. R. Johnson, A. D. Becke, *J. Chem Phys.* **2005**, *123*, 24101; c) E. R. Johnson, A. D. Becke, *J. Chem. Phys.* **2006**, *124*, 174104; d) S. Grimme, S. Ehrlich, L. Goerigk, *J. Comput. Chem.* **2011**, *32*, 1456–1465.

[9] F. Neese, *WIREs Comput Mol Sci* **2011**, *2*, 73–78.

[10] a) Perdew, Burke, Ernzerhof, *Phys. Rev. Lett.* **1996**, *77*, 3865–3868; b) J. P. Perdew, K. Burke, M. Ernzerhof, *Phys. Rev. Lett.* **1997**, *78*, 1396.

7.6 Supporting Information of Publication 6

In the case of this publication, only the NMR spectra of the precursor and the synthesis steps are shown. The additional STM images, DFT calculations and the single crystal X-ray structure determination have been contributed by co-workers.

Supporting Information for

On-Surface Synthesis and Characterization of a Cycloarene: C108 Graphene Ring

Qitang Fan,[1‡] Daniel Martin-Jimenez,[2‡] Simon Werner,[1‡] Daniel Ebeling,[2*] Tabea Koehler,[1] Tobias Vollgraff,[1] Jörg Sundermeyer,[1*] Wolfgang Hieringer,[3] André Schirmeisen,[2] J. Michael Gottfried[1*]

[1]Department of Chemistry and Material Sciences Center (WZMW), Philipps-Universität Marburg, Hans-Meerwein-Straße, 35032 Marburg, Germany

[2]Institute of Applied Physics (IAP) and Center for Materials Research (LaMa), Justus-Liebig-Universität Gießen, Heinrich-Buff-Ring 16, 35392 Gießen, Germany

[3]Theoretical Chemistry and Interdisciplinary Center for Molecular Materials (ICMM), Department of Chemistry and Pharmacy, Friedrich-Alexander-Universität Erlangen-Nürnberg, Egerlandstraße 3, 91058 Erlangen, Germany

[‡]Q.F., D.M.J, and S.W. contributed equally to this work.

(d4) NMR Spectra

3,6-Dibromophenanthrene-9,10-dione (**2**)

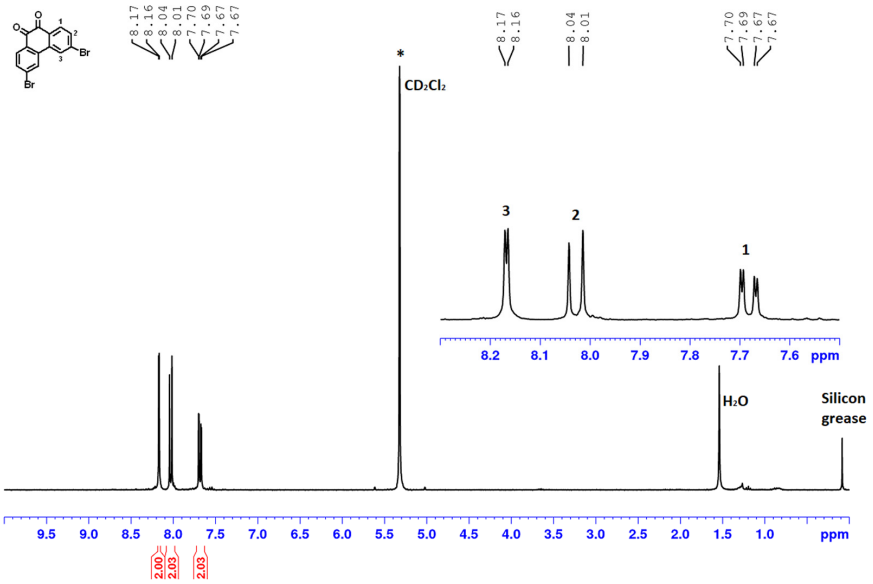

Figure S5. ^{1}H NMR of **2** (300 MHz, 298 K, CD_2Cl_2).

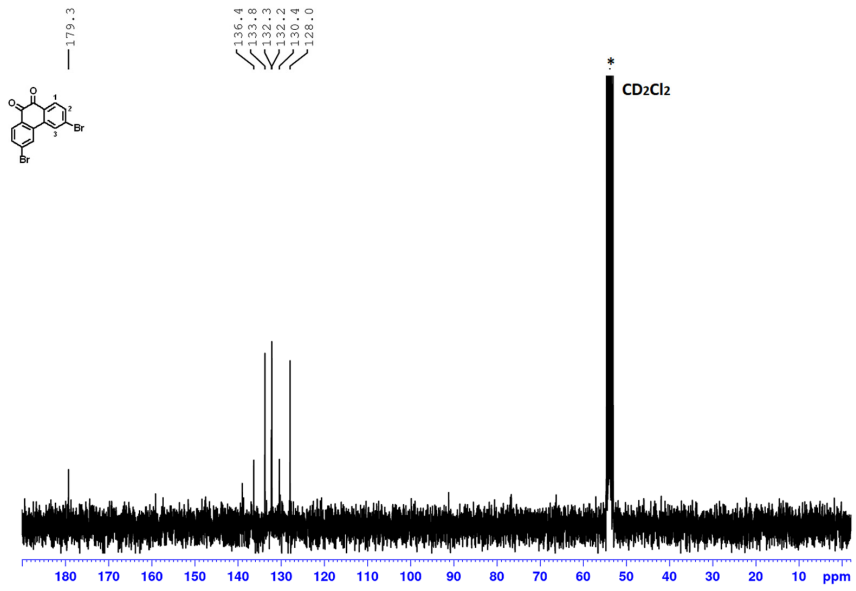

Figure S6. ^{13}C NMR of **2** (75 MHz, 298 K, CD_2Cl_2).

3,6-Dibromo-2-iodophenanthrene-9,10-dione (**3**)

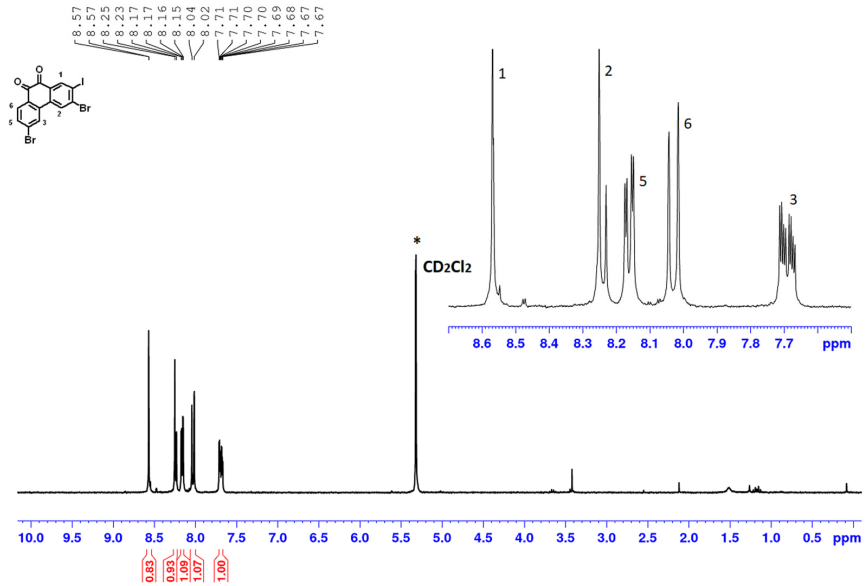

Figure S7. ^{1}H NMR of **3** (300 MHz, 298 K, CD_2Cl_2).

6,9-Dibromo-5-iodo-1,3-diphenyl-2H-cyclopenta[l]phenanthren-2-one (**4**)

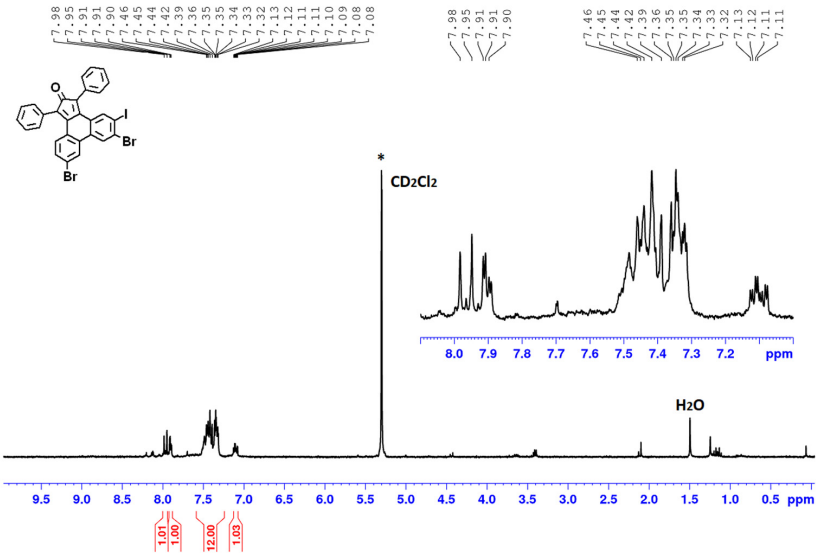

Figure S8. ^{1}H NMR of **4** (300 MHz, 298 K, CD_2Cl_2).

(7,10-Dibromo-11-iodo-1,4-diphenyltriphenylen-2-yl)trimethylsilane (**5**)

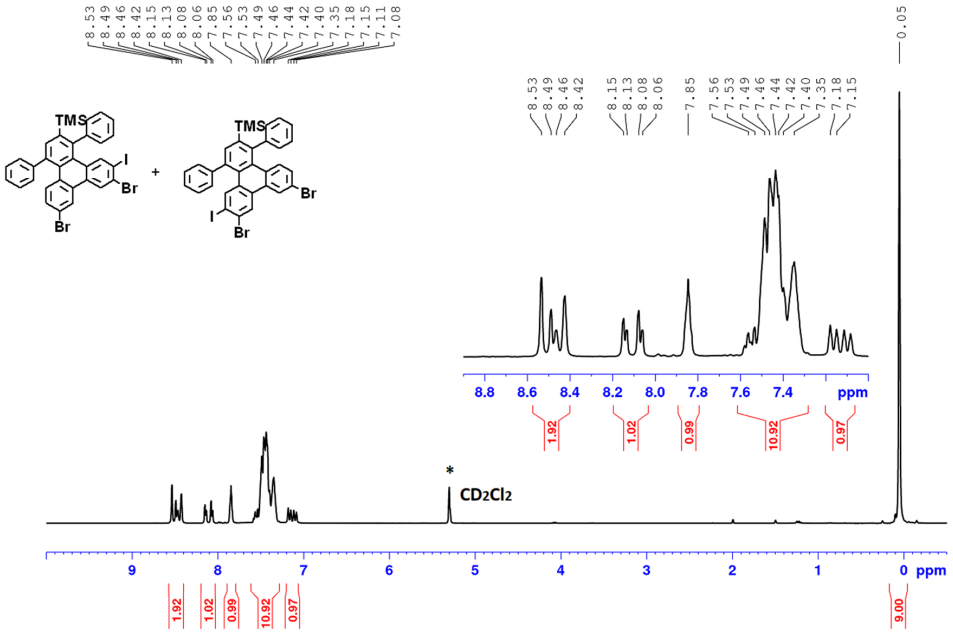

Figure S9. ^{1}H NMR of **5** (300 MHz, 298 K, CD_2Cl_2).

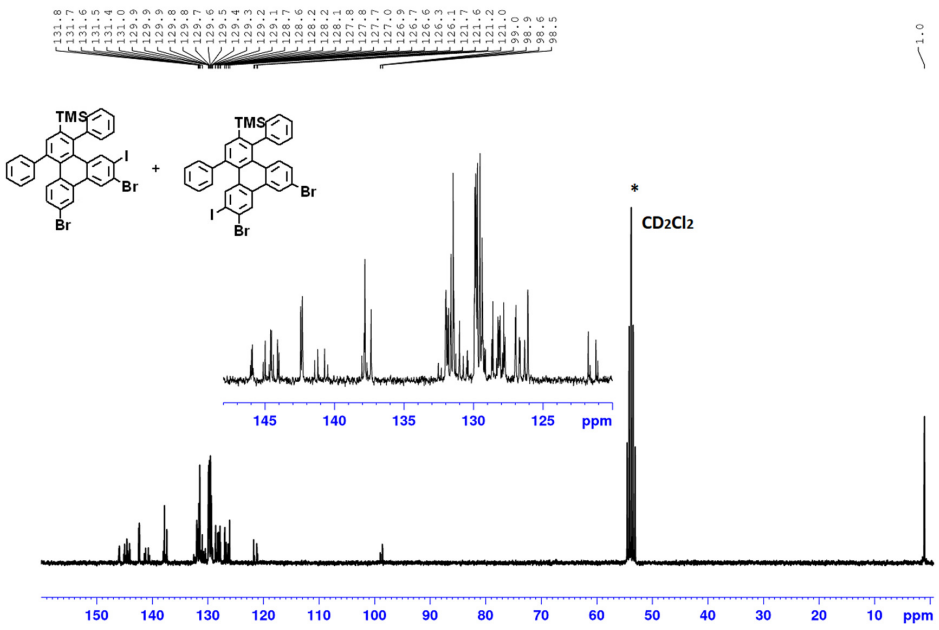

Figure S10. ^{13}C NMR of **5** (75 MHz, 298 K, CD_2Cl_2).

(7,10-Dibromo-1,4,11-triphenyltriphenylen-2-yl)trimethylsilane (**6**)

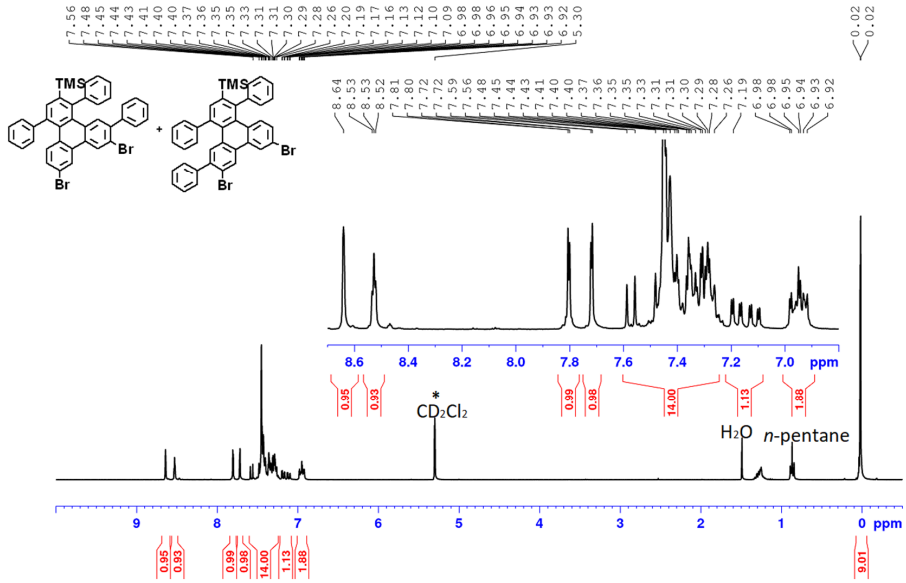

Figure S11. ^{1}H NMR of **6** (300 MHz, 298 K, CD_2Cl_2).

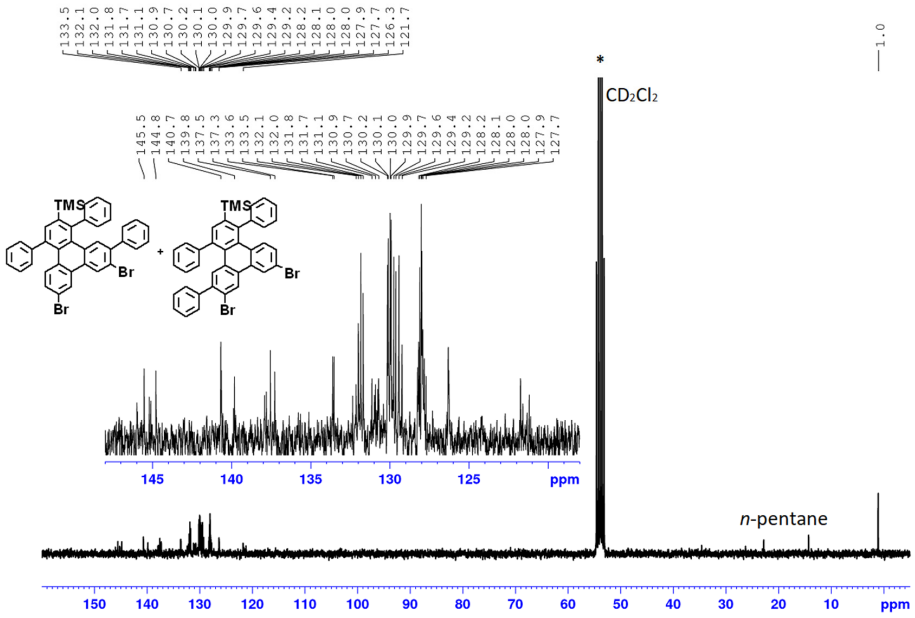

Figure S12. ^{13}C NMR of **6** (75 MHz, 298 K, CD_2Cl_2).

7,10-Dibromo-1,4,6-triphenyltriphenylene (**DBTT**)

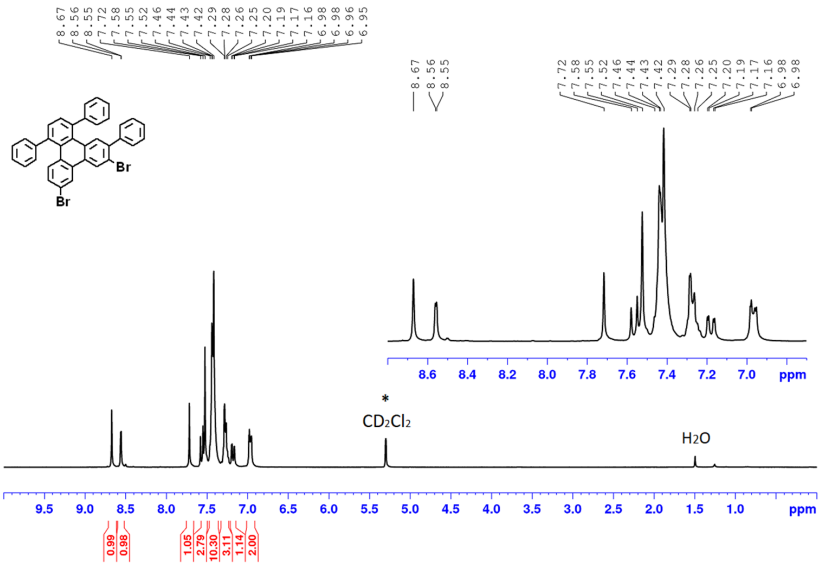

Figure S13. ^{1}H NMR of **DBTT** (300 MHz, 298 K, CD_2Cl_2).

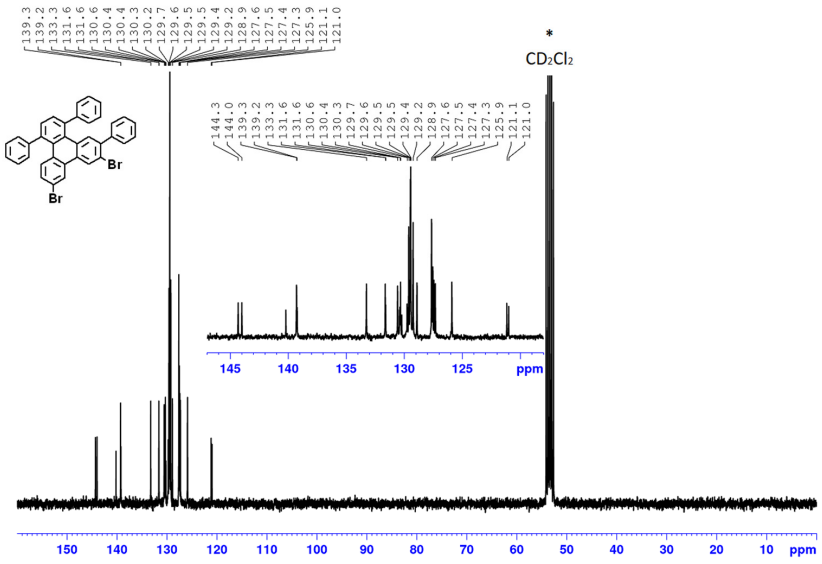

Figure S14. ^{13}C NMR of **DBTT** (75 MHz, 298 K, CD_2Cl_2).

References

1. Sheldrick, G. SHELXT - Integrated Space-Group and Crystal-Structure Determination. *Acta Cryst. A* **2015,** *71,* 3-8.

2. Sheldrick, G. Crystal Structure Refinement with SHELXL. *Acta Cryst. C* **2015,** *71,* 3-8.

3. Spek, A. Structure Validation in Chemical Crystallography. *Acta Cryst. D* **2009,** *65,* 148-155.

4. Brandenburg, H. P. K. Diamond. *Crystal Impact GbR, Bonn* **2012**.

5. Kobin, B.; Grubert, L.; Blumstengel, S.; Henneberger, F.; Hecht, S. Vacuum-Processable Ladder-Type Oligophenylenes for Organic–Inorganic Hybrid Structures: Synthesis, Optical and Electrochemical Properties upon Increasing Planarization as well as Thin Film Growth. *J. Mater. Chem.* **2012,** *22,* 4383-4390.

6. Shirai, Y.; Osgood, A. J.; Zhao, Y.; Yao, Y.; Saudan, L.; Yang, H.; Yu-Hung, C.; Alemany, L. B.; Sasaki, T.; Morin, J.-F.; Guerrero, J. M.; Kelly, K. F.; Tour, J. M. Surface-Rolling Molecules. *J. Am. Chem. Soc.* **2006,** *128,* 4854-4864.

7.7 Supporting Information of Publication 7

In the case of this publication, only the NMR spectra of the precursor and the synthesis steps are shown. The additional STM images, additional measurements, DFT calculations and the single crystal X-ray structure determination have been contributed by co-workers.

Supporting Information for

Kekulene: On-Surface Synthesis, Orbital Structure, and Aromatic Stabilization

Anja Haags[1,2,3‡], Alexander Reichmann[4‡], Qitang Fan[5‡], Larissa Egger[4], Hans Kirschner[6], Tim Naumann[5], Simon Werner[5], Tobias Vollgraff[5], Jörg Sundermeyer[5], Lukas Eschmann[7], Xiaosheng Yang[1,2,3], Dominik Brandstetter[4], François C. Bocquet[1,2], Georg Koller[4], Alexander Gottwald[6], Mathias Richter[6], Michael G. Ramsey[4], Michael Rohlfing[7], Peter Puschnig[4], J. Michael Gottfried[5], Serguei Soubatch[1,2], and F. Stefan Tautz[1,2,3]

[1] Peter Grünberg Institut (PGI-3), Forschungszentrum Jülich, 52425 Jülich, Germany
[2] Jülich Aachen Research Alliance (JARA), Fundamentals of Future Information Technology, 52425 Jülich, Germany
[3] Experimental Physics IV A, RWTH Aachen University, 52074 Aachen, Germany
[4] Institute of Physics, University of Graz, NAWI Graz, 8010 Graz, Austria
[5] Fachbereich Chemie, Philipps-Universität Marburg, Hans-Meerwein-Straße 4, 35032 Marburg, Germany
[6] Physikalisch-Technische Bundesanstalt (PTB), 10587 Berlin, Germany
[7] Institut für Festkörpertheorie, Westfälische Wilhelms-Universität Münster, 48149 Münster, Germany

[‡] A.H., A.R., and Q.F. contributed equally to this work.

S1.5. NMR spectra of chemical species

2,7-dibromophenanthrene (**3**)

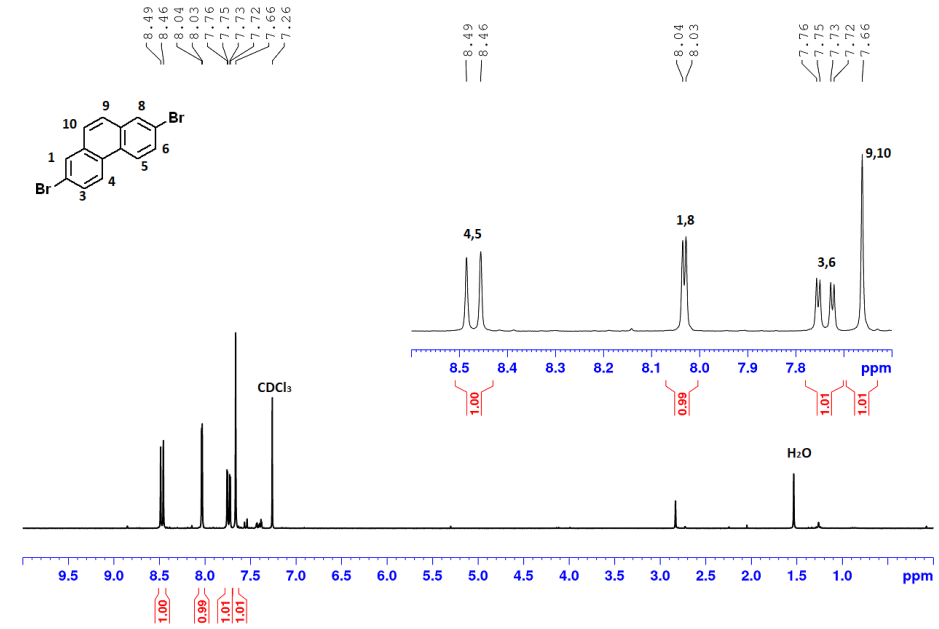

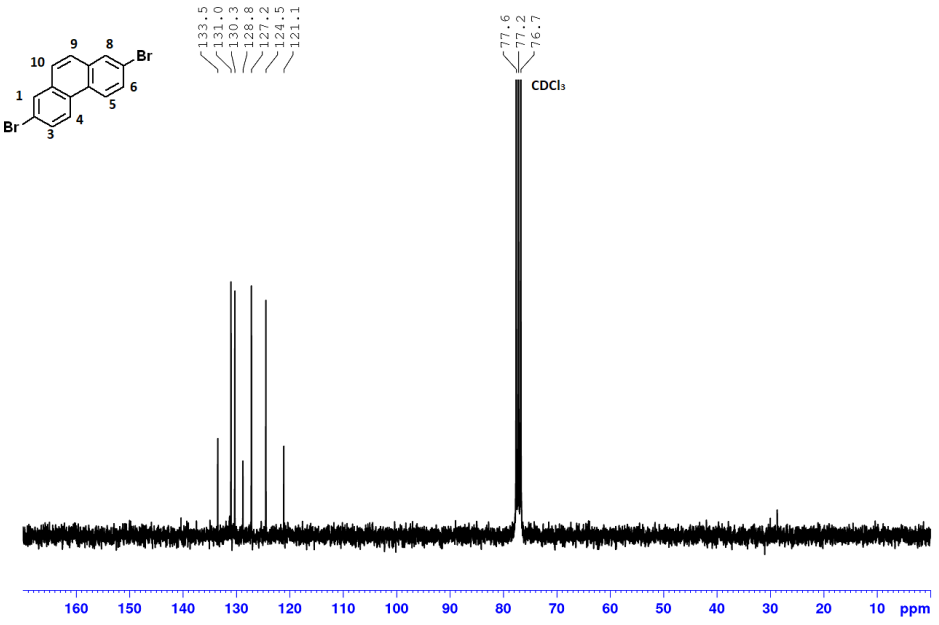

Phenanthrene-2,7-dicarbaldehyde (**4**)

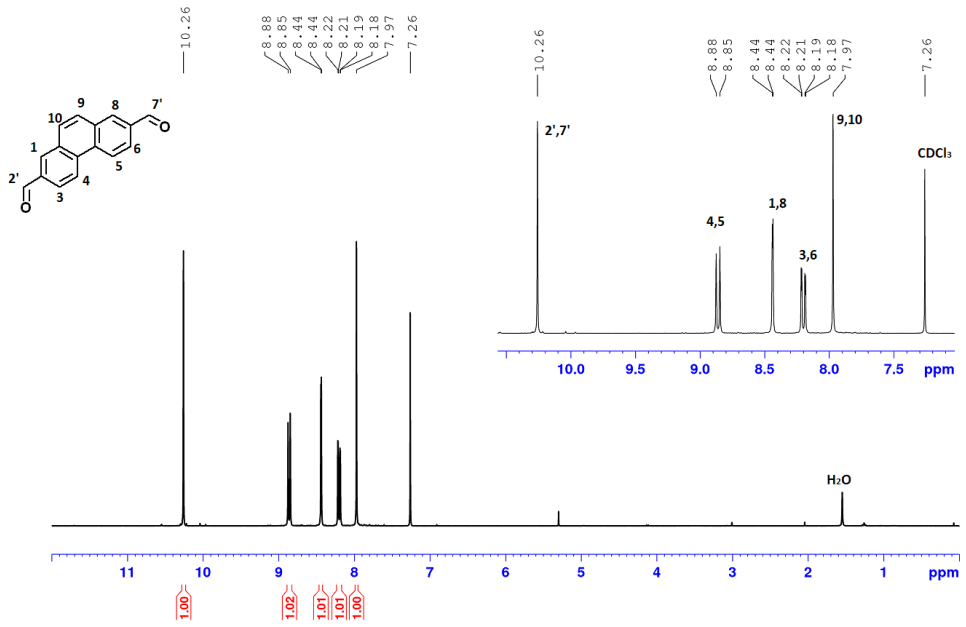

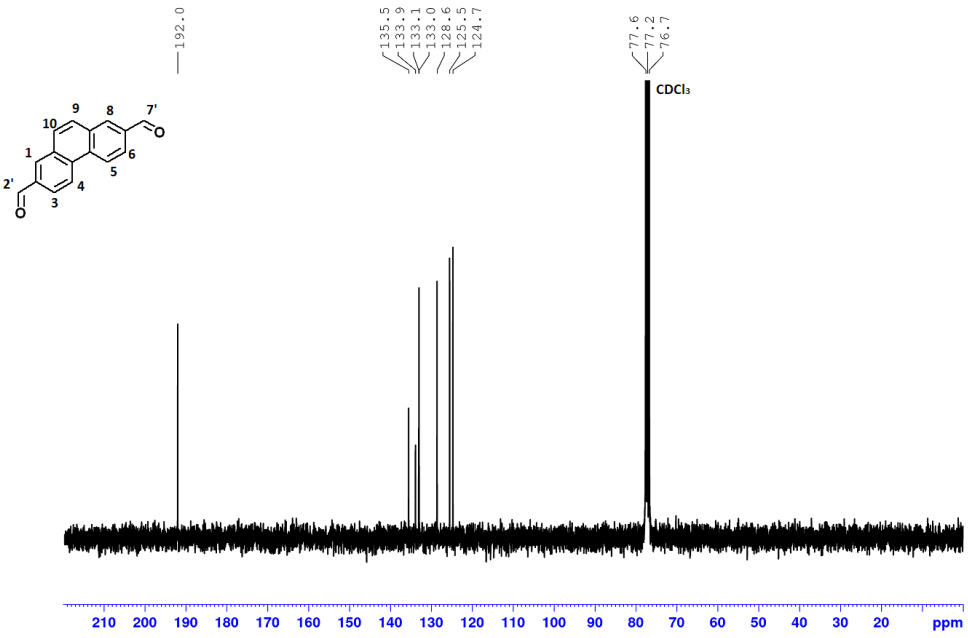

S10

1,4,7(2,7)-triphenanthrenacyclononaphane-2,5,8-triene (**5**)

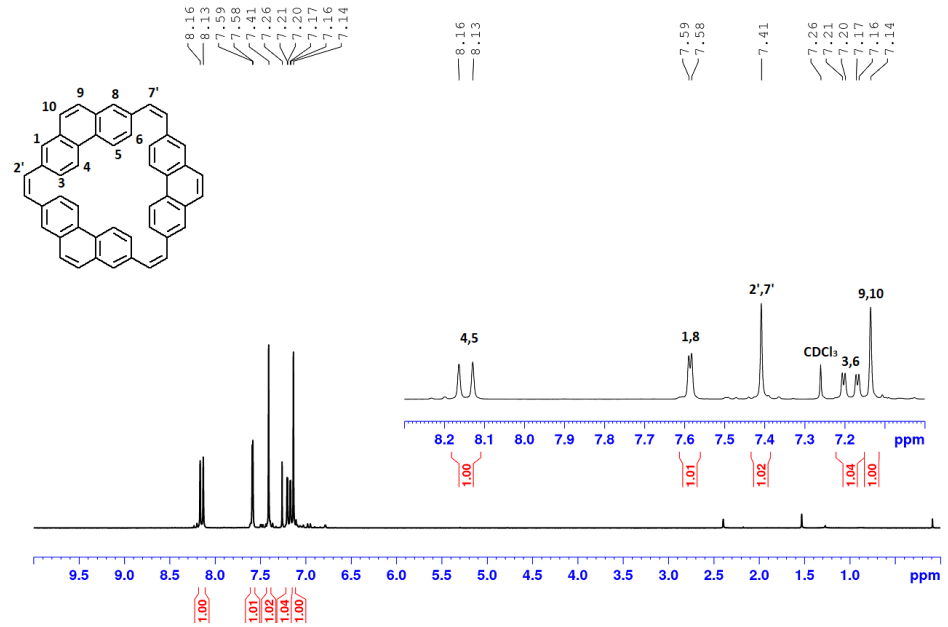

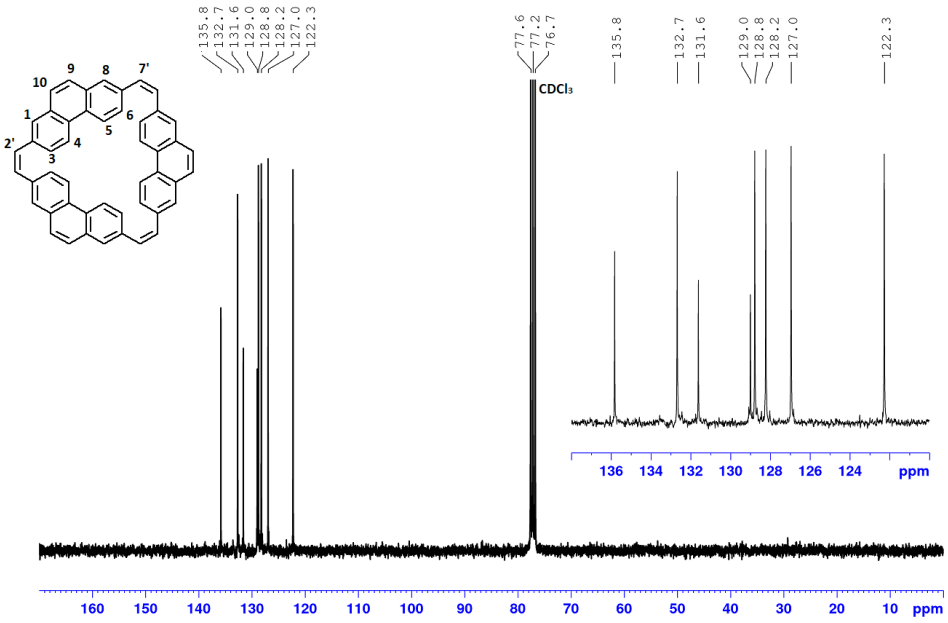

7.8 Supporting Information of Publication 9

In the case of this publication, only the NMR spectra of the precursor and the synthesis steps are shown. The additional STM images, DFT calculations and the single crystal X-ray structure determination have been contributed by co-workers.

WILEY-VCH

SUPPORTING INFORMATION

Supporting Information

Porous Graphene Nanoribbon and Porous Nanographene by Precursor- and Substrate-Controlled On-Surface Synthesis

Qitang Fan, Simon Werner, Tabea Koehler, Tobias Vollgraff, Jörg Sundermeyer,* Wolfgang Hieringer,* J. Michael Gottfried*

Table of contents

SUPPORTING INFORMATION

NMR Spectra

3,6-Dibromophenanthrene-9,10-dione (**M2**)

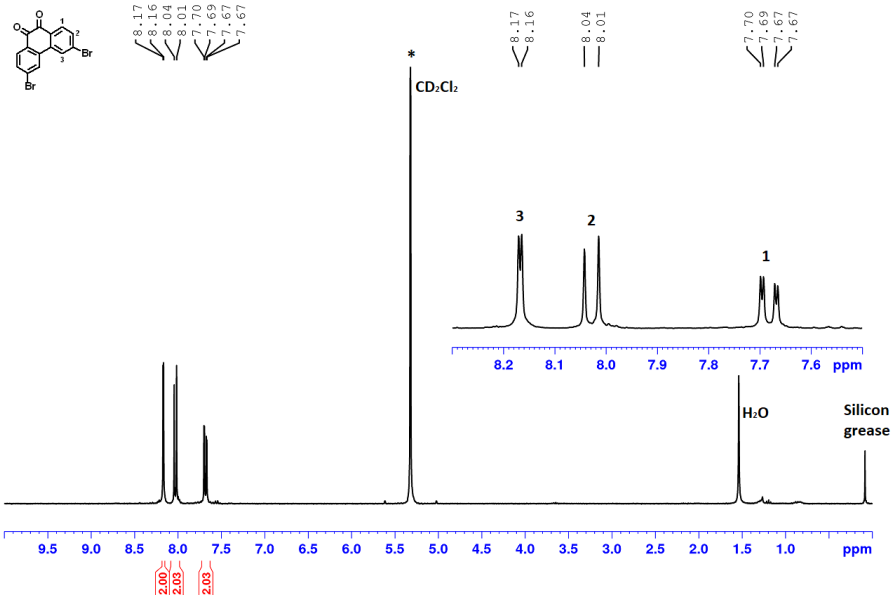

Figure S5. ^{1}H NMR of **M2** (300 MHz, 298 K, CD_2Cl_2).

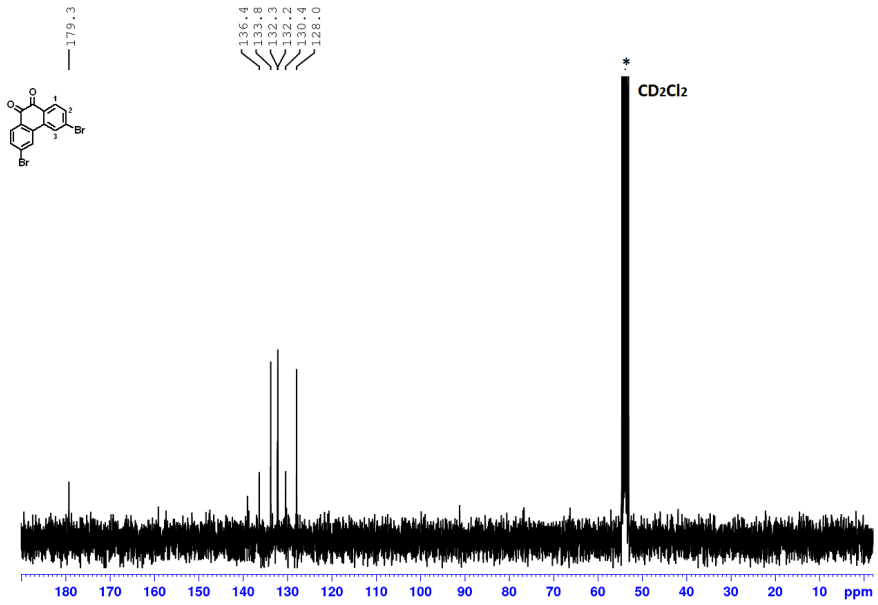

Figure S6. ^{13}C NMR of **M2** (75 MHz, 298 K, CD_2Cl_2).

SUPPORTING INFORMATION

6,9-Dibromo-1,3-diphenyl-2-*H*-cyclopenta[l]phenanthren-2-one (**M3**)

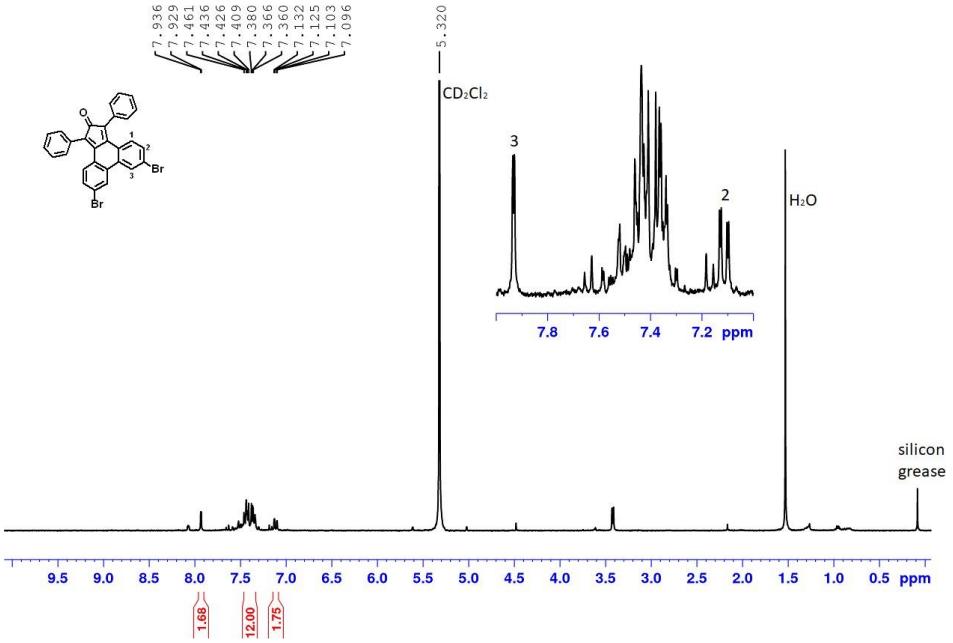

Figure S7. ^{1}H NMR of **M3** (300 MHz, 298 K, CD_2Cl_2).

(7,10-Dibromo-1,4-diphenyltriphenylen-2-yl)trimethylsilane (**M4**)

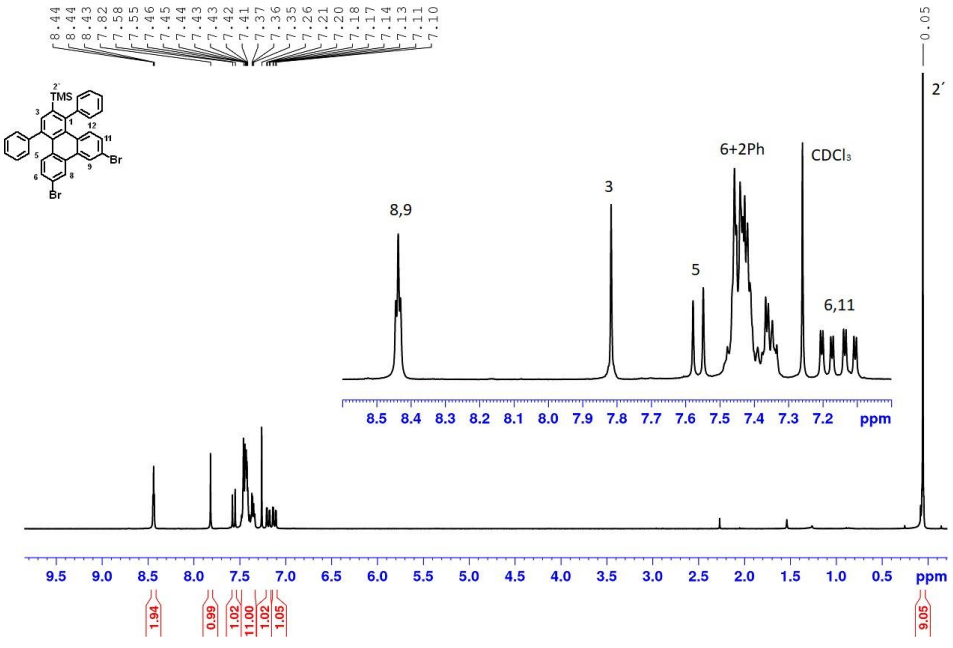

Figure S8. ^{1}H NMR of **M4** (300 MHz, 298 K, $CDCl_3$).

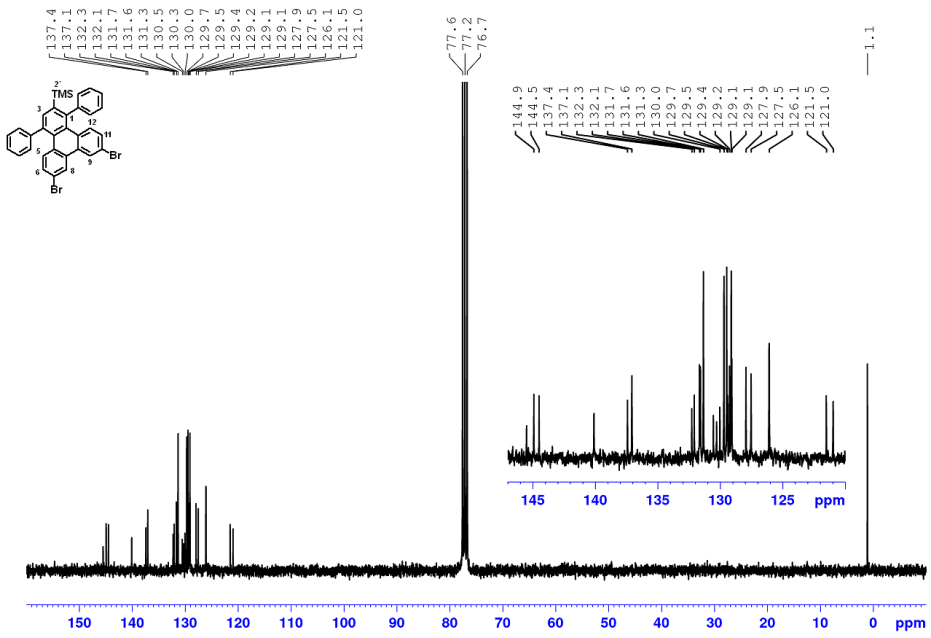

Figure S9. ^{13}C NMR of **M4** (75 MHz, 298 K, $CDCl_3$).

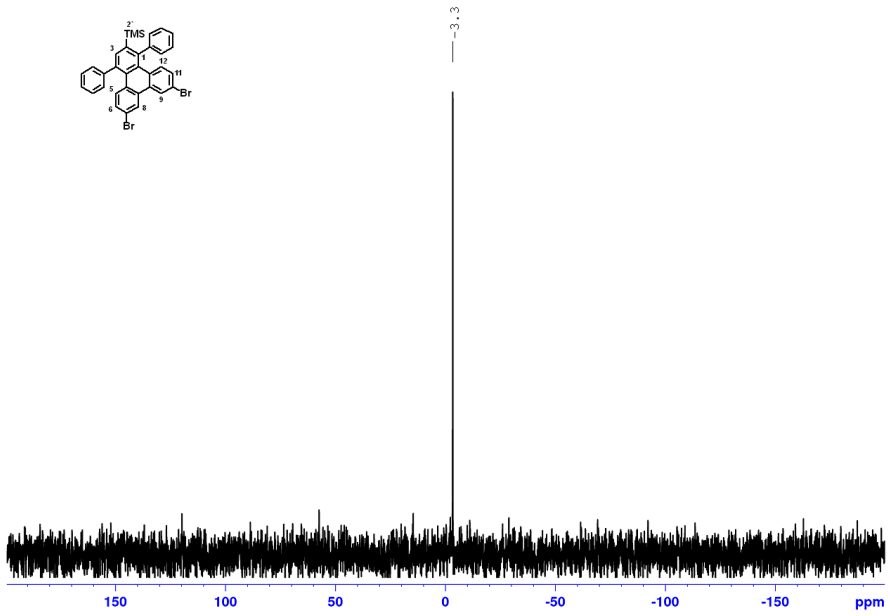

Figure S10. ^{29}Si NMR of **M4** (126 MHz, 298 K, $CDCl_3$).

7,10-Dibromo-1,4-diphenyltriphenylene (**DBDT**)

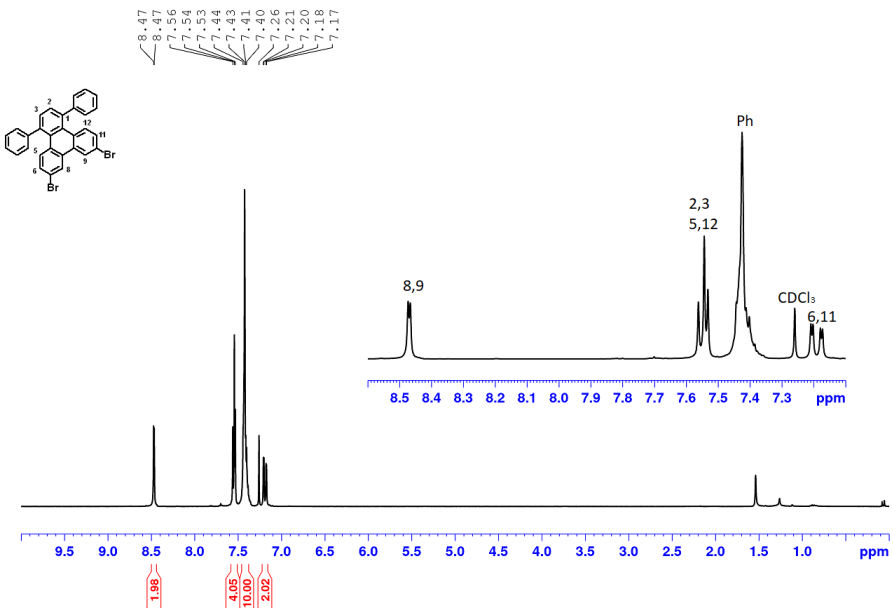

Figure S11. ^{1}H NMR of **DBDT** (300 MHz, 298 K, $CDCl_3$).

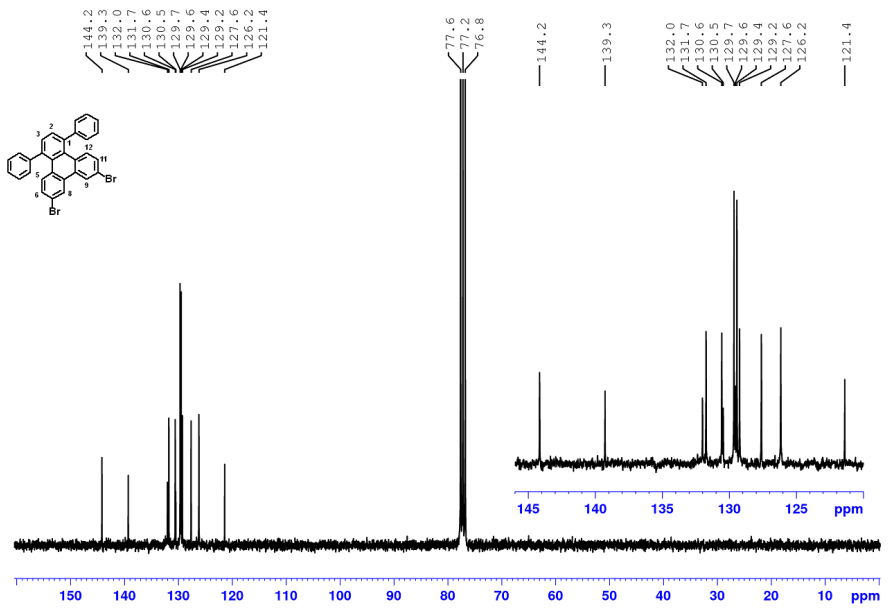

Figure S12. ^{13}C NMR of **DBDT** (75 MHz, 298 K, $CDCl_3$).

SUPPORTING INFORMATION

(1[5],1[8],2[5],2[8],3[5],3[8]-Hexaphenyl-1,2,3(2,11)-tritriphenylenacyclopropaphane-1[6],2[7],3[6]-triyl)tris(trimethylsilane) (**M5**)

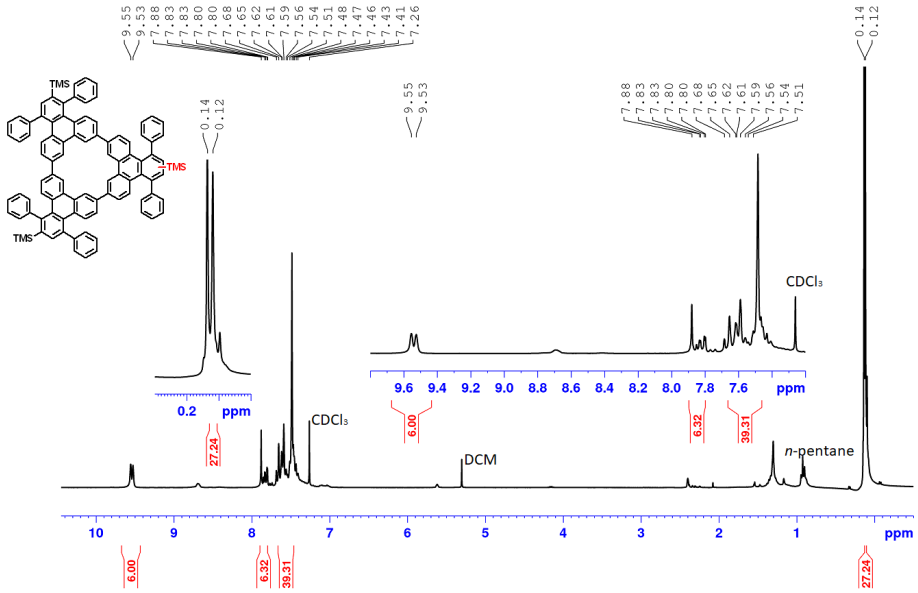

Figure S13. [1]H NMR of **M5** (300 MHz, 298 K, $CDCl_3$).

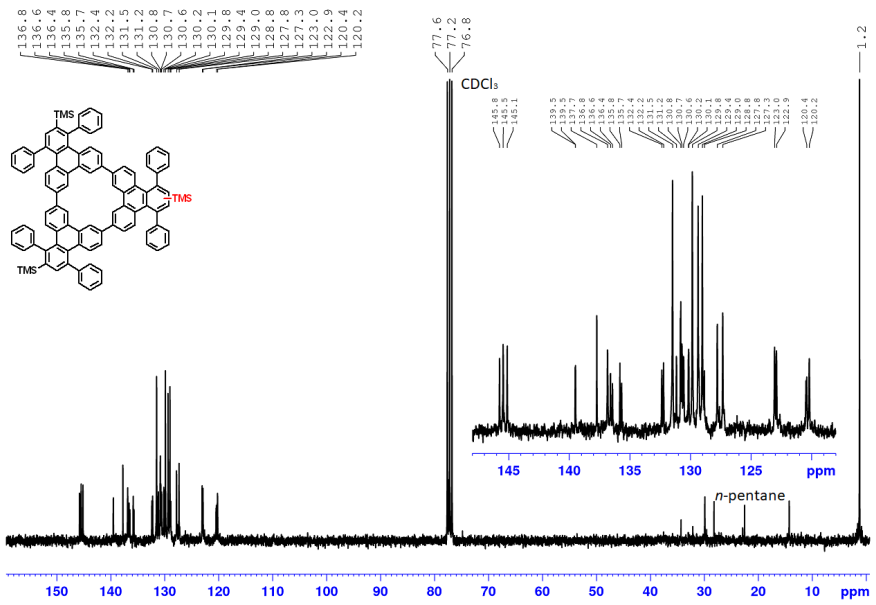

Figure S14. [13]C NMR of **M5** (75 MHz, 298 K, $CDCl_3$).

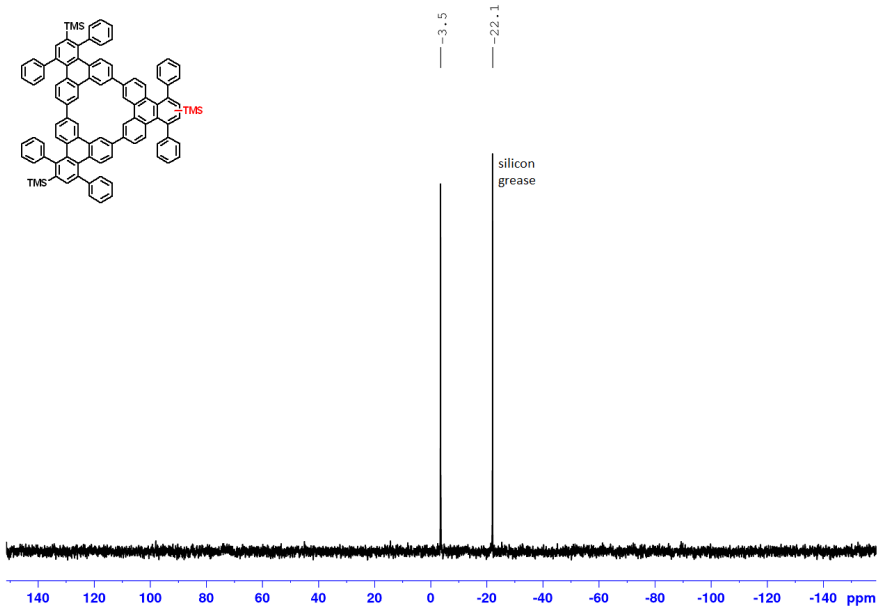

Figure S15. ^{29}Si NMR of **M5** (126 MHz, 298 K, $CDCl_3$).

(1^5,1^8,2^5,2^8,3^5,3^8-Hexaphenyl-1,2,3(2,11)-tritriphenylenacyclopropaphane (**M6**)

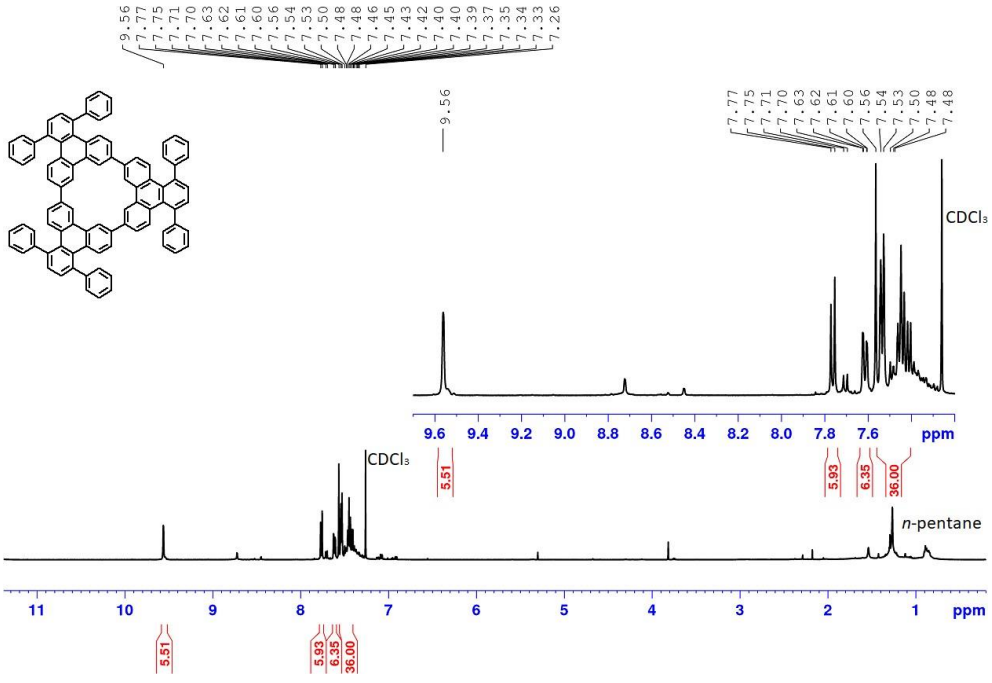

Figure S16. ^{1}H NMR of **M6** (300 MHz, 298 K, $CDCl_3$).

SUPPORTING INFORMATION

3. References

[1] G. Kresse, J. Hafner, Vienna Ab Initio Simulation Package (VASP), version 5.4.4; Institut für Materialphysik, Universität Wien, Vienna, since **1991**, *www.vasp.at.*

[2] J. P. Perdew, K. Burke, M. Ernzerhof, *Phys. Rev. Lett.* **1996**, *77*, 3865-3868.

[3] S. Grimme, J. Antony, S. Ehrlich, H. Krieg, *J. Chem. Phys.* **2010**, *132*, 154104.

[4] S. Grimme, S. Ehrlich, L. Goerigk, *J. Comput. Chem.* **2011**, *32*, 1456-1465.

[5] P. E. Blochl, *Phys. Rev. B* **1994**, *50*, 17953-17979.

[6] G. Kresse, D. Joubert, *Phys. Rev. B* **1999**, *59*, 1758-1775.

[7] Q. Fan, J. M. Gottfried, *ChemPhysChem* **2019**, *20*, 2311-2316.

[8] Stable organic light emitting diode. L. Xiaochang, Z. Jisen (Jiangxi Guan Neng Optoelectric Materials Co., Ltd), CN104447505A (B).

[9] M. G. Schwab, T. Qin, W. Pisula, A. Mavrinskiy, X. Feng, M. Baumgarten, H. Kim, F. Laquai, S. Schuh, R. Trattnig, E. J. W. List, K. Müllen, *Chem. Asian J.* **2011**, *6*, 3001–3010.

[10] X. Chen, F. Tian, C. Persson, W. Duan, N.-X. Chen, *Sci. Rep.* **2013**, *3*, 3026.

[11] W. Wang, N. Zhao, Y. Geng, S.-B. Cui, J. Hauser, S. Decurtins, S.-X. Liu, *RSC Advances* **2014**, *4*, 32639-32642.

[12] G. M. Sheldrick, *Acta cryst., Section A, Foundations and advances* **2015**, *71*, 3–8.

[13] G. M. Sheldrick, *Acta cryst., Section C, Structural chemistry* **2015**, *71*, 3–8.

[14] A. L. Spek, *Acta cryst., Section D, Biological crystallography* **2009**, *65*, 148–155.

[15] A. L. Spek, *Acta cryst., Section C, Structural chemistry* **2015**, *71*, 9-18.

[16] H. P. K. Brandenburg, *Diamond*; Crystal Impact GbR: Bonn, **2012**.

[17] B. Kobin, L. Grubert, S. Blumstengel, F. Henneberger, S. Hecht, *J. Mater. Chem.* **2012**, *22*, 4383–4390.

[18] H. Wettach, S. Höger, D. Chaudhuri, J. M. Lupton, F. Liu, E. M. Lupton, S. Tretiak, G. Wang, M. Li, S. de Feyter, S. Fischer, S. Förster, *J. Mater. Chem.* **2011**, *21*, 1404–1415

7.9 NMR Spectra of Chapter 3.10

Compound 79

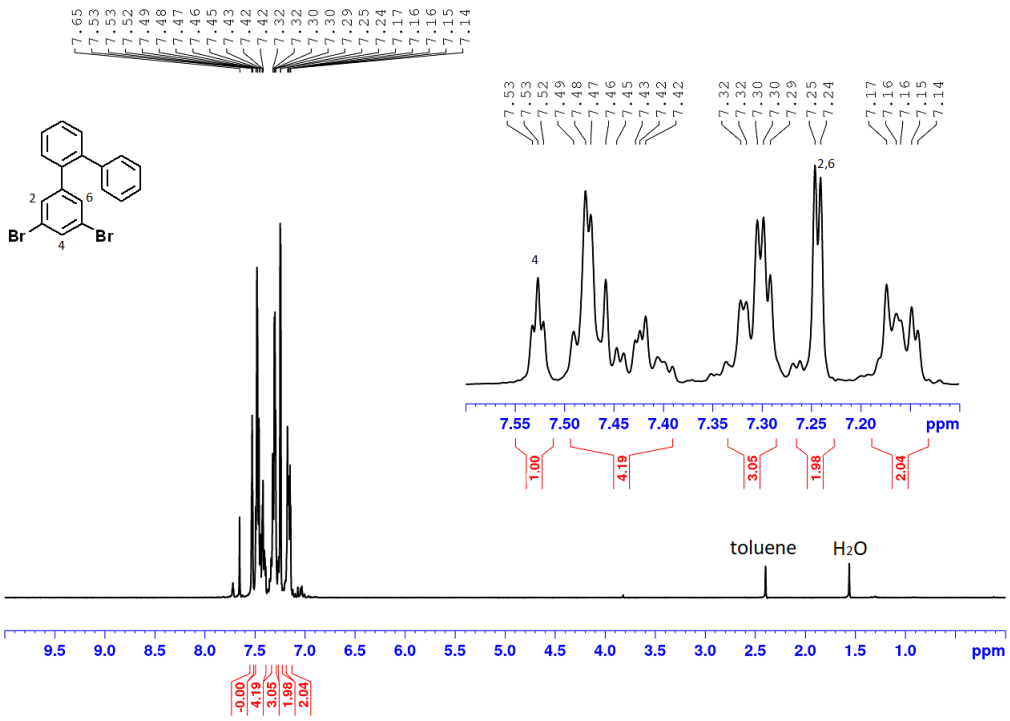

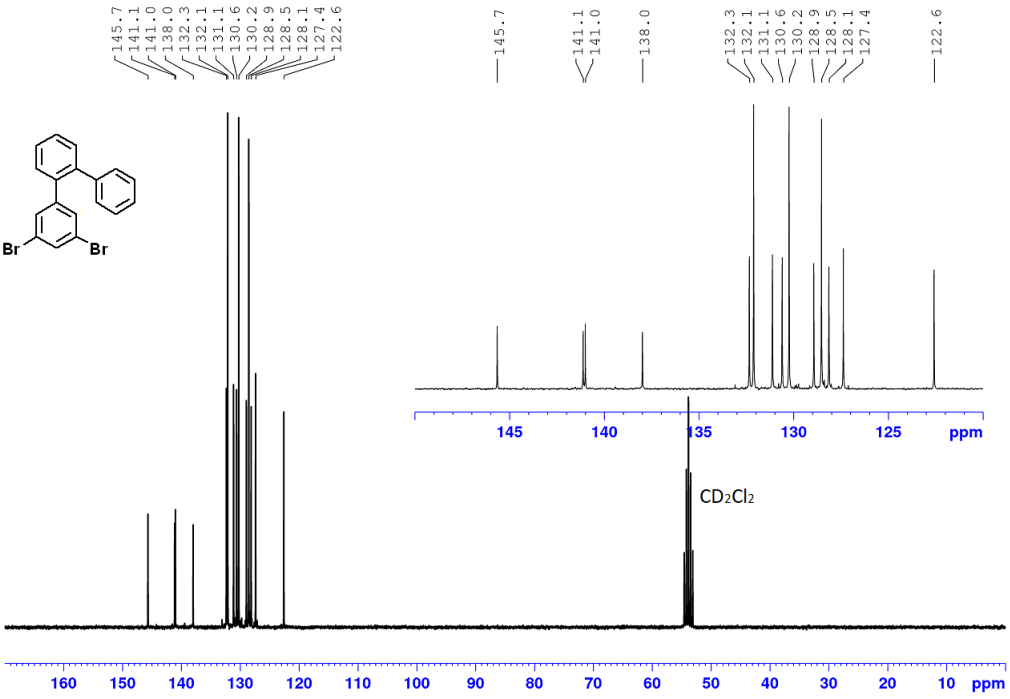

Compound 80

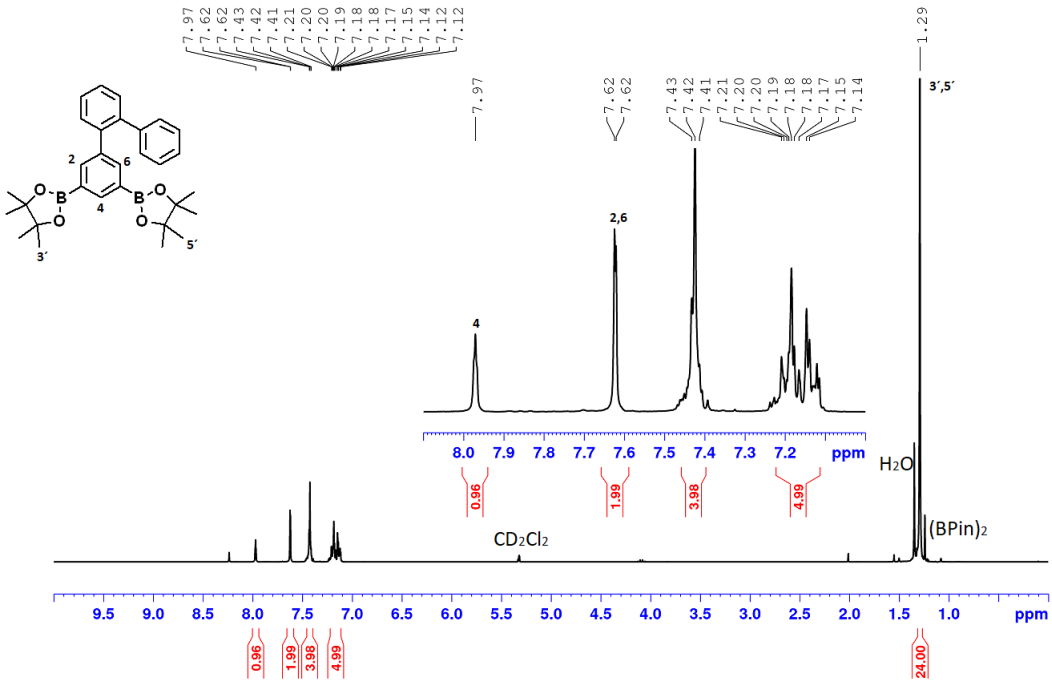
7.97
7.62
7.62
7.43
7.42
7.41
7.21
7.20
7.20
7.19
7.18
7.18
7.17
7.15
7.14
7.12
7.12
1.29
3',5'
2,6
4
8.0 7.9 7.8 7.7 7.6 7.5 7.4 7.3 7.2 ppm
0.96
1.99
3.98
4.99
H2O
CD2Cl2
(BPin)2
9.5 9.0 8.5 8.0 7.5 7.0 6.5 6.0 5.5 5.0 4.5 4.0 3.5 3.0 2.5 2.0 1.5 1.0 ppm
0.96
1.99
3.98
4.99
24.00

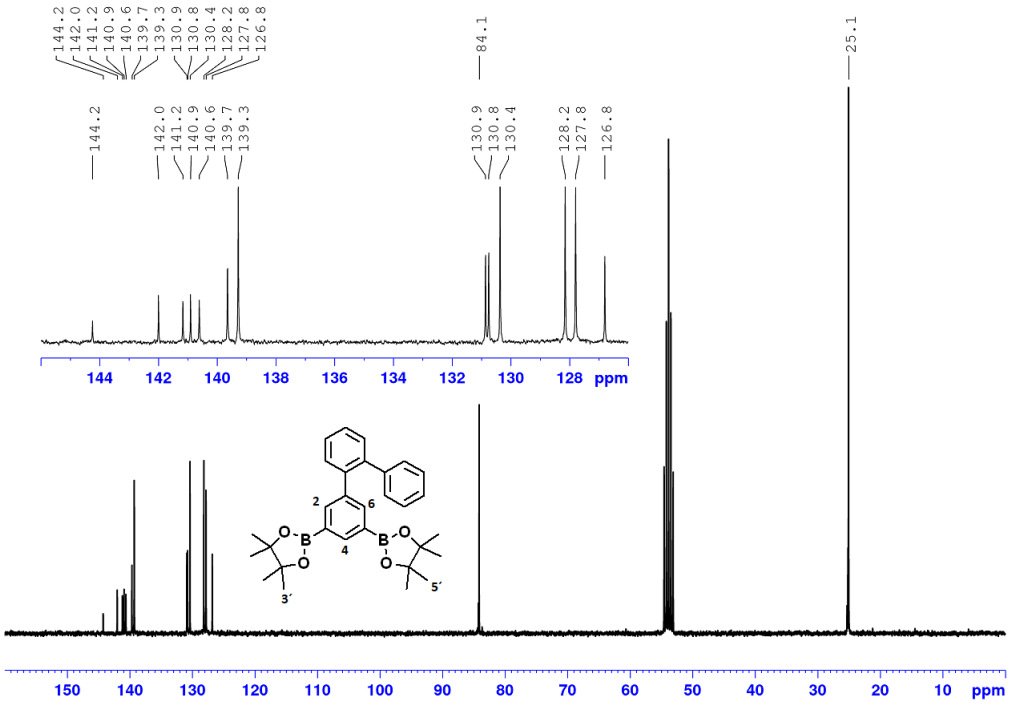
144.2
142.0
141.2
140.9
140.6
139.7
139.3
130.9
130.8
130.4
128.2
127.8
126.8
84.1
25.1
144 142 140 138 136 134 132 130 128 ppm
150 140 130 120 110 100 90 80 70 60 50 40 30 20 10 ppm

Compound 81

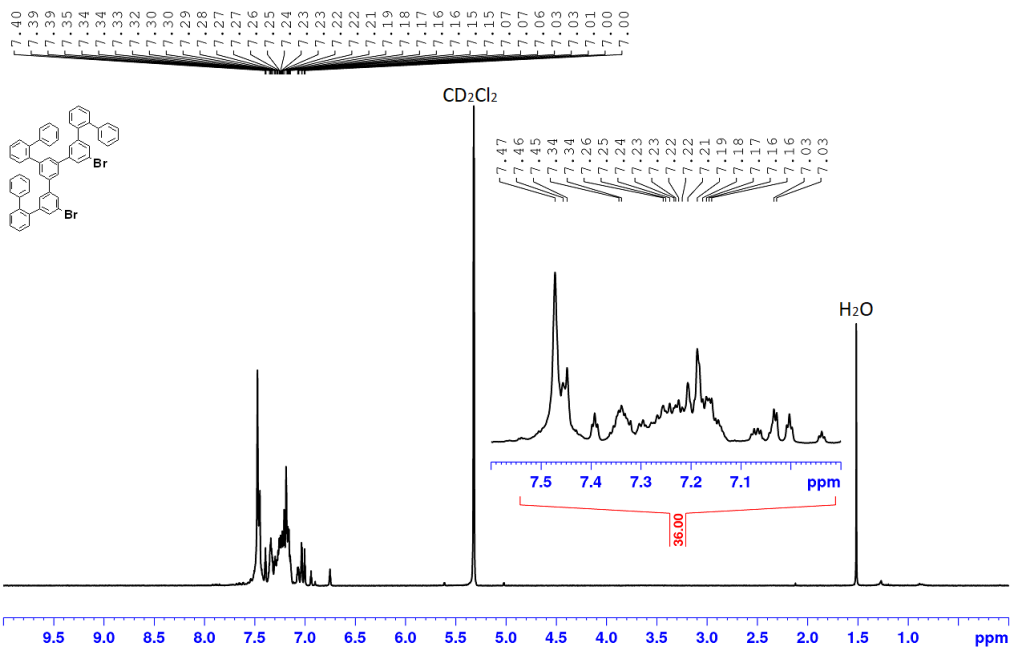
7.40
7.39
7.39
7.35
7.34
7.34
7.33
7.32
7.30
7.30
7.29
7.28
7.27
7.27
7.26
7.25
7.24
7.23
7.23
7.22
7.22
7.21
7.19
7.18
7.17
7.16
7.16
7.15
7.15
7.07
7.07
7.06
7.03
7.03
7.01
7.00
7.00
Br
Br
CD2Cl2
7.47
7.46
7.45
7.34
7.34
7.26
7.25
7.24
7.23
7.23
7.22
7.22
7.21
7.19
7.18
7.17
7.16
7.16
7.03
7.03
H2O
7.5
7.4
7.3
7.2
7.1
ppm
36.00
9.5
9.0
8.5
8.0
7.5
7.0
6.5
6.0
5.5
5.0
4.5
4.0
3.5
3.0
2.5
2.0
1.5
1.0
ppm

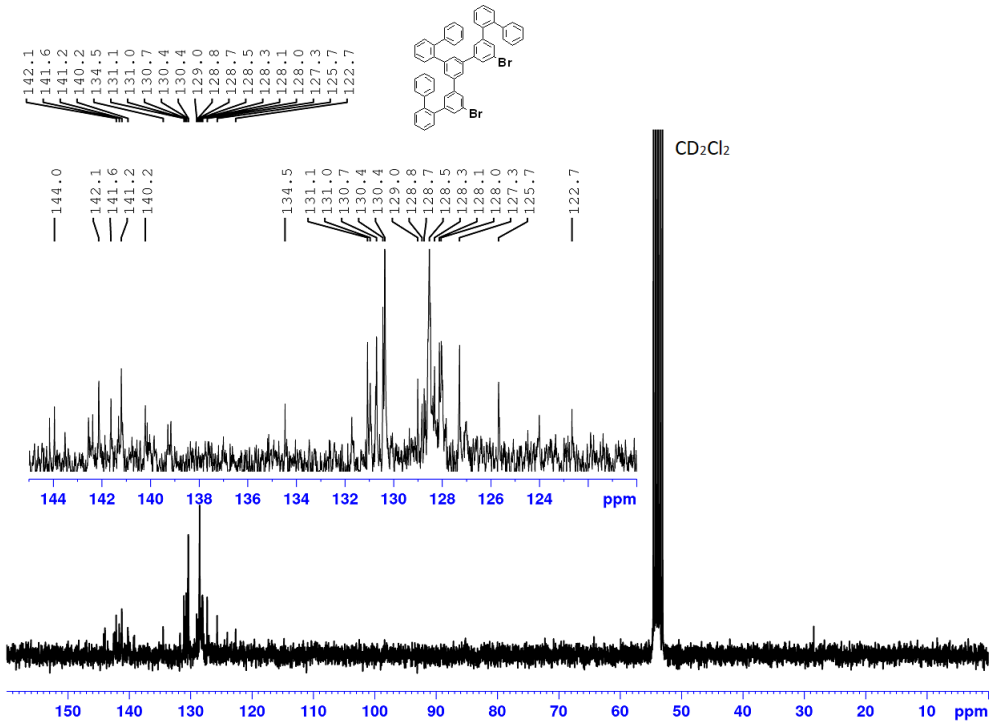
142.1
141.6
141.2
140.2
134.5
131.1
131.0
130.7
130.4
130.4
129.0
128.8
128.7
128.5
128.3
128.1
128.0
127.3
125.7
122.7
Br
Br
CD2Cl2
144.0
142.1
141.6
141.2
140.2
134.5
131.1
131.0
130.7
130.4
130.4
129.0
128.8
128.7
128.5
128.3
128.1
128.0
127.3
125.7
122.7
144
142
140
138
136
134
132
130
128
126
124
ppm
150
140
130
120
110
100
90
80
70
60
50
40
30
20
10
ppm

Compound 97

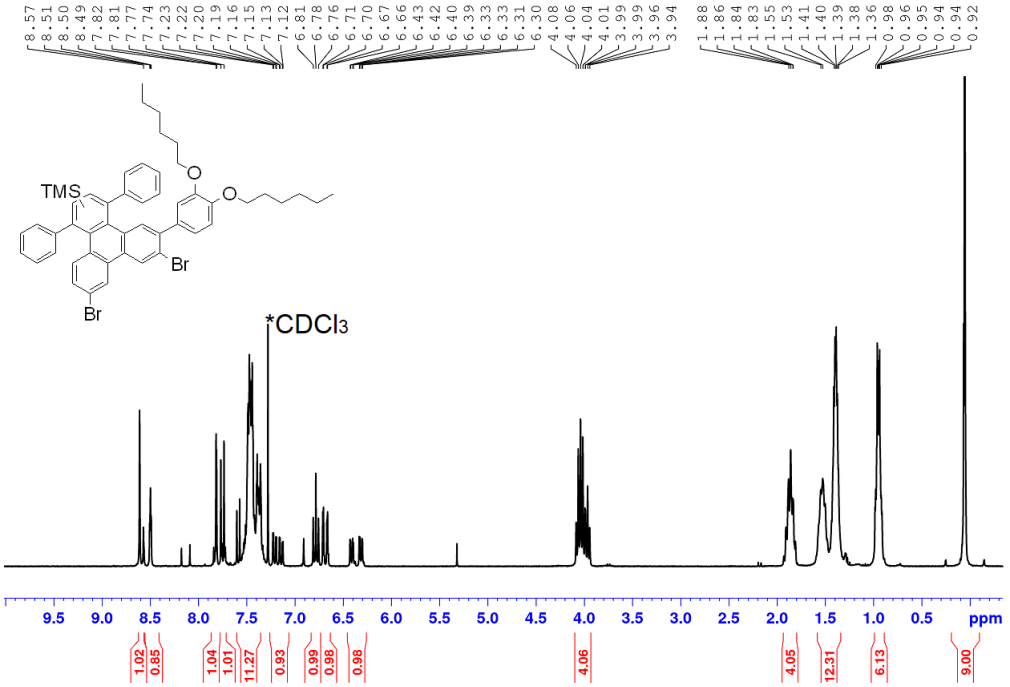
TMS
O
O
Br
Br
*CDCl3
9.5 9.0 8.5 8.0 7.5 7.0 6.5 6.0 5.5 5.0 4.5 4.0 3.5 3.0 2.5 2.0 1.5 1.0 0.5 ppm

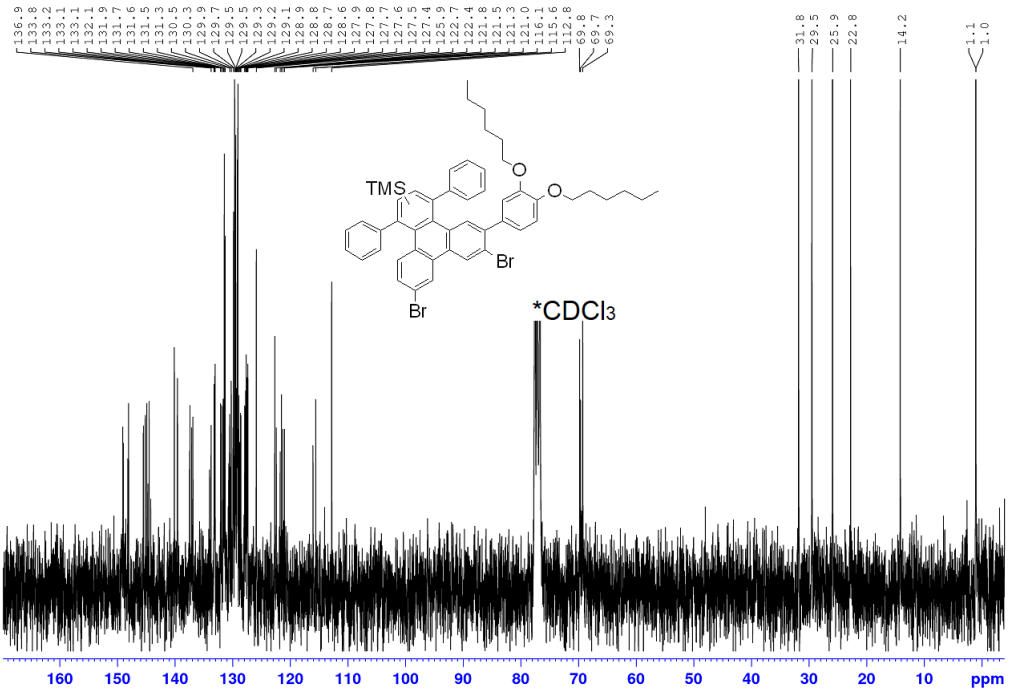
TMS
O
O
Br
Br
*CDCl3
160 150 140 130 120 110 100 90 80 70 60 50 40 30 20 10 ppm

Compound 98

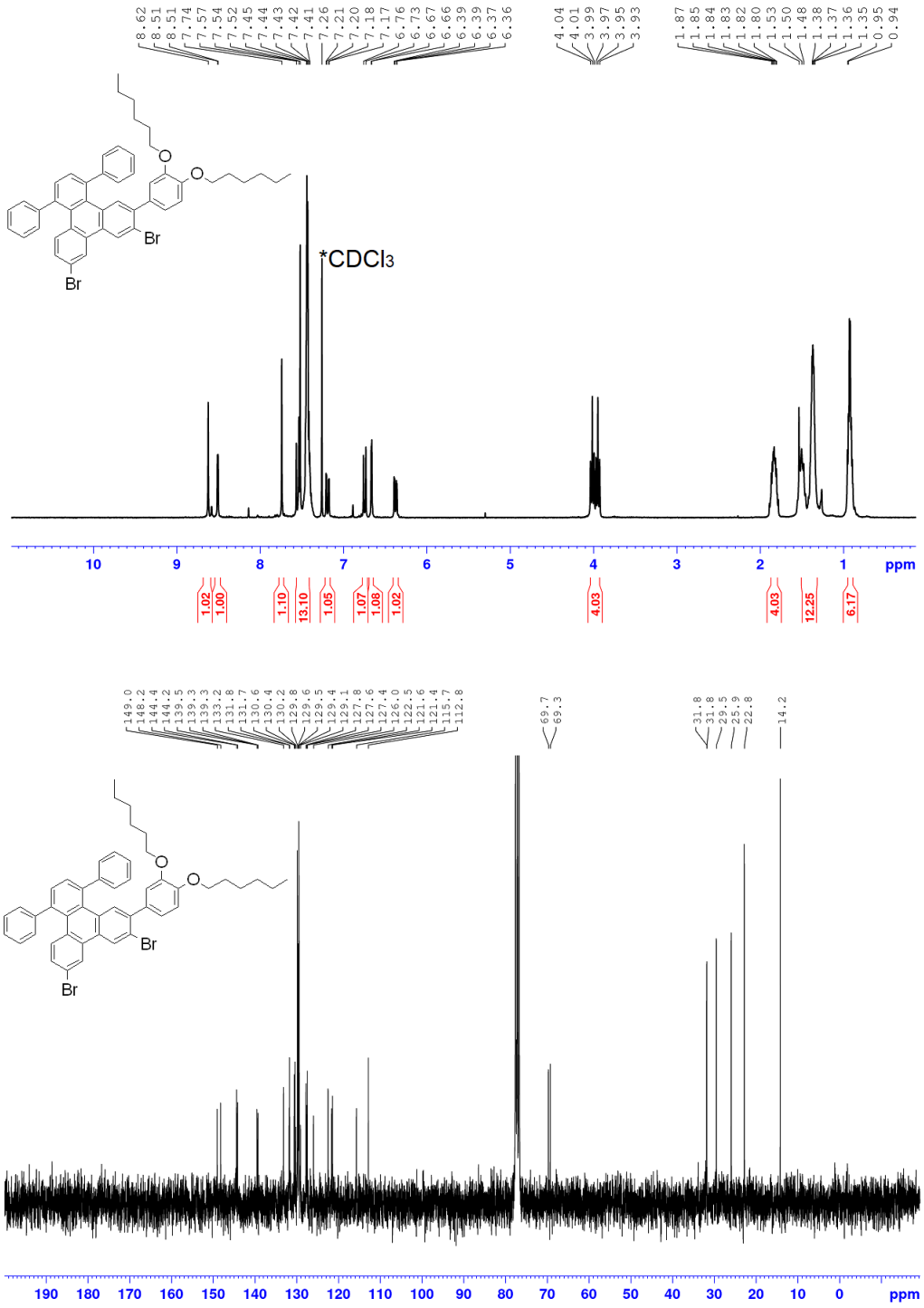
8.62
8.51
8.51
7.74
7.57
7.54
7.52
7.45
7.44
7.43
7.42
7.41
7.26
7.21
7.20
7.18
7.17
6.76
6.73
6.67
6.66
6.39
6.39
6.37
6.36
4.04
4.01
3.99
3.97
3.95
3.93
1.87
1.85
1.84
1.83
1.82
1.80
1.53
1.50
1.48
1.38
1.37
1.36
1.35
0.95
0.94
Br
Br
*CDCl3
10
9
8
7
6
5
4
3
2
1
ppm
1.02
1.00
1.10
13.10
1.05
1.07
1.08
1.02
4.03
4.03
12.25
6.17
149.0
148.2
144.4
144.2
139.5
139.3
139.3
133.2
131.8
131.7
130.6
130.4
130.2
129.8
129.6
129.5
129.4
129.1
127.8
127.6
127.4
126.0
122.5
121.6
121.4
115.7
112.8
69.7
69.3
31.8
31.8
29.5
25.9
22.8
14.2
Br
Br
190
180
170
160
150
140
130
120
110
100
90
80
70
60
50
40
30
20
10
0
ppm

Compound 99

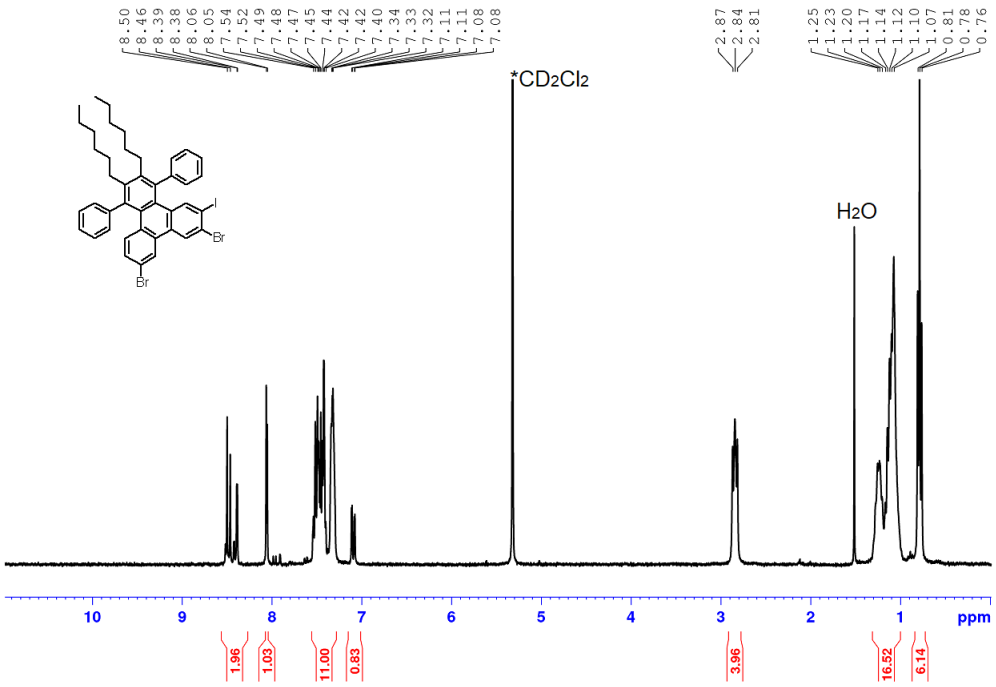

Compound 100

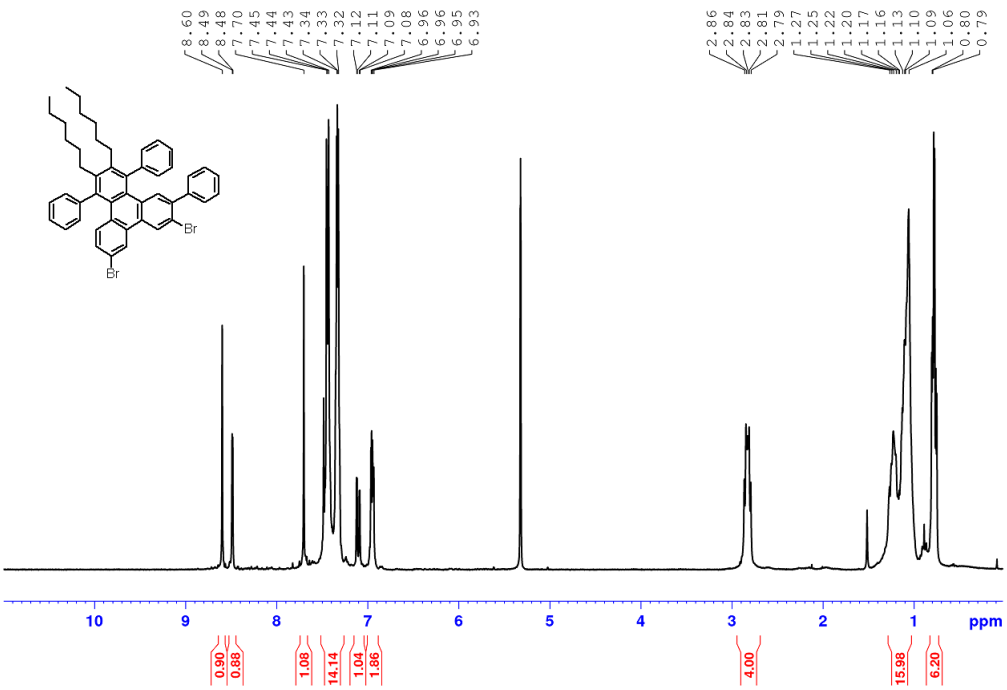

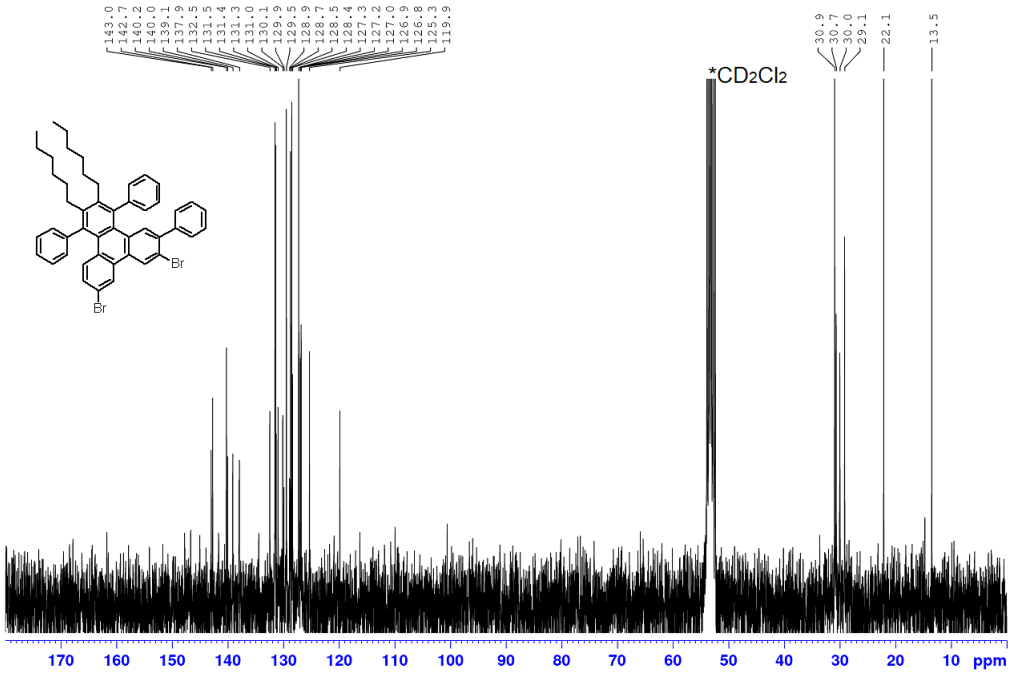

Compound 101

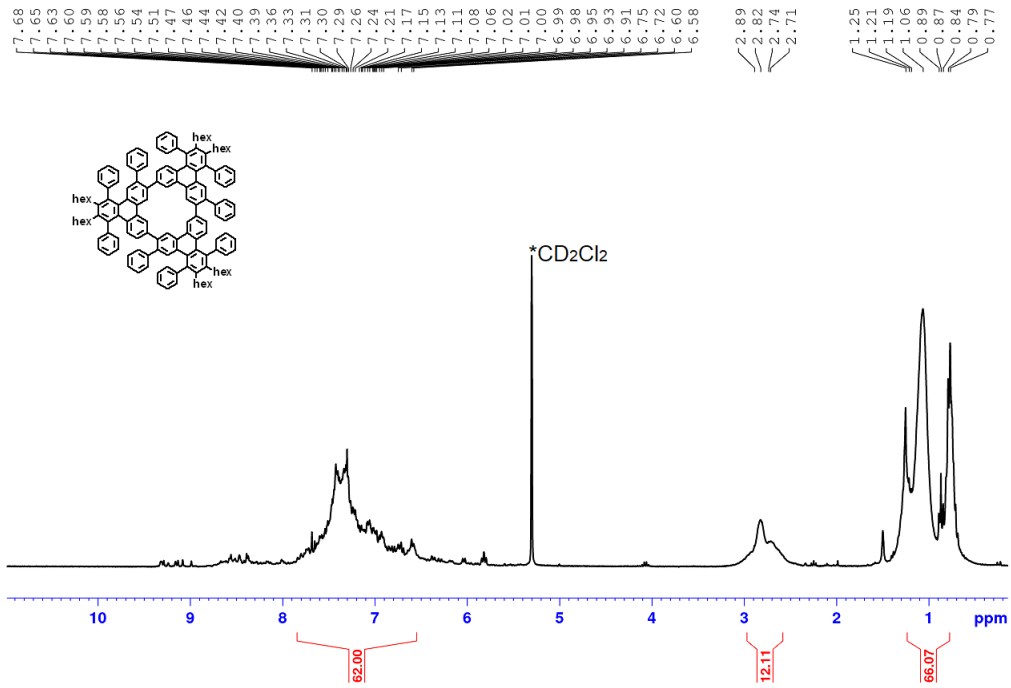

Compound 112

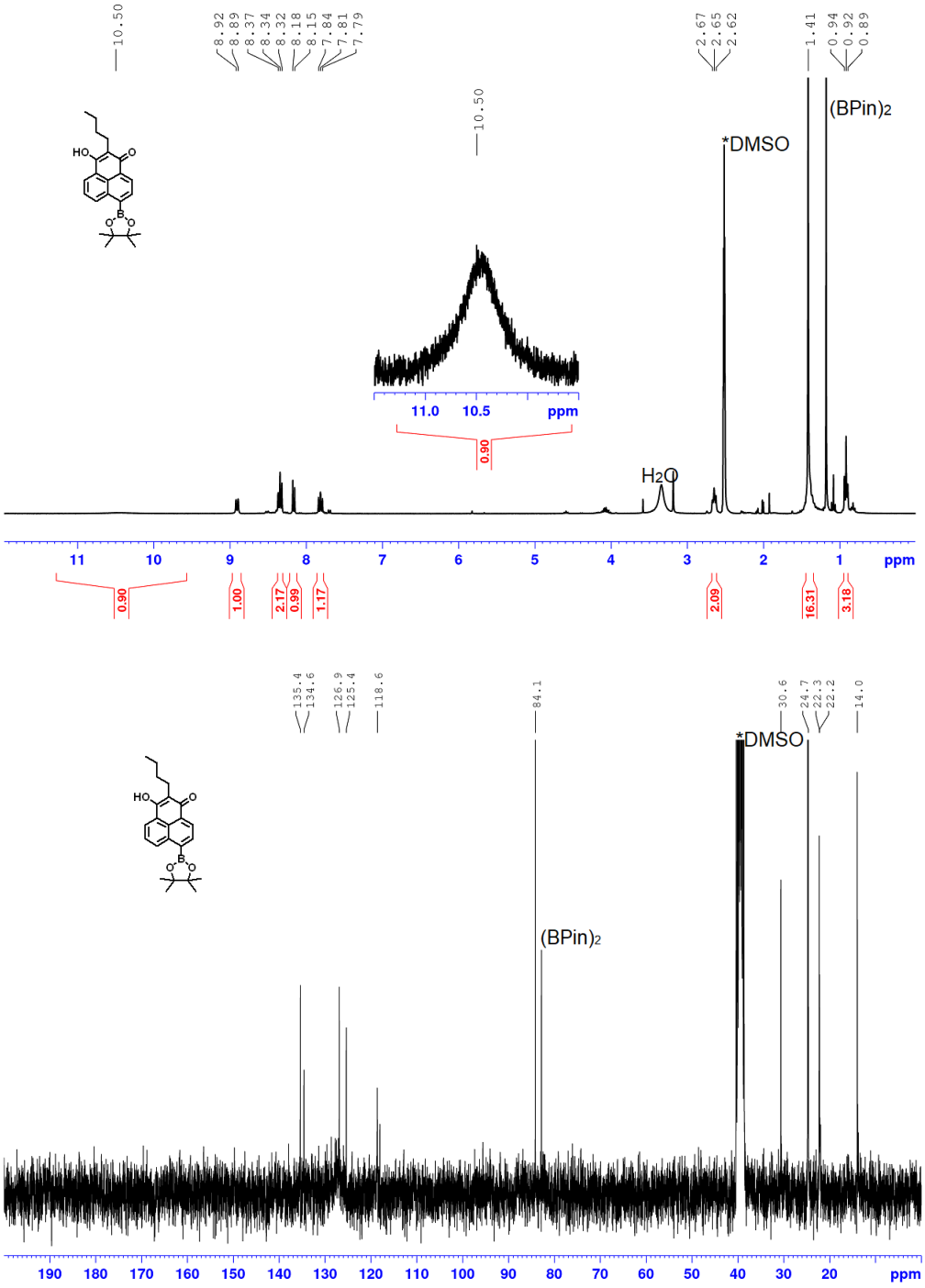

Compound 109

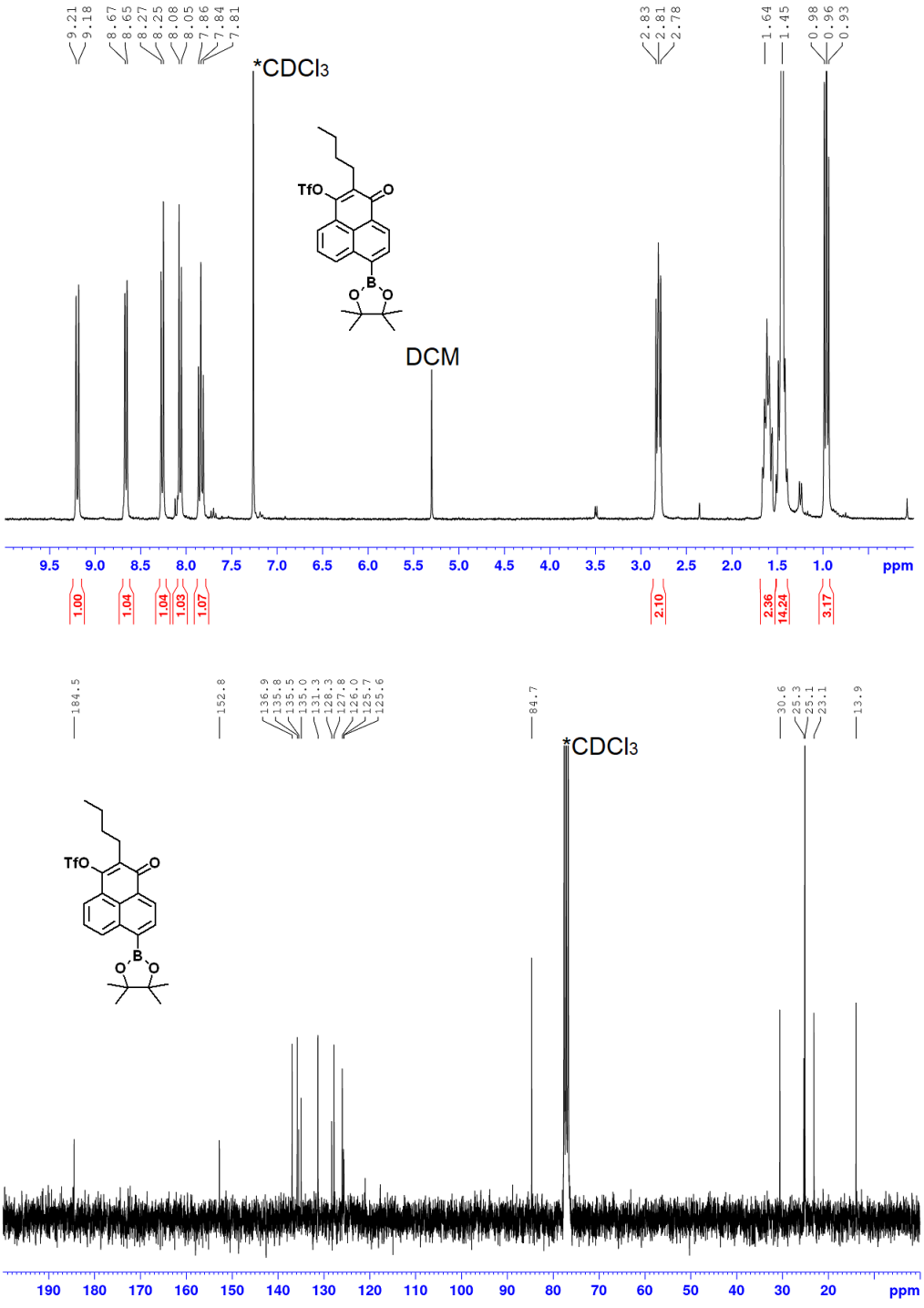

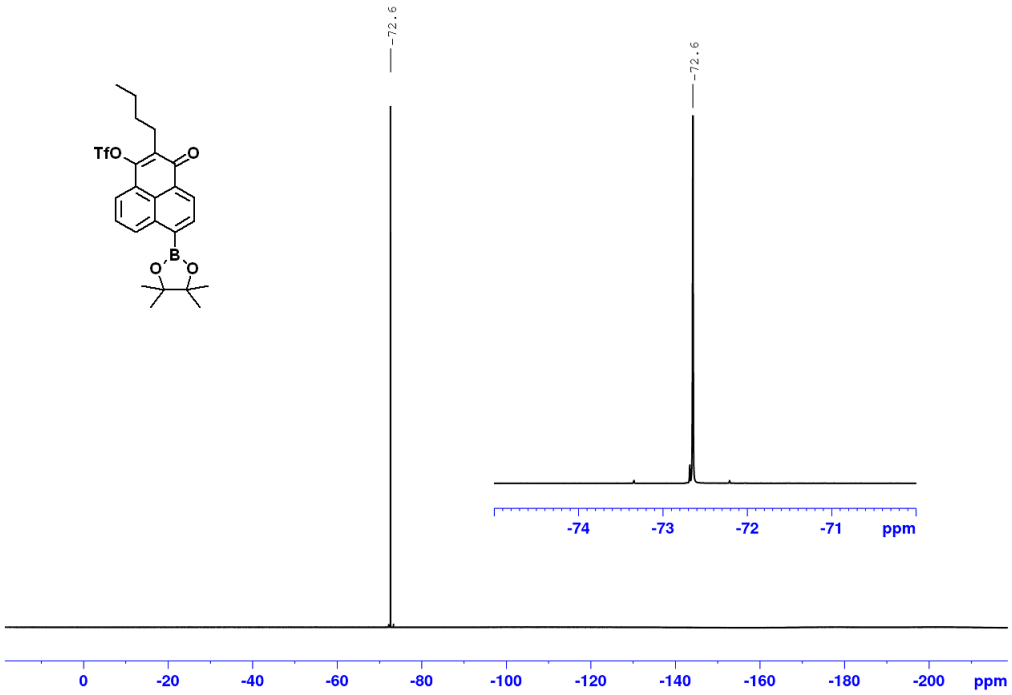

Compound 116

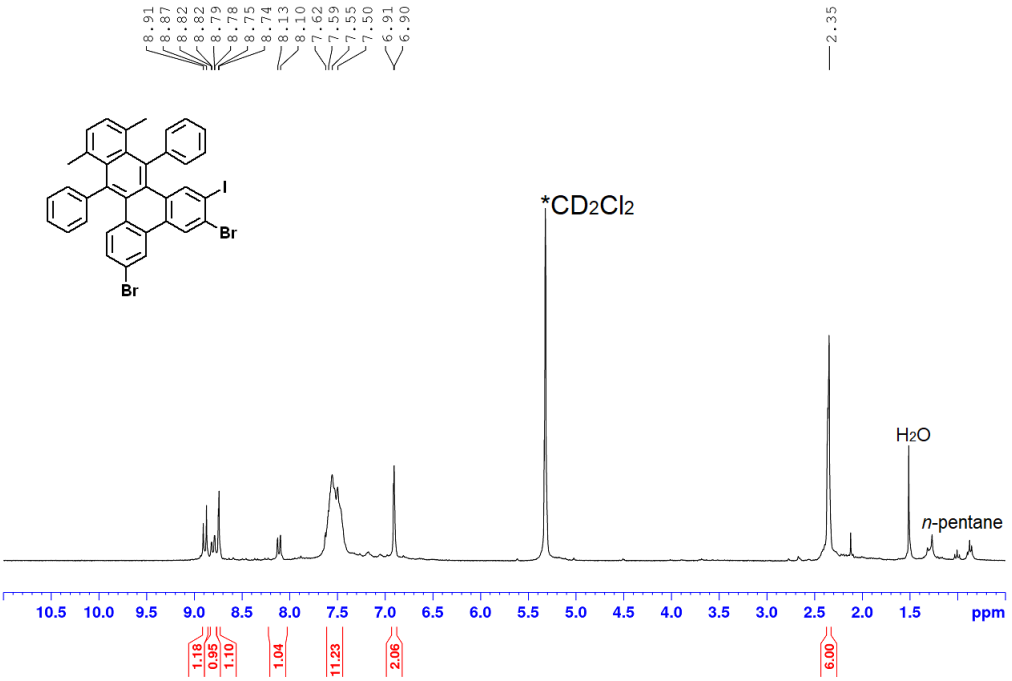

Compound 114

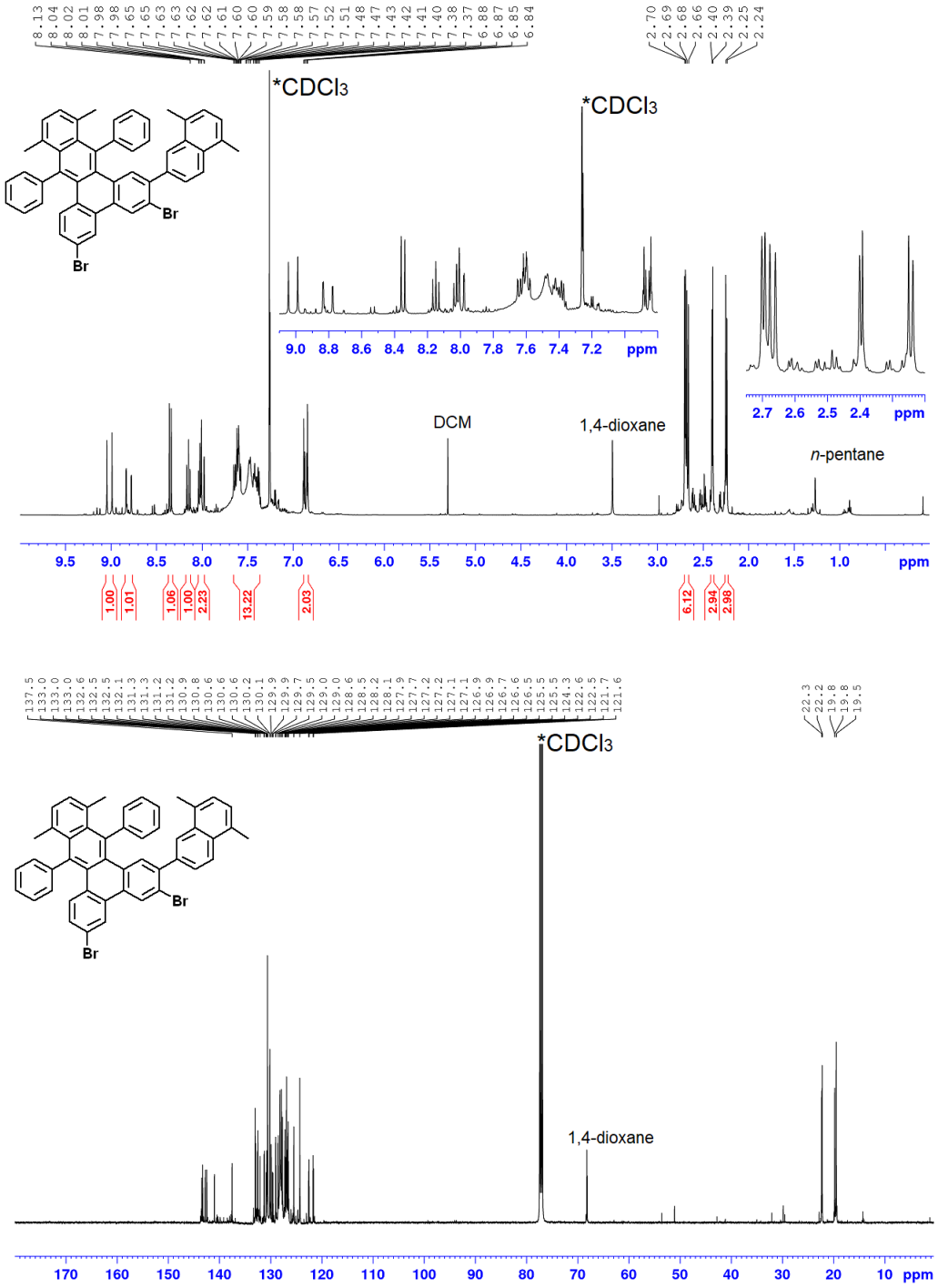

Compound 122

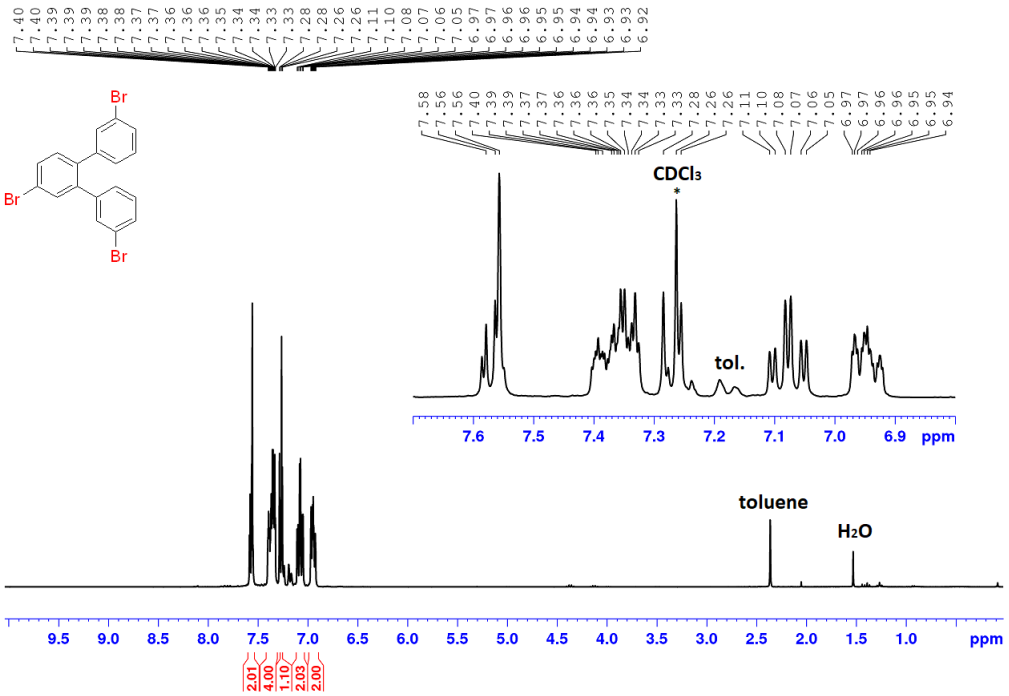

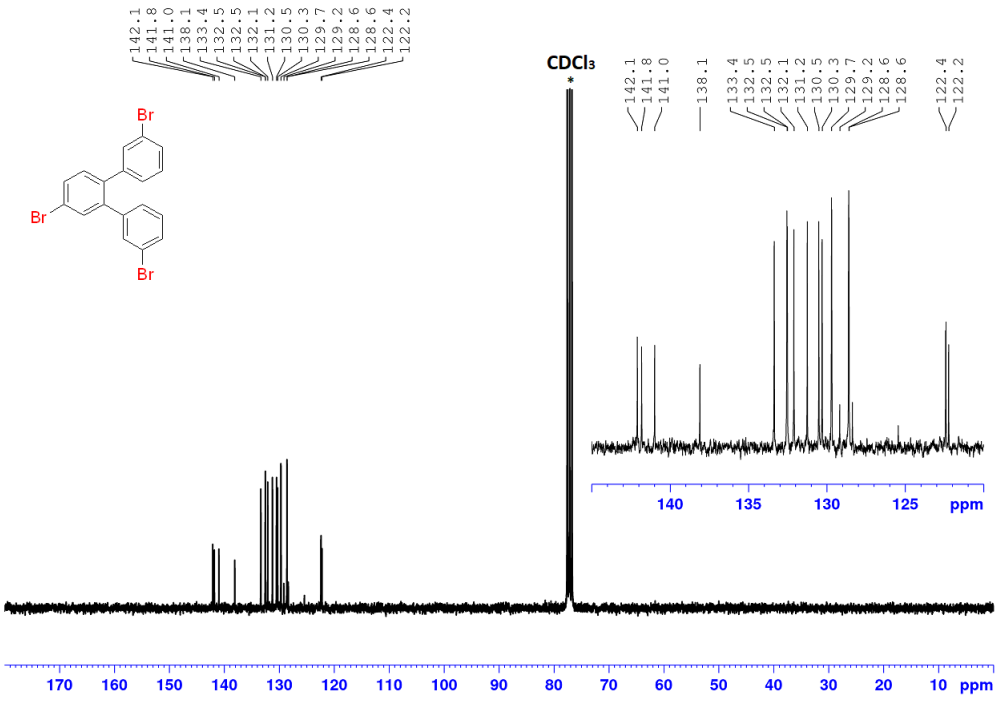

Compound 120

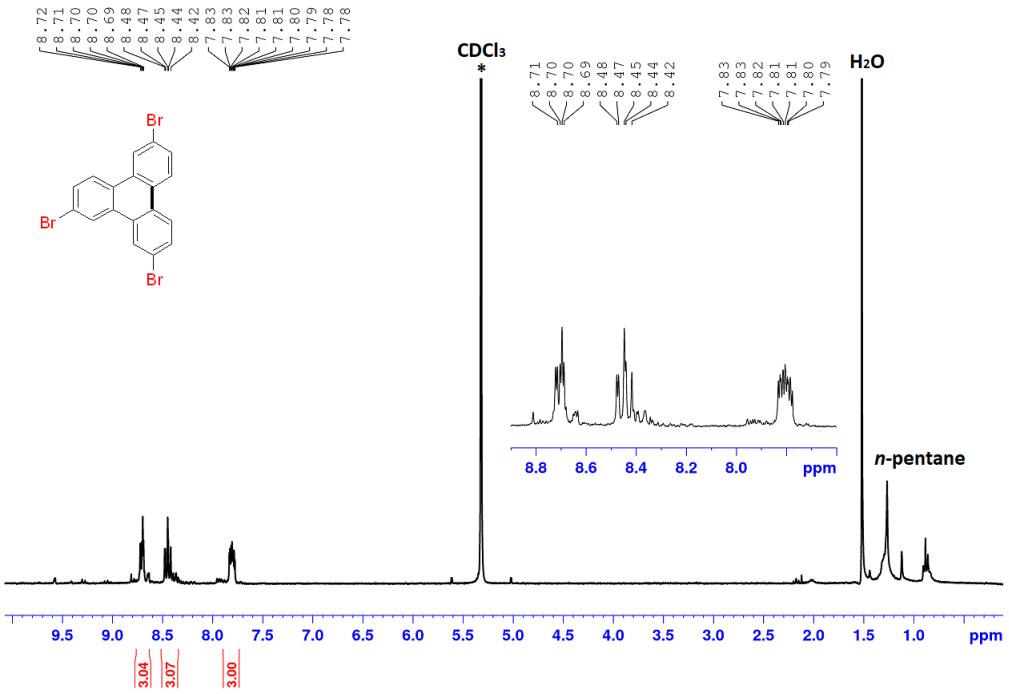

Compound 127

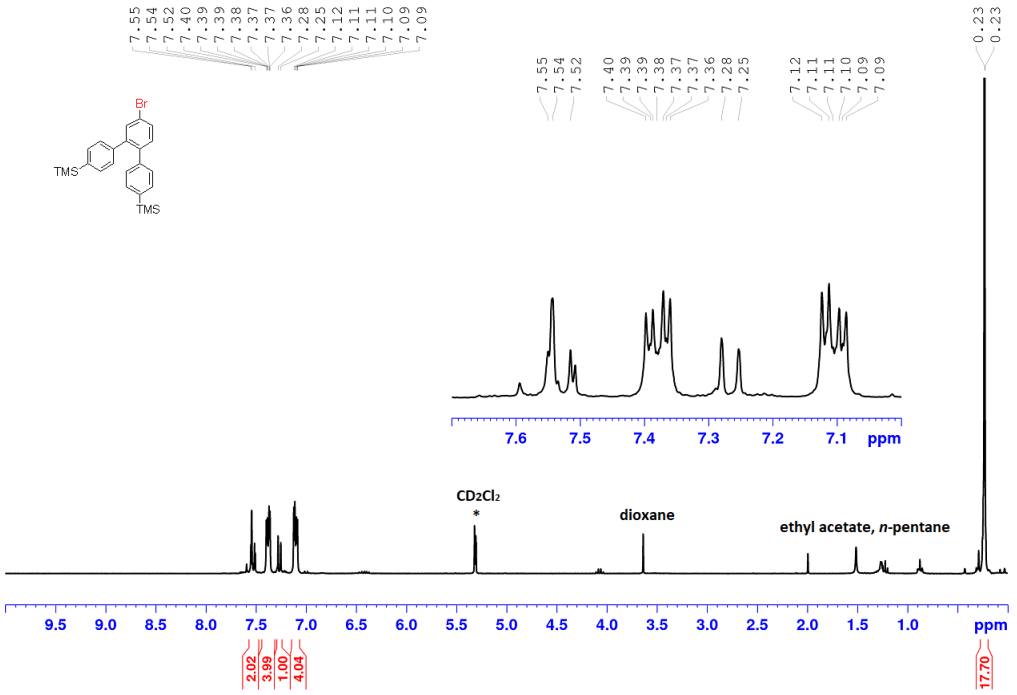

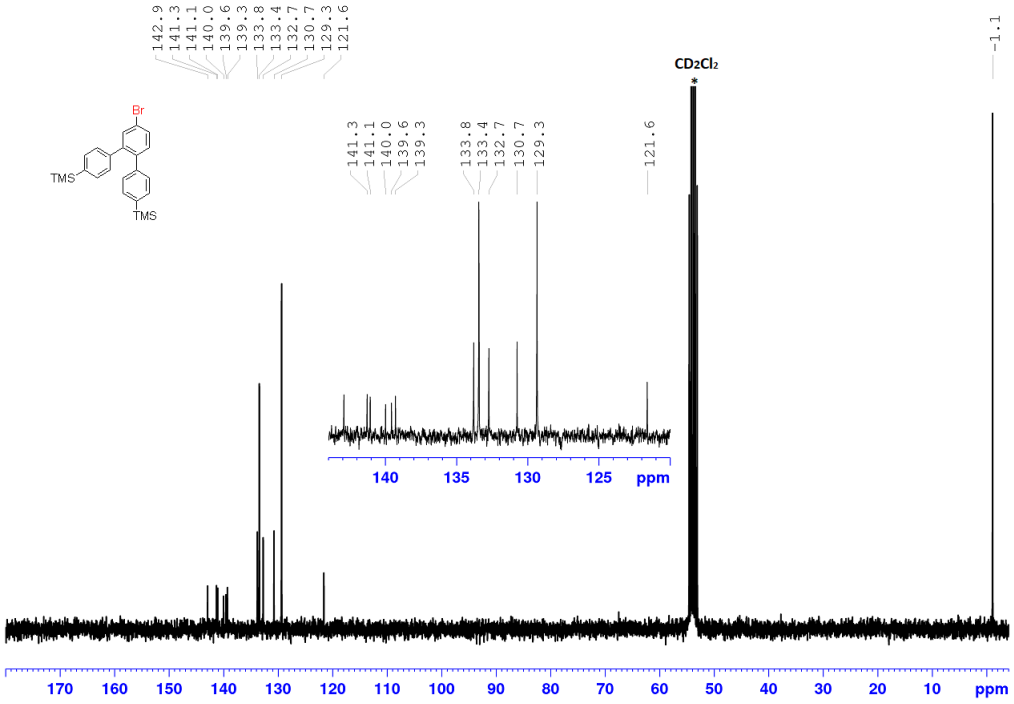

Compound 128

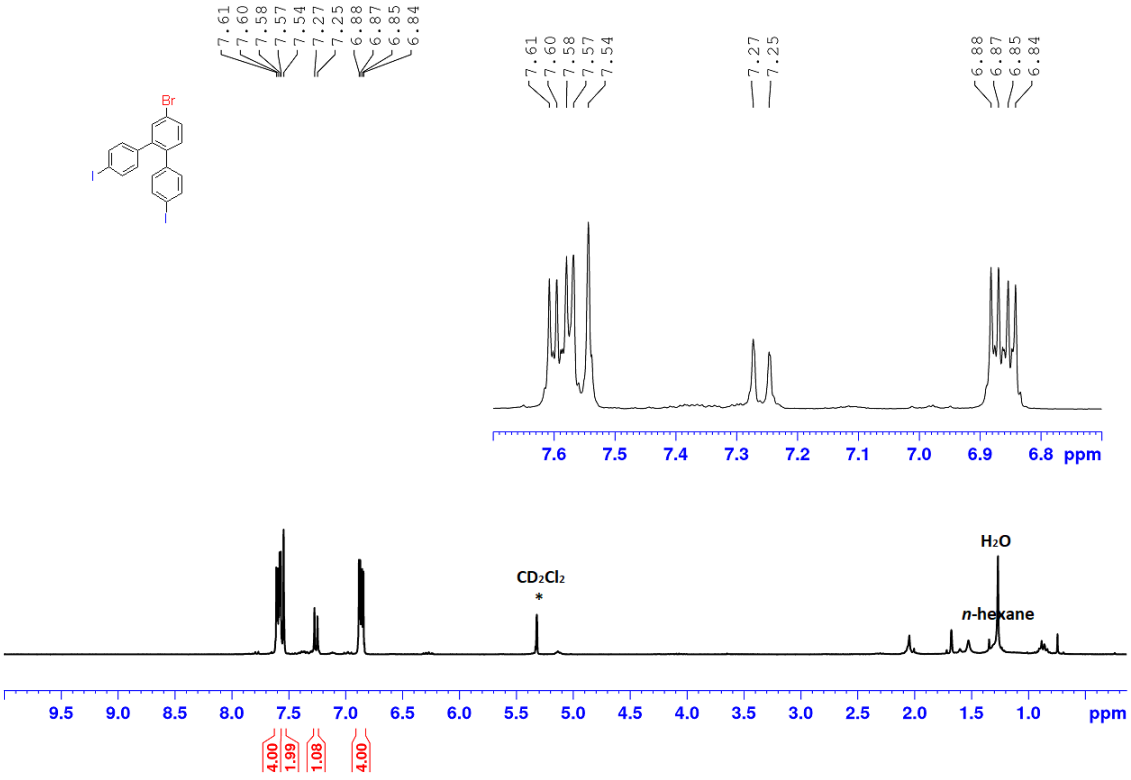

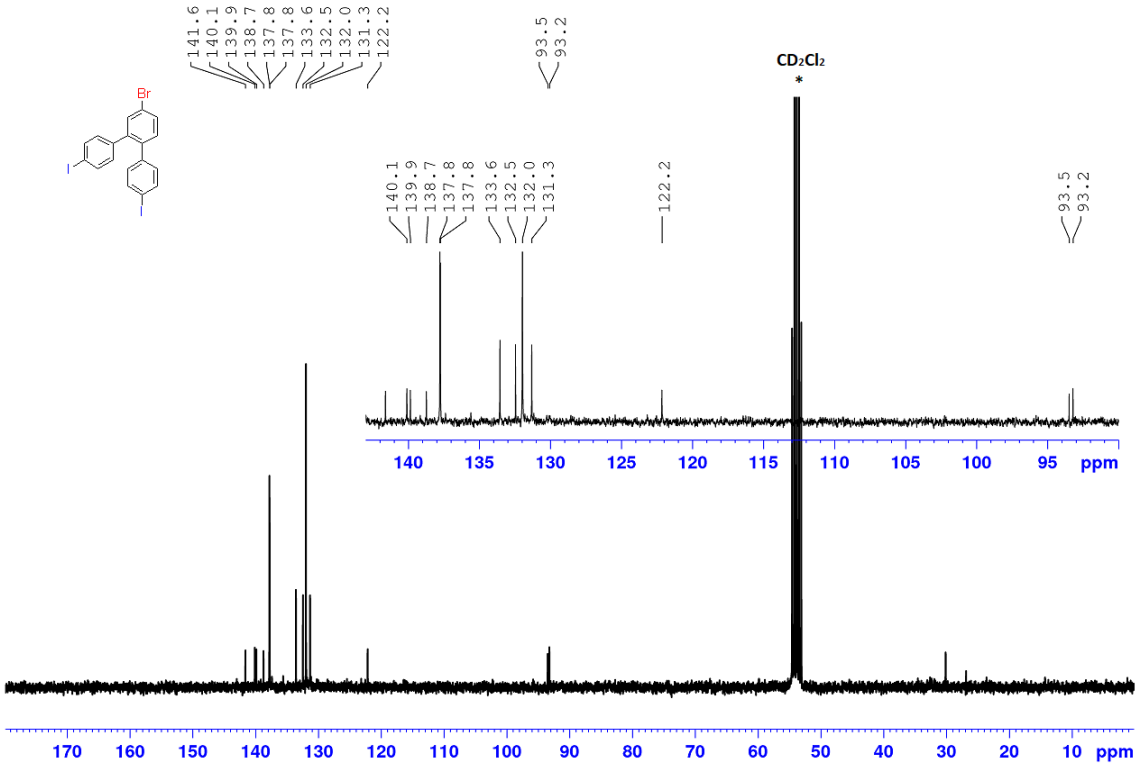

Compound 119

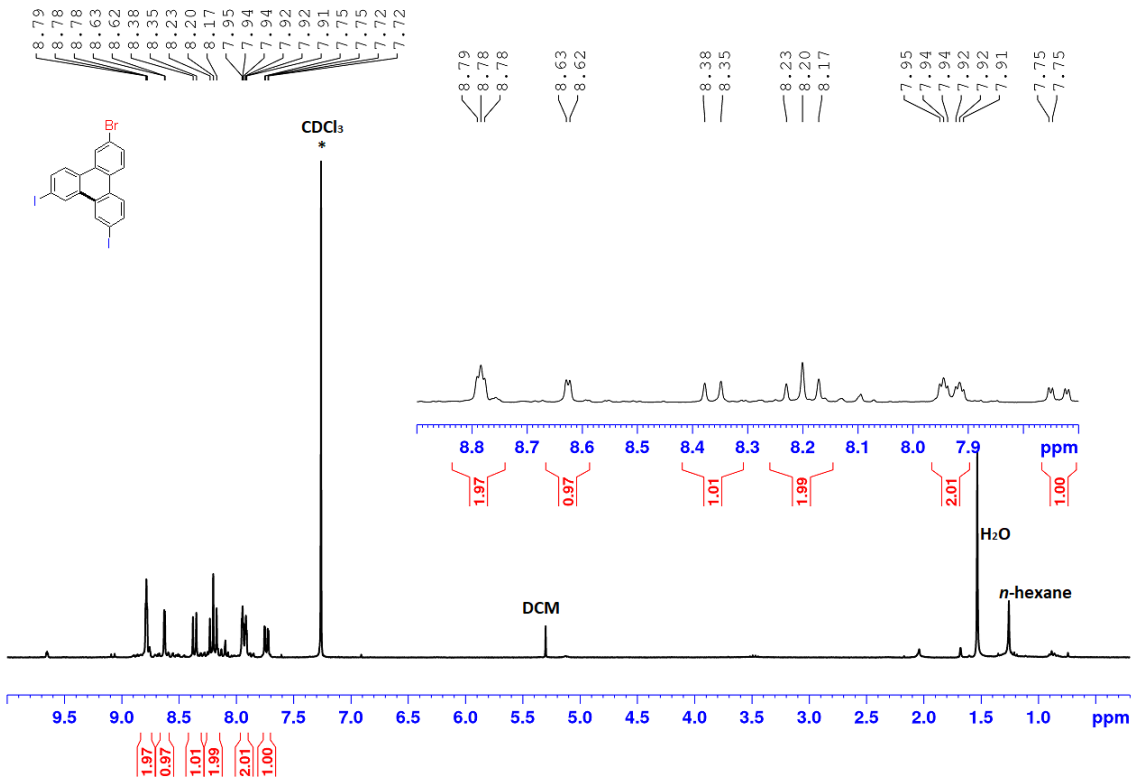

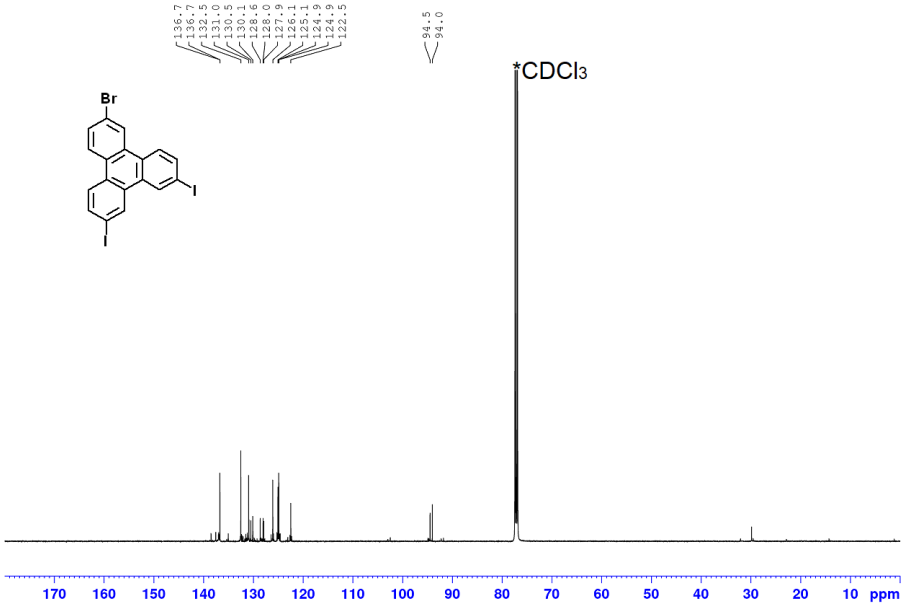

Compound 134

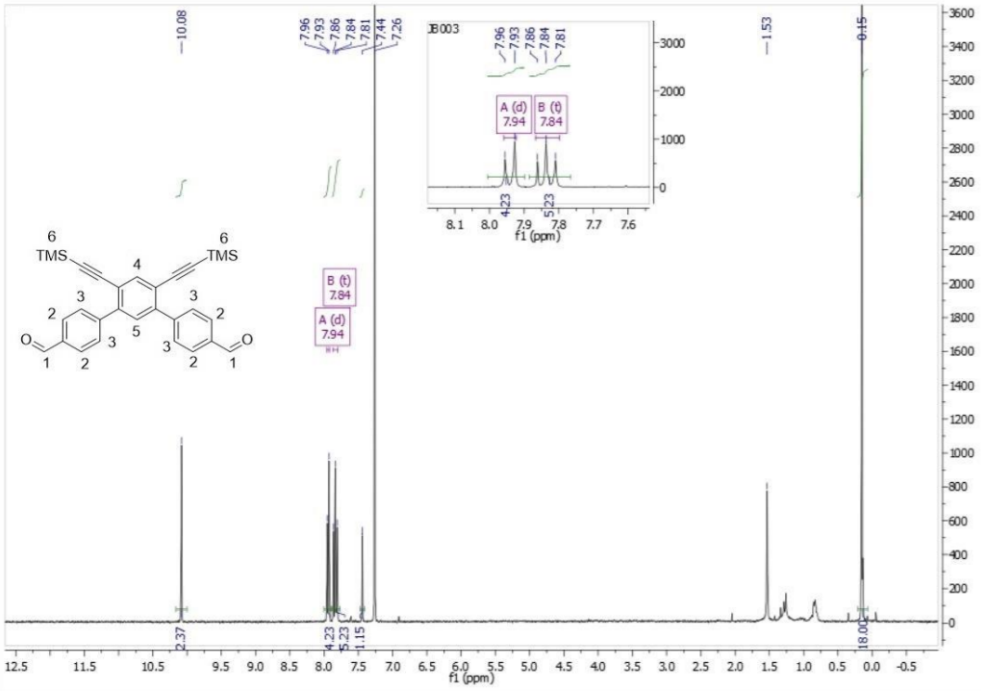

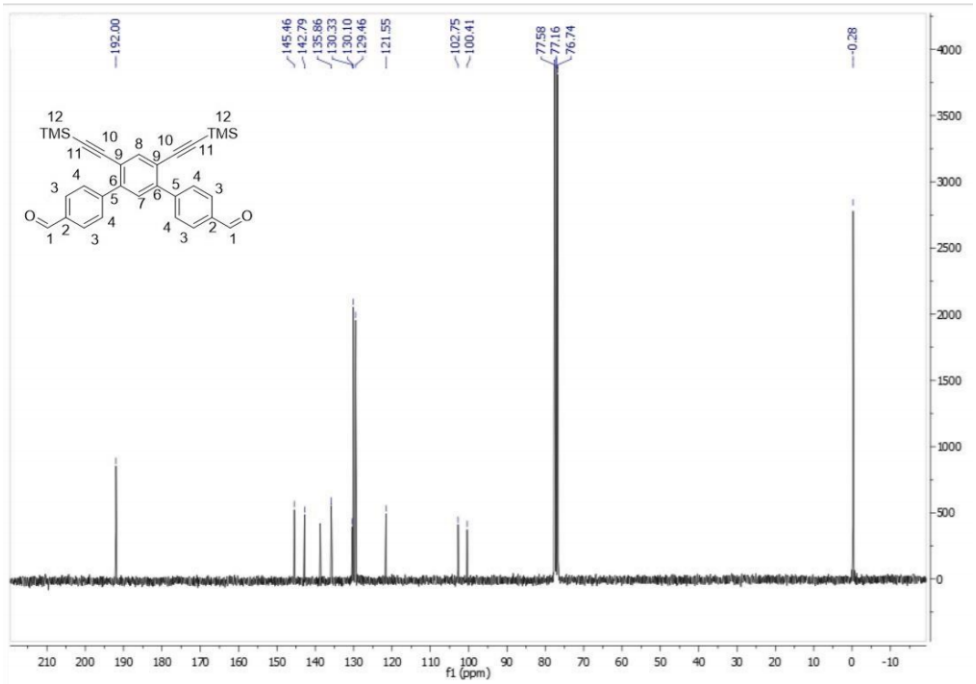

Compound 135

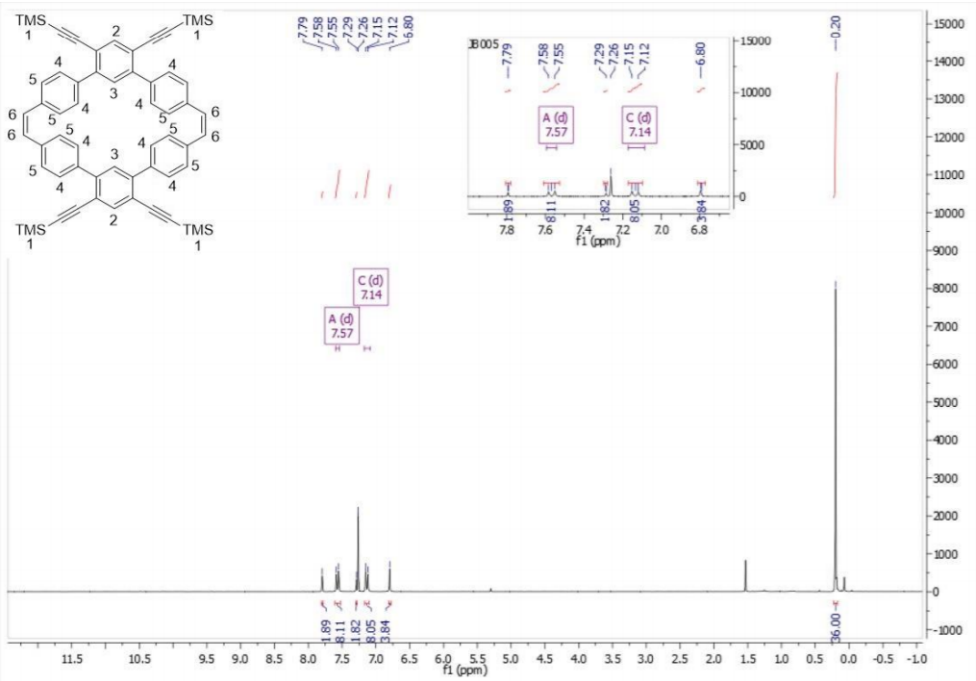

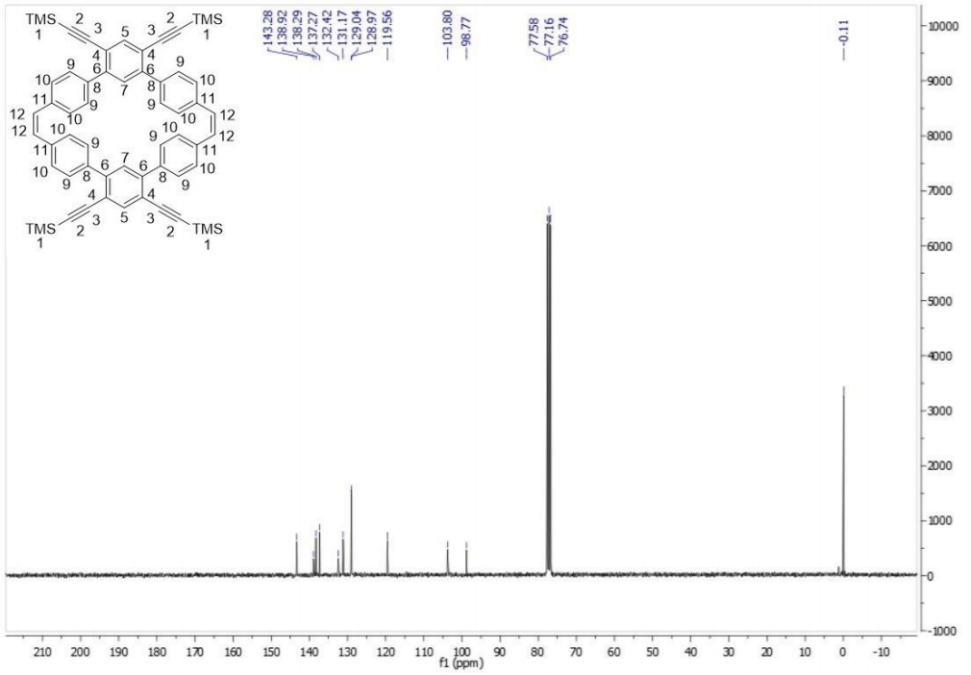

Compound 141

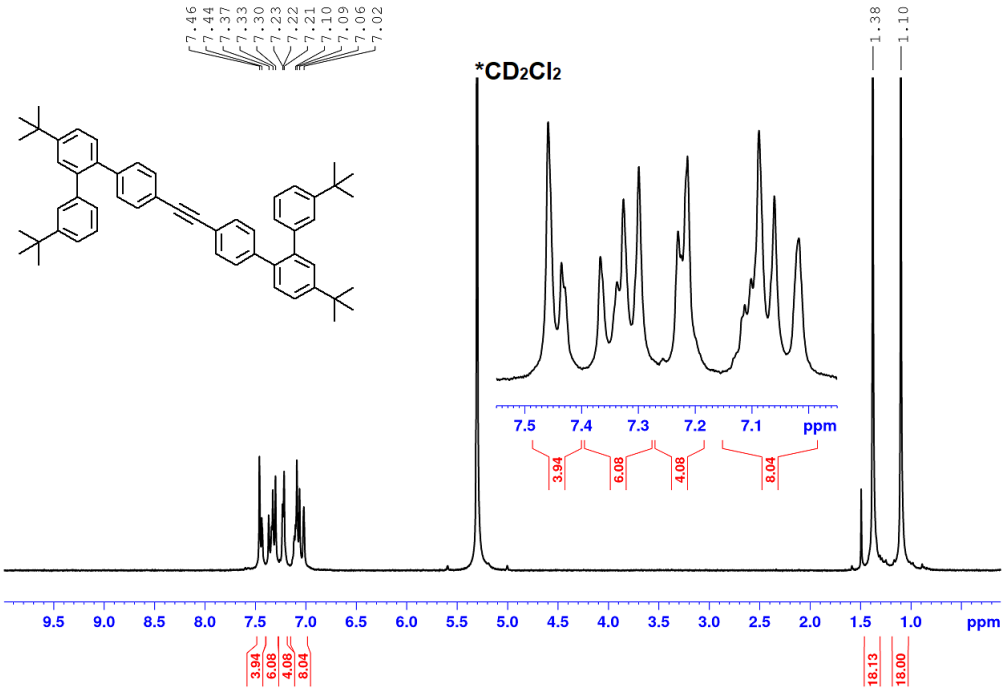

Compound 150

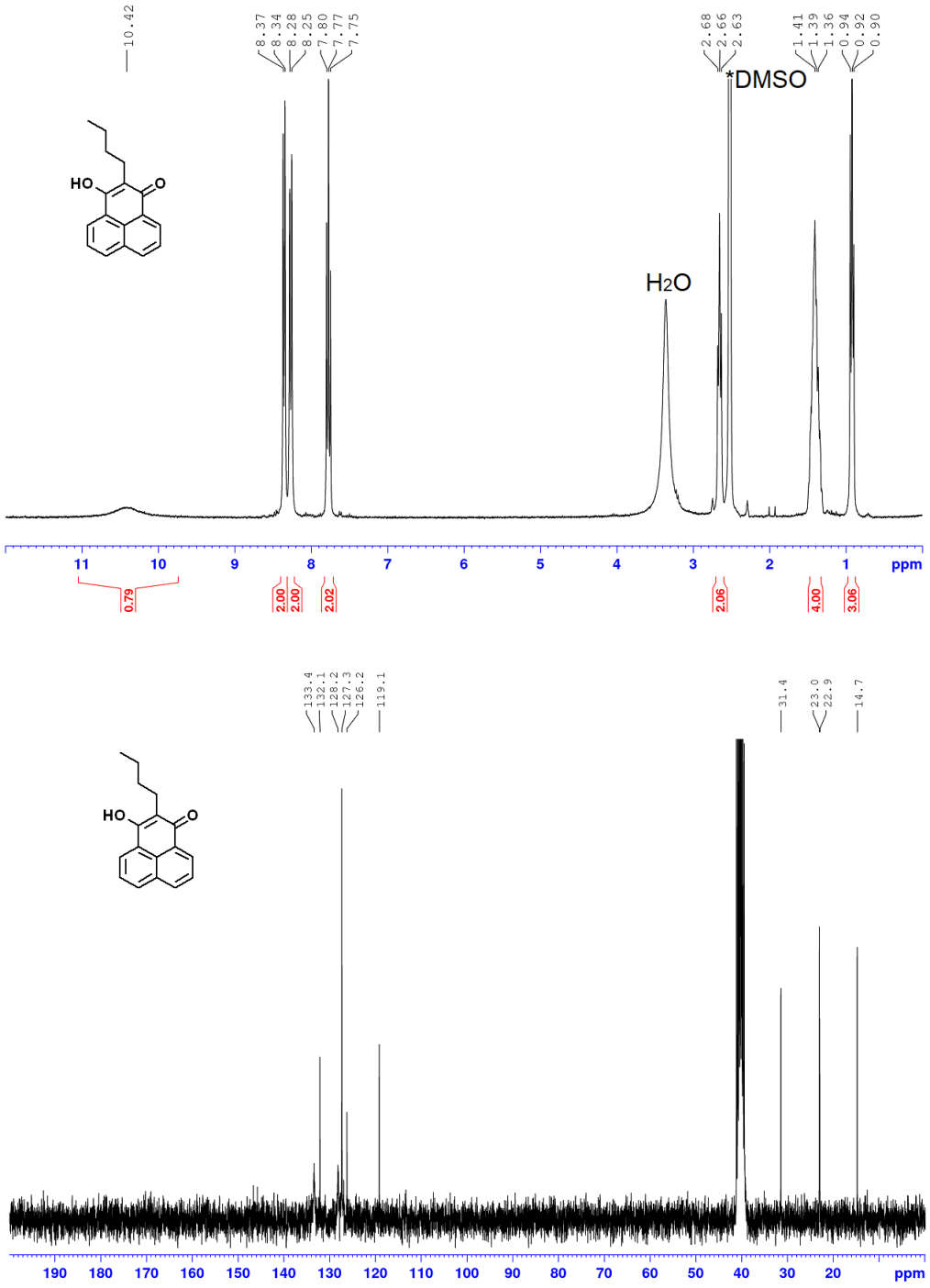

Compound *cis*-152

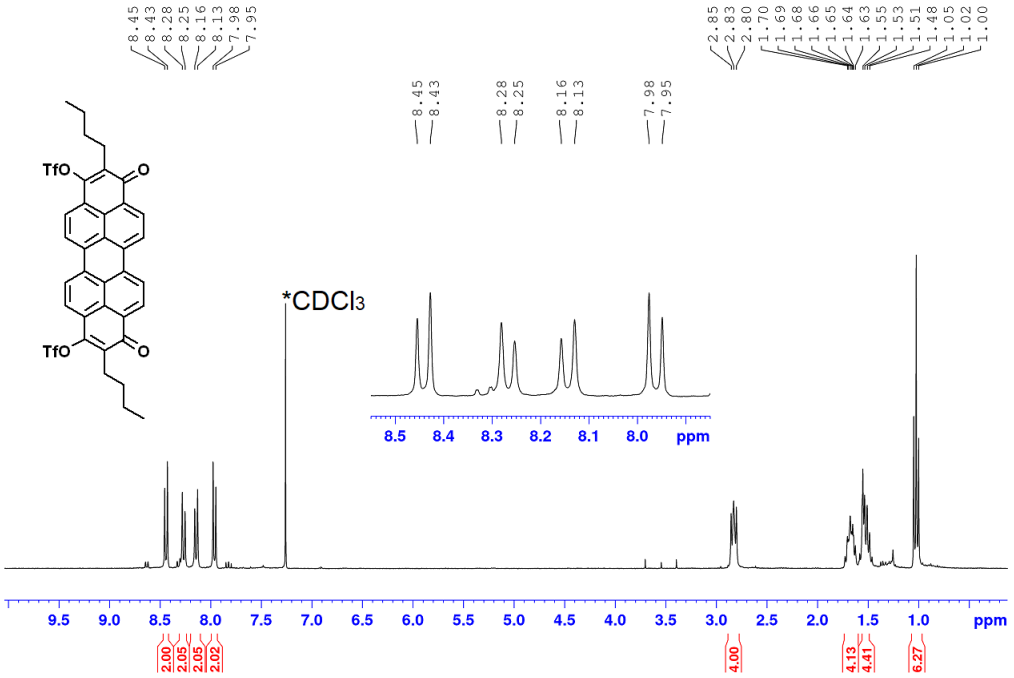

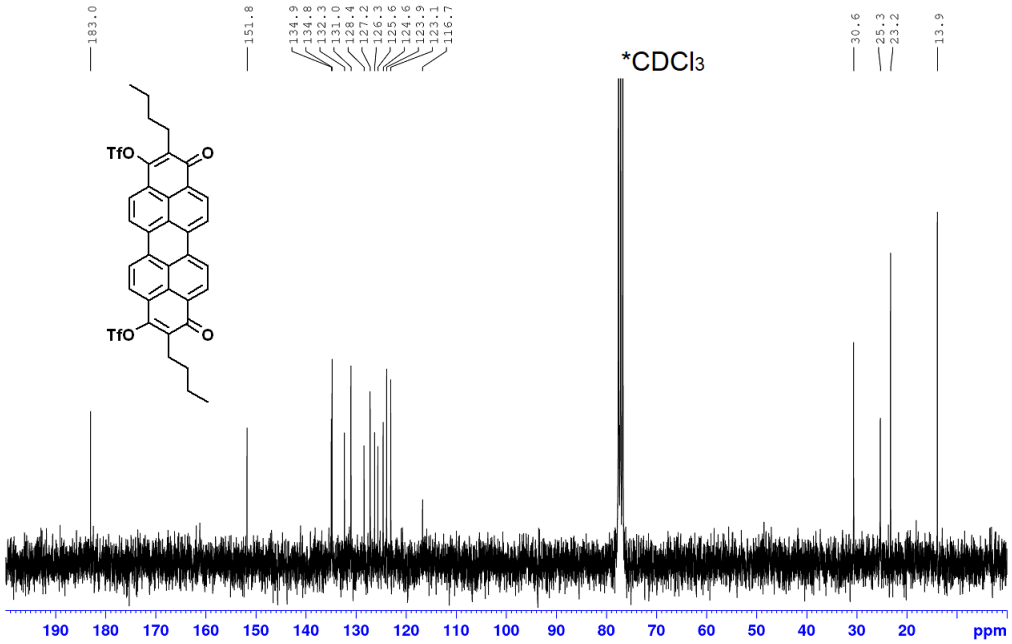

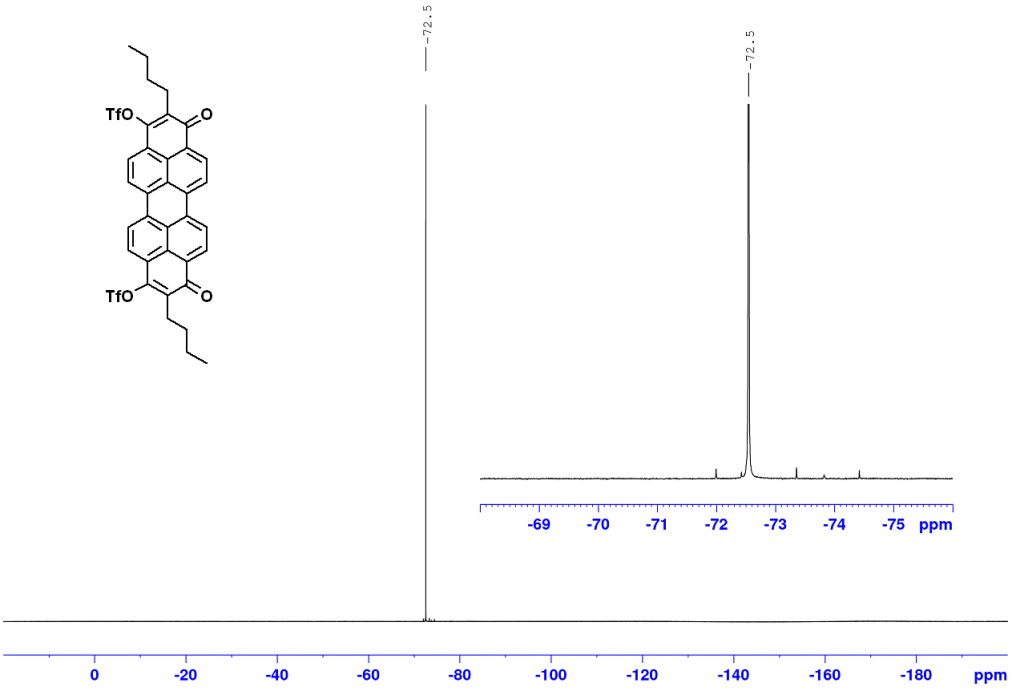
TfO
O
TfO
O
-72.5
-72.5
-69
-70
-71
-72
-73
-74
-75
ppm
0
-20
-40
-60
-80
-100
-120
-140
-160
-180
ppm

8 Acknowledgements

I first want to thank my supervisor Prof. Dr. Jörg Sundermeyer for the challenging and fascinating projects as well as for the helpful discussions. He gave me the opportunity and the freedom to realize many ideas and encouraged me constantly with my work on my projcts .

I want to thank Prof. Dr. J. Michael Gottfried not only for acting as the second referee, also for the fruitful collaboration during the PhD time.

I also want to thank Prof. Dr. Eric Meggers for acting as third member of the examination committee.

I also owe a lot of gratitude to Dr. Qitang Fan who teached me a lot about surface science and the technique of scanning tunneling microscopy. Also my credits go to the other cooperation partners (AG Schirmeisen in Gießen, Forschungszentrum Jülich) for their great work.

I want to thank the Sundermeyer group (all present and past members) for the nice (many times also funny, sometimes a little bit bizarre) working atmosphere! Especially I want to say thank you to Tobias Vollgraff for solving 1001 crystall structures for me and the nice time also outside the lab!

I also want to thank Stella Maris Schenk for her administrative support as well as my engaged students (Kevin, Jaqueline and Calotta), who partizipated in my research.

Furthermore I want to give props to the staff of the electronical and mechanical workshop for their support in the case of technical problems and the precise and fast fabrication of components.

Also the coworkers of the NMR-, XRD- and mass spectroscopy department shall be gratefully acknowledged for the fast and professional measurement of difficult samples.

Last but not least I am very grateful to my family and friends their moral support not only during this work but during the whole studies. Especially I want to thank Kerstin who was always there for me during this time. Thank you for always having an open ear for me, the supporting and building up discussions and for the great time we have together!